THE PHYSICS AND CHEMISTRY OF SOLIDS

AN INTERNATIONAL JOURNAL

VOLUME 21 1961

EDITORS

Editor-in-Chief HARVEY BROOKS *Cambridge, Mass.*

Associate Editors
H. B. G. CASIMIR *Eindhoven*
G. J. DIENES *Brookhaven*
JACQUES FRIEDEL *Paris*
E. M. LIFSHITZ *Moscow*

Supported by an International Advisory Editorial Board

Vol. 21
1961

Copyright © 1962
Pergamon

PERGAMON PRESS

NEW YORK · LONDON · PARIS · LOS ANGELES

THE JOURNAL OF THE PHYSICS AND CHEMISTRY OF SOLIDS

Editors

PROF. HARVEY BROOKS (*Editor-in-Chief*), 217 *Pierce Hall, Harvard University, Cambridge* 38, *Mass. U.S.A.*

PROF. Dr. H. B. G. CASIMIR, *N.V. Philips' Gloeilampenfabrieken, Eindhoven, The Netherlands*

DR. G. J. DIENES, *Brookhaven National Laboratory, Upton, Long Island, New York, U.S.A.*

PROF. JACQUES FRIEDEL, *Service de Physique des Solides, Faculté des Sciences (Group II), B.P. No.* 11, *Orsay (S. & O.) France*

PROF. E. M. LIFSHITZ, *Institute for Physical Problems, Vorobievskoye Chaussee,* 2, *Moscow V*–334, *U.S.S.R.*

Editorial Advisory Board

U.S.A.

E. N. ADAMS, New York
D. ALPERT, Illinois
L. APKER, Schenectady
J. BARDEEN, Illinois
D. S. BILLINGTON, Oak Ridge
R. G. BRECKENRIDGE, Cleveland
LEO BREWER, Berkeley, Calif.
E. BURSTEIN, Penn.
J. A. BURTON, New Jersey
N. CABRERA, Virginia
G. C. DANIELSON, Iowa
J. C. FISHER, Schenectady
F. HERMAN, Palo Alto
CONYERS HERRING, New Jersey
A. R. VON HIPPEL, Cambridge, Mass.
J. H. HOLLOMON, Schenectady
W. V. HOUSTON, Houston
H. B. HUNTINGTON, Troy
H. M. JAMES, Purdue
C. KITTEL, Berkeley, Calif.
W. KOHN, La Jolla, Calif.
J. A. KRUMHANSL, Ithaca
A. W. LAWSON, Riverside, Calif.
H. W. LEVERENZ, Princeton
O. T. MARZKE, Pittsburgh
B. T. MATTHIAS, New Jersey
L. R. MAXWELL, Silver Spring
JOSEPH E. MAYER, La Jolla, Calif.
J. W. MITCHELL, Charlottesville
E. W. MONTROLL, Yorktown Heights, N.Y.
DAVID PINES, Princeton
GEORGE T. RADO, Washington, D.C.
H. REISS, Canoga Park, Calif.
J. R. REITZ, Cleveland
A. ROSE, Princeton
R. SMOLUCHOWSKI, Princeton
F. H. SPEDDING, Iowa
D. TURNBULL, Schenectady
J. H. VAN VLECK, Cambridge, Mass.
B. E. WARREN, Cambridge, Mass.
EUGENE P. WIGNER, Princeton
B. H. ZIMM, La Jolla, Calif.

Canada

R. E. BURGESS, Vancouver
D. K. C. MACDONALD, Ottawa
W. B. PEARSON, Ottawa

United Kingdom

A. CHARLESBY, Shrivenham, Berks.
W. J. DUNNING, Bristol
I. ESTERMANN, London
F. C. FRANK, Bristol
H. K. HENISCH, Reading
H. JONES, London
A. B. PIPPARD, Cambridge
M. H. L. PRYCE, Bristol
O. C. SIMPSON, Baldock
R. A. SMITH, Sheffield
K. W. H. STEVENS, Nottingham
F. C. TOMPKINS, London

France

E. F. BERTAUT, Grenoble
A. GUINIER, Orsay
LOUIS NÉEL, Grenoble
LOUIS WEIL, Grenoble

Germany

M. BORN, Bad Pyrmont
ULRICH DEHLINGER, Stuttgart
R. HILSCH, Göttingen
G. LEIBFRIED, Aachen
E. MOLLWO, Erlangen
H. PICK, Stuttgart
H. WELKER, Erlangen

Italy

F. G. FUMI, Pavia

Czechoslovakia

J. TAUC, Praha

Japan

TOSHINOSUKE MUTO, Tokyo

The Netherlands

A. MICHELS, Amsterdam
G. W. RATHENAU, Amsterdam

Sweden

J. O. LINDE, Stockholm
PER-OLOV LÖWDIN, Uppsala

Switzerland

G. BUSCH, Zurich
P. SCHERRER, Zurich

U.S.S.R.

G. S. ZHDANOV, Moscow

Publishing Offices

American Continent: Pergamon Press, Inc., 122 East 55th Street, New York 22, N.Y.

Rest of the World: Pergamon Press Ltd., Headington Hill Hall, Oxford

Issued in parts. Annual Subscription: (A) for libraries, £35 (U.S.A. $100.00); (B) for subscribers who write directly to the publisher certifying that the subscriptions is for their own personal use, £5 5s. (U.S.A. $15.00) including postage.

Surcharge for airmail subscriptions:

U.S.A. and South America	$28.00 (£10) per annum
Far East	$40.00 (£14) per annum
European countries	£5 ($14.00) per annum

Copyright © 1962 Pergamon Press Ltd.

PERGAMON PRESS, INC.

122 EAST 55TH STREET, NEW YORK 22, N.Y. 4 & 5 FITZROY SQUARE, LONDON, W.1

Vol. 196

CONTENTS LISTS FOR VOLUME 21, NOS. 1–4

Volume 21 Numbers 1/2

	page
R. M. Barrer and B. E. F. Fender: The diffusion and sorption of water in zeolites—I Sorption	1
R. M. Barrer and B. E. F. Fender: The diffusion and sorption of water in zeolites—II Intrinsic and self-diffusion	12
A. Tauber, G. G. Whinfrey and E. Banks: The crystal chemistry of some germanium garnets	25
O. Jäntsch: Contribution to the theory of chemisorption	33
H. E. Resing and N. H. Nachtrieb: Self-diffusion of lead, thallium and bismuth in the solid lead–thallium system	40
J. S. Kouvel: The ferromagnetic–antiferromagnetic properties of Cu–Mn and Ag–Mn alloys	57
J. E. Zimmerman and H. Sato: Electronic specific heat of Mn–Cu alloys	71
R. Parker and M. S. Smith: The solubility of nickel in nickel ferrite	76
H. A. Papazian: Color centers in the alkali metal azides	81
R. E. Coovert: Surface magnetoconductivity experiments in silicon	87
Y. Yafet: Hyperfine interaction due to the orbital magnetic moment of electrons with large g factors	99
G. Gergely: Space charge effects in ambipolar diffusion of carriers induced by electron bombardment in photoconducting insulator crystals	105
W. E. Spear: Carrier mobility and charge transport in monoclinic Se crystals	110

Letters to the Editor:

T. Boniszewski and G. C. Smith: A note on nickel hydride	115
E. F. Bertaut and J. Dulac: On the isomorphism of trivalent Chromium and Rhodium ternary oxides	118
J. B. Grun, M. Sieskind and S. Nikitine: A study of very low temperature absorption and reflection of Cuprite in the short wave length side of the visible range	119
D. W. J. Langer: Solidification of helium at 77°K	122
L. E. Orgel: The van Vleck temperature-independent magnetism of metals	123
A. Ascoli and A. C. Damask: Migration energy of a vacancy adjacent to an impurity	124
A. D. Brailsford and A. W. Overhauser: Theory of the resistance minimum in dilute paramagnetic alloys	127
P. M. Gruzensky and A. B. Scott: Ionic conductivity of KCl containing sulfate ions	128
D. W. G. Ballentyne: On the behaviour of electroluminescent phosphors on irradiation with ultra-violet	131

Book Reviews:

S. Mrozowski (Editor): "Proceedings of the Fourth Conference on Carbon" (reviewed by J. A. Krumhansl)	134
A. E. Green and J. E. Adkins: "Large Elastic Deformations and Non-Linear Continuum Mechanics" (reviewed by R. T. Shield)	134
E. H. Putley: "The Hall Effect and Related Phenomena" (reviewed by J. H. Crawford, Jr.)	135

Errata:

Ryoichi Kikuchi: Statistical dynamics of crystalline diffusion—II and III	136
J. S. Smart: Magnetic short range and specific heat in ferromagnets and anti-ferromagnets	136

Volume 21 Numbers 3/4

E. Antončík: On the theory of surface states	137
M. L. Canut and J. L. Amorós: Temperature dependence of the X-ray diffuse scattering of molecular crystals. Naphthalene	146
J. P. Suchet: Ionicities, effective charges and electronic mobilities in mineral semiconductors compounds	156
M. O'Keeffe: Cation valencies and distributions in spinel structures containing manganese	172
H. Hasegawa and R. E. Howard: Optical absorption spectrum of hydrogenic atoms in a strong magnetic field	179
R. Nitsche, H. U. Bölsterli and M. Lichtensteiger: Crystal growth by chemical transport reactions—I. Binary, ternary and mixed-crystal chalcogenides	199
B. S. Chandrasekhar and J. M. Bardeen: The paramagnetic susceptibilities of some uranium–molybdenum alloys between 100°K and 300°K	206
M. J. Weber: Nuclear magnetic resonance in gallium phosphide	210
D. Shooter and H. E. Farnsworth: Hydrogen–deuterium exchange on clean nickel surfaces	219
E. T. Kornhauser: On the feasibility of phonon diffraction in liquid helium	228
E. F. Bertaut, L. Corliss, F. Forrat, R. Aleonard and R. Pauthenet: A study of bivalents transition metals niobates and tantalates	234
R. D. Blaugher, B. S. Chandrasekhar, J. K. Hulm, E. Corenzwit and B. T. Matthias: Superconducting titanium–molybdenum alloys	252

Vol. 21
1961

page

E. F. BERTAUT: Magnetic configurations. Fourier method 256
PER KOFSTAD and PER BJØRN ANDERSON: Gravimetric studies of the defect structure of $\alpha-Nb_2O_5$ . . 280
Y. A. ROCHER and J. FRIEDEL: On the electronic structure of liquid transitional metals and some complex phases 287
E. F. BERTAUT: Magnetic configurations. Direct Method 295

Letters to the Editor:

A. ENGLERT and H. TOMPA: The energy and the configuration of the atoms in a simple model of an edge dislocation 306
D. W. OVENALL: Paramagnetic resonance absorption in molecular crystals: Some comments on the paper by WIGEN and COWEN 309
L. T. CRANE and J. E. ZIMMERMAN: The specific heats of single Cu–Mn crystals between 1·4 and 5°K. 310
J. ROSS MACDONALD: Photocapacitance effects in additively colored alkali halide crystals . . . 313
E. SONDER and S. T. SEKULA: Effects of gaseous impurities on the magnetic properties of copper . . 315
L. J. VIELAND: The effect of arsenic pressure on impurity diffusion in gallium arsenide 318
P. N. BUTCHER, J. A. HULBERT and K. F. HULME: Indium antimonide tunnel diodes in high magnetic fields 320
E. LOH and R. NEWMAN: The absorption edge of zinc telluride 324

Notices 327

Tôme 21 Nos 1/2

R. M. BARBER et B. E. F. FENDER: Diffusion et sorption de l'eau dans les zéolithes—I Sorption . . . 1
R. M. BARBER et B. E. F. FENDER: Diffusion et sorption de l'eau dans les zéolithes—II Diffusion intrinsèque et auto-diffusion 12
A. TAUBER, C. G. WHINFREY et E. BANKS: Chimie cristalline de quelques grenats de germanium . . . 25
O. JÄNTSCH: Sur la théorie de la sorption chimique 33
H. E. RESING et N. H. NACHTRIEB: Auto-diffusion du plomb, du thallium et du bismuth dans le système solide plomb–thallium 40
J. S. KOUVEL: Propriétés ferromagnétiques et antiferromagnétiques des alliages CuMn et AgMn . . 57
J. E. ZIMMERMAN et H. SATO: Chaleur spécifique électronique des alliages Mn–Cu 71
R. PARKER et M. S. SMITH: La solubilité du nickel dans les ferrites de nickel 76
H. A. PAPAZIAN: Centres colorés dans les nitrures alcalins 81
R. E. COOVERT: Expériences sur la magnétoconductivité de surface du Silicium 87
Y. YAFET: Interaction hyperfine due au moment magnétique orbital des électrons de grand facteurs *g*. . . 99
G. GERGELY: Effet de charge d'espace dans la diffusion ambipolaire de porteurs induite par bombardement électronique de cristaux isolants photoconducteurs 105
W. E. SPEAR: Mobilité des porteurs et transport de charge dans les cristaux de Se monoclinique . . . 110

Lettres au Rédacteur:

T. BONISZEWSKI et G. C. SMITH: Une note sur l'hydrure de nickel 115
E. F. BERTAUT et J. DULAC: Sur l'isomorphisme d'oxydes ternaires de chrome et de rhodium trivalents . 118
J. B. GRUN, M. SIESKIND et S. NIKITINE: Etude de l'absorption et de la réflexion de la cuprite aux très basses températures dans le visible de très courtes longueurs d'onde 119
D. W. J. LANGER: Solidification de l'helium à 77°K. 122
L. E. ORGEL: Le paramagnétisme de Van Vleck indépendent de la température pour les métaux . . 123
A. ASCOLI et A. C. DAMASK: Energie de migration d'une lacune au voisinage d'une impureté . . . 124
A. D. BRAILSFORD et A. W. OVERHAUSER: Théorie du minimum de résistance dans les alliages paramagnétiques dilués 127
P. M. GRUZENSKY et A. B. SCOTT, Conductibilité ionique de KCl contenant des ions sulfate . . . 128
D. W. G. BALLENTYNE: Sur le comportement des matériaux électroluminescents irradiés à l'ultraviolet . 131

Revue des livres:

S. MROZOWSKI (Editeur): "Rapports de la quatrième conférence sur le carbone" (revu par J. A. KRUMHANSL) 134
A. E. GREEN et J. E. ADKINS: "Grandes déformations élastiques et phénomènes non linéaires dans la mécanique des milieux continus" (revu par B. T. SHIELD) 134
E. H. PUTLEY: "Effet Hall et phénomènes qui s'y rapportent" (revu par J. H. CRAWFORD, Jr.) . . 135

Errata:

RYOICHI KIKUCHI: Dynamique statistique de la diffusion cristalline II et III 136
J. S. SMART: Ordre magnétique à courte distance et chaleur spécifique dans les ferromagnétiques et les anti-ferromagnétiques 136

Vol. 2
196

Tôme 21 Nos 3/4

page

E. Antončík: Sur la théorie des états de surface . . . 137
M. L. Canut et J. L. Amorós: Dépendence en température de la diffusion des rayons X par les cristaux moléculaires. I—Napthalène . . . 146
J. P. Suchet: Ionicités, charges effectives et mobilités electroniques dans les composes semiconducteurs mineraux . . . 156
M. O'Keeffe: Valences et distribution des cations dans les spinelles contenant du manganèse . . . 172
H. Hasegawa et R. E. Howard: Spectre d'absorption optique d'atomes hydrogénoides placés dans un fort champ magnétique . . . 179
R. Nitsche, H. U. Bölsterli et M. Lichtensteiger: Croissance de cristaux par réactions chimiques de transport—I. Chalcogénides binaires, ternaires et cristaux mixtes . . . 199
B. S. Chandrasekhar et J. M. Bardeen: Susceptibilité paramagnétique de quelques alliages Uranium-Molybdène entre 100°K et 300°K . . . 206
M. J. Weber: Résonance magnétique nucléaire dans le Phosphure de Gallium . . . 210
D. Shooter et H. E. Farnsworth: Echange Hydrogène-Deutérium sur des surfaces de Nickel propres . 219
E. T. Kornhauser: Sur la possibilité de la diffraction des phonons dans l'Hélium liquide . . . 228
E. F. Bertaut, L. Corliss, F. Forrat, R. Aleonard et R. Pauthenet: Etude de Niobates et Tantalates de métaux de transition bivalents . . . 234
R. D. Blaugher, B. S. Chandrasekhar, J. K Hulm, E. Corenzwit et B. T. Matthias: Alliages Titane-Molybdène supraconducteurs . . . 252
E. F. Bertaut: Configurations magnétiques. Méthode de Fourier . . . 256
Per Kofstad et Per Bjørn Anderson: Études gravimétriques de la structure de défaut de $\alpha-Nb_2O_5$. 280
Y. A. Rocher et J. Friedel: Sur la structure électronique des métaux de transition liquides et de certaines phases complexes . . . 287
E. F. Bertaut: Configuration magnétique. La méthode directe . . . 295

Lettres au Rédaeteur:

A. Englert et H. Tompa: L'énergie et la configuration des atomes dans un modèle simple de dislocation-coin . . . 306
D. W. Ovenall: Absorption par résonance paramagnétique dans les cristaux moléculaires: commentaires sur l'article de Wigen et Cowen . . . 309
L. T. Crane et J. E. Zimmermann: Chaleur spécifique de monocristaux de Cu-Mn entre 1,4 et 5°K . 310
J. Ross Macdonald: Effets de photocapacité dans des cristaux d'halogénures alcalins colorés additivement 313
E. Sonder et S. T. Sekula: Effets d'impuretés gazeuses sur les propriétés magnétiques du Cuivre . . 315
L. J. Vieland: L'effet de la pression d'arsenic sur la diffusion des impuretés dans l'arséniure de Gallium . 318
P. N. Butcher, J. A. Hulbert et K. F. Hulme: Comportement à grand champ magnétique de diodes à effet tunnel d'antimoniure d'indium . . . 320
E. Loh et R. Newman: Limite d'absorption du tellurure de zinc . . . 324

Notes . . . 327

Band 21 Nr. 1/2

R. M. Barrer und B. E. F. Fender: Die Diffusion und Adsorbtion des Wassers in Zeolithen—I. Adsorbtion . 1
R. M. Barrer und B. E. F. Fender: Die Diffusion und die Adsorption des Wassers in Zeolithen—II. Diffusion und Selbstdiffusion . . . 12
A. Tauber, C. G. Whinfrey und E. Banks: Die Kristallchemie einiger Germaniumgranate . . . 25
O. Jäntsch: Zur Theorie der Chemisorption . . . 33
H. E. Resing und N. H. Nachtrieb: Selbstdiffusion von Blei, Thallium und Bismuth im festen Blei-Thallium-System . . . 40
J. S. Kouvel: Die ferromagnetischen und antiferromagnetischen Eigenschaften der Kupfer-Mangan-und Silber-Mangan-Legierungen . . . 57
J. E. Zimmerman und H. Sato: Spezifische Elektronenwärme von Mn-Cu-Legierungen . . . 71
R. Parker und M. S. Smith: Die Löslichkeit des Nickels in Nichelferriten . . . 76
H. A. Papazian: Farbzentren in den Alkalimetallaziden . . . 81
R. E. Coovert: Experimente zur magnetischen Leitfähigkeit der Oberfläche von Silizium . . . 87
Y. Yafet: Hyperfein-Wechselwirkung der magnetischen Bahnommente von Elektronen mit grossen g-Faktoren . . . 99
G. Gergely: Raumladungseffekte bei der ambipolaren Diffusion von Ladungen, die durch Elektronen-beschuss in photoleitenden Isolatorkristallen erzeugt wurden . . . 105
W. E. Spear: Beweglichkeit der Ladungsträger und Ladungstransport in monoklinen Se-Kristallen . . . 110

Vol. 21
1961

Briefe an den Herausgeber: page

T. Bonizewski und G. C. Smith: Ein Beitrag zum Nickelhydrit 115
E. F. Bertaut und J. Dulac: Über die Isomorphie der ternären Oxyde des Chroms und des dreiwertigen Rhodiums 118
J. B. Grun, M. Sieskind und S. Nikitine: Eine Untersuchung der Absorption und der Reflexion von Kupferoxyd bei sehr tiefen Temperaturen im sichtbaren Bereich der kurzwelligen Wellen . . . 119
D. W. J. Langer: Die Erstarrung des Heliums bei 77°K 122
L. E. Orgel: Der temperaturunabhängige van Vleckschе Magnetismus bei Metallen 123
A. Ascoli und A. C. Damask: Die Wanderungsenergie von Leerstellen die an Verunreinigungen gebunden sind 124
A. D. Brailsford und A. W. Overhauser: Zur Theorie des Widerstands minimums in verdünnten paramagnetischen Legierungen 127
P. M. Gruzensky und A. B. Scott: Ionenleitfähigkeit von KC1 das Sulfationen enthält 128
D. W. G. Ballentyne: Über das Verhalten elektroluminszierender Phosphore bei Bestrahlung mit ultraviolettem Licht 131

Buchbespruchungen:

S. Mrozowsky (Herausgeber): "Proceedings of the Fourth Conference on Carbon" (besprochen von J. A. Krumhansl) 134
A. E. Green und J. E. Adkins: "Large Elastic Deformations and Non-Linear Continuum mechanics" (besprochen von R. T. Shield) 134
E. H. Putley: "The Hall Effect and Related Phenomena" (besprochen von J. H. Crawford, Jr.) . . 135

Errata:

Ryoichi Kikuchi: Statistische Dynamikder Diffusion in Kristallen—II, III 136
J. S. Smart: Magnetische Nahordnung und spezifische Wärme in ferromagnetischen und antiferromagnetischen Stoffen 136

Band 21 Nr. 3/4

E. Antončík: Über die Theorie der Oberflächenzustände 137
M. L. Canut und J. L. Amorôs: Die Temperaturabhängigkeit der diffusen Streuung von Röntgenstrahlen durch Molekülkristalle—I. Naphthalin 146
J. P. Suchet: Ionisierbarkeit, effektive Ladungen und Elektronenbeweglichkeit in den Halbleiterkristallen . 156
M. O'Keeffe: Die Wiertigkeit der Kationen und ihre Verteilung in Spinellstrukturen die Mangan enthalten . 172
H. Hasegawa und R. E. Howard: Das optische Absorptionsspektrum der Wasserstoffatome in einem starken magnetischen Feld 179
R. Nitsche, H. V. Bölsterli und M. Lichtensteiger: Kristallwachstum durch chemische Transportreaktionen—I 199
B. S. Chandrasekhar und J. M. Bardeen: Die paramagnetischen Suszeptibilitäten einiger Uran–Molybdän-Legierungen zwischen 100°K und 300°K 206
M. J. Weber: Kernmagnetische Resonanzen in Galliumphosphiden 210
D. Shooter und H. E. Farnsworth: Wasserstoff-Deuteron Austausch auf reinen Nickeloberflächen . 219
E. T. Kornhauser: Über die Möglichkeit der Beugung von Phononen in flüssigem Helium 228
E. F. Bertaut, L. Corliss, F. Forrat, R. Aleonard und R. Pauthenet: Eine Untersuchung der Niobate und Tantalate zweiwertiger Übergangsmetalle 234
R. D. Blaugher, B. S. Chandrasekhar, J. K. Hulm, E. Corenzwit und B. T. Matthias: Supraleitende Titan-Molybdän-Legierungen 252
E. F. Bertaut: Magnetische Konfigurationen. Die Fouriermethode 256
Per Kofstad und Per Bjørn Anderson: Gravimetrische Untersuchungen der Fehlstruktur von $\alpha-Nb_2O_5$. 280
Y. A. Rocher und J. Friedel: Über die Elektronenstruktur der flüssigen Übergangsmetalle und einiger komplexer Phasen 287
E. F. Bertaut: Magnetische Konfigurationen. Die direkte Methode 295

Briefe an der Herausgeber:

A. Englert und H. Tompa: Die Energie und die Anordnung der Atome in einem einfachen Modell einer Stufenversetzung 306
D. W. Ovenall: Paramagnetische Resonanzabsorption in Molekülkristallen: Einige Bemerkungen zur Veröffentlichung von Wigen und Cowen 309
L. T. Crane und J. E. Zimmermann: Die spezifische Wärme von Cu-Mn-Einkristallen zwischen 1,4 und 5°K 310
J. Ross Macdonald: Der Bestrahlungseinfluss auf die Kapazität in durch Zusätze gefärbten Alkalihalogenidkristallen 313
E. Sonder und S. T. Sekula: Der Einfluss gasartiger Verunreinigungen auf die magnetischen Eigenschaften von Kupfer 315

Vol. 2
196

page

L. J. VIELAND: Der Einfluss der Arsendampfdruckes auf die Diffusion von Verunreinigungen in Gallium-arsenid . . . 318
P. N. BUTCHER, J. A. HULBERT und K. F. HULME: Indiumantimonid-Tunneldioden in grossen magnetischen Feldern . . . 320
E. LOH und R. NEWMAN: Die Absorptionskante von Zinktellurid . . . 324
Kündigungen: . . . 327

Том 21 На. 1/2

Р.М. Баррер, Б. Е. Ф. Фендер: Диффузия и сорбция воды в зеолитах—I . . . 1
Р. М. Баррер, Б. Е. Ф. Фендер: Диффузия и сорбция воды в зеолитах—II . . . 12
А. Таубер, К. Уинфри, Е. Банкс: Кристаллохлмия некоторых гранатов германия . . . 25
О. Ентш: К теории хемисорбции . . . 33
Г. А. Резинт, Н. Г. Нахтриб: Самодиффузия свинца, таллия и висмута в твердых растворах свинца и таллия . . . 40
Ж. С. Кувель: Ферромагнитно-антиферромагнитные свойства сплавов меди с марганцем и серебра с марганцем . . . 57
Дж. Е. Циммерман, Г. Сато: Электронная теплоемкость сплавов Ми–Сц . . . 71
Р. Паркер, М. С. Смит: Растворимость никкеля в феррите никкеля . . . 76
Г. А. Папазян: Центры окраски в азиДах Шелочных металлов . . . 81
Р. Е. Куверт: Зксперименты по поверхностной Магнитопроводимости на кремнии . . . 87
П. Яфет: Сверхтонкое взаимодействие, обусловленное орбитальным магниным моментом злектронов с больщими знлчениями фактора g . . . 99
Дь. Гергель: Эффекты пространственного заряда в амбиполярной диффуэии носителей, индуцированной злектронной бомбардировкой в фотопроводящих диэлектрических кристаллах . . . 105
В. Е. Спир: Подвижности носителей и перенос заряда в моноклинных кристаллах селена . . . 110

Письма в редакцию:

Т. Бонижевский, Г. Смит: Замечание о гидриде лития . . . 115
Е. Ф. Берто, Ж. Дюлак: Об изоморфизме тройных окислов тривалентных хрома и родия . . . 118
Ж. Б. Грюн, М. Сискинд, С. Никитин: Изучение поглощения и отражения купритом при очень низких температурах в области коротких видимых длин волн . . . 119
Д. В. Лангер: затвердевание гелия при 77°К . . . 122
Л. Е. Оргел: Ван-Флековский независящий от температуры магнетизм металлов . . . 123
А. Асколи, А. Цамаск: Миграция знергии вакансии, близкой к примеси . . . 124
А. Д. Брейиьсфорд, А. В. Оверхаузер: Теория минимума сопротивления в разведенных парамагнитных сплавах . . . 127
П. М. Грузенски, А. Б. Скотт: Ионная проводимость Кц, содержащего сульфатные ионы . . . 128
Д. В. Баллентайн: О поведении электролюминесцирующих фосфоров при ультрафиолетовом облучении . . . 131

Рецензия На книги:

С. Мрозощи (редактори): "Proceedings of the Fourth Conference on Carbon" (рецнзент ДЖ. А. Крумьансл) . . . 134
А. Е. Греен, ДЖ. Е. Адкинс: "Large Elastic Deformations and Non-Linear Continuum Mechanics" (рецнзент Р. Т. Шелд) . . . 134
Е. Г. Лутле: "The Hall Effect and Related Phenomena" (рецнзент ДЖ. Г. Крафорц) . . . 135

Опеуака:

Р. Кикууи: Статистиуеская динамика диффузии в кристаллах. II, III . . . 136
ДЖ. С. Смарт: Магнитный порядок и теплоемкость ферромагнетиков и антиферромагнетиков . . . 136

Том 21 На. 3/4

Е. Антончик: К теории поверхностных состоянии . . . 137
М. Д. Канут и Дж. Л. Аморос: Зависимость от температуры рентгеновского излучения рассеянного молекулярными кристаллами. Нафталин . . . 146
Ж. П. Сюше- Ионная структура, эффективные заряды и электронные подвижности в полупроводящих минеральных соединениях . . . 156
М. О'Киффе: Катионные валентности и распределения в шпинельных структурах, содержащих марганец . . . 172
Г. Хасегава, Р. Е. Ховард: Спектр оптического поглощения водородоподобных атомов в сильном магнитном поле . . . 179
Р. Нитше, Г. Болстерли, М. Ильхтенштейгер: Рост кристаллов путем химических реакций переноса. 1 . 199

Vol. 21
1961

page

Б. С. Чандрасекар, Дж. М. Бардин: Парамагнитные восприимчивости некоторых уран-молибденовых сплавов между 100 и 300°К 206
М. Вебер: Ядерный магнитный резонанс в фосфиде галлия 210
Д. Шутер, Г. Е. Фарнсворт: Водородно-дейтериевый обмен на чистых поверхностях никкеля . . 219
Е. Т. Корнгеузер: О возможности наблюдения диффракции нейтронов в жидком гелии 228
Е. Ф. Берто, Л. Корлисс, Ф. Форра, Р. Алеонард, Р. Потене: Изучение ниобатов и танталатов двухвалентных переходных металлов 234
Р. Д. Блаугер, Б. С. Чандрасекар, Дж. К. Хели, Е. Коренцвит, Б. Т. Маттиас: Сверхпроводимость сплавов титана и молибдена 252
Е. Ф. Берто: Магнитные конфигурации. Метод Фурье 256
П. Кофстад, П. Б. Андерсон: Гравиметрическое изучение дефектной структуры α—Nb_2O_5 280
И. А. Роше, Ж. Фридель: Об электронной структуре жидких переходных металлов и некоторых сложных фаз 287
Е. Ф. Берто: Магнитные конфигурации. Прямой метод 295

Письмо в редакцию:

А. Зиглерт, Г. Томпа: Энергия и конфигурация атомов в простой модели краевой дислокации . . 306
Д. В. Овенал: Парамагнитное резонансное поглощение в молекулярных кристаллах. Замечания к работе Вигена и Коуэна 309
Л. Т. Крейн, Дж. Е. Циммерман: Теплоемкость монокристаллов Си–Ми между 1,4 и 5°К . . . 310
Дж. Р. Макдональд: Фотоемкостные эффекты в аддитивно окрашенных кристаллах галогенидов щелочных металлов 313
Е. Сондер, С. Т. Секула: Влияние газовых примесей на магнитные свойства меди 315
Л. Виланд: Влияние давления мышьяка на диффузию примесей в Ga As 318
П. Н. Батчер, Дж. Хулберт, К. Ф. Хелм: Туннельные диоды из антимонида индия в сильных магнитных полях 320
Е. Ло, Р. Ньюмен: Край поглощения теллурида 324

Информация 327

AUTHOR INDEX TO VOLUME 21

(B) denotes book review (E) denotes erratum

Aleonard, R. 234
Amorôs, J. L. 146
Anderson, P. B. 280
Antončík, E. 137
Ascoli, A. 124

Ballentyne, D. W. G. 131
Banks, E. 25
Bardeen, J. M. 206
Barrer, R. M. 1, 12
Bertaut, E. F. 118, 234, 256, 295
Blaugher, R. D. 252
Bölsterli, H. U. 199
Bonizewski, T. 115
Brailsford, A. D. 127
Butcher, P. N. 320

Canut, M. L. 146
Chandrasekhar, B. S. 206, 252
Crane, L. T. 310
Crawford, J. H. 135
Corliss, L. 234
Coovert, R. E. 87
Corenzwit, E. 252

Damask, A. C. 124
Dulac, J. 118

Englert, A. 306

Farnsworth, H. E. 219
Fender, B. E. F. 1, 12
Forrat, F. 234
Friedel, J. 287

Gergely, G. 105
Grun, J. B. 119
Gruzensky, P. M. 128

Hasegawa, H. 179
Howard, R. E. 179
Hulbert, J. A. 320
Hulm, J. K. 252
Hulme, K. F. 320

Jäntsch, O. 33

Kikuchi, R. 136 (E)
Kofstad, P. 280
Kornhauser, E. T. 228
Kouvel, J. S. 57
Krumhansl, J. A. 134 (B)

Langer, D. W. J. 122
Lichtensteiger, M. 199
Loh, E. 324

Macdonald, J. R. 313
Matthias, B. T. 252

Nachtrieb, N. H. 40
Newman, R. 324
Nikitine, S. 119
Nitsche, R. 199

O'Keeffe, M. 172
Orgel, L. E. 123
Ovenall, D. W. 309
Overhauser, A. W. 127

Papazian, H. A. 81
Parker, R. 76
Pauthenet, R. 234

Resing, H. E. 40
Rocher, Y. A. 287

Sato, H. 71
Scott, A. B. 128
Sekula, S. T. 315
Shield, R. T. 134 (B)
Shooter, D. 219
Sieskind, M. 119
Smart, J. S. 136 (E)
Smith, G. C. 115
Smith, M. S. 76
Sonder, E. 315
Spear, W. E. 110
Suchet, J. P. 156

Tauber, A. 25
Tompa, H. 306

Vieland, L. J. 318

Weber, M. J. 210
Whinfrey, C. G. 25

Yafet, Y. 99

Zimmerman, J. E. 71, 310

J. Phys. Chem. Solids Pergamon Press 1961. Vol. 21, Nos. 1/2, pp. 1–11. Printed in Great Britain.

THE DIFFUSION AND SORPTION OF WATER IN ZEOLITES—I. SORPTION

R. M. BARRER and B. E. F. FENDER

Physical Chemistry Laboratories, Imperial College, London, S.W.7.

(*Received* 21 *February* 1961)

Abstract—Equilibrium sorption measurements have been made for D_2O and H_2O in the crystalline zeolites chabazite, gmelinite and heulandite, at relative coverages greater than $\theta = 0{\cdot}85$. The water contents, the shape of the isotherms, the isosteric heats and the partial molar entropies are almost identical for H_2O in chabazite and gmelinite; in heulandite isotherms are more rectangular but isosteric heats and partial molar entropies do not differ greatly from those in the other zeolites. Differences in these properties as between sorbed D_2O and H_2O are small, but heats of sorption are slightly greater for D_2O and slightly larger molar amounts of D_2O are probably sorbed in the crystals at the same relative pressures and temperatures. The sorbed water has certain fluid-like characteristics as shown by the similarity of the thermal entropies of sorbed and liquid water and by the thermal expansivities of sorbed water in chabazite and gmelinite. In heulandite there is some evidence from the thermal expansion data that the aluminosilicate lattice is sensitive to small changes in water content.

Vol. 21
1961

INTRODUCTION

THE state of water in zeolites has commanded interest since the early dehydration studies.[1] Techniques which have been used to investigate the properties of occluded water include thermogravimetric[2] and optical studies,[1] dielectric absorption,[3, 4] differential thermal analysis,[5] infra-red absorption,[6, 7, 8] equilibrium sorption[9, 10, 11] and diffusion measurements.[12, 13] It is with the sorption and diffusion properties of intracrystalline water that this present work is concerned. Studies of equilibrium sorption of water in zeolites have been reported by HEY[9], TISELIUS and BROHULT[10] and recently by BARRER and BRATT[11]. The present results refer to three naturally occurring zeolites: chabazite (source: Nova Scotia, Canada) and gmelinite (Antrim, Northern Ireland), two related minerals with robust three-dimensional crystal structures; and heulandite (Iceland), a lamellar zeolite. Equilibrium sorption measurements lead to isosteric heats, free energies and partial molar entropies of occluded water, and to information concerning the thermal expansion of intracrystalline water. Investigation of sorption of both H_2O and D_2O as well as illustrating differences in behaviour between the two isotopic species, is necessary for the interpretation of self-diffusion measurements.[14]

EXPERIMENTAL

The zeolite crystals were hand-picked, well-formed and free from visible surface impurities. They were lightly scrubbed, and washed with distilled water. Each sample consisted of a collection of crystals. For chabazite there were 22 crystals weighing together about 0·5 g, and as further chabazite samples will be described,[14] this sample will be called chabazite A. The gmelinite sample of 34 crystals weighed approximately 0·3 g, and the 2 crystals of heulandite weighed about 0·7 g. As sorbate, conductivity water was outgassed and redistilled under vacuum, the middle fraction being collected. The D_2O used was supplied by I.C.I. Ltd., and was also outgassed and redistilled under vacuum. The specified D_2O concentration varied between 99·77 and 99·83 per cent D_2O.

The sorption of water was measured gravimetrically. The apparatus was of conventional

design suitable for vapours in the temperature range 30–80°C. Minor modifications of the present apparatus included a ground-glass cone and cap, sealed with "Apiezon T" grease, at the top of the balance case, which allowed easy access to the sample; and a coarse-meshed fibreglass bucket to contain the crystals. The observations on heulandite were made using a thermostat tank with plate-glass windows; this reduced aberrations caused by the glass in the cylindrical tanks and thus enhanced the accuracy.

Prior to sorption measurements the crystals were not dehydrated completely as it was expected that dehydration or subsequent rehydration would cause the crystals to crack and break up. This had to be avoided in order that subsequent diffusion experiments could be carried out on the same crystals. The following procedure was adopted before H_2O sorption. Crystals were subjected to a high vacuum for ten minutes, isolated for thirty minutes and dehydrated for a further ten minutes. The temperature was then raised to, and maintained between, 65 and 75°C, and a dose of H_2O vapour between 100 and 150 mg was admitted to the balance case. This dosing procedure was repeated about twelve times in eight days. Finally the last dose was removed and isotherm measurements made. To replace the intracrystalline H_2O with D_2O a similar dosing procedure was adopted. In this case the heavy water doses were renewed twice every twenty-four hours. The crystal was considered fully deuterated four days after there was no detectable change in weight of the crystal sample, in successive daily readings taken at a particular temperature and pressure. The dehydrated weight of each crystal sample was determined at the end of all experiments by heating the crystals in a platinum crucible at 1200°C for one hour. Continued heating for a further hour showed that dehydration was complete. In other respects the sorption procedure was as described earlier.[15]

RESULTS

Isotherms

For each crystal sample, and for both H_2O and D_2O, isotherms were determined at five temperatures in the range 30–80°C. The pressures in mm of mercury were corrected to relate to mercury at 0°C. A correction was made for the capillary depression of the mercury using the data of GOULD and VICKERS[16] but assuming the surface tension of mercury in contact with water vapour to be the same as that in contact with liquid water.[17] A further correction was made for the difference in mercury vapour pressure between the limb of the manometer connected to the balance case and the high vacuum limb. About twenty x–p points were measured at each temperature; x is the amount sorbed in g/g of dehydrated crystal at pressure p (mm). The maximum experimental error in x, including spring reading and cathetometer calibration errors, is estimated as $\pm 0{\cdot}0006$ g for chabasite, $\pm 0{\cdot}0010$ g for gmelinite and $\pm 0{\cdot}0004$ g for heulandite. The maximum error in the corrected pressures is estimated as 0·10 mm. In addition to the above errors there are a number of errors affecting the over-all value of x which are constant for each isotherm point. These are (a) a possible error in x of $\pm 0{\cdot}0002$ g arising from spring calibrations; (b) uncertainty in the determination of the dehydrated weight of the crystal; this has been discussed by BARRER and LANGLEY[2] whose results imply that there could be an uncertainty in x of $\pm$ 0·005 g arising from this source; and (c) a further error in the D_2O isotherms only may be caused by incomplete replacement of H_2O by D_2O. The highest D_2O concentration in the crystals is governed by the concentration of D_2O in the water used (99·77–99·83 per cent). Replacement of H_2O is unlikely to be quite complete and the actual D_2O concentration in the crystals is probably little greater than, though not less than, 99 per cent. A value of 99 per cent D_2O implies that the values of x in the D_2O isotherms may be 0·0003 g (chabazite, gmelinite) or 0·0002 g (heulandite) too low. The effect of the small quantity of DOH which occurs naturally in H_2O is negligible.

All the isotherms were found to be reversible within experimental error. Detailed results have been tabulated[18] and are not reproduced here. The results obtained at 55°C shown in Fig. 1, clearly illustrate the rectangular nature of the isotherms. The liquid–vapour pressure data of RIESENFELD and CHANG[19] for D_2O was used in determining the relative pressures for the D_2O isotherms. Capillary or surface condensation becomes apparent at relative pressures near 0·95 by an upward inflection of the isotherms. The

amount sorbed (x) is the total amount sorbed, i.e. it includes both intracrystalline water and water sorbed or condensed on the external surface of the crystal. The present sorption experiments were made with crystal samples having low surface areas compared with powder samples. Assuming in the first place that the crystals are smooth and regularly shaped then approximately 10^3 layers of evenly distributed close packed water molecules on the surface of chabazite and gmelinite crystals and 5×10^3 layers on heulandite crystals would have caused an increase in x of only 0·0003. This would appear to be a greater amount of water than would be required to fill small cracks in the crystal where capillary condensation occurs at low relative pressures. It is also of interest to note that BARRER, MCKENZIE and REAY[20] have made calculations of the capillary condensation of water in single pores of regular shapes, which indicate that in the shapes studied (e.g. cones, wedges and cylinders) a rapid increase in capillary condensation at relative pressure of 0·95 can correspond to very little condensation at a relative pressure of 0·8. It seems reasonable to suppose in the present studies capillary condensation makes no significant contribution to the value of x below a relative pressure of 0·8. To obtain estimates of the amount of intracrystalline water (x_{sat}) at a relative pressure of 1·0, x–p and log x–log p plots were extrapolated to the saturation water vapour pressure. Both extrapolations gave values in close agreement, the average value being taken to obtain coverages θ, where $\theta = x/x_{sat}$.

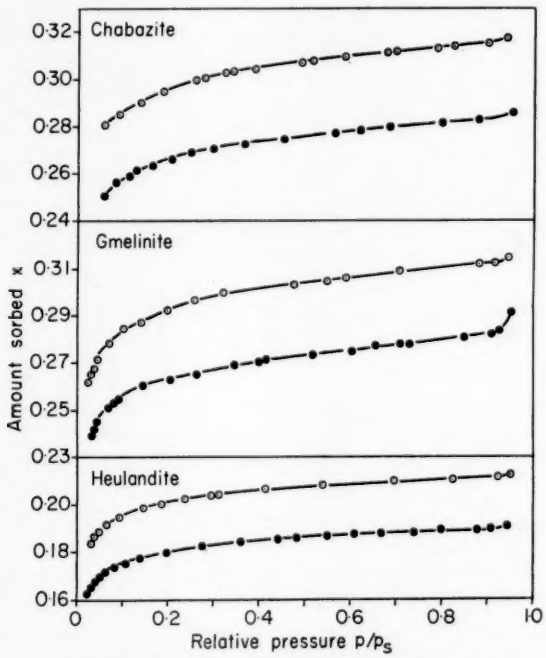

FIG. 1. Typical water–zeolite isotherms at 55°C.
○, D_2O ●, H_2O

Two features of ideal localized sorption are the applicability of the Langmuir isotherm equation $K = p(1-\theta)/\theta$ and the constancy of the differential entropy, $\bar{S}_{Th}$, of the sorbed molecules with coverage. The differential thermal entropy is given by

$$\bar{S}_{Th} = \bar{S}_s - \bar{S}_c \qquad (1)$$

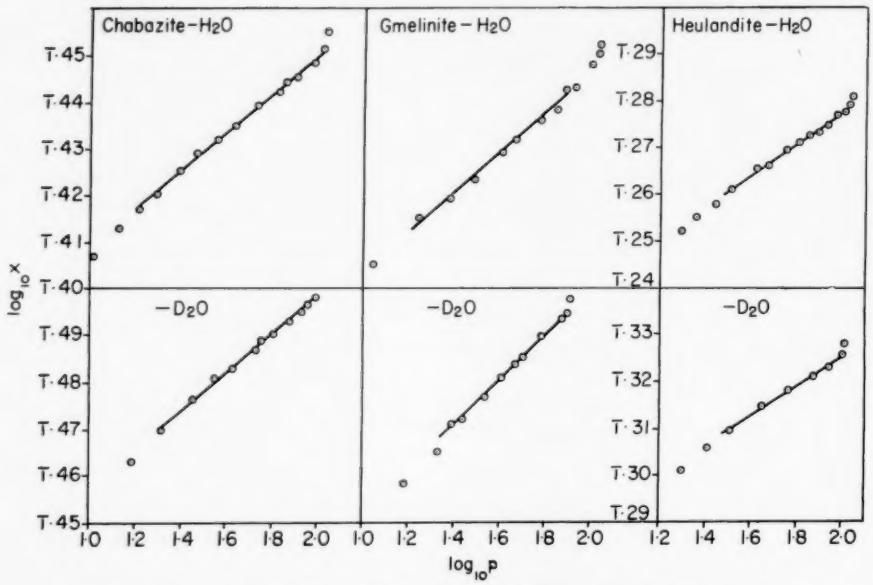

FIG. 2. Curves of log x vs. log p showing nearly linear sections (x denotes amount of water sorbed in g/g, and p is the equilibrium pressure).

where $\bar{S}_s$ is the partial molar entropy of sorption and $\bar{S}_c$ is the partial molar configurational entropy, which for ideal localized sorption is $\bar{S}_c = R\ln(1-\theta)/\theta$. Tables 1 and 2 give values of K and $\bar{S}_{Th}$ respectively and indicate the applicability of the relationships in the present range in θ. The constancy of K is a sensitive test of the Langmuir equation so that these values with the reasonably constant values of $\bar{S}_{Th}$ can be said to show that the equation is a fairly satisfactory description of the isotherms of water in all three zeolites in the range $0{\cdot}86 < \theta < 0{\cdot}96$. However plots of log x − log p show linear regions (Fig. 2) which indicate decreasing isosteric heats with increasing coverage, and emphasize the approximate nature of the fit between the measured isotherms and the ideal localized isotherm equation. Values of d log p/d log x for the linear region are given in Fig. 3 and the trend of decreasing values with increasing temperature illustrates how the isotherms become less rectangular with rising temperature. In particular these values are important in diffusion

Table 1. *Values of* $K = p(1-\theta)/\theta$ *at* 55°C

θ	Chabazite A		Heulandite		Gmelinite	
	H_2O	D_2O	H_2O	D_2O	H_2O	D_2O
0·98	0·146	0·136	0·115	0·113	0·157	0·141
0·96	0·179	0·163	0·131	0·122	0·195	0·176
0·94	0·162	0·154	0·119	0·111	0·176	0·160
0·92	0·137	0·130	0·097	0·090	0·137	0·130
0·90	0·111	0·103	0·077	0·071	0·108	0·103
0·88	0·091	0·081	0·057	0·055	0·087	0·081

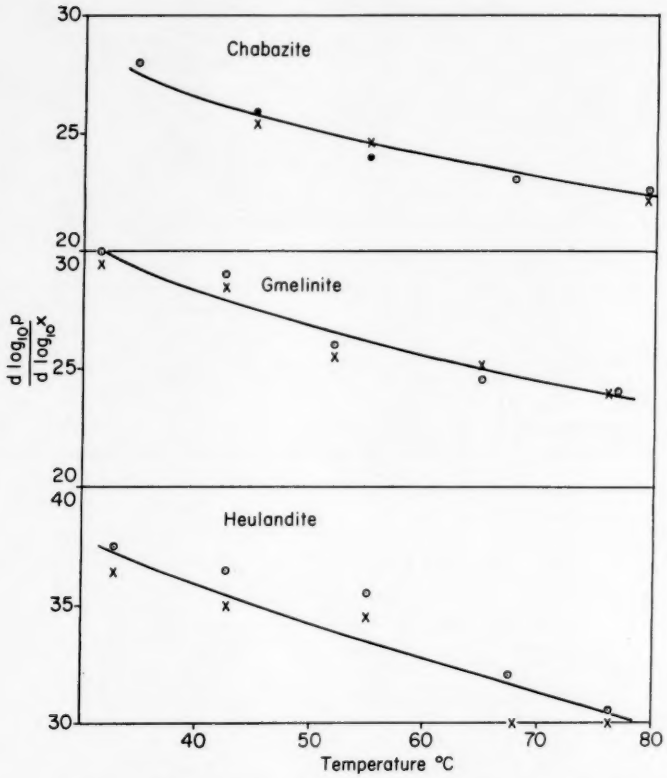

FIG. 3. The activity correction term $d \log p/d \log x$ as a function of temperature for the water–zeolite systems in the nearly linear regions shown in Fig. 2.

studies because $d \log p/d \log x = d \log a/d \log x$, where a is the activity of the occluded water (this assumes the water vapour behaves ideally). This term is the relevant activity factor related to the diffusion of intracrystalline water under the influence of a gradient of chemical potential.[14]

Table 2. Values of $\bar{S}_{Th}$ in e.u. at 55°C

θ	Chabazite A		Heulandite		Gmelinite	
	H_2O	D_2O	H_2O	D_2O	H_2O	D_2O
0·98	17·9	19·0	23·3	23·3	20·2	21·0
0·96	14·9	16·2	20·1	21·1	15·8	16·4
0·94	14·4	15·7	18·8	20·1	14·5	15·5
0·92	14·4	15·9	18·1	19·8	14·1	15·1
0·90	14·8	16·3	17·9	20·0	14·2	15·6
0·88	15·1	—	18·5	20·7	14·6	16·0
0·86	—	—	18·9	21·4	14·9	16·4

To compare the sorption of the two isotopic species, the ratio of molar amounts of D_2O and H_2O at constant values of the free energy of sorption (ΔG°) (see below) were determined (Table 3). The deviation of this ratio from unity is small and close to the maximum experimental error of ± 0·004 for chabazite and heulandite and ±0·006 for gmelinite. The results however show a consistent tendency for a slightly larger molar amount of D_2O to be occluded which is particularly marked in the case of heulandite.

Table 3. Values of $x_{D_2O}/M_{D_2O} \div x_{H_2O}/M_{H_2O}$

Crystal	Temperature (°C)	$-\Delta G^\circ = 0$ (x_{sat} values)	$-\Delta G^\circ$=1000 cal/mole
Chabazite A	34·35	1·001	1·002
	45·00	1·002	1·003
	55·00	1·002	1·002
	67·70	1·004	1·002
	79·40	1·000	1·002
Heulandite	32·85	1·008	1·009
	42·70	1·008	1·007
	54·95	1·008	1·006
	67·40	1·009	1·008*
	76·10	1·006	1·006
Gmelinite	31·40	1·008	1·004
	42·50	1·007	1·002
	54·95	1·003	1·002
	64·90	1·007	1·002
	76·80	1·002	1·002*

* Corrected value as D_2O isotherms measured at slightly different temperatures.

Isosteric heats, partial molar entropies and free energies of sorption

Log p vs. $1/T$ plots gave straight lines within experimental error and the calculated isosteric heats ($-\Delta\bar{H}$) are shown in Fig. 4. Maximum errors in the values of $-\Delta\bar{H}$ are 200–250 cal/mole for chabazite and heulandite and 250–300 cal/mole for gmelinite. The higher value in each case refers to the heats at the lower coverages. Partial molar entropies and differential entropies of sorption at 55°C are given in Table 4. The partial molar entropy of sorption is given by

$$\bar{S}_s = \bar{S}_g^T + \Delta\bar{S} + R\ln\frac{p^0}{p} - \alpha p \qquad (2)$$

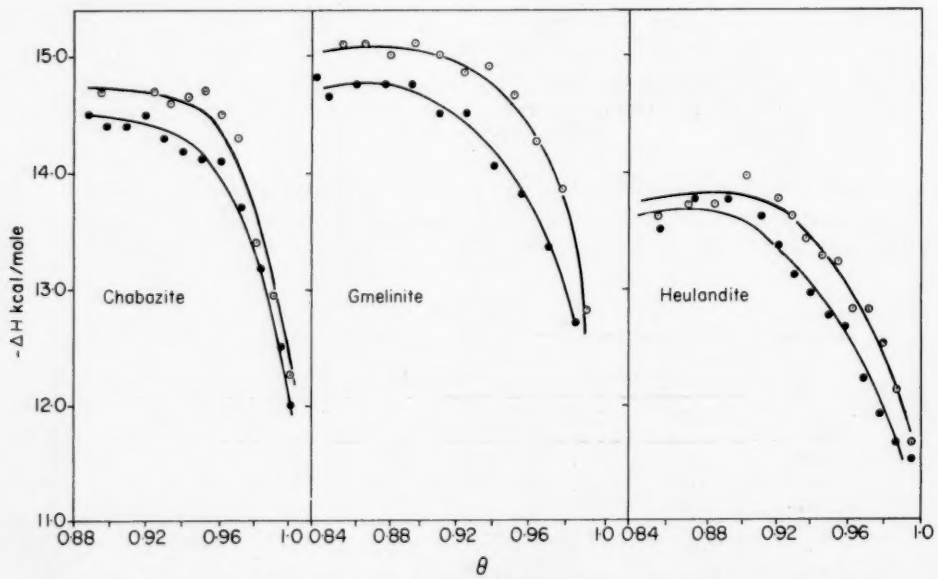

FIG. 4. Isosteric heats of sorption as a function of the degree of saturation, θ, of the zeolites by water.
⊙, D_2O ●, H_2O

Table 4

θ	$-\Delta G^\circ$ (cal/mole)	$-\Delta\bar{S}$(e.u.)	$\bar{S}_s$(e.u.)
	Chabazite A–H_2O		
1·00	0	35·50	14·05
0·98	330	40·40	10·15
0·96	660	43·00	8·55
0·94	985	43·75	8·85
0·92	1315	44·05	9·50
0·90	1610	44·05	10·40
0·88	1860	44·05	11·15
	Chabazite A–D_2O		
1·00	0	36·55	15·50
0·98	315	41·75	11·25
0·96	660	44·20	9·87
0·94	975	44·80	10·21
0·92	1285	44·95	11·01
0·90	1600	44·95	11·96
0·88	1850	—	—
	Heulandite–H_2O		
1·00	0	34·31	15·25
0·98	490	36·39	14·61
0·96	860	38·32	13·82
0·94	1205	39·92	13·29
0·92	1535	41·02	13·21
0·90	1845	41·66	13·52
0·88	2165	41·63	14·52
0·86	2390	41·50	15·34

θ	$-\Delta G^\circ$ (cal/mole)	$-\Delta\bar{S}$(e.u.)	$\bar{S}_s$(e.u.)
	Heulandite–D_2O		
1·00	0	34·74	17·30
0·98	430	37·79	15·57
0·96	845	39·74	14·88
0·94	1195	41·05	14·63
0·92	1520	41·81	14·87
0·90	1840	42·06	15·59
0·88	2130	41·81	16·72
0·86	2375	41·44	17·75
	Gmelinite–H_2O		
1·00	0	—	—
0·98	300	38·10	12·45
0·96	595	41·90	9·45
0·94	945	43·45	9·00
0·92	1310	44·35	9·20
0·90	1625	44·75	9·75
0·88	1885	44·75	10·55
0·86	2125	44·75	11·30
	Gmelinite–D_2O		
1·00	0	—	—
0·98	285	39·65	13·25
0·96	605	43·75	10·15
0·94	950	45·00	9·95
0·92	1285	45·75	10·20
0·90	1595	45·75	11·15
0·88	1870	45·75	12·00
0·86	2115	45·75	12·75

where $\bar{S}_g^T$ is the gas phase entropy at temperature T and pressure p^0, p^0 is a standard pressure in this case 760 mm of mercury, α is a gas phase non-ideality correction, $\Delta\bar{S}$ is the differential entropy of sorption ($\Delta\bar{S} = \Delta\bar{H}/T$) and R is the gas constant. $\bar{S}_g^T$ is calculated from the equation

$$\bar{S}_g^T = \bar{S}_g^0 + \int_{T^0}^{T} \frac{C_p(T)}{T}\,dT \qquad (3)$$

where $\bar{S}_g^0$ is the standard gas phase entropy at temperature T^0 and pressure p^0, $C_p(T)$ is the heat capacity of the gaseous phase. Using the heat capacity data of SPENCER and FLANAGAN[21] and taking a value of $\bar{S}_g^0$ equal to 45·14 cal/mole[22] ($T = 25°C$), $\bar{S}_g^T(H_2O)$ at 55°C is calculated as 4·84 e.u. For D_2O equation (3) was replaced by

$$\bar{S}_g^T = \bar{S}_l^0 + \frac{\Delta L}{T} + \int_{T^0}^{T} \frac{C_p}{T}\,dT - R\ln\frac{p'}{p^0} - \alpha p' \qquad (4)$$

where $\bar{S}_l^0$ is the entropy of the liquid at 25°C, ΔL is the latent heat of vapourization at 55°C, $C_p(T)$ is the heat capacity of the liquid, p' is the saturation vapour pressure of D_2O at 55°C. Using thermodynamic data given by KIRSCHENBAUM[22] $\bar{S}_g^T$ at 55°C is calculated as 48·16 e.u. In calculating gas phase entropies and values of $\bar{S}_s$ the non-ideality correction is negligible.

Free energies of sorption are given by

$$\Delta G^0 = -RT\ln p^0/p \qquad (5)$$

and are also recorded in Table 3. p^0, the standard gas pressure, is in this case the saturation vapour pressure of the relevant isotopic species.

Comparison of thermal entropies of sorbed and liquid water

Assuming as a first approximation ideal localized sorption given by the Langmuir isotherm it is possible to compare the thermal entropies of sorbed molecules with the molar thermal entropies of the corresponding liquids. This has been described by BARRER and SUTHERLAND[15] with reference to the sorption of hydrocarbon in faujasite. The relation between $\bar{S}_{\mathrm{Th}}$ and $\tilde{S}_{\mathrm{Th}}$ for n_s moles sorbed is

$$\bar{S}_{\mathrm{Th}} = \tilde{S}_{\mathrm{Th}} + n_s \left(\frac{\partial \tilde{S}_{\mathrm{Th}}}{\partial n_s}\right)_{p,T,n_s}.$$

$\bar{S}_{\mathrm{Th}}$ and $\tilde{S}_{\mathrm{Th}}$ are equal either when $n_s = 0$ or when $\tilde{S}_{\mathrm{Th}}$ is independent of n_s. Conversely, if $\bar{S}_{\mathrm{Th}}$ is constant it must either be equal to $\tilde{S}_{\mathrm{Th}}$ or else the concentration dependences of $\tilde{S}_{\mathrm{Th}}$ and n_s $[(\partial \tilde{S}_{\mathrm{Th}})/(\partial n_s)]$ must compensate. In view of the first of these possibilities the comparison of $\bar{S}_{\mathrm{Th}}$ of sorbate with $\tilde{S}_{\mathrm{Th}}$ of its liquid is of interest. For a liquid

$$\tilde{S}_l = {}_l\tilde{S}_c + {}_l\tilde{S}_{\mathrm{Th}} \qquad (6)$$

where $\tilde{S}_l$ is the molar entropy of the liquid and ${}_l\tilde{S}_c$ and ${}_l\tilde{S}_{\mathrm{Th}}$ are the molar configurational and thermal entropies of the liquid respectively. The values of ${}_l\tilde{S}_c$ should be small[25] so that $\tilde{S}_l$ is approximately equal to ${}_l\tilde{S}_{\mathrm{Th}}$ and $\tilde{S}_l - \bar{S}_{\mathrm{Th}}$ represents the difference in thermal entropies between the sorbate and the liquid. The entropy of liquid water at 55°C is 18·5 e.u. and the entropy of liquid D_2O, calculated from the entropy of the liquid at 25°C[22] and the heat capacity data for liquid, D_2O is 20·1. The results given in Table 5 suggest that the thermal entropies of sorbate and liquid are not very different.

Thermal expansion of sorbed water

The free energy values $-\Delta G^0$ described earlier relate to the liquid, i.e. the standard pressure is the saturation vapour pressure, and these are also Polyanyi sorption potentials ϵ. In a zeolite crystal where x is the amount sorbed and δ the density of the sorbate in the crystal, it has been shown[15] that for any chosen value of ΔG^0 or ϵ

$$\frac{1}{V_i\delta}\left(\frac{dx}{dT}\right)_\epsilon = \frac{1}{x}\left(\frac{dx}{dT}\right)_\epsilon = \alpha - \alpha_i$$

$$\alpha = \frac{1}{\delta}\left(\frac{\partial \delta}{\partial T}\right); \quad \alpha_i = \frac{1}{V_i}\left(\frac{\partial V_i}{T}\right).$$

α and α_i are the thermal expansivities of the intracrystalline water and the interstitial volume respectively. Differences in the two thermal expansivities were determined from plots of amount sorbed (x) against temperature (T) at constant ϵ. Some of the x–T plots showed slight curvature indicating higher values of dx/dT at higher temperatures but the experimental accuracy was not sufficient to warrant calculation of $\Delta x/\Delta T$ values for small ranges of temperature. (Δx is the change in amount sorbed for a change in temperature ΔT). Mean values of $\alpha - \alpha_i$ at different sorption potentials were calculated from $1/\bar{x}\ \Delta x/\Delta T$ where $\bar{x}$ is the average amount of sorbed water in the full temperature range of the measurements. The expansivities are relatively small so that the

Table 5. *Temperature* 55°C. $\theta = 0{\cdot}92$. $\bar{S}_c = R\ln(1-\theta)/\theta = -4{\cdot}9$ e.u.

Crystal	$\bar{S}_s$(e.u.)	$\bar{S}_{\mathrm{Th}}$(e.u.)	$\tilde{S}_l$(e.u.)	$\tilde{S}_l - \bar{S}_{\mathrm{Th}}$ (e.u.)
Chabazite A–H_2O	9·5	14·4	18·5	4·1
Chabazite A–D_2O	11·0	15·9	20·1	4·2
Heulandite–H_2O	13·2	18·1	18·5	0·4
Heulandite–D_2O	14·9	19·8	20·1	0·3
Gmelinite–H_2O	9·2	14·1	18·5	4·4
Gmelinite–D_2O	10·2	15·1	20·1	5·0

Table 6

Crystal	(cal/mole)	Temperature range (°C)	$\alpha-\alpha_i$ per °C	Mean cubical thermal expansion coefficient of liquid H_2O per °C.
Chabazite A–H_2O	0	34·35–79·4	0·00048	0·000517
	500	34·35–79·4	0·00048	
	1000	34·35–79·4	0·00050	
	1500	34·35–79·4	0·00050	
Chabazite A–D_2O	0	34·35–79·4	0·00048	
	500	34·35–79·4	0·00051	
	1000	34·35–79·4	0·00051	
	1500	34·35–79·4	0·00052	
Heulandite–H_2O	0	32·85–76·1	0·00016	0·000481
	1000	32·85–76·1	0·00023	
	2000	32·85–76·1	0·00029	
Heulandite–D_2O	0	32·85–76·1	0·00016	
	1000	32·85–76·1	0·00026	
	2000	32·85–76·1	0·00028	
Gmelinite–H_2O	0	31·6–76·8	0·00045	0·000483
	1000	31·6–76·8	0·00043	
	2000	31·6–76·8	0·00045	
Gmelinite–D_2O	0	31·6–76·1	0·00047	
	1000	31·6–76·1	0·00049	
	2000	31·6–76·1	0·00050	

maximum errors in $\alpha-\alpha_i$ for the temperature range of about 45°C are approximately 10, 20 and 15 per cent for water in chabazite, heulandite and gmelinite respectively. The measured values of $\alpha-\alpha_i$ are given in Table 6 with the corresponding values of the cubical thermal expansion coefficients of liquid water.

The results show that in chabazite and gmelinite values of $\alpha-\alpha_i$ are slightly less than the thermal expansivity of liquid water. The $\alpha-\alpha_i$ values appear to be slightly larger the higher the value of ϵ, but this trend is very slight. Making the reasonable assumption that the coefficient of thermal expansion of the interstitial volume (α_i) is proportional to the expansivity of the external volume of the crystals, and that the value of $2{\cdot}07\times10^{-5}$ of this coefficient in the synthetic *A*-zeolite is a typical value for chabazite and gmelinite also, then the true thermal expansion of the sorbed water (α) is about 5 per cent greater than the values of $\alpha-\alpha_i$ and is very close to that of liquid water. For comparison the mean cubical thermal expansion of ice in the temperature range −20°C to −1°C is 0·00012. In contrast to chabazite and gmelinite, the values of $\alpha-\alpha_i$ for the heulandite–water systems are exceptional, they are considerably less than the liquid water coefficient and show a marked tendency to increase with increasing values of ϵ.

DISCUSSION

(a) *The different zeolites.* A feature of the isotherm results is the close similarity in behaviour between chabazite–water and gmelinite–water systems; this similarity is emphasized in closely comparable isosteric heats, partial molar entropies, free energies of sorption and thermal expansivity of occluded water. If this is not unexpected because of their similarity in crystal structure[23] it nevertheless indicates that the sorption of water in zeolites, at least at high coverages, is insensitive to appreciable differences in crystal structure. This view is reinforced in a more general way when the present results are compared with those reported by BARRER and BRATT[11] (Table 7) for the sorption of H_2O in ion-exchanged forms of the synthetic near-faujasite, zeolite X. Apart from KX the ranges of values of $-\Delta\bar{H}$ and $\bar{S}_s$ are small

Table 7

Crystal	$\theta^* = 0{\cdot}94$ $-\Delta\bar{H}$(kcal/mole)	$\bar{S}_s$
Chabazite A–H_2O	14·4	9·0
Gmelinite–H_2O	14·3	8·35
Heulandite–H_2O	13·0	13·30
LiX–H_2O	14·8	7·1
NaX–H_2O	13·5	9·2
KX–H_2O	17·8	−0·8
CaX–H_2O	12·2	—
CsCaX–H_2O	14·0	8·8

* θ values for Chabazite, Gmelinite and Heulandite at 55°C.

θ values for ion-exchanged near-faujasite (Linde Sieve X) at 70°C.

supporting the view[11] that at least as θ approaches unity interaction between water molecules and the anionic oxygen and self-interaction between water molecules predominate in determining sorptive properties, rather than differences in cation composition or structural arrangement of the aluminosilicate framework. Oxygen atoms are the most numerous atoms in these crystals, they are exposed to the sorbate and they do not vary greatly in number per cm^3 among the zeolites under discussion.

The comparison between the thermal entropies of sorbed and liquid water suggests that sorbed water molecules at these high coverages have freedom in terms of vibrations, rotations and librations comparable with that which they possess in liquid water. This conclusion differs from that reached by BARRER and SUTHERLAND[15] for the sorption of hydrocarbons (smallest C_4H_{10}, largest C_8H_{18}) in faujasite. In this case they found considerable differences between $\bar{S}_l$ and $\bar{S}_{Th}$ and they interpreted this as meaning that molecular freedom was much restricted. Such a difference in behaviour is not surprising for it is to be expected that even in the open structure of faujasite the confining effect of the aluminosilicate lattice is greater for the larger hydrocarbon molecules than it is, in the zeolites studied, for the smaller water molecules.

(b) *Thermal expansion of zeolitic water.* The thermal expansion results support the similarity between occluded and liquid water already inferred from the entropies, except in the case of heulandite. Here two reasons are possible for the small values of $\alpha - \alpha_l$: either the low values reflect thermal expansion coefficients of intracrystalline water a good deal less than in liquid water or alternatively in presence of water the expansivities of the interstitial volume α_l are relatively large. The latter explanation is more likely for WYART[24] has shown that the heulandite lattice is sensitive to small changes in water content so that it is feasible that thermal expansion of intracrystalline water also causes the aluminosilicate lattice to expand giving higher apparent values of α_l. That the values of $\alpha - \alpha_l$ are higher the larger the values of ϵ, suggests that the lower the total water content of the crystal the smaller is the effect on the lattice of the expansion of the water in it. If this conclusion is valid it also means that the isosteric heats and partial molar entropies of water sorption in heulandite include particular effects arising from lattice changes associated with water sorption.*

(c) *Isotope effects.* The differences between the sorption of D_2O and H_2O at the same relative pressures have been noted (Table 3). It is possible that the slightly greater sorption of D_2O arises from a difference in size between the two isotopic species. This is unlikely however, at least on the evidence of the molar volumes in the liquid state, which, when calibrated from densities,[22] are virtually identical at 40°C. A more probable reason for the difference lies in the higher sorptive energies of D_2O (Fig. 3) causing slightly greater sorption. As comparisons are made at the same relative pressures this implies a greater free energy difference between sorbed D_2O and H_2O than exists between the respective liquids. This latter result should be viewed with some reserve because it is strictly true only if the interstitial volume of the crystal available to the water molecules is independent of isotopic water species sorbed. This is probably correct for the rigid crystal framework of chabazite and gmelinite but in the case of heulandite it has been seen that the aluminosilicate lattice may be less rigid and the greater "excess" sorption of D_2O may result if the more strongly sorbed D_2O causes a greater expansion of the crystal lattice than H_2O. Differences in the isosteric heats (average about 350 cal

* All partial molar quantities of sorbates depend of course on properties both of sorbent and sorbate.

Vol. 196

greater for D_2O) are similar to the differences in the latent heat of vaporization of the liquids and probably reflect the smaller zero point energies of vibrations of sorbed D_2O relative to the crystal lattice. The experimental accuracy was not sufficient to detect any possible change in the isosteric heat difference from one zeolite to another, or any variations of this difference with coverage. Values of the partial molar entropies of sorption are slightly higher for D_2O indicating the higher contributions to $\bar{S}_s$ for D_2O of the rotational (and librational) entropies which are larger for D_2O because of the higher moments of inertia. Comparisons of isotopic species in different environments are important and if the experimental techniques are developed to give greater accuracy further studies in aluminosilicate structures would be valuable.

Acknowledgements—We are grateful to Dr. G. P. L. WALKER of the Geology Dept., Imperial College, for providing the samples of heulandite and gmelinite crystals. One of us, B.E.F.F., acknowledges support from a D.S.I.R. Research Studentship.

Vol. 21
1961

REFERENCES

1. RINNE F., *Neues Jb. Min. Geol. Paläont.* **1,** 41 (1897).
2. BARRER R. M. and LANGLEY D. A., *J. Chem. Soc.* 3817 (1958).
3. GLEMSER O., *Z. anorg. Chem.* **252,** 305 (1944).
4. WETZLAR K., *Z. angew. Min.* **1,** 125 (1938).
5. BARRER R. M. and LANGLEY D. A., *J. Chem. Soc.* 3804 (1958).
6. DUVAL C. and LECOMTE J., *J. Chim. Phys.* **50,** C64 (1953) Centre Nat. de Recherche Scientifique, No. 53 C64.
7. PASSERINI L., *Gazz. Chim. Ital.* **65,** 534 (1935).
8. FROHNSDORFF G., Thesis, University of London (1959).
9. HEY M. H., *Miner. Mag.* **24,** 99 (1935); HEY M. H. and BANNISTER F. A., *ibid.* **23,** 51, 243 (1932); 421 (1933); **24,** 227 (1936).
10. TISELIUS A. and BROHULT S., *Z. Phys. Chem.* **168A,** 248 (1934).
11. BARRER R. M. and BRATT G., *J. Phys. Chem. Solids* **12,** 130, 146, 154 (1959); BRATT G., Thesis, University of London (1958).
12. TISELIUS A., *Z. Phys. Chem.* **169**A, 425 (1934); **174**A, 40 (1935).
13. TISELIUS A., *J. Phys. Chem.* **40,** 223 (1936).
14. BARRER R. M. and FENDER B. E. F., following paper.
15. BARRER R. M. and SUTHERLAND J. W., *Proc. Roy. Soc.* **237A,** 439 (1956).
16. GOULD F. A. and VICKERS T., *J. Sci. Instrum.* **29,** 85 (1952).
17. *Handbook of Chemistry and Physics*, Chemical Rubber Publishing Co., Cleveland (1956).
18. FENDER B. E. F., Thesis, University of London (1959).
19. RIESENFELD E. H. and CHANG T. L., *Z. Phys. Chem.* **B33,** 120 (1936).
20. BARRER R. M., MCKENZIE N. and REAY J. S., *J. Colloid Sci.* **11,** 479 (1956).
21. SPENCER H. M. and FLANAGAN G. N., *J. Amer. Chem. Soc.* **64,** 2511 (1942).
22. KIRSCHENBAUM I., *Physical Properties and Analysis of Heavy Water*. McGraw-Hill, New York (1951).
23. DENT L. S. and SMITH J. V., *Nature, Lond.* **181,** 1794 (1958); BARRER R. M. and KERR I. S., *Trans. Faraday Soc.* **55,** 1915 (1959).
24. WYART J., *C.R. Acad. Sci., Paris* **191,** 1343 (1930).
25. SLATER J. C., *Introduction to Chemical Physics* p. 263. McGraw-Hill, New York (1939).

J. Phys. Chem. Solids Pergamon Press 1961. Vol. 21, Nos. 1/2, pp. 12–24. Printed in Great Britain.

THE DIFFUSION AND SORPTION OF WATER IN ZEOLITES—II. INTRINSIC AND SELF-DIFFUSION*

R. M. BARRER and B. E. F. FENDER

Physical Chemistry Laboratories, Imperial College, London, S.W.7

(*Received* 21 *February* 1961)

Abstract—The solution of three-dimensional diffusion equations is discussed with respect to the applicability of a $\sqrt{t}$ relationship to describe diffusion. The kinetics of the rates of H_2O sorption and of D_2O–H_2O exchange have been followed in the zeolites chabazite, gmelinite and heulandite in the temperature range 30–80°C, and intrinsic diffusion coefficients and self-diffusion coefficients of water in the crystal evaluated from the respective sets of measurements. Self-diffusion coefficients in all three zeolites have values intermediate between the self-diffusion coefficients of liquid water, at the same temperature, and ice near its melting point. Small changes in total water content near saturation produce a slight decrease in the self-diffusion coefficients in chabazite and gmelinite and a more marked decrease in heulandite. Using equilibrium sorption data it is shown that the equation $D = D^*(d\ln a/d\ln c)$ is a reasonably satisfactory description of the relationship between the diffusion coefficients and this provides an indication that both intrinsic and self-diffusion processes involve molecules as diffusing units.

AMONG extensive diffusion and transport measurements reported in recent years, there is little information concerning the mobility of water in hydrated crystalline compounds. TISELIUS[1,2] evaluated diffusion coefficients of water in heulandite from rates of water sorption in this crystal and PEMSLER[3] has measured diffusion coefficients associated with the exchange of light and heavy water in a number of zeolite crystals. Among stoichiometric hydrates diffusion coefficients have been reported from isotopic exchange measurements in potassium ammonium sulphate[4] and boehmite.[5] The aim of the present work has been to extend the earlier studies in zeolites, and by observing both the kinetics of D_2O–H_2O exchange and the sorption of H_2O, to allow a discussion of the diffusion process involved. The crystals studied were naturally occurring samples of chabazite, gmelinite and heulandite.[6]

Evaluation of the diffusion coefficients from kinetic measurements involves the use of appropriate three-dimensional diffusion equations. Earlier papers[7,8,9] have stressed the importance in these equations of the dependence of the amount of diffusion with the square-root of time. The $\sqrt{t}$ relationship is in most cases an approximation and the degree of approximation for diffusion in different three-dimensional shapes requires discussion in the present context, since crystalline blocks of rather definite shapes provide the diffusion media.

* The work described in this paper and in Part I is part of a programme on the properties of water originally sponsored at Imperial College by the D.S.I.R., and by the Rockefeller Foundation.

THEORETICAL

Diffusion in three dimensions

(a) *Plane sheet or slab. D constant.* For unidirectional diffusion in a finite plane sheet or slab, with boundary condition of zero surface concentration and a uniform constant initial concentration M_t, the amount of diffusing material remaining after time t, is given by[10,11]

$$M_t/M_\infty = \sum_{m=0}^{\infty} \frac{8}{(2m+1)^2\pi^2} \times \exp\left(-D\frac{(2m+1)^2}{4a^2}\pi^2 t\right) \qquad (1)$$

or

$$M_t/M_\infty = 1-2\left(\frac{Dt}{a^2}\right)^{1/2}\left[\frac{1}{\pi^{1/2}}+2\sum_{m=1}^{\infty}(-1)^m i\mathrm{erfc}\frac{ma}{\sqrt{Dt}}\right] \quad (2)$$

where M_∞ is the total amount of diffusing material in the slab, D is the diffusion coefficient and a is the thickness of the slab. Equation (1) is the solution suitable for computation with large values of t, and equation (2) is the relationship appropriate for small values of t.

(b) *Diffusion in a rectangular parallelopiped. D constant.* With the same conditions of constant initial concentration and zero surface concentration, the solution for a rectangular parallelopiped of sides a, b, c, can be written as a product solution of three one-dimensional solutions[12] so that for large times

$$M_t/M_\infty = \sum_{m=0}^{\infty}\sum_{n=0}^{\infty}\sum_{p=0}^{\infty}\frac{512}{\pi^6}\frac{1}{(2m+1)^2(2n+1)^2(2p+1)^2} \times \exp\left\{\frac{-D\pi^2}{4}\left[\frac{(2m+1)^2}{a^2}+\frac{(2n+1)^2}{b^2}+\frac{(2p+1)^2}{c^2}\right]t\right\} \quad (3)$$

and for small times

$$M_t/M_\infty = \left[1-2\left(\frac{Dt}{a}\right)^{1/2}\frac{1}{\pi^{1/2}}+2\sum_{m=1}^{\infty}(-1)^m i\mathrm{erfc}\frac{ma}{(Dt)^{1/2}}\right] \times \left[1-2\left(\frac{Dt}{b}\right)^{1/2}\frac{1}{\pi^{1/2}}+2\sum_{n=1}^{\infty}(-1)^n i\mathrm{erfc}\frac{nb}{(Dt)^{1/2}}\right] \times \left[1-2\left(\frac{Dt}{c}\right)^{1/2}\frac{1}{\pi^{1/2}}+2\sum_{p=1}^{\infty}(-1)^p i\mathrm{erfc}\frac{pc}{(Dt)^{1/2}}\right] \quad (4)$$

which for the special case of a cube of side "a" reduces to

$$M_t/M_\infty = 1-\frac{6}{a}\left(\frac{Dt}{\pi}\right)^{1/2}-\frac{8}{a^3}\left(\frac{Dt}{\pi}\right)^{3/2}+\frac{12}{a^2}\left(\frac{Dt}{\pi}\right)+\ldots \quad (5)$$

This latter equation has been deduced by JAIN[13] in a discussion of approximate solutions. It is stressed here that this equation can be obtained directly from equation (4).

(c) *Diffusion in a sphere of radius a. D constant.* The solutions of the equations for a sphere with initial and boundary conditions as above are for long times and short times respectively:[9,10]

$$M_t/M_\infty = \frac{6}{\pi^2}\sum_{n=1}^{\infty}\frac{1}{n^2}\exp\left(\frac{-Dn^2\pi^2 t}{a^2}\right) \quad (6)$$

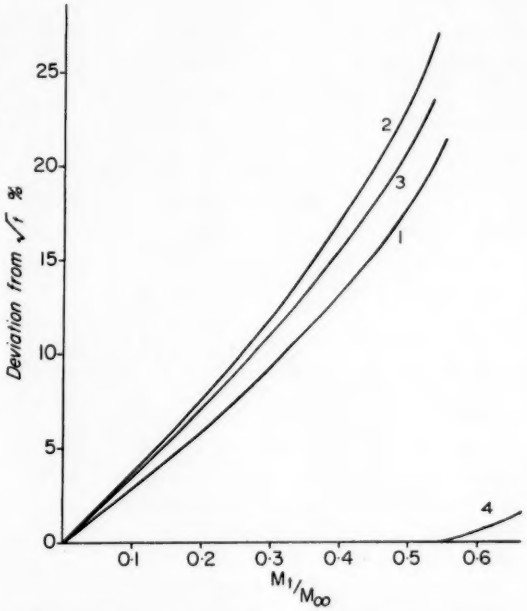

FIG. 1. Deviation from $\sqrt{t}$ for different shapes as a function of the amount of diffusion M_t/M_∞. Curve 1 a sphere, curve 2 a cube, curve 3 a rectangular parallelopiped (2:2:1), and curve 4 a plane sheet.

and

$$M_t/M_\infty = 1-6\left(\frac{Dt}{a^2}\right)^{1/2} \times \left[\pi^{-1/2}+2\sum_{n=1}^{\infty} i\mathrm{erfc}\frac{na}{(Dt)^{1/2}}\right]+\frac{3Dt}{a^2} \quad (7)$$

To obtain a measure of the deviation of M_t/M_∞ from a function dependent only on $\sqrt{t}$, a particular value of D and a volume V was assumed for

each shape discussed above. M_t/M_∞ for each shape was calculated first by including all significant terms, and then including only the $\sqrt{t}$ term (and unity), this latter value is designated as $(M_t/M_\infty)_{\sqrt{t}}$. $[(M_t/M_{\infty\sqrt{t}} - M_t/M_\infty]/M_t/M_\infty$ gives the fractional deviations of M_t/M_∞ from a $\sqrt{t}$ function for each shape and this is illustrated in Fig. 1. This figure shows that even in early stages of diffusion in a cube or sphere considerable deviation from linear dependence on $\sqrt{t}$ is apparent. The rectangular parallelopiped is not a fixed shape and the deviation in this case depends on the ratio of $a{:}b{:}c$. For example with $a = b$ then as $c \to a$ curve 3 approaches curve 2 and as $c \to 0$ curve 3 approaches curve 4. In all cases the extent of the deviation is independent of the particular value of D or V.

Diffusion coefficients in zeolites

A zeolite crystal can be considered as a two-component system; the dehydrated aluminosilicate lattice is composed of repeating units of component B, and water or other occluded species is component A. Diffusion in a two-component system can be represented by five diffusion coefficients[14] D_A, D_B, D_A^*, D_B^* and D_{AB}. D_A and D_B are intrinsic diffusion coefficients of A and B, D_A^* and D_B^* are the corresponding self-diffusion coefficients, and D_{AB} is a mutual diffusion coefficient describing interdiffusion of A and B, which is dependent on the particular reference system chosen. The surface of the crystal represents a section such that the mass of B is fixed on each side and the mutual diffusion coefficient D_{AB} relative to this section is given by HARTLEY and CRANK[18] as

$$D_{AB} = V_B C_B^V (V_B^0 C_B^V)^2 \times \left[D_A + D_B \frac{C_A^V V_A + C_A^V dV_A/dC_A^V}{C_B^V V_B + C_B^V dV_B/dC_B^V} \right] \quad (8)$$

where V_A and V_B are the constant volumes of the unit amounts used to define A and B. V_B^0 is the specific volume of pure B, and C_B^V and C_A^V are the concentrations of B and A in unit volume of solution. Two special properties simplify the description of diffusion in most zeolite systems; these are (a) $D_B = 0$ (and also $D_B = 0$); and (b) solutions of A and B, at least for zeolites with robust three-dimensional crystalline structures, have a virtually constant volume which is independent of the concentration of A and is equal to the volume of pure B. Under these conditions $V_B^0 = V_B$ and $C_B^V V_B = 1$ and equation (8) reduces to

$$D_{AB} = D_A. \quad (9)$$

This can be seen directly from the definition of the intrinsic diffusion coefficient of A as the diffusion of A relative to a section fixed so that there is no combined mass flow of A and B across it, but it is emphasized that the appropriate equation is equation (8) if conditions (a) and (b) above are not valid. If (a) and (b) do hold, diffusion in the two component systems can be represented by the two diffusion coefficients D_A and D_A^*. If chemical potential is assumed to be the driving force of the diffusion process the usual Darken relationship between them is

$$D_A^* = D_A \frac{d \ln a_A}{d \ln c_A} \quad (10)$$

where a_A and c_A are the activity and concentration of A respectively.

EXPERIMENTAL

(a) *Crystal and water samples*

The samples of heulandite and gmelinite used in sorption experiments were also employed in diffusion experiments. Two different chabazite samples, from the same geological source as chabazite A, were prepared as described previously.[6] Chabazite B was a single crystal weighing about 0·5 g and the chabazite C sample consisted of eight crystals weighing in total about 0·35 g. Samples of D_2O and H_2O used were also prepared as described in Part I.

(b) *Crystal surface area and size determinations*

External surface areas of the crystal samples were estimated in three ways. In the case of chabazite B and heulandite samples, a direct projection was traced of each crystal face and the total area summed, to give a direct projected area. An indirect projected area was obtained by using a travelling microscope to obtain length measurements in different directions on each crystal face.

These were plotted on an enlarged scale to give a magnified projection and this magnified area was summed and scaled down to give an estimate of the total surface area of each crystal. Thirdly for all crystal samples a regular shape to which the crystal(s) approximated was assumed. Then from the weight of the crystal(s) and their density, (which was determined pycnometrically) the volume and hence the surface area for the regular shape was calculated.

(c) *Apparatus*

Rates of H_2O sorption and of D_2O–H_2O exchange were followed gravimetrically using a modification of the apparatus used in sorption experiments.[6] In both types of experiment it was necessary to replace continually the water vapour around the crystal. This was achieved by passing a continuous stream of vapour with nitrogen as a carrier gas through the crystal sample. The sample was placed on a loose-mesh fibreglass bucket to allow easy flow of the N_2–H_2O stream round individual crystals. An inlet and outlet tube at the top and bottom of the balance case respectively allowed free passage of the nitrogen–water vapour stream. The inlet tube included a copper coil immersed in the balance case thermostat to ensure that the nitrogen–water vapour flow attained the balance case temperature. Incorporated into the outlet tube was a rotameter flow meter to measure the nitrogen flow rate. Water vapour was introduced into a dry nitrogen stream by passing the nitrogen through a series of four all-glass bubblers, the first containing distilled water and the remaining bubblers saturated potassium sulphate solutions. All four bubblers were placed in a thermostat tank with a temperature range 25–70°C. By adjusting the temperature of this tank a required water vapour pressure could be obtained. Within the limit of detection (i.e. the weight of a zeolite crystal with known H_2O sorption characteristics) the water vapour pressure was as predicted from saturated potassium sulphate–water vapour data[15] and was independent of time and flow rate (up to a maximum measured rate of 600 ml/min).

(d) *Rates of* H_2O *sorption*

Initially the procedure adopted for determining an H_2O isotherm point was followed, the pressure of H_2O surrounding the crystal being adjusted to give the required water content of the crystal. The inlet tube to the balance case was then opened to admit rapidly a different water vapour pressure in the nitrogen–water vapour stream. The nitrogen–water vapour flow was continued as the change in weight of the crystal was followed with time. Small corrections to the weight of the crystal were necessary for the buoyancy effect of the nitrogen–water vapour mixture and the slight pressure exerted on the crystal sample and bucket by the gas stream.

(e) D_2O–H_2O *exchange*

A similar procedure to that described for the rate of H_2O sorption was adopted in following D_2O–H_2O exchange, except that in this case the initial procedure was as in determining a D_2O isotherm point, and the H_2O vapour pressure in the nitrogen stream was adjusted to be equal to the D_2O vapour pressure initially surrounding the crystal. In some early experiments with chabazite B dry nitrogen was admitted to the balance case prior to the commencement of the nitrogen–water vapour flow. With this procedure some D_2O vapour was swept into the connecting tube so that on admitting the N_2–H_2O stream some direct H_2O sorption as well as exchange took place (see Results section). In subsequent experiments the N_2–H_2O stream was admitted directly to the balance case.

RESULTS

(a) *Rates of* H_2O *sorption and intrinsic diffusion coefficients*

The loss or gain of water by a zeolite can be described as shown earlier by an intrinsic diffusion coefficient of water in the crystal, if $D_B = 0$ and the volume of the crystal remains unchanged during sorption or desorption. For the crystals chabazite and gmelinite both conditions are effectively valid, but in the case of heulandite the thermal expansion of occluded water[6] and dehydration data[16] indicate the possibility of a small change in lattice dimension, normal to the plane of cleavage, with water content. However the Tiselius experiments[1,2] show that diffusion occurs predominantly parallel to this plane so that rates of sorption, at least for small increments of water can still be represented by an intrinsic diffusion coefficient.

Table 1. *Surface areas of zeolite crystals*

	Chabazite B	Heulandite	
		Area ‖ to (010) plane	Area ⊥ to (010) plane
Indirect projected area	2·60 cm²	2·02 cm²	2·00 cm²
Direct projected area	2·48 cm²	2·14 cm²	2·04 cm²
Area calculated assuming crystal to be a rectangular parallelopiped (2:2:1)	2·57 cm²		
Area calculated assuming cubic crystal	2·43 cm²		

Chabazite

The chabazite B crystal approximated in shape to a rectangular parallelopiped of sides 2:2:1, as indicated by the external surface areas shown in Table 1. This shape was assumed in calculating the intrinsic diffusion coefficient. It was further assumed that the crystal behaved isotropically and D was independent of water content in the rather small sorption range covered. The boundary and initial conditions for the sorption process are now constant initial concentration throughout the crystals and constant but different surface concentration for $t \geqslant 0$. The solution for this case is

$$(M_t/M_\infty)_{H_2O} = 1 - \text{R.H.S. of equation (3)}$$

$$\text{or (4)} = \frac{\Delta W_t}{\Delta W_\infty} \qquad (11)$$

where M_t is the amount of H_2O occluded in time t, M_∞ is the total H_2O increment, ΔW_t is the corresponding change in weight after time t and ΔW_∞ is the total change in weight associated with the increment M_∞. The value of D taken to represent the diffusion process was the value which

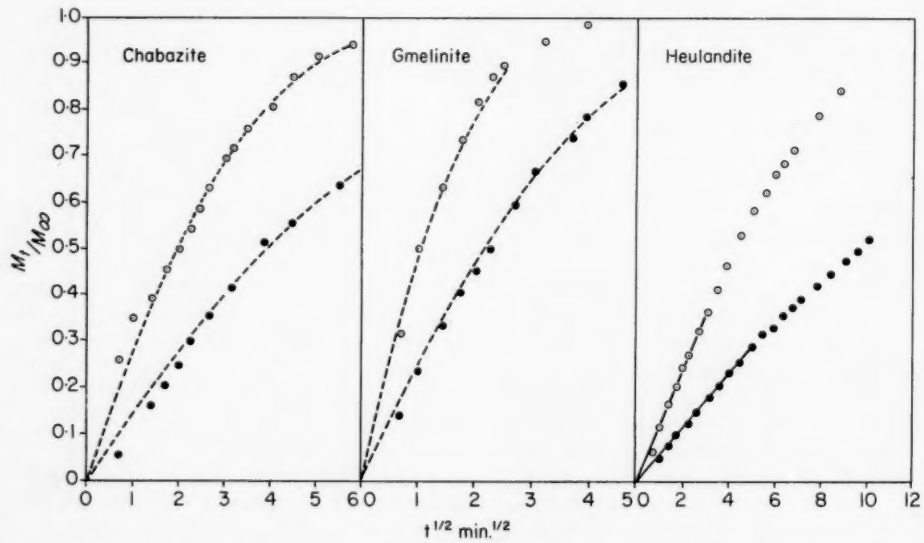

FIG. 2. Intrinsic diffusion: curve fit of calculated and experimental values of $(M_t/M_\infty)_{H_2O}$. – – – – – calculated, experimental: chabazite ⊙ 75·4°C, ● 30·8°C, gmelinite ⊙ 62·5°C, ● 31·7°C, heulandite –⊙– 77·8°C, –●– 37·4°C.

gave the best agreement between curves of $(M_t/M_\infty)_{H_2O}$ vs. $\sqrt{t}$ calculated from equation (11) and the experimentally determined points. Fig. 2 illustrates the curve-fit agreement achieved, and Fig. 3 shows the temperature dependence of D.

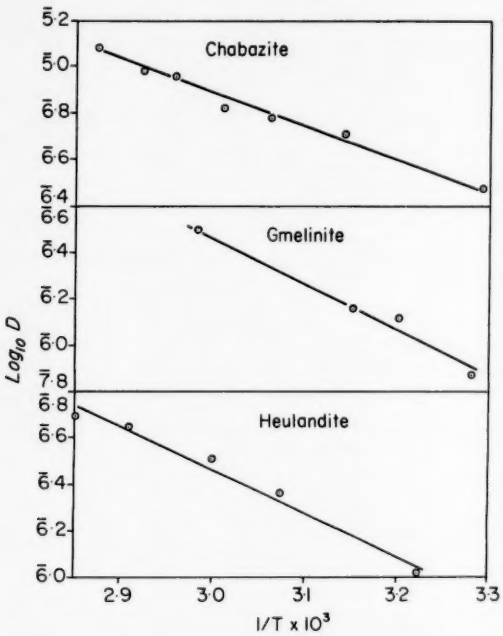

FIG. 3. Intrinsic diffusion plot of log D vs. 1/T.

The parameters D_0 and E associated with the usual Arrhenius equation

$$D = D_0 \exp\left(\frac{-E}{RT}\right) \qquad (12)$$

are given in Table 2.

Experiments were performed on crystals with water contents in the range x(g of H_2O/g dehydrated crystal) = 0·2626–0·2837. Within this range it was found that D (at constant T) was independent of (a) total water content, (b) total increment of H_2O up to the largest Δx value of 0·0108 and (c) nitrogen–water vapour flow rate.

In addition a single experiment was made using the chabazite C sample. Each crystal was assumed to be a rectangular parallelopiped of sides 2:2:1 and $(M_t/M_\infty)_{H_2O}$ was calculated as the sum of contributions from individual crystals. The measured value of D in this sample at 53·6°C was $4{\cdot}55 \times 10^{-6}$ cm^2 sec^{-1} compared with a value of $D = 6{\cdot}1 \times 10^{-6}$ cm^2 sec^{-1} measured at 53·9°C in chabazite B. A comparison of these values gives some measure of the reproducibility of the measured diffusion coefficients from one crystal sample to another.

Gmelinite

For the individual gmelinite crystals, isotropic diffusion, with D independent of water content a rectangular parallelopiped shape (2:2:1) was assumed. Intrinsic diffusion coefficients were calculated from the rates of sorption as for the chabazite C sample. The calculated curves of $(M_t/M_\infty)_{H_2O}$ vs. $\sqrt{t}$ are compared with those for $\Delta W_t/\Delta W_\infty$ in Fig. 2; Fig. 3 shows the temperature coefficients of D and Table 2 summarizes the results obtained in terms of the Arrhenius equation $D = D_0 \exp(-E/RT)$. Experiments were limited to lower temperatures because rates of sorption were too rapid to measure accurately at elevated temperatures. Within this temperature range, and for the narrow range in water content, no dependence of D on water content, water increment or nitrogen–water vapour flow rate was detected.

Heulandite

The experiments of TISELIUS on rates of water sorption in heulandite showed that diffusion normal to the cleavage plane, i.e. normal to the (010) plane is small, $< 0{\cdot}7 \times 10^{-12}$ cm^2. If diffusion

Table 2. Intrinsic diffusion coefficients

Crystal	D(at 45°C) (cm^2 sec^{-1})	D_0(cm^2 sec^{-1})	E(kcal/mole)
Chabazite B	$4{\cdot}8 \times 10^{-6}$	$1{\cdot}2 \times 10^{-3}$	$6{\cdot}7 \pm 0{\cdot}3$
Gmelinite	$1{\cdot}5 \times 10^{-6}$	$5{\cdot}6 \times 10^{-2}$	$8{\cdot}5 \pm 2{\cdot}0$
Heulandite	$1{\cdot}6 \times 10^{-6}$	$4{\cdot}9 \times 10^{-2}$	$8{\cdot}4 \pm 0{\cdot}4$

is confined solely to directions parallel to the (010) plane then equations (3) and (4) referring to isotropic media are no longer applicable. To interpret the present measurements, it is first assumed that the crystal behaves as a finite slab. Then with the present boundary conditions the appropriate equation for small times is

$$\frac{\Delta W_t}{\Delta W_\infty} = \left(\frac{M_t}{M_\infty}\right)_{H_2O} = 1 - \text{R.H.S. of equation (2)}$$

which reduces to

$$\frac{\Delta W_t}{\Delta W_\infty} = \left(\frac{M_t}{M_\infty}\right)_{H_2O} \approx \frac{2A}{V}\sqrt{\frac{Dt}{\pi}} \qquad (13)$$

as the term including *i*erfc is negligibly small for small values of M_t/M_∞. A is the area of the crystal normal to the direction(s) of diffusion, and V is the volume of the crystal. Even though the heulandite crystals are not slabs and diffusion probably occurs in more than one direction parallel to the (010) plane, equation (13) can be used as an approximation in the early stages of diffusion where deviation from the $\sqrt{t}$ law will be small. The deviation will be between curves 2 and 4 in Fig. 1. A is now the total projected crystalline area parallel to the (010) plane (see Table 1) and D describes a mean diffusion coefficient for diffusion parallel to this plane. Fig. 2 shows $\Delta W_t/\Delta W_\infty$ as a function of $\sqrt{t}$ and Fig. 3 gives the temperature dependence of D. Values of D_0 and E are given in Table 2.

The values obtained in the present study are somewhat larger than those reported by TISELIUS[1,2] for diffusion normal to the (201) plane. Extrapolation of the log $D - 1/T$ plot gives a value of 5×10^{-7} cm^2 sec^{-1} compared with the value of 4×10^{-7} cm^2 sec^{-1} at 30°C reported by TISELIUS. The activation energies of diffusion reported by TISELIUS of 5·4 kcal/mole normal to the (201), and 9·1 kcal/mole normal to the (001) plane are both lower and slightly higher than the present mean value of 8·4 kcal. Detailed comparisons between the two sets of measurements cannot be made because we have measured the mean diffusion coefficient and TISELIUS measured the diffusion coefficients in two specific directions. Other factors which may contribute to differences in measured values include differences in the crystal samples. Evidence for this is indicated by the fact that the results of TISELIUS quoted above related to a heulandite sample of maximum water content $x_{sat} = 0{\cdot}1967$, compared with a value of $x = 0{\cdot}1901$ for the present sample. There is also the possibility that dehydration of the crystal to a value of $x/x_{sat} < 0{\cdot}5$ in the Tiselius experiments and subsequent sorption of relatively large increments of water, with a corresponding thermal flux associated with the heat of sorption, has some effect on the diffusion coefficients.

D_2O–H_2O *exchange and self-diffusion coefficients*

The change in weight associated with D_2O–H_2O exchange cannot be immediately attributed to a direct D_2O–H_2O molecular exchange process, since this change measures only a flux of deuterium-containing water leaving the crystal or of hydrogen-containing water entering the crystal. To interpret the process in terms of a single self-diffusion coefficient it is necessary to assume that the "excess" molar amount of deuterium arising from the slightly different sorptive properties of D_2O and H_2O is proportional to the deuterium concentration at any point. This is a correct assumption if the two isotopic species form an ideal solution in the crystal, and, as the molar excess is in any case small, deviation from ideality will have little influence on interpretation of the exchange process.

If D_H describes the diffusion of hydrogen (contained in the water) into the crystal and D_D the diffusion of deuterium out of the crystal as a result of the exchange process, then to describe a self-diffusion coefficient D^*, we must have $D_H = D_D = D^*$. This must be true for a diffusion process involving direct atom–atom, ion–ion, or molecule–molecule exchange, but is not necessarily strictly valid for vacancy or interstitial mechanisms. The coefficient D^* will be referred to as the self-diffusion coefficient of water in the crystal. It does not necessarily imply that the deuterium–hydrogen exchange process involves molecules as units. It is further assumed that D^* is independent of isotopic concentration. For all crystals the approximate crystal shape was that described in the evaluation of intrinsic diffusion coefficients from rates of H_2O sorption. Experiments were carried out for water contents near to saturation.

Chabazite

If the loss of deuterium in the crystal is

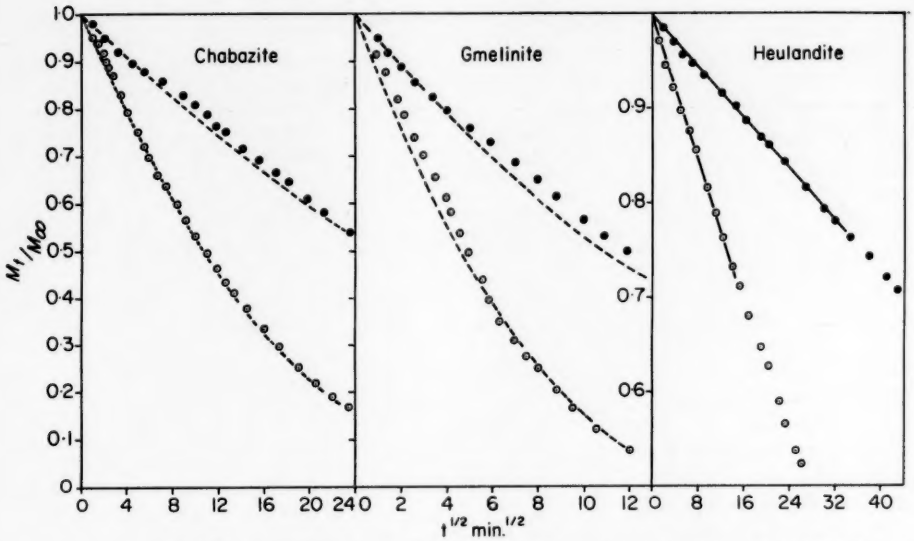

FIG. 4. Self-diffusion: curve fit of calculated and experimental values of $(M_t/M_\infty)_{D/H}$. ----- calculated, experimental: chabazite ⊙ 75·0°C, ● 31·4°C, gmelinite ⊙ 76·9°C, ● 31·7°C, heulandite -⊙- 76·1°C, -●- 36·1°C.

Vol. 21
1961

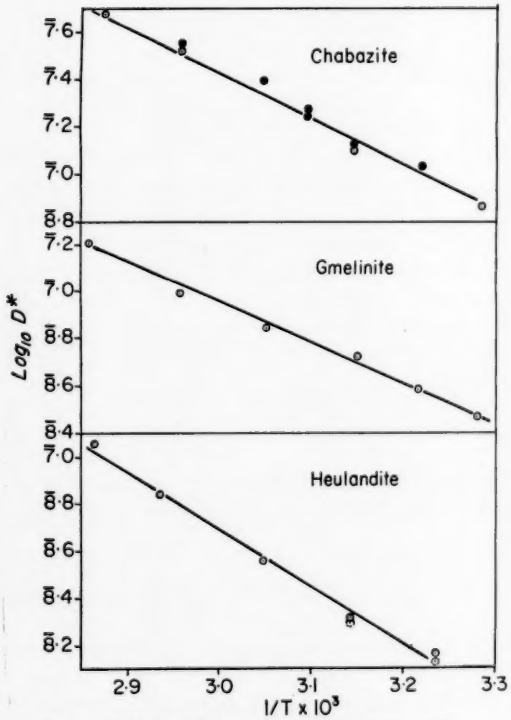

FIG. 5. Self-diffusion: plot of log D^* vs. $1/T$.

considered when the initial and boundary conditions are constant deuterium concentration throughout the crystal and zero surface deuterium concentration respectively, then the solution of the diffusion equation is given by equations (3) or (4). That is

$$\left(\frac{M_t}{M_\infty}\right)_{D/H} = \text{R.H.S. of equations (3) or (4)}$$

$$= 1 - \frac{\Delta W_t^*}{\Delta W_\infty^*} \qquad (14)$$

where ΔW_t^* is the loss in weight of the crystal after time t, and ΔW_∞^* is the total loss in weight of the crystal, i.e. $(x_{D_2O} - x_{H_2O})X$. x_{D_2O} and x_{H_2O} are the D_2O and H_2O water contents of the crystal, in g per g of dehydrated crystal, at the experimental water vapour pressure and temperature. X is the weight of the dehydrated crystal sample used. Appropriate values of x_{D_2O} and x_{H_2O} were determined from equilibrium sorption experiments. D was determined as for intrinsic diffusion coefficients, by comparison of calculated curves of $(M_t/M_\infty)_{D/H}$ with experimental curves of $(1 - \Delta W_t^*/\Delta_\infty^*)$ vs. $\sqrt{t}$. Typical examples are illustrated in Fig. 4. Fig. 5 shows the temperature dependence of D^* and Table 3 gives values of the

Table 3. Self-diffusion in zeolites

Crystal	D^*(at 45°C) (cm² sec⁻¹)	D_0^*(cm² sec⁻¹)	E^*(kcal/mole)
Chabazite B	$1{\cdot}26\times10^{-7}$	$1{\cdot}2\times10^{-1}$	$8{\cdot}7\pm0{\cdot}3$
Gmelinite	$5{\cdot}4\times10^{-8}$	$2{\cdot}0\times10^{-2}$	$8{\cdot}1\pm0{\cdot}3$
Heulandite	$2{\cdot}07\times10^{-8}$	$7{\cdot}6\times10^{-1}$	$11{\cdot}0\pm0{\cdot}3$

Self-diffusion in water and ice

	D^*(cm² sec⁻¹)	D_0^*(cm² sec⁻¹)	E^*(kcal/mole)
Water	$3{\cdot}87\times10^{-5}$ (45°C)	$5{\cdot}6\times10^{-2}$	4·6 (Ref. 22)
Ice	$1{\cdot}0\times10^{-10}$ (−2°C)		(Ref. 20)

pre-exponential parameters D_0^* and activation energy of self-diffusion.

As mentioned previously, in some of the early chabazite experiments a known increment of H_2O direct sorption took place in addition to the exchange process. Using the experimentally determined values of the intrinsic diffusion coefficient equations (11) and (14) were combined and D^* again evaluated from the best curve fit. Fig. 4 indicates that values obtained in this way are compatible with the normal case where no direct H_2O sorption takes place.

The measured self-diffusion coefficients were reproducible over the full time of the experiments; they were independent of N_2–H_2O flow rate confirming that the observed diffusion coefficients relate to diffusion in the crystal and not to vapour phase controlled diffusion. This is also evident from the form of the curves of $(1-\Delta W_t^*/\Delta W_\infty^*)$ vs. $\sqrt{t}$. The results (see Table 5) also indicate that within the narrow concentration range studied there is no marked dependence of D^* on total water content.

Values of the self-diffusion coefficient of water obtained by PEMSLER[3] in chabazite varied between $2{\cdot}2\times10^{-7}$ cm² sec⁻¹ and $4{\cdot}1\times10^{-7}$ cm² sec⁻¹ at 60°C depending on the crystal size. These values are similar to the value of $2{\cdot}8\times10^{-7}$ cm² sec⁻¹ obtained in this study. Close agreement is not to be expected, first because some variation in D^* between different crystal samples is likely and secondly because PEMSLER made the assumption that the crystals were spherical and all the same size.

Gmelinite

Self-diffusion coefficients of water were calculated in a similar way to that described above for Chabazite B except that as in the case of intrinsic diffusion $(M_t/M_\infty)_{D/H}$ was calculated as the sum of contributions from each member of the crystal sample. The agreement between experimental and calculated curves is only moderately satisfactory (Fig. 4). Reduction of the N_2–H_2O flow rate 3–4 times had no significant effect on the shape of the curve or the value of D^* evaluated from it, thus discounting the possibility that the water vapour in close contact with the crystal was not 100 per cent H_2O rich in the initial stages of the exchange process. However, agreement between calculated and experimental curves may be affected if

(i) there are differences in shape between individual crystals, so that the assumed shape is not the best for every crystal, and

(ii) the crystals are anisotropic.

Gmelinite is hexagonal in structure so that some diffusion anisotropy would be expected. Experimental results are summarized in Fig. 5 and Table 3. As with chabazite B there is no significant dependence of D^* on total water content (Table 5).

Heulandite

Self-diffusion coefficients for heulandite were evaluated, as in the case of the intrinsic diffusion coefficients, by assuming the $\sqrt{t}$ law appropriate for diffusion in a finite slab. Diffusion normal to the (010) plane was again assumed to be negligible as shown by TISELIUS[1,2]. The appropriate

equation becomes

$$\left(\frac{\Delta M_t}{\Delta M_\infty}\right)_{D/H} = \text{R.H.S. of equation (13)}$$

$$= 1 - \frac{\Delta W_t^*}{\Delta W_\infty^*}$$

$(1-\Delta W_t^*/\Delta W_\infty^*)$ is shown as a function of $\sqrt{t}$ in Fig. 4. The plot of log D^* against $1/T$ is given in Fig. 5, and values of D^* and E^* in Table 3. PEMSLER[3] gives values of D^* at the saturation water content for heulandite of $1{\cdot}3\times10^{-10}$, $2{\cdot}0\times10^{-10}$ cm^2 sec^{-1} at 30°C, the increase being associated with an eight-fold decrease in crystal size. These values are 25–100 times less than ours. One probable reason for the disparity lies in the anisotropic diffusion behaviour of heulandite. PEMSLER, apart from assuming the crystals to be spherical, calculated diffusion coefficients assuming diffusion across the whole surface area of the crystal. Since diffusion is relatively very slow normal to the (010) plane and if the ratio of surface area parallel to the (010) plane (A_1) to the area normal to the plane (A_2) was in his heulandite crystals between 4 and 10 then this would account for the difference. Such ratios are possible for PEMSLER describes the crystals as "thin flat parallelopipeds". He further states that nearly perfect cleavage was observed along the c-axis, i.e. parallel to the (010) plane when the size of the crystals was reduced. The implication is that reduction of the crystal size resulted in a greater increase in A_1 than A_2. This, with slow diffusion normal to A_1, would result in the measured value of D^* being greater for the large crystals as he observed.

A feature of the measured D^* values in heulandite is that unlike chabazite and gmelinite, heulandite shows a considerable dependence of D^* on total water content, as Table 5 shows. This effect is discussed below.

Errors

Both systematic and non-systematic errors affect the evaluation of diffusion coefficients. An error of the former type arises from an assumption of a regular shape for the crystal. For example the values of D for chabazite would be about 20 and 60 per cent larger if the crystals had been assumed to be cubic and spherical respectively. Surface roughness will also affect the rate of sorption though this effect may not be large, for as diffusion proceeds the concentration contours will be smoothed out minimizing the effect of irregularities. In heulandite a systematic error may be introduced in the area measurements.

Non-systematic errors arise from spring reading errors, and the uncertainty in D from curve fitting. In intrinsic diffusion in gmelinite and chabazite C there is some uncertainty in the time measurements. Reasonable estimates of the systematic errors are chabazite B ± 15 per cent, heulandite ± 5 per cent, gmelinite ± 20 per cent. Maximum non-systematic errors in individual measurements are estimated for self-diffusion coefficients as: chabazite B ± 5–10 per cent, heulandite ± 5 per cent, gmelinite ± 10 per cent. For intrinsic diffusion the respective values are ± 5–10 per cent, ± 5 per cent, ± 15–20 per cent, with a total systematic and non-systematic error of about ± 30 per cent for chabazite C.

DISCUSSION

(a) *The relationship between D^* and D*

Equation (10) relating intrinsic and self-diffusion coefficients is valid only if the intrinsic mobilities for both self-diffusion and intrinsic diffusion of water are equal. Where equation (10) is valid it is thus implied that the mechanisms for the two diffusion processes are the same. Actual or interpolated values of D, D^* and $d\ln a/d\ln c$ were used in compiling Table 4 which indicates how the present experimental data fit this relationship. $d\ln a/d\ln c$ was obtained from equilibrium sorption measurements,[6] and this term largely accounts for the difference between the two sets of diffusion coefficients. The Darken relationship may not hold exactly, even if the mechanism for diffusion is the same in both types of diffusion, because intrinsic diffusion may be non-Fickian because of the importance of terms higher than $\partial c/\partial x$.[17] Another factor which could be important is that in intrinsic diffusion there is a heat flow coupled with the occlusion of the H_2O molecules. This arises from the liberation of the heat of sorption (~14 kcal/mole), and may be one reason why D is consistently larger than D^* ($d\ln a/d\ln c$). Experiments in which D was found to be independent, within the narrow range studied, of the magnitude of the H_2O

Vol. 21
1961

Table 4

	Temp. (°C)	$D^* \times 10^8$ (cm² sec⁻¹)	$\frac{d \log a^{\ddagger}}{d \log c}$	$D^*\left(\frac{d \log a}{d \log c}\right) \times 10^6$ (cm² sec⁻¹)	$D(\text{expt}) \times 10^6$ (cm² sec⁻¹)
Chabazite B	75	46·2	23·0†	10·65	11·7
	65	31·8	24·0†	7·60	8·9
	55	21·4	25·5†	5·45	6·6
	45	14·1	27·0†	3·80	4·8
	35	9·0	28·0†	2·50	3·4
Heulandite	75	9·77	30·0	3·00	4·9
	65	6·07	32·0	1·95	3·5
	55	3·70	34·0	1·26	2·4
	45	2·19	35·5	0·780	1·6
	35	1·24	37·0	0·465	1·05
Gmelinite	55	7·33	26·5	1·95	2·3
	45	4·99	28·0	1·40	1·5
	35	3·31	29·5	0·97	1·0

† Values obtained for chabazite A.[6]

‡ Value over region of flat maximum (Part I).

increment, and thus of the total heat flow, seem to rule out this possibility. A third factor which may influence the relationship in the observed way, concerns the nature of the measured D^*. This is a mean diffusion coefficient related to deuterium–hydrogen exchange. Higher heats of D_2O sorption, and the larger mass of diffusing deuterium-containing water molecules or ions, compared with H_2O, suggest that the measured diffusion coefficients may be smaller than true self-diffusion coefficients of H_2O in the crystals. Finally for intracrystalline diffusions the equation 10 should be replaced by

$$D = D^* \frac{d \ln a}{d \ln c_i}$$

where c_i is the concentration of the intracrystalline water, whereas c is the sum of c_i and of the concentration c_a of water sorbed upon external surfaces of crystallites. As the intracrystalline free volume becomes nearly saturated c_a may begin to increase more rapidly than c_i so that

$$\frac{d \ln a}{d \ln c_i} > \frac{d \ln a}{d \ln c}.$$

Indeed $d \ln a / d \ln c_i$ should in the limit tend towards infinity whereas Fig. 2 of Part I shows that $d \ln a / d \ln c$ increases to a flat maximum and then decreases. It is to be expected therefore that $D^*(d \ln a / d \ln c)$ will begin to become less than D once dc_a/dc_i becomes appreciable.

Taking into account all these considerations, together with experimental error, the relative validity of the Darken equation suggests that the diffusion process is predominantly the same for both intrinsic and self-diffusion, though some reservations should be held in the case of heulandite. This restricts the diffusion mechanism to one involving discrete water molecules, for intrinsic diffusion involves the transport of water molecules. Since they would not contribute to intrinsic diffusion direct molecular place exchanges are eliminated, together with molecule–ion exchanges, such as

$$H_3O^+ + D_2O \rightarrow H_2O + D_2OH^+ \rightarrow H_2OD^+ + DOH$$

Processes involving the simultaneous transport of H^+ or D^+ with OH^- and OD^- are not strictly eliminated but must be considered unlikely. Specific diffusion processes which can be considered are thus either molecule–vacancy exchange,

or interstitial in type, or both. It is relevant that extensive self-diffusion experiments in liquid water[19,21,22] indicate a molecular diffusion process as does a single experiment with ice near its melting point.[20]

*Concentration dependence of D**

It is unlikely that the diffusion of water in these crystal systems takes place by one diffusion mechanism only. The water has fluid-like properties, and clusters of molecules exist in each of a large number of interconnected cavities in, for example, the chabazite and gmelinite structures.[23] Diffusion of molecules involves, at some stage, their escape through "windows" of considerably smaller diameter than that of the cavities which they join. The mobility of water molecules may be governed either by their rate of escape through such windows, or by molecule exchanges with holes in the clusters. Molecule–hole exchanges would be expected to give D^* dependent upon the product of the amount sorbed, x, and of some function of the free volume V_f, i.e.

$$D^* \propto xf(V_f).$$

The rate of escape of molecules through the windows would also be expected to depend on x and on a function of the free volume, since the chance of a molecule striking the target area of a window being reflected back by collision with water molecules on its far side should depend on V_f. Therefore, two factors operate, one of which reduces D^* as $x/x_{sat} \rightarrow 1$ and the other of which increases it. It might be expected that, as the intracrystalline volume becomes more tightly packed with water molecules, molecular migration would be more difficult, i.e. $f(V_f)$ would tend to dominate. However, the data in Table 5 suggest a trend in the opposite direction.

The statistical–kinetic treatment of diffusion gives approximately[24]

$$D^* = d^2 \nu \rho_f \left(\frac{E_0}{RT}\right)^{f-1} \frac{1}{(f-1)!} \exp - E_0/RT$$

where E_0, the total energy of activation, is related to the Arrhenius energy, E, by $E_0 = E+(f-1)RT$, the energy E_0 being distributed in f degrees of freedom. ρ_f is a factor expressing the need for co-operation between directions of movement of the oscillators sharing E_0, and is therefore < 1. d is the average jump distance per unit act of diffusion and ν the average vibration frequency of the diffusing molecule relative to its environment. The parameters d, ρ_f, f, E and ν could all depend upon x or upon V_f. It has for instance been found that ν tends to increase as x increases.[25] d could either decrease, if it depended on free volume, or it could represent the nearly constant distance between neighbouring sites in "ice-like" water clusters. ρ_f might in turn decrease as the packing density of water molecules increased.

*Table 5. Concentration dependence of D**

I(°C)	x/x_{sat}	D^*(cm^2 sec^{-1})
	Chabazite B	
75·00	0·976	4·85
75·00	0·939	4·17
75·00	0·913	4·39
	Gmelinite	
76·90	0·978	16·1
76·90	0·944	15·4
76·90	0·916	14·8
	Heulandite	
76·10	0·984	11·40
76·10	0·952	9·67
76·10	0·918	8·29

Evidently then no firm theoretical conclusion can be drawn regarding the trend of D^* as $x/x_{sat} \rightarrow 1$, or as to the dominant molecular mechanism. Lattice changes may play a further part in determining the x-dependence of D^*, especially in the case of heulandite. In this case, if the diffusion is predominantly controlled by the framework spacing normal to the (010) plane, then an increase in this spacing could increase D^*.

Values of D_0^* and E

The pre-exponential factor D^* given in Table 3, allows a calculation of the entropy of activation

ΔS^* as

$$D_0^* = \frac{kT}{h} \times 2{\cdot}72\, d^2 \exp\left(\frac{\Delta S^*}{R}\right)$$

where k and h are Boltzmann and Planck constants respectively, $R = 1{\cdot}98$ cal mole^{-1} deg^{-1} and d is the distance in each single diffusion process. Assuming a jump distance of 3·0 Å, ΔS^* is $+4{\cdot}0$ cal mole^{-1} deg^{-1} for chabazite, $+0{\cdot}5$ cal mole^{-1} deg^{-1} for gmelinite, and $+7{\cdot}5$ cal mole^{-1} deg^{-1} for heulandite compared with a value of $+2{\cdot}5$ cal mole^{-1} deg^{-1} for water. These values with those given in Table 3 show that the self-diffusion coefficients of water in zeolites are lower than in liquid water primarily because of the higher activation energy of the diffusion process, for the entropy values appear to be similar. Without detailed knowledge of the diffusion mechanism it is not possible to speculate on the reasons for the higher activation energy, though the "confining" effect of the aluminosilicate framework is likely to be important.

CONCLUSIONS

The similarity in properties of chabazite and gmelinite crystals, and the lamellar character of heulandite noted in equilibrium sorption measurements, is further substantiated in these diffusion studies. The diffusion results indicate a rather narrow range of values for self-diffusion coefficients of water in the three different zeolite crystals. All self-diffusion coefficients measured are intermediate in magnitude between corresponding values at the same temperature for liquid water and ice just below its melting point. Although a detailed model of the diffusion process has yet to be proposed, and the concentration dependence of D^* to be explained, present evidence favours a mechanism involving molecules diffusing as units. Further progress may depend on the development of an experimental technique to study diffusion coefficients at lower total water contents.

REFERENCES

1. Tiselius A., *Z. Phys. Chem.* **A169,** 425 (1934).
2. Tiselius A., *J. Phys. Chem.* **40,** 223 (1936).
3. Pemsler P., Thesis, New York University, *Diss. Abs.* **18,** 2005 (1958).
4. Kraft H., *Z. Phys.* **110,** 303 (1938).
5. Wel Y. K. and Bernstein R. B., *J. Phys. Chem.* **63,** 738 (1959).
6. Barrer R. M. and Fender B. E. F., preceding paper.
7. Barrer R. M., *Trans. Faraday Soc.* **45,** 358 (1949).
8. Barrer R. M. and Brook D. W., *Trans. Faraday Soc.* **49,** 1040 (1953).
9. Barrer R. M. and Falconer J. D., *Proc. Roy. Soc.* **A236,** 227 (1956).
10. Barrer R. M., *Diffusion in and through Solids.* Cambridge University Press (1941).
11. Crank J., *Mathematics of Diffusion.* Oxford University Press (1956).
12. Carslaw H. S. and Jaeger J. C., *Conduction of Heat in Solids,* (2nd ed.). Oxford University Press (1959).
13. Jain S. C., *Proc. Roy. Soc.* **A243** 359 (1957).
14. Barrer R. M., *J. Phys. Chem.* **61,** 178 (1957).
15. *International Critical Tables,* McGraw-Hill, New York (1953).
16. Wyart J., *C.R. Acad. Sci., Paris* **191,** 1343 (1930).
17. Le Claire A. D., *Phil. Mag.* **3,** 921 (1958).
18. Hartley G. S. and Crank J., *Trans. Faraday Soc.* **45,** 801 (1949).
19. Wang J. H., *J. Amer. Chem. Soc.* **73,** 4181 (1951).
20. Kuhn W. and Thurkauf M., *Helv. Chim. Acta.* **41,** 938 (1958).
21. Douglass D. G. and McCall D. W., *J. Chem. Phys.* **31,** 569 (1959).
22. Wang J. H., Robinson C. V. and Edelman I. S., *J. Amer. Chem. Soc.* **75,** 466 (1953).
23. Barrer R. M. and Kerr I. S., *Trans. Faraday Soc.* **55,** 1915 (1959).
24. Barrer R. M., *Trans. Faraday Soc.* **38,** 322 (1942).
25. Barrer R. M. and Reucroft P. J., *Proc. Roy. Soc.* **A258,** 431 (1960).

Vol. 2
196

J. Phys. Chem. Solids Pergamon Press 1961. Vol. 21, Nos. 1/2, pp. 25–32. Printed in Great Britain.

THE CRYSTAL CHEMISTRY OF SOME GERMANIUM GARNETS*

A. TAUBER and C. G. WHINFREY

U.S. Army Signal Research and Development Laboratory, Fort Monmouth, New Jersey

and

E. BANKS

Polytechnic Institute of Brooklyn, Brooklyn, New York

(*Received* 26 *January* 1960; *revised* 23 *March* 1961)

Abstract—Germanium-containing compounds isostructural with naturally occurring silicate garnets have been synthesized dry and at 1 atm of steam by solid state reaction. The general formula for these compounds is $A_3B_2Ge_3O_{12}$ in which A is divalent Cd, Ca or Mn, and B is trivalent Fe, Al, Cr, Sc or Ga. Of these possible combinations only $Mn_3Sc_2Ge_3O_{12}$ and $Ca_3Ga_2Ge_3O_{12}$ could not be prepared in this investigation. X-ray fluorescence analysis indicates that most of the compounds contain less than the stoichiometric amount of Ge. Reaction studies from 800°C to the melting points revealed several phases which could not be identified. Several of the compounds yielded glasses upon quenching of their melts.

The determination of cation distribution in $Ca_3Al_2Ge_3O_{12}$ based on intensity data from X-ray diffraction was inconclusive.

INTRODUCTION

SINCE the discovery of ferrimagnetic ferrogarnets, the investigation of compounds isostructural with garnet has been pursued in several laboratories. GELLER has recently reviewed our present knowledge of the crystal chemistry and its relation to magnetic interactions in garnets.[1] He has formulated some rules governing the substitution and ionic site preferences in these compounds.

The magnetic rare-earth garnets are isostructural with the mineral orthosilicate garnet of general formula $A_3^{2+}B_2^{3+}Si_3^{4+}O_{12}$ (space group $Ia3d = O_h^{10}$). There are eight formula units to a unit cell, totalling 160 atoms.

The first successful synthesis of a garnet with a trivalent cation in tetrahedral coordination was accomplished by YODER and KEITH[2], who synthesized $Y_3AL_2Al_3O_{12}$. ABRAHAMS and GELLER[3] have refined the grossularite ($Ca_3Al_2Si_3O_{12}$) structure and found that the oxygen tetrahedra and octahedra are more regular in the silicate than in yttrium iron garnet although the CaO_8 dodecahedra are less regular in grossularite than are the YO_8 dodecahedra in yttrium iron garnet. The presence of a trivalent cation (Fe^{3+})[4,5,6] approximately 50 per cent larger than Si^{4+} in the tetrahedral site, suggested some variability in the size and charge of cations which might occupy that position. Consequently the substitution of Ge^{4+} for the slightly smaller Si^{4+} in tetrahedral coordination seemed quite possible on the basis of size, charge, and electronic configuration.

An investigation of garnets, in which tetravalent germanium is expected to occupy the tetrahedral position, was undertaken. The crystal chemistry of these garnets was compared with that of other garnets to learn more about the magnetic interactions. The initial stages of this work have been reported.[7,8]

* Presented at the Meeting of the Electronics Division, American Ceramic Society, Detroit, Michigan, 23–25 September 1959. (Part of this material was condensed from Mr. Tauber's thesis submitted in partial fulfillment of the requirements for the Degree of Master of Science in Chemistry at the Polytechnic Institute of Brooklyn, June 1959.)

EXPERIMENTAL PROCEDURES

1. *Sample preparation*

The syntheses of germanium garnets were accomplished by solid state reaction between oxides. The general methods of preparation are described elsewhere.[7,8] In addition to an air atmosphere, oxygen, nitrogen, and steam atmospheres were employed in preparing some of the samples used in this study. The reactions of most of the compositions were examined from 800°C to the melting point at 100° intervals.

2. *X-ray diffraction measurements*

X-ray photographs (Debye–Scherrer) of all samples were prepared. Lattice constants, d spacings, and intensity measurements (I/I_1) were obtained using a Geiger-counter diffractometer. Filtered FeK radiation was used on all the samples containing Fe. Filtered CuK radiation was used occasionally on samples containing no Fe. The diffractometer traces were calibrated with a silicon standard before and after scanning and were read according to the method of DONNAY[9]. The reported lattice constants were obtained by extrapolation of a_0 vs. $\frac{1}{2}(\cos^2\theta/\sin\theta+\cos^2\theta/\theta)$.[10]

3. *Melting points*

A strip heater, similar to one described by KEITH and ROY[11] was used to observe the melting points of the compounds. Temperatures were measured with an optical pyrometer, which was calibrated with Ag, Au, Ni, and Pt.

4. *X-ray fluorescence analysis*

In comparison to some of the reaction temperatures employed in this study, hexagonal GeO_2 has a low melting point (1115°C). Furthermore, when GeO_2 is exposed to water vapor at elevated temperatures the volatility increases,[12] which makes it important to ascertain whether any of the compounds which may form are non-stoichiometric with respect to GeO_2. Samples were analyzed by means of a standard Norelco X-ray fluorescence analysis unit. Calibration curves bracketing the compositions of GeO_2 used were prepared from unfired mixtures, diluted with starch if the sample had been diluted; the latter was done where insufficient sample material was available.

DISCUSSION

1. *Reactions attempted*

Germanium-containing garnets were successfully synthesized in thirteen different reactions. Their composition, lattice constant and color are given in Table 1. Although some of the lattice constants were previously reported, they are given here for the sake of completeness. Of these synthetic garnets, all of which are analogues of the mineral garnets, were prepared with the exception of those corresponding to almandite ($Fe_3Al_2Si_3O_{12}$) and pyrope ($Mg_3Al_2Si_3O_{12}$). ROY and GENTILE[13] could not prepare $Mg_3Al_2Ge_3O_{12}$ by hydrothermal reaction between constituent oxides at 800°C and 15,000 p.s.i. It is possible that this compound could be formed at higher pressures. $Mn_3Sc_2Ge_3O_{12}$ and $Ca_3Ga_2Ge_3O_{12}$ did not form under the experimental conditions employed in this study. Recently, $Ca_3Ga_2Ge_3O_{12}$ was prepared by hydrothermal means.[14]

The five garnets synthesized with Cd^{2+} in the dodecahedral position, as well as all those with Ga^{3+} and Sc^{3+}, do not have silicate analogues in nature. Divalent cadmium, intermediate in radius between divalent manganese and calcium, would be expected to exist in eight-fold coordination. ROY and GENTILE[13] have prepared $Cd_3Al_2Si_3O_{12}$ dry, and $Cd_3Cr_2Si_3O_{12}$, $Ca_3Fe_2Si_3O_{12}$, and $Ca_3Ga_2Si_3O_{12}$ hydrothermally. HUMMEL[15], GELLER and MILLER[16], GLASSER and OSBORN[17], and GLASSER[18] have all claimed the synthesis of uvarovite, $Ca_3Cr_2Si_3O_{12}$, from the dry oxides at atmospheric pressure and temperatures between 800°C and 1400°C.

GELLER and MILLER[19] have reported that they did not obtain $Mn_3Fe_2Si_3O_{12}$ and $Mn_3Cr_2Si_3O_{12}$ in syntheses carried out at atmospheric pressure. They did succeed, however, in partially replacing Al^{3+} by Fe^{3+} in $Mn_3Al_2Si_3O_{12}$.

In the present study, attempts to place Ni^{2+} and Co^{2+} in eight-fold coordination resulted primarily in spinel formation. Garnets with Ni^{2+} and Co^{2+} occupying only such positions are probably unstable at low pressures because of the small size of these ions. This is also the case with Mg^{2+} and Fe^{2+}. The replacement of Ge^{4+} by Sn^{4+} in $Ca_3Cr_2Ge_3O_{12}$ did not lead to a garnet, although GELLER and MILLER[21] have synthesized $Ca_3Fe_2Sn_3O_{12}$. BOZORTH and GELLER[22] and GELLER *et al.*[23] have shown that Sn^{4+} ion has a

Table 1. *Synthetic end-member garnets*

No. batch composition	Lattice constant in Å		Color
	Experimental	Calculated	
1. $3CaO+Cr_2O_3+GeO_2$	12·265 ± 0·004 [12·262][14]	12·262	Green
2. $3CaO+Fe_2O_3+3GeO_2$	12·312 ± 0·004 [12·320 ± 0·004][20] [12·325][14]	12·322	Tan–gray
3. $3CaO+Al_2O_3+3GeO_2$	12·120 ± 0·003 [12·12 ± 0·01][20] [12·117][14]	12·112	White
4. $3CaO+Sc_2O_3+3GeO_2$	12·504 ± 0·003	12·496	White
5. $3CaO+Ga_2O_3+3GeO_2$	(12·251)[14]	12·281	
6. $Mn_3O_4+Cr_2O_3+3GeO_2$	12·027 ± 0·003 [12·027 ± 0·003][20]	12·032	Green
7. $Mn_3O_4+Fe_2O_3+3GeO_2$	12·087 ± 0·004 [12·087 ± 0·003][20]	12·087	Light-brown
8. $Mn_3O_4+Al_2O_3+3GeO_2$	11·901 ± 0·004 [11·902 ± 0·005][20] [11·91 ± 0·01][13]	11·895	Rose-beige
9. $Mn_3O_4+Ga_2O_3+3GeO_2$	12·043 ± 0·004(12·043)*	12·046	Beige
10. $Mn_3O_4+Sc_2O_3+3GeO_2$		12·245	
11. $3CdO+Cr_2O_3+3GeO_2$	12·213 ± 0·003	12·216	Green
12. $3CdO+Fe_2O_3+3GeO_2$	12·261 ± 0·003	12·273	Yellow–beige
13. $3CdO+Al_2O_3+3GeO_2$	12·077 ± 0·004	12·073	White
14. $3CdO+Sc_2O_3+3GeO_2$	12·447 ± 0·003	12·438	White
15. $3CdO+Ga_2O_3+3GeO_2$	12·191 ± 0·003 (12·189)*	12·230	White

* Reaction carried out in a sealed quartz tube.

great preference for octahedral sites in garnets. Because Cr^{3+} ion has an even greater preference for octahedral sites and because it is much smaller than Sn^{4+} ion, there would be little likelihood of the formation of a garnet of formula $Ca_3Cr_2Sn_3O_{12}$. However, it is not impossible that some Sn^{4+} ion could be substituted for the Ge^{4+} ion.

2. *Reactions as a function of temperature*

The first appearance of a garnet phase generally occurred at approximately 900°C in the thirteen compositions investigated (Table 2). Near 1100°C, the reactions were almost complete. For reaction temperatures near 1200°C, the X-ray diffraction patterns usually showed that garnet was the only phase present. The course of the reaction could be followed qualitatively by observation of the colored reaction products. The concentration of phases was estimated from the intensities of powder diffraction lines.

If either Cd^{2+} or Mn^{2+} was a constituent in a given reaction, a spinel phase was frequently identified as an intermediate phase at low temperatures. At higher temperatures it usually disappeared.

The appearance of new and unidentified phases in the course of many of the reactions is not surprising. Little is known about the solid state chemical reactions between GeO_2 and other oxides. The possible binary products formed in reactions between GeO_2 and most of the oxides employed in this study have not been extensively investigated. The appearance of extra phases in the present experiments is probably enhanced by the loss of volatile oxides such as GeO_2, CdO, and Ga_2O_3. Extra phases may also arise as a result of failure to maintain equilibrium, as well as changes in metal–oxygen ratios in those cases involving transition metals.

The unidentified phases appearing in the preparation of the compounds $Mn_3Fe_2Ge_3O_{12}$ and $Cd_3Fe_2Ge_3O_{12}$ at elevated temperatures are strongly attracted to a magnet. In an earlier paper (TAUBER *et al.*[7]) we described some samples of $Mn_3Fe_2Ge_3O_{12}$ as ferrimagnetic; the observed magnetism, however, should be attributed rather to the co-existing, unidentified phase. We are grateful to GELLER[24] for calling our attention to this error. Further investigation (Table 2) demonstrated that the unknown phase is absent when

Table 2. Representative reaction conditions and results

Batch composition	Method of reaction	Temperature (°C)	Time at temperature	Phases identified in X-ray powder patterns		
				Major	Intermediate	Minor
$3CaO+Cr_2O_3+3GeO_2$	Heated in air	900	5 hr	GeO_2	Unidentified phase	Cr_2O_3 Garnet
$3CaO+Cr_2O_3+3GeO_2$	Heated in air	1200	5 hr	Garnet		
$3CaO+Fe_2O_3+3GeO_2$	Heated in air	900	5 hr	Garnet	GeO_2	Fe_2O_3
$3CaO+Fe_2O_3+3GeO_2$	Heated in air	900	5 hr	Garnet	GeO_2	Fe_2O_3
$3CaO+Fe_2O_3+3GeO_2$	Heated in air	1425	5 min	Tan glass	Amorphous	
$3CaO+Al_2O_3+3GeO_2$	Heated in air	900	5 hr	GeO_2	Al_2O_3	CaO Garnet
$3CaO+Al_2O_3+3GeO_2$	Heated in air	1100	5 hr	Garnet		
$3CaO+Al_2O_3+3GeO_2$	Heated in air	1375	5 min	Colorless glass		
$3CaO+Al_2O_3+3GeO_2$	Heated in steam	1200	3 hr	Garnet	Unidentified phase	
$Mn_3O_4+Cr_2O_3+3GeO_2$	Heated in air	900	5 hr	GeO_2	Garnet	Mn_3O_4
$Mn_3O_4+Cr_2O_3+3GeO_2$	Heated in air	1200	5 hr	Garnet		
$Mn_3O_4+Fe_2O_3+3GeO_2$	Heated in air	900	5 hr	GeO_2	Fe_2O_3	Mn_3O_4 Trace unidentified phase
$Mn_3O_4+Fe_2O_3+3GeO_2$	Heated in air	1200	5 hr	Garnet		
$Mn_3O_4+Fe_2O_3+3GeO_2$	Heated in air	1200	20 hr	Garnet	Spinel	
$Mn_3O_4+Fe_2O_3+3GeO_2$	Heated in air	1255	5 min	Garnet	Unidentified phase	
$Mn_3O_4+Fe_2O_3+3GeO_2$	Heated in steam	1200	3 hr	Garnet	Spinel	
$Mn_3O_4+Fe_2O_3+3GeO_2$	Heated in O_2	1200	5 hr	Garnet	Unidentified phase	
$Mn_3O_4+Fe_2O_3+3GeO_2$	Heated in N_2	1200	5 hr	Garnet	Spinel	
$3CdO+Fe_2O_3+3GeO_2$	Heated in air	900	5 hr	Fe_2O_3	Garnet	Spinel Trace unidentified phase
$3CdO+Fe_2O_3+3GeO_2$	Heated in air	1200	5 hr	Garnet		
$3CdO+Fe_2O_3+3GeO_2$	Heated in steam	1200	3 hr	Garnet		
$3CdO+Al_2O_3+3GeO_2$	Heated in air	900	5 hr	Spinel	Unidentified phase	
$3CdO+Al_2O_3+3GeO_2$	Heated in air	1100	5 hr	Garnet		Trace unidentified phase
$3CdO+Al_2O_3+3GeO_2$	Heated in air	1290	5 min	Colorless glass		
$3CdO+Al_2O_3+3GeO_2$	Heated in steam	1180	3 hr	Garnet		

preparations are made in atmospheres less oxidizing than air, viz. nitrogen and steam. In some of these preparations, a spinel phase is present, instead of the unidentified phase.

3. *Melting points*

Melting and decomposition characteristics of many of the garnet compounds were observed. Although accurate temperature measurements have not yet been made, the relative order of melting was noted and is here recorded, without distinguishing between congruent and incongruent melting. Within the series $Mn_3(Ge,Fe,Al,Cr)_2Ge_3O_{12}$ the melting temperature increases in the order shown for the octahedrally coordinated cations. In the series $Cd_3(Ga,Al,Fe,Sc,Cr)_2Ge_3O_{12}$ the corresponding sequence is as shown. The sequence in the Ca–Ge garnets is similarly Al,Fe,Sc,Cr.

Data obtained with a strip heater indicate that the melting range is about 1200°C for compounds containing gallium to more than 1650°C for those containing chromium. The melting range of the chromium compounds could not be reached; mechanical strains caused localized hot spots in the heating strips at about 1700°C, leading to failure of the strips.

The following compounds yielded glasses on quenching their melts:

$Ca_3Fe_2Ge_3O_{12}$	Tan glass
$Ca_3Al_2Ge_3O_{12}$	Colorless glass
$Cd_3Al_2Ge_3O_{12}$	Colorless glass
$Cd_3Ga_2Ge_3O_{12}$	Yellow glass

Quenching of the melts of other compositions yielded polyphase crystalline products. In most instances these quenched materials contained one or more phases which could not be identified. It appears that in these cases the garnet compounds melt incongruently.

4. *Linear lattice constant relationship*

Comparison of the lattice constant of germanium garnets with different cations in dodecahedral coordination, but with the same cation in octahedral coordination, shows a constant difference (Table 3). This suggests a linear dependence of lattice constant upon the ionic radii of six-fold coordinated cations. BERTAUT and FORRAT[25] have derived linear equations for the lattice parameters of ferrogarnets and silicate garnets investigated by LEVIN[26]. GELLER and MILLER[19] and GELLER and MITCHELL[27] have observed a similar linear dependence among other garnets. When lattice constants of the germanium garnets were plotted as a function of ionic radii (Fig. 1), a linear relationship was also observed.

Table 3. Constant difference in lattice constant for end member germanates

Dodecahedral site	Octahedral site	Difference in lattice constant	Average
Cd–Mn	Al	0·176	0·18
	Cr	0·186	
	Fe	0·174	
	Ca	1·172	
Ca–Mn	Al	0·219	0·23
	Cr	0·238	
	Fe	0·225	
Ca–Cd	Al	0·043	0·051
	Cr	0·052	
	Fe	0·051	
	Sc	0·057	

The following equations were fitted to the data:

Ca compounds:

$$a_0 = 7{\cdot}923 + 3{\cdot}002(r_{\text{oct.}}) + 2{\cdot}544(r_{\text{dod.}}) \quad (1)$$

Mn compounds:

$$a_0 = 8{\cdot}475 + 2{\cdot}729(r_{\text{oct.}}) + 2{\cdot}272(r_{\text{dod.}}) \quad (2)$$

Cd compounds:

$$a_0 = 8{\cdot}760 + 2{\cdot}849(r_{\text{oct.}}) + 2{\cdot}808(r_{\text{dod.}}) \quad (3)$$

where $(r_{\text{oct.}})$ is the ionic radius of trivalent 6-coordinated cations as determined by GELLER[28] and $(r_{\text{dod.}})$ is the ionic radius of divalent 8-coordinated cations ($Mn^{2+} = 0{\cdot}82$ Å, $Ca^{2+} = 1{\cdot}01$ Å, and $Cd^{2+} = 0{\cdot}98$ Å). The calculated lattice constants agree fairly well with the experimental values except for the cadmium gallium and calcium gallium garnet (Table 1).

5. *Non-stoichiometry*

All of the germanium garnets prepared in this

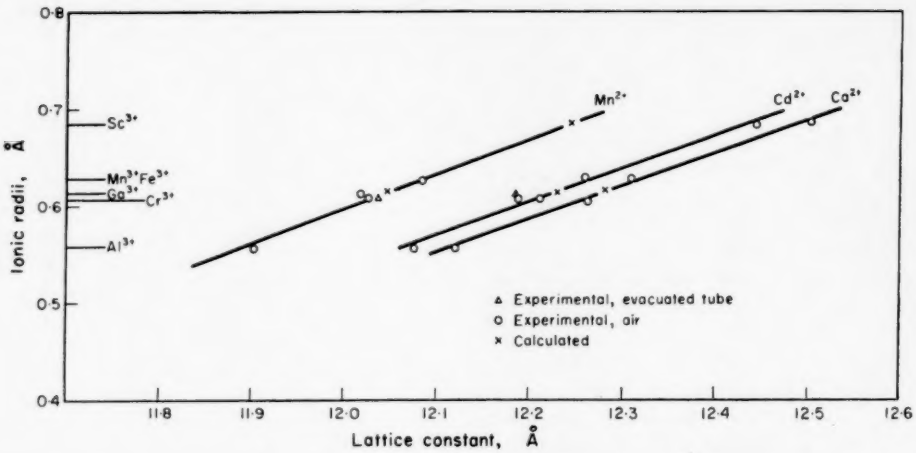

FIG. 1. Lattice constant vs. ionic radii[28] of trivalent octahedrally coordinated cations.

study contained less GeO_2 than was introduced originally. The results of X-ray fluorescence analysis for GeO_2 in compounds prepared under specific conditions are given in Table 4.

Thus, germanium garnets tend to form defect compounds when germanium is permitted to volatilize during preparation. GELLER *et al.*[20] have shown that defect germanium garnet structures exist. If it is true that the GeO_2 loss is not accompanied by other extra phases, then many of the germanium garnets reported here are also defect structures. Calcium chromium and calcium iron germanium garnet samples heated in steam generally showed greater losses of GeO_2 than samples prepared in air for the same firing times. The compounds consisting of elements whose oxides are refractory tend to lose less germanium dioxide.

On the basis of data obtained in this study, it is not possible at this time to account for the loss of germanium dioxide in terms of the formation of specific products. The other oxides may have formed separate phases which are not detected by X-ray techniques, or solid solutions which are

Table. 4. *Analysis for* GeO_2

Initial composition	Method of preparation	Per cent loss in weight of GeO_2
$3CaO+Cr_2O_3+3GeO_2$	Fired in air at 1150°C for 1 hr	3·6
$3CaO+Cr_2O_3+3GeO_2$	Fired in steam at 1200°C for 3 hr	12·0
$3CaO+Fe_2O_3+3GeO_2$	Fired in air at 1200°C for 2 hr	2·5
$Mn_3O_4+Fe_2O_3+3GeO_2$	Fired in air at 1200°C for 3 hr	15·0
$3CdO+Cr_2O_3+3GeO_2$	Fired in air at 1200°C for 2 hr	11·3
$3CdO+Cr_2O_3+3GeO_2$	Fired in steam at 1180°C for 3 hr	9·8
$Mn_3O_4+Al_2O_3+3GeO_2$	Fired in air at 1200°C for 3 hr	2·6
$Mn_3O_4+Al_2O_3+3GeO_2$	Fired in steam at 1200°C for 3 hr	9·5
$3CaO+Al_2O_3+3GeO_2$	Fired in air at 1200°C for 5 hr	6·1
$3CaO+Al_2O_3+3GeO_2$	Fired in steam at 1200°C for 3 hr	5·9
$3CdO+Fe_2O_3+3GeO_2$	Fired in air at 1200°C for 5 hr	18·0
$3CdO+Fe_2O_3+3GeO_2$	Fired in steam at 1200°C for 3 hr	19·0

Table 5. *Comparison of calculated and observed relative intensities of* $\{Ca_3\}[Al_{2-x}Ge_x](Ge_{3-x}Al_x)O_{12}$

hkl	$I_{obs.}$	$I_{calc.}$(1)*	$I_{calc.}$(2)*	$I_{calc.}$(3)*
211	10	17	16	14
220	5	7	5	2
321	9	10	9	8
400	29	24	26	31
420	99	100	100	100
332	19	19	19	18
422	23	13	15	19
431	7	11	12	13
440	7	5	5	4
611, 532	1	4	4	6
541	0·5	0·5	0·1	0·5
631	3	3	3	3
444	15	17	17	15
640	30	26	26	27
721, 633, 552	1	2	2	2
642	28	31	33	39
732, 651	1	2	2	2
800	8	8	9	9
653	1	3	3	3
822, 660	0·5	0·5	0·8	0·1
752	0·5	2	2	2
840	6	7	8	9
842	16	17	17	17
921, 761, 655	2	4	2	2
664	6	5	5	6
941, 853	1	1	2	2
10,2,0, 862	2	3	2	2
10,4,0, 864	15	14	15	14
10,4,2	9	3	4	4
880	7	7	7	8
11,3,2, 10,5,3, 972, 776	1	1	1	0·6
12,0,0, 884	5	4	2	3
12 2,0	3	3	3	3
12,2,2, 10,6,4	7	7	7	8
12,4,4	3	4	3	3
12,6,0, 10,8,4	10	9	9	10
12,6,2	1	3	3	4
888	4	3	4	4
14,1,1, 13,5,2, 10,7,7, 996	1	1	1	1
12,8,0	1	2	2	3
14,4,0, 12,8,2	8	11	11	11
14,4,2, 12,6,6, 10,10,4	10	12	13	15

* (1) $x = 0{\cdot}0$; (2) $x = 0{\cdot}15$; (3) $x = 0{\cdot}45$.

deficient in GeO_2. In the case of $Mn_3Ga_2Ge_3O_{12}$ (nominal) there is some evidence that the latter is the case, as seen from the difference in lattice constant between samples prepared in air and in sealed tubes. Finally, the germanium and oxygen may be lost in ratios other than 1:2, which could be compensated by oxidation or reduction of transition metal ions. However, we have no evidence bearing on this point.

6. *Calculation of the intensities of* $\{Ca_3\}[Al_{2-x}Ge_x](Ge_{3-x}Al_x)O_{12}$†

In order to examine cation distribution, a calculation of the intensities of $Ca_3Al_2Ge_3O_{12}$ was made using a powder sample. This compound was selected because it has analogue in silicate garnets (grossularite) on which ABRAHAMS and GELLER[3] have carried out a very careful refinement of the structure.

The grossularite structure was taken as a model. The germanium compound has a volume 6·7 per cent larger than the silicate. It was assumed that this increase in volume is primarily the result of a uniform expansion, without marked departure from the oxygen parameters in the silicate. Consequently, the oxygen parameters used were those obtained by ABRAHAMS and GELLER[3]. The atomic scattering factors (f_0) employed were those calculated by JAMES *et al.*[30] for Ca^{2+} and by

† After the convention of GELLER *et al.*[29], where {} is a *c* or dodecahedral site, [ ] is an *a* or octahedral site and ( ) is a *d* or tetrahedral site.

BERGHUIS *et al.*[31] for Al^{3+}, O^{2-}, and Ge^{4+}, the latter two being modified. The BERGHUIS[31] value for Ge was taken as 28·00 for $f_{Ge^{4+}}$ at $\sin\theta/\lambda = 0$ and $f_{Ge^{4+}} = f_{Ge}$ when $\sin\theta/\lambda \geqslant 0{\cdot}3$. Similarly, for oxygen, $f_{O^{2-}} = 10{\cdot}00$ at $\sin\theta/\lambda = 0$ and $f_{O^{2-}} = f_O$ when $\sin\theta/\lambda \geqslant 0{\cdot}25$. The temperature corrections used were based on those given by ABRAHAMS and GELLER[3] for the grossularite structure. Calculations were performed on an L.G.P. 30 Royal McBee Digital Computer programmed for solutions in I. Observed intensities were obtained with an X-ray diffractometer using filtered CuK radiation. No absorption correction as a function of diffraction angle was necessary.[32]

Six calculations between $x = 0$ and 0·45, based on $\{Ca_3\}[Al_{2-x}Ge_x](Ge_{3-x}Al_x)O_{12}$, were carried out. The data for the calculations using $x = 0{\cdot}0$, 0·15, and 0·45 are given in Table 5 with the observed intensities.

The results indicate that there is little difference between the three calculated values. This reflects the insensitivity of the X-ray powder diffraction method for determining the cation distribution in octahedral and tetrahedral sites in this compound.

Acknowledgement—The authors are grateful to Drs. S. B. LEVIN, H. H. KEDESDY and J. A. KOHN for informative discussions, throughout the course of this investigation. We gratefully acknowledge the assistance of J. FINNEGAN in the analysis of many samples.

REFERENCES

1. GELLER S., *J. Appl. Phys.* **31,** 30S (1960).
2. YODER H. S. and KEITH M. L., *Amer. Min.* **36,** 519 (1951).
3. ABRAHAMS S. C. and GELLER S., *Acta. Cryst. Camb.* **11,** 437 (1958).
4. BERTAUT F. and FORRAT F., *C.R. Acad. Sci., Paris* **241,** 382 (1956).
5. GELLER S. and GILLEO M. A., *Acta. Cryst., Camb.* **10,** 239 (1957).
6. GELLER S. and GILLEO M. A., *J. Phys. Chem. Solids* **3,** 30 (1957).
7. TAUBER A., BANKS E. and KEDESDY H. H., *J. Appl. Phys.* **29,** 385 (1958).
8. TAUBER A., BANKS E. and KEDESDY H. H., *Acta Cryst., Camb.* **11,** 893 (1958).
9. DONNAY G. and DONNAY J. D. H., *Amer. J. Sci.* Bowen Vol., p. 115 (1952).
10. KLUG H. P. and ALEXANDER L. E., *X-ray Diffraction Procedures*, p. 464. John Wiley, New York (1954).
11. KEITH M. L. and ROY R., *Amer. Min.* **36,** 519 (1951).
12. MARGRAVE J. L., *J. Phys. Chem.* **60,** 715 (1956).
13. GENTILE A. L. and ROY R., *Amer. Min.* **45,** 701 (1960).
14. SWANSON H. E., COOK M. I., EVANS E. H. and DE GROOT J. H., *Standard X-ray Diffraction Powder Patterns* **9,** 15–20 (1960).
15. HUMMEL F. A., *Amer. Min.* **35,** 324 (1950).
16. GELLER S. and MILLER C. E., *Amer. Min.* **44,** 445 (1959).
17. GLASSER E. P. and OSBORN E. F., *J. Amer. Ceram. Soc.* **41,** 358 (1958).
18. GLASSER E. P., *Amer. Min.* **44,** 1301 (1959).
19. GELLER S. and MILLER C. E., *Amer. Min.* **44,** 665 (1959).
20. GELLER S., MILLER C. E. and TREUTING R. G., *Acta Cryst., Camb.* **13,** 179 (1960).
21. GELLER S. and MILLER C. E., Milwaukee ACA Meeting, Paper No. A10, June (1958).
22. BOZORTH R. M. and GELLER S., *J. Phys. Chem. Solids* **11,** 263 (1959).
23. GELLER S., BOZORTH R. M., GILLEO M. A. and MILLER C. E., *J. Phys. Chem. Solids* **12,** 111 (1960).
24. GELLER S., private communication.
25. BERTAUT F. and FORRAT F., *C.R. Acad. Sci., Paris* **244,** 96 (1957).
26. LEVIN S. B., *Bull. Geol. Soc. Amer.* **61,** 519 (1950).
27. GELLER S. and MITCHELL D. W., *Acta Cryst., Camb.* **12,** 936 (1959).
28. GELLER S., *Acta Cryst., Camb.* **10,** 248 (1957).
29. GILLEO M. A. and GELLER S., *J. Phys. Chem. Solids* **10,** 187 (1959).
30. JAMES R. W. and BRINDLEY G. W., *Z. Kristallogr.* **78,** 470 (1931).
31. BERGHUIS J., HAANAPPEL I. W., POTTERS M., LOEPSTRA B. O., MACGILLAVRY C. W. and VEENENDAAL A. L., *Acta Cryst., Camb.* **8,** 478 (1955).
32. KLUG H. P. and ALEXANDER L. E., *X-Ray Diffraction Procedures*, p. 377. John Wiley, New York (1954).

J. Phys. Chem. Solids Pergamon Press 1961. Vol. 21, Nos. 1/2, pp. 33–39. Printed in Great Britain.

ZUR THEORIE DER CHEMISORPTION

O. JÄNTSCH

Apparatewerk München der Siemens-Schuckertwerke A.G.

(*Received* 27 *December* 1960; *revised* 24 *February* 1961)

Zusammenfassung—Mit der Theorie, dass bei der Chemisorption ein Ladungsaustausch zwischen den Molekülen und dem Adsorbens bzw. dem Katalysator stattfindet, werden die Isotherme, die Isostere und die Isobare der Chemisorption aufgestellt. Aus geringen Änderungen der Adsorptionsdichte vom Gleichgewicht lässt sich die Lebensdauer der chemisorbierten Moleküle bestimmen. Die Lebensdauer ist für die Geschwindigkeit der Chemisorption massgebend. Die freien Valenzen der Oberflächenatome stellen wahrscheinlich die "Aktiven Zentren" des Katalysators dar. Ihre energetischen Lagen relativ zum elektrochemischen Potential bestimmen die Transmissionskoeffizienten der Ladungsübergänge.

Abstract—The isotherm, the isoster and the isobar of chemisorption are derived on the basis of the assumption that during the chemisorption, charge is exchanged between the molecules and the adsorbant or the catalyst. The lifetime of the chemisorbed molecules is determined by considering small deviations of the density of the adsorbed molecules from the equilibrium value. This lifetime determines the rate of the chemisorption process. The "active centers", responsible for the adsorption, are probably the free valencies of the surface atoms. The position of the energy levels of these centers relative to the electrochemical potential determines the transmission coefficients of the various charge transitions.

ol. 21
1961

LISTE DER SYMBOLE

n = chemisorbierte Moleküle pro Flächeneinheit
g = Moleküle pro Zeit- und Flächeneinheit des Übergangs $P \rightarrow C$
v = Moleküle pro Zeit- und Flächeneinheit des Übergangs $C \rightarrow P$
τ = Lebensdauer der chemisorbierten Moleküle
t = Zeit
t_P = Verweilzeit eines physikalisch adsorbierten Moleküls an einem Potential-minimum
Z = aus dem Gasraum auftreffende Moleküle pro Zeit- und Flächeneinheit
W = zeitunabhängige Wahrscheinlichkeit des Übergangs $P \rightarrow C$ für ein Molekül
σ = Kondensationskoeffizient
k = Boltzmannkonstante
R = Gaskonstante
T = absolute Temperatur
p = Gasdruck
m = Masse eines Moleküls
n_m = monomolekulare Besetzung
A, A', A^*, b = Konstanten
α = Transmissionskoeffizienten
ΔH = Enthalpien
ΔG = freie Enthalpien
w = Übergangswahrscheinlichkeiten eines Moleküls pro Zeiteinheit

Indizes :

AP = Aktivierung des Übergangs $P \rightarrow C$
AC = Aktivierung des Übergangs $C \rightarrow P$
D = Aktivierung bei der Diffusion der physikalisch adsorbierten Moleküle
P = physikalische Adsorption
C = Chemisorption

EINLEITUNG

NACH neueren Theorien der Chemisorption und der Katalyse besteht zwischen den adsorbierten Molekülen und dem Adsorbens, bzw. dem Katalysator ein Ladungsaustausch.[1] Die physikalisch adsorbierten Moleküle (ungeladen) geben entweder an das Adsorbens Elektronen ab oder nehmen Elektronen von ihm auf.

Das Verhalten eines Adsorbens wird zum Teil durch die Lage seines elektrochemischen Potentials (Ferminiveau) bestimmt. So werden die Donatorreaktionen, bei denen die adsorbierten Moleküle Elektronen abgeben, besser an Katalysatoren mit *tiefem* elektrochemischen Potential vonstatten gehen, als an solchen mit hohem. Dass die elektrochemischen Potentiale jedoch *nicht* die *einzigen* Faktoren sind, die die Chemisorption und damit die Katalyse bestimmen, zeigen die Untersuchungen an Einkristallen.[2] Obwohl das elektrochemische Potential im gesamten Kristall konstant ist, haben verschiedene Kristallflächen unterschiedliche Aktivitäten. Die einzelnen Kristallflächen unterscheiden sich lediglich durch die unterschiedliche Struktur der Oberflächenatome.

Die Tatsache, dass die Oberfläche eines Katalysators nicht an allen Stellen gleich wirkt, hat zur Theorie der "Aktiven Zentren" geführt. Es blieb jedoch die Frage, welcher Art diese Zentren sind und auf welche Weise sie wirken.

Im Halbleiterinnern finden Reaktionen der Elektronen und Defektelektronen fast ausschliesslich über Rekombinationszentren statt.[3] Rekombinationszentren sind Gitterstörstellen (Fremdatome oder Gitterbaufehler), die diskrete Energieniveaus im verbotenen Band erzeugen. Die Lage der Energieniveaus innerhalb des verbotenen Bandes bestimmt die Wirksamkeit der Zentren. Es lassen sich quantenmechanische Gründe anführen, weshalb die Reaktionen über Rekombinationszentren und nicht direkt von Band zu Band stattfinden.

An der Oberfläche sind Rekombinationszentren auch unter dem Namen schnelle oder auch innere Oberflächenzustände bekannt[4]. In Analogie zum Halbleiterinnern ist es denkbar, dass der Ladungsaustausch zwischen den adsorbierten Molekülen und dem Adsorbens (Metall oder Halbleiter) fast ausschliesslich über solche Oberflächenrekombinationszentren stattfindet. Inwieweit eine direkte Reaktion mit dem Kristallinnern überhaupt möglich ist, müsste eine quantenmechanische Rechnung zeigen.

Im atomistischen Kristallmodell entsprechen die Oberflächenrekombinationszentren den äusseren nicht gebundenen Valenzen der Oberflächenatome, sofern es sich nicht um Fremdatome handelt. Ins atomistische Bild übertragen bedeutet ein hohes elektrochemisches Potential ein Überangebot an Elektronen, und somit sind die freien Valenzen der Oberflächenatome weitgehend mit Elektronen besetzt. Eine Donatorreaktion kann daher ihr zusätzliches Elektron schlecht unterbringen, eine Akzeptorreaktion kann den freien Valenzen leicht ein Elektron entreissen. Eine Akzeptorreaktion wird daher durch ein hoch liegendes elektrochemisches Potential begünstigt. Bei einem Katalysator mit tief liegendem elektrochemischen Potential sind die äusseren Valenzen weitgehend unbesetzt.

Die bei der Chemisorption und der Katalyse angenommenen "Aktiven Zentren" sind nach diesem Modell mit freien Valenzen der Oberflächenatome oder mit gewissen Fremdatomen identisch.

KINETIK DER CHEMISORPTION

Der Zustand der Chemisorption wird erreicht, indem ein Molekül aus der Gasphase auf die Oberfläche trifft, dort zunächst physikalisch adsorbiert wird und erst durch Ladungsaustausch chemisorbiert. Bei der Desorption wird der Weg rückwärts durchlaufen. Ein direktes Verdampfen der chemisorbierten Moleküle ist unwahrscheinlich. Die Berechnungen von EHRLICH[5] berücksichtigen bereits diesen Mechanismus. Die Bilanzgleichung für die Zahl der chemisorbierten Moleküle n pro Flächeneinheit lautet somit :

$$\partial n/\partial t = g - v. \qquad (1)$$

Es bedeuten g der Gewinn und v der Verlust an chemisorbierten Molekülen, die pro Zeit- und Flächeneinheit aus bzw. in den Zustand der physikalischen Adsorption überwechseln.[6] Die Differenz $g-v$ ist gleich Null, wenn sich das System im *stationären* Gleichgewicht befindet. Ist das stationäre Gleichgewicht gestört, so gibt der zeitliche Differentialquotient $\partial n/\partial t$ die Abnahme der Konzentration n der chemisorbierten Moleküle pro Zeit- und Flächeneinheit an, die

Vol. 2
1961

die Abweichung vom stationären Gleichgewicht ausgleicht.†

Bei den folgenden Betrachtungen wird eine gleichmässige Dichte an aktiven Zentren vorausgesetzt, so dass sich keine Dichteunterschiede in n ergeben. Befinden sich n chemisorbierte Moleküle auf der Flächeneinheit des Adsorbens und gibt τ die mittlere Verweilzeit eines Moleküls in diesem Zustand an (Lebensdauer der chemisorbierten Moleküle), so folgt

$$v = n/\tau. \tag{3}$$

Die Lebensdauer τ lässt sich leicht bestimmen[6]: Hat sich bei bestimmten Versuchsbedingungen eine Gleichgewichtskonzentration eingestellt und geht man plötzlich zu anderen Versuchsbedingungen über (z.B. Änderung des Dampfdrucks), so stellt sich die neue Gleichgewichtskonzentration n_∞ erst allmählich wieder ein. Handelt es sich nur um eine *geringe* Störung n^* vom neuen Gleichgewichtswert n_∞, so fällt die Störung nach der Funktion

$$n^* = |n_0 - n_\infty| \exp(-t/\tau) \tag{4}$$

mit der Zeit t ab. Die Lebensdauer ergibt sich also als die Zeit, in der eine *geringe* Störung auf $1/e$ abgeklungen ist. Das gleiche gilt für jede Messgrösse, die zumindest in dem untersuchten *kleinen* Intervall eine annähernd lineare Abhängigkeit von der Konzentration n zeigt (z.B. elektrischer Widerstand[7] oder innere Totalreflektion[8] eines Adsorbens). Auch *geringe* Störungen dieser Messgrössen klingen nach Gleichung (4) mit der Zeitkonstanten τ ab. Die Lebensdauer der chemisorbierten Moleküle liegt bei Raumtemperatur in der Grössenordnung von Minuten.[6]

Die Zahl der aus dem Gasraum pro Zeiteinheit auf die Flächeneinheit des Adsorbens treffenden Moleküle sei Z. Mit dem Kondensationskoeffizienten σ wird von ihnen ein Teil reflektiert, $(1-\sigma)Z$, der andere, nämlich σZ, physikalisch adsorbiert. Ferner kommen noch n/τ Moleküle aus dem Zustand der Chemisorption hinzu, so dass die Gesamtzahl der pro Zeit- und Flächeneinheit physikalisch adsorbierten Moleküle $\sigma Z + (n/\tau)$ beträgt. Die Wahrscheinlichkeit, dass ein physikalisch adsorbiertes Molekül überhaupt (zeitunabhängig) chemisorbiert wird und nicht wieder die Oberfläche verlässt, sei W. So ergibt sich

$$g = [\sigma Z + (n/\tau)]W. \tag{5}$$

Nach Einsetzen von (3) und (5) in (2) folgt für den Gleichgewichtsfall $\partial n/\partial t = 0$, wenn nach der Dichte der chemisorbierten Moleküle n aufgelöst wird

$$n = \sigma Z \tau W/(1-W). \tag{6}$$

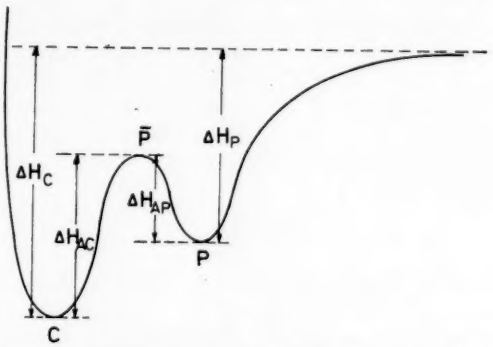

ABB. 1. Potentialverlauf für die physikalische Adsorption und für die Chemisorption

P = Zustand der physikalischen Adsorption
C = Zustand der Chemisorption
$\bar{P}$ = Aktivierter Zustand beim Übergang $C \rightleftarrows P$
ΔH_P = Enthalpie der physikalischen Adsorption
ΔH_C = Enthalpie der Chemisorption
ΔH_{AP} = Aktivierungsenthalpie des Übergangs $P \rightarrow C$
ΔH_{AC} = Aktivierungsenthalpie des Übergangs $C \rightarrow P$

DIE ÜBERGANGSWAHRSCHEINLICHKEITEN

Ähnlich wie bei chemischen Reaktionen ist beim Übergang vom Zustand der physikalischen Adsorption in den Zustand der Chemisorption eine Potentialschwelle zu überwinden[5] (Abb. 1). Die Höhe der Potentialschwelle ist die Aktivierungsenthalpie ΔH_{AP}, und die Aktivierungsenthalpie des Übergangs Chemisorption → physikalische Adsorption ist ΔH_{AC}.

Für die Wahrscheinlichkeit w_{AP}, dass ein physikalisch adsorbiertes Molekül pro Zeiteinheit chemisorbiert wird, ergibt sich

$$w_{AP} = (\varkappa_{AP} kT/h) \exp(-\Delta G_{AP}/RT) \tag{7}$$

aus der Theorie der Reaktionsgeschwindigkeiten.[9] Es bedeuten k die Boltzmannkonstante,

† Tritt ein weiterer Verlust ϕ an chemisorbierten Molekülen pro Zeit- und Flächeneinheit durch Strömung oder durch Umwandlung bei katalytischen Reaktionen ein, so gilt

$$\partial n/\partial t = g - v - \phi. \tag{2}$$

h die Plancksche Konstante, R die Gaskonstante, T die absolute Temperatur und

$$\Delta G_{AP} = \Delta H_{AP} - TS_{AP} \tag{8}$$

die molare freie Enthalpie der Aktivierung.

Der Transmissionskoeffizient α_{AP} gibt die Wahrscheinlichkeit an, dass ein Molekül, das durch thermische Anregung in den aktivierten Zustand $\overline{P}$ versetzt wurde, auch tatsächlich chemisorbiert wird. α_{AP} ist daher stark von der Beschaffenheit der Oberfläche abhängig, von der Zahl und Art der freien Oberflächenvalenzen (Aktiven Zentren), von der Höhe des elektrochemischen Potentials, von der Besetzung der Oberflächenplätze usw.

Die Wahrscheinlichkeit, dass ein physikalisch adsorbiertes Molekül in der Zeiteinheit weder chemisorbiert wird, noch verdampft, sondern auf den nächsten Platz diffundiert oder auf dem gleichen Platz bleibt, ist

$$w_D = (\alpha_D kT/h) \exp(-\Delta G_D/RT). \tag{9}$$

Beim Kristallwachstum aus der Schmelze konnte gefunden werden, dass die freie Aktivierungsenthalpie der Anlagerung von Molekülen an den Kristall mit der freien Aktivierungsenthalpie der Selbstdiffusion in der Schmelze (erhalten aus der Viskosität) übereinstimmt.[10] Da beim Kristallwachstum ebenfalls Elektronenreaktionen mit den äusseren freien Valenzen des Kristalls stattfinden, ist auch bei der Chemisorption zu erwarten, dass ΔG_{AP} gleich der freien Aktivierungsenthalpie der Oberflächendiffusion ΔG_D ist. Da sich ΔG_D jedoch eliminieren lässt, wäre dies ohne Einfluss auf die allgemeine Temperatur- und Druckabhängigkeit der Chemisorption. α_D ist der Transmissionskoeffizient der Oberflächendiffusion.

Weiter gibt es noch die Möglichkeit, dass das Molekül aus dem Zustand der physikalischen Adsorption verdampft mit der Wahrscheinlichkeit pro Zeiteinheit

$$w_P = (\alpha_P kT/h) \exp(-\Delta G_P/RT). \tag{10}$$

Die mittlere Zeit, die zwischen zwei Anregungen vergeht, sei t_P; dann ist die Wahrscheinlichkeit, dass das Molekül bereits nach dem ersten Aufenthalt in einem Potentialminimum chemisorbiert wird : $W_1 = t_P w_{AP}$,

dass es verdampft: $W_{P1} = t_P w_P$,

und dass es wieder in ein Potentialminimum gelangt: $W_{D1} = t_P w_D$.

Ferner ergibt sich für den zweiten Aufenthalt in einem Potentialminimum : $W_2 = t_P^2 w_D w_{AP}$,

$W_{P2} = t_P^2 w_D w_P$,

$W_{D2} = t_P^2 w_D^2$,

usw.

Als Wahrscheinlichkeit W, dass ein physikalisch adsorbiertes Molekül überhaupt chemisorbiert wird, folgt

$$W = \sum_{\nu=1}^{\infty} W_\nu = t_P w_{AP} \sum_{\nu=0}^{\infty} t_P^\nu w_D^\nu, \tag{11}$$

oder nach Summation der geometrischen Reihe

$$W = t_P w_{AP}/(1 - t_P w_D). \tag{12}$$

Ein ähnliches Verfahren zur Berechnung der Wahrscheinlichkeit der Chemisorption wurde bereits von KISLIUK[11] angewendet.

Da $W_1 + W_{P1} + W_{D1} = 1$ sein muss, ergibt sich

$$t_P = 1/(w_{AP} + w_P + w_D), \tag{13}$$

und somit nach kurzer Rechnung aus (12) unter Berücksichtigung von (7) und (10)

$$W = \{1 + (\alpha_P/\alpha_{AP}) \exp[-(\Delta G_P - \Delta G_{AP})/RT]\}^{-1}. \tag{14}$$

Analog wie in Gleichung (7) ergibt sich die Wahrscheinlichkeit pro Zeiteinheit des Uebergangs vom Zustand der Chemisorption in den der physikalischen Adsorption zu

$$w_{AC} = (\alpha_{AC} kT/h) \exp(-\Delta G_{AC}/RT). \tag{15}$$

Nach Gleichung (3) gilt

$$w_{AC} = 1/\tau. \tag{16}$$

Als Temperaturabhängigkeit der Lebensdauer ergibt sich

$$\tau = h \exp(-\Delta S_{AC}/R) \cdot (\alpha_{AC} kT)^{-1} \times \exp(\Delta H_{AC}/RT). \tag{17}$$

Hieraus lässt sich die Enthalpie ΔH_{AC} bestimmen. Da die Temperaturabhängigkeit weitgehend von der e-Potenz beherrscht wird, stimmt Gleichung (17) bis auf die Konstanten mit der von ROGINSKI[12] angegebenen Formel für die Lebensdauer überein.

Aus der kinetischen Gastheorie lässt sich die Auftreffwahrscheinlichkeit zu

$$z = p/(2\pi mkT)^{1/2} \tag{18}$$

berechnen, wobei p der Druck und m die Masse des Moleküls bedeuten.

Nach Einsetzen (15) in (16) und (16), (14) und (18) mit dem Kondensationskoeffizienten σ in (6) folgt

$$n = \frac{\sigma\alpha_{AP}hp\exp(\Delta G_C/RT)}{(2\pi mkT)^{1/2}\alpha_{AC}\alpha_P kT}, \tag{19}$$

wenn man

$$\Delta G_C = \Delta G_{AC} + \Delta G_P - \Delta G_{AP} \tag{20}$$

setzt (Abb.1).

DIE CHEMISORPTIONSISOTHERME

Bei der Ableitung der Gleichung (19) wurden bis jetzt alle chemisorbierten Moleküle als gleichwertig betrachtet. Dies ist in Wirklichkeit nicht der Fall, wenn es sich um mehrmolekulare Schichten handelt. Selbst bei einer monomolekularen Schicht werden sich Plätze mit unterschiedlicher Aktivität auch unterschiedlich auf den Transmissionskoeffizienten α_{AP} auswirken. Es wird ausserdem α_{AP} eine Funktion der Besetzung n sein.

Für den Fall, dass bei der monomolekularen Schicht die Aktivität für alle Plätze gleich ist, für weitere Schichten jedoch gleich Null, ergibt sich

$$\alpha_{AP} = \alpha_{AP0}[1-(n/n_m)], \tag{21}$$

wobei n_m die Zahl aller Oberflächenplätze bedeutet und α_{AP0} den Transmissionskoeffizienten für $n = 0$.

Im Gegensatz hierzu wird jedoch angenommen, dass in dem Bereich merklicher Chemisorption die Menge der physikalisch adsorbierten Moleküle zu gering ist, als dass sich eine Abhängigkeit des Kondensationskoeffizienten σ von der Besetzung ergibt.

Nach Einsetzen von (21) in (19) und Auflösung nach der relativen Besetzung n/n_m folgt die Langmuirsche Gleichung

$$n/n_m = bp/(1+bp) \tag{22}$$

wie sie auch für die physikalische Adsorption gilt, jedoch mit einer anderen Konstanten b,

$$b = \frac{\sigma\alpha_{AP0}h\exp(\Delta G_C/RT)}{n_m(2\pi mkT)^{1/2}\alpha_{AC}\alpha_P kT} \tag{23}$$

Für mehrmolekulare Schichten muss α_{AP} entsprechend der Theorie von BRUNAUER und Mitarbeitern[13,14] abgewandelt werden. Für geringe Adsorptionen ergibt sich

$$n \approx n_m bp. \tag{24}$$

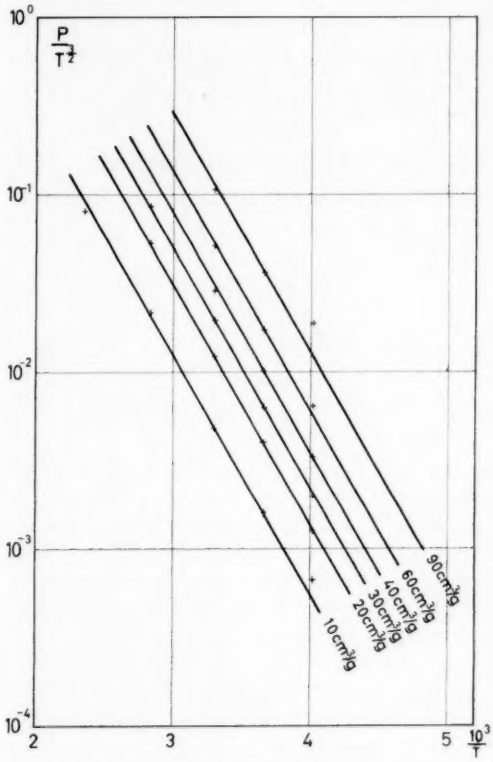

ABB. 2. Theoretische Chemisorptionsisosteren. Die Werte wurden aus Messungen von TITOFF für Ammoniak an Kohle erhalten.

DIE CHEMISORPTIONSISOSTERE

Eine Isostere gibt den Gleichgewichtsdruck als Funktion der Temperatur bei konstanter adsorbierter Menge an. In diesem Fall ist α_{AP} im Mittel konstant. Aus Gleichung (19) folgt daher die Chemisorptionsisostere

$$p = AT^{3/2}\exp(-\Delta H_C/RT). \tag{25}$$

Wird der Logarithmus von $p/T^{3/2}$ als Ordinate über der Abzisse $1/T$ aufgetragen, so ergeben sich Geraden, wie sie in Abb. 2 mit einer einheitlichen

Chemisorptionsenthalpie $\Delta H_C = 6000$ cal/Mol dargestellt sind. Die eingezeichneten Werte wurden aus Adsorptionsmessungen von TITOFF[15] für NH_3 an Aktivkohle erhalten. Nach TRAPNELL[16] handelt es sich bei NH_3 an Aktivkohle zumindest für die anfängliche Adsorption um Chemisorption. Mit dem Faktor $T^{3/2}$ der Chemisorptionsisostere ergibt sich für alle Isosteren der Abb. 2 eine einheitliche Enthalpie. Im Gegensatz hierzu steht die Auswertung von BRUNAUER[14] für die physikalische Adsorption.

DIE CHEMISORPTIONSISOBARE

Aus Gleichungen (19) und (21) folgt die Chemisorptionsisobare zu

$$\frac{n}{n_m} = \frac{A'}{T^{3/2}}\left(1-\frac{n}{n_m}\right)\exp(\Delta H_C/RT), \quad (26)$$

oder nach Umwandlung

$$\frac{n}{n_m}T^{3/2}\left(1-\frac{n}{n_m}\right)^{-1} = A'\exp(\Delta H_C/RT). \quad (27)$$

In Abb. 3 sind Isobaren ebenfalls für die Chemisorptionsenthalpie von $\Delta H_C = 6000$ cal/Mol dargestellt. Die eingezeichneten Werte wurden wieder aus Messungen von TITOFF[15] für NH_3 an Aktivkohle erhalten. Die entsprechenden relativen Bedeckungen n/n_m wurden hierfür aus einer Isotherme nach Gleichung (22) bestimmt. Die Abweichungen für kleine Besetzungen könnten auf Unregel mässigkeiten der Oberfläche zurückzuführen sein, die unterschiedliche Transmissionskoeffizienten bedingen.

Für den linearen Druckbereich, in dem Gleichung (24) noch gilt, ergibt sich die Chemisorptionsisobare zu

$$V = A^* T^{-3/2}\exp(\Delta H_C/RT), \quad (28)$$

mit V der chemisorbierten Menge.

Die von TAYLOR[17] und anderen gefundenen Isobaren mit Maximum setzen sich aus drei Teilen zusammen. Der absteigende Ast für tiefe Temperaturen ist die Isobare der physikalischen Adsorption. Hier bestimmt ΔH_P die Temperaturabhängigkeit. Der absteigende Ast für hohe Temperaturen stellt die eigentliche Chemisorptionsisobare mit ΔH_C dar. Der verbindende ansteigende Teil ist keine Gleichgewichtskurve, sondern eine Isochrone der Chemisorption.

DIE GESCHWINDIGKEIT DER CHEMISORPTION

Für den Nichtgleichgewichtsfall ergibt sich aus Gleichungen (2), (3) und (5) die Differentialgleichung

$$\frac{\partial n}{\partial t} = -\left(\frac{1-W}{\tau}\right)n + \sigma ZW. \quad (29)$$

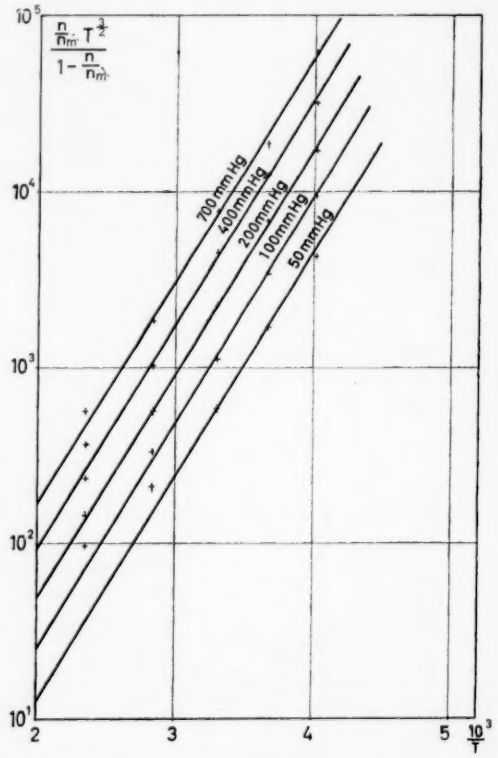

ABB. 3. Theoretische Chemisorptionsisobaren. Die Werte wurden aus Messungen von TITOFF für Ammoniak an Kohle erhalten.

Die Lösung lautet im linearen Druckbereich, in dem Gleichung (24) gilt, mit der Randbedingung $n = 0$ für $t = 0$

$$n = \sigma\tau ZW(1-W)^{-1}\{1-\exp[-(1-W)t/\tau]\}. \quad (30)$$

Diese Gleichung entspricht äusserlich bis auf die Konstanten der von LANGMUIR[18] für die physikalische Adsorption angegebenen. Sie wurde z.B. von BERL und WEINGAERTNER[19] für die Adsorption von Methan, Aethan und Propan an Aktivkohle geprüft. Die Temperaturabhängigkeit der

Exponentialfunktion in Gleichung (30) wird weniger durch W sondern vielmehr durch die Lebensdauer τ und somit nach Gleichung (17) durch die Aktivierungsenthalpie ΔH_{AC} bestimmt. Es steht hier nicht die Chemisorptionsenthalpie $\Delta H_C V$, wie es die Langmuirsche Formel analog für die physikalische Adsorption fordert. Falls es sich bei der Adsorption von Methan, Aethan und Propan an aktiver Kohle um Chemisorption handeln sollte, würde die Kritik von DAMKÖHLER[20] an der Arbeit von BERL und WEINGAERTNER[19] entfallen, wenn $\Delta H_{AC} < \Delta H_C$ ist.

Anerkennung—Herrn Prof. G. M. SCHWAB danke ich für eine wertvolle Diskussion.

LITERATURVERZEICHNIS

1. AIGRAIN P. und DUGAS C., *Z. Elektrochem.* **56,** 363 (1952); HAUFFE K. und ENGELL H. J., *Z. Elektrochem.* **56,** 366 (1952); WEISZ P. B., *J. Chem. Phys.* **20,** 1483 (1952); ENGELL H. J. und HAUFFE K., *Z. Elektrochem.* **57,** 762 (1953); ENGELL H. J., *Halbleiterprobleme,* Bd. I, S. 249. (herausgegeben von SCHOTTKY W.). Vieweg, Braunschweig (1954); HAUFFE K., *Angew. Chem.* **67,** 189 (1955); SCHWAB G. M., *Angew. Chem.* **67,** 433 (1955); SCHWAB G. M., GREGER G., KRAWCYNSKI ST. und PENZKOFER J., *Z. Phys. Chem.* N.F. **15,** 363 (1958); GARRETT C. G. B., *J. Chem. Phys.* **33,** 966 (1960).
2. GWATHMEY A. T. und CUNNINGHAM R. E., *Advanc. Catalys.* **10,** 57 (1958); LEIDHEISER H. und MEELHEIM R., *J. Amer. Chem. Soc.* **71,** 1122 (1949); LEIDHEISER H., GWATHMEY A. T., *J. Amer. Chem. Soc.* **70,** 1200, 1206 (1948), zitiert bei SCHWAB G. M., NOLLER H. und BLOCK J., *Handbuch der Katalyse,* Bd. 5/II, S. 409 Springer, Wien, (1957).
3. SHOCKLEY W. und READ W. T., Jr., *Phys. Rev.* **87,** 835 (1952); SPENKE E., *Elektronische Halbleiter.* Springer, Berlin (1954); HOFFMANN A., *Halbleiterprobleme,* Bd. II, S. 109. (herausgeben von SCHOTTKY W.). Vieweg, Braunschweig (1955).
4. BRATTAIN W. H., *Nobelvortrag* 1956, *Phys. Bl.* 10, 457 (1957); BARDEEN J., *Halbleiter und Phosphore* S. 81. (herausgegeben von SCHÖN M. und WELKER H.). Vieweg, Braunschweig, Akad.-Verlag, Berlin (1958); KINGSTON R. H., *J. Appl. Phys.* **27,** 101 (1956); HARTEN H. U. und SCHULTZ W., *Halbleiterprobleme,* Bd. III. S. 76 (herausgegeben von SCHOTTKY W.). Vieweg, Braunschweig (1956).
5. EHRLICH G., *J. Phys. Chem. Solids* **1,** 3 (1956).
6. JÄNTSCH O., *Z. Naturf.* **15a,** 141 (1960).
7. SUHRMANN R., WEDLER G. und KRÜGER G., *Z. Phys. Chem.* N.F. **16,** 131 (1958); SUHRMANN R. und WEDLER G., *Advanc. Catalys.* **9,** 223 (1957); RIENÄCKER G. und NANSEN N., *Z. Elektrochem.* **60,** 887 (1956); RIENÄCKER G. und NANSEN N., *Z. Anorg. Chem.* **284,** 162 (1956).
8. HARRICK N. J., *J. Phys. Chem. Solids* **14,** 60 (1960); HEILAND G., *Uber ein optisches Verfahren zur Beobachtung von Adsorptionsvorgängen an festen Körpern.* Vortrag Physiker-Tagung, Wiesbaden (1960).
9. GLASSTONE S., LAIDLER J. und EYRING H., *The Theory of Rate Processes.* McGraw-Hill, New York (1941); KINCAID J. F., EYRING H. und STEARN A. E., *Chem. Rev.* **28,** 301 (1941).
10. JÄNTSCH O., *Z. Kristallogr.* **108,** 185 (1956).
11. KISLIUK P., *J. Phys. Chem. Solids* **3,** 95 (1957).
12. ROGINSKI S. S., *Adsorption und Katalyse an inhomogenen Oberflächen* (Übersetzung aus dem Russischen) S.54. Akad.-Verlag, Berlin (1958).
13. BRUNAUER ST., EMMETT P. H. und TELLER E., *J. Amer. Chem. Soc.* **60,** 309 (1938).
14. BRUNAUER ST., *The Adsorption of Gases and Vapors.* Princeton University Press, Princeton, N.Y. (1945).
15. TITOFF A., *Z. Phys. Chem.* **74,** 641 (1910).
16. TRAPNELL B. W. W., *Chemisorption.* Academic Press, New York (1955).
17. TAYLOR H. S. und WILLIAMSON A. T., *J. Amer. Chem. Soc.* **53,** 2168 (1931).
18. LANGMUIR I., *J. Amer. Chem. Soc.* **40,** 1361 (1918) zitiert bei BRUNAUER, Literaturnote 23, S. 458.
19. BERL E. und WEINGAERTNER E., *Z. Phys. Chem.* A **173,** 35 (1935).
20. DAMKÖHLER G., *Z. Phys. Chem.* A **174,** 222 (1935).

Vol. 21
1961

J. Phys. Chem. Solids Pergamon Press 1961. Vol. 21, Nos. 1/2, pp. 40–56. Printed in Great Britain.

SELF-DIFFUSION OF LEAD, THALLIUM AND BISMUTH IN THE SOLID LEAD–THALLIUM SYSTEM

H. A. RESING* and N. H. NACHTRIEB

Institute for the Study of Metals, The University of Chicago

(*Received* 3 *August* 1960; *revised* 22 *March* 1961)

Abstract—Results are reported for the self-diffusion of both lead and thallium over the whole range of solid solution for these elements (0–87 atomic per cent Tl) for the temperature interval, 206–323°C. Data for the trace impurity diffusion of bismuth over the same concentration range are also given for a more limited temperature range. All three elements show the same qualitative dependence of their diffusion coefficient upon alloy composition: namely, a slight maximum at about 35 atomic per cent thallium and a deep minimum at about 75 atomic per cent thallium at all temperatures. The results are compared with the predictions of the corresponding states principle and with theories based upon the Johnson vacancy-solute complex mechanism. A correction applied to the corresponding states principle, based upon lattice parameter deviations from Vegard's Law, leads to agreement with observation. Some evidence for the existence of a superlattice at alloy compositions in the neighborhood of $PbTl_7$ is inferred from trends in the ratios D_{Tl}/D_{Pb} and D_{Bi}/D_{Pb} with thallium concentration.

1. INTRODUCTION

THERE have been several reports in the literature giving theoretical treatments of diffusion in solid solutions, most of them being concerned with solutions in the limit of infinite dilution.[1–4] As far as more concentrated solutions are concerned there have been two ideas stimulating experimental studies, the one being concerned with the justification of the Darken equation,[5, 6] and the other being concerned with the relation between melting and diffusion.[7] The latter idea has found expression in a correlation between the melting temperature of an alloy and the diffusion coefficient therein, and can be expressed in the equation

$$D(N_2P) = A \exp(-BT_m(N_2,P)/T) \qquad (1)$$

in which $D(N_2,P)$ is the diffusion coefficient of the solvent atom at a given concentration, N_2, of solute at a pressure P, $T_m(N_2,P)$ is the melting temperature of that solution, T is the temperature of the diffusion measurement, and A and B are constants determined by the behavior of the diffusion coefficient as a function of temperature in the pure solvent at one atmosphere of pressure. It can be seen that if this relation is of general validity the behavior of the diffusion coefficient as a function of composition can be predicted from the phase diagram of the given system once diffusion has been studied in the pure solvent.

NACHTRIEB *et al.*[7] noted that equation (1) agreed well with the data determined by HOFFMAN *et al.*[1] in various silver alloys. They noted further that in all of those systems T_m was a decreasing function of solute concentration. They then undertook the study of diffusion in silver rich silver–palladium alloys in which T_m is an increasing function of solute concentration, in contrast to the first-mentioned alloys. The expectation that D_{Ag} would decrease as the atom fraction of palladium was increased was fulfilled, and equation (1) was in quantitative agreement with the data obtained.

NACHTRIEB *et al.*[8] then found that equation (1) also was in quantitative agreement with the data obtained in a study of the effect of pressure on

* N.R.C.–N.R.L. Post-Doctoral Research Associate, the U.S. Naval Research Laboratory, Washington 25, D.C. This work is based upon the doctoral dissertation of Henry A. Resing, submitted to the Department of Chemistry of The University of Chicago.

diffusion of lead in lead, where T_m is a function of pressure alone rather than of solute concentration.

The correlation expressed in equation (1) therefore was a good summary of past experience. In fact, RICE and associates have more recently succeeded in building a theoretical support for this equation and its predictions in a series of papers entitled *Dynamical Theory of Diffusion in Crystals.*[9–12]

In order to test once more equation (1) and its predictions in an alloy system in which T_m is an increasing function of solute concentration, the study of the diffusion of lead in lead-rich lead–thallium alloys was undertaken. When the first results showed that the predictions of equation (1) were not fulfilled, it was decided to expand the study to include both lead and thallium diffusion in the entire range of solid solution of thallium in lead (i.e. up to 0·87 atom fraction thallium).

2. EXPERIMENTAL PROCEDURE

Alloy specimens were made in the form of rods six inches long and 9/16 in. in diameter by solidifying the well-mixed liquid phase in evacuated Pyrex tubes. Because of the existence of a maximum in the liquidus and solidus of the lead–thallium phase diagram[13] at 62·3 atomic per cent thallium there exists an opportunity to grow a single crystal of this composition by the Bridgman method without introducing a concentration gradient along the direction of growth.[14] Since a single crystal specimen would offer information concerning the extent of the error introduced by grain boundary diffusion in the polycrystalline specimens, both single and polycrystalline specimens were made at 62·3 atomic per cent thallinm. The rods were cut into cylinders approximately $\frac{1}{2}$ in. in length and $\frac{3}{8}$ in. in diameter. All specimens were annealed at temperatures close to the solidus to increase the grain size. In the specimens of low thallium content the grain size increased to the point at which the specimen consisted of three or four large grains. At higher thallium concentration the average grain size was about 1 mm.

The starting materials were 99·99 per cent pure as determined by spectrographic analysis;* the impurities consisted of copper, silicon, silver, magnesium, iron, and bismuth. A spectrographic check of each of the alloys showed that no additional impurities were introduced during specimen preparation. To show that none of the starting materials had been lost it was necessary to analyze the specimens after preparation. Analyses of specimens taken from each end of the rods showed that no concentration gradients existed on a macroscopic scale of dimensions. The specimen for analysis was dissolved in nitric acid and the resulting solution was made 6N in HCl. Three aliquots were carried through the analytical

* These spectrographic analyses were carried out by A. J. LEONI of the Institute for the Study of Metals, and his help is gratefully acknowledged.

Table 1

Alloy designation	Wt. per cent Tl as made up	Wt. per cent Tl found	Wt. per cent Pb found	Atomic per cent Tl	Density (g cm^{-3})	Melting temperature (°C)
0	0	—	—	0	$11{\cdot}35_3$	327
5	5·22	5·14 ± ·02	—	5·21	$11{\cdot}36_8$	331
10	10·17	10·14 ± ·01	—	10·27	$11{\cdot}38_6$	335
20	20·19	20·0 ± ·1	—	20·2	$11{\cdot}41_7$	342
34	34·63	34·0 ± ·3	65·5 ± ·1	34·6	$11{\cdot}47_9$	358
50	50·00	49·7 ± 1	50·03 ± ·05	50·3	$11{\cdot}55_2$	370
62-*s*	62·30	62·3 ± 7	37·67 ± ·15	62·6	$11{\cdot}63_4$	380
62-*p*	62·15	—	37·91 ± ·03	62·4	—	380
74	74·17	—	25·82 ± ·07	74·5	$11{\cdot}71_7$	362
76	75·82	—	24·00 ± ·13	76·2	$11{\cdot}73_9$	356
82	81·64	—	18·40 ± ·18	81·8	$11{\cdot}78_8$	338
87	86·93	—	13·06 ± ·10	87·1	$11{\cdot}84_2$	316

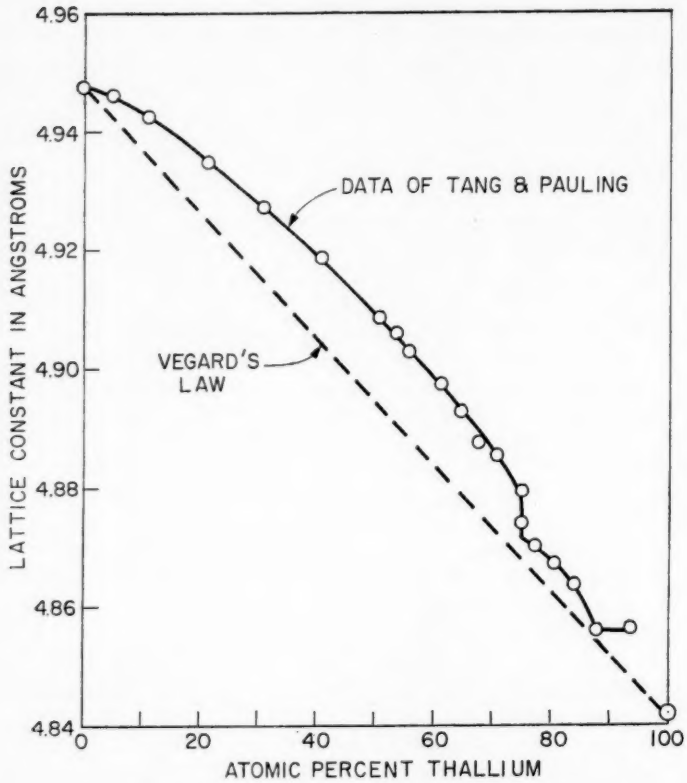

FIG. 1. Lattice constant vs. atomic per cent thallium.

procedure. Each aliquot was extracted with *iso*-propyl ether, the thallium passing into the ethereal phase and the lead remaining in the aqueous phase.[15] Thallium was determined by precipitation with thionalide*[16] and lead was determined by the anodic deposition of PbO_2.†[17] The results of the analyses are listed in Table 1. The precision indices indicate, for the most part, the difference in composition between the specimens taken from the opposite ends of the cast rod.

The densities of the specimens were determined from their weights in water and in air. Corrections were made for the buoyant effect of the air, but not for the effects of surface tension on the suspending wire.[18] Three determinations were made on each of three specimens of a given composition. The temperature at which the determinations were made was $23 \pm 1°C$. It is estimated that an upper limit to the error of the values given in Table 1 is $0{\cdot}01 g/cm^3$. The lattice constant as a function of composition is shown in Fig. 1[19]. Observed values of the density are in good agreement with those calculated from the lattice constant except in the region of the cusp in the latter. Because that region is represented by so few points in this density study there will be no attempt to draw any conclusions from the discrepancy.

Pb^{210} was obtained from the Canadian Radium and Uranium Corporation. Tl^{204} was obtained from Oak Ridge National Laboratory. Both were in the form of nitric acid solutions and were reduced to metallic form by soldium borohydride

* Thionalide is a trade name for α-mercapto-N-2 naphthylacetamide.

† The gravimetric factor used was 0·8627 g Pb per g PbO_x and was suggested by M. C. BACHELDER.

after dilution with inactive isotopes.[20] The radioactive metal so obtained was further diluted by melting together with the corresponding inactive metal.

The surface of the specimen on which the radioactive layer was to be deposited was machined to flatness within 2μ on a microtome. The slight amount of cold work introduced in this surface was very shallow with respect to the thickness of a section, and was disregarded. Six crystals so prepared were carried as a group through the steps outlined in the following paragraph. Vapor deposition of the active metal was carried out in an evacuated (ca. 10^{-5} mm Hg) bell jar. The six specimens were mounted on a rotating plate so that the prepared face of each passed, in turn, over a source of active metal vapor. The thickness of the deposited layer was usually less than $0{\cdot}6\mu$. After the evaporation the specimens were placed in a stainless steel tube and were separated from one another by mica spacers. This tube was then sealed in an evacuated Pyrex tube. No trace was ever found in the Pyrex or stainless steel tubes of any activity which could have been evaporated from the specimens.

The evacuated tube was then placed in the iron core of a cylindrical nichrome-wound furnace. The temperature of the furnace was controlled to $\pm$ 0·5°C by a Micromax controller which was fed by four series-connected chromel–alumel thermocouples. The temperature was measured with a chromel–alumel thermocouple which was frequently compared to an N.B.S. calibrated platinum–13 per cent rhodium thermocouple. The maximum uncertainty in the temperature is less than $\pm$ 1°C. The time of the anneal at the diffusion temperature ranged from one to forty days. For the anneals of short duration a heat-up correction was applied.

The precaution was taken of removing 0·01 in.

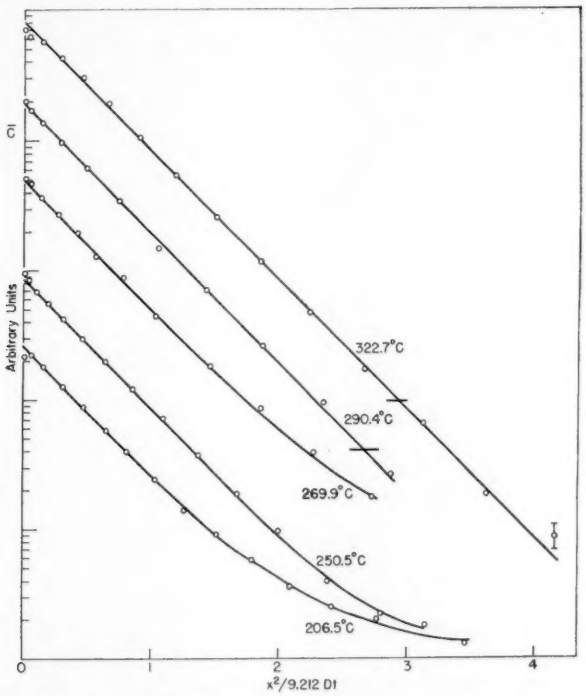

FIG. 2. Lead diffusion profiles for a 50 per cent thallium polycrystalline alloy.

of the cylindrical surface to remove surface diffusion effects (before sectioning the specimens). The specimens were sectioned on a sledge base microtome, either two or four micron thick slices being taken. These slices were combined into groups for weighing and counting, each group containing from one to fifteen slices depending on the penetration depth. In certain cases the slices curled up into tight rolls which were suitable for counting. If such were not the case, or if the rolls oxidized rapidly, the groups were placed in one inch diameter planchets, dissolved in HNO_3, and evaporated to uniformily thin residues of the metal nitrates under an infrared lamp to render them suitable for counting. Groups of slices were weighed on a Mettler microbalance to the nearest 5μg. The aggregate weight of the slices for a given specimen agreed within 0·5 per cent in every case with the loss in weight of the specimen on sectioning. Cylinder diameters were measured with a micrometer which had been checked against a half-inch gauge block. From the diameter and the weight of a group the thickness of the group was calculated.

The activity was determined on several methane flow counters in the proportional region, and at least 10,000 counts above background were taken for each group. It was not necessary to apply decay corrections because of the long half-lives involved (Pb^{210}, 22 years; Tl^{204}, 4 years). In the case of Pb^{210}, however, it was necessary to allow thirty days after the end of the anneal (about six half-lives of Bi^{210}) for secular equilibrium to be established between Pb^{210} and its daughter, and then to count the Bi^{210}.[23] A 12·5 mg/cm^2 aluminum absorber foil was used to prevent the Po^{210} α-radiation from entering the counter. From the activity and the weight of a group the specific activity of a section was determined.

Various semilogarithmic plots of specific activity vs. distance squared (penetration profiles) are shown in Figs. 2 and 3. In these figures the plots have been displaced along the ordinate by arbitrary amounts so that they do not interfere with one another. For the same reason the abscissas are expressed in terms of the variable $X^2/(9{\cdot}212\,Dt)$. From the slopes of the best straight line drawn through the points on plots such as these the diffusion coefficients were calculated. This method of analysis is based on the solution of Fick's second law for the boundary conditions of this experiment[,21] i.e.

$$D = \frac{a}{(\pi Dt)^{1/2}} \exp\frac{-X^2}{4Dt}. \qquad (2)$$

When a tail was observed on these plots only the upper, linear portion was used in the calculation of

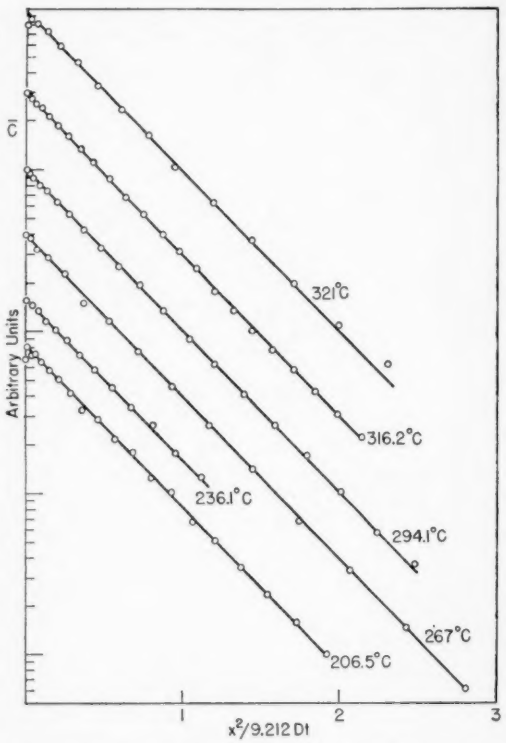

FIG. 3. Lead diffusion profiles for a 62·3 per cent thallium single-crystalline alloy.

D. The absence of tails on any of the penetration profiles of the single crystal specimens (see Fig. 3) and their presence on the profiles of the polycrystalline specimens (see Fig. 2) illustrate the effects of grain boundary diffusion. Diffusion coefficients (corrected for the thickness of the sections misalignment during sectioning[22] and expansion on heating) are listed in Tables 2 and 3.

Figures 4 and 5 show that semilogarithmic plots *D* vs. $1/T$ ($^\circ K^{-1}$) conform with activated state

Table 2. Diffusion coefficients in the alloys ranging in composition from 0 *to* 50 *per cent thallium. The units of D are* $cm^2\ sec^{-1}$. *Each value of D has been multiplied by* 10^{12}

Alloy designation	D_{Pb}					D_{Tl}						D_{Bi}	
	T°C	322·7	290·4	269·9	250·5	206·5	322·4	310·6	283·4	257·8	239·2	206·5	322·7	290·4
0		414	106	41·9	19·0	1·92	657	412	146	47·6	20·7	4·59	1006	266
5		427	116	48·8	19·8	2·18		439	152	51·6	22·4	5·27	1109	265
10		441	118	49·2	20·6	2·40		449	162	55·9	23·5	5·61	1139	281
20		448	125	50·3	23·4	2·65		466	163	56·5	24·9	5·65	1150	307
34		388	111	47·8	22·0	2·54		450	162	56·2	26·6	6·23	978	248
50		266	76·8	30·9	14·9	1·86		351	135	46·0	21·4	5·60	703	210

Table 3. Diffusion coefficients in the alloys ranging in composition from 62·3 *to* 87 *per cent thallium. The units of D are* $cm^2\ sec^{-1}$. *Each value of D has been multiplied by* 10^{12}

Alloy designation	D_{Pb}						D_{Tl}					D_{Bi}
	T°C	231·0	316·2	294·1	267·0	236·1	206·5	320·7	293·8	266·6	236·2	206·4	316·2
62-*s*		152	126	50·0	16·3	3·62	·932	378	145	50·1	13·6	3·51	315
62-*p*		155	128	53·9	17·8	3·65	·921	386	143	51·0	14·5	3·80	327
74		99·1	78·9	31·1	9·30	1·90	·479	330	121	39·6	10·6	2·79	184
76		97·5–97·6	75·4	30·2	8·74	1·78	·436	341	120	39·3	10·2	2·73	174
82		115	91·0	32·8	9·31	1·66	·419	469	153	50·2	12·8	3·08	180
87		248	159·3	62·6	15·8	2·80	·531	—	308	91·4	20·9	5·34	236

Table 4. ΔH_{act} *and* D_0 *as a function of thallium concentration. The units of* ΔH_{act} *are* kcal/mole *and of* D_0 *are* $cm^2\ sec^{-1}$

Alloy designation	Pb diffusion		Tl diffusion	
	ΔH_{act}	D_0	ΔH_{act}	D_0
0	26·06 ± 0·39	1·372 ± 0·5	24·33 ± 0·44	0·511 ± 0·2
5	25·75 ± 0·30	1·108 ± 0·3	23·89 ± 0·52	0·364 ± 0·2
10	25·45 ± 0·41	0·880 ± 0·3	23·83 ± 0·50	0·361 ± 0·2
20	25·05 ± 0·41	0·647 ± 0·2	23·78 ± 0·43	0·353 ± 0·1
34	24·53 ± 0·27	0·367 ± 0·1	23·12 ± 0·46	0·193 ± 0·1
50	24·44 ± 0·54	0·231 ± 0·1	22·52 ± 0·50	0·091 ± 0·05
62–*s*	25·29 ± 0·39	0·287 ± 0·1	23·20 ± 0·21	0·126 ± 0·03
62–*p*	25·64 ± 0·41	0·393 ± 0·2	22·93 ± 0·29	0·101 ± 0·03
74	26·83 ± 0·53	0·691 ± 0·4	23·86 ± 0·41	0·194 ± 0·07
76	27·13 ± 0·49	0·862 ± 0·4	24·48 ± 0·61	0·330 ± 0·2
82	28·24 ± 0·70	2·575 ± 1·8	25·37 ± 0·59	0·957 ± 0·5
87	29·71 ± 0·61	17·0 ± 10	25·53 ± 0·89	1·20 ± 0·8

Vol. 21
1961

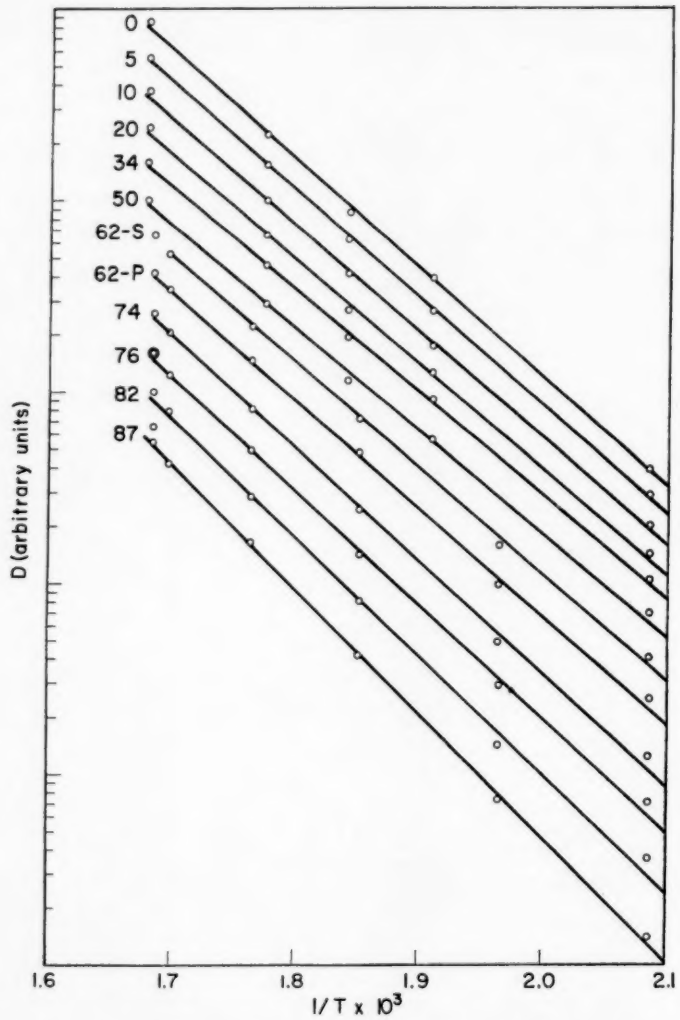

FIG. 4. Log D vs. $1/T$ for lead self diffusion. The plots have been displaced arbitrarily along the ordinate in order not to interfere with one another.

formulations of the diffusion process[23]:

$$D = \gamma a^2 \nu \exp(-\Delta F_{act}/RT)$$
$$= D_0 \exp(-\Delta H_{act}/RT). \quad (3)$$

It is clear from the penetration profiles that the diffusion coefficients should not be given equal weight in the calculation of ΔH_{act} and D_0, and a weighting procedure was chosen based on (a) the length of the linear portion of the profile in order of magnitude, and (b) the numbers of points on this linear portion of the curve. The least square values of ΔH_{act} and D_0 so obtained are listed in Table 4, and the lines drawn on Figs. 4 and 5 are based on these values.

In the lead diffusion runs of short duration it

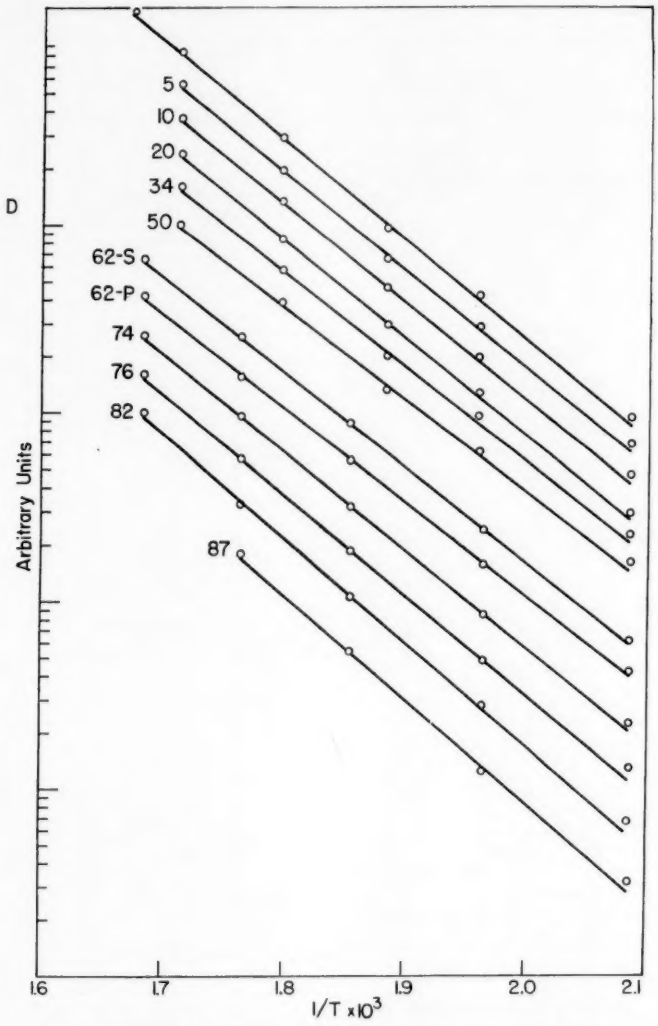

FIG. 5. Log D vs. $1/T$ for thallium self diffusion. The plots have been displaced arbitrarily along the ordinate in order not to interfere with one another.

was possible to determine also the diffusion coefficients for bismuth within the limitations of the assumption that no Bi^{210} was formed during the time in which diffusion was occurring and that all of the Bi^{210} present in a section at the end of the diffusion time was due to diffusion. Because of the five day half-life of Bi^{210} it can be seen that this assumption tended to become valid only for short diffusion times, i.e. for higher temperature experiments. Thus, when the diffusion time was close to one day in length the diffusion specimens were sectioned and counted as soon as possible after the end of the diffusion time, and then counted again after the normal thirty-day waiting period. The Bi^{210} activity could then be extrapolated back to the end of the diffusion time, and a diffusion

profile for bismuth could be plotted. In Fig. 6 are plotted both the lead and bismuth diffusion profiles obtained for a 62-*s* specimen at 316°C, and it is evident that the bismuth diffusion profile is in accord with equation (2), i.e. that a bismuth diffusion coefficient can be calculated from the slope of the straight line obtained. The bismuth

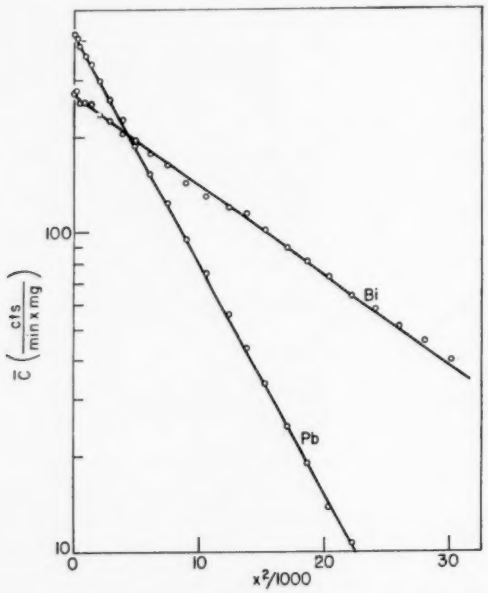

FIG. 6. Penetration profiles for lead and bismuth diffusion in a 62·3 per cent Tl alloy. The plot labeled Bi represents the penetration profile at the end of the diffusion time. The plot labeled Pb represents the same groups of slices counted 30 days later.

diffusion coefficients are listed also in Tables 3 and 4. Further remarks concerning the procedure of obtaining bismuth coefficients are given in an appendix.

3. RESULTS

The values of D, D_0, and ΔH_{act} are listed in Tables 2, 3 and 4. The most notable features of the concentration dependence of the diffusion coefficients (Fig. 7) are the slight maximum near 35 per cent thallium, and the deep minimum near 75 per cent thallium. It is interesting that the lead, thallium, and bismuth diffusion coefficients show approximately the same dependence on concentration. In Fig. 8, ΔH_{act} is plotted vs. atomic per cent thallium and in Fig. 9, log D_0 is plotted vs. atomic per cent thallium. It is to be noted that despite the undulatory behavior of the diffusion

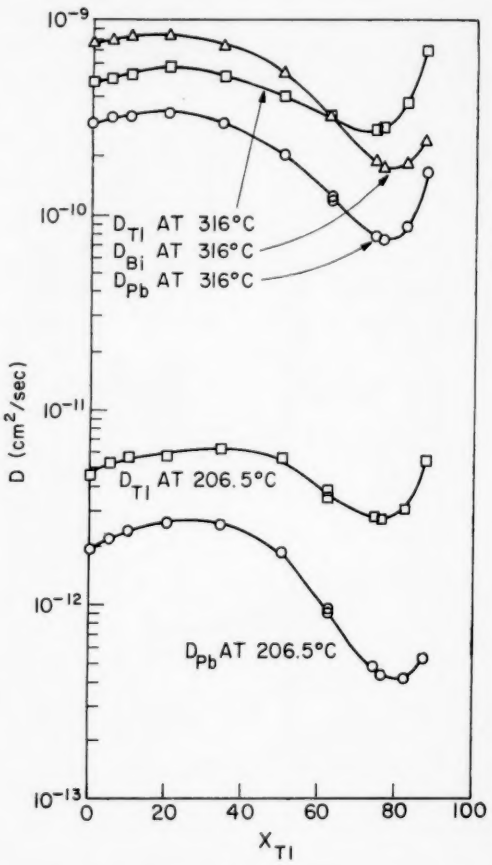

FIG. 7. Log D vs. X_{Tl} at two temperatures.

coefficients, ΔH_{act} and D_0 show only minima close to 50 per cent thallium.

Self-diffusion in lead has been studied by VON HEVESY *et al.*[24], OKKERSE[25], and NACHTRIEB and HANDLER[26]. The data obtained in these previous studies and those presented here are compared in Table 5. The discrepancy between the value of ΔH_{act} reported by NACHTRIEB and HANDLER and that reported here is about twice

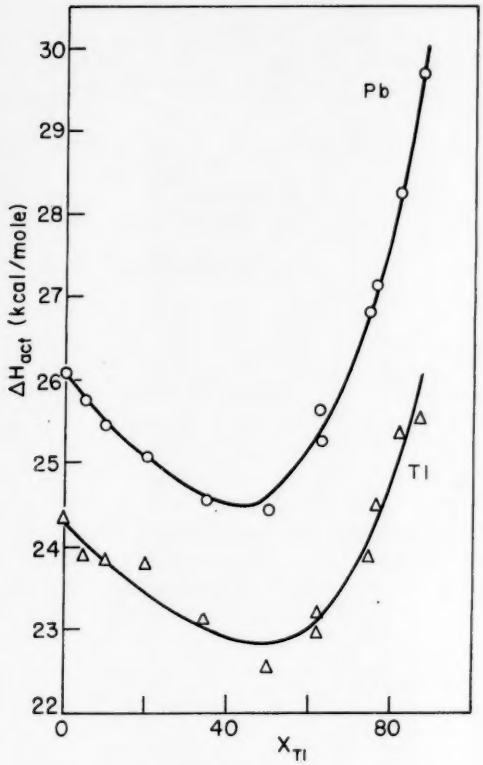

FIG. 8. ΔH_{act} vs. X_{Tl}.

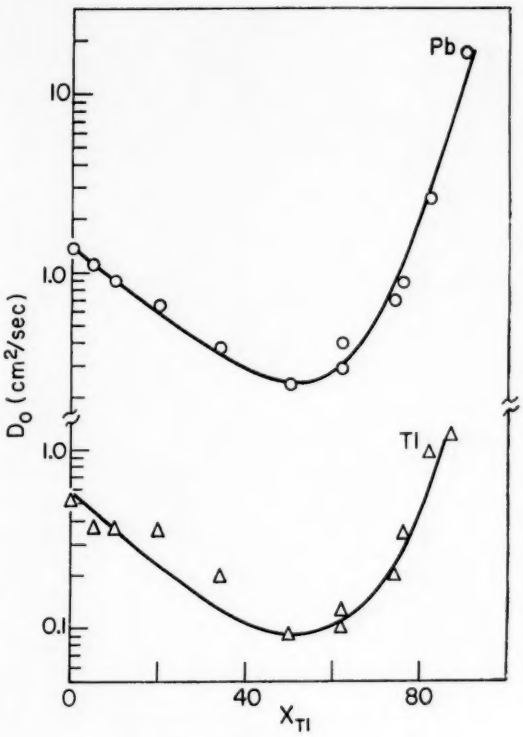

FIG. 9. D_0 vs. X_{Tl}.

Table 5. Self diffusion in lead

Reference	ΔH_{act}(kcal/mole)	D_0 (cm²/sec)
VON HEVESY	27,680 ± (2500)	5·56
OKKERSE	25,700	1·17
NACHTRIEB	24,210 ± 770	0·281
Present	26,060 ± 390	1·37

the sum of the limits of error claimed in each case. The remarkable fact is that the present value of ΔH_{act} is larger despite the fact that polycrystalline specimens were used in obtaining it. Since in this study ΔH_{act} was found to be a smooth function of thallium concentration, the discrepancy is not just due to random error but must be due to some systematic error. Perhaps in the measurement of temperature a systematic error arose, due to the fact that the thermocouple used in the present study was not calibrated directly but was checked (frequently) against an N.B.S. calibrated thermocouple.

Diffusion in the Pb–Tl system was studied using chemical diffusion methods by SEITH and HERMANN[27]. They observed no composition dependence for the thallium diffusion coefficient in the range 0–50 per cent thallium, which is in agreement with the data reported here within the limits of their error. They obtained a value of 24,600 kcal/mole as the enthalpy of activation for the diffusion of thallium in pure lead. This is in agreement with the value of 24,300 kcal/mole reported here. The value of D_{Tl}/D_{Pb} at 315°C is about $\frac{5}{3}$, in close agreement with the present data.

SEITH and LAIRD[28] studied the diffusion of bismuth in Pb–Bi alloys. However, they worked in a lower temperature range, and comparison to the limited bismuth diffusion data presented here is not possible.

Vol. 21
1961

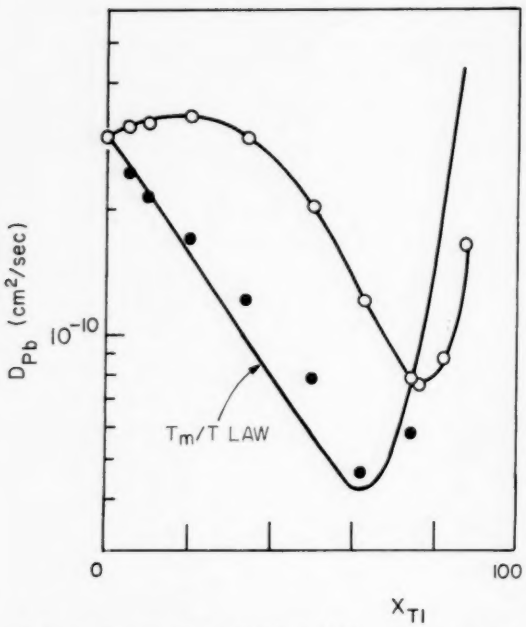

FIG. 10. D_{Pb} vs. X_{Tl} at 316°C. ⊙ indicate experimental points, ● represent the experimental values to which the volume correction has been applied. The dependence predicted by the T_m/T postulate is indicated.

4. THE T_m/T POSTULATE

At a given temperature and composition equation (1) allows a predicted value of the lead diffusion coefficient to be calculated from the self-diffusion coefficient of pure lead at that temperature and the melting temperature characteristic of that composition. The values of T_m shown in Table 1 have been read from the solidus of the phase diagram as reported by HANSEN[13]. In Fig. 10 the predicted and experimental values of the lead diffusion coefficients at 316°C are plotted vs. thallium concentration. The experimental values rise to a slight maximum in qualitative disagreement to the prediction of equation (1). If the T_m/T postulate were assumed to hold for solute diffusion as well, it can be seen in Fig. 11 that the same lack of agreement between experiment and theory exists. On a plot of log D vs. T_m/T the postulated values of D_{Pb} at the various compositions necessarily lie on a straight line determined only by the diffusion coefficients in pure lead. In Fig. 12 the experimental values of D_{Pb} representing two isotherms are shown on such a plot, and can be observed to curl away from the predicted line and to cross it again at a point corresponding to approximately 75 atomic per cent thallium.

If the temperature dependence of equation (1) is compared with that of the usual expression for the diffusion coefficient given by equation (3) another prediction is obtained, namely,[8]

$$\Delta H_{act} = RBT_m.$$

In Fig. 13 the expected values of ΔH_{act} are plotted vs. thallium concentration along with the observed values for lead, and again there is qualitative disagreement between equation (1) and experiment.

The lattice constants, as measured by TANG and PAULING[19], are plotted vs. composition in Fig. 1 along with the values to be expected from Vegard's Law. It can be seen that the lattice constant, as X_{Tl} is increased, departs from the predictions of Vegard's Law, reaching a maximum departure at about 50 per cent thallium and then returning to the predictions of Vegard's Law at

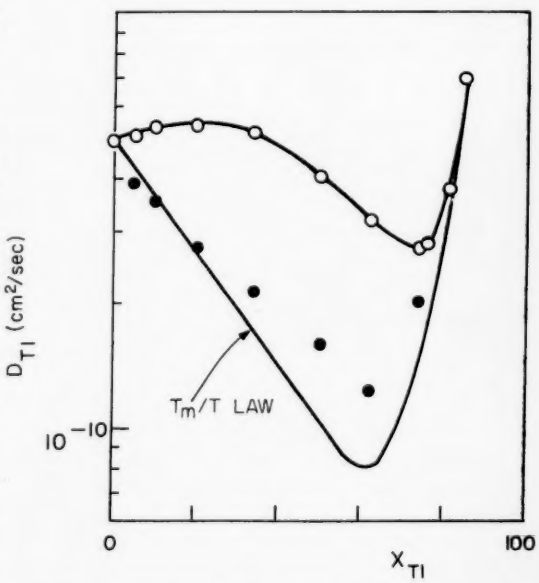

FIG. 11. D_{Tl} vs. X_{Tl} at 316°C. ⊙ indicate experimental points, ● represent the experimental values to which the volume correction has been applied. The dependence predicted by the T_m/T postulate is indicated.

Vol. 2
196

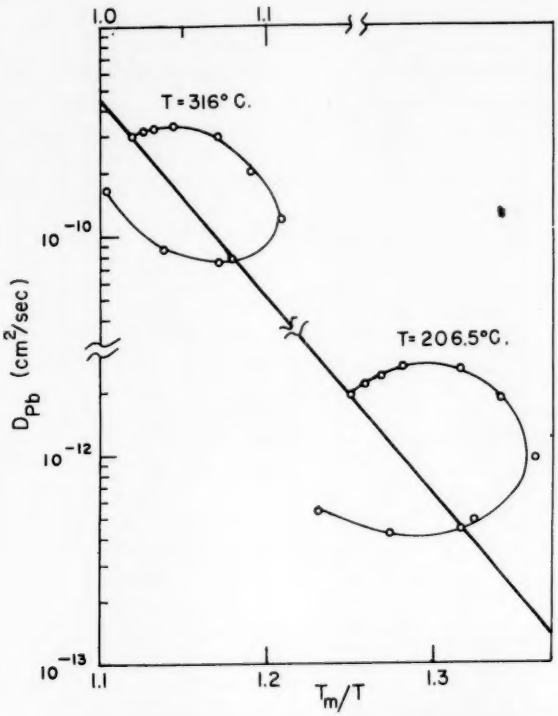

FIG. 12. Log D_{Pb} vs. T_m/T. The straight line represents the prediction of the T_m/T postulate. The curves represent two experimentally determined isotherms.

75 per cent thallium—remaining close thereto to the end of the solid solution range (87 per cent thallium). These departures from Vegard's Law are of the proper sign to account for the departure from the T_m/T postulate if it is assumed that diffusion but not melting is sensitive to the lattice dilatation. Both the lattice dilatation and the anomalously high diffusion coefficients show the same concentration dependence. Figs. 10 and 11 show that the downward trend of the diffusion coefficients is suddenly reversed at about 75 per cent thallium, after which the observed and expected values parallel one another more closely. These facts suggest that in the region 0–75 per cent thallium a correction may be applied to the diffusion coefficients.

Fortunately, the effect of a change in volume on the diffusion coefficient is known because the effect of pressure on self-diffusion in lead has been studied.[8] If the three derivatives

$$\frac{\partial \ln(D/\gamma a^2 \nu)}{\partial P} = \frac{-\Delta V_{act}}{RT}$$

$$\frac{\partial P}{\partial \ln V} = \frac{1}{\kappa}$$

$$\frac{\partial \ln V}{\partial \ln a} = 3$$

are multiplied together, an equation relating the diffusion coefficient to the lattice constant is obtained, which upon integration yields the following result:

$$\ln \frac{D}{D(0)} = \frac{3\Delta V_{act}}{\kappa RT} \times \frac{\Delta a}{a}. \qquad (4)$$

$\gamma a^2 \nu$ is independent of volume to within an error of less than 1 per cent and its volume dependence is neglected; ΔV_{act} is the volume of activation,[8] 13·0 cm^3; P is the pressure in atmospheres; V is the molar volume; κ, the compressibility of lead, is $2{\cdot}4 \times 10^{-6}$ cm^3/kg,[29] and is used at all compositions; a is the lattice constant, and Δa is the departure from Vegard's Law (read from Fig. 1); D

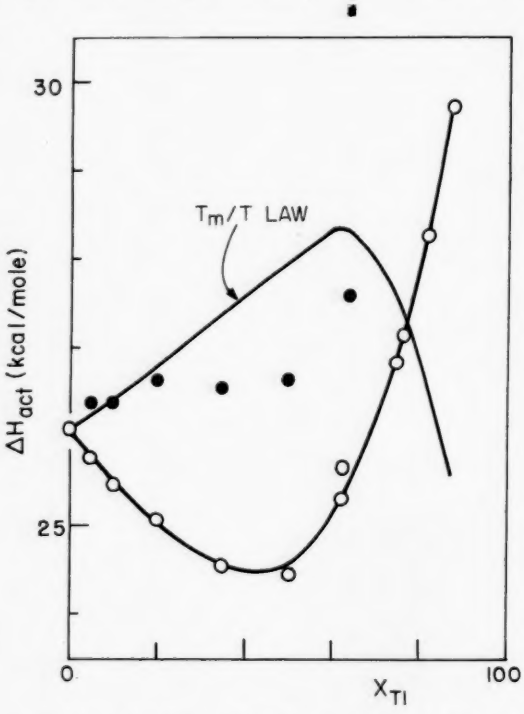

FIG. 13. ΔH_{act} for Pb diffusion vs. X_{Tl}. ○ indicate experimental points, ● represent experimental values to which the volume correction has been applied. The dependence predicted by the T_m/T postulate is indicated.

is the observed diffusion coefficient at a given composition and thus has $a\,(\Delta a)$ associated with it, and $D(0)$ is the value of D corrected to $a = 0$. At each composition in the range 0–75 per cent thallium a value of $D(0)$ was calculated. These values of D_{Pb} have been plotted in Fig. 11 along with the observed and expected values. These corrected values lie very close to the predicted values, and the agreement may be considered highly satisfactory.

The value of ΔV_{act} for thallium diffusion is not available, but should not be far different from that of lead in pure lead. Thus the same correction was also applied to the thallium diffusion coefficients. and the results are shown in Fig. 11.

Since the temperature appears in equation (4) it was also possible to make a correction to the enthalpy of activation, i.e.

$$\Delta H_{act} - \Delta H_{act}^{(0)} = 3\Delta V_{act}\Delta a/\kappa a$$

where ΔH_{act} is the observed value, and $\Delta H_{act}^{(0)}$ is the former corrected to $\Delta a = 0$. In Fig. 13 the corrected values are plotted along with curves representing the observed and predicted values. Here the agreement is at best qualitative, implying the corrections to the diffusion coefficients at other temperatures will probably not work out as well as they did at 316°C. Another disagreeable feature is that in the region 75–87 per cent thallium where no correction is possible, the observed values and those predicted by the T_m/T postulate go in opposite directions as X_{Tl} increases.

In this correction procedure probably the worst assumption is made in using the room temperature values of the lattice constant to correct the high temperature diffusion coefficients. Using the values of the compressibility and ΔV_{act} of pure lead for the correction at all compositions should be a good assumption in comparison.

The main implication of this correction procedure is that only solutions which obey Vegard's Law should follow the T_m/T postulate. In the silver–palladium system where the T_m/T postulate is followed,[7] the lattice constant does obey Vegard's Law more closely.

5. THE JOHNSON MECHANISM

The JOHNSON mechanism[30] was introduced in order to explain the fact that in many cases of impurity diffusion in metals the impurity diffusion coefficient is much greater than the solvent diffusion coefficient and that, correspondingly, ΔH_{act} for impurity diffusion was sometimes less than half the values of ΔH_{act} for solvent diffusion. These effects could not be assigned merely to an increased jump frequency for the impurity atom over that of the solvent atom because such a condition leads to much redundant jumping of the impurity atom. JOHNSON was able to show that

Vol. 2
1961

if there were a binding energy between impurity atoms and vacancies, solute vacancy molecules would result which could climb "amoeba-like" through the lattice, thus giving a higher impurity diffusion coefficient and a lower ΔH_{act}.

Certain quantities which have found use in treating the JOHNSON mechanism will be enumerated here before proceeding with the discussion:

(a) D_1, the diffusion coefficient of solvent atoms as measured by the radioactive tracer technique at an atom fraction N_2 of solute, D_1^0 indicating the diffusion coefficient when N_2 is zero;

(b) D_2 and D_2^0, the respective diffusion coefficients of the solute;

(c) ω, the frequency with which a solvent atom jumps into a nearest neighbor vacancy, the jump occurring either in pure solvent or in a region of solution remote from a solute atom (this and all over ω's to be defined are of the form $\nu \exp(-\Delta F_m/RT)$ where ν is of the order of magnitude of the lattice vibration frequency and where ΔF_m is the free energy required to move the atom into the vacant lattice site; $\Delta F_m = \Delta H_m - T\Delta S_m$);

(d) ω_S, the frequency with which a solute atom jumps into an FCS2 vacancy. The notation FCS2 is used to mean "first coordination sphere of a solute atom";

(e) ω_T, the frequency with which an FCS2 solvent atom jumps into a nearest neighboring FCS2 vacancy;

(f) ω_A, the frequency with which an FCS2 solvent atom jumps into a nearest neighboring non-FCS2 vacancy, and creates a solute vacancy complex;

(g) ω_D the frequency with which a non-FCS2 solvent atom jumps into a nearest neighboring FCS2 vacancy and destroys a solute vacancy complex;

(h) W, the solute vacancy binding energy. ΔF_f is the free energy of formation of a vacancy in pure solvent, i.e. a non-FCS2 vacancy, and $\Delta F_f + W$ is the free energy of formation of an FCS2 vacancy. If W is negative a solute vacancy complex can be said to exist. Indicate $\exp(-W/RT)$ by α.

MANNING[31] has shown that when ω_S/ω is infinite D_2/D_1^0 can be at most 4·58 unless the notion of solute vacancy binding is introduced. For thallium and lead diffusion in pure lead D_2^0/D_1^0 is 1·59 at 600°K and 2·12 at 500°K. Combining equations (8) and (36) of MANNING's paper yields the following expression for an f.c.c. lattice:

$$\frac{D_2^0}{D_1^0} = \frac{(2\omega_T + 5{\cdot}151\omega_D)\,[\omega_S/\omega \exp(-W/RT)]}{0{\cdot}78146(2\omega_T + 2\omega_S + 5{\cdot}151\omega_D)}. \quad (5)$$

Assuming that ω_S is the only frequency different from ω and that W is zero allows a value of ω_S/ω

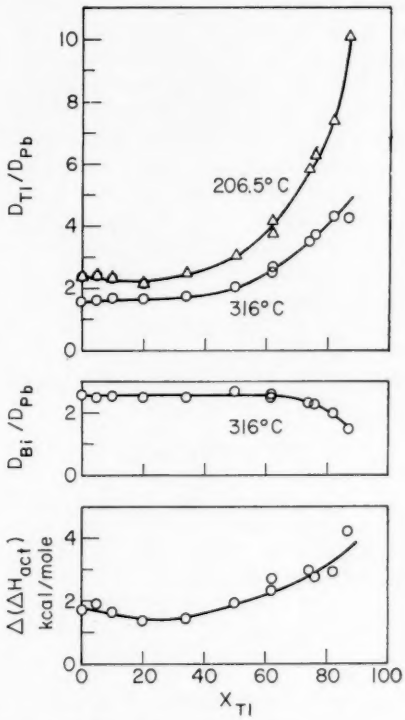

FIG. 14. Upper: D_{Tl}/D_{Pb} vs. X_{Tl}
Middle: D_{Bi}/D_{Pb} vs. X_{Tl}.
Lower: $(\Delta H_{act})_{Pb} - (\Delta H_{act})_{Tl}$ as a function of X_{Tl}.

to be calculated which in the lead–thallium case is 1·91 at 600°K and 3·09 at 500°K. Log (ω_S/ω), determined at these and at intermediate temperatures, was found to be linear in T^{-1} with an activation energy of −2·9 kcal/mole. These values are not extreme, and suggest that it may not be necessary to invoke solute vacancy binding.

The opposite conclusion is reached if the results

are examined from the point of view of LAZARUS' theory He derived the expression for D_2/D_1 as a function of composition:

$$\frac{D_2^0}{D_1^0} = \frac{D_2}{D_1}\left[1-4N_2+4N_2\exp\left(-\Delta E_{mi}/RT\right)\right] \quad (6)$$

where ΔE_{mi} is the extra energy required to move a solute atom as compared to a solvent atom. From Fig. 14 it can be seen that D_2/D_1 is constant up to 30 atomic per cent thallium. Therefore, ΔE_{mi} must be zero. However, ω_S/ω should be equal to $\exp\left(-\Delta E_{mi}/RT\right)$ and hence $\omega_S = \omega$. D_2 must then be greater than D_1 purely because of solute vacancy binding. LAZARUS states that ΔE_{mi} is also the change in energy of motion for FCS2 solvent atoms; hence, $\omega_T = \omega_S = \omega$. REISS[4] suggests the assumption that $\omega_A = \omega$ and that $\omega_D = \omega\exp(W/RT) = \omega/\alpha$. Making these substitutions in equation (5) yields values for α of 1·74 at 316°C and 2·47 at 206°C. Log α has approximately the same temperature dependence as the ratio of the diffusion coefficients so that $W = -1{\cdot}7 \pm 0{\cdot}8$ kcal/mole.

The theory of REISS[4] furnishes two expressions for the quantity b in the equation:

$$D_1 = D_1^0(1+bN_2).$$

Using only the data for the 0 and 5 per cent thallium alloys the values of b obtained are 1·05 at 316°C and 2·37 at 206°C. The first of the expressions presented by REISS,

$$b = 0{\cdot}306h(\gamma)\frac{12\omega_T}{\alpha\omega} - 13, \quad (7)$$

is derived under the assumption that both bound and free vacancies have long lifetimes. This situation corresponds to large negative W and large values of b according to REISS, and should thus not be applicable to the present case. The second expression,

$$b = 0{\cdot}28\frac{12\omega_T}{\omega\alpha} + 16 - 13 \quad (8)$$

was derived specifically for small values of b, and takes into account the association and dissociation of solute vacancy complexes. In an ideal solution, however, no concentration dependence is expected, and b should be zero. For an ideal solution all of the frequencies should be equal, and W should be zero. Making these substitutions in (8) yields a value of seven, not zero, for b. Thus the theory of REISS does not account for values of b between zero and seven, the region in which the data of the present study lie.

6. THE POSSIBILITY OF ORDER IN THE SYSTEM

One consideration which has not yet been discussed in the possible existence of order in the Pb–Tl system. Much indirect evidence has accumulated for the existence of order at compositions ranging from 62–87 per cent thallium although no direct evidence such as that from X-ray measurements has been obtained. A superlattice has not been detected because of the similar scattering factors of Pb and Tl. The indirect evidence consists of the following facts.

(1) The lattice parameter determination of TANG and PAULING shows a cusp at 75 per cent Tl.[19]

(2) TANG and PAULING[19] derived the liquidus and solidus lines of the temperature–composition diagram on the basis of an assumed order at 75 per cent Tl.

(3) The alloys are formed exothermically with the integral heat of solution reaching its greatest negative value in the neighborhood of 75–78 per cent Tl.[32]

(4) The entropy of formation of the alloys becomes 0 at about 87 per cent Tl.[33]

(5) The electrical conductivity of the alloys rises to a maximum close to 87 per cent thallium.[34]

(6) TANG and PAULING[19] have shown that there are possible superlattices in the f.c.c. structure at AB_3 and AB_7.

Thus it is likely that there is order at either 75 or 87 per cent thallium or possibly at both compositions. Intuitively one would expect (other things remaining the same) that order would lower the diffusion coefficient and raise the enthalpy of activation. It has been shown[35] that for an interstitial C atom diffusing in an ordered AB lattice there is a minimum in its diffusion coefficient when plotted versus composition and that its activation enthalpy does not increase. KUPER *et al.*[36] have studied diffusion in β-brass and the effect of ordering upon it. They observed that the enthalpy of activation did increase with order.

An examination of the data here presented shows a minimum in the diffusion coefficients of Pb, Tl, and Bi in the vicinity of 75 per cent thallium. This fact as it stands would suggest order at 75 atomic per cent thallium.

Further examination of the data, however, shows that a plot of ΔH_{act} vs. composition passes through 75 per cent thallium without even a hint of a maximum. Indeed, it steeply rises to 87 per cent thallium, and this latter fact, taken alone, would argue for the existence of order at 87 per cent thallium.

It would be expected that a change in the melting temperature or a change in volume would affect both lead and thallium diffusion coefficients in the same manner, i.e. the ratio D_{Tl}/D_{Pb} would not be much affected. This ratio as a function of thallium concentration would show the existence of factors which would affect D_{Pb} and D_{Tl} differently. If order exists at $PbTl_7$ the lead sites have no lead sites as nearest neighbors, while the thallium sites are of two kinds—those having two nearest neighbor lead sites and those having no nearest neighbor lead sites. Therefore, a lead atom in its ordered site would have to introduce disorder into the lattice if it is to jump, while a thallium atom would jump freely without introducing disorder. Intuitively, then, the existence of order at $PbTl_7$ would lead to an increase in the ratio D_{Tl}/D_{Pb} and probably also in the quantity $\Delta H_{act}(Pb) - \Delta H_{act}(Tl)$ vs. thallium concentration. In Fig. 14 are plotted the ratios D_{Tl}/D_{Pb} and D_{Bi}/D_{Pb}, the former being plotted for both 20·6 and 316°C. The difference in the activation enthalpies is also plotted in Fig. 14. These plots seem to support the conclusion that there is order at 87 per cent thallium.

7. CONCLUSIONS

(1) The postulate that T_m/T is the only factor governing diffusion in solid solutions is not supported by the data on diffusion obtained in the lead–thallium system.

(2) The fact that a correction can be made for a dilatation of the lattice, i.e. a positive deviation of the lattice constant from Vegard's Law, implies that the T_m/T postulate might hold for "ideal" solutions in the sense of there being no deviation from Vegard's Law.

(3) Although the ratio D_{Tl}/D_{Pb} in pure lead is not so great as to make it absolutely necessary to consider vacancy binding, the theory of LAZARUS indicates that vacancy binding is the only contributing factor toward making D_{Tl}/D_{Pb} greater than one.

(4) The theory of REISS will have to be re-examined to account for the data of this study.

(5) The data tend to support the idea of order at 87 per cent thallium.

Acknowledgements—This research was carried out in part with the support of the United States Air Force under Contract No. AF 18(600)–1489 with the University of Chicago. HENRY A. RESING gratefully acknowledges the receipt of several National Science Foundation Fellowships during the period of his graduate studies. The assistance of the U.S. Naval Research Laboratory in the preparation of the manuscript for publication is gratefully acknowledged.

REFERENCES

1. HOFFMAN R. E., TURNBULL D. and HART E. W., *Acta Met.* **3,** 417 (1955).
2. HART E. W., HOFFMAN R. E. and TURNBULL D., *Acta Met.* **5,** 74 (1957).
3. LAZARUS D., *Imperfections in Solids*, p. 107. American Society for Metals, Chicago, Illinois (1954).
4. REISS H., *Phys. Rev.* **113,** 1445 (1959).
5. DARKEN L. S., *Trans. A.I.M.E.* **175,** 184 (1948).
6. REYNOLDS J. E., AVERBACH B. L. and COHEN M., *Acta Met.* **5,** 29 (1957).
7. NACHTRIEB N. H., PETIT J. and WEHRENBERG J., *J. Chem. Phys.* **26,** 106 (1957).
8. NACHTRIEB N. H., RESING H. A. and RICE S. A., *J. Chem. Phys.* **31,** 135 (1959).
9. RICE S. A., *Phys. Rev.* **112,** 804 (1958).
10. RICE S. A. and NACHTRIEB N. H., *J. Chem. Phys.* **31,** 139 (1959).
11. LAWSON A. W., RICE S. A., CORNELIUSSEN R. D. and NACHTRIEB N. H., *J. Chem. Phys.* **32,** 447 (1960).
12. RICE S. A. and FRISCH H. L., *J. Chem. Phys.* **32,** 1026 (1960).
13. HANSEN M., *Constitution of Binary Alloys*, 2nd Ed. p. 1115. McGraw Hill, New York (1958)
14. RHINES F. N., *Phase Diagrams in Metallurgy*, p. 31. McGraw Hill, New York (1956).
15. LUNDELL G. E. F. and HOFFMAN J. D., *Outlines of Methods of Chemical Analysis*, p. 108. John Wiley, New York (1938).
16. BERG R. and FAHRENKAMPF E. S., *Z. Anal. Chem.*, **109,** 305 (1937).
17. HILLEBRAND W. F. and LUNDELL G. E. F., *Applied Inorganic Analysis*, p. 187. John Wiley, New York (1948).
18. EGERTON A. C. and LEE W. B., *Proc. Roy. Soc.* **103,** 487 (1923).

Vol. 21
1961

19. TANG Y. and PAULING L., *Acta Cryst., Camb.* **5,** 39 (1952).
20. NACHTRIEB N. H. and HANDLER G. S., *J. Chem. Phys.* **23,** 1569 (1955).
21. JOST W., *Diffusion in Solids, Liquids, Gases*, p. 19. Academic Press, New York (1952).
22. SHIRN G. A., WAJDA E. S. and HUNTINGTON H. B., *Acta Met.* **1,** 513 (1953).
23. WERT C. and ZENER C., *Phys. Rev.* **32,** 1026 (1949).
24. VON HEVESEY G., SEITH W. and KEIL A., *Z. Phys.* **79,** 197 (1932).
25. OKKERSE B., *Acta Met.* **2,** 551 (1954).
26. NACHTRIEB N. H. and HANDLER G. S., *J. Chem. Phys.* **23,** 1569 (1955).
27. SEITH W. and HERMANN J., *Z. Elektrochem.* **46,** 213 (1940).
28. SEITH W. and LAIRD J. G., *Z. Metallk.* **24,** 194 (1932).
29. PARTINGTON J. R., *An Advanced Treatise on Physical Chemistry*, Vol. III, p. 166. Longmans, Green and Co., New York (1952).
30. JOHNSON R. P., *Phys. Rev.* **56,** 814 (1939).
31. MANNING J. R., *Phys. Rev.* **116,** 819 (1959).
32. KUBASHEWSKI O. and CATTERALL J. A., *Thermochemical Data of Alloys*, p. 117. Pergamon Press, New York (1956). The values listed here are calculated from the data of A. ÖLANDER, *Z. Phys. Chem.* **A168,** 274 (1934).
33. KUBASHEWSKI O. and SCHNEIDER A., *Z. Elektrochem.* **49,** 261 (1943).
34. ÖLANDER A., *Z. Phys. Chem.* **A168,** 274 (1934).
35. SMIRNOV A. A., *J. Tech. Phys. U.S.S.R.* **23,** 56 (1953).
36. KUPER A. B., LAZARUS D., MANNING J. R. and TOMIZUKA C. T., *Phys. Rev.* **104,** 1536 (1956).

APPENDIX

BISMUTH DIFFUSION COEFFICIENTS

The quantity "a" which appears in the numerator on the right side of equation (2) is given by

$$a = \int_0^\infty C(x,t)\,dX. \qquad \text{(a)}$$

Both in the determination of the lead diffusion coefficient and of the bismuth diffusion coefficient only the Bi^{210} is counted. Therefore, once secular equilibrium has been attained in the vapor deposited layer, the quantity "a" is no longer subject to change with time and is the same whether D_{Bi} or D_{Pb} appears in equation (2). Because of this fact the ratio of the intercepts of the two penetration profiles (see Fig. 6) is equal to the reciprocal of the square root of the ratio of the diffusion coefficients. D_{Bi} is calculated by this method from D_{Pb} and the ratio of the intercepts for a 62-s crystal at 316°C was $2{\cdot}84\times10^{-10}$ cm^2 sec^{-1}, which is to be compared to the value $3{\cdot}08\times10^{-10}$ cm^2 sec^{-1} obtained from the slope of the penetration profile. This method also is subject to the assumption that no Bi^{210} is formed during the diffusion time.

In order to evaluate the assumption mentioned in the preceding paragraph an attempt was made to solve the true equation relating C_{Bi} to time of diffusion and distance from the interface:

$$\frac{\partial C_{Bi}}{\partial t} = D_{Bi}\frac{\partial^2 C_{Bi}}{\partial X^2} + k_{Pb}C_{Pb} - k_{Bi}C_{Bi}, \qquad \text{(b)}$$

where k_{Pb} and k_{Bi} are the decay constants of Pb^{210} and Bi^{210}, respectively, and where C_{Pb} is a function of time and coordinate. If D_{Bi} and D_{Pb} are equal, then

$$k_{Pb}C_{Pb} = k_{Bi}C_{Bi}$$

equation (b) reduces to Fick's second law, and no error in the determination of D_{Bi} is caused by the assumption. Since $D_{Bi} > D_{Pb}$ the next limiting case evaluated was that of $D_{Pb} = 0$. For a diffusion time of one day and a penetration profile going through one order of magnitude in C_{Bi}, the error in D_{Bi} was determined to be 15 per cent. Thus the error in D_{Bi} as reported due to the assumption mentioned is certainly less than 15 per cent.

It seems appropriate to discuss here the procedure used in determining D_{Pb} of allowing 30 days to elapse before counting the Bi^{210}. The user of this procedure tacitly assumes that $D_{Bi} \sim D_{Pb}$, i.e. that the amount of Bi^{210} in a section at the end of the diffusion time is less than, or at least not much greater than, the amount of Bi^{210} that will grow into equilibrium with the Pb^{210} which has diffused to that section. For example, in the alloys used in this study $D_{Bi} = 2D_{Pb}$ and from Fig. 6 it can be seen that when the activity has fallen through two orders of magnitude on the lead diffusion profile, it has fallen only one on the bismuth diffusion profile. Thus the specific activity ascribed to lead after a 30 day wait is still 16 per cent too high. This condition becomes worse farther out on the lead diffusion profile and leads to upward curvature as X^2 increases. The relative magnitude of D_{Bi} and D_{Pb} are important since the error becomes worse as the ratio D_{Bi}/D_{Pb} increases; however, for D_{Bi}/D_{Pb} less than one the lead diffusion is not markedly affected. In conclusion, it may be stated that a larger waiting period would be advisable in certain cases.

J. Phys. Chem. Solids Pergamon Press 1961. Vol. 21, Nos. 1/2, pp. 57–70. Printed in Great Britain.

THE FERROMAGNETIC–ANTIFERROMAGNETIC PROPERTIES OF COPPER–MANGANESE AND SILVER–MANGANESE ALLOYS

J. S. KOUVEL

General Electric Research Laboratory, Schenectady, New York

(*Received* 22 *March* 1961)

Abstract—Magnetic hysteresis loops displaced from their symmetrical positions about the origin are observed when the alloys of about 5–30 per cent Mn in Cu and 10–25 per cent Mn in Ag are cooled to 1·8°K in a magnetic field. The two remanent magnetizations from each loop are equal both in magnitude and direction and represent a ferromagnetic alignment of a significant fraction of the Mn atomic moments. For each alloy, the hysteresis loop displacement decreases with increasing temperature and its disappearance is attended by large hysteresis losses. At a somewhat higher temperature, the losses vanish and the magnetic susceptibility reaches a maximum. However, the only anomaly in the electrical resistivity vs. temperature curve, indicative of a magnetic transition, occurs at a still higher temperature.

All these properties and their dependence on alloy composition are shown to be qualitatively consistent with a microscopic exchange anisotropy model. According to this model, the coexistence of antiferromagnetic and ferromagnetic interactions between Mn atoms of different separation, together with the statistical fluctuations in the local Mn concentration, gives rise to unusual magnetic states in these atomically-disordered alloys.

Vol. 21
1961

INTRODUCTION

CONSIDERABLE attention has been recently given to the magnetic behavior of dilute alloys of manganese in copper down to liquid helium temperatures. Whereas earlier experiments had shown that their magnetic susceptibilities at higher temperatures obeyed the Curie–Weiss relation, $\chi = C/(T-\theta)$, with values of θ that were small but positive, it was observed by OWEN *et al.*[1, 2] and by SCHMITT and JACOBS[3] that these alloys did not become ferromagnetic at low temperatures. On the contrary, except for those extremely dilute in manganese ($< 0{\cdot}4$ at. per cent), the alloys were found to exhibit susceptibility maxima which were indicative of antiferromagnetic order. These observations led OWEN *et al.*[2] to propose a molecular field model in which the Mn ions are divided into two sublattices. For the assumptions that the short range interactions within each sublattice be ferromagnetic and stronger than the short range antiferromagnetic interactions between sublattices, this model was able to give antiferromagnetic ordering at low temperatures and a positive paramagnetic Curie point (θ). However, as the authors pointed out, such a model with a limited number of interaction parameters can be valid only for an atomically ordered structure whereas the copper–manganese alloys in question are highly, though perhaps not completely, disordered. Thus, the perfect antiferromagnetic order predicted by this model is undoubtedly a simplification of the actual magnetic state of these alloys at low temperatures.

In fact, two magnetic phenomena revealed by the same investigations[1–3] suggested that the antiferromagnetic order in the copper–manganese alloys is imperfect and can be easily disturbed by an applied magnetic field. First, when an alloy that exhibited a susceptibility maximum was cooled to liquid helium temperatures in zero field, it was found upon subsequent application and removal of a magnetic field that there was a small but measurable isothermal remanent magnetization (IRM). Secondly, a non-zero thermoremanent

magnetization (TRM) was observed when the alloy was cooled to these temperatures in a magnetic field and the field then removed. It was later demonstrated that as the maximum field applied during these experiments was raised, both the IRM and the TRM increased (the latter more rapidly) until they reached the same saturation value.[4]

The presence of these remanences and especially their saturation strongly suggest that the dilute alloys of manganese in copper are in a mixed ferromagnetic–antiferromagnetic state at low temperatures. This complicated magnetic state could very well be the outcome of antiferromagnetic and ferromagnetic interactions between nearest-neighbor and more distantly separated Mn–Mn atom pairs, respectively, as assumed previously for the two-sublattice model[2] but now applied more realistically to an atomically disordered system with its inherent statistical fluctuations in chemical composition. Under these circumstances, the antiferromagnetic interactions would predominate in regions in the alloy that are relatively rich in Mn while the ferromagnetic couplings would be decisive in the Cu-rich regions.

A coexistence of small regions of antiferromagnetic and ferromagnetic order, analogous in origin to that discussed above, has been recently proposed as an essential part of a magnetic model for the disordered alloys of nickel–manganese[5] and cobalt–manganese.[6] It had been observed that compositions near 25 atomic per cent manganese exhibited a remarkable change in their magnetic behaviour when they were cooled to liquid helium temperatures in a magnetic field. Under this condition, their magnetic hysteresis loops were displaced from their symmetrical positions about the origin, the remanent magnetizations for both branches of each loop having the same direction as the field applied during cooling. This unidirectional anisotropy behavior is similar to that previously found in partially-oxidized cobalt particles[7] and attributed to exchange interactions between the ferromagnetic Co and the antiferromagnetic CoO. Hence, in the more microscopic exchange anisotropy model for the Ni–Mn and Co–Mn alloys, it was necessary to justify not only the coexistence of antiferromagnetic and ferromagnetic regions but also an appreciable coupling between these regions. In addition, it had to be assumed that at low temperatures the moments within the antiferromagnetic regions were prevented from reversing by strong anisotropy forces and that this gave rise to the observed magnetic asymmetry.

This tentative interpretation of the exchange anisotropy effects found in Ni–Mn and Co–Mn alloys raised the intriguing possibility that these effects might also be displayed by Cu–Mn alloys whose low-temperature properties, described above, indicated a mixed ferromagnetic–antiferromagnetic state. This was further suggested by previous observations that the remanent magnetizations of dilute alloys of Mn in Cu cooled to 4·2°K in a magnetic field, could not be reversed by large reverse fields.[2, 3] However, no attempt had been made to study this phenomenon more closely as possible evidence for exchange anisotropy. Subsequently, STREET and SMITH found that when Cu–Mn alloys of 40–50 per cent Mn were cooled to 80°K in a magnetic field, their magnetizations in the direction of this field were much larger than those obtained by cooling in zero field.[8] However, complete hysteresis loops were not investigated, and the observed behavior could not be attributed to a particular mechanism.

It was not until our recent report of some preliminary measurements[9] that the magnetic behavior of a Cu–Mn alloy could be associated unambiguously with an exchange anisotropy process. We had found that a Cu–Mn alloy of about 25 per cent Mn (and a Ag–Mn alloy of similar composition) had the same unusual properties as those previously observed in Ni–Mn and Co–Mn alloys. This similarity included not only hysteresis loops that were displaced from the origin for the alloys cooled in a field but also the fact that the loop displacement decreased monotonically with increasing temperature, its eventual disappearance being accompanied by large magnetic losses. Moreover, for the alloys cooled in zero field, these losses caused the remanent magnetization to rise to a maximum, and this occurred at temperatures somewhat lower than those of maximum susceptibility. It was shown, however, that the alloys did not become truly paramagnetic until they reached much higher temperatures. From these measurements, we concluded that all the basic conditions given above for a microscopic exchange anisotropy mechanism were also fulfilled by these Cu–Mn

and Ag–Mn alloys. Furthermore, it was demonstrated that a fairly simple model, based on the coexistence of antiferromagnetic and ferromagnetic regions arising from competing short-range exchange interactions and the atomic disorder of these alloys, could account for most of the gross features of their anomalous magnetic properties.[9]

The results of these measurements on the Cu–Mn and Ag–Mn alloys of about 25 per cent Mn encouraged us to explore more thoroughly the magnetic properties and associated electrical properties of both these alloy systems over a wide composition range. In particular, we were interested in the possibility that an exchange anisotropy mechanism may be operative in the alloys of fairly low Mn concentration and that many of the peculiarities previously found in the low-temperature behaviour of these alloys may be manifestations of this mechanism. More generally, it was hoped that a more extensive study of these materials would provide the information required for a meaningful elaboration of our simple exchange anisotropy model.[9] In its present qualitative form, this model will serve as a useful framework for the discussion of our experimental results in the following section of this paper. Its development into a more quantitative model has been left for a future report.

EXPERIMENTAL RESULTS AND DISCUSSION

For this investigation, ingots of several Cu–Mn and Ag–Mn compositions were made by induction-melting in an argon atmosphere. Chemical analyses of the different ingots gave the following results: 5·5, 8·9, 14·0, 18·9, 24·1, and 28·6 atomic per cent Mn in Cu, and 11·9, 15·9, 20·0, and 23·7 atomic per cent Mn in Ag, with about 0·01 atomic per cent Fe in each. Cylindrical specimens 0·5 in. long by 0·25 in. in diameter for our magnetization measurements were machined out of the ingots, annealed 15 hr at 800°C (Cu–Mn) or 900°C (Ag–Mn), and then quenched into water. X-ray diffraction study of filings given the same heat treatment revealed no evidence of any phase other than f.c.c. for any of these alloys; the lattice parameters obtained were in good agreement with published values.[10] For our electrical resistivity specimens, a part of each ingot was cold-drawn down to a wire 0·02 in. in diameter, which was then given a similar heat treatment; in this case, however, the annealing temperature was kept at 800°C to avoid excessive loss of Mn from the relatively large external surface of the wire.[11]

Magnetic measurements were made between 1·8°K and room temperature in the apparatus described previously,[12] which, as in more recent work,[5, 6, 9] had

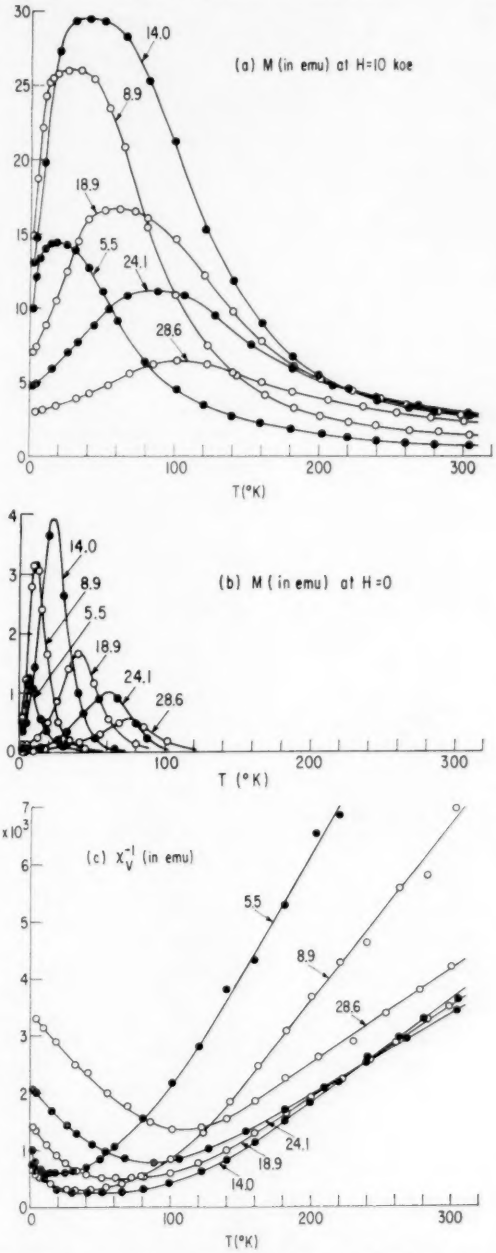

FIG. 1. Temperature variation of (a) the magnetization measured in a 10 kOe field, (b) the remanent magnetization, and (c) the reciprocal volume susceptibility, for different Cu–Mn alloys (designated by at. per cent Mn) cooled to 1·8°K in zero field.

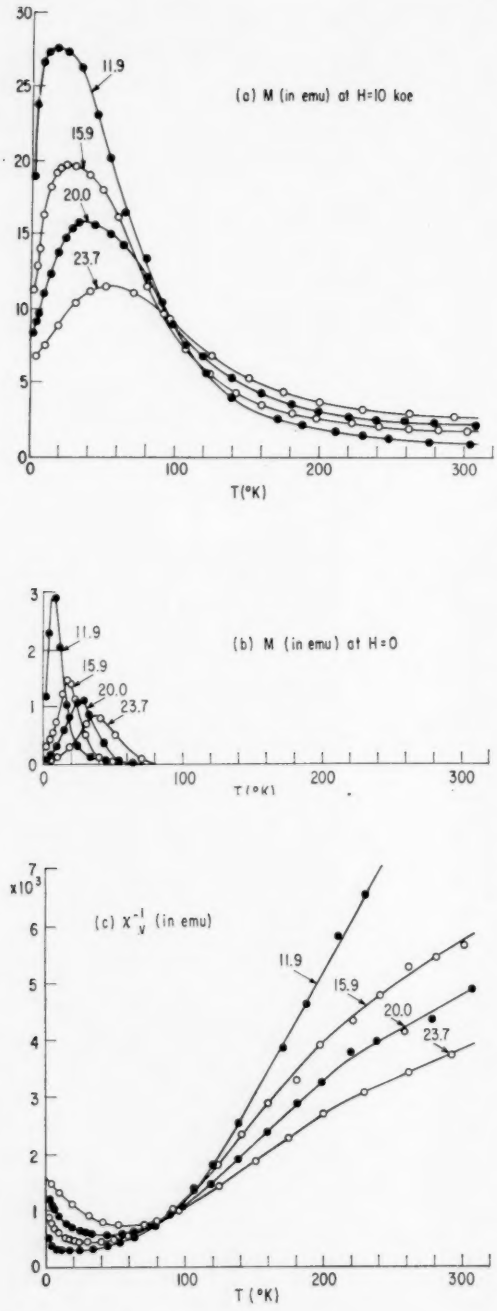

FIG. 2. Same as Fig. 1 for Ag–Mn alloys.

been modified by the substitution of cadmium for the lead in the thermal block in order to avoid any extraneous fields introduced by the superconducting lead. The magnetizations of the specimens were measured while the applied field was slowly cycled between ± 10 kOe; thus, we always obtained complete hysteresis loops. For all the data presented here the applied fields have been corrected for demagnetizing fields calculated from the magnetizations and physical dimensions of the specimens.

The magnetization measured in a 10 kOe field and the remanent magnetization for the Cu–Mn and Ag–Mn specimens cooled initially to 1·8°K in zero field are plotted in (a) and (b) of Figs. 1 and 2 as functions of temperature. It is evident that at the lowest temperature the remanence of most of these alloys is zero; although this is not quite true for the alloys most dilute in Mn, the remanence in these cases appears to extrapolate to zero at 0°K. With increasing temperature, the remanence of all these alloys rises to a maximum, decreases rapidly while the magnetization at 10 kOe reaches its maximum, and finally vanishes. In both alloy systems, the temperature of the maximum remanence, as well as that of the maximum magnetization at 10 kOe, increases monotonically with increasing Mn concentration. From the results of these measurements, we have also obtained values for the initial volume susceptibility. At temperatures where the remanent magnetization is not zero, the susceptibility was determined from the slope of the hysteresis loop at the remanence point. The reciprocal of this susceptibility has been plotted against temperature in Figs. 1(c) and 2(c); the curves shown in these figures will be discussed later.

In the following experiments, the Cu–Mn and Ag–Mn specimens were cooled down to 1·8°K from 300°K in a 5 kOe field applied in the direction of magnetization measurement; hysteresis loops were again measured at 1·8°K and at higher temperatures. These experiments were then repeated with a 10 kOe field applied during cooling. The loops measured at 1·8°K, including those obtained for zero field during cooling, are shown as solid curves in Figs. 3 and 4. It is obvious from these figures that the low-temperature magnetic properties of all these alloys have been very profoundly changed by the fields applied during cooling. Particularly striking is the fact that under these conditions their hysteresis loops are displaced from symmetrical positions about the origin.

Moreover, all the displaced loops as well as the symmetrical loops, are almost completely reversible, indicating that the hysteresis losses at 1·8°K are very low. It should also be noted that despite the displacement of these loops, the magnetizations in large negative fields are equal and opposite to those in large positive fields, except for the alloys of high Mn concentration where it appears that the negative fields needed to achieve this symmetry exceed our maximum available field of 10 kOe. This high-field symmetry indicates that the displaced hysteresis loops in Figs. 3 and 4 cannot be attributed to ordinary anisotropy effects but, instead, are fairly conclusive evidence for an exchange anisotropy mechanism.

previously observed in Ni–Mn alloys[5] and in the Cu–Mn and Ag–Mn alloys of about 25 per cent Mn[9] and was shown to be contrary to the predictions of the model in which the exchange anisotropy is simply given a preferred orientation by the field applied during cooling. A different and probably more meaningful correlation is suggested by the curves in Figs. 3 and 4 for the alloys of low Mn concentration. The magnetizations of these alloys when cooled in a 5 kOe perpendicular field have virtually the same values at high fields as the magnetizations obtained after cooling in 5 kOe applied parallel to the measurement axis. It seems reasonable from these figures

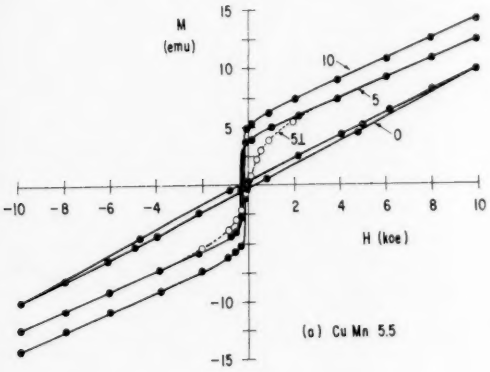

FIG. 3(a)

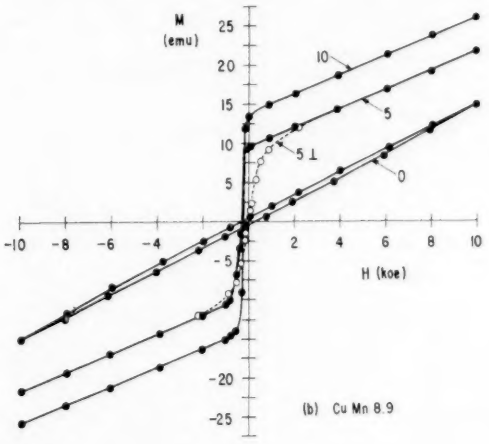

FIG. 3(b)

The different alloy specimens were also cooled to 1·8°K in a 5 kOe field applied perpendicular to the axis of measurement, and the hysteresis loops measured at this temperature are shown as dashed curves in Figs. 3 and 4. As it might be expected, all these loops are perfectly symmetrical about the origin. They are also similar in their extremely small remanent magnetizations to the loops for zero field during cooling. However, it should be noted that at high fields their magnetizations are considerably larger than those of the loops for zero field during cooling. This effect was to suppose that the magnetizations for these two conditions of cooling are also converging with increasing field (but more slowly) for the alloys of higher Mn concentration.

Many important features of the hysteresis loops in Figs. 3 and 4 are simplified by the fact that the loops enclose very little area. In particular, the two branches of each displaced loop give remanent magnetizations that are almost identical in magnitude and having the same direction as the field applied during cooling. Moreover, for all these alloys, this remanence is increased but not quite

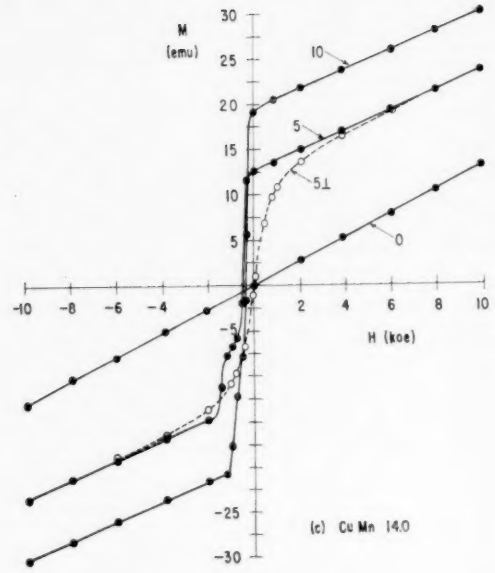

FIG. 3(c)

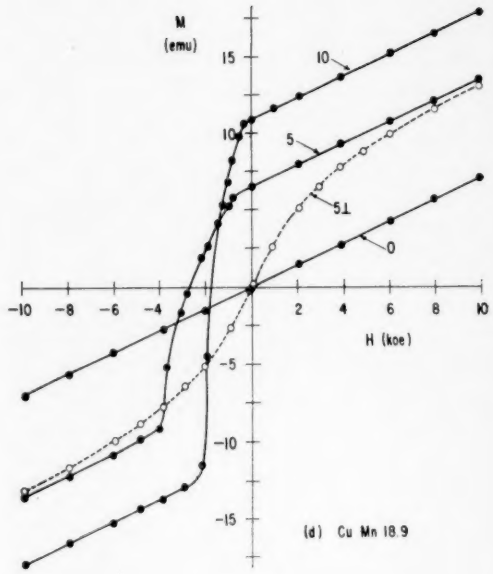

FIG. 3(d)

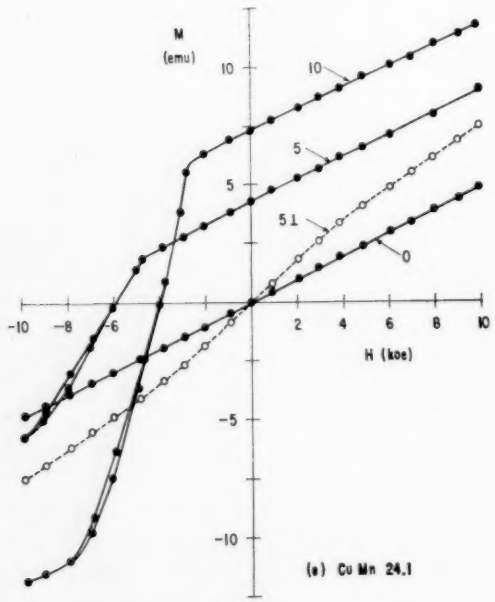

FIG. 3(e)

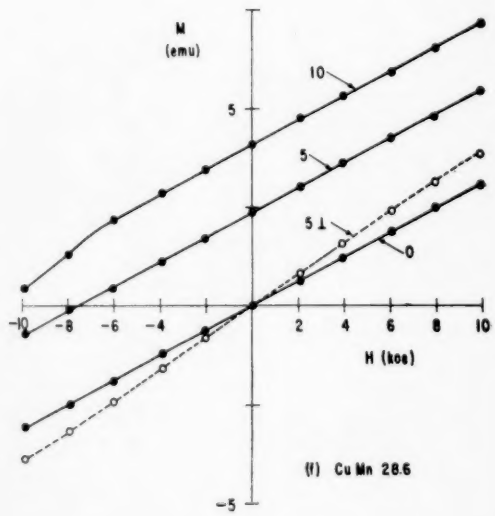

FIG. 3(f)

FIG. 3. Hysteresis loops measured at 1·8°K for different Cu–Mn alloys (designated by at. per cent Mn) cooled in +5 kOe or +10 kOe field applied parallel to measurement axis, or in zero field, or in 5 kOe field perpendicular to measurement axis.

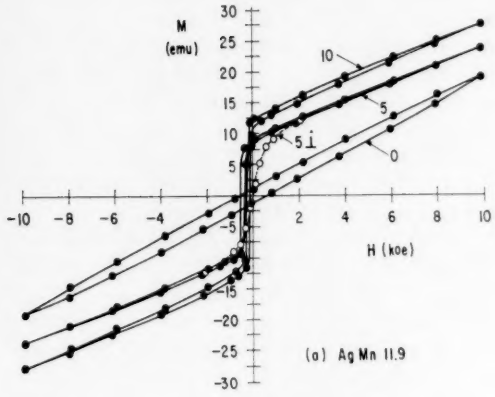

FIG. 4(a)

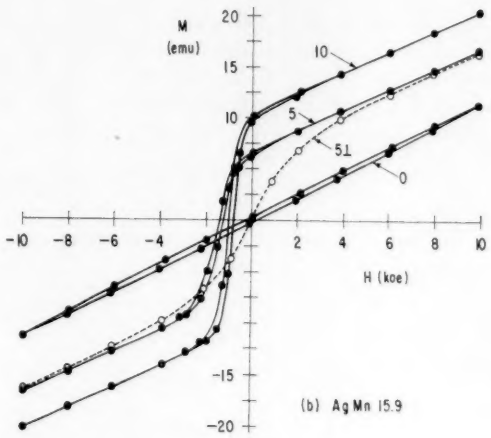

FIG. 4(b)

Vol. 21
1961

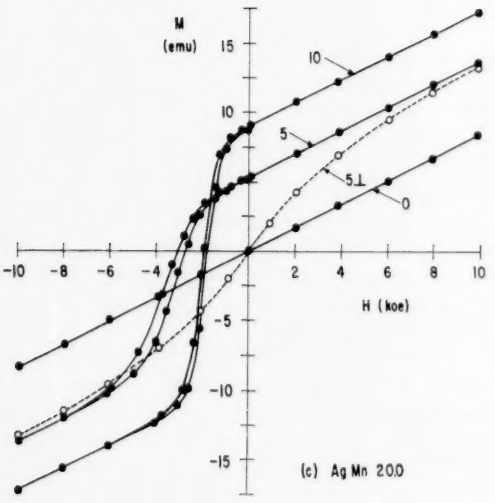

FIG. 4(c)

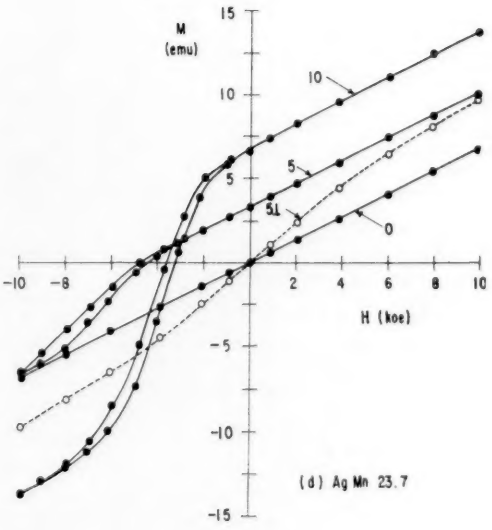

FIG. 4(d)

FIG. 4. Same as Fig. 3 for Ag–Mn alloys.

doubled when the field during cooling is raised from 5 to 10 kOe. The non-linearity of this relationship becomes so exaggerated for the alloys of lowest Mn concentration that it suggests a possible leveling off of the remanence values at higher fields applied during cooling. This is therefore consistent with the recent experiment

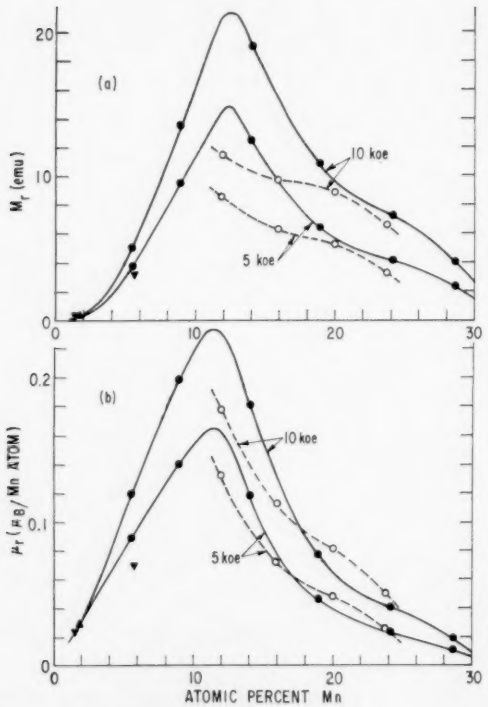

FIG. 5. (a) Remanent magnetization and (b) remanent moment per Mn atom, measured at 1·8°K, vs. Mn concentration in alloys of Cu–Mn (closed symbols) and Ag–Mn (open symbols) cooled in 5 kOe or 10 kOe field parallel to measurement axis. Circles represent present work: triangles and inverted triangles represent previous measurements [Refs. (3) and (2), respectively].

in which the thermoremanent magnetization (TRM) of an alloy of 1·8 per cent Mn in Cu was found to have a constant value for cooling-fields above 1·6 kOe.[4] Presumably, a saturation of the TRM at relatively low fields applied during cooling would also occur in the very dilute alloys of Mn in Ag.

The thermoremanence values taken from the displaced loops in Figs. 3 and 4 and also some from previous measurements[2, 3] have been plotted against alloy composition in Fig. 5(a). It is clear that the earlier TRM values for the dilute alloys of Mn in Cu join smoothly with those of the present work, which continue to rise with increasing Mn concentration and reach a maximum at about 12 per cent Mn in Cu. For the more restricted composition range of Ag–Mn alloys, there is a monotonic decrease of TRM with increasing Mn; nevertheless, this signifies that the thermoremanence (for any given cooling-field) must have a maximum value at some lower Mn concentration before dropping to zero for pure Ag. Since there are large discrepancies in lattice parameter between the two alloy systems, we converted all the TRM values to average moments per Mn atom (in Bohr magnetons), and these are shown as functions of alloy composition in Fig. 5(b). In contrast to the unnormalized remanences, the atomic remanent moments of the Ag–Mn alloys are fairly close to those of the Cu–Mn alloys of comparable composition. Moreover, since the atomic moment of Mn is probably about $4\,\mu_B$ in all these compositions,[9] it follows from Fig. 5(b) that about 5 per cent of the atomic moments are ferromagnetically aligned in the alloys of 12 per cent Mn in Cu or Ag cooled to 1·8°K in a 10 kOe field. Although the fractional ferromagnetic alignment is lower at other compositions, it is still appreciable in the dilute alloys of Mn in Cu that were studied previously[2, 3] and are represented in the figure.

Starting at its remanence value, the magnetization of each displaced hysteresis loop in Figs. 3 and 4 rises almost linearly with increasing positive field, and, as noted previously, it assumes equal but opposite values in sufficiently large reverse fields. Hence, as shown in Fig. 6, each of these loops may be resolved into two component parts: one of them is a straight line passing through the origin with a slope that is fairly independent of the field applied during cooling, while the other is constant at a positive magnetization value equal to the remanence for all positive fields but then decreases in negative fields until it levels off at a negative value of the same magnitude. The latter component, which is asymmetrical about the origin, is therefore characterized by (1) the

thermoremanence which represents the ferromagnetic polarization induced by the field applied during cooling, and (2) the negative fields required for the complete reversal of this polarization, or, more significantly, the energy involved in this magnetization reversal. This energy (per unit volume of material) can be easily shown to equal the area that is bounded on the left by the asymmetrical component of the displaced loop and on the right by the magnetization axis, as indicated in Fig. 6. For consistency with previous terminology,[7] we define the unidirectional anisotropy coefficient, K, as half this energy (per unit volume).

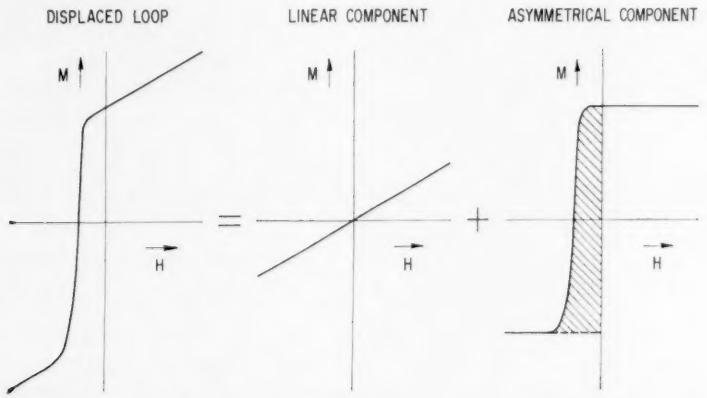

FIG. 6. Resolution of displaced hysteresis loop into linear and asymmetrical components. The shaded area associated with the latter component equals twice the unidirectional anisotropy coefficient.

This graphical integration method for evaluating K was applied to all the displaced loops in Figs. 3 and 4, except those for which the magnetization was not completely reversed in our maximum negative field of 10 kOe: namely, the curves in Figs. 3(e) and 4(d) for 5 kOe applied during cooling and those in Fig. 3(f) for both 5 and 10 kOe applied during cooling. Curiously enough, the computations for each of the alloys analyzed in this way gave an anisotropy value for the case of 10 kOe applied during cooling that was only slightly lower (by about 5 to 10 per cent) than the value for the 5 kOe cooling-field case. Hence, only our results for the former case have been plotted vs. alloy composition in Fig. 7(a), where it is clear that the strength of the unidirectional anisotropy rises at an increasing rate with the Mn concentration in both alloy systems. For a better comparison of these results for the two alloy systems, they have been converted to values of anisotropy energy per Mn atom. These are shown in Fig. 7(b) as functions of alloy composition, and it is evident that for high Mn concentrations, the atomic anisotropy values for the Ag–Mn alloys are slightly greater than those for Cu–Mn. This figure also indicates, however, that the unidirectional anisotropy of the Ag–Mn alloys (at least, that measured at 1·8°K) probably disappears at about 10 per cent Mn, whereas this anisotropy persists in much more dilute alloys of Mn in Cu.

Our results, therefore, suggest that the simple model recently proposed[9] as a qualitative explanation of these unusual low-temperature magnetic phenomena in the Cu–Mn and Ag–Mn alloys of about 25 per cent Mn is valid for a wide range of compositions in both alloy systems. According to this model, the coexistence of short-range ferromagnetic and antiferromagnetic interactions, together with the inherent composition fluctuations of an atomically disordered system, gives rise to a spatially inhomogeneous magnetic state. Specifically, within each group or cluster of nearest-neighbor Mn atoms, the moments are

Vol. 21
1961

aligned antiferromagnetically whereas the interactions between next-nearest-neighbor Mn atoms in different clusters are ferromagnetic. Although, in general, the net moment of each Mn cluster will not be zero, it is shown that for the lowest energy state the net moments of the different clusters will be aligned antiferromagnetically to give zero net moment for the total system. This ground state will be attained when the system is cooled to low temperatures in the absence of a magnetic field, and we note from Figs. 3 and 4 that under these conditions the remanent magnetizations of all our alloys are essentially zero, in agreement with the model.

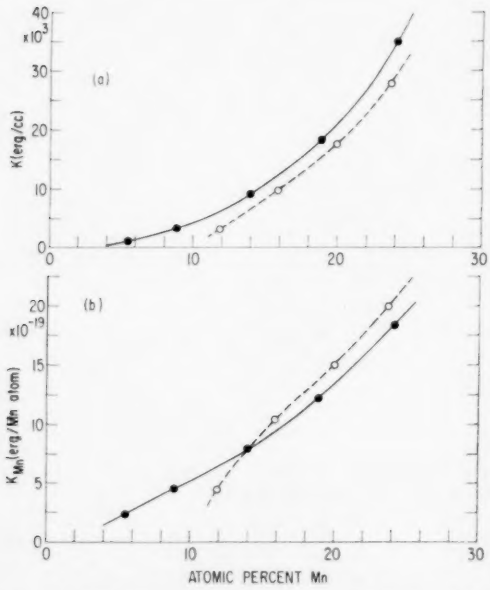

FIG. 7. (a) Unidirectional anisotropy coefficient and (b) unidirectional anisotropy per Mn atom, from hysteresis loops at 1·8°K, vs. Mn concentration in alloys of Cu–Mn (closed circles) and Ag–Mn (open circles) cooled in 10 kOe field parallel to measurement axis.

However, according to this model,[9] the existence of net moments in various Mn clusters makes it possible for a field applied during cooling to turn all the atomic moments of some of these clusters so that their net moments are aligned along the field direction, even at the cost of a slight rise in exchange energy. Furthermore, if a strong local anisotropy at low temperatures prevents these moments from returning to their original orientations even when the cooling-field is removed, the system will remain in a metastable state having a non-zero remanent magnetization. Under these circumstances, the magnetization will be reversed only by a reverse field large enough to turn the more loosely-bound atomic moments at the outer surfaces of the clusters against their antiferromagnetic coupling with their neighbors within the cluster cores, which are being held by the anisotropy. Thus, when the reverse field is removed, the magnetization will revert back to the direction of the field applied during cooling. This model, therefore, can account for a displaced hysteresis loop of the kind observed in all our Cu–Mn and Ag–Mn specimens when they are cooled to low temperatures in a magnetic field. Moreover, the relatively small thermoremanence for an alloy of high Mn concentration, as shown in Fig. 5, can be readily explained by the large average size of the antiferromagnetic Mn clusters; in this case, only a relatively small number (per unit volume) of loosely-bound atomic moments can participate in the magnetization process.

After cooling our different alloy specimens down to 1·8°K in various fields and measuring the displaced hysteresis loops shown in Figs. 3 and 4, we continued these measurements as the specimens were slowly warmed up. In each case, the asymmetry of the hysteresis loops decreased monotonically and finally disappeared. Concurrently, the hysteresis losses (as determined from the area of the loops) rose to a maximum value at the temperature where maximum losses had been observed for the same alloy cooled in zero field [and which is identical, therefore, to the temperature of maximum remanence indicated in Figs. 1(b) and 2(b)]. At a somewhat higher temperature, the hysteresis losses also disappeared and the initial susceptibility reached its maximum value [represented by the minimum in each curve in Figs. 1(c) and 2(c)]. Our experimental values for the temperatures of maximum losses, T_l, and for the temperatures of maximum susceptibility, T_s, are plotted in Fig. 8 as functions of alloy composition, and it is evident that both these temperatures for the two alloy systems increase monotonically with increasing Mn concentration. A linear variation of T_s for the Cu–Mn alloys has

also been observed by OWEN *et al.*[1] and by STREET[13]; however, our values agree very closely with those of the latter over this entire composition range, whereas those of the former are consistently about twice as high.

Within the context of our microscopic exchange anisotropy model, the increase in hysteresis losses exhibited by all our alloy specimens with increasing temperature can be regarded as a consequence

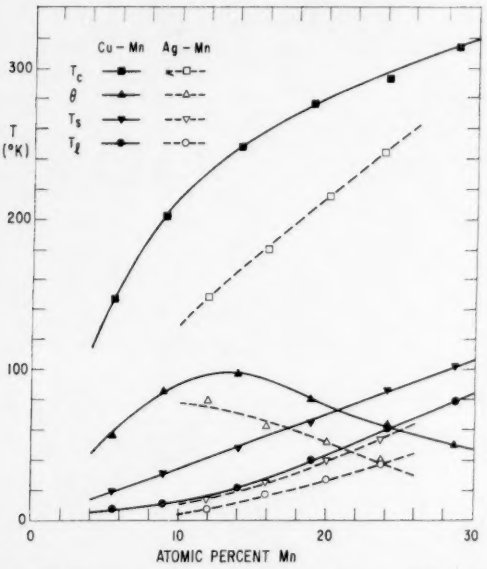

FIG. 8. Temperatures of maximum losses (T_l) and maximum susceptibility (T_s), paramagnetic Curie point (θ), and magnetic transition temperature (T_c), vs. Mn concentration in alloys of Cu–Mn (closed symbols) and Ag–Mn (open symbols).

of discontinuous rotations of the antiferromagnetically aligned moments of Mn clusters. This presumably occurs in a particular cluster when the thermal energy becomes comparable to the local anisotropy energy summed up over the volume of the cluster. Since the average volume of these clusters increases with increasing over-all concentration of Mn in the alloy, it seems reasonable to expect a corresponding rise in the temperature of maximum losses, which is borne out by the T_l vs. per cent Mn curves in Fig. 8 for both alloy systems. Furthermore, for any given alloy composition, there is a wide distribution of cluster volumes (and shapes) which contributes to the spread in the temperatures over which magnetic losses take place and, therefore, to the width of the remanence vs. temperature curves in Fig. 1(b) and 2(b). It also follows that as the temperature rises through this region and the local anisotropy gradually loses its hold on the small net moments of the Mn clusters, the hysteresis loop of the system originally cooled in a magnetic field will become less and less asymmetrical and the remanent magnetization will vanish. For the same reason, the susceptibility of the system cooled in zero field can be expected to increase with increasing temperature until the net moments of all the clusters are participating freely in the magnetization process, which will occur when the magnetic losses disappear.

Previous measurements on Cu–Mn alloys have disclosed various other dissipative properties that are consistent with our exchange anisotropy model. OWEN *et al.*[2] have observed that as the temperature of the alloys of 1·4 and 5·6 per cent Mn (originally cooled to 4·2°K in a magnetic field) was raised, the decrease of the remanent magnetization was not continuous but consisted of many small abrupt changes. More recently, STREET[13] reported a time dependence of the magnetization measured at constant field (10 kOe) and temperature (78°K) for a 30 per cent Mn alloy that had been cooled to this temperature in a field of −10 kOe. The functional form of this magnetic viscosity effect was found to be the same as that previously observed in high coercivity alloys under similar conditions. In our model, the magnetic units whose moments are thermally agitated against restraining anisotropy forces are the small almost-antiferromagnetic clusters of Mn atoms rather than the comparatively large ferromagnetic domains of the high coercivity materials; otherwise, the two relaxation mechanisms are closely analogous. Furthermore, an anomalously high specific heat has been recently observed[14] in several dilute alloys of Mn in Cu (and in Ag) at temperatures that coincide with reasonable extrapolations of our T_l vs. composition curves in Fig. 8. Hence, the excessive heat capacity of these alloys is probably associated with the large magnetic losses whose origin we have been discussing, and may therefore be another indication that the Mn-cluster model is valid down to very low Mn concentrations.

Vol. 21
1961

In our discussion of this model, it has been implicit that the antiferromagnetic alignment of nearest-neighbor Mn moments within the different clusters remains essentially intact at least up to the temperature of maximum susceptibility. Moreover, at this temperature where the magnetic losses disappear, we consider these clusters with their small net moments as being in a superparamagnetic state. Consequently, the system is not truly paramagnetic until the magnetic order within the clusters breaks down at some higher temperature. In our recent study of the Cu–Mn and Ag–Mn alloys of about 25 per cent Mn,[9] their magnetic disordering temperatures were identified with anomalous kinks in their $1/\chi$ vs. T curves at about 320° and 220°K, respectively. It is evident from Fig. 2(c) that although this anomaly persists (at about 200°K) in the more dilute alloys of Mn in Ag, its effect on the curves is more subtle and, in the 11·9 per cent Mn alloy, is not detectable at all. The kink in the curve for the 24·1 per cent Mn in Cu alloy occurs just above the maximum temperature shown in Fig. 1(c); however, as we will show later, any anomalies in the curves for the alloys of less Mn should appear well within this figure and it is obvious that they do not. Fortunately, the results of our electrical resistivity measurements, which will be discussed below, make it unnecessary for us to rely on subtle variations in the $1/\chi$ vs. T curves in order to identify the magnetic disordering temperatures of these alloys.

The electrical resistivities of our alloys, obtained between 4·2°K and 650–700°K by standard potentiometric techniques, are plotted vs. temperature in Fig. 9. The most obvious feature common to all the curves in this figure is the rapid drop in resistivity below some temperature, above which there is a more gradual variation that is fairly linear over a temperature range of at least 150 degrees. When the linear portion of each curve is extended to lower temperature by a dotted line, as shown, the decrease of our experimental points below this line becomes highly suggestive of an onset of magnetic order. Although the magnetic transition in each alloy appears to be very gradual, its characteristic temperature has been reasonably, though arbitrarily, defined as the temperature where the difference between the experimental resistivity curve and the dotted line

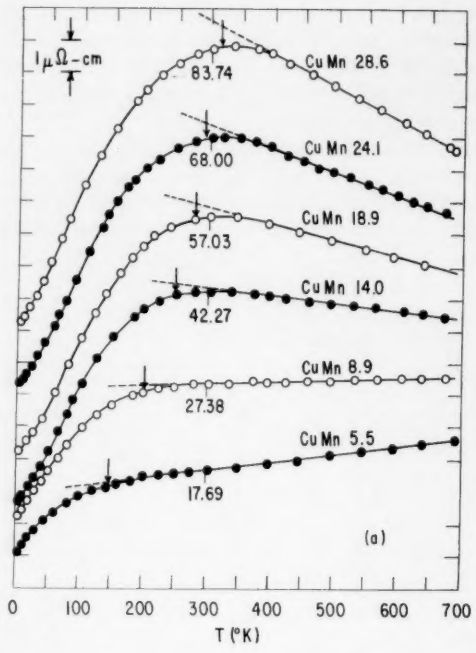

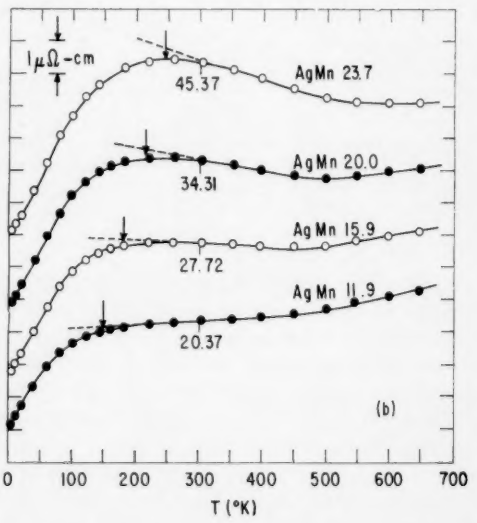

FIG. 9. Electrical resistivity vs. temperature for (a) Cu–Mn and (b) Ag–Mn alloys of composition designated by at. per cent Mn. Resistivity values at 300°K are given in μΩ-cm. Arrows indicate approximate magnetic transition temperatues.

Vol. 2
196

is 5 per cent of the difference at 4·2°K. The magnetic transition temperatures thus defined are indicated by arrows in Fig. 9, and their values (T_c) are plotted against alloy composition in Fig. 8. It is clear from the latter figure that the T_c value for each alloy is considerably higher than its value for T_s. Thus, as we have suggested earlier, the alloys do not undergo complete magnetic disorder immediately above their temperatures of maximum susceptibility. This is further emphasized by the fact that at these temperatures nothing unusual can be detected in the resistivity–temperature curves of Fig. 9, in contrast to the significant behavior of these curves at the higher temperatures that we associate with magnetic disordering.

Both T_c vs. alloy composition curves in Fig. 8 are concave-downwards, heading rapidly toward $T_c = 0$ with decreasing per cent Mn. It seems reasonable that at low Mn concentrations, where the average size of the clusters of nearest-neighbor Mn atoms is very small, the antiferromagnetic order within these clusters will be substantially weaker than in the large clusters of the more Mn-rich alloys. This is probably also the reason why there is hardly any effect on the $1/\chi$ vs. T curves of the low-Mn alloys when they transform at T_c from a super-paramagnetic to a truly paramagnetic state. Hence, the curves for these low-Mn alloys in Figs. 1(c) and 2(c), at temperatures above the broad minima where they are linear, may be considered as representing classical paramagnetic behavior. Values for the paramagnetic Curie points, θ, obtained by linear extrapolations to the T axis, are shown in Fig. 8 and are fairly consistent with previous results.[2, 15] Also plotted are the θ values for the more Mn-rich alloys, obtained from the linear portions of their $1/\chi$ vs. T curves at temperatures below the anomalous kinks. In these cases, however, as our recent work on the alloys of 24·1 per cent Mn in Cu and 23·7 per cent Mn in Ag has shown,[9] the more valid θ values taken from the portions of the curves above the anomalies are much lower and even negative. Thus, the variation of θ with composition, which correctly represents the paramagnetic state of these alloys, is a rise to a positive maximum value followed by a rapid decrease to negative values as the Mn concentration increases. Since θ corresponds to an algebraic average of all the interactions in a system, the composition variation just described can be attributed to an increasing predominance of antiferromagnetic interactions between nearest-neighbor Mn moments over the ferromagnetic interactions between more distant Mn moments. The coexistence of both these interactions has been a fundamental premise of our exchange anisotropy model for these alloys.

Another basic ingredient of our model has been the atomic disorder of these alloys. Stated more accurately, our model requires that there be a significant departure from perfect long-range atomic order. Any short-range atomic order would give rise to only a quantitative modification of the inhomogeneous magnetic state we have envisioned for a perfectly random solid solution. Recently, SCHEIL and WACHTEL[16] found that the magnetic behavior of Cu–Mn alloys (especially those of 20–25 per cent Mn) was changed by a long anneal between 100° and 450°C; the changes were attributed to short-range atomic order. To avoid these effects as much as possible in the present work, we found it necessary to store both our Cu–Mn and Ag–Mn specimens in liquid nitrogen between the time they were quenched and the time of our measurements. Prolonged exposure even at room temperature was observed to have an appreciable (though only quantitative) effect on their magnetic properties, and this will be the subject of a future report.

SUMMARY

For a wide composition range of Cu–Mn and Ag–Mn alloys cooled to liquid helium temperatures in a magnetic field, the hysteresis loops measured parallel to this field are found to be displaced from their symmetrical positions about the origin. The remanent magnetizations from the two branches of each of these loops are equal in magnitude and have the same direction as the field applied during cooling. In all the alloys studied, they represent a ferromagnetic alignment of a significant fraction of the Mn atomic moments, which increases (though not linearly) with the field applied during cooling. However, for each alloy, the strength of the unidirectional anisotropy associated with the displaced loop is only slightly dependent on the field applied during cooling. Although this anisotropy is stronger in the more Mn-rich alloys, it

is still measurable in fairly dilute alloys of Mn in Cu.

As the temperature of these alloys is raised, the displacement of their hysteresis loops decreases monotonically, and its disappearance is accompanied by large hysteresis losses. At somewhat higher temperatures, the losses vanish and the differential magnetic susceptibility reaches a maximum. The temperatures of maximum losses and of maximum susceptibility both increase with the Mn concentration of the alloy. However, at neither of these two temperatures is there any corresponding anomaly in the electrical resistivity of these alloys, whereas the resistivity vs. temperature curves of all these materials give a clear indication of a magnetic transition at considerably higher temperatures. These latter temperatures are higher for the more Mn-rich alloys, where they coincide with the temperatures at which the reciprocal susceptibility vs. temperature curves have peculiar kinks. In the alloys with less Mn, the susceptibility anomalies are much less distinct.

All the magnetic properties mentioned above (except the resistivity behavior) were recently reported for the alloys of about 25 per cent Mn in Cu and in Ag and were considered as evidence of an exchange anisotropy mechanism.[9] In the model proposed for these alloys and now extended to other compositions, the moments of nearest-neighbor and more distantly separated Mn–Mn pairs are considered to be coupled antiferromagnetically and ferromagnetically, respectively. Moreover, it is shown that the coexistence of these two types of interaction, together with the statistical composition fluctuations in these atomically-disordered alloys, gives rise to unusual spatially-inhomogeneous magnetic states. These states can be visualized in terms of clusters of nearest-neighbor Mn atoms with antiferromagnetically aligned moments, but where the net moments of the different clusters are not, in general, zero. From the interaction of these clusters with other neighboring clusters, with local anisotropy fields, and with magnetic fields applied during and after cooling, a consistent interpretation is developed for all the low temperature magnetic properties of these alloys, including the displaced hysteresis loops. Furthermore, the observed variation of these properties with increasing temperature can be readily attributed to the thermal excitation of the Mn clusters against the restraining forces of anisotropy and exchange. It is proposed that above the temperatures of the susceptibility maxima the clusters are probably behaving as superparamagnetic units and that the magnetic order within these clusters is disrupted only at the higher temperatures marked by anomalies in the resistivity–temperature curves.

Acknowledgements—The author is particularly grateful to G. W. Rathenau for his very valuable advice on the theoretical aspects of this problem, to I. S. Jacobs and W. H. Meiklejohn for many enlightening discussions, and to H. N. Treaftis for his capable assistance in the experiments.

REFERENCES

1. Owen J., Browne M., Knight W. D. and Kittel C., *Phys. Rev.* **102,** 1501 (1956).
2. Owen J., Browne M. E., Arp V. and Kip A. F., *J. Phys. Chem. Solids* **2,** 85 (1957).
3. Schmitt R. W. and Jacobs I. S., *Canad. J. Phys.* **34,** 1285 (1956); *J. Phys. Chem. Solids* **3,** 324 (1957).
4. Jacobs I. S. and Schmitt R. W., *Phys. Rev.* **113,** 459 (1959).
5. Kouvel J. S., Graham C. D., Jr. and Jacobs I. S., *J. Phys. Radium* **20,** 198 (1959); Kouvel J. S. and Graham C. D., Jr., *J. Appl. Phys.* **30,** 312S (1959); *J. Phys. Chem. Solids* **11,** 220 (1959).
6. Kouvel J. S., *J. Phys. Chem. Solids* **16,** 107 (1960).
7. Meiklejohn W. H. and Bean C. P., *Phys. Rev.* **102** 1413 (1956); *Phys. Rev.* **105,** 904 (1957).
8. Street R. and Smith J. H., *J. Phys. Radium* **20,** 18 (1959).
9. Kouvel J. S., *J. Appl. Phys.* **31,** 142S (1960).
10. Valentiner S. and Becker G., *Z. Phys.* **80,** 735 (1933); Raub E. and Engel A., *Z. Metallk.* **37,** 62 (1946).
11. Domenicali C. A. and Christensen E. L., *J. Appl. Phys.* **31,** 1730 (1960).
12. Kouvel J. S., Graham C. D., Jr. and Becker J. J. *J. Appl. Phys.* **29,** 518 (1958).
13. Street R., *J. Appl. Phys.* **31,** 310S (1960).
14. de Nobel J. and du Chatenier F. J., *Physica* **25,** 969 (1959); Zimmerman J. E. and Hoare F. E., *J. Phys. Chem. Solids* **17,** 52 (1960).
15. Morris D. P. and Williams I., *Proc. Phys. Soc. Lond.* **73,** 422 (1959).
16. Scheil E. and Wachtel E., *Z. Metallk.* **48,** 571 (1957).

J. Phys. Chem. Solids Pergamon Press 1961. Vol. 21, Nos. 1/2, pp. 71–75. Printed in Great Britain.

ELECTRONIC SPECIFIC HEAT OF Mn–Cu ALLOYS

J. E. ZIMMERMAN and H. SATO

Scientific Laboratory, Ford Motor Company, Dearborn, Michigan

(*Received* 10 *March* 1961; *revised* 13 *April* 1961)

Abstract—The specific heats of face-centred-cubic manganese–copper alloys at liquid helium temperatures have been measured for copper concentrations between 3½ and 90 wt. per cent. Analysis of the results shows that the major specific heat component is electronic, and that this exhibits a broad maximum of about 12×10^{-3} J/mol deg^2 between 10 and 30 wt. per cent Cu. At lower Cu concentration the electronic component dips sharply and it is estimated that for pure Mn (γ-phase) the electronic component should be of the same magnitude or lower than in the other transition elements, in contrast to the anomalously large values found in the α- and β-phases of Mn. Implications of the specific heat data on the electronic density of states curve and on the magnetic properties of MnCu alloys are discussed. The lattice component of the heat capacity appears to vary only moderately with concentration.

INTRODUCTION

THE ELECTRONIC structure of transition metals and its relation to the origin of ferromagnetism is not fully understood. Furthermore, there are discussions which indicate an essential difference between the electronic structures of the f.c.c. and of the b.c.c. transition elements which is reflected in their magnetic behavior.[1, 2, 3] Unfortunately, among the transition elements of the iron group, only nickel and cobalt have close-packed structures, cobalt being h.c.p. which is very similar to the f.c.c. structure. Because of this, any comparison of properties depending upon the number of electrons per atom cannot be done extensively, and the conclusions regarding the effect of electronic structure (as distinct from crystal structure) cannot be clear cut. Therefore, it would be very helpful if we could study the transition metal series without changing the crystal structure. In this respect, γ-iron has attracted much attention, particularly in attempts to understand the basis of the difference between the magnetic properties of the usual b.c.c. form (α-iron) and of the f.c.c. form (γ-iron). Magnetic susceptibility measurements on a γ-iron (18 per cent Cr, 9 per cent Ni, balance Fe) show it to be antiferromagnetic,[4] in contrast to α-iron which is ferromagnetic. Also, the electronic specific heat of a γ-iron (12 per cent Mn, 0·5 per cent C, balance Fe) was measured and found to be unusually high[5] (12 mJ/mol deg^2) compared to the value for pure α-iron[6] (5·0 mJ/mol deg^2). However, the γ-phase of iron can only be retained at low temperatures through the addition of considerable amounts of alloying elements which obscures the conclusion.

It is of interest, therefore, to study the f.c.c. form of manganese (γ-manganese), the element preceding iron in the transition series. Pure γ-manganese is, however, rather unstable at low temperatures, although it has been prepared by electrolytic deposition.[7] However, this γ-phase can be stabilized through the addition of a few per cent of copper and rapid cooling from a high temperature. Copper–manganese alloys in fact form an uninterrupted series of f.c.c. solid solutions over the whole composition range, at least at high temperatures, and with more than about 3 per cent copper this phase is retained at low temperatures after quenching from the equilibrium region.[8] With less than 25 per cent copper there is a slight deformation to face-centered-tetragonal because of antiferromagnetic ordering. It is thus possible in principle to determine the properties of pure f.c.c. manganese by extrapolation of measurements on the alloys. It was with this point of view that we undertook the measurement of an electronic specific heats of γ-phase Mn–Cu alloys.

The electronic specific heats of α-Mn as well as β-Mn have been measured and these values are sometimes used in estimating the general shape of the 3*d* band of the transition series. As a matter of fact, the values found are extremely high. The former was found to be 13·8 mJ/mol deg^2[9, 10] and the latter, 50 mJ/mol deg^2.[11] These high values and the difference between them leads to the conclusion that the value is very sensitive to crystal structure and that the use of either value in estimating the general shape of the 3*d* band is meaningless. Indeed, HOARE and MATTHEWS found the electronic specific heat of σ-phase Fe–Cr to be extremely high[12] and, actually, the σ-structure bears a close resemblance to the α-Mn structure. Specific heat measurements on Mn–Fe, Cr–Mn, and Cr–Fe alloys by WEI *et al.*[13, 14] indicate that the high electronic specific heat of α- and β-Mn might arise from the complicated crystal structure. Again, this conclusion is based on measurements on high-concentration alloys. On the other hand, there is a certain empirical correlation between antiferromagnetism and high electronic specific heat, as exemplified by α-Mn, β-Mn, γ-Fe alloys, and others. Since γ-Mn is believed to be a typical antiferromagnetic metal, it might thus be expected to have a high electronic specific heat. The present measurements are intended to show whether crystal structure or magnetic structure correlates in a significant way with electronic specific heat.

Specific heat measurements on the γ-phase Mn–Cu system are of interest in another respect, in that the electron/atom ratio covers a rather wide range, including the respective values for Fe, Co, and Ni. Measurements over the entire concentration range, therefore indicate the nature of the dependence of electronic specific heat on electron concentration. At the same time, it would be interesting to compare the specific heat with the rather complicated magnetic behavior. At the copper end, the system seems to be antiferromagnetic with positive paramagnetic Curie temperatures of the order of a few degrees Kelvin.[15] At about 25 per cent Mn, the system becomes ferromagnetic upon prolonged annealing,[16] presumably with the formation of Cu_3Mn. And with low Cu content, the alloys behave in typical antiferromagnetic fashion, with Néel temperatures in the neighborhood of room temperature, which is extrapolated to about 650°K for γ-Mn.[17, 18]

EXPERIMENTAL

A total of nine samples covering the composition range 3½ to 90 wt. per cent Cu were prepared by the Metallurgy Department of this Laboratory from extra pure copper and electrolytic manganese having a stated purity better than 99·9 per cent. After homogenizing, each sample was annealed in an argon atmosphere for several hours at a temperature at which the γ-phase was stable, and water quenched. The samples averaged around 10 g in weight, the relatively small size being desirable in the interest of rapid quenching. High-manganese samples were extremely brittle before heat treatment but became relatively soft afterward, indicating that the γ-phase was retained. Each sample was checked metallographically and by X-rays to determine if retention of the γ-phase was perfect. This turned out to be the case for all samples except that with 3½ per cent

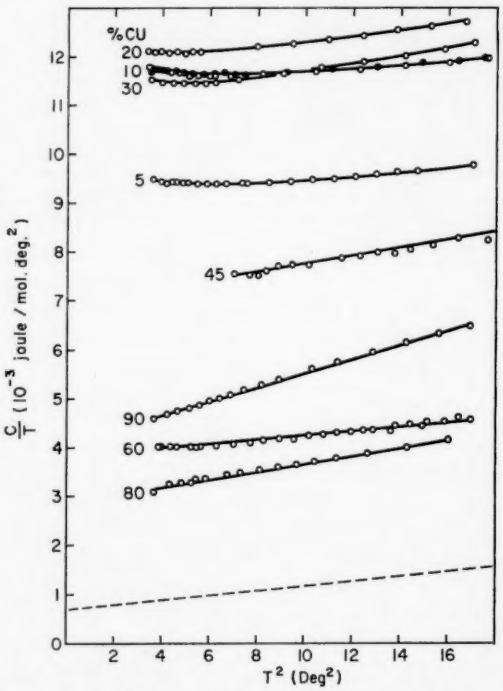

FIG. 1. Specific heat data for several γ-phase Mn–Cu alloys. Copper concentration is given in wt. per cent, and the straight dashed line is for pure copper. Two different sets of data are indicated for 10 per cent Cu.

Cu, which upon metallographic examination seemed to show a small amount of a second phase, presumably β. We estimated the amount of the second phase as 2 ± 1 per cent by volume. That some β-phase might have precipitated in this sample is reasonable, since a sample containing 2 per cent Cu transformed almost completely to the β-phase when heat treated in the same way. With 5 per cent or more copper there was no evidence of a second phase in any of the samples.

Measurements were made at helium temperatures by the method already described.[19] and the results, plotted as c/T vs. T^2, are shown in Fig. 1.

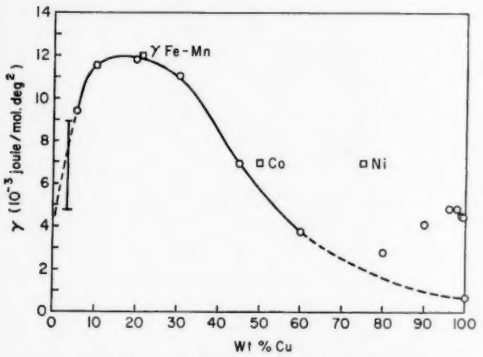

FIG. 2. Electronic specific heat coefficient derived from the data of Fig. 1. The estimated value and the uncertainty for $3\frac{1}{2}$ per cent copper is indicated by the vertical line segment. Points for γ-phase Fe–Mn, Co and Ni are included for comparison.

The dashed line showing the specific heat of pure copper, and the results for 90 per cent copper are from the previous paper. The relatively large scatter and restricted range of the 45 per cent data was caused by malfunctioning of the equipment, so these results are somewhat less reliable than the rest. Two sets of points, the open and the closed circles, are shown for the 10 per cent sample. The open circles represent measurements made after heat treatment as described above. This sample was then heat treated again at a slightly higher temperature, and remeasured, as represented by the closed circles. The agreement between these two sets of data indicates excellent reproducibility for the whole procedure. Since the $3\frac{1}{2}$ per cent sample apparently included a small amount of the β-phase, the results are not included in Fig. 1. The measured specific heat of this sample was in fact nearly the same (slightly lower) as that of the 5 per cent sample.

The coefficient γ of the linear term in the specific heat, as a function of wt. per cent Cu, is shown in Fig. 2. This coefficient is obtained in the usual way, by fitting each set of data in Fig. 1 by a straight line and extrapolating to absolute zero, ignoring for the moment the slight upward curvature shown by the specimens of low copper content. The value of γ for the $3\frac{1}{2}$ per cent Cu alloy is estimated using the value of β-Mn.

DISCUSSION

The existence of a steep rise in γ from low copper contents to a maximum at about 20 per cent Cu means that either there is some unknown mechanism by which foreign atoms increase the linear term in the specific heat, or in accordance with the usual interpretation of the linear term, that the density of electronic states changes rather rapidly near pure Mn. A possible antiferromagnetic contribution does not seem to be responsible for the maximum as explained below. A rather anomalous increase in the linear term has been observed with the addition of foreign atoms even in non-transition metals,[20] and this fact casts some doubt on the usual interpretation of the relation between the density of states and the linear term in the specific heat. These results indicate the difficulty in estimating the linear term in γ-Fe from measurements on, for example Fe–Mn alloys,[5] and also emphasize the inaccuracy of estimating the electronic specific heat of γ-Mn by extrapolation of measurements on only the 10, 20 and 30 per cent specimens.[21]

With regard to the question raised in the introduction concerning a correlation between high electronic specific heat and antiferromagnetism, we see that γ drops rather sharply as the Cu content exceeds 30 per cent, which is near the boundary of the antiferromagnetic region. It might indeed be suggested that the high γ value between 10 and 30 per cent represents the low temperature end of the magnetic specific heat anomaly at the Néel point. However, the Néel point for the dilute alloys in this range lies at several hundred degrees K, and it seems unlikely that a specific heat anomaly of the magnitude observed here should persist to low temperatures.

Vol. 21
1961

Also the fact that there is a sharp drop in specific heat below 10 per cent Cu is inconsistent with this view. Therefore, the origin of the maximum of γ near 20 per cent Cu should be sought in something other than the antiferromagnetic contribution, though the latter may be appreciable.

Susceptibility and neutron diffraction data on 85 and 90 per cent[17] alloys indicate that the magnetic transition is suppressed somewhat in temperature, probably because of the rather large lattice strains accompanying the tetragonal deformation. At low temperatures where the lattice strains are frozen in, the change of magnetic order with temperature and consequently the magnetic specific heat should become very small. The temperature dependence of the strength of magnetic scattering in neutron diffraction indicates this fact. However, there is no reliable way of estimating the magnitude of the antiferromagnetic contribution to the low temperature specific heat of these alloys.

Extrapolating the Néel point to higher Cu concentration indicates it will vanish near 40 per cent Cu.[17, 22] There one should expect a very large low-temperature specific heat anomaly. However, we see no evidence of this in our alloys. Probably in this concentration range where the magnetic contribution to the free energy becomes small, the lattice strain accompanying the tetragonal deformation suppresses the transition altogether. More data in this range of concentration and temperature are needed to clarify this point.

Disregarding the above ambiguities and going on the assumption that the linear term in the specific heat really represents the density of states, the behaviour of the electronic specific heat of f.c.c. Mn–Cu alloys as a function of concentration should give some idea of the shape of the 3*d* band of the f.c.c. transition elements. Since it is believed that f.c.c. metals obey the predictions of the collective electron theory better than the b.c.c. metals,[3] it is of interest to compare the electronic specific heats of γ-Fe, Mn, Co and Ni with the present results at the corresponding electron/atom ratios. This comparison has been made in Fig. 2. The agreement is reasonable except perhaps in the case of Ni.

Because of the rapid drop in γ below 10 per cent Cu and of the inclusion of β-phase in the $3\frac{1}{2}$ per cent Cu sample, one cannot extrapolate to pure γ-Mn with any accuracy. Apparently however, a value of 3 to 6×10^{-3} J/mol deg^2 is reasonable. This is much smaller than the values for the α- and β-phases but agrees very well with the value extrapolated[11] from the specific heat curve of γ-Mn at high temperature.[23] This probably arises from the fact that γ-Mn is quite metallic in character and has a broad *d*-band, whereas the α and β forms are more ionic in character, as the neutron diffraction[24] and other physical properties show, and therefore have much narrower *d*-bands. These results emphasize the importance of taking crystal structure into account when using electronic specific heats to get an idea of the shape of the 3*d* band.

Since the close packed transition elements, γ-Mn, Co, and Ni have similar electronic specific heats, it may be interesting to consider this fact in view of the magnetic properties of these elements and their alloys. It would appear that the density of states at the Fermi surface bears no definite relation to the magnetic behavior. On the contrary, the lattice constant seems to have a much closer relation. The Curie point or the Néel point of these elements as well as the magnetic properties of alloys of these elements and of iron with platinum indicate that the dependence of the calculated interaction on the atomic distance just corresponds to a "Bethe–Slater" type curve, the border between plus and minus being near γ-iron.[25]

At the Cu-rich end of the alloy system there is a low temperature antiferromagnetic ordering, accompanied by a specific heat anomaly which has already been investigated.[19] This anomaly is approximately linear in temperature near absolute zero. The linear coefficients from this previous work have been included in Fig. 2. These are the points at 90, 96, 98, 99 and 99·5 per cent Cu. The probable behavior of the electronic specific heat in this concentration range has been indicated by the dashed line between 60 per cent and pure Cu.

There is one additional bit of information which may merit consideration, although outside the aim of this work. Debye characteristic temperatures for the alloys can be calculated from the slopes of the various curves in Fig. 1. If we include the value for pure γ-Mn obtained by SHOMATE[23], this leads to the curve (θ vs. per cent Cu) shown in Fig. 3. If the points at 80 and 90 per cent Cu

are discounted as being affected by the magnetic contribution to the specific heat at low Mn concentrations, then the curve can be joined smoothly onto WALDORF's curve for dilute Cu–Mn alloys[26] calculated from elastic constants. His results are shown by the straight dashed line. For low copper

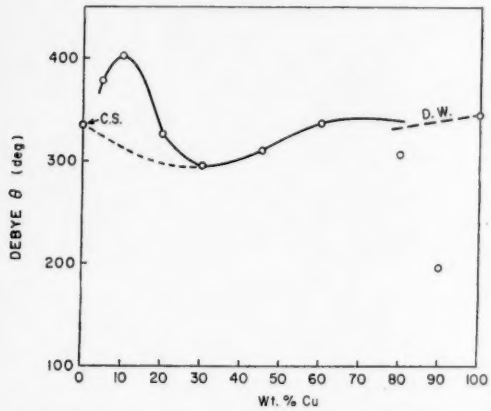

FIG. 3. Debye characteristic temperature derived from the data of Fig. 1. The point labeled "C.S." and the line labeled "D.W." are from SHOMATE[23] and WALDORF[26], respectively.

contents we have used the slope of the high-temperature end of each curve (Fig. 1) to determine θ. Doing this gives a smaller Debye temperature than the value which would be obtained if an average slope were used. If in fact the curvature for the high specific heat specimens persists to temperatures above the helium range, then the true Debye temperature may be lower still. In short, one cannot take the peak in the Debye θ curve near the Mn end too seriously. The true behavior may be closer to that indicated by the dotted curve.

Acknowledgements—The authors would like to express their thanks to the Metallurgy Department for their help in the preparation of samples. Thanks are also due to the late Mr. FRED MELLER for his help in X-ray analysis and Mr. R. MUNSON for his metallographic analysis.

REFERENCES

1. WEISS R. J. and DE MARCO J. J., *Rev. Mod. Phys.* **30,** 59 (1958).
2. MOTT N. F. and STEVENS K. W. H., *Phil. Mag.* **2,** 1364 (1957).
3. LOMER W. H. and MARSHALL W., *Phil. Mag.* **3,** 185 (1958).
4. KONDORSKY E. I. and SEDOV V. L., *Zh. exsp. teor. fiz.* **35,** 1104 (1958).
5. GOLDMAN J. E. and GUTHRIE G. L., *Bull. Amer. Phys. Soc.* **1,** 148 (1956).
6. DUYCKAERTS G., *Physica* **6,** 401 (1939).
7. SCHLAIN D. and PRATER J. D., *Trans. Electrochem. Soc.* **94,** 58 (1948).
8. HANSEN M. and ANDERKO K., *Constitution of Binary Alloys*, p. 597. McGraw-Hill, New York (1958).
9. ELSON R. G., GRAYSEN-SMITH H. and WILHELM J. O., *Canad. J. Res.* **A18,** 83 (1940).
10. GUTHRIE G. L., FRIEDBERG S. A. and GOLDMAN J. E., *Phys. Rev.* **98,** 1181 (1955).
11. WEISS R. J. and TAUER K. V., *J. Phys. Chem. Solids* **4,** 135 (1958).
12. HOARE F. E. and MATHEWS J. C., *Proc. Phys. Soc. Lond.* **71,** 220 (1958).
13. WEI C. T., CHENG C. H. and BECK P. A., *Phys. Rev.* **112,** 696 (1958).
14. WEI C. T., CHENG C. H. and BECK P. A., *Phys. Rev. Letters* **2,** 95 (1959).
15. SCHMITT R. W. and JACOBS I. S., *J. Phys. Chem. Solids* **3,** 324 (1957).
16. SCHEIL E. and WACHTEL E., *Z. Metallk.* **48,** 571 (1957).
17. BACON G. E., DUNMUR I. W., STREET R. and SMITH J. H., *Proc. Roy. Soc.* **A241,** 223 (1957).
18. MYERS H. P., *Canad. J. Phys.* **34,** 527 (1956).
19. ZIMMERMAN J. E. and HOARE F. E., *J. Phys. Chem. Solids* **17,** 52 (1960).
20. RAYNE J. A., *Phys. Rev.* **108,** 22 (1957).
21. ZIMMERMAN J. E. and SATO H., *Bull. Amer. Phys. Soc.* (ser. 2) **4,** 150 (1959).
22. BASINSKI Z. S. and CHRISTIAN J. W., *J. Inst. Met.* **80,** 659 (1952).
23. SHOMATE C. H., *J. Chem. Phys.* **13,** 326 (1945).
24. KASPER J. S. and ROBERTS B. W., *Phys. Rev.* **101,** 537 (1956).
25. SATO H., *J. Appl. Phys.* **31,** 327S (1960).
26. WALDORF D., *J. Phys. Chem. Solids* **16,** 90 (1960).

Vol. 21
1961

J. Phys. Chem. Solids Pergamon Press 1961. Vol. 21, Nos. 1/2, pp. 76–80. Printed in Great Britain.

THE SOLUBILITY OF NICKEL IN NICKEL FERRITE

R. PARKER

Department of Mathematics and Physics, Portsmouth College of Technology

and

M. S. SMITH*

Department of Physics, University College of North Wales, Bangor

(*Received* 30 *March* 1961)

Abstract—A method is described for preparing high resistivity nickel ferrites with nickel excess. High resistivity materials can be made by suppressing Fe^{++} and Ni^{+++} ions in the spinel lattice by suitable heat treatment. Electrical measurements indicate that excess nickel dissolves in the ferrite lattice up to a nickel to iron ratio of 1·029 : 2. This result is consistent with available data of saturation magnetic moment.

1. INTRODUCTION

In a recent publication Jonker[1] has shown that the semiconducting properties of the spinel cobalt ferrite system

$$Co_{3-x}\,Fe_xO_4 \text{ with } 2{\cdot}1 > x > 1{\cdot}9$$

can be described adequately in terms of an activation process of electron transport between cobalt and iron ions. Jonker's analysis cannot directly be applied to the structurally similar nickel ferrite system for two reasons. In the first place, it is known that excess nickel has a very limited solubility in the ferrite lattice so that in compositions corresponding to x say 1·9 a second phase, probably simple cubic NiO, is present.[2] Secondly, in the process of ferrite formation by sintering a stoichiometric mixture of nickelous and ferric oxides, a certain amount of oxygen is irreversibly lost and this loss has a dominant influence in determining the electrical properties of the ferrite formed. Since this oxygen loss depends critically upon the firing and cooling process during formation it is perhaps not surprising that different authors quote widely differing results for the value of the resistivity for pure nickel ferrite of apparently the same composition.[1, 3, 4]

It has been shown by Lord and Parker[5] (to be referred to as I), that either nickel excess or oxygen deficiency can reduce the electrical resistivity of nickel ferrites by lowering the activation energy, ϵ in the equation $\rho = A\exp(\epsilon/KT)$, the symbols having their usual meaning; this reduction is due to the creation of like metal ions of the same element with differing valencies. In the case of a ferrite where δ, the relative oxygen deficiency, is small compared to γ, the relative nickel excess dissolved in the ferrite lattice, the ionic formula may be represented by

$$Ni^{++}_{1+2\delta}Ni^{+++}_{\gamma-2\delta}Fe^{+++}_{2-\gamma}O^{--}_{4-\delta} \quad (\text{with } 1 \gg \delta > 2\delta).$$

For this case ϵ represents the activation energy of the motion of some $\gamma-2\delta$ positive holes per molecule through the crystal lattice. If on the other hand $2\delta > \gamma$, the ionic formula may be represented by

$$Ni^{++}_{1+\gamma}Fe^{++}_{2\delta-\gamma}Fe^{+++}_{2-2\delta}O^{--}_{4-\delta}$$

and ϵ now represents the activation energy associated with the transport of $2\delta-\gamma$ electrons per molecule away from divalent and towards trivalent iron ions along the applied electric field vector. The parameter δ depends primarily upon the partial oxygen pressure and the maximum temperature which prevails during the sintering process. In Fig. 1 curves of activation energy vs.

* Present address: Denbighshire Technical College, Wrexham.

oxygen pressure are reproduced for various firing temperatures for specimens prepared from spectroscopically pure materials of a starting composition

$$NiO(Fe_2O_3)_{0\cdot95}.$$

For each specimen, thermoelectric measurements revealed *n*-type conduction to the left, and *p*-type

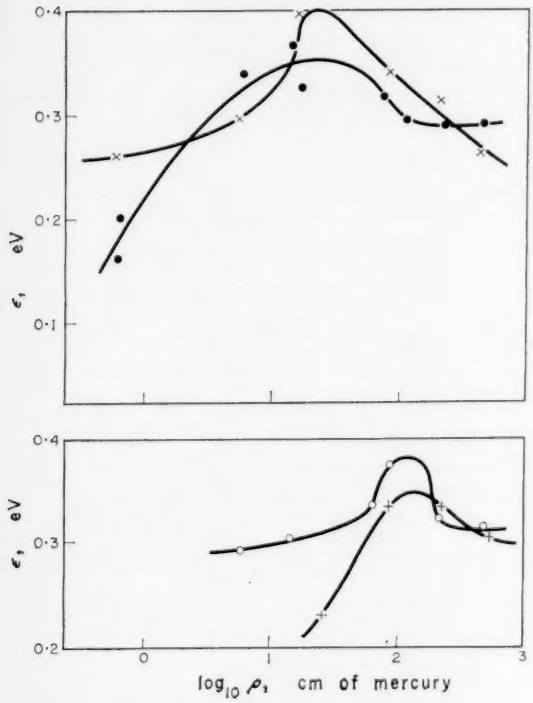

FIG. 1. Firing temperature: ● 1100°C.
× 1150°C.
○ 1200°C.
\+ 1250°C.

With acknowledgements to the Editor of *Nature*.

conduction to the right of the activation energy peak. It can be assumed therefore that the peak in ϵ occurs for specimens in which the surplus electrons from oxygen vacancies reduce the charge on all excess nickel ions to a valency 2, i.e. where $\gamma = 2\delta$ in the present notation. It was suspected by LORD and PARKER[5] that the true peak might be much higher and was not obtained for any specimen on account of the difficulties inherent in achieving adequate control in the oxygen pressure inside the furnace tube containing the specimens. An alternative method of preparing specimens has therefore been developed and this is described in the following paragraph. It will be shown that by the new method nickel ferrites can be made with much greater activation energy (and room temperature resistivity) than any which have been reported hitherto. From the results obtained the solubility limit of excess nickel in the ferrite lattice is estimated with considerable accuracy in a novel manner.

2. EXPERIMENTAL

A range of nickel ferrites with nickel excess, as listed in Table 1, were prepared as follows: powders of nickelous oxide (NiO) and ferric oxide (Fe_2O_3) of spectroscopic purity (total impurity content approximately 1 part in 10^5) of the required proportion were mixed in a rubber lined ball mill for 24 hr, prefired at 800°C for several hours and milled again for several hours. The mixture was slightly moistened with distilled water and compressed in a die into cylindrical pellets of approximately 1 cm length and diameter. The pellets were placed into a fused alumina crucible and inserted into the furnace, in which an oxygen pressure of one atmosphere was maintained by a slow stream from a cylinder and reducing valve at one end and a water seal at the other. The furnace was maintained at a temperature θ which was just below the temperature estimated to yield specimens corresponding to the peak activation energy condition in Fig. 1. After a time known to be adequate to complete the reaction

$$NiO + Fe_2O_3 \rightarrow NiFe_2O_4$$

the specimens were removed from the furnace tube and cooled in air as rapidly as their thermal resistance allowed. After surface grinding, resistivity measurements were made and the activation energy determined. The procedure was repeated with a different set of pellets at slightly higher sintering temperatures until the temperature θ' was determined which yielded the peak activation energy; this was presumed to yield a compensated specimen with $\gamma = 2\delta$. The degree of control obtained by this method is very much greater than by varying the oxygen pressure as described in I. It

was subsequently ascertained by thermoelectric measurements that specimens sintered below θ' were *p*-type conductors and those fired above θ' *n*-type.

Specimens fired at temperature θ' were found to have very high values of ϵ and therefore of electrical resistivity. The whole procedure was then repeated for other starting compositions. It was ascertained that specimens had reached their equilibrium composition by noting that subsequent reheating at θ' for an indefinite period did not alter the electrical properties in any way. It was found that a compensation temperature was only achieved if the nickel oxide excess was greater than that corresponding to the composition

$$NiO\,(Fe_2O_3)_{0.974};$$

for smaller nickel content, samples were found to be always *n*-type even at the lowest temperature at which ferrite formation takes place, i.e. $\sim$ 1050°C. Table 1 lists the composition of powders, θ' in °C, and the activation energy in electron volts obtained from resistivity measurements.

It will be noted that values of activation energy in Table 1 are substantially higher than any which have hitherto been quoted in the literature for nickel ferrites. They are practically identical with those estimated by JONKER[1] for stoichiometric cobalt ferrite and this would suggest that the conduction mechanism proposed by him is applicable to the nickel ferrite system.

Resistivity measurements were made in a frequency range up to 5 Mc/s above 100°C; a block diagram of the circuit is given in Fig. 2. No significant frequency dispersion of resistivity was observed. Below 100°C the resistivity of specimens was too high to be amenable to measurements described in Fig. 2. One may conclude that activation energies quoted in Table 1 are characteristic of the resistivity of the bulk material and not of surface layers on crystal grains as have been observed in some ferrites by KOOPS[6] and DERRY *et al.*[2]

Table 1

Composition of mixture	Ferric oxide molecular deficiency (per cent)	θ'(°C)	ϵ(eV)
$NiO(Fe_2O_3)_{0.974}$	2·6	—	—
$NiO(Fe_2O_3)_{0.973}$	2·7	1131–1135	0·68
$NiO(Fe_2O_3)_{0.972}$	2·8	1216–1221	0·62
$NiO(Fe_2O_3)_{0.970}$	3·0	1234–1237	0·625
$NiO(Fe_2O_3)_{0.950}$	5·0	1225–1231	0·59

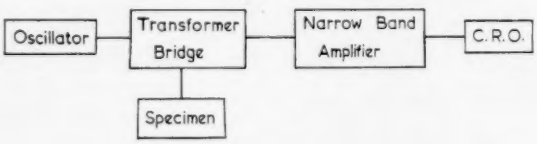

FIG. 2

3. DISCUSSION

The activation energies governing conductivity reported in the previous paragraph are about 50 per cent higher than those reported for nickel

ferrites made by more conventional methods. This has been achieved by approximately compensating the trivalent excess nickel ions with electrons released by the removal of oxygen ions by careful control of firing conditions. The easy conduction mechanism involving either iron or nickel ions of two valencies is thus virtually eliminated and the intrinsic conduction process involving the removal of electrons from Ni^{++} ions to Fe^{+++} ions comes into play. Expressed in terms of JONKER's nomenclature, the Fermi level in a compensated specimen lies approximately half way in energy space between the full Ni^{+++} and the empty Fe^{++} level. Since the oxygen deficiency in ferrites increases rapidly with firing temperature,[7] it is possible to estimate the excess nickel dissolved in nickel ferrite with some accuracy in the following manner.

It will be noted from Table 1 that θ' rises rapidly for a ferric oxide molecular deficiency up to 2·7–2·8 per cent and remains virtually constant near 1230°C for a deficiency greater than 3 per cent. Specimens have also been prepared with iron deficiencies up to 10 per cent and θ' remains around 1230°C; these have not been recorded in the table since they provide little additional relevant information. One may conclude that while θ' increases with nickel concentration of the original mixture, excess nickel dissolves in the ferrite lattice and requires an increasing loss of oxygen for the attainment of a compensated specimen. Once θ' remains constant the excess nickel oxide does not dissolve in the ferrite lattice and presumably precipitates as a separate phase. θ' remains practically constant according to Table 1 with a nickel to iron ratio greater than 1·029 : 2 and this ratio may therefore be assumed to represent the solubility limit of excess nickel in the ferrite lattice at the temperature of formation.

The ionic formula of a p-type nickel saturated ferrite can be written as

$$Ni_1^{++}Ni_\alpha^{+++}Fe_{2-\beta}^{+++}O_{4-\delta}^{--}$$

where, in order to satisfy the requirements of electrical neutrality and of the spinel structure

$$\alpha = \frac{2}{3}\times\frac{(3y-\delta-\delta y)}{(3+y)} \qquad (1a)$$

$$\beta = \frac{2}{3}\times\frac{(3y+2\delta)}{(3+y)} \qquad (1b)$$

$(1+y)/2$ represents the nickel : iron ratio, i.e. $y_{max} = 0{\cdot}029 \pm 0{\cdot}001$ according to Table 1.

It is of some interest to compare this deduction with results available from other types of measurement. In principle it should be possible to detect the precipitation of a second phase of nickelous oxide by X-ray diffraction and from a determination of saturation magnetic moment. The X-ray method however, is of little practical use. Owing to the similarity in lattice parameters of simple cubic nickelous oxide and the spinel nickel ferrite the presence of the former phase yields recognisable diffraction lines only for concentrations in excess of about 5 per cent. The magnetic method depends upon the difference in the contribution to the total magnetic moment of excess nickel dissolved in the ferrite from that of the non-ferromagnetic oxide. This difference is approximately $y/3$ Bohr magnetons per molecule if the theoretical moment of 3 Bohr magnetons is assigned to Ni^{+++} ions. With $y = 0{\cdot}029$ the calculated reduction in saturation moment is 0·85 per cent. Saturation moment determinations have been reported by DERRY *et al.* and in I and both lead to the conclusion that the solubility of excess nickel in the ferrite lattice could not be detected. The accuracy of both experiments was approximately $\pm$ 1 per cent, so that the negative result is in satisfactory agreement with the conclusions drawn from the present work.

The results of the present work allow an estimate to be made of the oxygen deficiency, δ. It has been pointed out in Section 2 that for a compensated specimen $y = 2\delta$ and it follows from equation (1a) that for such a specimen $\delta \simeq 3y$, since y is very small compared to unity. Using this value of δ one calculates a loss in weight on sintering of 0·65 per cent. This may be compared with the conclusion by SNOEK[8] from gravimetric experiments that the oxygen loss on sintering of many ferrites is a few tenths of one per cent.

Acknowledgements—The authors wish to express their gratitude to Professor E. R. ANDREW for his encouragement of the present work. One of us, M.S.S., is indebted to the Council of the D.S.I.R. for the award of a Research Studentship.

REFERENCES

1. JONKER G. H., *J. Phys. Chem. Solids* **9,** 165 (1959).
2. DERRY R., WHITEHEAD C. S. and WILLS M. S., A.R.L. Report R1/100 (1956).
3. KAMIYOSHI K., *Sci. Rep. Res. Inst. Tôhoku Univ.* **A3,** 716 (1951).
4. VAN UITERT L. G., *J. Chem. Phys.* **23,** 1883 (1955).
5. LORD H. and PARKER R., *Nature, Lond.* **188,** 929 (1960).
6. KOOPS C. G., *Phys. Rev.* **83,** 121 (1951).
7. GORTER E. W., Thesis, Leiden (1954).
8. SNOEK J. L., *New Developments in Ferromagnetic Materials.* Elsevier, Amsterdam (1949).

Vol. 2
196

J. Phys. Chem. Solids Pergamon Press 1961. Vol. 21, Nos. 1/2, pp. 81–86. Printed in Great Britain.

COLOR CENTERS IN THE ALKALI METAL AZIDES

H. A. PAPAZIAN*

Convair Scientific Research Laboratory, San Diego, California

(*Received* 23 *December* 1960; *revised* 29 *March* 1961)

Abstract—A study has been made of the spectral bands in NaN_3, KN_3, RN_3, and CsN_3 produced by u.v. irradiation. The ultraviolet, visible, and infrared regions were studied. A very strong correlation was found between the behavior of the bands produced in the visible and infrared. A new model based upon a "charge-transfer" complex has been proposed for the *F* band.

INTRODUCTION

RECENTLY, the spectra of azide crystals colored by ultraviolet and X-ray irradiation have been published,[1, 2, 3] and by analogy with color centres in the alkali halides the absorption band in the ultraviolet region was attributed to the *V* center and the bands in the visible to *F*, *R*, and *M* centers etc.

The present work describes a rather extensive study of the u.v. photolysis of the isomorphous body centered tetragonal crystals CsN_3, RbN_3, KN_3, and the body centered rhombohedral NaN_3. The spectra of these crystals were investigated in the ultraviolet, visible, and infrared regions of their absorption before and after irradiation. The study included growth of spectral bands, their thermal bleaching, and the subsequent photolysis of the crystals.

A very strong correlation between the behavior of the bands in the infrared and in the visible was found and a new model has been suggested for the *F* band in the azides.

EXPERIMENTAL

The crystals were grown from saturated aqueous solutions of the appropriate azide salts. Saturated solutions were made in distilled water at room temperature, and the solutions were placed in desiccators using $CaSO_4$ as desiccant. In two or three days crystals approximately 40 mm^2 in area were obtained. Crystals could be grown equally well in glass or polyethylene beakers. The CsN_3 crystals grew, approximately 0·13 mm thick, in a maze of thin sheets which could easily be separated from each other. The RbN_3 and KN_3 plates were approximately 0·35 mm thick. NaN_3 grew on the surface of the solution in a very thin and fragile sheet; the entire surface of the solution was essentially one large crystal which broke easily into smaller pieces. Because the crystals were so fragile, their thickness was not measured but they appeared to be intermediate between CsN_3 and RbN_3. The CsN_3, RbN_3 and NaN_3 crystals were "water clear". The best description which can be given for the Kn_3 crystals is that they were not completely "water clear"; in general they had regions that looked "white" and to the observer's eye appeared to scatter the visible light.

The spectra of RbN_3 and KN_3 were taken along the *c* axis of the plate-like crystals. (DREYFUS and LEVY[4] have described KN_3.) The similarity of the infrared spectrum of CsN_3 to the RbN_3 and KN_3 spectra suggests that it too was studied along the *c* axis. A crystal orientation determination of NaN_3 was not made. (The complete infrared spectra of these crystals have been published elsewhere[5].)

In order to produce minimum irradiation effects, the crystals were irradiated for short times and with a relatively weak source of irradiation. The lamp used for irradiation was an 85 W G.E. H3FE with its outer envelope removed. The spectrum of this lamp was photographed and it showed lines down to about 225 mμ (5·5 eV). The lamp was placed approximately 12 in. from

* Presently on leave at the Department of Chemistry, Imperial College of Science and Technology, Imperial Institute Road, London, S.W.7.

the crystal and the radiation passed through the $\frac{1}{4}$ in. NaCl Dewar windows so that it is unlikely that any heating occurred during irradiation. The sample holder was a Dewar with NaCl windows and a massive copper crystal holder sealed in with a copper-to-glass seal. An iron–constantan thermocouple was soldered to the crystal holder and the temperature was recorded continuously.

All irradiations and all spectra were taken at $-196°C$ *under vacuum.* To study thermal bleaching effects the liquid nitrogen was allowed to boil off permitting the Dewar to warm up to any desired temperature, and when this temperature was reached liquid nitrogen was reintroduced. (The spectrum at any given warmup temperature is constant for at least 20 min.) After the temperature dropped back to $-196°C$ a short period of time was allowed to insure thorough cooling of the crystal and then the spectrum was remeasured. The crystals reached liquid nitrogen temperature almost as soon as the copper crystal holder (this was known from previous work[5]). *In all of the following, this is the experiment carried out when any statement concerning warmup is made.*

All the azides were first surveyed for general irradiation effects, and then each different azide was studied in detail in the regions of interest. The infrared region was examined to 500 cm^{-1}. A different crystal had to be investigated in each region (i.e. u.v., visible, i.r.) but several crystals of each azide were studied in any one region.

The spectra were studied with a Perkin–Elmer Model 13 spectrophotometer using interchangeable prisms. The NaCl prism was calibrated against NH_3, CO_2, HBr, CO, CH_4, H_2O vapor and a Hg arc; the KBr prism was calibrated against CO_2 and H_2O vapors, and the SiO_2 prism with a Hg arc.

The Dewar was mounted in the light path of the spectrophotometer in such a manner that a 45° turn of the Dewar allowed the u.v. radiation to fall on the crystal. After irradiating for the desired length of time the Dewar was turned back into the light path and the spectrum was recorded. To obtain the spectra due to the irradiation, the spectrum of the unirradiated crystal was subtracted from that of the same crystal after irradiation. To equalize the optical density readings before and after irradiation the zero adjustment for the visible was set at 950 mμ and checked at 450 mμ. In the infrared region the spectrophotometer zero was made in a similar manner. Confidence in this technique was established in the following manner. After the last experiment on the growth of a band (see for example Fig. 1), the crystal was bleached without moving the Dewar and the spectrum was remeasured. The background was the same as in the unirradiated crystal. In the ultraviolet there was a general increase in background which may have been due to light scattering perhaps caused by the gas which evolves from the crystal during the thermal bleach. For this reason the ultraviolet region was not investigated in detail.

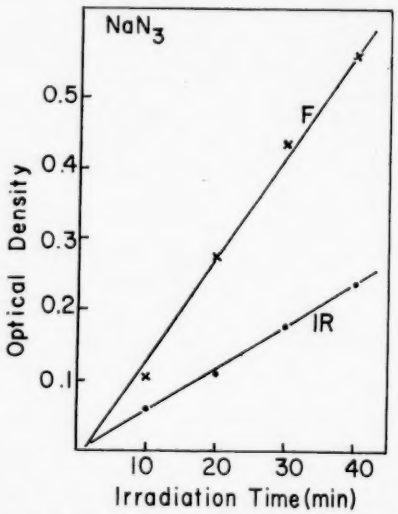

FIG. 1. Growth of the *F* band and i.r. band on irradiating NaN_3.

To check for possible bleaching effects during the spectrum measurement repeated measurements of the spectrum were made. No bleaching effects were found. The check was repeated periodically during the course of the work.

Reported optical densities are $\log_{10} I_0/I$.

RESULTS

Table 1 shows the frequencies of the ultraviolet and visible bands obtained by previous workers[2, 3] and the present work. To be consistent, band designations are those used by the previous authors. The work of CUNNINGHAM and TOMPKINS[2] is labelled (CT), the work of HEAL

Table 1. Band frequencies identified by various investigators

	Crystal fundamental band (mμ)			*V* band (mμ)			*F* band (mμ)			*F* band width* (eV)		Bands to red side of *F* (mμ)		
	(CT)	(HP)	(P)	(CT)	(HP)	(P)	(CT)	(HP)	(P)	(HP)	(P)	(CT)	(HP)	(P)
NaN_3	242	249	242	—	330	—	610	612	615	0·32	0·35	740	740	740
KN_3	254	259	267	360	361	360	572	568	575	0·60	0·65	770	790	775
RbN_3	—	280	268	—	374	375	—	578	575	0·50	0·38	—	820	750
CsN_3	—	263	268	—	390	380	—	592	595	0·43	0·42	—	850	—

* Full band width at half height.

and PRINGLE[3] is labelled (HP), and the present work is labelled (P). From (CT) we have listed the bands produced by u.v. irradiation. HEAL and PRINGLE used only X-ray irradiation. It is apparent that there is quite excellent agreement. The difference in the bands on the red side of the *F* band between (HP) and (P) can be attributed to the very great difference in the energies used to produce the color centers. In RbN_3, (HP) point out that their value for the fundamental absorption edge appeared to be anomalous and our value does appear to be more nearly what might be expected.

Since attention will be focused on the visible and infrared regions, only a short discussion of results of the ultraviolet region will be given. The broad band in the near ultraviolet was a weak band. The maximum optical densities for irradiation times used here (of the order of 40 min) were 0·06, 0·05, and 0·10 for KN_3, RBN_3, and CsN_3, respectively. (No band was observed in NaN_3.) They were also the most unstable bands, disappearing when the crystal was warmed to approximately −115°C. In CsN_3, at this temperature a new fairly strong band is formed in the infrared at 1568 cm^{-1} with a band width at half height of approximately 0·0023 eV (20 cm^{-1}). It appears with its maximum intensity at this temperature and decays with warmup disappearing at approximately −60°C. This suggests that the two bands are intimately related.

A definitive statement about this band cannot be made except for the following comments. Vibrations of N—N bonds near 1568 cm^{-1} have been discussed by several authors. LEFEVRE *et al.*[6] have come to the conclusion that the —N=N— vibration should be assigned the value 1579 cm^{-1}. HERZBERG[7] in discussing azomethane lists $\nu_{N=N}$ as 1576 cm^{-1}. Since no other infrared vibration related to this one was found, a possible assignment for the 1568 cm^{-1} vibration would be a structure N=N—N=N (the single bond in this configuration would not be expected to be infrared active). It is of interest to point out here that SHUSKUS *et al.*[8] have suggested the N_4^- molecule-ion to explain their ESR spectra in KN_3. Why

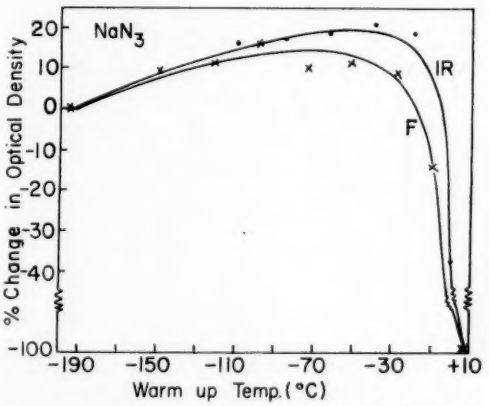

FIG. 2. Change with temperature of the *F* and i.r. band peak heights in NaN_3 (all measurements taken at −196°C).

this 1568 cm^{-1} band was not observed in the other azides which yielded V bands is not clear.

NaN_3: Figure 1 shows typical growth curves for the F band at 615 mμ and the i.r. band at 1721 cm^{-1} (band width at half height approximately 0·0023 eV) produced by u.v. irradiation.

The two bands may be correlated by their monotonic increase of the optical density with the irradiation time. A further correlation is shown by Fig. 2. It shows the per cent change in optical density during warmup of the F band and the i.r. band. The thermal behavior gives strong evidence for the intimate association of the two bands. Both bands appear together, undergo similar thermal effects, and disappear together (at approximately +10°C).

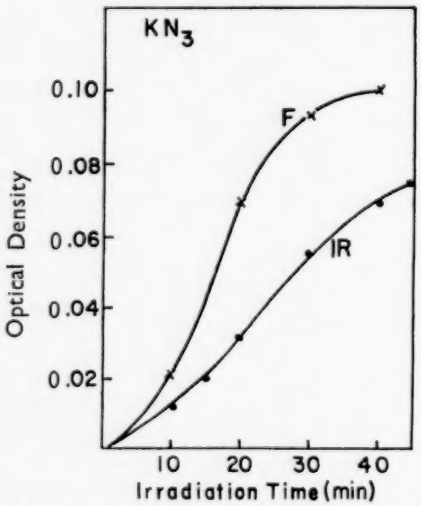

FIG. 3. Growth of the F band and i.r. band on irradiating KN_3.

KN_3: Upon irradiation a band appears at 575 mμ and in the infrared at 1637 cm^{-1} (band width at half height approximately 0·0023 eV). Both bands grow with irradiation and thermally bleach in the same manner. Fig. 3 shows growth curves for both bands. Both the F band and the i.r. band increase in peak height in a manner similar to NaN_3. Both bands increase approximately 15 per cent in the region between −196° and −20°C before beginning decay, and both are gone at room temperature.

When the warmup temperature reaches +15°C a new band appears at 775 mμ with a band width similar to the F band. In the infrared, a band appears at 1666 cm^{-1} (band width at half height < 0·0023 eV). Both bands decay with increasing temperature and are gone at room temperature. Apparently, the bands found by the previous workers on the red side of the F band (740–790 mμ) are not produced by radiation but by thermal effects caused by the radiation.

RbN_3: Upon irradiation, a band appears in the visible at 575 mμ, and in the infrared a band appears at 1623 cm^{-1} (band width at half height approximately 0·0023 eV). The growth curves and the thermal bleaching behavior of these bands again suggests that they are intimately related. The growth curves are depicted in Fig. 4. Both bands begin to decay at approximately −100°C, are 50 per cent gone by approximately −30°C, and are all gone at room temperature.

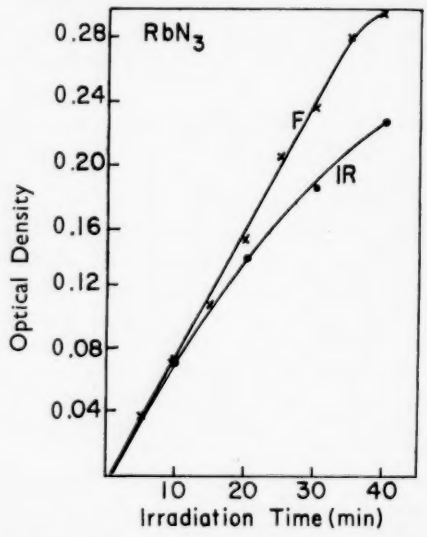

FIG. 4. Growth of the F band and i.r. band on irradiating RbN_3.

At approximately −45°C a new band appears at 750 mμ with a band width at half height of 0·42 eV and at this temperature a band at 1635 cm^{-1} (band width at half height < 0·0023 eV) appears in the infrared. Both grow slightly with temperature before decaying completely at room

temperature. Again, as in KN_3 these bands are not produced by radiation.

CsN_3: Upon irradiation a band appears in the visible at 595 mμ, and in the infrared a band appears at 1613 cm^{-1} (band width at half height approximately 0·0023 eV). The growth curves and the thermal bleaching behavior of these bands suggests that they are intimately related. Fig. 5 shows the growth for these bands. Both bands begin to decrease in peak height at approximately −100°C, are approximately 50 per cent gone by −75°C, and are all gone by −60°C. These bands did not undergo any increase in peak height before beginning to decay. However, another correlation exists. Fig. 5 also shows the rate of growth for both bands for the first and second irradiation (after thermal bleach of the first growth). Both slopes are decreased approximately 60 per cent.

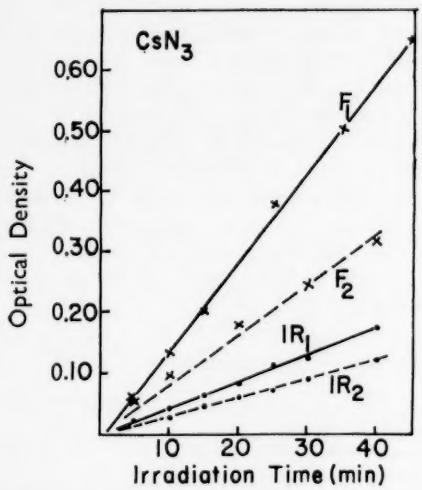

FIG. 5. Growth of the *F* band and i.r. band on irradiating CsN_3.
F_1 and $i.r_1$: First irradiation.
F_2 and $i.r_2$: Irradiation after thermal bleach.

DISCUSSION

Even a cursory examination of the results of this investigation shows that in these azides there is a strong correlation between the visible spectra and the infrared spectra produced by ultraviolet irradiation. In Table 2, the frequencies of the irradiation produced bands are correlated with the fundamental asymmetric stretching vibration of the azide ion.

MULLIKEN[9] has pointed out that all of the electrons of the azide ion contribute to the internal binding of the three nitrogen atoms. The isomorphous azides show that indeed this is the case. From the table it can be seen that for the case of the more electronegative cation, potassium, the azide ion is the least tightly bound internally and for the least electronegative cation, cesium, the orbitals in the azide ion are relatively more localized. The comparison cannot be carried to NaN_3 because of its different crystal structure. The table shows that the i.r. band formed on irradiation is displaced furthermost from the

Table 2. Relationship between the azide ion fundamental vibration and irradiation produced bands

	Crystal structure	Fundamental i.r. vibration of azide ion* ν_a	*F* band	Irradiation formed i.r. band ν_b	$\nu_a - \nu_b$
NaN_3	Body-center rhombohedral	2189 cm^{-1}	615 mμ	1721 cm^{-1}	468 cm^{-1}
CsN_3	Body-center tetragonal	2015	595	1613	402
RbN_3		2008	575	1623	385
KN_3		2002	575	1637	365

* PAPAZIAN H. A., *J. Chem. Phys.* **34,** 1614 (1961).

fundamental of the azide ion for the ion with the more localized orbitals, i.e. 468 cm^{-1} for NaN_3 and only 365 cm^{-1} for KN_3.

Table 2 also shows a correlation between the F band energy and the frequency of the fundamental vibration of the azide ion. It can be seen that the azide ion with the most localized orbitals has the smallest F band energy.

The results depicted in Table 2 show all the characteristics of "charge-transfer" phenomena well known in liquid systems and discussed extensively in the chemical literature especially by MULLIKEN[10]. Here we will state only generally what is observed and expected when "charge-transfer" occurs (for further details the reader is referred to a recent review by MCGLYNN[11]). In a suitable donor-acceptor (DA) system an exchange of charge occurs giving rise to a chemical "dative" bond with a concomitant appearance of a strong electronic absorption band belonging to the complex as a whole. In the infrared the following should ensue[11]:

(a) A decrease of bond order for at least one bond in each component of the complex (i.e. D–A) because of a partial removal of an electron from a bonding orbital of the donor to an antibonding orbital of the acceptor.

(b) Thus, there should be a decrease in the vibrational modes whose force constants are sensitive to the active orbitals involved in the DA interaction. This decrease will be larger the more localized the particular orbital.

Table 2 shows just these effects. The new infrared band appears on the low frequency side of the fundamental and the decrease is the largest for the azide ion with the more localized orbitals (i.e. NaN_3). The acceptor (a cation) in this system having no internal vibrations, we obtain no other infrared vibration related to the complex.

It has been suggested[2, 3] that the V band may be due to N_3—N_3^-. It would be of considerable interest to investigate the i.r. region of 1600–1700 cm^{-1} in crystals with strong V bands. If new i.r. bands were found to be related to the V electronic band then it could be concluded that the V center was also due to "charge-transfer".

Since the bands on the red side of the F band in KN_3 and RbN_3 have an associated i.r. band these too are likely caused by "charge-transfer".

The following model is suggested as a possible cause for the "charge-transfer" phenomenon. The incoming photon ionizes an interstitial atom, the electron becoming trapped in an anion vacancy giving rise to ESR and the cation moving into a cation vacancy. Now in the region of the original cation vacancy the equilibrium crystal field is so perturbed as to cause "charge-transfer". Although no determination of interstitial metal in unirradiated azide crystals has been made, interstitial atoms are found in many ionic crystals; for example, HAESKAYLO and OTTERSON[12] have found $1{\cdot}5 \pm 0{\cdot}2 \times 10^{17}$ "free" Na atoms/cm^3 in normal NaCl.

REFERENCES

1. TOMPKINS F. C. and YOUNG D. A., *Proc. Roy. Soc.* **236A,** 10 (1956).
2. CUNNINGHAM J. and TOMPKINS F. C., *Proc. Roy. Soc.* **251A,** 27 (1959).
3. HEAL H. G. and PRINGLE J. P. S., *J. Phys. Chem. Solids* **15,** 261 (1960).
4. DREYFUS R. W. and LEVY P. W., *Proc. Roy. Soc.* **246A,** 233 (1958).
5. PAPAZIAN H. A., *J. Chem. Phys.*, **34,** 1614 (1961).
6. LEFEVRE J. A., SOUSA J. B. and WERNER R. L., *Aust. J. Chem.* **9,** 151 1956).
7. HERZBERG G., *Infra-red and Raman Spectra of Polyatomic Molecules,* Van Nostrand, New York (1945).
8. SHUSKUS A. J., YOUNG C. G., GILLIAM O. R. and LEVY P. W., *J. Chem. Phys.* **33,** 622 (1960).
9. MULLIKEN R. S., *J. Chem. Phys.* **3,** 720 (1935).
10. MULLIKEN R. S., *J. Phys. Chem.* **56,** 801 (1952).
11. MCGLYNN S. P., *Chem. Rev.* **58,** 1113 (1958).
12. HACSKAYLO M. and OTTERSON D., *J. Chem. Phys.* **21,** 552 (1953).

Vol. 2
1961

J. Phys. Chem. Solids Pergamon Press 1961. Vol. 21, Nos. 1/2, pp. 87–98. Printed in Great Britain.

SURFACE MAGNETOCONDUCTIVITY EXPERIMENTS ON SILICON*

R. E. COOVERT†

Electrical Engineering Research Laboratory, University of Illinois, Urbana, Illinois

(*Received* 3 *October* 1960; *revised* 11 *March* 1961)

Abstract—Measurements of the Hall coefficient and magnetoconductivity of holes and electrons trapped in the space charge region adjacent to a thermally oxidized silicon surface have been made. The experiments were performed on high resistivity silicon samples at approximately 90°C. The results have been compared with theories for random and specular surface scattering. It was found that *p*-type samples showed better agreement with random scattering than specular scattering. On an *n*-type sample, electrons in an accumulation layer were in agreement with the random scattering theory, while holes at an inversion layer indicated specular scattering. On a sample which converted from *p*-type to *n*-type in the oxidation treatment, better agreement with specular scattering was found for electrons at an *n*-type surface, while the results for holes at a *p*-type surface were in better agreement with the random scattering theory. It is suggested that surface scattering may be specular in the absence of ionized impurities in the surface region and random in the presence of such ionized impurities.

1. INTRODUCTION

THE assumption of random scattering of carriers at the surface of a semiconductor has been used in a number of theoretical treatments[1–7] of surface transport properties, although there is some evidence of at least partially specular scattering.[8,9] The present investigation concerns an experiment on silicon in which the influence of surface carrier mobilities on the Hall effect is measured as the surface conditions are varied by means of the field effect. The results are compared with theoretical calculations for the cases of random and specular surface scattering.

It has been pointed out that under certain conditions the mobilities of carriers in the surface region of a semiconductor may be reduced from the values existing in the bulk. If carriers are constrained at the surface within a potential well having a width of the order of a mean free path or less, the carriers will make frequent collisions with the surface in addition to the usual bulk scattering mechanism. The resulting reduction in the effective mobility of surface carriers in an inversion layer has been calculated by SCHRIEFFER[1] under the assumption that the carriers are scattered randomly at the surface. Additional modifications and extensions of this calculation have been given[2–7] which also utilize the random scattering condition, since a detailed knowledge of the surface scattering mechanism is not known. In order to check the validity of the random scattering assumption, experiments have been performed[8–13] on germanium and silicon. These experiments are designed to detect a change in the effective mobility as the surface conditions are varied. There is some lack of agreement among the results of the different experiments.

A rather direct study of surface mobilities by galvanomagnetic measurements on germanium has been made by ZEMEL and PETRITZ[10,11]. The results of this experiment are independent of the amount of surface trapping. Using expressions derived by PETRITZ[14], which are not dependent upon the detailed scattering mechanism or potential variation at the surface, they calculated theoretical curves to compare with their measured

* Based on a thesis submitted to the University of Illinois in partial fulfillment of the requirements for the Ph.D degree (unpublished). This work was supported by the Office of Naval Research.

† Present address: Tektronix, Inc., Research Division, Beaverton, Oregon.

galvanomagnetic coefficients. They found that for an n-type surface their data were in agreement with the diffuse scattering hypothesis if they assumed a two carrier model for the Hall effect and a three carrier model for the magnetoresistance. For a p-type layer, they also found good agreement with random scattering, using either the SCHRIEFFER[1] calculation or a treatment by ZEMEL[3] which takes into account the presence of the magnetic field. Magnetoresistance measurements on very thin n-type germanium filaments of lower resistivity (~ 10 ohm-cm) over a wide range of surface potential have been made by ALBERS and THOMAS[13]. Their results show evidence of some random scattering and are qualitatively similar to those of ZEMEL and PETRITZ.

On the other hand, field effect measurements on germanium and thermally oxidized silicon reported by MILLEA and HALL[8] indicate that the scattering of carriers by the surface may not be completely diffuse. They observe a larger change of conductance than is predicted by the SCHRIEFFER theory for the case of no surface state shielding. Because of the uncertainty introduced by the probable presence of surface states, they were only able to conclude from their measurements that the scattering is not completely random but may be partially so. The measurements they present are for an n-type surface condition on doped ($\sim 3 \times 10^{14}/\text{cm}^3$) n-type material, while the data reported by ZEMEL and PETRITZ are for nearly intrinsic germanium samples.

MANY[9] and co-workers have performed pulsed field effect measurements on n-type germanium below room temperature. They find that the measured reduction in mobility for electrons in an accumulation layer is less severe than would be expected by the application of SCHRIEFFER's random scattering calculation.

MISSMAN and HANDLER[12] have performed magnetoconductivity experiments on a germanium surface cleaned by ion bombardment, using an oxygen ambient to change the energy bands at the surface. They found that the Hall surface mobility of holes as a function of surface conductance was somewhat greater than but close to the values predicted by the diffuse scattering model of SCHRIEFFER.

Several workers[2,4–7] have modified SCHRIEFFER's calculation by the assumption of different potential functions used to describe the surface region, and ZEMEL[3] has extended the theory to include the presence of a magnetic field. Recently, GREENE, FRANKL and ZEMEL[6] have given a calculation which is generalized to apply to an accumulation layer as well as the inversion layer assumed by SCHRIEFFER. Galvanomagnetic coefficients for thin films and space charge layers for the case of random surface scattering have been calculated by AMITH[7]. A good review of semiconductor surface transport theory has been presented by GREENE[15].

Recently the conductivity and galvanomagnetic coefficients of the semimetal bismuth have been measured at low temperature by FRIEDMAN and KOENIG[16]. Using the theory of HAM and MATTIS[17] and of PRICE[18] to interpret their results, they have shown that the surface scattering of electrons is specular.

Our experiments were initiated to determine the relation between the surface mobility and the bulk mobility in silicon in order to interpret field effect data. Measurements have been made on thermally oxidized high resistivity silicon samples, using the experimental method of ZEMEL and PETRITZ[10]. The results, which were found to vary with sample type and oxidation treatment, indicate that random scattering at the surface is a function of the surface potential.

2. EXPERIMENTAL METHOD

The samples were made from the following three floating zone refined single crystals of silicon obtained from Merck and Company:

Merck I: p-type, 4000 to 4800 ohm cm, 2000 μsec lifetime.
Merck II: p-type, 1300 ohm cm, 1500 to 2000 μsec lifetime.
Merck III: n-type, 500 ohm cm, 100 μsec lifetime.

The specimens were prepared from slices cut normal to the [111] crystal axis, so that the thin samples have the [110] direction along their length and (111) surfaces. The samples were polished by wet lapping successively in slurries of 600 to 3200 mesh silicon carbide on plate-glass, and then in Linde A slurry on a nylon cloth lap. The final shaping of the specimens with side arm tabs as in Fig. 1 was done by sandblasting, with a protective

Table 1. *Sample run data*

Sample	162D	126F	148A	170A
Merck ingot and type	II (*p*)	I (*p*)	II (*p*)	III (*n*)
Approximate ingot resistivity (ohm cm)	1300	4800	1300	500
Sample thickness (cm)	0·066	0·103	0·075	0·066
Oxidation time (hr)	1·0	0·5	12·0	1·0
Oxidation temperature (°C)	1200	550	680	1200
Type and resistivity (ohm cm) after oxidation	3400 (*n*)	60,000 (*p*)	1250 (*p*)	640 (*n*)
Temperature of run (°K)	357	367	363	357
Minimum *G* (micromhos)	74·0	11·0	52·6	96·8
Average current density (mA/cm²)	0·9	0·3	6·0	0·9
Number of field plates used	1	2	1	1
Magnetic field induction (G)	6540	7000	7000	5900

mask covering the polished faces. The total length, *L*, of the specimens was 1·5 cm, the width, *w*, was 0·3 cm, and the tab separation, *l*, was 0·6 cm. The thickness of each sample is given in Table 1.

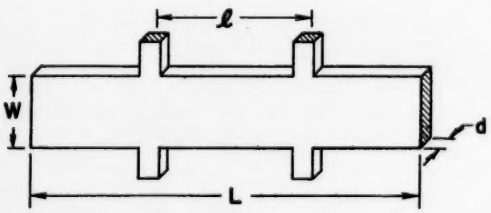

FIG. 1. Shape of silicon samples used.

In this geometry the ends of the sample are current contacts and the side arms are tabs for measuring the Hall and conductance voltages. The arms are positioned a distance of at least 1·5 times the width away from the ends of the sample in order to avoid diminishing the Hall voltage by the shorting effect of the end contacts.[19,20] The samples were etched in CP-4A (CP-4 without bromine), rinsed in deionized water and air dried.

In order to overcome the shielding by slow surface states in the d.c. field effect, the samples received an additional treatment of a thermally grown oxide on the surface. Although the lowest effective temperature was to be preferred, various temperatures from 300 to 1200°C were tried, with times varying from 80 hr down to several minutes. The oxidation was performed in the presence of wet oxygen, with the growth rate estimated from the data given by ATALLA *et al.*[21].

In the high resistivity *p*-type material it was noted that occasionally the bulk was converted from *p*- to *n*-type by heat treatment. It was concluded that this conversion was due to the donor-like[22] behavior of dissolved oxygen aggregates[23] rather than the introduction of a column V contaminant, since the material could be restored to *p*-type silicon by heating to 1200°C, annealing at 1000°C, and cooling slowly to room temperature.

It was found that acceptable ohmic contacts could be made to high resistivity silicon with the aid of an ultrasonic soldering apparatus, using ordinary tin–lead solder or indium. The end of each side arm as well as the ends of the sample were tinned with solder, and these tinned areas were placed in contact with spring clip electrodes in the sample holder. Floating potential measurements made with a traveling probe showed uniform resistivity along the length of the completed samples.

The sample was placed in the sample holder in the form of a sandwich, with the two high voltage field plates separated from the polished faces of the sample by sheets of mylar insulation. The sample mount was located at the upper end of a brass bar, while the lower end was placed in a Dewar flask into which liquid nitrogen could be placed for attaining colder than room temperatures. A heater coil wound around the middle of the bar was used to control and maintain the temperature

in the range 78–400°K. An inverted Dewar or a double-walled metal cover with glass wool inner insulation was placed down over the sample and heating coil for thermal and electrical shielding.[24]

The temperature of the sample was measured by means of a chromel–alumel thermocouple in contact with the sample. The temperature sensing element for the control heater was a thermistor which operated a commercial* furnace control unit. With the addition of an oscillating type[25] heating cycle "anticipator" the temperature could be stabilized to better than ± 0·1°C.

The experimental method and apparatus employed were similar to that described by ZEMEL and PETRITZ[10]. A constant direct current source was connected to the end contacts of the sample and a reversible transverse magnetic field was applied in a direction normal to the polished surfaces. The sum of a conductance voltage along the sample and the Hall voltage was measured by connecting an electrometer to a diagonally opposite pair of side arms. This conveniently produced a single output voltage to a recorder, from which the separate contributions were reclaimed by simple algebraic combinations of the values for the magnetic field on, off and reversed. Instead of using ambient gases to control the surface potential, a variable high voltage was connected to one or both of the insulated field plates to apply a transverse electric field to the polished faces.

Three separate digital type subtractors, using General Radio decade voltage divider boxes, were used for the conductance, Hall and magnetoresistance voltages. Each field effect run was carried out at constant temperature, usually at about 360°K. The magnetic field of approximately 7000 G was cycled continuously as the field plate voltage V_p, was varied at intervals to change the surface potential. The conductivity with zero magnetic field was used as a reference property for determining the relative surface potential. The absolute value of the surface potential may be determined from the bulk properties and the minimum value of surface conductivity, which occurs when the surface is nearly intrinsic. This conductivity minimum may not always be observed, due to the action of surface states which may shield the electric field set up by V_p. The allowed range of V_p is limited by dielectric breakdown between the field plate and the sample. With three thicknesses of 0·25 mil mylar, d.c. breakdown occurred at about 2000 V, limiting the applied electric field to about 10^6 V/cm. Breakdown was avoided because after the transfer of charge to the oxide the conductance minimum did not usually coincide with previous minima.

On etched silicon, after V_p is changed, the conductance usually changes immediately and then relaxes back to nearly the original value within a few minutes. On thermally oxidized surfaces there is usually a tendency for the conductance to drift forward in the same direction as the initial rapid jump. Thus, even when V_p has reached the maximum allowed value, the conductance may continue to drift onward for a half hour or longer. This forward drift effect, plus the observation that the minimum of conductance is not always unique on oxidized silicon surfaces, has been reported by MILLEA and HALL[26].

3. RESULTS OF MEASUREMENTS

Measurements of the conductivity, Hall voltage and magnetoresistance have been made as a function of field induced surface conductance on high resistivity silicon samples. Several typical runs are reported here.

The conductivity data is presented in terms of a "conductance per square", G, which is related to the total conductance, I/V_g, by the ratio of length to width of surface area:

$$G = \frac{LI}{wV_g} \tag{1}$$

where I is the current and V_g is the voltage along the sample.

The variation in the conductance per square, caused by a change in the potential of the electric field plate, and measured from the minimum value of conductance, is

$$\delta G = G - G_{\min}. \tag{2}$$

Since the energy bands are near the flat band position at the conductance minimum, δG will be regarded as the "surface conductance" and used as a reference property related to the surface

* Tagliabue Celectray Indicating Potentiometer Controller.

potential. Although δG is always positive as defined, it will be regarded as negative for a p-type surface and positive for an n-type surface when the surface conductance is used as the abscissa in plotting graphical data.

The measured Hall voltage, in terms of the usual Hall coefficient, R, is

$$V_H = \frac{RIH}{d} \tag{3}$$

where I is the current, and d is the thickness of the sample. It is convenient to define a "Hall coefficient per square" so that the Hall voltage is not explicitly dependent on sample thickness:

$$R_\square = \frac{R}{d} = \frac{V_H}{IH}. \tag{4}$$

The Hall mobility, μ_H, is given by

$$\mu_H = R\sigma = R_\square G. \tag{5}$$

The magnetoresistance data is presented in terms of the coefficient M, defined by

$$M = \frac{\Delta\rho}{\rho H^2}. \tag{6}$$

In terms of the above quantities, the equations derived by PETRITZ[14] may be written

$$\frac{G-G_B}{e} = \Delta N_1\mu_1\alpha_1+\Delta N_2\mu_2\alpha_2+\Delta N_3\mu_3\alpha_3 \tag{7}$$

$$R_\square G^2-(R_\square G^2)_B = q_1\Delta N_1\mu_1^2\alpha_1^2 + q_2\Delta N_2\mu_2^2\alpha_2^2+q_3\Delta N_3\mu_3^2\alpha_3^2 \tag{8}$$

$$G\{M+(R_\square G)^2\}-G_B\{M+(R_\square G)^2\}_B = q_1\Delta N_1\mu_1^3\alpha_1^3+q_2\Delta N_2\mu_2^3\alpha_2^3+q_3\Delta N_3\mu_3^3\alpha_3^3 \tag{9}$$

where the correlation terms as well as some terms which are negligible for high resistivity material have been dropped, and where the subscript B denotes the bulk value as measured at the flat band condition. Also, using subscripts b and s to distinguish between carriers in the bulk and surface regions, respectively, we define

$$\alpha_i \equiv \langle\mu_{is}\rangle/\langle\mu_{ib}\rangle \quad \text{and} \quad \langle\mu_{ib}\rangle = \mu_i$$

where the brackets denote averages over velocity space as used by PETRITZ.

The following approximations have also been made:

$$\langle\mu_{is}^2\rangle/\langle\mu_{ib}^2\rangle = \alpha_i^2, \quad \langle\mu_{is}^3\rangle/\langle\mu_{ib}^3\rangle = \alpha_i^3.$$

In the equations above, the carrier charge and mobility are denoted by q_i and μ_i respectively, and the quantities ΔN_i are products of the surface layer thickness with the effective densities of carriers and represent surface concentrations as used by KINGSTON and NEUSTADTER[27].

The above equations have been used to calculate theoretical curves, as in Figs. 2, 3, and 8, to compare with the experimental data. The subscripts 1, 2, 3, in the above equations are taken to refer, respectively, to electrons, slow holes, and fast holes. To take into account the fast holes assumed to be present in silicon, the values $n_3/n_2 = 0{\cdot}165$ and $\mu_3/\mu_2 = 3$ have been used.[28] The values of ΔN_i were obtained from KINGSTON and NEUSTADTER's computations[27], for which the bulk potential, u_b, was determined from the flat band conductivity. The bulk mobilities, determined from the measured Hall mobility near the flat band condition using the empirical mobility ratios[29]($\mu_{nH}/\mu_n = 1{\cdot}2$, $\mu_{pH}/\mu_p = 0{\cdot}7$), were used to calculate curve B in each figure, with $\alpha_i = 1$ in equations (7), (8) and (9). To obtain curve S for the random scattering case, the effective mobility ratios, α_i, were estimated from the SCHRIEFFER[1] calculation.

As explained above, all of the specimens were thermally oxidized in order to be able to induce appreciable changes in surface conductance, $\sim$ 10 micromhos. Without this treatment δG of freshly etched samples could not usually be varied more than about one or two micromhos due to the shielding effect of surface states. In general the oxidation treatment changed the resistivity of the samples and several converted from p-type to n-type. It is possible that after the oxidation the impurity concentration near the surface may not be uniform, which would cause some difficulty in the interpretation of the results. Typical results are presented from each of three groups: converted samples, p-type, and n-type.

Figure 2 shows the Hall coefficient per square for sample 162D, which converted to 3400 ohm cm

Vol. 21
1961

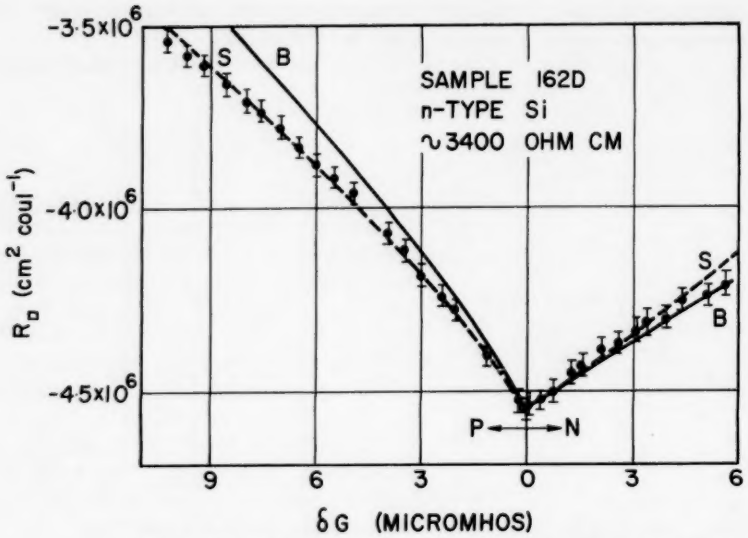

FIG. 2. Hall coefficient per square vs. surface conductance per square for a 3400 ohm cm *n*-type converted sample. Curve B: Theory based on bulk mobility. Curve S: Schrieffer theory for random surface scattering.

n-type silicon. It is seen that the Hall data on the *n*-type side are best fit by curve B for large values of δG where surface scattering might be expected to be appreciable, although curve S fits as well if not better at smaller values of δG. For the *p*-type surface the Schrieffer curve S fits the Hall data fairly well and is clearly superior to curve B. In Fig. 3 the experimental results of magnetoresistance measurements on this sample are presented. Neither of the two theoretical curves shown provide conclusive agreement with the magnetoresistance data.

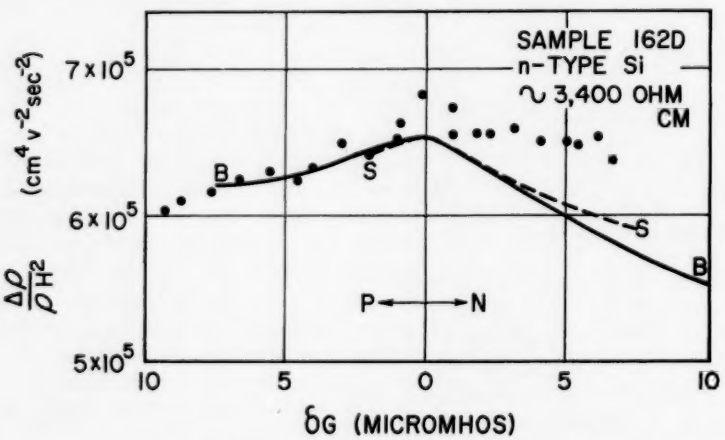

Fig. 3. Magnetoresistance coefficient vs. surface conductance per square for a 3400 ohm cm *n*-type converted sample.

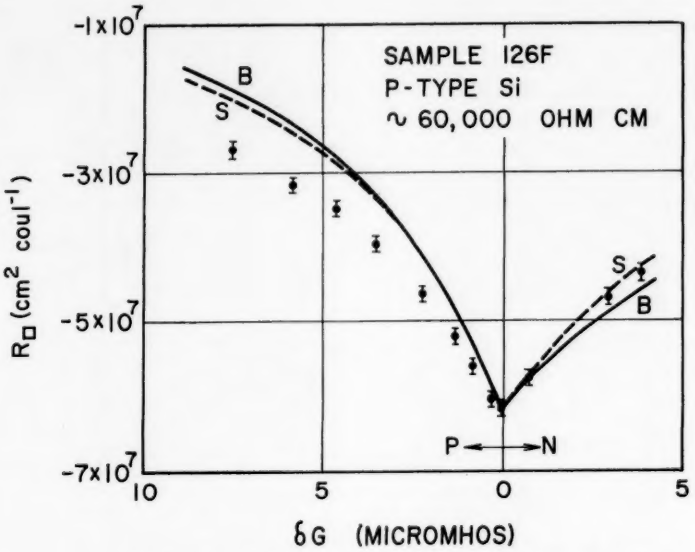

FIG. 4. Hall coefficient per square vs. surface conductance per square for a 60,000 ohm cm *p*-type sample.

Vol. 21
1961

p-type sample 126F was oxidized at a lower temperature than the other samples and its resistivity increased from 4800 to 60,000 ohm cm. The Hall coefficient per square in Fig. 4 for the *p*-type surface shows that the experimental points fall well below the theory curves, farthest from curve B. On the *n*-type side the measured values lie in between the two curves, slightly closer to curve S. Another *p*-type sample, 148A, did not convert or change its resistivity appreciably after

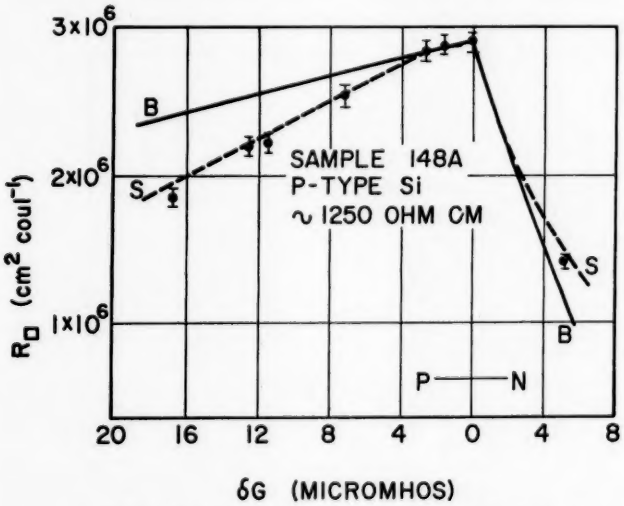

FIG. 5. Hall coefficient per square vs. surface conductance per square for a 1250 ohm cm *p*-type sample.

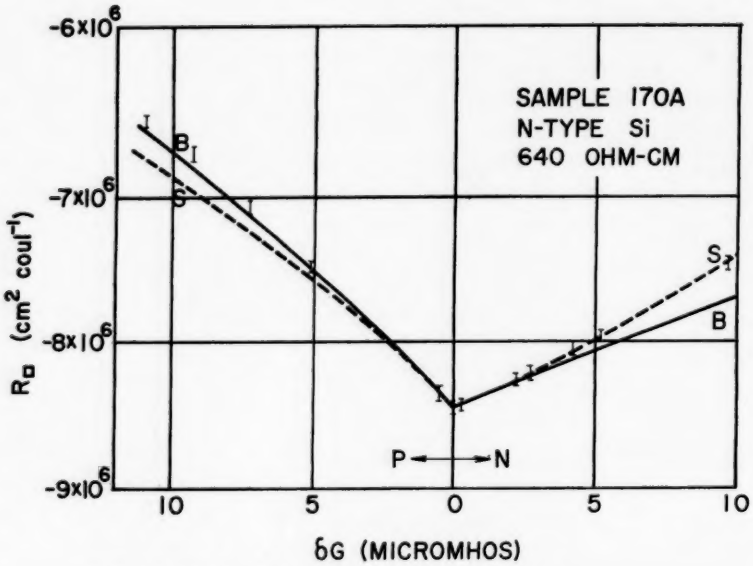

FIG. 6. Hall coefficient per square vs. surface conductance per square for a 640 ohm cm *n*-type sample.

oxidation for twelve hours at 680°C. The Hall results presented in Fig. 5 are in fairly good agreement with the Schrieffer curve S for the *p*-type surface, although the points tend to lie below curve S as for the previous sample. The measured value for the *n*-type surface lies between the two theory curves somewhat closer to the S curve.

An unconverted *n*-type sample, 170A, was found to have increased its resistivity slightly after

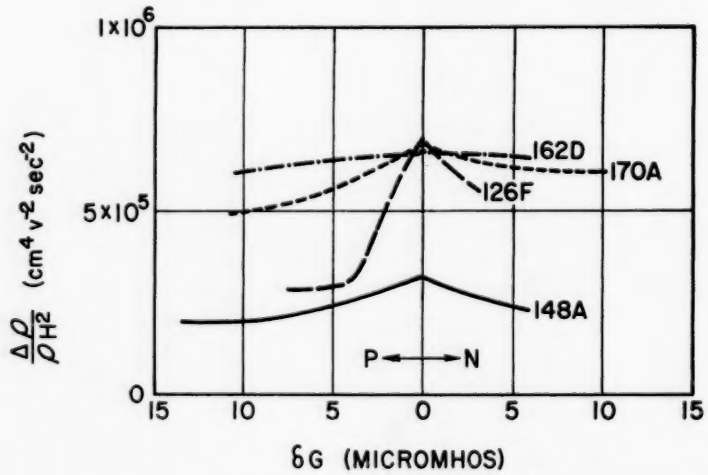

FIG. 7. Magnetoresistance coefficient vs. surface conductance for four silicon samples.

oxidation from 500 to 640 ohm cm. The Hall coefficient per square in Fig. 6 shows good agreement with curve S on the *n*-type side, while for a *p*-type surface the points lie close to but above curve B.

The magnetoresistance measurements for all the samples are summarized in Fig. 7 and are presented only for completeness, since the main conclusions of this report are based on the more accurate Hall data.

The quantity $R_\square G^2$ of equation (8) is plotted as in this representation. Since one carrier is usually predominant for band displacements large enough for surface scattering to become important, it is easy to detect deviations in surface mobility in this plot. Unfortunately, however, the drift effect observed in oxidized silicon[26] leads to experimental discrepancies in G, which are then magnified in the calculation of $R_\square G^2$. Therefore, theoretical curves for the Hall coefficient were calculated, so that they could be compared more directly with the measured Hall data.

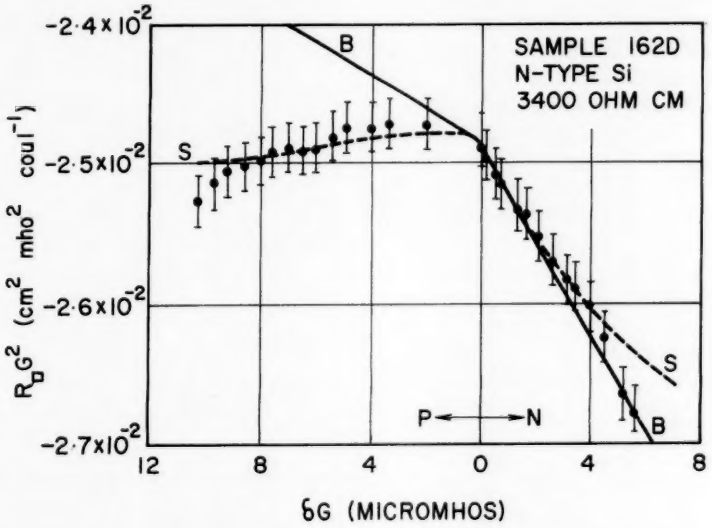

FIG. 8. A plot of the quantity $R_\square G^2$ for the sample data in Fig. 2.

in Fig. 8 together with some experimental results because it has the following significance. If equations (8) and (7) are divided, keeping only the large first term on the right hand side of each, the result is

$$\frac{R_\square G^2 - R_{\square B} G_B^2}{G - G_B} = \frac{\langle \mu_{is}^2 \rangle}{\langle \mu_{is} \rangle} = (\mu_{is})_H \quad (10)$$

where the subscript H denotes a Hall mobility. Thus in a range in which one carrier is sufficient to describe the effects, if $(R_\square G^2 - R_{\square B} G_B^2)$ is plotted vs. δG, the slope of a line from the origin yields the surface carrier Hall mobility. A constant mobility is indicated by a linear plot from the origin

The anomalous drift effect and lack of uniqueness of the conductance minimum is probably the greatest source of error in the measurements. Measurements of the d.c. field effect on thermally oxidized silicon surfaces have been made by ATALLA *et al.*[21]. They do not observe such anomalous drifts, but they stress the importance of cleanliness and a suitable preoxidation treatment, as impurities left on the surface partially remain at the Si–SiO_2 interface and may affect the surface characteristics. Additional care in this respect was taken in preparing samples 162D and 170A. The pretreatment for these samples consisted of boiling in concentrated nitric acid and then in deionized water immediately prior to the

oxidation. The detectable drift in these runs was not as large as in some of the other runs. All of the samples with oxides thick enough to produce interference colors appeared to have a macroscopically uniform coating. If the impurity concentration near the surface is not uniform there is a possibility of some error in the analysis.

The experimental method used does not distinguish between the Hall voltage and those due to the Ettingshausen, Nernst and Righi–Leduc effects.[30] These other effects are usually neglected in semiconductor measurements at the temperatures used. Preliminary work with a.c. Hall voltage measurements, in which the other effects are eliminated, agreed with d.c. measurements on the same specimen. Low current densities and moderately thick specimens with side tabs help in minimizing these other effects, which are primarily related to temperature gradients in the sample.

In addition to the above possibilities for the introduction of error, there are also experimental errors associated with the measuring apparatus. The largest relative errors in the measurements of the Hall coefficient are due to variations in the magnetic field ($\sim 0{\cdot}5$ per cent) and temperature ($\sim 0{\cdot}2$ per cent). The total relative error is about 0·7 per cent for both the Hall coefficient and $R_{\square}G^2$. The error in the magnetoresistance is estimated to be about 5 per cent. These relative errors have been used in the plots of experimental points. The use of the absolute errors in the magnetic field (2 per cent), sample dimensions (2 per cent), current (0·5 per cent), temperature (0·5 per cent) and subtractors (0·1 per cent) would lead to correspondingly larger tolerance limits. Since the theoretical curves have been based upon the values measured at the conductance minimum of each sample, the relative error was considered to be a better indication of the uncertainty in comparing the experimental results with theory.

4. DISCUSSION OF RESULTS

These results indicate that the type of scattering at the surface may change from specular to random as the energy bands are displaced at the surface. This suggests a mechanism of scattering by surface impurities that may change their state of ionization as the energy bands are displaced relative to the Fermi level.

The results may be understood qualitatively by the assumption that scattering from ionized impurities is random in character, and is essentially specular from a surface with neutral impurities. The presence of donor-like and acceptor-like levels at the surface will also be assumed.

RUPPRECHT[31] has reported measurement of a donor-like impurity level below midgap in *p*-type silicon and an acceptor-like impurity level above midgap in *n*-type silicon. It is presumed that both

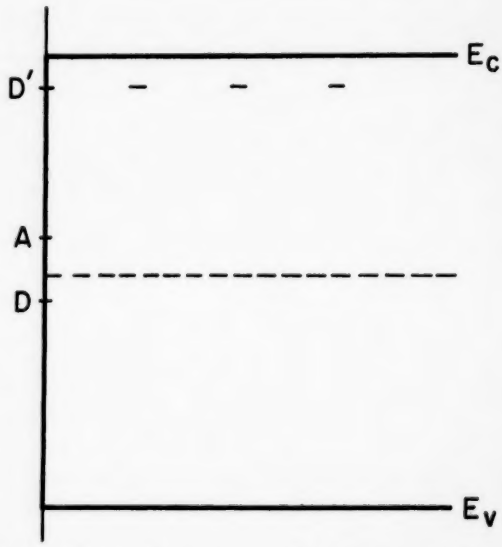

FIG. 9. Energy bands at a semiconductor surface for the flat band case, showing assumed positions of some donor and acceptor levels used in the interpretation of the results.

levels may be present simultaneously in a given specimen of either type.

In the case of the high resistivity *p*-type specimen, the Fermi level at the flat band condition is presumed to lie near midgap between the two surface levels. (See Fig. 9.) Since the Fermi level lies above the donor-like level D and below the acceptor-like level *A*, both levels are essentially neutral at the flat band condition. However, when the energy bands are displaced downward, *A* will become ionized and give rise to random scattering. Similarly, if the energy bands are displaced upward, *D* will become ionized. Thus the scattering

is random for a high resistivity p-type sample for both n-type and p-type surface conditions.

For a fairly high resistivity n-type sample, the Fermi level will lie in the vicinity of, perhaps slightly above, level A in the flat band condition. With the energy bands displaced downward A is ionized, and with the bands raised A becomes neutral. It is assumed that if level D is actually present it remains neutral because the extent of the band displacement is not sufficient to raise it above the Fermi level. Thus the scattering should be random for an n-type surface and specular for a p-type surface condition.

In the case of the sample which converted from p-type to n-type, the situation is less clear, but it is probable that a considerable density of additional donor levels, D', have been introduced near the conduction band as a result of the heating process. These are probably ionized at flat band and with the bands raised, but may become neutral when the bands are depressed at the surface. If these donors represent the dominant scattering centers for such a sample, the scattering would be random for a p-type surface and specular for an n-type surface condition, as observed.

It should be noted that the origin of any reduction of channel mobility in the above results is not determined by these measurements. We have compared our results with SCHRIEFFER's calculation for the reduction in mobility due to random scattering of carriers at the surface boundary plane. However, an increase in the concentration of scattering centers within the channel as compared to that of the bulk would also lead to reduced surface mobility. For example, besides the possibility of additional impurity scattering centers within the surface region, the Coulomb fields of charged surface states may be expected to extend over a substantial portion of the channel depth. Therefore a carrier may experience additional scattering while traveling along the channel as well as by collisions with the surface. Under these conditions a greater reduction of effective surface mobility than given by SCHRIEFFER's theory would be permitted. Such effects may have contributed to the considerable discrepancy between theory and experiment as in Fig. 4.*

5. CONCLUSION

An investigation of the surface mobilities of carriers in high resistivity thermally oxidized silicon has been carried out. The results are based on simultaneous conductance, Hall and magnetoresistance measurements as a function of a capacitively applied electric field to displace the energy bands at the surface with respect to the Fermi level. The measurements are compared with two theoretical curves, one for the specular reflection of carriers at the surface and the other for the random surface scattering hypothesis used by SCHRIEFFER.

Table 2. Comparison of experimental results with theory

	Sample	p-type surface	n-type surface
p-type samples	148A	S	—
	126F	S	S
n-type sample	170A	B	S
Sample converted to n-type	162D	S	B

The results are given for samples from three categories: p-type, n-type, and p-type that converted to n-type in the oxidation process. The results are summarized in Table 2, where the curve nearest to the experimental points is listed. In accordance with the labeling of the curves in the figures, the calculation using bulk mobilities for the case of specular surface scattering is denoted by B, and the calculation using SCHRIEFFER's effective mobility for the random scattering hypothesis is denoted by S.

* The author is indebted to the referee for pointing out this alternative interpretation.

Vol. 21
1961

In summary it may be said that the random scattering theory provides the better fit in the above cases, except for a *p*-type inversion layer on an *n*-type sample, and for an *n*-type surface in samples which converted from *p*-type to *n*-type. These results indicate that the type of scattering at the surface may depend upon the position of the energy bands at the surface relative to the Fermi level. It is further suggested that the surface scattering may be largely specular in the absence of ionized impurities in the surface region, whereas the scattering may be random in the presence of such ionized impurities.

Acknowledgement—The author wishes to thank Professor J. BARDEEN and Professor P. HANDLER for many valuable discussions during the course of this investigation.

REFERENCES

1. SCHRIEFFER J. R., *Phys. Rev.* **97,** 641 (1955).
2. ZEMEL J. N., *Bull. Amer. Phys. Soc.* (ser. 2) **3,** 255 (1958).
3. ZEMEL J. N., *Phys. Rev.* **112,** 762 (1958).
4. FLIETNER H., *Ann. Phys. Lpz. F.* 7, **3,** 396 (1959).
5. FRANKL D. R., *Bull. Amer. Phys. Soc.* (ser. 2) **4,** 179 (1959)
6. GREENE R. F., FRANKL D. R. and ZEMEL J. N., *Phys. Rev.* **118,** 967 (1960).
7. AMITH A., *J. Phys. Chem. Solids* **14,** 271 (1960).
8. MILLEA M. F. and HALL T. C., *Phys. Rev. Letters* **1,** 276 (1958).
9. MANY A., GROVER N. B., GOLDSTEIN Y., HARNIK E., *J. Phys. Chem. Solids* **14,** 186 (1960).
10. ZEMEL J. N. and PETRITZ R. L., *Phys. Rev.* **110,** 1263 (1958).
11. ZEMEL J. N. and PETRITZ R. L., *J. Phys. Chem. Solids* **8,** 102 (1959).
12. MISSMAN R. and HANDLER P., *J. Phys. Chem. Solids* **8,** 109 (1959).
13. ALBERS W. A., Jr., THOMAS J. E., Jr., *J. Phys. Chem. Solids* **14,** 181 (1960).
14. PETRITZ R. L., *Phys. Rev.* **110,** 1254 (1958).
15. GREENE R. F., *J. Phys. Chem. Solids* **14,** 291 (1960).
16. FRIEDMAN A. N. and KOENIG S. H., *IBM Journal* **4,** 158 (1960).
17. HAM F. S. and MATTIS D. C., *IBM Journal* **4,** 158 (1960).
18. PRICE P. J., *IBM Journal* **4,** 152 (1960).
19. ISENBERG I., RUSSELL B. R. and GREEN R. F., *Rev. Sci. Instrum.* **19,** 685 (1948).
20. DUNLAP W. C., Jr., *Phys. Rev.* **79,** 286 (1950).
21. ATALLA M. M., TANNENBAUM E. and SCHEIBNER E. J., *Bell Syst. Tech. J.* **38,** 749 (1959).
22. FULLER C. S. and LOGAN R. A., *J. Appl. Phys.* **28,** 1427 (1957).
23. KAISER W., *Phys. Rev.* **105,** 1751 (1957).
24. URE R. W., Jr., *Rev. Sci. Instrum.* **28,** 836 (1957).
25. American Institute of Physics, *Temperature, Its Measurement and Control in Science and Industry,* p. 611. Reinhold, New York (1941).
26. MILLEA M. F. and HALL T. C., *Second Conference on Semiconductor Surfaces,* U.S. Naval Ordnance Lab., White Oak, Maryland (1959).
27. KINGSTON R. H. and NEUSTADTER S. F., *J. Appl. Phys.* **26,** 718 (1955).
28. LAX B. and MAVROIDES J. G., *Phys. Rev.* **100,** 1650 (1955).
29. MORIN E. J. and MAITA J. P., *Phys. Rev.* **96,** 28 (1954).
30. LINDBERG O., *Proc. Inst. Radio Engrs. N.Y.* **40,** 1414 (1952).
31. RUPPRECHT G., *J. Phys. Chem. Solids* **14,** 208 (1960).

J. Phys. Chem. Solids Pergamon Press 1961. Vol. 21, Nos. 1/2, pp. 99–104. Printed in Great Britain.

HYPERFINE INTERACTION DUE TO ORBITAL MAGNETIC MOMENT OF ELECTRONS WITH LARGE g FACTORS

Y. YAFET

Bell Telephone Laboratories, Incorporated, Murray Hill, New Jersey

(*Received* 31 *March* 1961)

Abstract—The hyperfine interaction due to the orbital magnetic moment of conduction electrons is investigated. The effect can be split into two parts. One part is due to the long-range component of the interaction and it depends only on the macroscopic properties of the solid, i.e. on the magnetic susceptibility. This part depends on the shape of the sample via the demagnetizing factors; its magnitude is small, but the effect may be observable in a substance with very large g factor. The second part arises from the short-range component of the interaction and is the analogue of the atomic orbital hyperfine interaction; it reduces to it when the atoms are separated.

Vol. 21
1961

THERE has been interest recently in semimetals and semiconductors where the current carriers have very large g factors.[1] Nuclear resonance experiments on such substances provide an additional method of studying their electronic properties through interpretation of the Knight shift and the nuclear relaxation rate.[2] The theory of the Knight shift[3] shows that in metals it arises primarily from the contact part of the hyperfine interaction. With g factors of the order of 200 as in bismuth[1] a question which arises is whether such a large electronic moment can have an appreciable effect on the hyperfine interaction. This question is treated here; it is found that the hyperfine interaction with the orbital magnetic moment is small compared to the contact part of the interaction for a pure s state. Nevertheless in substances with predominantly non-s wave functions this effect may be observable through its dependence on the sample shape.

The magnetic field at the nucleus due to the carrier electrons (or holes) is the sum of the field due to the electron spin and the field due to the orbital current. Each of these is conveniently separated into two parts:

(a) The field due to the spin moment is the sum of the "contact part" or local interaction, and the dipolar part; the latter in turn gives two types of contributions in a crystal: long-range and short-range. They will be briefly mentioned later.

(b) The field due to the orbital current is our main concern; it can be split into a long-range contribution which depends only on the macroscopic magnetic properties of the crystal, and hence on the g factor via the susceptibility, and a short-range contribution which is the analogue of the field due to the atomic orbital hyperfine interaction. In the limit of infinite lattice constant, the long-range part reduces to zero and the short-range part reduces to the atomic value.

Let us first recall[4] the modification of the contact part of the Knight shift due to the departure of the g factor from 2. For free spins, the field at the nucleus resulting from the polarization of the spins is:

$$\Delta H = (8\pi/3)H\chi_P\Omega \langle|\psi(0)|^2\rangle_F$$

where H is the external field, $\psi(0)$ is normalized in the atomic volume Ω and χ_P is the paramagnetic susceptibility in the atomic volume; $\chi_P = (\partial n/\partial E)\beta^2$ where β is the Bohr magneton and $\partial n/\partial E$ is the density of states at the Fermi surface (assuming degeneracy of the electron gas).

For an arbitrary $g(\boldsymbol{k})$, function of the wave-vector, the magnetic field at the nucleus due to the contact interaction is given by the local density of

spin magnetic moment. Since the g factor gives the spin splitting of the orbital states, the excess population in one orientation of spin is:

$$\delta n = (1/2\pi)^3 \int \beta H g(\boldsymbol{k})(1/|\nabla_{\boldsymbol{k}} E|) dS_{\boldsymbol{k}},$$

where the integral is over the Fermi surface. With $\boldsymbol{\beta}(\boldsymbol{k})$ being the spin vector in the s part of $\psi_{\boldsymbol{k}}$, the field at the nucleus becomes:

$$\Delta \boldsymbol{H}_c = \frac{8\pi}{3} \frac{\Omega}{(2\pi)^3} \int \boldsymbol{\beta}(\boldsymbol{k}) \beta H g(\boldsymbol{k}) |\psi_{\boldsymbol{k}}(0)|^2 [dS_{\boldsymbol{k}}/|\nabla_{\boldsymbol{k}} E|]. \quad (1)$$

It is often the case, (although not in bismuth which is considered below) that when the g factor is very large, the electrons occupy a small region of $\boldsymbol{k}$ space, such that both $g(\boldsymbol{k})$ and $\psi_{\boldsymbol{k}}(0)$ are essentially constant. In this case (1) simplifies to:

$$\Delta \boldsymbol{H}_c = \frac{8\pi}{3} H \chi_P (2/g_i) \Omega |\psi(0)|^2. \quad (2)$$

Here $\boldsymbol{H}$ is assumed to lie along a principal axis i of the g tensor at the bottom of the band and χ_P is the paramagnetic susceptibility:

$$\chi_P = g_i^2 (\partial n/\partial E) \beta^2.$$

Finally, because of spin–orbit interaction the spin in the s part of the wave-function does not need to lie in the direction of the applied field so that the projection of $\Delta \boldsymbol{H}_c$ on $\boldsymbol{H}$, which is the relevant quantity for the Knight shift, may be smaller than (2).

We turn now to the hyperfine interaction arising from the orbital magnetic moment of the electron. For electrons localized in small regions of $\boldsymbol{k}$ space, the method of LUTTINGER and KOHN[5] (L–K) which consists in obtaining an equivalent one-band Hamiltonian expanded in powers of k is particularly appropriate and will be used. The form of the result thus obtained is quite general and it will easily be shown that it holds for an arbitrarily filled band.

Let $\boldsymbol{A} = (\boldsymbol{\mu} \times \boldsymbol{r})/r^3$ be the vector-potential of the nuclear moment $\boldsymbol{\mu}$ and $\boldsymbol{A}'$ be the vector potential of the externally applied field H. $\boldsymbol{A}$ is Fourier-analyzed and split into two parts:

$$\boldsymbol{A}(\boldsymbol{r}) = \int d\boldsymbol{q} \boldsymbol{A}(\boldsymbol{q}) \exp(i\boldsymbol{q} \cdot \boldsymbol{r}) = \boldsymbol{A}_0(\boldsymbol{r}) + \boldsymbol{A}_s(\boldsymbol{r})$$

where $\boldsymbol{A}_0$ is given by the Fourier components with $\boldsymbol{q}$ in the reduced zone and $\boldsymbol{A}_s$ is the rest. $\boldsymbol{A}_0$ contains the long-range part of $\boldsymbol{A}$ while $\boldsymbol{A}_s$ is effectively short-range, of the order of the lattice distance. Let

$$\chi_{n',\rho,\boldsymbol{k}} = u_{n',\rho}(\boldsymbol{r}) \exp(i\boldsymbol{k} \cdot \boldsymbol{r})$$

be the L–K function for band n' and spin state ρ, where $u_{n'\rho}(\boldsymbol{r})$ is the Bloch function at $\boldsymbol{k}_0$, the position of the energy minimum of the band n which contains the electrons under consideration. The wave vector $\boldsymbol{k}$ is measured from $\boldsymbol{k}_0$. The normalization is

$$(\chi_{n,\rho,\boldsymbol{k}}, \chi_{n',\rho',\boldsymbol{k}'}) = \delta_{nn'} \delta_{\rho\rho'} \delta(\boldsymbol{k} - \boldsymbol{k}').$$

The representative of the Hamiltonian in these states is readily obtained; to first order in $\boldsymbol{A}(\boldsymbol{r})$ it is:

$$\begin{aligned}
(n,\rho,\boldsymbol{k}|\mathcal{H}|n',\rho',\boldsymbol{k}') &= \epsilon_n \delta_{nn'} \delta_{\rho\rho'} (\boldsymbol{k}|\boldsymbol{k}') \\
&+ (1/mc) \boldsymbol{\Pi}_{n\rho,n'\rho'} \cdot (\boldsymbol{k}| -i\hbar c \nabla + e\boldsymbol{A}' + e\boldsymbol{A}_0|\boldsymbol{k}') \\
&+ (e/mc) \boldsymbol{\Pi}_{n\rho,n'\rho'} \cdot \sum_{\boldsymbol{K}\neq 0} \int d\boldsymbol{q} (n'\rho'|\boldsymbol{A}(\boldsymbol{K}+\boldsymbol{q}) \\
&\times \exp(i\boldsymbol{K} \cdot \boldsymbol{r})|n'\rho') \\
&\times (\boldsymbol{k}|\exp(i\boldsymbol{q} \cdot \boldsymbol{r})|\boldsymbol{k}') + \frac{e}{mc} \sum_{n'',\rho''} \int d\boldsymbol{k}'' \\
&\times \sum_{\boldsymbol{K}\neq 0} \int d\boldsymbol{q} (\boldsymbol{k}|\boldsymbol{\Pi}_{n\rho,n''\rho''} + \left(\frac{\hbar}{i}\nabla + \frac{e\boldsymbol{A}'}{c}\right) \delta_{nn''} \delta_{\rho\rho''} |\boldsymbol{k}'') \\
&\times (n''\rho''|\boldsymbol{A}(\boldsymbol{K}+\boldsymbol{q}) \exp[i\boldsymbol{K} \cdot \boldsymbol{r}]|n'\rho') \\
&\times (\boldsymbol{k}''|\exp(i\boldsymbol{q} \cdot \boldsymbol{r})|\boldsymbol{k}') \\
&+ \frac{1}{2mc^2} (\boldsymbol{k}|[-i\hbar c\nabla + e\boldsymbol{A}' + e\boldsymbol{A}_0]^2|\boldsymbol{k}'). \quad (3)
\end{aligned}$$

The $\boldsymbol{\Pi}_{n\rho,n'\rho'}$ are the matrix elements of the velocity operator v at $\boldsymbol{k}_0$ and the $|\boldsymbol{k})$ are plane-wave states. It is assumed that the crystal possesses a center of inversion symmetry so that there is spin-degeneracy throughout the zone and the matrix element $\boldsymbol{\Pi}_{n\rho;n\rho'}$ vanishes at $\boldsymbol{k}_0$. The integrations over $\boldsymbol{q}$ and $\boldsymbol{k}''$ are over the reduced zone; the $\boldsymbol{K}$s are reciprocal lattice vectors.

The reason for splitting $\boldsymbol{A}$ into $\boldsymbol{A}_0$ and $\boldsymbol{A}_s$ is apparent from (3): $\boldsymbol{A}_0$ having no interband matrix elements occurs only in the combination $\boldsymbol{A}'+\boldsymbol{A}_0$ and is the potential acting on the effective particle, the electron in band n. The interaction with $\boldsymbol{A}_0$ results in a field at the nucleus due to the mean, total orbital moment induced by the external field, i.e. the diamagnetic moment and the moment due to spin–orbit interaction. The terms involving $\boldsymbol{A}(\boldsymbol{k}+\boldsymbol{q})$ will contribute only for $q\to 0$; they represent the cell-periodic part of $\boldsymbol{A}$.

To first order in $\boldsymbol{A}$ and second order in $\boldsymbol{k}$ it is sufficient to eliminate by the transformation eS of L–K the interband terms of (3) which are independent of $\boldsymbol{A}$ and linear in $\boldsymbol{k}$. The matrix elements of S are:

$$S_{n\rho,n'\rho'} = -[1/mc(\epsilon_n-\epsilon_{n'})]\boldsymbol{\Pi}_{n\rho,n'\rho'}\cdot(\boldsymbol{k}|-i\hbar c\boldsymbol{\nabla}+eA'|\boldsymbol{k}').$$

The effective Hamiltonian thus obtained is:

$$(n\boldsymbol{k}|e^{-s}\mathscr{H}e^{s}|n\boldsymbol{k}') = \epsilon_n(\boldsymbol{k}|\boldsymbol{k}')+\sum_{\alpha\beta}\left\{\left[\frac{1}{2m}\delta_{\alpha\beta}+\frac{1}{2m^2}\sum_{n'\neq n}\frac{\Pi^{\alpha}_{nn'}\Pi^{\beta}_{n'n}+\Pi^{\beta}_{nn'}\Pi^{\alpha}_{n'n}}{E_n-E_{n'}}\right]\right.$$
$$\times\left(\boldsymbol{k}\left|\left[\frac{\hbar}{i}\nabla^{\alpha}+\frac{e(A'^{\alpha}+A_0^{\alpha})}{c}\right]\left[\frac{\hbar}{i}\nabla^{\beta}+\frac{e(A'^{\beta}+A_0^{\beta})}{c}\right]\right|\boldsymbol{k}'\right)$$
$$\left.+\frac{e\hbar}{2im^2c}\sum_{n'\neq n}\frac{\Pi^{\alpha}_{nn'}\Pi^{\beta}_{n'n}-\Pi^{\beta}_{nn'}\Pi^{\alpha}_{n'n}}{E_n-E_{n'}}(\boldsymbol{k}|\nabla^{\alpha}(A'^{\beta}+A_0^{\beta})|\boldsymbol{k}')\right\}$$
$$+\frac{e}{mc}\sum_{\alpha}\sum_{n'\neq n}\sum_{k\neq 0}\int d\boldsymbol{q}\,\Pi^{\alpha}_{nn'}A^{\alpha}(\boldsymbol{K}+\boldsymbol{q})(n'|\exp(i\boldsymbol{K}\cdot\boldsymbol{r})|n)(\boldsymbol{k}|\exp(i\boldsymbol{q}\cdot\boldsymbol{r})|\boldsymbol{k}')$$

+ terms in $A^{\alpha}(\boldsymbol{K}+\boldsymbol{q})$ of order k and k^2. (4)

In (4), the spin index ρ has been included in n, the α, β are Cartesian coordinates and the integration over $\boldsymbol{k}''$ has been performed. The first term on the right of (4) determines the zero of energy, the second term (in curly brackets) gives the motion of a free particle with an effective mass determined by the symmetric combination of $\Pi^{\alpha}_{nn'}$, $\Pi^{\beta}_{n'n}$ and a magnetic moment determined by the antisymmetric combination of the same. The only difference from free particle behavior is that instead of $\boldsymbol{A}$, the long-range part $\boldsymbol{A}_0$ only enters in the interaction. It will be seen that using $\boldsymbol{A}$ here instead of $\boldsymbol{A}_0$ would make no difference in the resulting Knight shift. We denote by $\mathscr{H}'_1$ the part of the second term that is first order in $\boldsymbol{A}_0$ and by $\mathscr{H}'_2$ the third term which contains the short-range part of $\boldsymbol{A}$. The terms of order k and k^2 are assumed to be small; they are in fact the first- and second-order terms in the expansion of $\boldsymbol{v}\cdot\boldsymbol{A}_s$ while $\mathscr{H}'_2$ is the zero-order term.

The orbital Knight shift for a sample in equilibrium is given by the trace of $\rho\times(\mathscr{H}'_1+\mathscr{H}'_2)$ where ρ is the density matrix. Consider $\mathscr{H}'_1$ first: it can be rewritten as

$$\mathscr{H}'_1 = (e/c)\boldsymbol{v}^*\cdot\boldsymbol{A}_0-\boldsymbol{\beta}^*\cdot\boldsymbol{\nabla}\times\boldsymbol{A}_0=\mathscr{H}'_{11}+\mathscr{H}'_{12} \quad (5)$$

where $\boldsymbol{v}^*$ and $\boldsymbol{\beta}^*$ are respectively the velocity and orbital magnetic moment. $\mathscr{H}'_{11}$ is the interaction of the nuclear moment with the orbital motion of an effective free particle. Since $\boldsymbol{A}_0$ depends on $\boldsymbol{r}$ alone it is convenient in taking the trace to use eigenstates of position, obtaining:

$$\langle\mathscr{H}'_{11}\rangle = \int(\boldsymbol{r}|(e/c)\boldsymbol{v}^*\rho|\boldsymbol{r})\cdot\boldsymbol{A}_0(\boldsymbol{r})\,d\boldsymbol{r}$$
$$= -(1/c)\int\langle\boldsymbol{j}(\boldsymbol{r})\rangle\cdot\boldsymbol{A}_0(\boldsymbol{r})\,d\boldsymbol{r} \quad (6)$$

where $\langle\boldsymbol{j}(\boldsymbol{r})\rangle$ is the statistical average of the current density at $\boldsymbol{r}$, due to the effective free particle of (4). In the presence of $\boldsymbol{H}$, $\langle\boldsymbol{j}(\boldsymbol{r})\rangle$ vanishes

Vol. 21
1961

in the interior of the sample, but does not vanish near the boundary.[6] The surface current $\langle \boldsymbol{j} \rangle_s$ must be such as to give rise to a magnetization $\boldsymbol{M} = \chi_d \boldsymbol{H}$ equal to the induced diamagnetic moment per unit volume and according to magnetostatics this is $\langle \boldsymbol{j} \rangle_s = c\boldsymbol{M} \times \boldsymbol{n}$ where $\boldsymbol{n}$ is the outer normal. Since for a point on the boundary, $\boldsymbol{A}_0(\boldsymbol{r}) \cong \boldsymbol{A}(\boldsymbol{r})$ the latter may be used and the field at the nucleus due to $\mathscr{H}'_{11}$ is then the same as that of a uniformly magnetized sample. This field is independent of the location of the nucleus in the sample only for ellipsoidal specimens and in the latter case it depends on the shape through the demagnetizing factors. Recently DAS and SONDHEIMER[7] have given a treatment of this effect but did not mention the shape dependence. In the absence of spin–orbit coupling $\mathscr{H}'_{11}$ gives the only contribution of orbital motion to the Knight shift at the bottom of a nondegenerate band. The magnetic field due to it is:

$$\Delta \boldsymbol{H}_d = (4\pi - \boldsymbol{D}) \cdot \boldsymbol{\chi}_d \cdot \boldsymbol{H} \tag{7}$$

where χ_d is the diamagnetic susceptibility tensor and D is the demagnetizing coefficients tensor.

The second term of (5), $\mathscr{H}'_{12}$, is the interaction with $\boldsymbol{A}_0$ of a free particle having a magnetic moment

$$\boldsymbol{\beta}^* = -\beta(n|\boldsymbol{X} \times \boldsymbol{\pi}|n)/\hbar$$

where

$$(n|\boldsymbol{X}|n') = \hbar(n|\boldsymbol{\pi}|n')/im(E_n - E_{n'}).$$

Since $\boldsymbol{X} \times \boldsymbol{\pi}$ changes sign under time reversal, its contribution to the trace is proportional to the excess population of one direction of spin and hence it is sufficient to use plane waves in taking the trace. When integrating over $\boldsymbol{r}$, the $\boldsymbol{\nabla} \times \boldsymbol{A}_0$ can be replaced by a surface term so that again it is permissible to use $\boldsymbol{A}$ instead of $\boldsymbol{A}_0$. The resulting field is that of a uniformly magnetized sample and is given by:

$$\Delta \boldsymbol{H}_P = (4\pi - \boldsymbol{D}) \cdot \boldsymbol{\chi}_P \cdot \boldsymbol{H}. \tag{8}$$

By using χ_P in (8) we have neglected the free-spin moment β versus β^*, which is consistent with $g \gg 2$. However, (8) gives correctly the total paramagnetic long-range contribution to ΔH as is easily seen by including the dipolar interaction with the electron spin. Equations (7) and (8) are of comparable magnitudes when $g \gg 2$ and of opposite signs.

It is illuminating to contrast (8) with (2) which gave the field due to the contact interaction, $-(n\boldsymbol{k}|\boldsymbol{\beta} \cdot \boldsymbol{\nabla} \times \boldsymbol{A}|n\boldsymbol{k})$. The difference is that for the contact interaction, $\boldsymbol{\beta} \cdot \boldsymbol{\nabla} \times \boldsymbol{A}$ is evaluated over the Bloch state $|n\boldsymbol{k})$ while $\boldsymbol{\beta}^* \cdot \boldsymbol{\nabla} \times \boldsymbol{A}$ is evaluated over a plane wave. Alternatively, (8) could be obtained by keeping only the part $-\boldsymbol{\beta}^* \cdot (\boldsymbol{\nabla} \times \boldsymbol{A})_{1.w.}$ that consists of the Fourier components with nearly zero wave vector and evaluating it over $|n\boldsymbol{k})$. The reason for keeping only the long-wave Fourier components can be understood in terms of a physical picture of electrons with large g factors, given by HERRING[8]: If one considers a wave packet formed from Bloch states in the vicinity of the energy minimum and having the same direction of spin, one finds that the packet has circulating currents. These are such that their magnetic moment is equal to β^* and is independent of the shape of the packet. Moreover since the energies of the states in the packet must be small compared to the smallest band gap, the minimum spatial expansion of the packet is of the order $\Delta X = |(n|X|n')|$, which is a large number of atomic distances when the gap is small. The large g factor is a consequence of the large value of ΔX which imposes a minimum size on the packet, and so is also the fact that only the long-wave part of $\boldsymbol{\nabla} \times \boldsymbol{A}$ can "feel" the g factor. The ratio

$$(n\boldsymbol{k}|(\boldsymbol{\nabla} \times \boldsymbol{A})_{1.w.}|n\boldsymbol{k})/(n\boldsymbol{k}|\boldsymbol{\nabla} \times \boldsymbol{A}|n\boldsymbol{k}) \text{ is } 1/\Omega|\psi(0)|^2$$

and this follows physically from the fact that the circulating currents having no singularity and being spread over a region large compared to the unit cell, the detailed nature of the wave function in the cell averages out when the contributions from all the current is integrated.

The term $\mathscr{H}'_2$ consists of the short-wave components of $\boldsymbol{\nabla} \times \boldsymbol{A}$. Its trace vanishes in absence of spin–orbit interaction (as with $\mathscr{H}'_{12}$) so that in lowest order in k, its contribution is proportional to $\chi_P \boldsymbol{H}$ and plane waves can again be used in taking the trace. The resulting field at the nucleus is the trace of the cell periodic part of

$$(-e/mc)(\boldsymbol{r} \times \boldsymbol{v}/r^3).$$

In the limit of infinite lattice distance this becomes the orbital part of the atomic hyperfine interaction. Since the value of the wave-function near the nucleus is important in determining the size of the

matrix element, the magnitude of the contribution from $\mathscr{H}'_2$ can be estimated from the value of the orbital interaction in the free atom. In addition, the non-contact part of the interaction with the electron spin magnetic moment gives a short-range contribution of the same order as that of $\mathscr{H}'_2$ and since treatments of these questions have been given,[2, 9] nothing further will be added. Their order of magnitude for a p state in the free atom is[9] from $\frac{1}{12}$ to $\frac{1}{5}$ of the contact part from an s state of the same shell.

A substance for which the field due to the orbital currents might be among the largest is bismuth. The calculation just made is not directly applicable to bismuth because the Fermi energy is of the same order of magnitude as the band gap.[10] Nevertheless, the following argument shows that quite generally, the field resulting from the orbital motion is the sum of a long-range part given by the susceptibility and a short-range part due to the cell periodic currents:

The orbital part of the hyperfine interaction is given by:

$$\text{trace}\quad (-1/c)\int \langle \boldsymbol{j}(\boldsymbol{r})\rangle \boldsymbol{A}(\boldsymbol{r})\, d\boldsymbol{r}.$$

We define the magnetic moment density $\boldsymbol{M}(\boldsymbol{r})$ by the two equations:

$$c\boldsymbol{\nabla}\times\boldsymbol{M}(\boldsymbol{r}) = \langle \boldsymbol{j}(\boldsymbol{r})\rangle \text{ and } \boldsymbol{\nabla}\cdot\boldsymbol{M}(\boldsymbol{r}) = 0$$

with the added condition that $\boldsymbol{M}$ vanishes far outside the sample. By a partial integration the interaction is also given by

$$-\text{trace}\int \boldsymbol{M}(\boldsymbol{r})\cdot\boldsymbol{\nabla}\times\boldsymbol{A}(\boldsymbol{r})\, d\boldsymbol{r}.$$

Now for an infinite solid the Hamiltonian is invariant under translation by a lattice vector followed by a gauge transformation, so that $\langle \boldsymbol{j}(\boldsymbol{r})\rangle$ has the same periodicity as the lattice. Therefore $\boldsymbol{M}(\boldsymbol{r})$ is the sum of a part which is essentially constant within the sample, and a part which has the lattice periodicity. The first contributes only with the long-range part of $\boldsymbol{A}$ and gives the field

$$\boldsymbol{\Delta H} = (4\pi - D)\chi\boldsymbol{H}$$

where χ is the total susceptibility (neglecting the spin moment); the second contributes with the short-range part of $\boldsymbol{A}$.

We now estimate the ratio of the hyperfine interaction that is due to the large g factor, to the contact interaction in bismuth. Consider the contribution from the electrons in one of the six conduction valleys, and assume the magnetic field to be along the direction of the principal axis of the g tensor for which $g \simeq 200$. The spin effective mass is close to the orbital effective mass and for a spherical sample the ratio of (7) and (8) to (2) is:

$$\frac{\Delta H_d + \Delta H_P}{\Delta H_c} = \frac{g}{3}\times\frac{1}{\Omega|\psi(0)|^2} \qquad (9)$$

For atomic bismuth in an s state $|\psi(0)|^2$ can be estimated from the value of the field at the nucleus in Bi^V given by KOPFERMANN[9]: $\bar{H}(0) = 6{\cdot}5\times10^7$ G. Using a correction,[12] $\bar{H}(0)$ in neutral bismuth is found to be about twelve times smaller leading to $|\psi_a(0)|^2 = 6{\cdot}5\times10^{25}\,\text{cm}^{-3}$. The value of Ω is $35{\cdot}5\times10^{-24}\,\text{cm}^3$ and the ratio (9) becomes 1/30 for a wave function of pure s character. Inclusion of all the valleys may lower this number by a factor of 2. However, a tight-binding calculation[13] suggests that s–p overlap is small and the wave function might be predominantly of p character. Using estimates[9] of the field at the nucleus due to p states, the shape-independent field due to $\mathscr{H}_2$ might be more than six times smaller than ΔH_c in which case the shape-dependent part due to $\mathscr{H}'_1$ may amount to 20 per cent of the total Knight shift which could be observable. The experiment was tried by HEBEL and SHULMAN[14]; they found a broad (of the order of 80 G) nuclear resonance line which saturated very easily, indicating $T_2 \ll T_1$ and no Knight shift measurement could be deduced.

Acknowledgements—The author wishes to thank L. C. HEBEL for stimulating conversations which initiated this work, C. HERRING for a communication of his unpublished treatment of the orbital magnetic moment and for useful comments on the manuscript, and E. I. BLOUNT for a helpful discussion.

REFERENCES

1. COHEN M. H. and BLOUNT E. I., *Phil. Mag.* **5,** 115 (1960); SMITH G. E., GALT J. K. and MERRITT F. R., *Phys. Rev. Letters* **11,** 276 (1960); ROTH L. M., LAX B. and ZWERDLING S., *Phys. Rev.* **114,** 90 (1959).
2. KORRINGA J., *Physica* **16,** 601 (1950).

3. TOWNES C. H., HERRING C. and KNIGHT W. D., *Phys. Rev.* **77,** 852 (1950).
4. Expression (2) for ΔH_c has been given previously by BLUMBERG W. E. and EISINGER J., *Phys. Rev.* **120,** 1965 (1960).
5. LUTTINGER J. M. and KOHN W., *Phys. Rev.* **97,** 869 (1955).
6. TELLER E., *Z. Phys.* **67,** 311 (1931).
7. DAS T. P. and SONDHEIMER E. H., *Phil. Mag.* **5,** 529 (1960). The author is indebted to C. HERRING for showing him this manuscript.
8. HERRING C., unpublished work.
9. KOPFERMANN H., *Nuclear Moments.* Academic Press, New York (1958).
10. BOYLE W. S. and RODGERS K. F., *Phys. Rev. Letters* **2,** 338 (1959).
11. GALT J. K., YAGER W. A., MERRITT F. R., CETLIN B. B. and BRAILSFORD A. D., *Phys. Rev.* **114,** 1396 (1959).
12. KNIGHT W. D., *Solid State Physics* Vol. II, p. 121, (Edited by SEITZ F. and TURNBULL D.), Academic Press, New York (1956).
13. MASE S., *J. Phys. Soc. Japan* **13,** 434 (1958).
14. HEBEL L. C., private communication.

Vol. 2
196

J. Phys. Chem. Solids Pergamon Press 1961. Vol. 21, Nos. 1/2, pp. 105–109. Printed in Great Britain.

SPACE CHARGE EFFECTS IN AMBIPOLAR DIFFUSION OF CARRIERS INDUCED BY ELECTRON BOMBARDMENT IN PHOTOCONDUCTING INSULATOR CRYSTALS

GY. GERGELY

Research Institute for Telecommunications, Budapest

(*Received* 7 *April* 1961)

Abstract—In a recent paper[1] a simplified model was proposed and an analysis of electron bombardment induced processes was given. The analysis considered only one type of carriers, neglecting space charge effects. It was shown that the dead voltage in cathodoluminescence and induced conductivity is related to the diffusion length of the induced carriers. The present paper being a continuation of the above, deals with a more elaborate model. An analysis of the ambipolar diffusion of induced carriers will be presented and some space charge effects will also be considered.

Vol. 21
1961

THE TWO-CENTER MODEL

THE ANALYSIS is restricted to photoconducting insulator crystals, containing two types of levels in the forbidden band: A centers having different capture cross-sections for electrons and holes, acting as hole traps; and H centers, acting as deep electron traps. These properties are characteristic for photoconductors and phosphors of the ZnS and CdS type. They are n-type crystals.

The model used is similar to that employed by SCHÖN[2] and KLASENS[3]. The steady state conductivity and luminescence excited by cathode rays can be calculated by solving the fundamental system of equations described by SCHÖN and RITTNER[4]. To facilitate calculations, some simplifying assumptions used in the preceding paper[1] will be applied in the analysis; such as:

(1) One dimensional plane geometry.
(2) Semi-infinite, homogeneous crystal.
(3) Validity of the Young–Feldman formula[1,5,6] for the energy dissipation of incident cathode rays.
(4) Neglect of thermal ejection of trapped carriers from A and H centers.

The rigorous solution of the fundamental equations is a hopeless task; in practice, however, a successive approximation may be used.

ANALYSIS UNDER NEUTRALITY CONDITION

In the analysis, the following symbols will be used:

$g(x)$ = The excitation density (electron–hole pairs generated $cm^{-3}\,sec^{-1}$).
n = Density of free electrons.
p = Density of free holes, $p \ll n$.
H = Density of H centers.
H^- = Density of electrons trapped in H centers.
A = Density of A centers.
A^+ = Density of holes captured by A centers.
α_{CA} = Capture coefficient of A^+ centers for free electrons, $\alpha_{CA} = 10^{-12}\ cm^3\,sec^{-1}$.
μ_n = Mobility of electrons.
μ_p = Mobility of holes, $\mu_p < \mu_n$.
D_p = Diffusion coefficient of holes.
e = The electronic charge.
ϵ = The dielectric constant.
ρ = Density of space charge.
τ_n = Lifetime of free electrons.
τ_p = Lifetime of free holes, $\tau_p \ll \tau_n$.
L_n = Diffusion length of electrons.
L_p = Diffusion length of holes.
S = Surface recombination velocity of holes.
ΔE = The work done to create an electron–hole pair.
i_0 = The bombarding beam current density.
V = The energy of bombarding electrons.
P_0 = $i_0 V$ the incident beam power.
R = Range of incident electrons.
$\sigma(V)$ = Induced conductivity for accelerating voltage V.

The distribution and transitions of electrons and holes between the electronic states in the

crystal are determined by the location, density, capture coefficients of A and H centers and by $g(x)$. The analysis is restricted to good phosphors and good photoconductors under medium energy (1–50 kV) and moderate beam current density ($< 2\ \mu A/cm^2$) excitation conditions.

As first step of approximation, the method of KLASENS[3] was used, neglecting diffusion and space charge effects. Under the above excitation conditions good phosphors can be characterized by code number 122122, good photoconductors either by 121222 or by 221222, according to KLASENS. In view of these processes the lifetime of free holes may be assumed as constant. It is allowed to do so for both types of hole recombination via A centers and via H centers, respectively. For good phosphors and photoconductors the density of free electrons may be given by relations:

$$n = a_1 p = \frac{\tau_n}{\tau_p} p \text{(monomolecular recombination)} \tag{1a}$$

$$n = a_2 \sqrt{p} \text{ (bimolecular recombination)} \tag{1b}$$

The conditions (1a), (1b) and τ_p = constant may be applied for certain special cases of the ROSE–BUBE model[7,8] too.

The second step of successive approximation involved the consideration of carrier diffusion but under neutrality condition. The distribution of holes can be calculated by an ambipolar diffusion equation derived from the fundamental equation. As shown by AUTH[9] for zero current density in the crystal:

$$0 = g(x) - \frac{p}{\tau_p} + D_p \frac{d^2p}{dx^2} - \mu_p \frac{D_p - s(p) D_n}{p[r(p)\mu_n + \mu_p]} \left(\frac{dp}{dx}\right)^2 - \frac{4\pi}{\epsilon} \mu_p p \rho \tag{2}$$

with the notations:

$$r(p) = \frac{n(p)}{p} \quad \text{and} \quad s(p) = \frac{dn(p)}{dp}$$

For $\rho = 0$ and cases (1a) and (1b) it is

$$0 = g(x) - \frac{p}{\tau_p} + 2D_p \frac{d^2p}{dx^2} \tag{3a}$$

and

$$0 = g(x) - \frac{p}{\tau_p} + \frac{3}{2} D_p \frac{d^2p}{dx^2} - \frac{3}{4} \frac{\mu_p}{\mu_n} D_p \frac{1}{a_2 \sqrt{p}} \left(\frac{dp}{dx}\right)^2 \tag{3b}$$

For n-type crystals $p/n \ll 1$, the quadratic term in equation (3b) can be neglected. The excitation density is given[1,5,6] by:

$$g(x) = \frac{P_0}{\Delta E R} \quad \text{for } 0 < x < R \tag{4a}$$

and

$$g(x) = 0 \quad \text{for } x > R \tag{4b}$$

with

$$R = K V^b \tag{4c}$$

K and b being material constants.

Solving equations (3a) and (3b) the boundary conditions are given by surface recombination and by the continuity of p.[1,4,10] In the excitation domain $0 < x < R$ the solution is given by:

$$p_1(x) = \frac{P_0 \tau_p}{\Delta E R 2 \exp(R/L_p)} \times \left\{ -\exp\frac{x}{L_p} + \left(2Q - 1 - 2Q \exp\frac{R}{L_p}\right) \times \exp\left(-\frac{x}{L_p}\right)\right\} + \frac{P_0 \tau_p}{\Delta E R} \tag{5}$$

For $x > R$ the solution takes the form:

$$p_2(x) = \frac{P_0 \tau_p}{\Delta E R 2 \exp(R/L_p)} \times \left\{ \exp\frac{2R}{L_p} + 2Q - 1 - 2Q \exp\frac{R}{L_p}\right\} \times \exp\left(-\frac{x}{L_p}\right) \tag{6}$$

with the notation:

$$Q = \frac{S}{(D_p/L_p) + S}$$

In equation (5), L_p denotes the diffusion length of holes. Its value depends on the type of recombination and on the electron/hole density relationship. For the case of monomolecular recombination (case 1a):

$$L_p = \sqrt{(2D_p\tau_p)} \tag{7a}$$

For the case of bimolecular recombinations (case 1b):

$$L_p = \sqrt{(\tfrac{3}{2}D_p\tau_p)} \tag{7b}$$

according to the solution of equations (3a) or (3b) respectively.

The distribution of electrons can be calculated by making use of equations (5), (6) and (1a) or (1b) respectively. The diffusion length of the majority carriers is given by[9] the following expressions:

(a) For monomolecular recombination:

$$L_n = L_p \tag{8a}$$

(b) For the case of bimolecular recombination:

$$L_n = 2L_p \tag{8b}$$

The neutrality approximation involves the assumption of a constant electric field within the crystal. This is hardly possible under the excitation conditions expressed by equations (4a–c) and it is inconsistent with the continuity condition.[11]

CONSIDERATION OF SPACE CHARGE EFFECTS

For incident electrons exhibiting $R \gg L_p$, in the excitation layer ($x < R$) $n_1(x)$ and $p_1(x)$ can be calculated by the approximate formulae of KLASENS[2]; in the diffusion tail ($x > R$), however, the electron and hole density is strongly decreasing, and H traps will be filled with electrons developing a space charge layer.[22] The build-up of a negative space charge layer is the consequence of $n \gg p$, $\mu_n > \mu_p$ and $\tau_n \gg \tau_p$ in ZnS type crystals and space charge accumulated in traps plays an important role in ambipolar diffusion of induced carriers.

As the third step of successive approximation, space charge effects in the excitation layer ($x < R$) have been neglected for $x > R$, however, the space charge term in equation (2), was considered. Assuming a ρ = constant negative space charge and for case (1a) of monomolecular recombination and the density of electrons being proportional to that of holes:

$$0 = -\frac{p}{D_p\tau_p} + \frac{d^2p}{dx^2} + \frac{1}{p}\left(\frac{dp}{dx}\right)^2 + \frac{p}{L_D} \tag{9}$$

where L_D is the Debye length associated with ρ

$$L_D = \sqrt{\frac{\epsilon kT}{4\pi e\rho}} \tag{10}$$

In practice, negative space charge is produced by electrons trapped in H centers, $\rho = -eH^-$. For $x \gg R$:

$$p_2(x) = \text{const. exp} - \left(\frac{x}{L_{\text{eff}}}\right) \tag{11}$$

$$L_{\text{eff}} = \sqrt{(2D_p\tau_p)}\frac{L_D}{\sqrt{(L_D^2 - D_p\tau_p)}} \tag{12a}$$

Let us now consider two extreme cases:

(1) Quasi-neutrality: $\rho \cong 0$, $L_D \gg L_p$. Then

$$L_{\text{eff}} = L_p$$

(2) The highest possible space charge is produced by filled traps with $H^- = H$, $H^- \gg A^+$ and n. In this case L_{eff} is given by equation (12a) and for appropriate ρ, a long diffusion tail can be developed.

The effective ambipolar diffusion length is a result of the negative space charge attracting holes and retarding electrons, preventing them reaching traps located deeper in the bulk. For zero current density in the crystal, the diffusion current of electrons has to be balanced by the action of negative space charge:

$$D_n\frac{dn}{dx} = \mu_n n\frac{4\pi}{\epsilon}\int_x^\infty \rho\, dx \tag{13}$$

Using equation (11) for the distribution of electrons in the diffusion tail and supposing a uniform space charge layer of thickness L_ρ

$$L\rho = \frac{L_D^2}{L_{\text{eff}}} \tag{14}$$

With equation (13) and (14) a rough estimation of L_ρ can be given. Taking the reasonable values

$L_{\text{eff}} = 1000$ Å, $H = 10^{15}\,\text{cm}^{-3}$, $L_D = 1070$ Å, $L_\rho = 1140$ Å. These values are in good agreement with experiments.[1,12,13] The crystal as a whole is neutral, thus the negative space charge layer has to be compensated. Two possible forms of space charge distribution will be mentioned:

(1) The negative space charge layer is suppressing the free electron density and enhancing the free hole density. Under equilibrium conditions:

$$A^+ = \frac{p}{\alpha_{CA}\tau_p n} \tag{15a}$$

In the neighbourhood of the negative (H^-) layer, a positive (A^+) layer is built up, forming a double layer. Outside of this double layer, the neutrality condition is fulfilled and the electric field strength is zero.

(2) The crystal surface contains a high density of acceptor states and a positive layer is built up in the surface layer. Its effect is manifested in the apparent value of surface recombination velocity. GROSCHWITZ[14] and BIR[15] have found such space charge layers on semiconductors.

Otherwise the space charge distribution of type (1) does not exclude the possibility of a surface space charge (double) layer.

The build-up of a double layer leads to polarization, this was observed by some authors.[16,17]

SOME EXPERIMENTAL ASPECTS

Finally, mention should be made of some experimental aspects. The study of diffusion phenomena in crystals excited by electrons was pursued by two experimental methods.

(1) Studying the voltage response of induced conductivity and cathodoluminescence.[1]
(2) Analysing the build-up of cathodoluminescence.[12]

Other possible methods are offered by the techniques used in photoconductivity experiments.[9,13,18]

The voltage dependence of cathodoluminescence was calculated in the preceding paper.[1] The formula derived under neutrality condition is in very good agreement with experiments. This is due to the fact that luminescence is mainly determined by surface recombination losses and it is little affected by space charge effects in the bulk. The value $L_p = 1130$ Å determined from the dead voltage, is the diffusion length of holes drifting towards the crystal surface. L_p is given by equation (7b). Taking $\tau_p = 4{\cdot}4 \times 10^{-10}$ sec we get $\mu_p = 7{\cdot}5\ \text{cm}^2\,\text{V}^{-1}\,\text{sec}^{-1}$ and $S = 4 \times 10^4\ \text{cm sec}^{-1}$, for a ZnS sample.

Comparing this value of L_p with the radius of excitation channel in ZnS (1800 Å) as found by KALLMANN[12], the agreement is remarkable, the latter being identical with $L_n = 2L_p$. A similar value was found by DIEMER[13] with photoelectromagnetic experiments. These experimental observations confirm the adequacy of the model used.

The induced conductivity can be calculated for weak transversal electric fields and large crystals neglecting carrier exhaustion and recombination on the contacts.[4] For cases (1a) and (1b)

$$\sigma(V) = e\mu_n\tau_n\frac{P_0}{\Delta E}\left\{1 - QL_p\frac{1-\exp-(KV^b/L_p)}{KV^b}\right\} \tag{15b}$$

$$\sigma(V) = e\mu_n a_2 \int_0^\infty \sqrt{(p(x))}\,dx \tag{15c}$$

The run of (15b) is linear. Equation (15c) gives $\sigma(V) \sim \sqrt{V}$ for higher voltages. In practice both types occur, the linear voltage relationship was observed by BLEIL[19], the saturating type by LAPPE[20] on CdS crystals. Long range carrier diffusion for photon excitation was observed on CdS crystals by AUTH[9], DIEMER[13] and BROPHY[21].

SUMMARY

An analysis is given of the ambipolar diffusion of carriers induced by electron bombardment. Induced conductivity and cathodoluminescence in ZnS and CdS crystals are discussed. The distribution of carriers is calculated, considering diffusion, surface recombination and space charge effects. The effective ambipolar diffusion length is a result of negative space charge accumulated in traps, attracting holes and retarding electrons, preventing them reaching traps located deeper in the bulk and balancing the diffusion current. The negative space charge layer has to be compensated

Vol. 196

by a positive layer. Formulae are derived for linear and saturating type induced processes. Comparing the theoretical and experimental voltage response curves of cathodoluminescence and induced conductivity, the diffusion length L_p and surface recombination velocity S of holes can be determined. $L_p = 0{\cdot}1\,\mu$, $S = 4 \times 10^4$ cm sec^{-1}, were found on a ZnS–AgCl sample.

Acknowledgement—The author is indebted to Dr. Z. Bodó for valuable discussions.

REFERENCES

1. Gergely Gy., *J. Phys. Chem. Solids* **17,** 112 (1960).
2. Schön M., *Physica* **20,** 930 (1954).
3. Klasens H. A., *J. Phys. Chem. Solids* **7,** 175 (1958).
4. Rittner E., *Proceedings of the Conference on Photoconductivity, Atlantic City*, p. 215. John Wiley, New York (1955).
5. Young J. R., *J. Appl. Phys.* **28,** 524 (1957).
6. Feldman C., *Phys. Rev.* **117,** 455 (1960).
7. Rose A., *Phys. Rev.* **97,** 322 (1955).
8. Bube R. H., *J. Phys. Chem. Solids* **1,** 234 (1957).
9. Auth J. and Ridder R., *Ann. Phys., Leipzig* **20,** 210 (1957); **2,** 351 (1959).
10. DeVore H. B., *Phys. Rev.* **102,** 86 (1956).
11. Bodo Z., *Acta Phys. Acad. Sci. Hung.* **11,** 1 (1960).
12. Kallmann H. and Dresner J., *Phys. Rev.* **114,** 71 (1959).
13. Diemer G. and Hoogenstraaten W., *J. Phys. Chem. Solids* **2,** 119 (1957).
14. Groschwitz E., *Solid State Physics in Electronics and Telecommunication Conference, Bruxelles*, (1958). Vol. I. p. 575. Academic Press, (1959).
15. Bir L. G., *Soviet Phys. Solid State* **1,** 62 (1956).
16. Ben Sira M. Y., Pratt B., Harnik E. and Many A., *Phys. Rev.* **115,** 554 (1959).
17. Kallmann H. and Rosenberg B., *Phys. Rev.* **97,** 1596 (1955).
18. Broser I. and Broser-Warminsky R., *J. Phys. Chem. Solids* **6,** 386 (1958).
19. Bleil C. E., Snyder D. D. and Sihvonen Y. T., *Phys. Rev.* **111,** 1522 (1958).
20. Lappe F., *Z. Phys.* **164,** 267 (1959).
21. Brophy J. J., *Phys. Rev.* **119,** 591 (1960).
22. Newton R. R., *Phys. Rev.* **75,** 234 (1949).

Vol. 21
1961

J. Phys. Chem. Solids Pergamon Press 1961. Vol. 21, Nos. 1/2, pp. 110–114. Printed in Great Britain.

CARRIER MOBILITY AND CHARGE TRANSPORT IN MONOCLINIC Se CRYSTALS

W. E. SPEAR

Physics Department, University of Leicester, Leicester, England

(*Received* 22 *May* 1961)

Abstract—Crystals of α-monoclinic Se (Se_8 ring structure) have been grown from solution by a circulation method, and their electrical properties studied. In the experiments a 10 mμ sec pulse of 40 keV electrons produced free carriers near the top electrode, and generated electrons or holes could be drawn across the specimen in a pulsed applied field. Transit time measurements led to an electron mobility $\mu \simeq 2\,cm^2\,V^{-1}\,sec^{-1}$ at 21°C. At temperatures above 0°C, $\mu \propto T^{-3/2}$ for all specimens. With decreasing T a sharp transition takes place from the lattice mobility to a charge transport controlled by a level of states $\epsilon = 0{\cdot}25$eV below the conduction band. A comparison of experimental and calculated μ vs. T curves leads to a density of centres $N_t \simeq 10^{14}\,cm^{-3}$. The same value of ϵ was found in similar experiments on vitreous Se (chain molecules) suggesting that this type of centre is common to both forms. The hole mobility in monoclinic Se is found to be trap controlled throughout the temperature range investigated.

1. INTRODUCTION

THE STUDY of the electrical properties of the Se allotropes allows a comparison between the charge transport in a chain and a ring structure of the same element. In contrast to the hexagonal and vitreous modifications the monoclinic form of Se consists of a lattice of puckered Se_8 rings.[1,2] An α- and β-monoclinic form have been distinguished but there appears to be little structural difference between them.[3] Photoconductivity in these crystals was first investigated by GUDDEN and POHL[4] and recently a detailed investigation of the optical properties has been carried out by PROSSER[5]. Virtually nothing is known about the electrical properties of monoclinic Se.

This paper describes an investigation of the carrier mobility and the conduction mechanism using an electron pulse method developed for the study of wide gap semiconductors.[6] Since similar experiments have been carried out on the vitreous form[7] which consists of Se chain molecules, a comparison of the charge transport in the two forms can be made.

An interesting feature of the present experiments is the transition from the lattice mobility to a charge transport controlled by a level of discrete states. A similar behaviour has been observed by BROWN and KOBAYASHI[8] in AgCl crystals.

2. SPECIMEN PREPARATION

The growing of crystals of sufficient size and perfection presents one of the main problems. The circulating method originally used by KYROPOULOS[9] was tried under various experimental conditions but the crystals were imperfect and too small. An improved method due to PROSSER[5] led to far better results.

The solvent, re-distilled CS_2, is boiled in a flask fitted at its side with a water-cooled circulation tube. The condensed vapour passes into a Soxhlet Extractor and drips through a filter funnel filled with precipitated red Se powder. In this way the solvent is gradually saturated with Se and red monoclinic crystals begin to form in the circulation tube. The advantage over the Kyropoulos method lies in the fact that the solvent remains completely free from small particles of Se powder which previously appeared to form nucleation centres and led to a large number of small crystals.

With this method up to twenty crystal plates

Vol. 21
1961

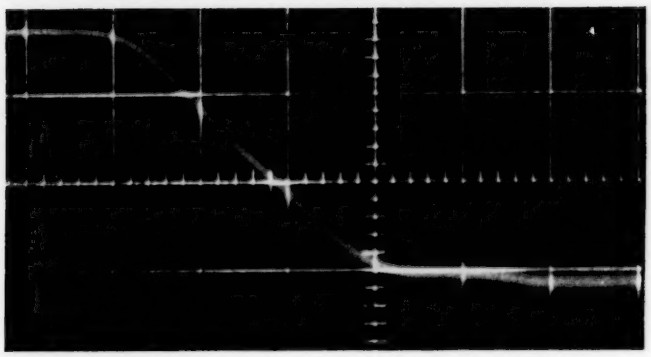

FIG. 1. Observed oscilloscope trace showing the transit of about 10^6 electrons generated at $t = 0$ by a short excitation pulse. Time scale: 1 cm $\equiv$ 20 mμ sec.

facing p. 110

BLANK
PAGE

Vol. 2
196

40–70 μ thick, and measuring $2\frac{1}{2}$–3 mm across, could normally be obtained in a run lasting about 20 hr. An X-ray examination* of a number of crystals led to lattice parameters in close agreement with those of the α-monoclinic form. According to the structure determined by BURBANK[2] the (101) plane coincides with the surface of the crystal plates; the average planes containing the puckered Se rings are almost perpendicular to the surface. Microscopic examination showed pronounced surface steps and striations on many of the crystals. A number of specimens with little or no surface structure were selected and fitted with evaporated gold electrodes of 1–2 mm^2 area on opposite sides of the crystal plate. Thin connecting wires were attached with silver paste. The specimen was mounted in a vacuum chamber designed for temperature measurements. The bottom electrode was connected directly to the input of a cathode follower which formed part of the specimen holder.

Vol. 21
1961

3. EXPERIMENTAL METHOD AND PROCEDURE

As this has been described in a previous publication[6] only a brief outline will be given here.

A pulse of 40 keV electrons and less than 10 mμsec duration enters the top electrode of the specimen and generates electron–hole pairs to within a depth of a few microns below the electrode. About 2 msec before the arrival of the excitation pulse a pulsed electric field is applied across the specimen for a few milliseconds and, depending on its polarity, either electrons or holes are drawn out of the surface region and drift across the specimen. The charge displacement is integrated and displayed on wide band electronic equipment. During application of the field pulse the input is gated to prevent paralysis of the sensitive amplifying system.

Figure 1 shows a photograph of the oscilloscope trace when generated electrons are drawn across a crystal in an applied field of $4{\cdot}5 \times 10^4$ V cm^{-1} at room temperature. The linear edge of the pulse implies a uniform drift velocity of the carriers indicating that (a) the internal field is uniform, and (b) the number of electrons per pulse leaving the recombination region near the top electrode remains constant during transit. The sharp levelling off of the trace marks the arrival of the generated electrons at the bottom electrode and defines a transit time t_t, in this case 60 mμ sec. The pulse height corresponds to the transit of about 10^6 carriers produced at $t = 0$ by the short excitation pulse of $2{\cdot}5 \times 10^4$ electrons (not resolved in Fig. 1).

The experimental procedure consisted in measuring t_t as a function of the applied field E which ranged from about 5×10^3 to 7×10^4 V cm^{-1}. The graph of $1/t_t$ against E was found to be linear except for a small range of values at low applied fields. As explained previously,[6] this is most likely due to space charge build-up in the surface region. A value for the mobility $\mu = d/Et_t$ where d denotes the specimen thickness, was obtained from the gradient of the graph.

Experiments on these and other insulating crystals have shown that the use of a pulsed applied field largely prevents the gradual build-up of a volume space charge which leads to a non-uniform internal field. This effect seems to be connected with the filling of deeper trapping centres which possess a release time far longer than t_t.

4. EXPERIMENTAL RESULTS

The twelve specimens investigated were selected partly from a number of batches grown in this laboratory and partly from crystals supplied by Dr. PROSSER of Prague University. They all showed the same general behaviour. At room temperature the electron mobilities were found to lie between 1·7 and 2·3 cm^2 sec^{-1} V^{-1}. On a given specimen the values of t_t were reproducible to within a few per cent; the main error in μ arose from the difficulty of measuring the thickness of the fragile crystals to a comparable accuracy. In the following the mobilities have therefore been normalized to the value μ_r at room temperature T_r, to facilitate the correlation of results from different specimens.

The experimental points in Fig. 2 show the temperature dependence of μ/μ_r for three specimens typical of the crystals investigated. The continuous lines were calculated from equation (3) of Section 5. Above 0°C the mobility of all the specimens was proportional to $T^{-3/2}$ which

* Carried out by Dr. M. EHRENBERG of University College, London.

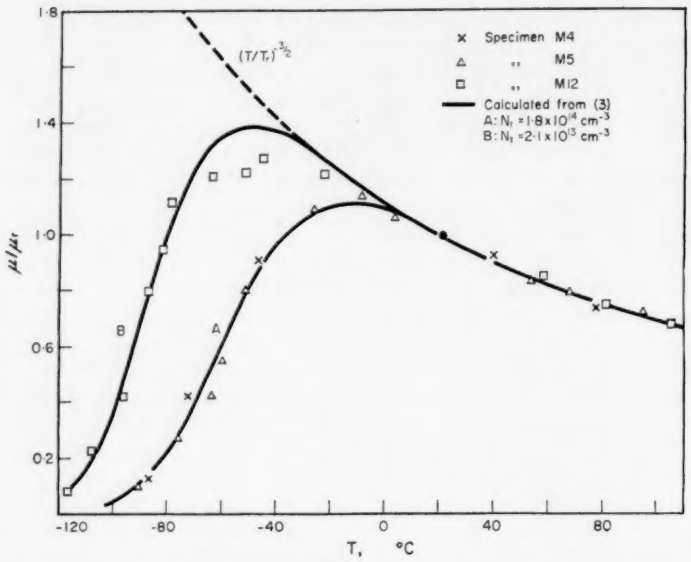

FIG. 2. Graph of the measured mobility μ, normalized to the room temperature value μ_r, against temperature. The continuous lines were calculated from equation (3), Section 5.

would be expected in a non-polar crystal from the interaction of the generated electrons with the lattice vibrations.[10] As the temperature is lowered, however, μ/μ_r goes through a maximum and then decreases sharply. In Fig. 3 the same experimental data have been plotted on a semi-logarithmic graph against $10^3/T$. It shows fairly convincingly that with decreasing temperature the mobility–temperature dependence goes over into a relation of the form $\mu \propto \exp(-\epsilon/kT)$ with $\epsilon = 0{\cdot}25$ eV. It is of interest to compare these results with the electron mobility in the vitreous form.[7] As can be seen from Fig. 3 this shows an exponential dependence throughout the temperature range which is associated with practically the same value of ϵ.

At temperatures in the region of the mobility maximum and below, it is observed that the levelling off of the pulse becomes less sharp than is shown in Fig. 1. The initial part of the pulse, however, retains its linearity and the more gradual rounding off affects at most the final 30 per cent of the pulse length. It appears, therefore, that the generated electron cloud spreads out during transit. As diffusion is an unlikely explanation this straggling in the arrival times is almost certainly connected with trapping in a level of centres with release times which are short, but not negligibly so, in comparison with t_t. The mechanism of trap controlled charge transport will be discussed further in Section 5. In presence of the straggling of transit times it appeared reasonable to use an average value of t_t defined by the point of intersection of the linear portion with the final horizontal level.

The charge gain, i.e. the number of electrons drawn out of the surface region per incident electron, has been determined for a number of specimens at $E = 3 \times 10^4$ V cm^{-1} and is found to be about 40. It is about $\frac{1}{4}$ of that observed for vitreous specimens under identical conditions.

When the field across the specimen is reversed a positive signal is observed corresponding to the drift of generated holes. This has been investigated for a number of specimens with the following results:

(a) At room temperature and below there exists a marked difference in the height of the electron and hole signals. For example, at room temperature and $E \sim 10^4$ V cm^{-1} the positive signal is only $\frac{1}{5}$ of the electron amplitude and increases to about $\frac{1}{2}$ at maximum E. This fact, together with the observed pulse shape, indicates that deep trapping occurs during transit. Above 50°C, however, the ratio of the amplitudes approaches unity at the higher fields and the pulse possesses a linear edge as in the case of electrons. Transit time measurements could be carried out in this temperature range.

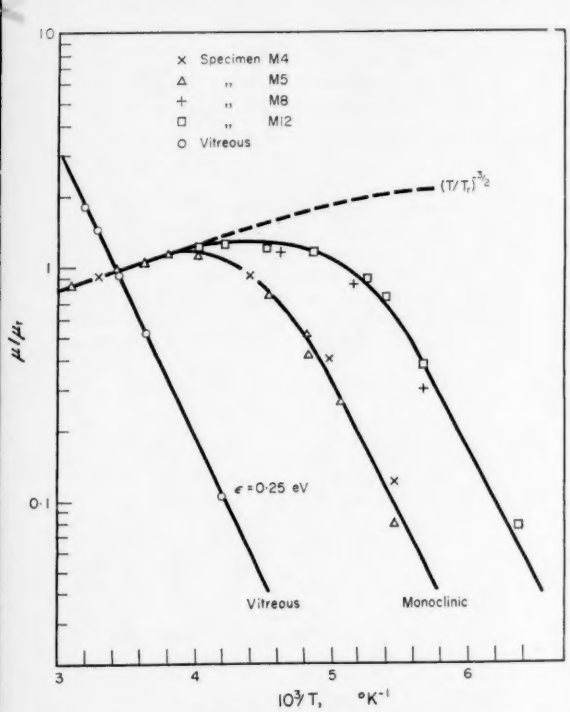

FIG. 3. Semi-logarithmic plot of μ/μ_r against $10^3/T$ for monoclinic and vitreous Se specimens.

(b) The measured hole mobility increases with T up to the highest temperatures used. At 105°C $\mu_h = 1{\cdot}3$ cm^2 V^{-1} sec^{-1}; it is then nearly equal to the lattice controlled electron mobility at that temperature. Because of the limited temperature range that could be investigated, these results are less conclusive than those for the electron mobility. Above 50°C the experimental values could be fitted approximately to a relation of the form $\mu_h \propto \exp(-\epsilon/kT)$ with $\epsilon \sim 0{\cdot}3$ eV.

5. DISCUSSION

The rapid decrease of the electron mobility shown in Fig. 2 is of interest because it suggests a change in the mechanism of charge transport. Normally the decrease in carrier mobility at low temperatures is connected with the transition from lattice to impurity scattering.[11] The latter varies approximately as $T^{3/2}$ and leads to a far shallower mobility maximum.[12] Impurity scattering can obviously not explain the rapid decrease of μ within a comparatively small temperature range. The experimental temperature dependence at lower T suggests that the observations are connected with the transition from a mobility determined by lattice scattering to one controlled by a fairly narrow level of states of density N_t, ϵ eV below the conduction band. With decreasing temperature the mean free path between lattice scattering increases, and in the region of the mobility maximum becomes comparable with that between trapping events. This transition may be formulated in the following simple way if it is assumed that the effective drift velocity of the electron cloud is small enough to allow a description in terms of the equilibrium distribution between free and trapped carriers.

The measured mobility is given by

$$\mu = d/[(t_0 + \sum t_\epsilon)E] \qquad (1)$$

where t_0 denotes the transit time in absence of trapping; this is determined by the lattice mobility $\mu_L = d/Et_0$. t_ϵ, the average time an electron remains in the level at ϵ is obtained by equating the rate of thermal release with the rate of trapping. This leads to $t_\epsilon = \tau(n_t/n)$ where $n_t(\ll N_t)$ denotes the density of trapped electrons and τ the free electron lifetime. As the average number of trapping events during transit is t_0/τ, $\sum t_\epsilon = t_0 (n_t/n)$. If the Fermi level lies below ϵ by more than a few kT,

$$\sum t_\epsilon = \frac{N_t}{N_c} t_0 \exp(\epsilon/kT). \qquad (2)$$

The effective density of states is $N_c = 2{\cdot}5 \times 10^{19} (T/T_r)^{3/2}(m^*/m)^{3/2}$. Equations (1) and (2) together

Vol. 21 1961

with $\mu_L/\mu_T = (T/T_T)^{-3/2}$ then lead to

$$\mu/\mu_T = [(T/T_T)^{3/2} + 0{\cdot}4\times 10^{-19} N_t(m^*/m)^{-3/2}\exp(\epsilon/kT)]^{-1}. \quad (3)$$

Using the value $\epsilon = 0{\cdot}25$ eV obtained from Fig. 3, $N_t(m^*/m)^{-3/2}$ can be found from the position of the mobility maximum in Fig. 1. For specimens M4 and M5, $N_t = 3{\cdot}5\times 10^{13}(m^*/m)^{3/2}$ cm^{-3}, for M12 it is $4\times 10^{12}(m^*/m)^{3/2}$ cm^{-3}. Other specimens lead to values within this range. It can be seen from Fig. 1 that with these constants equation (3) leads to a satisfactory agreement with experiment over the complete temperature range.

Moss[13] has applied the deformation potential theory[10] to obtain an estimate of the lattice mobility in Se. He finds $\mu(m^*/m)^{3/2} \simeq 32$ at room temperature which leads to $m^* \simeq 3m$ in reasonable agreement with the value 2·5 m obtained from the Faraday effect.[13] This may well be fortuitous in view of the uncertainty of the data used for the estimate of the deformation potential. With the above value of m^* the specimens lead to an average value of 10^{14} cm^{-3} for N_t.

At a low temperature in the trap controlled range (e.g. −80°C, specimen M5) a transit time of about 300 mμ sec is observed at a normal value of E. From the extent of the straggling of transit times (~90 mμ sec), t_t might be estimated as 30 mμ sec. τ which is given by $(\mu/\mu_L)t_e$ would then be about 3 mμ sec. With $N_t = 10^{14}$ cm^{-3} this leads to a capture cross section of the order of 10^{-13} cm^2. One would expect such a comparatively high value to be associated with charged centres which exert a Coulomb attraction on the free electrons.

It is not possible at present to decide whether the centres arise from impurities or from structural defects. The close agreement in the value of ϵ for monoclinic and vitreous Se suggests that the type of centre controlling the electron mobility is common to both forms. A comparison of the measured mobility values indicates that N_t should be about 10^{18} cm^{-3} in the vitreous form. With a density of this order the transition to a lattice mobility would be expected only at temperatures well above the melting point.

It has been pointed out that the investigation of the hole mobility was complicated by the presence of deeper trapping effects; an interpretation of the results in terms of a single level at $\epsilon \sim 0{\cdot}3$ eV is therefore doubtful. As would be expected there appears to be no connection between the hole mobility in the monoclinic and the vitreous (or hexagonal) forms. In the latter $\epsilon = 0{\cdot}14$ eV, a value which is characteristic of the hole transport along a Se chain.

Acknowledgements—The author wishes to thank Dr. MARIANNE EHRENBERG of University College, London for an X-ray examination of the crystals and Dr. V. PROSSER of the Charles University, Prague for a number of specimens and for advice on the growing of monoclinic crystals. The work described was supported by the European Research Office of the U.S. Department of the Army.

REFERENCES

1. KLUG H. P., *Z. Kristallogr.* **88,** 128 (1934).
2. BURBANK R. D., *Acta Cryst., Camb.* **4,** 140 (1951).
3. MARSH E., PAULING L. and MCCULLOUGH J. D., *Acta Cryst., Camb.* **6,** 71 (1953).
4. GUDDEN B. and POHL R., *Z. Phys.* **35,** 243 (1925).
5. PROSSER V., *Czech. J. Phys.* **A10,** 35 (1960); *Proceedings of the International Conference on Semiconductor Physics* (1960), in press.
6. SPEAR W. E., *Proc. Phys. Soc., Lond.* **76,** 826 (1960).
7. SPEAR W. E., *Proc. Phys. Soc., Lond.* **B70,** 669 (1957).
8. BROWN F. C. and KOBAYASHI K., *J. Phys. Chem. Solids* **8,** 300 (1959).
9. KYROPOULOS S., *Z. Phys.* **40,** 620 (1927).
10. BARDEEN J. and SHOCKLEY W., *Phys. Rev.* **80,** 72 (1950).
11. CONWELL E. and WEISSKOPF V. F., *Phys. Rev.* **77,** 388 (1950).
12. See for example SHOCKLEY W., *Electrons and Holes in Semiconductors* p. 288. Van Nostrand, Princeton (1950).
13. MOSS T. S., *Optical Properties of Semiconductors* p. 155. Butterworths, London (1959).

LETTERS TO THE EDITOR

A note on nickel hydride

(*Received* 17 *February* 1961)

NICKEL saturated with hydrogen from a gaseous atmosphere or from cathodic charging or deposition has been studied previously by X-ray diffraction techniques [literature reviewed in Ref. (1)]. The conclusion reached was that hydrogen has virtually no effect on the lattice parameter of nickel. However, marked broadening of diffraction lines has been observed in both cathodically charged and electrodeposited nickel. This indicates that processes associated with the cathodic evolution of hydrogen on nickel can produce effects similar to those caused by local lattice strains.

Sputtered nickel films have been shown to have a hexagonal structure due to absorption of hydrogen, nitrogen, or carbon monoxide during sputtering [literature reviewed in Refs. (1) and (2)]. On heating to 300–400°C the hexagonal structure transforms into a f.c.c. nickel structure. It is thought that hexagonal nickel hydrides, nitrides, hydronitrides or possibly carbides and carbonitrides may be formed depending on the atmosphere used. However, very little is known about these substances and in recent reference books, the hexagonal nickel hydride is accompanied by a question mark[2] or is thought to be a hydrogen-metastabilized modification of nickel.[3]

In the present note evidence is given for the existence of a f.c.c. nickel hydride. The hydride can be obtained at room temperature by saturating nickel with hydrogen, using cathodic charging.

Fig. 1(a) shows part of the X-ray front-reflection diffraction pattern recorded from a nickel specimen treated to produce nickel hydride. Fig. 1(b) shows a corresponding part of the diffraction pattern from a hydrogen-free specimen. The two extra peaks in Fig. 1(a) at 2Θ angles equal approximately to 42° and 49°, are due to the Bragg reflections from (111) and (200) planes of the nickel hydride.

Both the figures were obtained using copper radiation and a nickel filter in a counter-tube diffractometer, Siemens Kristalloflex 4. The specimens were prepared from annealed 99·0 per cent pure Mond nickel strip (grain size 35μ). Before saturation with hydrogen, the specimens were electropolished to 200μ thickness. The saturation was conducted at room temperature in a 1*N* aqueous solution of H_2SO_4 with the addition of 0·04g As_2O_3 per litre. The current density was 0·3A/cm^2 and the charging time was 48 hr. The layer of the hydride produced at the surface was of the order of 10μ thick.

Figure 2 shows part of the X-ray back-reflection diffraction pattern for a similarly prepared specimen. (420), (331) and (400) sets of lines for both the nickel and the nickel hydride are present. This was obtained using a small Philips powder camera (Straumanis method) and filtered copper radiation. The specimen was of the same material as the previous two, but only 60μ thick and 3 mm wide. It was mounted in the holder with its flat surface normal to the X-ray beam. Although the grain size was 15μ in this case, the diffraction lines are still spotty, as no rotation was applied during the

Table. 1. *The indexing of the diffraction patterns of nickel hydride*

X-ray diffraction method	Θ	$\sin^2\Theta$	N $(h^2+k^2+l^2)$	Indices (hkl)
Front reflection in counter-tube diffractometer, Siemens Kristalloflex 4	21°02′	0·1288	3	(111)
	24°28′30″	0·1717	4	(200)
	35°53′30″	0·3441	8	(200)
Back reflection in Philips powder camera (Straumanis method)	55°50′	0·6841	16	(400)
	64°20′	0·8123	19	(331)
	67°42′	0·8560	20	(420)

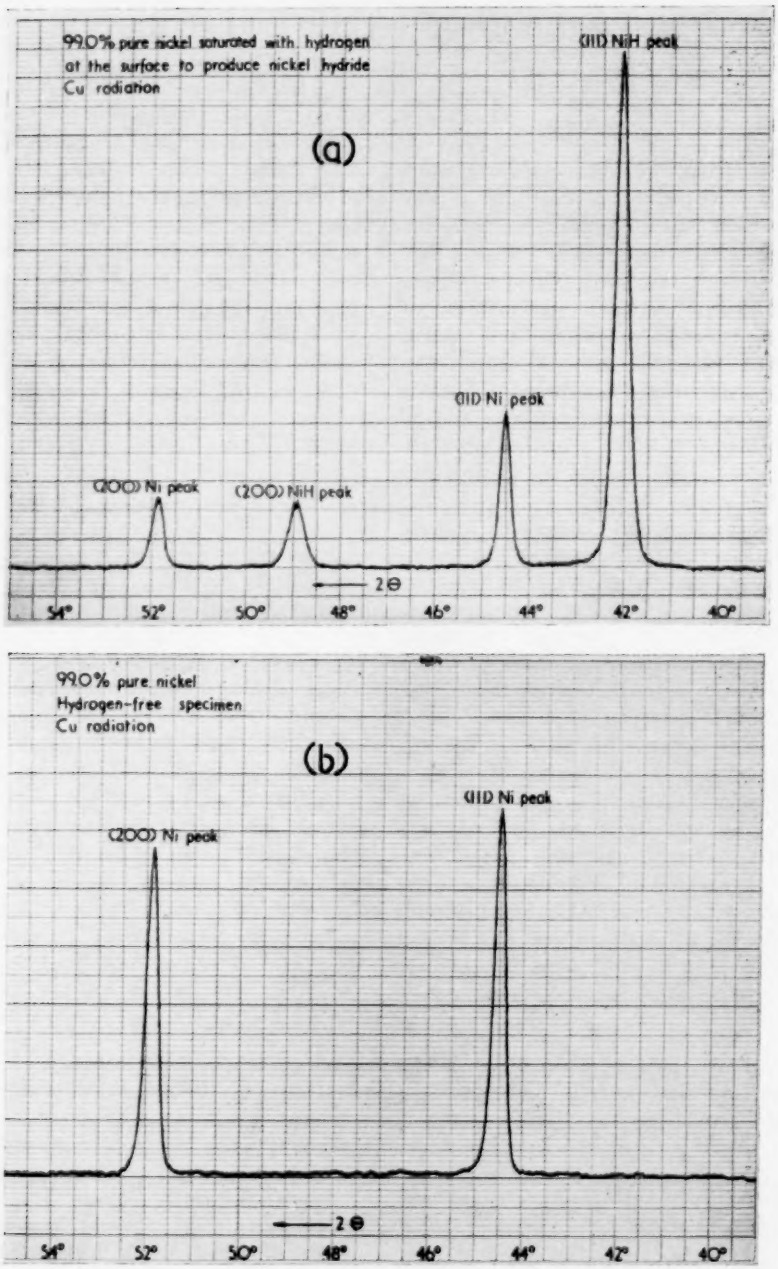

FIG. 1. The X-ray diffraction graphs of the part of the front-reflection pattern obtained at room temperature with Siemens Kristalloflex 4 using Cu radiation and Ni filter. Material: 99·0 per cent pure nickel. Grain size 35μ. (a) Charged with hydrogen in 1N H_2SO_4+0·04g As_2O_3/litre at 0·3 A/cm^2 for 48 hr at room temperature. Examined 20 min after the charging. (b) Hydrogen-free specimen.

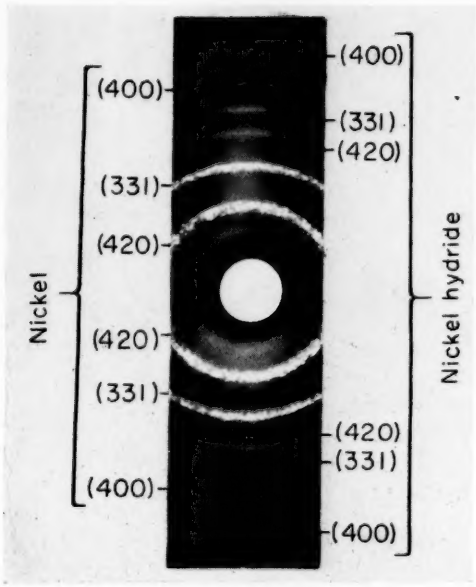

FIG. 2. Part of the X-ray back-reflection diffraction pattern obtained at room temperature with a small Philips powder camera (Straumanis method) using Cu radiation and Ni filter. Material as in Fig. 1. Grain size 15μ. Charged with hydrogen as in Fig. 1, but for 24 hr. Examined 2 hr after charging.

[*facing p.* 116

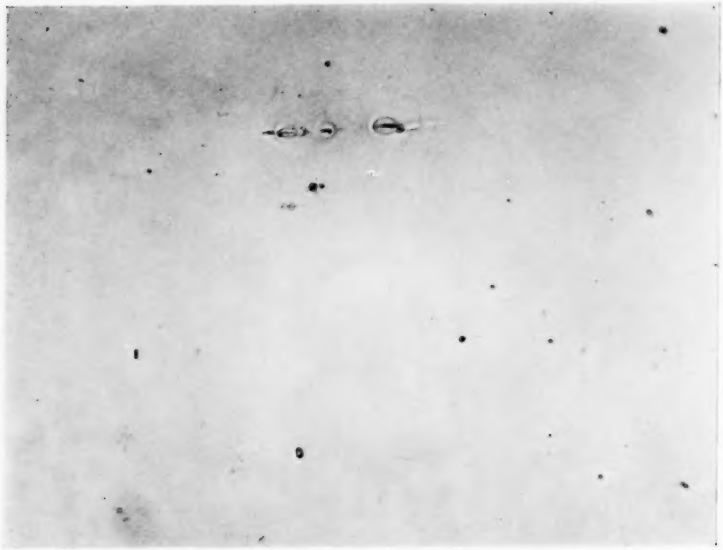

FIG. 3. The appearance of an electrolytically polished nickel surface before cathodic charging with hydrogen. Material and grain size as in Fig. 1. Magnification × 580. The non-metallic inclusion identifies the examined area.

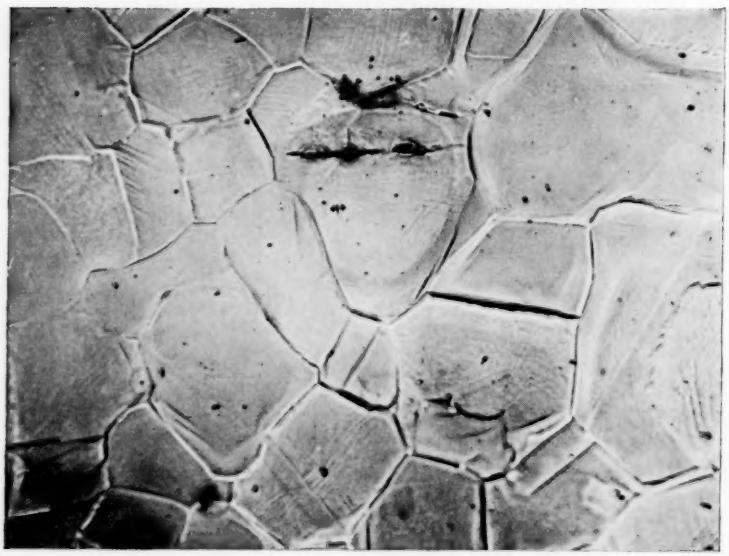

FIG. 4. The same area as in Fig. 3 photographed 12 min after charging was ended. Charging conditions as in Fig. 2. Magnification × 580. Note the delineation of grain boundaries, and slip lines due to the volume expansion associated with the formation of nickel hydride.

FIG. 5. The same area as in Fig. 4 after complete decomposition of nickel hydride. Magnification ×580.

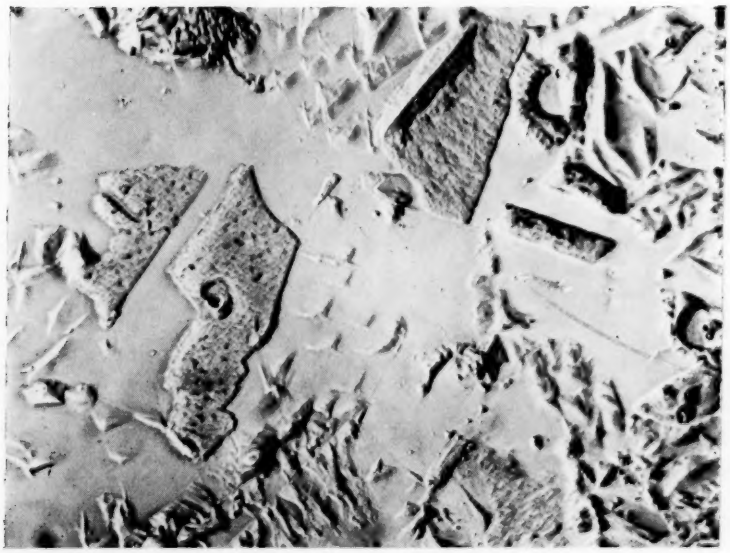

FIG. 6. Surface appearance after charging in 1N Analar H_2SO_4 at 94°C and 0·15 A/cm^2 for 1 hr. Material and grain size as in Fig. 1. Photographed 30 min after charging. Magnification ×580. Oblique illumination falling from left to right. Note that the formation of nickel hydride is structure sensitive (twins).

BLANK
PAGE

Vol.
196

exposure. The layer of hydride was much less than 10μ thick as the charging time was only 24 hr with the other conditions being as above.

The crystal structure of nickel hydride has been determined by indexing the diffraction patterns as shown in Table 1.

The values of N thus correspond to a face centred cubic structure. A full pattern of eight f.c.c. diffraction lines was observed but the remainder were too weak to be measured accurately.

There does not appear to be any gradual increase in the lattice parameter of nickel during the saturation with hydrogen. The formation of the hydride appears to be a discontinuous process.

The diffraction patterns were taken from specimens transformed to the hydride only at the surface, so that reflections for both the nickel (α-phase) and the hydride (β-phase) were present. The lattice parameter of the hydride (a_β) was obtained from the relation

$$a_\alpha \sin \Theta_\alpha = a_\beta \sin \Theta_\beta$$

in which the Bragg angles (Θ) belong to the reflections with the same indices.

Taking $a_\alpha = 3{\cdot}524$ Å[2] the parameter of the nickel hydride is $a_\beta = 3{\cdot}721 \pm 0{\cdot}001$ Å at room temperature ranging from 16–22°C. This corresponds to a 5·6 per cent increase in lattice parameter during transformation of the nickel to the hydride.

It has not been possible to determine the positions of the hydrogen atoms in the hydride due to the low scattering factor of a hydrogen atom, and the internal stresses produced by the volume change on transformation. However they must occupy either the tetrahedral or octahedral interstices in the f.c.c. lattice although on the size factor basis the tetrahedral interstices would probably be preferred. It appears from approximate determinations of the hydrogen concentration in the surface layer transformed to hydride, that the ratio of hydrogen atoms to nickel atoms is about 0·8. Hence the hydride should have a NiH type formula and zinc blende type or sodium chloride type structures could be expected for hydrogen in the tetrahedral or octahedral interstices respectively. Thus the f.c.c. nickel hydride might be classified as an interstitial phase (compound) having the structure of the parent metal, but with the metal atoms no longer in contact with one another but with the hydrogen atoms.

The diffraction lines of the hydride always appear at the same Bragg angles irrespective of variation in the conditions of cathodic charging, providing the build-up of hydrogen concentration has been sufficient to cause the transformation. When the hydride decomposes its diffraction lines fade away gradually whilst the lines of nickel become stronger, but there appears to be no shift in their angular positions.

The rate of decomposition of the hydride depends on temperature, size of crystallites (determined by the grain size of the parent metal) and the amount of deformation the specimen undergoes during handling.

At room temperature decomposition occurs on standing after charging and in specimens with a grain size of 35μ, and charged electrolytically for 24 hr, the intensity of (111) peaks of the hydride falls considerably in 2–3 hr, but the peaks fade away completely only after times in excess of 40 hr. At 100°C complete decomposition occurs in 1–2 hr. If a specimen is hammered decomposition occurs at room temperature in a matter of minutes.

The hydride can be obtained with a variety of electrolytic conditions. Electolytes ranging in composition from 0·1–1N aqueous solution of H_2SO_4 have been used, with or without additions of 0·004–0·04g of As_2O_3 per litre. When the charging is carried out in 1N H_2SO_4 + 0·04gAs_2O_3/litre at a current density 0·3A/cm^2, the hydride is formed in a matter of minutes. On the other hand, if the solution is free of the cathodic poison (AnalaR H_2SO_4 and no As_2O_3), the first traces are not found until after 2 hr. If the charging is carried out at 90°C the hydride forms but decomposes very rapidly. It is also formed when spectroscopically pure nickel is used instead of 99·0 per cent purity.

The presence or the prior existence of nickel hydride can be readily detected by a metallographic examination. Before charging a specimen, the surface is polished electrolytically so that no grain boundaries are visible (Fig. 3). The formation of a uniform layer of hydride then produces a bulging of grain surfaces, due to volume expansion. This results in a delineation of grain boundaries (Fig. 4). During decomposition of the hydride tensile stresses are set up in the surface layers. These and the simultaneous "precipitation" of gaseous hydrogen result in extensive grain

Vol. 21
1961

boundary cracking, and rumpling and cracking within the grains. Fig. 5 shows the same area as Fig. 4 after complete decomposition of the hydride. The depth of cracking depends on the thickness of the hydride layer. Thus after charging for 48 hr in 1N H_2SO_4+0·04g As_2O_3/litre at a current density 0·3A/cm^2, the depth of cracking is about 10μ after complete decomposition.

The decomposition may be followed directly under the microscope since the reflectivity of the hydride is lower than that of nickel, and it appears as dark patches. Thus the nickel hydride/nickel interface is defined not only by the relief effect due to difference in volume, but also by the difference in reflectivity of the two phases.

The conditions of electrolytic charging may be arranged so that the amount of hydrogen absorbed by the nickel is not sufficient to produce a uniform layer of nickel hydride. In this case only some grains are transformed to hydride and these can be identified by the characteristic relief on an electropolished surface (Fig. 6). The metallographic technique is more sensitive than an X-ray method for the detection of small amounts of hydride.

The formation and decomposition of nickel hydride clearly has considerable implications in connection with the mechanical properties of nickel charged with hydrogen.

Acknowledgements—The authors wish to thank Professor A. H. Cottrell, F.R.S. for his help and interest in this work, and for the provision of laboratory facilities. They are also grateful for help received from the British Welding Research Association who also provided a maintenance grant (T.B.).

Department of Metallurgy T. Boniszewski
University of Cambridge G. C. Smith
England

References

1. Smith, D. P., *Hydrogen in Metals*, p. 65. University of Chicago Press (1948).
2. Pearson, W. B., *A Handbook of Lattice Spacings and Structures of Metals and Alloys*, pp. 228, 781, 973. Pergamon Press, London (1958).
3. Hansen M., *Constitution of Binary Alloys*, p. 788. McGraw-Hill, New York (1958).

Sur l'isomorphisme d'oxydes ternaires de chrome et de rhodium trivalents*

(*Received* 23 *March* 1961)

Nous établissons l'isomorphisme des composés oxydes ternaires Cr^{3+} et de Rh^{3+} dans trois classes d'oxydes. Deux d'entre elles ont pour formule ABO_2, la troisième appartient aux spinelles.

(1) *Type* $NiLiO_2$. Cette structure[1] cristallise dans le groupe d'espace $R\,\bar{3}\,m-(D^5_{3d})$. Elle dérive de la structure de NaCl par l'établissement d'un ordre des cations Ni et Li qui forment des couches alternées selon [111] et par une dilatation selon [111]. L'etude cristallographique des composés rhomboédriques isomorphes $CoLiO_2$[2], $VLiO_2$, $CrLiO_2$[3] a été faite récemment.

Nous avons préparé les composés $CrLiO_2$ et $RhLiO_2$ par réaction directe, en chauffant un mélange de $LiCO_3$ et de l'oxyde du métal de transition. $RhLiO_2$ est isomorphe des composés précédents. A titre de comparaison nous avons rassemblé dans le Tableau 1 les paramétres cristallographiques de $MLiO_2$ (M = Co, Ni, Cr, Rh). Les coordonnées de position (en notation hexagonale) sont M en 3*a*, (000), Li en 3*b* (00$\frac{1}{2}$) et O en 6*c* $\pm$ (00*z*) avec $z \sim 0{,}25$. Les cations M et Li ont une coordination octaédrique.

Tableau 1. $MLiO_2$. *Paramètres en* Å

Composés M	Notation hexagonale		Notation rhomboédrique	
	a	*c*	*a*	α
Co	2,814	14,06	4,96	32°58′
Ni	2,88	14,20	5,02	33°22′
Cr	2,905	14,44	5,10	33°07′
Rh	3,02	14,30	5,075	34°37′

(2) *Type* $NaHF_2$. La structure rhomboédrique de $FeCuO_2$[4] dans laquelle Fe est trivalent et Cu monovalent[5] est isotype de $NaHF_2$[6]. Elle appartient encore au groupe $R\,\bar{3}\,m$, mais possède la particularité d'avoir un cation Cu^+ coordiné à 2 atomes d'oxygène. La coordination de Fe^{3+} est octaédrique. D'autres auteurs ont réalisé la synthèse

* Communiqué au 5ème Congrès International de Cristallographie Août 1960, Cambridge, Angleterre.

de $CrCuO_2$[7], $CoCuO_2$[8] et $AlCuO_2$[9]. Tous ces corps sont isomorphes et les résultats de leurs études cristallographiques ont été résumés dans la Réf. (9).

Nous avons réussi à préparer le composé $RhCuO_2$, isomorphe des précédents par chauffage à l'air d'un mélange de CuO et de Rh_2O_3 en proportion calculée. Le Tableau 2 résume les paramètres cristallographiques pour Fe, Cr, Rh. Les coordonnées de position (notation hexagonale) sont Cu en $3a$ (000), M = Al, Fe, Cr, Co, Rh en $3b$ $(00\frac{1}{2})$, O en $6c \pm (00z)$ $z \sim \frac{1}{9}$.

Tableau 2. $MCuO_2$. *Paramètres en* Å

Composés M	Notation hexagonale		Notation rhomboédrique	
	a	c	a	α
Fe	3,03	17,09	5,96	29°26′
Cr	2,97	17,07	5,94	29°
Rh	3,075	17,165	5,99	29°45′

(3) *Type spinelle.* Nous avons réalisé la synthèse de Rh_2NiO_4 quadratique (c/a = 1,037), Rh_2CuO_4 quadratique (c/a = 0,909) et de Rh_2CoO_4 cubique. Nous avons déjà fait remarquer[10] que la déformation est due à un effet Jahn–Teller. *Elle varie dans le même sens que dans les chromites isomorphes.* Tous ces spinelles sont normaux, c'est-à-dire Rh^{3+} et Cr^{3+} sont dans les positions octaédriques. Les exemples 1°, 2° et surtout 3° montrent que Rh^{3+} a la même prédilection que Cr^{3+} pour une coordination octaédrique. Selon la théorie du champ cristallin, les 5 orbites d se décomposent en orbitales t_{2g} triplement dégénérées et e_g doublement dégénérées, l'état t_{2g} étant le plus bas dans une configuration octaédrique. Si Δ est la séparation des niveaux, l'énergie de stabilisation de la configuration $(t_{2g})^m(e_g)^n$ est[11] $(4m-6n)\Delta$. D'aprés les mesures d'absorption d'ions de transition dans les verres Δ est approximativement constant pour un ion d'une valence donnée.[11] L'ion Cr^{3+} dans l'état $(t_{2g})^3$ posséde une énergie de stabilisation de 12Δ. Nous en concluons que Rh^{3+} n'a pas la configuration $(t_{2g})^4(e_g)^2$ à laquelle on est conduit normalement et dont l'énergie de stabilisation n'est que de 4Δ. Le cas extrême, c'est-à-dire l'état $(t_{2g})^6$, diamagnétique de Rh^{3+} peut être envisagé soit par la théorie de champ cristallin en supposant la séparation des énergies t_{2g} et e_g très grande,[12] soit par la théorie des orbitales.[13]

En effet, on peut construire un complexe de 18 électrons particulièrement stable, avec les 6 électrons d de Rh^{3+} dans les orbitales t_{2g} (dxy, dyz, dzx) et les 12 électrons de l'octaèdre de coordination dans les orbitales qui sont formées par l'hybridisation des orbitales $2p_\sigma$ ou $2p_\pi$ de l'oxygène avec les orbitales vides $3d^24s4p^3$ de l'ion de transition.

Les deux méthodes ont été envisagées[12,13] pour expliquer le diamagnétisme fréquent de Co^{3+} qui a la même configuration d^6 que Rh^{3+} (et dont la coordination semble toujours être octaédrique)[14].

Des mesures de susceptibilité trancheront certainement cette question.

Laboratoire d'Electrostatique et de Physique du Métal
Institut Fourier
Grenoble
France

E. F. Bertaut
J. Dulac

Bibliographie

1. Dyer L., Borie B. et Smith G., *J. Amer. Chem. Soc.* **76,** 1479 (1954).
2. Johnston W. D., Heikes R. R. et Sestrich D., *J. Phys. Chem. Soc.* **7,** 1 (1958).
3. Rüdorff W., *Z. Naturforsch.* **96,** 614 (1954)
4. Soller W. et Thompson A. J., *Bull. Amer. Phys. Soc.* **10,** 17 (1935).
5. Delorme C. et Bertaut F., *J. Phys. Radium* **148,** 129 (1953).
6. *Strukturbericht* Vol. 1, p. 271 (1913–1928).
7. Stroupe J. D., *J. Amer. Chem. Soc.* **71,** 569 (1949).
8. Bertaut F. et Delorme C., *C.R. Acad. Sci., Paris* **238,** 1829 (1954).
9. Delorme C., *Acta Cryst., Camb.* **9,** 200 (1956).
10. Bertaut F., Forrat F. et Dulac J., *C.R. Acad. Sci., Paris* **249,** 726 (1959).
11. Dunitz J. P. et Orgel L. E., *J. Phys. Chem. Soc.* **3,** 318 (1957).
12. Penney W. G. et Schlapp R., *Phys. Rev.* **42,** 666 (1932).
13. Van Vleck J. H., *J. Chem. Phys.* **3,** 807 (1935).
14. Cossee P., Thèse, Leiden (1956).

Etude de l'absorption et de la réflexion de la cuprite aux très basses températures dans le visible de courtes longueurs d'onde

(*Received* 27 *March* 1961)

Cette étude a été effectuée avec des échantillons

épais (épaisseur supérieure à 10μ) et des échantillons minces (épaisseur de l'ordre du micron), ces derniers étant déposés sur des lames de quartz et de coryndon.

Echantillons épais

Ces échantillons ont été obtenus par oxydation de lames de cuivre dans un four porté à 1000°C sous une pression réduite d'oxygène.

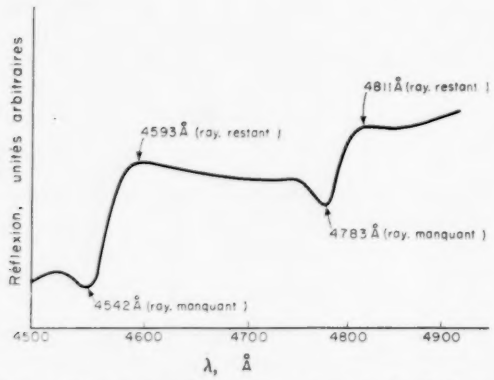

FIG. 1. Courbe de réflexion d'une lame de Cu_2O d'une épaisseur supérieure à 10μ à 77°K.

Les lames polycristallines de cuprite ainsi obtenues ont été étudiées par réflexion aux très basses températures.[1] On observait, dans la partie bleue et violette du spectre, deux anomalies de réflexion formées chacune d'un minimum suivi d'un maximum de réflexion (Fig. 1). Nous avons vérifié que ces anomalies n'étaient pas dues à des phénomènes de surface, car les surfaces attaquées par des acides et polies montraient les deux anomalies. On pouvait donc supposer que l'on observait des réflexions sélectives avec rayon restant (R.R.) et rayon manquant (R.M.), dues à l'existence de fortes raies d'absorption appartenant à des spectres de première classe, comme l'ont montré NIKITINE et REISS dans le cas de CuI[2].

Nous avons cherché à observer les raies d'absorption correspondant à ces anomalies. Mais l'absorption de la cuprite après la série verte est très importante; pour l'étudier, nous avons dû utiliser des échantillons très minces déposés sur support.

Echantillons sur coryndon

Ces échantillons ont été obtenus en déposant, par sublimation, une couche mince de cuivre sur des lames de coryndon et en les oxydant dans un four porté à 1000°C sous pression réduite d'oxygène.

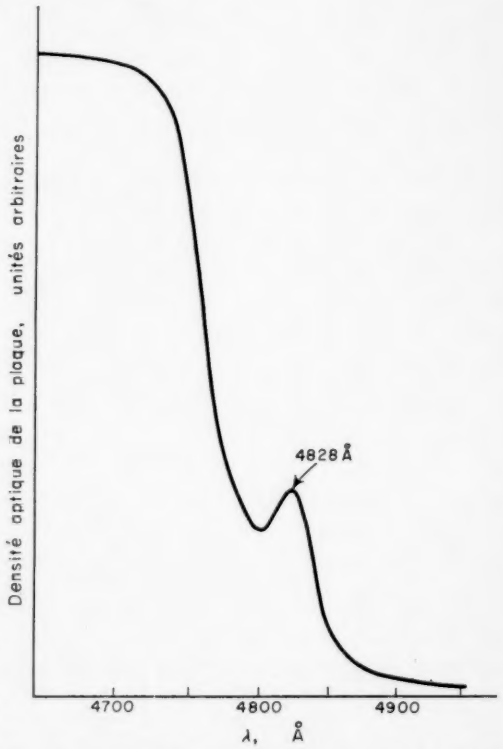

FIG. 2. Courbe d'absorption d'une couche de Cu_2O d'une épaisseur inférieure à 1μ sur support de coryndon à 77°K.

Les anomalies de réflexion n'ont pu être observées par suite de la mauvaise qualité des surfaces des lames de coryndon utilisées. Par contre, nous avons pu observer, avec des couches épaisses, les séries jaune et verte et, avec des couches plus minces, une forte raie d'absorption dans le bleu (Fig. 2). Mais cette raie est systématiquement décalée vers les grandes longueurs d'onde par rapport aux anomalies de réflexion observées avec les échantillons épais sans support. Le décalage varie de 10 à 40 Å selon le support de coryndon.

On peut supposer qu'il est dû au support. Pourtant, les séries jaune et verte observées avec ces échantillons épais sur support de coryndon ne sont pas déplacées dans le spectre.

Echantillons sur quartz

Ces échantillons ont été obtenus en déposant, par sublimation, une couche mince de cuivre sur

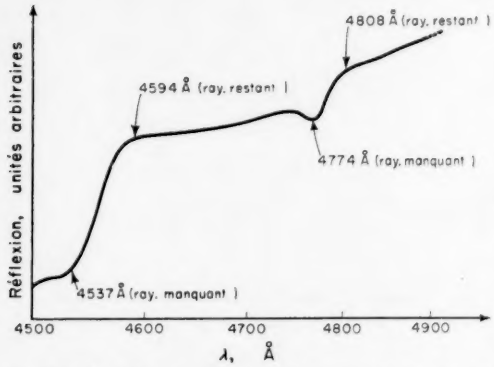

FIG. 3(a). Courbe de réflexion d'une couche de Cu_2O d'une épaisseur inférieure à 1μ sur support de silice fondue à 20°K.

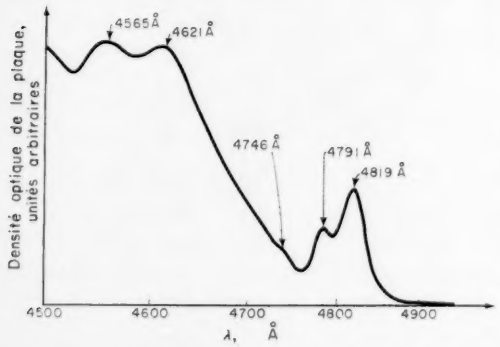

FIG. 3(b). Courbe d'absorption d'une couche de Cu_2O d'une épaisseur inférieure à 1μ sur support de silice fondue à 20°K.

des lames de silice fondue, en les chauffant à la flamme d'un bec Bunsen à la pression atmosphérique, puis en les trempant brusquement dans un Dewar rempli d'azote liquide. On procède ainsi afin d'éviter la diffusion du cuivre, puis de la cuprite dans le quartz. Ces lames observées par réflexion présentent, comme les échantillons épais, deux réflexions sélectives dans le bleu et le violet (Fig. 3a). Les longueurs d'onde des R.R. et R.M. sont identiques, à la précision des mesures près, pour les échantillons minces sur support et pour les échantillons épais sans support.

D'autre part, par absorption ces lames présentent deux doublets : l'un dans le bleu, l'autre dans le violet qui correspondent chacun à une des réflexions sélectives observées (Fig. 3a et b).

$$\lambda_{\text{bleu}} = 4819 \text{ Å et } 4791 \text{ Å}$$

$$\lambda_{\text{violet}} = 4621 \text{ Å et } 4565 \text{ Å}.$$

La position des raies ne varie pratiquement pas d'un échantillon à un autre. On peut se demander si le dédoublement des raies ne serait pas dû aux traitements thermiques ou à l'effet du support.

Il résulte de cette étude que l'on observe donc deux raies d'absorption intenses avec réflexion sélective dans le bleu et le violet.*

Ces raies ne se déplacent pratiquement pas avec la température. Les réflexions sélectives des échantillons épais ont été étudiées à différentes températures. Leur variation thermique est faible et correspond plutôt à un élargissement des rayons restants et manquants lorsque la température croît. D'autre part, les échantillons sur support, étudiés aux températures de l'azote et de l'hydrogène liquides, ne montrent aucun déplacement des raies. Rappelons que les séries jaune et verte, par contre, se déplacent considérablement dans le spectre avec la température.

Enfin, la distance entre les raies bleue et violette est du même ordre que celle entre les séries jaune et verte, environ 1000 cm^{-1}.

ELLIOTT suggère le modèle de bandes d'énergie au voisinage de $K = 0$, représenté sur le diagramme (Fig. 4). Les séries jaune et verte seraient liées aux transitions entre les deux niveaux de la bande de valence, dédoublée par le couplage spin–orbite, et la bande de conduction.[4] Si l'on suppose qu'il existe une autre bande de conduction environ 4500 cm^{-1} plus élevée que la première, on obtient deux nouvelles séries de

* Dans un travail récent[3] dont nous venons de prendre connaissance, GORBAN et TIMOFEEV ont obtenu des résultats assez différents.

Vol. 21
1961

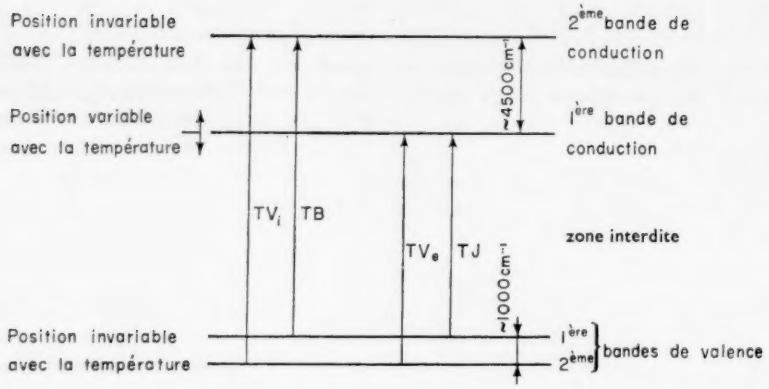

FIG. 4. Diagramme des bandes d'énergie de Cu_2O au voisinage de $K = 0$. La variation thermique de la position des bandes est relative. La première bande de conduction pourrait être invariante, les deux autres se déplaçant par rapport à celle-ci avec la température.

raies correspondant aux transitions entre les deux niveaux de la bande de valence et la deuxième bande de conduction. Ces deux séries distantes de 1000 cm^{-1} correspondraient aux absorptions observées dans le bleu et le violet.[5] Ainsi, cette étude permet, conformément à une suggestion de ELLIOTT, de montrer que c'est la bande de valence qui est dédoublée.

Laboratoire de Spectroscopie et d'Optique du Corps Solide
Institut de Physique
Université de Strasbourg

J. B. GRUN
M. SIESKIND
S. NIKITINE

Bibliographie

1. NIKITINE S., GRUN J. B. et SIESKIND M., Communication à la *Conférence Internationale de la Physique des Semiconducteurs, Prague* (à paraître).
2. REISS R., *Cah. Phys.* **13,** 129 (1959); NIKITINE S. et REISS R., *C.R. Acad. Sci., Paris.* **242,** 238 (1956).
3. GORBAN J. S. et TIMOFEEV V. S., *Fiz. Tverdogo Tela.* **2,** 111 (1960).
4. ELLIOTT R. J., *Phys. Rev.* **108,** 1384 (1957).
5. ELLIOTT R. J., *Conférence Internationale de la Physique des Semiconducteurs, Prague* et communication privée. Les auteurs remercient le Dr. ELLIOTT pour l'autorisation de reproduire le diagramme (Fig. 4).

Solidification of helium at 77°K

(*Received* 27 *March* 1961)

A PHASE change of He^4 has been observed to occur at 77·3°K at 14,140 bars. The maximal temperature deviation is estimated to be between 77·0 and 78·2°K. The maximal error in the determination of pressure is estimated to be ± 1·4 per cent (or ± 200 bars).

This phase change was observed by the piston displacement method. The gas pressure is generated in a helium reservoir at room temperature as described previously.[1] This reservoir is connected by a ten foot tubing of 0·025 in. inner diameter—which is further reduced by introducing a steel wire of 0·020 in. diameter—to the test chamber, which has a volume of approximately 1·63 cm^3. The test chamber is immersed in liquid nitrogen.

The pressure was measured in the room temperature reservoir by the resistance change of a manganin wire. An estimated nonlinearity of ± 0·7 per cent of the resistance change with pressure is included in the above estimation of error.

The observed phase change is evidently the transition between the gaseous and the solid phase, for it is in good agreement with the extrapolation from experimental values[2,3] and with predicted sublimation curves.[4]

The predicted equilibrium pressure at 77·3°K according to SIMON's formula[6] is 14,135 bars, and according to the expression given by MILLS and GRILLY[7] it is 14,285 bars. Both values fall within the limits of experimental error.

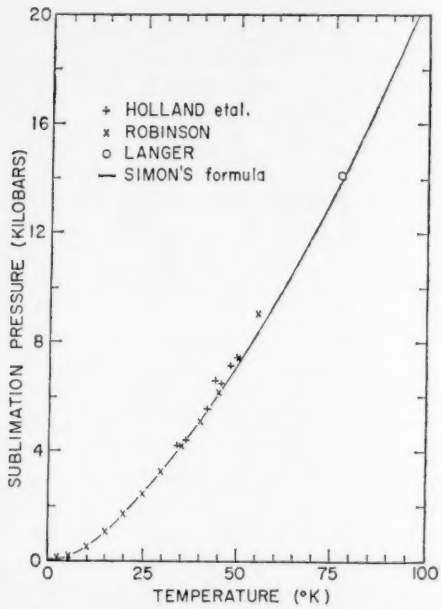

FIG. 1. The melting curve of He^4. Points give experimental values. The curve is calculated according to SIMON's formula:

$$P = 16{\cdot}235[(T/0{\cdot}992)^{1{\cdot}5544} - 1]$$

where P is measured in bars.

Thus the verification of the theoretical curves at a higher pressure range reaffirms the assumptions underlying the calculations as pointed out by DUGDALE[5] and therefore may justify even further extrapolation.

D. W. J. LANGER

Aeronautical Research Laboratory
Wright–Patterson AFB
Ohio, U.S.A.

References

1. LANGER D., WARSCHAUER D. M., *Rev. Sci. Instrum.* **32,** 32 (1961).
2. HOLLAND F. A., HUGGILL J. A. and JONES G. O., *Proc. Roy. Soc.* **A207,** 268 (1951).
3. ROBINSON D. W., Thesis, *The Properties of Solid and Liquid Helium at High Pressures,* Oxford (1952).
4. DOMB C. and DUGDALE J. S., *Progress in Low Temperature Physics,* Vol. II, p. 351. North Holland Publishing Co., Amsterdam (1957).
5. DUGDALE J. S., *Nuovo Cim.* (ser. 10) **9,** 25S (1958).
6. SIMON F., RUHEMANN M. and EDWARDS W., *Z. Phys. Chem.* **B6,** 62 (1929).
7. MILLS R. L. and GRILLY E. R., *Phys. Rev.* **99,** 480 (1955).

The van Vleck temperature-independent magnetism of metals

(*Received* 3 *April* 1961)

THE paramagnetic susceptibility of metals is usually attributed to the alignment of electron spins. Here we suggest that the van Vleck paramagnetism due to induced orbital motion may also be important, particularly for the transition metals.

To make possible an order of magnitude estimate we accept the picture of the body-centred metals in which the conduction band is made up of s, p and $d(t_{2g})$ orbitals, while the $d(e_g)$ orbitals form a narrow band some way above the Fermi surface.[1,2] We assume:

(1) That there are three electrons in the d orbitals; this seems reasonable for, say, vanadium or molybdenum.

(2) That the contribution to the susceptibility is determined by the usual van Vleck formula as applied to $t_{2g}d$ electrons[3] but with an average energy denominator E which corresponds to the distance from the middle of the conduction band to the e_g band. Here we arbitrarily set this quantity equal to 2 eV.

(3) That the contribution of the three t_{2g} electrons is half of that which would be obtained from a filled $(t_{2g})^6$ shell.

Then we obtain for the orbital contribution to the molecular-susceptibility a value of 125×10^{-6}.

We do not suggest that this value be taken seriously but we do believe that it shows that for any reasonable d electron distribution the van Vleck paramagnetism must make an important contribution to the susceptibility of body-centred transition metals. It may provide at least part of

the explanation of the disagreement between the observed susceptibility of these metals and that estimated from the density of states as the Fermi-surface.[4]

The van Vleck orbital paramagnetism also makes an important contribution to the magnetic shielding of nuclei. It seems possible that it may be relevant, for example, to the large Knight-shift in superconducting vanadium[5] and to the anomalous relaxation-time of normal vanadium.[4] The importance of this term in non-transition metals is likely to be smaller, but not necessarily negligible.

Acknowledgement—I am indebted to Professor W. D. KNIGHT for a helpful discussion.

University Chemical Laboratory L. E. ORGEL
Lensfield Road
Cambridge
England

References

1. GRIFFITH J. S. and ORGEL L. E., *Nature, Lond.* **181,** 170 (1958).
2. MOTT N. F. and STEVENS K. W. H., *Phil. Mag.* **2** (8) 1364 (1957).
3. GRIFFITH J. S. and ORGEL L. E., *Trans. Faraday Soc.* **53,** 601 (1957).
4. BUTTERWORTH J., *Phys. Rev. Letters* **5,** 305 (1960).
5. KNIGHT W. D., private communication.

Migration energy of a vacancy adjacent to an impurity*

(*Received* 17 *April* 1961)

THE interpretation of impurity diffusion by means of the "Johnson molecule" requires a vacancy to be attached to the impurity atom during its migration. Theoretical calculations made of the binding energy and the interchange energy of the impurity with the vacancy have been fairly successful in explaining experimental observations.[1] However, the migration of the impurity–vacancy molecule must also involve the interchange of the vacancy with a lattice atom in order to transport the impurity. Since the slower exchange is the rate-determining step, the reasonable agreement of the impurity exchange energy with experiment implies that it is the slower step. In fact HART *et al.* have shown that if the rate of exchange of the solvent atom with the vacancy is the faster, the acceleration of solvent diffusion in impure metals can be readily explained.[2] The change in migration energy of a solvent atom into a vacancy, both of which are adjacent to an impurity, has been treated by considering the lattice strain[3] and the electrostatic charge of the impurity.[4] However, the path of the jumping lattice atom is also influenced by the impurity atom. The purpose of the present calculation is to explore the details of the effect of altering the path on the lattice atom–vacancy interchange, using a Morse function as a potential.

The greatest contribution to the interchange energy of a vacancy with a lattice atom arises from a barrier of four atoms through which the moving atom must pass at a distance closer than the nearest neighbor. The mid-point of this plane of four atoms is, therefore, the saddle point. These four atoms are shown in Fig. 1 as the three solid circles and the large atom with concentric circles. The moving atom–vacancy interchange is represented by the two shaded atoms. Divacancy migration energies calculated by this method have been very low,[5] because not only has one of these four large repulsive terms been removed, but with its removal the moving atom can deviate in its path away from the other three atoms so that it does not come closer than nearest neighbor to any. Instead of completely removing one of these four atoms, a foreign atom is added in this calculation, indicated by the large atom with concentric circles, whose repulsive energy interaction with the lattice atoms is weaker that that of the lattice atoms themselves.

The interaction energy of the atoms was represented by a Morse function, according to which the potential energy $E(r_{ij})$ of two atoms i and j separated by a distance r_{ij} is given as

$$E(r_{ij}) = D\{\exp[-2\alpha(r_{ij}-r_0)] - 2\exp[-\alpha(r_{ij}-r_0)]\} \quad (1)$$

where α and D are constants, and r_0 is the equilibrium distance of approach of two atoms outside

* Supported in part by the U.S. Atomic Energy Commission.

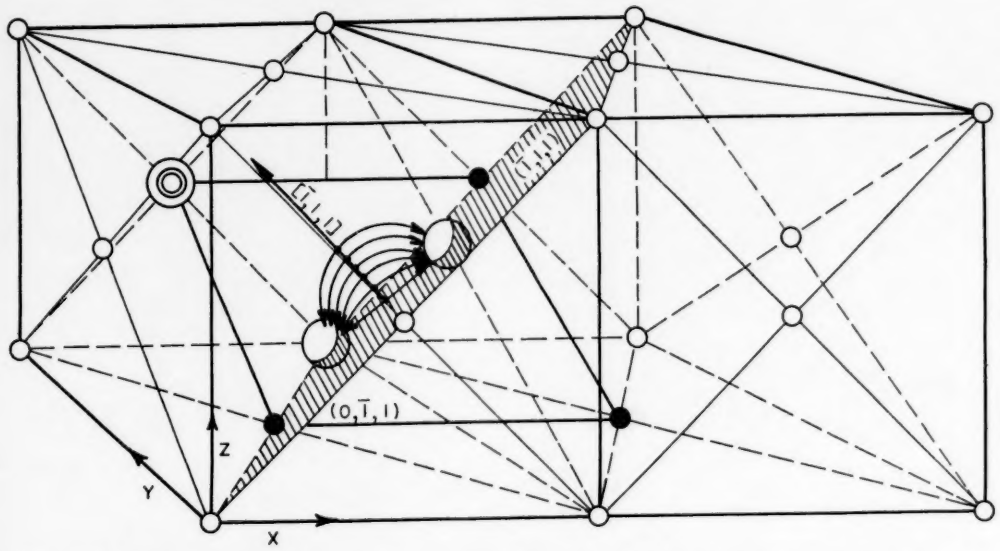

FIG. 1. Calculation model. Shaded atoms—vacancy atom interchange; [1̄, 1, 1] direction—locus of saddle points and maximum path deviation; concentric circles—impurity atom; solid circles—lattice atoms which give greatest repulsive energy contribution.

Vol. 21
1961

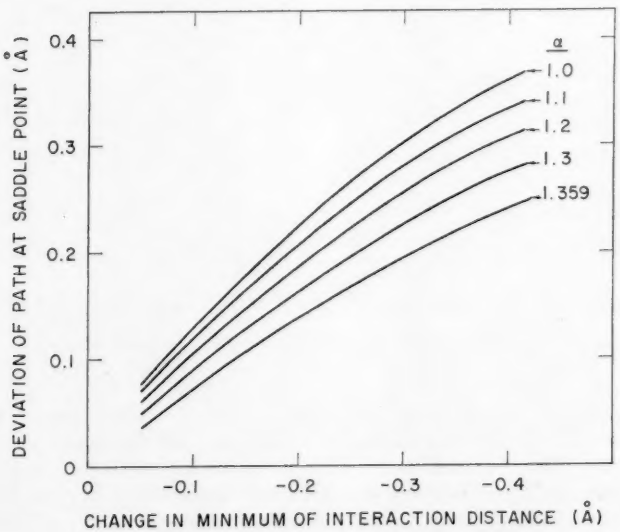

FIG. 2. Curves of saddle point deviation vs. change in minimum interaction distance for a series of α's.

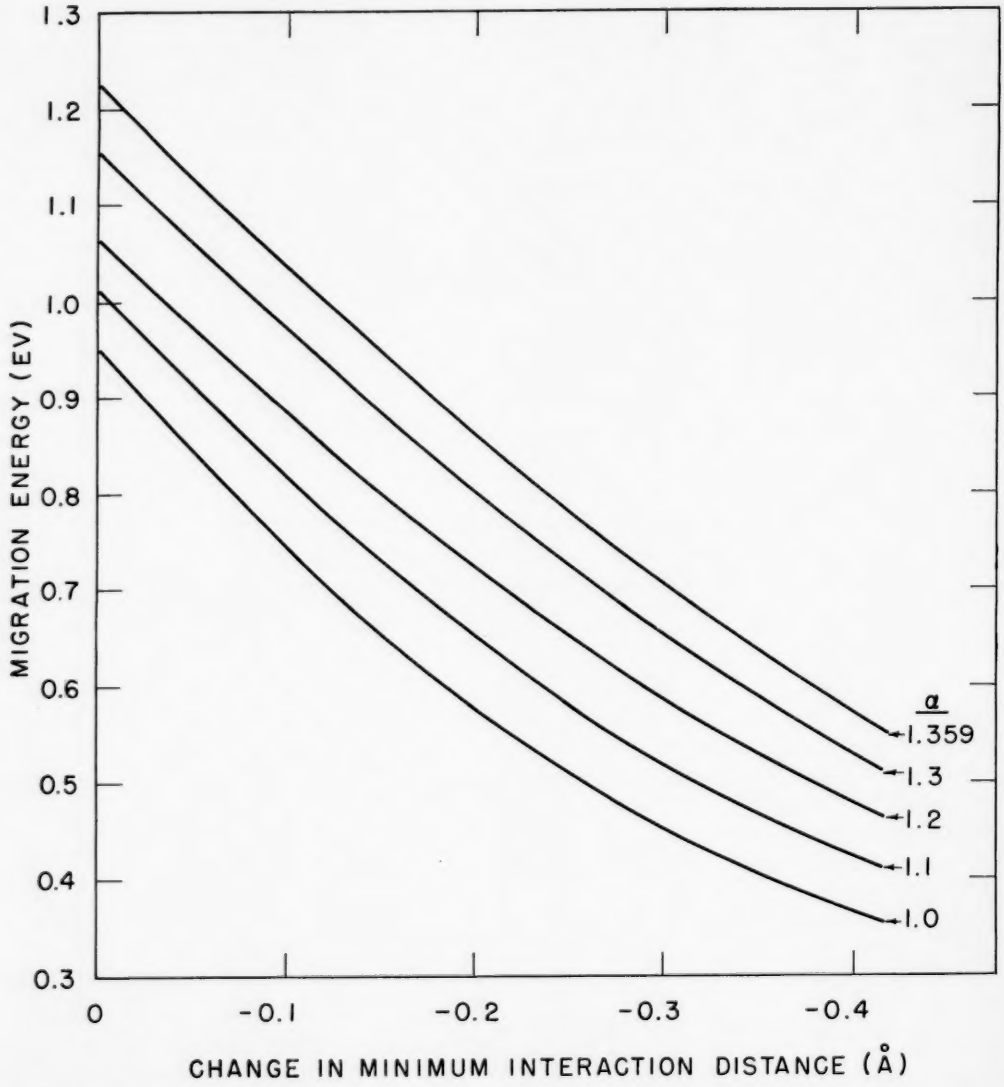

FIG. 3. Variation of vacancy migration energy vs. change in minimum interaction distance for a series of α's.

of the crystal and, therefore, the minimum of the pairwise potential; not the nearest neighbor distance within the crystal. The calculation was done for a copper lattice using $r_0 = 2{\cdot}866$ Å, $D = 0{\cdot}3429$ eV, and $\alpha = 1{\cdot}359$ Å^{-1}, the constants calculated by GIRIFALCO and WEIZER[6]. The potential energy of the moving atom was calculated with respect to all the nearest neighbors of the moving atom, the vacancy, and the impurity. The single interaction with the impurity was calculated separately for a variety of r_0's and α's. The path of deviation, shown as the $[\bar{1}, 1, 1]$ direction in Fig. 1, is also the locus of saddle points. The energy of the moving atom was calculated along this line and the

minimum in energy was found. A change in the potential of the impurity will cause an initial relaxation of the moving atom. This relaxation was calculated along the line between the moving atom and the vacancy and also along the line connecting the moving atom and the midpoint between the impurity and the vacancy, the [1, $\bar{2}$, 1] direction. For the α's and r_0's of interest here, the lower initial energy was found along the [1, $\bar{2}$, 1] direction. For the largest variations in r_0 and α the difference in initial energy in these two directions was 0·15 eV so that the inherent error in not performing a complete calculation in three dimensions is expected to be less than this in these extreme cases, and considerably less for the more moderate changes of α and r_0. The migration energy is the difference between the initial energy and the energy at the saddle point.

The deviation in the path of the moving atom is represented by the concentric arcs in Fig. 1, and the intercept of the path arc with the line of the [$\bar{1}$, 1, 1] direction is the point of maximum deviation. The results are shown in Fig. 2 where the maximum deviation in path is plotted against the decrease of r_0 for a series of α's. Fig. 3 shows the corresponding migration energy of the vacancy against the decrease in r_0 for a series of α's. It is clear that a small change in the path can cause a large change in the migration energy. The upper curve should approach 0·2 eV asymptotically, the value calculated for the divacancy using the same potential. It is obvious that if r_0 and α are larger than those of the lattice atoms the migration energy would increase as the moving atom is forced towards one of the lattice atoms. The left hand intercept of the upper curve is the migration energy of a single vacancy in copper, and the value 1·23 eV is in good agreement with both previous calculations and experiments.

Two important factors have not been included in this calculation. (a) The electronic relaxation was shown by SEEGER and BROSS to be important,[7] and its inclusion would probably give a more realistic value for divacancy migration. (b) A reduction of the r_0 and α of the impurity should cause a relaxation of all the neighbors, thereby increasing the potential energy of the moving atom at all points in its path. This would have a tendency to increase the migration energy and the curves of Fig. 3 would be displaced increasingly upward with decreasing r_0 and α. This correction would require a three dimensional calculation with successive relaxations which is beyond the scope of this demonstration. Such a correction, however, would not alter the general characteristics of the curves of Fig. 3, and would only be worth doing for an accurately known potential.

Acknowledgement—Appreciation is expressed to Dr. G. J. Dienes for helpful discussions.

Brookhaven National Laboratory A. ASCOLI*
Upton A. C. DAMASK†
New York

References

1. LAZARUS D., *Phys. Rev.* **93,** 973 (1954); ALFRED L. C. R. and MARCH N. H., *Phys. Rev.* **103,** 877 (1956); *Phil. Mag.* **46,** 759 (1955); TOBIN J. M. *Acta Met.* **8,** 781 (1960).
2. HART E. W., HOFFMAN R. E. and TURNBULL D., *Acta. Met.* **5,** 74 (1957).
3. OVERHAUSER A. W., *Phys. Rev.* **90,** 393 (1953).
4. LECLAIRE A. D., to be published.
5. BARTLETT J. H. and DIENES G. J., *Phys. Rev.* **89,** 848 (1953); DAMASK A. C., DIENES G. J. and WEIZER V. G. *Phys. Rev.* **113,** 781 (1959).
6. GIRIFALCO L. A. and WEIZER V. G., *Phys. Rev.* **114,** 687 (1959).
7. SEEGER A. and BROSS H., *Z. Phys.* **145,** 161 (1956).

Theory of the resistance mimimum in dilute paramagnetic alloys

(*Received* 17 *May* 1961)

IT HAS kindly been pointed out by a colleague that, in our previous paper[1] (hereafter called I) the formula we derived for the resistivity is inexact at low temperatures, owing to certain approximations which were made in evaluating an energy integral. Whereas the result given in I for the resistivity arising from elastic exchange scattering is correct, namely

$$\rho_{el} = \alpha B_+ \sum_{I=0}^{2S} p_I(2I+1)I(I+1)/4, \qquad (1)$$

* Guest Scientist from Laboratori C.I.S.E., Milano, Italy.

† Guest Scientist from Pitman-Dunn Laboratories, Frankford Arsenal, Philadelphia, Pennyslvania. Supported in part by a U.S. Secretary of the Army Fellowship.

a better approximation for the contribution resulting from inelastic processes is

$$\rho_{\text{inel}} = \alpha B_- \sum_{I=1}^{2S} p_I p_{I-1} W I^2 [(2S+1)^2 - I^2]/2kT(p_I - p_{I-1}). \quad (2)$$

The notation used here is the same as in I.

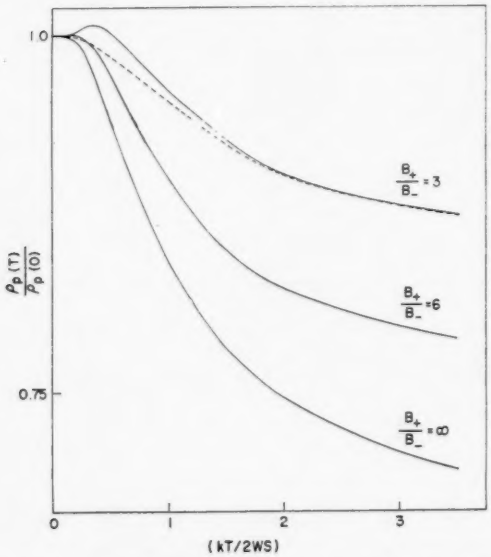

FIG. 1. Resistivity contribution of ferromagnetically coupled nearest-neighbor pairs.

The high temperature expansions of (1) and (2) are identical with those given in I(19) and consequently the total resistivity from ion pairs, $\rho_p(=\rho_{el}+\rho_{inel})$, still yields a minimum when combined with the phonon resistivity. On the other hand, it is apparent that at sufficiently low temperatures the minimum is always preceded by a maximum since, when $kT < W$ and $W > 0$, (1) and (2) are approximately

$$\rho_{el} \simeq \alpha B_+ \{\tfrac{1}{2}S(2S+1) - S[(4S-1)/(4S+1)] \times \exp(-2WS/kT)\}, \quad (3)$$

and

$$\rho_{inel} \simeq \alpha B_- (2WS^2/kT) \exp(-2WS/kT). \quad (4)$$

Clearly the "freezing out" of inelastic scattering processes dominates at sufficiently low temperatures. However, as we shall now show, the size of this maximum is extremely small and over most of the temperature range, the variation of the resistivity is qualitatively the same as described in Reference 1.

The variation of ρ_p with temperature depends of course upon the relative magnitudes of B_+ and B_-. We have discussed this point at length in I and indicate there that the ratio (B_+/B_-) can be significantly greater than unity. Accordingly, in Fig. 1, we have plotted ρ_p vs. T, as calculated from (1) and (2) for an ion spin $S = 3/2$ and values of (B_+/B_-) equal to 3, 6 and ∞—the latter corresponding to purely elastic scattering. Only for the smallest value is a maximum readily discernable and even then the initial resistivity increase amounts to less than 5 per cent of the subsequent decrease with increasing temperature. For the sake of comparison we have also included a plot of ρ_p as derived from our previous formulae (broken line) for the value $(B_+/B_-) = 3$. It is evident that the latter approximation underestimates the relative importance of ρ_{inel}, but apparently there is no essential difference in the variation of ρ_p with temperature above $(kT/2SW) \sim 0{\cdot}5$.

Additional calculations have indicated that the size of the maximum becomes even smaller with a larger spin quantum number S, and for values of (B_+/B_-) which we consider pertinent. We conclude therefore that the *s–d* exchange scattering of conduction electrons by ferromagnetically coupled ion pairs still constitutes a very plausible mechanism for the occurrence of a resistivity minimum in dilute paramagnetic alloys.

Scientific Laboratory A. D. BRAILSFORD
Ford Motor Company A. W. OVERHAUSER
Dearborn, Michigan

Reference

1. BRAILSFORD A. D. and OVERHAUSER A. W., *J. Phys. Chem. Solids* **15**, 140 (1960).

Ionic conductivity of KCl containing sulfate ions

(*Received* 15 *May* 1961)

IT IS WELL known that the effect of divalent

cations dissolved in alkali halide crystals is to increase the extrinsic ionic conductivity, presumably by increasing the positive-ion vacancy concentration.[1] An opposite effect might be predicted for divalent anions, which, if they occupy single halide ion sites, will increase the negative-ion vacancy concentration. These vacancies do not contribute appreciably to conduction except at temperatures near the melting point; by the operation of the mass action principle, an increase of negative-ion vacancy concentration will decrease the concentration of positive-ion vacancies and thus decrease the conductivity.

On the other hand, a large divalent anion such as SO_4^{--} may replace two halide ions, with no direct effect upon the concentration of vacancies.

K_2SO_4 is somewhat soluble in solid KCl. Enough SO_4^{--} ion is incorporated in a single KCl crystal grown from a melt containing 0·1 mole per cent K_2SO_4 so that it may be detected by means of infrared absorption spectroscopy.* The effect of sulfate is definitely to depress ionic conductivity in the extrinsic region. Surprisingly, by sulfate-doping, the conductivity was reduced virtually to the value of the intrinsic conductivity, even at temperatures as low as 360°C.

The crystals were grown from twice-recrystallized KCl and K_2SO_4, by the Czochralski method, using a platinum crucible with a nitrogen atmosphere. Their conductivity was compared with that of good quality undoped crystals.† Specimens for conductivity measurements were approximately 18 mm square by 5 mm thick. Silver electrodes of 0·5 cm² area were evaporated on to the opposite faces of each specimen to insure good electrical contact. The conductivity apparatus held the crystal specimen between nickel-plated brass electrodes under a constant pressure of 2 kg/cm². This pressure assured good contact, but was not great enough to cause any deformation measureable with a micrometer. The assembly, which was kept under a positive pressure of dry argon during measurement, was enclosed in a Vycor container and heated with a nichrome resistance furnace. A square-wave d.c. pulse of 0·66 sec duration was sent through the crystal in series with a ballistic galvonometer, by means of batteries and a motor-driven switch. The voltage used was varied between 1·6 and 930 V. At each voltage used the throw of the galvanometer was standardized by replacing the crystal by a series of precision resistors supplied by Dale Products, Inc. Current direction was reversed on alternate measurements. A chromel–alumel thermocouple, calibrated at the steampoint and the freezing points of tin, lead, zinc, and antimony, was inserted in a well drilled in the upper electrode as a means of measuring the temperature of the crystal.

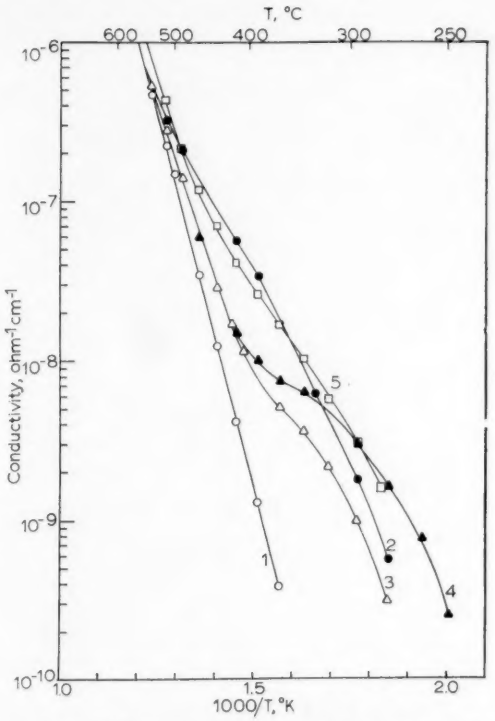

FIG. 1. Conductivity of sulfate doped KCl single crystal. 1. (○) Initial curve; measurements taken with increasing temperature. 2. (●) Measurements with decreasing temperature. 3. (△) Recycle (increasing temperature). 4. (▲) Measurements with increasing temperature after quenching from 500°C. 5. (□) Harshaw crystal.

Figure 1 illustrates the effect of sulfate ion upon the temperature dependence of ionic conductivity.

* We are now investigating the solubility quantitatively using ^{35}S tracer.

† Supplied by Harshaw Chemical Co.

Measurements of Curve 1 were made upon a fresh sample, starting at room temperature and determining the resistance as the temperature increased. Curve 1 is to be compared with Curve 5, that of an undoped good quality crystal. It is seen that the slope of Curve 1 is essentially the intrinsic (high temperature) slope throughout its entirety. On allowing the crystal to cool* while continuing the resistivity measurement, Curve 2 was obtained; increasing the temperature a second time yielded Curve 3. The crystal was then rapidly quenched from 500°. On increasing the temperature, the conductivity then followed Curve 4. When the crystal was annealed at 600°, and brought slowly to room temperature during a period of two days, it was returned to the original condition and followed Curve 1 during subsequent heating.

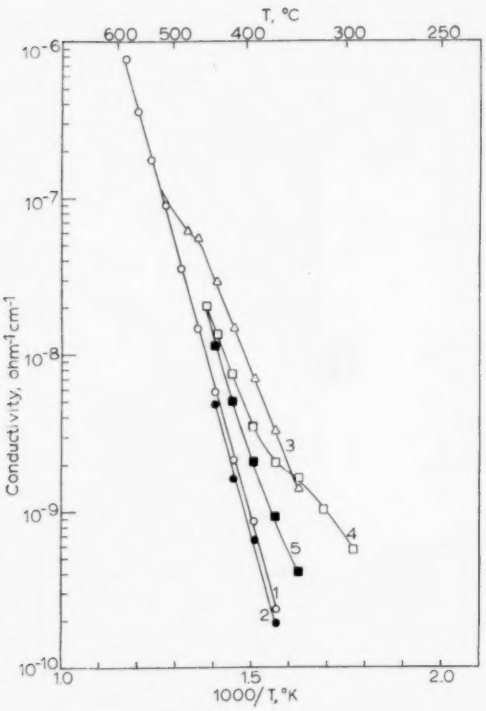

FIG. 2. Conductivity of sulfate-doped KCl single crystal. 1. (○) Initial curve with increasing temperature. 2. (●) Conductivity with decreasing temperature if crystal is not heated above 450°C. 3. (△) Temperature decreasing from 600°C. 4. (□) Increasing temperature after specimen held at room temperature for 68 days. 5. (■) Decreasing temperature from 450°C (continuing from curve 4).

A second sample was subjected to the treatment illustrated in Fig. 2. Provided the temperature was not higher than 450°, the conductivity followed the "intrinsic" curve with increasing or decreasing temperature (Curves 1 and 2). On warming the crystal to 600° and cooling during measurement the conductivity followed Curve 3. On subsequent warming just to 450°, the conductivity tended toward the intrinsic value with increasing temperature (Curve 4) and on subsequent cooling followed nearly the intrinsic slope (Curve 5).

The conductivity hysteresis exhibited upon heating and cooling enables us to select which of the two mechanisms described above is responsible for the repression of extrinsic conductivity by sulfate ion. We believe that SO_4^{--} in solid solution occupies two halide ion sites. At the lower temperatures divalent impurity cations (e.g. Ca^{++} ions) are precipitated as sulfate as a second phase* (e.g. $CaSO_4$), the solubility of which is small enough that the concentration of dissolved divalent cations is less than the intrinsic concentration of positive ion vacancies. An excess of sulfate would have no observable further effect. As the second phase dissolves on warming, the divalent cations effect the positive-ion vacancy concentration, but the dissolved SO_4^{--} is without effect. Thus on rapid cooling, the conductivity is initially enhanced but as the precipitation of the impurities slowly proceeds, it tends toward the intrinsic value; at room temperature the rate of precipitation is essentially nil. Below 450°, equilibrium, once established, is not appreciably disturbed, either because of low solubility of the second phase, or low rate of dissolution, or both. The slow cooling following growth of the original crystals was evidently sufficient for establishment of equilibrium.

* Cooling rate: from 600° to 250° in about 45 min.

* The existence of a second phase has not been established, except in heavily doped crystals, in which case light scattering is observed. An alternative process is the aggregation of divalent cations, positive-ion vacancies and sulfate ions to form complexes of less than colloidal size.

This interpretation relies upon the recent conductivity measurements of GRÜNDIG[2], performed upon very pure KCl. In these experiments no hysteresis upon heating or cooling was reported, showing that equilibrium between the ideal crystal and the vacancies themselves is readily established at temperatures above 350°.

Acknowledgement—We are indebted to Professor H. KANZAKI for valuable discussions concerning the interpretation of this experiment, and to H. COKER who prepared the sulfate-doped crystals. This work was supported by the National Science Foundation.

Department of Chemistry P. M. GRUZENSKY
Oregon State University A. B. SCOTT
Corvallis, Oregon

References

1. KELTING H. and WITT H., *Z. Phys.* **126,** 697 (1949).
2. GRÜNDIG H., *Z. Phys.* **158,** 577 (1960).

Vol. 21
1961

On the behaviour of electroluminescent phosphors on irradiation with ultra-violet

(*Received* 16 *February*; *revised* 21 *April* 1961)

ELECTROLUMINESCENCE is attributed to impact ionization of the luminescence centres in the vicinity of an exhaustion barrier.[1] The electrons in the conduction band are assumed to obtain sufficient energy by acceleration in a high field zone in the exhaustion barrier to cause the ionization by collision. It is assumed that virtually the whole field is concentrated across the barrier, because of the high positive space charge formed in the barrier region by the field excitation of electrons in trapping states below the conduction band. As all these processes occur in a thin barrier (10^{-5} cm), irradiation with ultra-violet during electroluminescence can have little effect.

Whilst investigating the relationship between electroluminescence and infra-red emission,[2] it was observed that the irradiation of an electroluminescent phosphor with ultra-violet caused enhancement of the visible emission. This effect cannot be detected by means of a d.c. system (i.e. a photomultiplier feeding a galvanometer or an oscilloscope) as there is a large increase in the intensity of emission due entirely to the photoluminescence response of the phosphor. In this particular work the phosphor in an electroluminescent cell[3] was energized by a 400 cycle alternating potential and thus the brightness of the emitted light was modulated at 800 cycles. This radiation was detected and the signal obtained fed to an 800 cycle amplifier. The large d.c. component of the radiation was rejected at the amplifier. The results obtained are shown in Fig. 1. The ultra-violet source alone gave no effect but

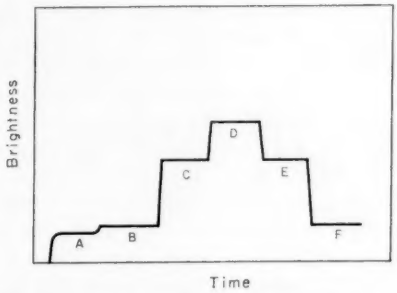

FIG. 1. Effect of ultra-violet on the electroluminescence of ZnS: Cu, Al phosphors. A: field along; B and F: field and ultra-violet; C and E: field emission of electroluminescent phosphor; D: field emission of electroluminescent phosphor enhanced by ultra-violet.

in conjunction with an electroluminescent panel a large enhancement of the signal was obtained. By means of filters it was shown that this emission and the enhanced emission was in the green.

Previous workers[4,5] have reported a similar effect. The enhancement has been explained using the impact ionization model. The field in the exhaustion barrier is thought to be enhanced by increasing the positive space charge by trapping the holes in deep levels above the valence band. Such transitions should give rise to emission in the infra-red but with the equipment described no such emission could be detected using a PbS cell. Unless the holes are trapped and the electrons swept to the other end of the crystal it is difficult to understand the enhancement of electroluminescence on the impact ionization model.

It would appear that the ultra-violet radiation will cause the transition of electrons from the

valence band into the conduction band. The release of these electrons and the production of holes will increase the conductivity and will, therefore, effectively decrease the voltage across the barriers. As there is a negligible field in the region between the barriers it is not possible for these electrons to gain sufficient energy for the field to ionize luminescent centres by impact. After an initial build-up period, it may be assumed that a very large proportion of the centres in the barrier take part in the process giving rise to emission and further ionization of these centres by the radiation cannot cause a large increase in the electroluminescent emission.

The effect reported here may alternatively be explained by the assumption that the holes take some part in the processes of electroluminescence. It has been shown[5] that excess copper has a considerable effect upon the crystal structure of zinc sulphide. The separation of a phase of copper sulphide leads to the conversion of a large proportion of the wurtzite to sphalerite. It is possible that this effect is due to nucleation by the cubic copper sulphide. The islands of copper sulphide will cause the growth of cubic zinc sulphide containing very large concentrations of copper ions. From this point of view it is to be expected that solubility of copper in hexagonal zinc sulphide will be small. It is possible, therefore, that the effect of the excess copper is to produce a phase of cubic material containing hexagonal material with a low concentration of copper ions.* Under these conditions in the cubic phase the wave functions of the pertubed states may overlap and an impurity band may be formed and one may assume that regions of such material are in contact with less heavily doped *n*-type material, Fig. 2, of hexagonal structure. Electroluminescence may then be ascribed to the following processes.

(1) With A negative, electrons in the centres L may tunnel into the impurity band ($L \rightarrow C$). The observation that there is no infra-red emission makes it improbable that the valence band is involved in the processes occurring during this cycle, as recombination between free holes in the valence band and electrons in the centres should give rise to such emission.

(2) With the field reversed, electrons from the impurity band may tunnel either into the states of the conduction band or into the traps T. The first process is likely and will be followed by two other processes, (a) direct recombination of the electrons with the ionized luminescent centres, (b) trapping of the electrons in the states T. The electrons trapped in T will be released thermally into the conduction band and recombine with the luminescent centre L with the emission of photons of energy $h\nu$. This process will be field dependent and sufficient energy can be acquired by combination of electrical and thermal process. A long mean free path is not implied so that the failure to detect extinction in a magnetic field can be explained.[6]

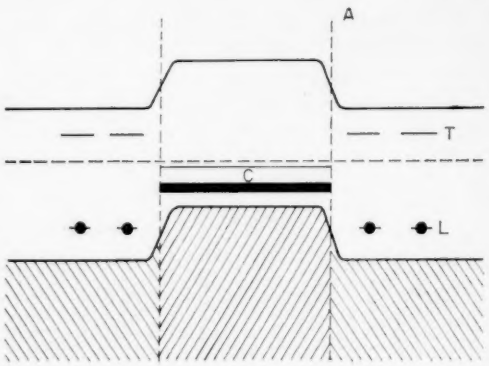

FIG. 2. A proposed simplified model for electroluminescence. No attempt has been made to depict the probable shapes of the various bands, they are shown schematically.

On this model the effect of ultra-violet is easily explicable. Absorption of ultra-violet by the impurity band will decrease the occupancy of the band, and hence the number of electrons which can tunnel from the level L will be increased. As it is these electrons which are finally transferred to T, the brightness of the emitted light will be enhanced.

The model proposed in this note is being investigated in more detail and the results will be published shortly. Qualitatively, such a model gives the correct temperature dependence as the electroluminescence cannot occur until the traps

* The evidence here is still far from certain. See AVEN M., and PARODI J. A., *J. Phys. Chem. Solids* **13,** 56 (1960) and GOLDBERG P., *et. al., J. Electrochem. Soc.* **108,** 21 (1961).

T can be emptied thermally. The build-up of trapped electrons which cannot obtain sufficient energy to be released thermally will cause a potential which will nullify the effect of the applied field. This field may prevent tunneling to the conduction band. If direct tunneling to the traps is probable the effect of the non-emptying of traps is obvious. The saturation of the emission at higher frequencies is implied due to the relaxation time of the traps.[1]

Department of Physics D. W. G. BALLENTYNE
University of Hull
Hull, England

References

1. See for example IVEY H. F. and DESTRIAU G., *Proc. Inst. Radio Engrs., N.Y.* **43,** 1911–1940 (1955).
2. BALLENTYNE D. W. G., *J. Phys. Soc.*, in press.
3. BALLENTYNE D. W. G., *J. Electrochem. Soc.* **107,** 807 (1960).
4. GUMLICH H. E., thesis, Tech. University of Berlin (1958).
5. CUSANO D. A., thesis, Rensselaer Polytechnic Inst. Troy, N.Y. (1959).
6. INCE H. F., *Proc. Phys. Soc. Lond.* **67B,** 870 (1954).

Vol. 21
1961

BOOK REVIEWS

Proceedings of the Fourth Conference on Carbon. (Edited by S. MROZOWSKI) Pergamon Press, Oxford, 1960. 778 pp., £7 10*s*.

THE Proceedings on the Fourth Conference on Carbon held at the University of Buffalo, January 15–19, 1959, is a massive collection of information on the status of carbon and graphite science and technology at the time of the conference. It is a beautifully prepared volume on which the editor can be complimented.

The program of the conference was divided into five parts: Part I, Surface Properties, Adsorption and Reactivity; Part 2, Electronic Properties; Part 3, Carbonization, Graphitization and Structure; Part 4, Mechanical and Thermal Properties; Part 5, Carbon Technology, Friction and Wear.

Under the heading of Surface Properties, Adsorption and Reactivity were included papers on surface chemistry, physical adsorption, and various aspects of catalysis involving graphite and graphite compounds. Part 2 on the Electronic Properties comprised a comprehensive presentation of the energy band structure, transport phenomena and resonance behavior of graphite. Also included was a discussion of the effect of doping on the properties of carbons and graphites. Part 3 on Carbonization included several papers, which presented X-ray electron microscopy and other special techniques for investigating the structure of metamorphous carbons and graphites. Section 4 on Mechanical and Thermal Properties included discussions of both graphite and carbons. The mechanical strength of pyrolytic graphites was discussed; the defects produced by irradiation were also mentioned. In the last session on Carbon Technology, several aspects of carbon and graphite processes were reviewed. In addition, the properties of graphites and carbons relevant to certain applications were presented in papers on wear and friction.

Although this conference was held in mid-1959 and is just being published, the information is still quite timely. The Proceedings can be recommended to anyone who wishes to obtain in one volume a rather complete survey of the field.

J. A. KRUMHANSL

A. E. GREEN and J. E. ADKINS: **Large Elastic Deformations and Non-Linear Continuum Mechanics.** Oxford University Press, 1961. xiii+347 pp., $8.80.

THE mathematical theory of large elastic deformations has progressed at a rapid pace during the last decade. Indeed, the progress has been such that the theory may be said to have begun with the publications of R. S. Rivlin in the late nineteen-forties, despite the much earlier work on the foundations of the theory. An account of most of the work prior to 1953 can be found in *Theoretical Elasticity* by A. E. Green and W. Zerna, published in 1954, and the present volume supplements this previous book and brings the account up to date.

As in the earlier volume, tensor notation is used systematically throughout. In Chapter I a summary of the notation and of the basic formulae for large elastic deformations is given, the reader being referred to *Theoretical Elasticity* for a detailed exposition. Chapter I then continues with a discussion of the form of the strain-energy function for the various crystal classes and the derivation of the stress–strain relations for particular kinds of anisotropic materials. The effect of imposed geometrical constraints on the stress–strain relations is also considered and this theory is applied in Chapter VII to the important technological problem of elastic materials reinforced by systems of inextensible cords.

Chapter II presents exact solutions to problems for both isotropic and anisotropic materials and for the most part with a completely general form of the strain-energy function. The problems for which exact solutions exist are necessarily simple and usually involve a high degree of symmetry. Nevertheless the problems are important as their solutions can be used in conjunction with experimental results, as described in Chapter X, to evaluate the mechanical properties of real materials.

The simplifications which result if the body is assumed to undergo a deformation in which the displacement component in a fixed direction is either zero (finite plane strain) or proportional to distance along that direction are considered in Chapter III. For this two-dimensional situation the theory can be formulated in complex variable

notation, but the governing equations are still highly non-linear and again only special problems are exactly solvable. Some approximate solutions to plane strain problems are exhibited in Chapter VI, the solutions being obtained by an adaptation of the method of successive approximations developed in Chapter V for a general three-dimensional deformation. This method assumes that the displacement vector can be expanded as a power series in a parameter ϵ which is typical of the deformation. The coefficients of the powers of ϵ in the series can be determined in principle by the successive solution of a sequence of problems in classical infinitesimal elasticity theory.

Chapter IV treats plane stress and the deformation of membranes. Axially symmetric membranes are examined in detail and some solutions are provided.

The thermodynamics of deformation and the heat-conduction law for strained bodies are discussed in Chapter VIII, while Chapter IX deals with the theory of stability for finite deformations.

The eleventh and last chapter is concerned with rheological equations of state for more general materials which exhibit inelastic effects such as stress relaxation and creep. After some kinematical preliminaries, attention is confined to materials whose constitutive equations involve the state of stress and its time rates of variation and also the displacement, velocity and successive acceleration gradients. The effect of isotropy at some instant of time in the history of the material is considered, and the forms of the constitutive relations for some simple types of materials, including the hypoelastic material, are derived.

This book should be of value to all interested in the mathematical theory of large deformations.

R. T. SHIELD

E. H. PUTLEY : **The Hall Effect and Related Phenomena**. Butterworths, London, 1960. viii + 263 pp., 50*s*.

PERHAPS the first reaction that comes to mind on examining this book is that its name is not a very good description of its contents. Although as a specific physical property, the Hall effect does occupy a position of prominence, all other electronic transport properties are treated in nearly the same depth, and the electronic structure of a variety of semiconductors is given rather thorough coverage. Therefore, one feels that the author would have done more justice to his efforts if the title *Transport Properties and Electronic Structure of Semiconductors* had been chosen.

In the preface, the author states that his approach in this volume is primarily from the experimental side. However, adequate theoretical background is included to provide a coherent treatment of the properties themselves, and their relation to fundamental parameters of electronic structure in various semiconducting systems. For example, an entire chapter is devoted to semiconductor statistics and the solution of the Boltzmann transport equation in the presence of electric and magnetic fields and thermal gradients. From this development, expressions are obtained for the galvanomagnetic effects, the thermomagnetic effects, and thermoelectric effects. An excellent tabulation of both the pertinent formulae and the transport coefficients is included for the various important cases such as classical statistics, complete degeneracy, mixed conduction, etc.

The following chapter relates transport properties to the electronic structure of typical semiconductors in a lucid and effective treatment of the subject and the final chapter discusses results that have been obtained on a variety of semiconductors, both elemental and compound.

This book fulfills its objective of covering the field of electronic transport phenomena in semiconductors in a competent and useful way. The author's long standing activity within this field of research has made him sensitive to the needs of experimenters as the organization and treatment of subject matter demonstrates. Although the references and bibliography are not as complete as might be desired in a comprehensive treatise, and there are certain minor omissions of subject matter, the reviewer feels that this book is of considerable value to both the newcomer and the experienced worker in the field.

J. H. CRAWFORD, JR.

ERRATA

RYOICHI KIKUCHI, Statistical dynamics of crystalline diffusion—II and III, *J. Phys. Chem. Solids* **20,** 17, 35 (1961).

Ann. Phys., Paris should read *Ann. Phys., New York,* in Refs. 1, 10, p. 33 and Refs. 2, 3, p. 40.

J. S. SMART, Magnetic short range order and specific heat in ferromagnets and antiferromagnets, *J. Phys. Chem. Solids* **20,** 41 (1961).

Ann. Phys., Paris should read *Ann. Phys., New York,* in Ref. 11, p. 46.

J. Phys. Chem. Solids Pergamon Press 1961. Vol. 21, Nos. 3/4, pp. 137–145. Printed in Great Britain.

ON THE THEORY OF SURFACE STATES

E. ANTONČÍK

Institute of Technical Physics, Czechoslovak Academy of Sciences, Prague

(*Received* 24 *April* 1961)

Abstract—A new method is elaborated for calculating Shockley-type surface states; this method is analogous to a certain modification of the OPW method, using a repulsive potential. The symmetry of the wave functions of surface states is discussed in this connection. Some concrete conclusions reached by this method are illustrated on the example of the energy spectrum of crystals having a diamond lattice.

Vol. 21
1961

INTRODUCTION

IN THIS paper we shall only deal with Shockley-type surface states, i.e. we shall assume that by limiting the crystal by a plane the periodic potential inside the crystal does not change. This problem had been dealt with before SHOCKLEY's paper[1] by a number of authors, in particular by MAUE[2] from the point of view of the method of nearly free electrons and by GOODWIN[3], who apart from this method also used the tight binding method.[4] In later papers this problem is solved from the aspect of high energy approximation by STATZ[5] and LIPPMANN[6], from the point of view of the tight binding method or its equivalent by ARTMANN[7], KOUTECKÝ and TOMÁŠEK[8] etc. Nearly all these papers start out from a one-dimensional crystal or from very simplified models of a real crystal and its band structure, so that the general validity of the conclusions reached in these papers is sometimes problematic. Moreover, in papers using the method of nearly free electrons or its equivalent, the solution of the Schrödinger equation is not always correctly formulated, which in some cases[2, 5] leads to an incorrect interpretation of the results. In view of further considerations it would be wise to deal with the results of these papers in somewhat greater detail.

A simple but intuitive case is given by STATZ[5], who deals in detail with the conditions for the formation of Shockley-type surface states in one-dimensional crystals. One of his cases is shown in Fig. 1; the potential energy of the electron in the crystal is given in the lower part of the figure, and the energy levels both of the band and of the localized states in the upper part. The potential term in Schrödinger's equation is $\alpha V(x)$ for STATZ's type, where the parameter α characterizes the degree of binding of the electron and its sign the course of the potential energy in a one-dimensional crystal. It is clear from Fig. 1 that surface states are produced only for $\alpha < 0$. STATZ, however, thinks that the course of the potential for $\alpha < 0$ does not correspond to the real conditions in the crystal; on the other hand, the formation of surface states can easily be explained in this case by the existence of potential holes on the crystal surface.[6]

Apart from the potential energy plotted in Fig. 1, STATZ also considered square-well potentials. Without going into detail, we shall give merely the conclusions of his considerations: from an analysis of both cases STATZ judges that in the case, which is the only physically justified one, i.e. the plane limiting the crystal is led in the centre between the lattice planes of the originally infinite crystal, one must confine oneself to the case $\alpha > 0$; it follows from this, of course, that as long as the lowest energy band is ascribed to the valence band in the one-dimensional case (and this classification cannot be made without certain difficulties according to STATZ), no surface state exists in any case in the forbidden band between the valence and conduction bands.

STATZ also shows that his case also includes MAUE's results.[2] The validity of his conclusions can also be extended to GOODWIN's work,[3]

which deals with a simple cubic crystal but in the case in question the formulation of this problem is quite analogous to MAUE's one-dimensional case.

It is obvious from all this that the conclusions of all these papers are confined either to a one-dimensional crystal or to a simple three-dimensional crystal, which of course is far from corresponding to a real crystal lattice, not to mention the fact that the method of nearly free electrons used in this formulation is not suitable for practically calculating a band spectrum[9] and its application to surface states is questionable. In order to avoid all these difficulties, it seems best to use some proved method for calculating the band spectrum in a real crystal, modified for calculating surface states. This means that the accuracy of the results can be estimated at least approximately beforehand and that the surface levels can be correlated with the volume levels within the framework of one method.

The existence of surface states plays a very important role in the theory of surface phenomena in semiconductors and metals. One of the most successful methods used for calculating the energy spectrum of these materials is the OPW method and it thus seems suitable for use in further considerations. We shall confine ourselves below to the use of a simple variation of this method in which the strict orthogonality condition is replaced by the repulsive potential.[10] This method, in which the wave functions are chosen in the form of the linear combination of plane waves, is formally close to the methods used in previous papers,[1,2,3,5] so that the results and conclusions of all these methods can be directly correlated.

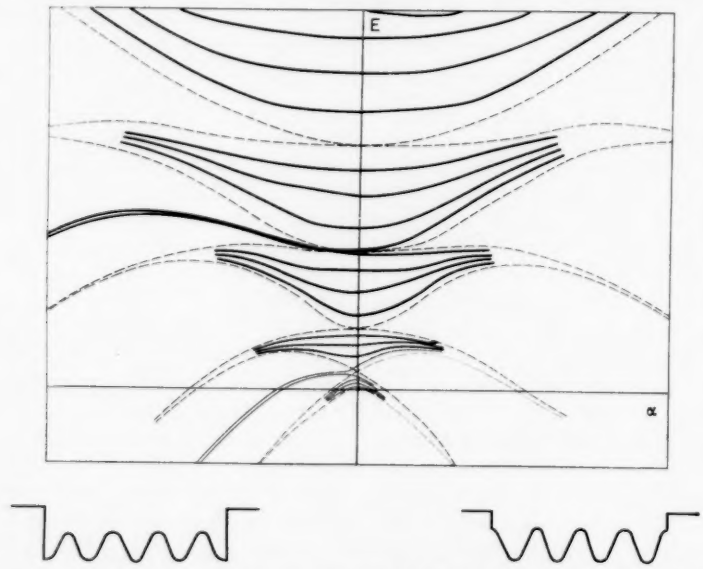

FIG. 1. Energy spectrum of a one-dimensional finite crystal as a function of the parameter α (after STATZ[5]).

SYMMETRY OF WAVE FUNCTIONS IN LIMITED CRYSTAL

According to the approximate formulation of the OPW method[10] the Hamiltonian operator inside the crystal can be written in the form

$$\mathscr{H} = -\Delta + V + V_{\text{rep}}; \qquad (1)$$

Δ is the Laplace operator, V the potential energy of the electron and V_{rep} an operator by means of which the orthogonality condition for wave functions of the valence or conduction bands is respected. As was mentioned above, these functions are chosen in the form of a linear combination of plane waves, which in general are not

orthogonal to the wave functions of core electrons; in the special case, when the orthogonality condition is satisfied, the term V_{rep} is identically zero according to Ref. (10).

A very important condition, which must be respected when solving the Schrödinger equation with a Hamiltonian operator (1), is the symmetry of the crystal lattice and thus also the symmetry of the wave functions. If we consider an infinite crystal, the group of the Schrödinger equation is the space group of the crystal. It can be proved[11] that the wave functions, which are the solution of the Schrödinger equation with the Hamiltonian operator (1), must form the basis for the irreducible representation of the group of $\boldsymbol{k}$; they can thus be written in the form of a linear combination of symmetrized plane waves.

When studying volume properties we consider an infinite crystal lattice, in which we choose a certain cyclic domain and require the Born–Kármán conditions to be valid with respect to it, but when investigating surface states we start out from a crystal limited by a certain plane (or several planes). Obviously the simplest form of a limited crystal is a half-space in which, as in the case of volume states, we choose a suitable domain, one plane of which coincides with the limiting plane of the crystal lattice half-space. In this plane of course, the periodic Born–Kármán conditions are replaced by other conditions, which will be dealt with later in greater detail. It is obvious that the symmetry of such a limited crystal lattice is smaller than that of the originally infinite crystal.

When the crystal has the form of a half-space, an analogous procedure may be followed in group analysis as when the crystal is infinite except that only those operators from the space group, which transform the crystal into itself, should be taken into consideration; in the case in question this is analogous to the two-dimensional problem. Those operators of the group of $\boldsymbol{k}$, which satisfy this condition, form a sub-group, which will be denoted below by $S_{\boldsymbol{k}}$. The wave functions of the electrons in this crystal must form the basis for the irreducible representation of the sub-group $S_{\boldsymbol{k}}$.

An analogous procedure may be followed in a crystal limited by two parallel planes, which is the three-dimensional analogy of a one-dimensional finite crystal. This form of crystal differs from the case of a half-space introduced by us in that the generating elements of the sub-group $S_{\boldsymbol{k}}$ are joined by another element corresponding to the operator which transforms the crystal into itself, whereby one limiting plane is transformed into another. Even in this case the wave functions must be constructed so that they form the basis for the irreducible representation of the sub-group $S_{\boldsymbol{k}}$ extended in this way. This form of crystal is particularly suitable for studying the origin of surface states with respect to the energy spectrum of an infinite crystal since we can easily pass from a limited to an infinite crystal by introducing suitable boundary conditions on the boundary planes. It also follows from this that it is convenient to use the surface states of wave functions corresponding to the originally infinite crystal when constructing wave functions, since then the surface states can be directly correlated with the volume states.

SHOCKLEY-TYPE SURFACE STATES

For the sake of simplicity we shall confine ourselves below to investigating the conditions for the existence of surface states on the surface of a crystal having the shape of a half-space, assuming that the plane defining the surface is chosen so that it passes in the centre between two neighbouring lattice planes of an infinite crystal. The orientation of this plane obviously defines the elements of the sub-group $S_{\boldsymbol{k}}$ and the symmetry of the wave functions and the existence of surface states will depend on the orientation of the crystal surface.

The solution of the Schrödinger equation thus has two parts: the solution of this equation inside the crystal and outside the crystal. In the first case we write the Hamiltonian operator in the form of (1), and in the second case choose $V = V_{\text{rep}} = 0$.

From the general form of the Hamiltonian operator (1) we can immediately reach two conclusions which from the general point of view somewhat clarify STATZ's conception. First and foremost, it is obvious that the course of the potential energy is not determined, as STATZ thinks, only by the course of the potential energy V inside the crystal but by the course of the effective potential energy $V+V_{\text{rep}}$. Since the term V_{rep} can to a certain extent compensate or even exceed the term V[12], this means that STATZ's criterion must be applied to the course of the effective potential energy. And this may have a quite different character to that

Vol. 21
1961

of the term V, on which STATZ bases his considerations. Of course, in quite exceptional cases, when V_{rep} is identically zero, STATZ's original criterion is valid.

The introduction of the repulsive potential eliminates another ambiguity, which STATZ also mentions; this is the ambiguity in ascribing the different bands of the one-dimensional model to the valence and conduction band of a real crystal. According to Ref. (10) the wave functions of core electrons should be used in constructing the operator V_{rep}. Then, of course, the lowest band corresponds quite unambiguously to the valence electrons, whereby the problem of classification is solved.

For the general construction of the wave functions of surface states the somewhat modified method of MAUE[2] may be used, supplemented by group analysis, as was mentioned earlier.

We choose a suitable coordinate system ξ,η,ζ so that the ζ axis is normal to the plane of the crystal surface, and denote the corresponding coordinate of the point of intersection of the ζ axis with this plane by ζ_0; the coordinates ξ,η then define the position of any point on the crystal surface. MAUE shows that when solving the Schrödinger equation inside the crystal there exist N^2 suitable solutions $\psi_{\lambda\mu}$ for given k_ξ and k_η and energy E. N is the number of elementary cells of the domain in the ξ or η direction. The general wave function inside the crystal must be written in the form of a linear combination

$$\Psi = \sum_{\lambda\mu} a_{\lambda\mu}\psi_{\lambda\mu} \quad \zeta < \zeta_0. \tag{2}$$

The wave function outside the crystal can be written analogously

$$\Psi = \sum_{lm} b_{lm}\phi_{lm} \quad \zeta > \zeta_0 \tag{3}$$

where ϕ_{lm} has the form

$$\phi_{lm}(\xi,\eta,\zeta) = w_{lm}(\zeta)\exp i[(k_\xi + K_{\xi l})\xi + (k_\eta + K_{\eta m})\eta]. \tag{4}$$

Since the wave functions (2) and (3) must be continuous and have a continuous derivative for $\zeta = \zeta_0$, it is convenient to write the functions $\psi_{\lambda\mu}$ in the form of an expansion

$$\psi_{\lambda\mu}(\xi,\eta,\zeta) = \sum_{lm} v_{lm}^{\lambda\mu}(\zeta)\exp i[(k_\xi + K_{\xi l})\xi + (k_\eta + K_{\eta m})\eta]. \tag{5}$$

The fulfillment of the boundary condition gives the following system of equations

$$\sum_{\lambda\mu} a_{\lambda\mu} v_{lm}^{\lambda\mu}(\zeta_0) = b_{lm} w_{lm}(\zeta_0)$$

$$\sum_{\lambda\mu} a_{\lambda\mu} v'^{\lambda\mu}_{lm}(\zeta_0) = b_{lm} w'_{lm}(\zeta_0). \tag{6}$$

In order to determine the coefficients $a_{\lambda\mu}$, we must solve the equation

$$\det|v_{lm}^{\lambda\mu} w'_{lm} - v'^{\lambda\mu}_{lm} w_{lm}| = 0. \tag{7}$$

Since the functions $v_{lm}^{\lambda\mu}$ and w_{lm} depend on k_ξ and k_η and the energy E, equation (7) may be regarded as the equation defining the energy of the surface state.

However, as GOODWIN states,[3] this general procedure is not very suitable for practical calculation and therefore, as usual,[13] we shall confine ourselves to the simple case when only one term corresponding to a certain function $v_{lm}^{\lambda\mu}$ plays the dominating role in the expansion (5) so that the contribution of the other terms can be neglected. It is obvious that we have chosen this procedure mainly because of the simplicity of the calculations since the general solution of this problem is numerically relatively complicated. At the same time our results can be directly correlated with previous papers,[1,2,3,5,6] which are substantially confined to the same approximation.

If it is assumed, therefore, that with the exception of one term in expansion (5) all the others can be practically neglected, then the whole procedure is greatly simplified since the determinant (7), which is of the order of N^2, reduces to a determinant of the first order and can be written in the form

$$\frac{v'^{\lambda\mu}_{lm}}{v_{lm}^{\lambda\mu}} = \frac{w'_{lm}}{w_{lm}}. \tag{8}$$

It thus remains to determine the function $\psi_{\lambda\mu}$ and the corresponding function ϕ_{lm}. At the same time we shall deal with the question of the symmetry

Vol. 196

of these functions and their transformation properties with respect to the operators of the sub-group S_k, which has so far not been considered for the sake of simplicity.

If the surface state is to be localized in the neighbourhood of the surface plane, it is obvious that the ζ-th component of the wave vector must be complex; the energy of this state falls into the region of the forbidden band and it can be proved[1,2,3] that the value of the real part of the ζ-th component of the wave vector corresponds to the boundary plane of the Brillouin zone. Since the boundary conditions may become the Born–Kármán condition by a gradual change, which corresponds to the transition of possible surface states to volume states, we can assume for the sake of simplicity that the wave function of the surface state for $\zeta < \zeta_0$ has the form

$$\psi_{\lambda\mu} = e^{q\zeta} \sum_i c_i \varphi_i; \tag{9}$$

the functions φ_i are suitable linear combinations of the wave functions of the volume spectrum corresponding to the point on the boundary of the Brillouin zone in question chosen so that the functions $\psi_{\lambda\mu}$ form the basis for the irreducible representation of the sub-group S_k. The coefficients c_i are determined in the usual manner by substituting $\psi_{\lambda\mu}$ into the Schrödinger equation with the Hamiltonian operator (1). The function determined in this way is then expanded according to expansion (5), by which we get the corresponding $v_{lm}^{\lambda\mu}$. The function ϕ_{lm} is determined in an analogous manner, care being taken that the function transforms in the same way as $\psi_{\lambda\mu}$; from equation (8) we then get the energy value of the surface state.

Up to now we have considered a crystal limited by one plane. It is quite easy to pass to a crystal limited by two parallel planes but of course on condition that its thickness is sufficiently great.[13] It can be proved that by using the reflection operator a second function can be formed from that determined on one surface plane, which corresponds to the surface at the second plane with the same energy. From a linear combination of both functions it is then possible to form two functions, one of which is symmetrical and the other antisymmetrical with respect to the reflection operator which transforms one surface plane into another.

THE SURFACE STATES OF A DIAMOND LATTICE

In this section we shall try to illustrate some of the general conclusions of the above paragraphs on the example of a diamond lattice. Although this lattice is somewhat more complicated than the lattices of some other materials, particularly metals, the energy spectrum of the volume states of some materials crystallizing in this structure, such as diamond, silicon and germanium, is relatively well known, and the surface states of such elements play a very important role in some effects and for this reason are relatively well studied.

As is known,[14] the extended Brillouin zone of a diamond lattice is defined by the planes given by the equation

$$\boldsymbol{k} \cdot \boldsymbol{K} = \tfrac{1}{2}K^2, \tag{10}$$

where

$$\boldsymbol{K} = \left(0, \pm\frac{4\pi}{a}, \pm\frac{4\pi}{a}\right)$$

and cyclic permutations. In the band spectrum the states corresponding to the centres of the areas of the dodecahedron, defined by the vector

$$\boldsymbol{k}_X = \left(0, \pm\frac{2\pi}{a}, \pm\frac{2\pi}{a}\right)$$

and cyclic permutations, are usually denoted as the point X. It is shown[15] that in the band spectrum of diamond, silicon and germanium the two-dimensional representation of X_4 corresponds to the valence band and likewise the two-dimensional representation of X_1[2] to the conduction band. The general point in the plane defined by equation (10) is characterized merely by two one-dimensional representations, which correspond to the appropriate discontinuity of the energy on the boundary of the Brillouin zone.

As has already been mentioned, the orientation of the boundary planes of the Brillouin zone also defines the plane of the crystal surface on which surface states may be formed. In the case in question, therefore, we can expect the formation of surface states primarily on the surface limited by the (011) plane. Due to the symmetry of the problem it will be more convenient to choose a new coordinate system (ξ,η,ζ) so that the ζ axis coincides with the normal of the (011) plane and the x axis $\equiv \xi$. The sub-group S_k then contains

Vol. 21
1961

only two elements, the identity and the reflection on the $\eta = 0$ plane.

Due to the degeneration of the states $X_1^{(2)}$ and X_4 the conditions in this point are somewhat more complicated than in a general point on this plane of the Brillouin zone. Despite this, however, we shall first deal with the point X since it can easily be proved that the surface states in a general point on the boundary plane of the Brillouin zone have the same character, and the derivation of the appropriate relations is practically performed by solving for the point X, which is the more general case.

As has already been stated, always two wave functions correspond to the volume states X_4 and $X_1^{(2)}$, and these form the basis for the corresponding two-dimensional representation. In general, these functions have the form of a Fourier expansion; due to our approximation, however, we can confine ourselves to the dominating terms in this expansion. It can easily be proved that, for example, for diamond the wave functions and corresponding energies are given in this approximation by the expressions[10, 16]

$$X_4\colon\ \varphi_4' = \sqrt{\frac{2}{\Omega}} \sin k_X \zeta$$

$$\varphi_4'' = \sqrt{\frac{2}{\Omega}} \sin k_X \eta$$

$$E_4 = k_X^2 + V_0 - V_{4\sqrt{(2)}(\pi/a)}$$

$$X_1^{(2)}\colon\ \varphi_1' = \sqrt{\frac{2}{\Omega}} \cos k_X \zeta$$

$$\varphi_1'' = \sqrt{\frac{2}{\Omega}} \cos k_X \eta \qquad (11)$$

$$E_1 = k_X^2 + V_0 + V_{4\sqrt{(2)}(\pi/a)} + 2V_{\mathrm{rep}}^s,$$

where Ω is the volume of the domain, V_K the Fourier coefficient of the potential V and $2V_{\mathrm{rep}}^s$ the corresponding matrix element of the repulsive potential, which for diamond respects the orthogonality of the wave functions of the valence electrons to the wave functions of the core electrons in the state $1s^2$.[10] For silicon or germanium the wave functions have the same form except that the expressions for the energies contain other repulsive terms. Since a knowledge of the band spectrum, i.e. also of the energies E_4 and E_1, is assumed below, our conclusions will be valid for all the materials given for which $E_4 < E_1$.

It now remains to investigate how the wave functions are transformed when operators from the sub-group S_k are applied. It is obvious from the form of the wave functions that the functions $\varphi_4', \varphi_1', \varphi_1''$ do not change their sign when reflected from the $\eta = 0$ plane and φ_4'' changes its sign. The wave functions of the surface states—inasfar as they exist—will be either symmetrical or anti-symmetrical with respect to reflection on the $\eta = 0$ plane.

The wave functions of the surface states inside the crystal are constructed according to equation (9). The symmetrical state in our approximation will have a wave function of the form

$$\Psi = e^{q\zeta}(c_1\varphi_1' + c_2\varphi_1'' + c_3\varphi_4'), \qquad (12)$$

while the anti-symmetrical state will be described only by the function φ_4'' with the corresponding exponential expression. The coefficients c_i are determined in the usual way, which leads to a solution of the secular equation. It is obvious from the form of φ_1'' that it is orthogonal to both functions φ_1' and φ_4', from which it follows that the corresponding secular equation becomes the product of two determinants, the first of which corresponds to the linear combination of the functions φ_1' and φ_4', and the second to the function φ_1''.

In the first case we get the following equation for the energy W of the surface state, in a manner analogous to that of papers (2) and (3) after a certain simplification of the matrix elements

$$(\alpha - W)(\beta - W) + \kappa^2 = 0, \qquad (13)$$

where

$$\alpha = E_1 - q^2, \quad \beta = E_4 - q^2, \quad \kappa = 2qk_X.$$

The following ratio can be determined for the two values of the energy W_i ($i = 1,4$)

$$c_1^i : c_3^i = \frac{\kappa}{\alpha - W_i}. \qquad (14)$$

The wave function outside the crystal must be transformed in the same manner as the function (12). In our case this function has the form

$$\Psi = \text{const. } e^{-p\zeta}, \tag{15}$$

where $p = \sqrt{(-W)} > 0$.

As has already been mentioned, we shall assume that the surface plane is led between two neighbouring lattice planes, i.e. the corresponding coordinate ζ_0 may be chosen e.g. as follows

$$\zeta_0 = Na\sqrt{2} + \frac{a}{8}\sqrt{2} \quad (N \text{ is an integer}). \tag{16}$$

The condition of continuity Ψ'/Ψ of function (12) and (15) leads to the equation

$$-q + \frac{\kappa}{\alpha - W} k_X = \sqrt{-W}. \tag{17}$$

After slight changes we get for q, which in our case must be positive,

$$q = -\frac{\Delta\sqrt{-E_4}}{2(E_4 - k_X^2)}, \tag{18}$$

where $\Delta = E_1 - E_4$ is the width of the forbidden band. The corresponding energy of the surface state is given by

$$W = \frac{E_1 + E_4}{2} - q^2 - \frac{1}{2}\sqrt{(\Delta^2 - 16q^2k_X^2)}, \tag{19}$$

where q is defined by equation (18).

Analogous expressions are obtained for the surface states occurring in the forbidden band near to the state corresponding to the vector (0, 0, k_X). If the corresponding vector components are denoted by (k_ξ, k_η, k_X) and the corresponding energies in the conduction and valence bands again by E_1 and E_4, an expression similar to (18) can easily be derived for q except that the energy E_4 is replaced by the expression $E_4 - k_\xi^2 - k_\eta^2$.

It is interesting to compare our results with those of MAUE and GOODWIN. It should be borne in mind, of course, that such a comparison can only be formal since the orthogonality condition is not taken into consideration in either paper. If, however, V_{rep} in the Hamiltonian operator (1) is put identically equal to zero, it is easily seen that in the case considered by us a surface state would exist only if $V_{4\sqrt{(2)}(\pi/a)} > 0$, which—as we mentioned before—is the condition for the existence of a surface state according to MAUE and GOODWIN. It could also be proved that after substituting the expressions for the energy (11) E_4 and E_1 into (18) and (19) we should get the corresponding relations derived by GOODWIN[3]. It is thus obvious that our first approximation, leading to the derivation of expressions (18) and (19), is formally equivalent to the procedure in papers (2) and (3). In addition it respects the orthogonality condition of the wave functions which—as will be seen on an example—permits direct correlation with volume states, for which this condition must also be taken into consideration if physically senseless results are to be avoided.

It remains to pay attention to the origin of surface states. If, like MAUE and GOODWIN, we considered a crystal limited by two planes and investigated the change in distribution of the states in the band spectrum at the transition from the Born–Kármán conditions to conditions corresponding to the limited crystal, we would find that, in agreement with papers (2) and (3), the existence of two surface states with the same energy, one of which is described by a symmetrical and the other by an antisymmetrical wave function, is connected with the disappearance of the two states of the band spectrum, one of which corresponds to the highest state with the corresponding wave vector in the valence band and the other to the lowest state in the conduction band. In the case considered by us these are the states characterized by the wave functions φ_1' (state $X_1^{(2)}$) and φ_4' (state X_4). It can be proved that in the approximation used by us surface states do not exist which would correspond to the volume states described by the wave functions φ_1'', and φ_4''. These states remain in the band spectrum and their energies are somewhat displaced due to the other boundary conditions for wave functions.

For the purpose of illustration we give the values of q and W for a surface state produced from the states $X_1^{(2)}$ and X_4 of the band spectrum of diamond. The same procedure can be followed for silicon or germanium. According to paper (10) the following values are obtained from equation (11) for the energy (in Rydberg units) in the states $X_1^{(2)}$ and X_4:

$$E_4 = -0{\cdot}705, \quad E_1 = -0{\cdot}423.$$

Vol. 21 1961

Substituting into (17) and (18) we get

$$q = 0{\cdot}048 \text{ and } W = -0{\cdot}627.$$

It is seen that the energy of the surface state lies somewhat lower than in the middle of the forbidden band limited by the energies E_4 and E_1. The values E_4 and E_1 are defined in our case by equations (11). Since both matrix elements V_0 and $V_{4\sqrt{(2)}(\pi/a)}$ are negative, it is obvious that the neglection of the repulsive potential (for diamond concretely $2V^s_{\text{rep}}$ for the $X_1^{(2)}$ state) would not only lead to the fact that a surface state would not exist, but simultaneously it would mean the incorrect order of the energies E_4 and E_1, for which it would then hold that $E_4 > E_1$, which does not correspond to reality. It thus follows that, as in the same way the orthogonality condition of the wave functions cannot be neglected for volume states, so it also cannot be neglected when solving the Schrödinger equation for surface states.

Analogous conclusions are valid for surface states lying in the forbidden band limited by the energy discontinuity on the Brillouin zone boundary, corresponding to another orientation of the plane limiting the crystal. From the point of view of physical interpretation a very important case is that of a crystal limited by the (111) plane, where we are chiefly interested in the surface states in the forbidden band near to the point characterized by the wave vector $\boldsymbol{k} = (\pm 2\pi/a, \pm 2\pi/a, \pm 2\pi/a)$. In this case, too, the above procedure can be used. The sub-group $S_{\boldsymbol{k}}$ contains altogether six elements for this point. The wave function of the surface state inside the crystal (9) is constructed in our approximation from the functions φ_t, which correspond to the states Γ_{25}', Γ_{15}, Γ_2' and $\Gamma_1^{(2)}$ of the band spectrum. The calculation is then somewhat more complicated and assumes a knowledge of the energy values of the volume states E_t in the point Γ. Not all these values are always known with sufficient accuracy, particularly if it is remembered that not only the relative order of the energies E_t but at least their absolute values in correct order of magnitude must be known (the latter condition is not satisfied for example with Ge[15]). It can be proved for diamond and silicon on the basis of the known values of E_t that even in this case a surface state exists; its wave function remains invariant with respect to the operators of the sub-group $S_{\boldsymbol{k}}$ and the corresponding energy value, like the preceding case, lies approximately in the middle of the forbidden band, defined by the values E_{25}' and E_{15} (E_{25}', $E_{15} < 0$). A similar conclusion would be reached even if for the sake of simplicity and clarity we used in expansion (9) only the mean values of the wave functions on the crystal surface corresponding only to the states Γ_{25}' and Γ_{15}. If it were assumed that the forbidden band in the point Γ is defined by the states Γ_{25}' and Γ_2' (where $E_{25}' < E_2' < 0$), which would for example correspond to the energy spectrum of germanium, we should get an analogous result.

It is clear from the above that the parameters characterizing the surface states depend on the parameters of the volume states. These, however, are for the most part not determined with sufficient accuracy, which is seen to a certain extent in the calculation of the surface states. Inaccuracy in knowing the band spectrum involves yet another difficulty: since the surface states hitherto considered by us are only one half occupied, localization of the electrons from the volume states on the unoccupied surface levels may occur in some cases, or vice versa some electrons from the surface states may pass to the volume states. This obviously depends on the relative position of the spectrum of the volume and surface states. It is seen that this problem to a certain extent depends on the accuracy in determining the band spectrum and can hardly be definitively solved, the present accuracy in calculating the band spectrum being what it is.* It should be noted here that when solving this problem it is also necessary to start out from a somewhat more detailed model of the surface, which would better represent the real conditions on the crystal surface than the assumptions made by us; this will be dealt with in greater detail in a later paper.

***Note added in proof:*

However, if we compare the surface states energy spectrum for different crystallographic orientations of the surface plane, semiquantitative conclusions sometimes can be drawn. For example, it is obvious from the energy band spectrum of the crystals with diamond structure that the number of Shockley-type surface states having energy lower than the energy of the conduction band bottom for $\boldsymbol{k} = 0$ is much smaller for the (111) crystallographic orientation of the surface plane than for the (011) orientation.

CONCLUSION

A new method has been proposed for calculating Shockley-type surface states. Particular emphasis has been laid on the fact that the orthogonality condition of the wave functions of valence electrons to the wave function of core electrons must be respected at least approximately if physically incorrect conclusions are to be avoided; it is also convenient to start out from group analysis of the wave functions of a finite crystal. The general conclusions of the given method were illustrated on the example of a diamond lattice, and cases when the crystal is limited by a (011) or (111) plane were in particular discussed. It was proved that from the energy point of view Shockley-type surface states fall approximately into the middle of the forbidden band, characterized by the energy discontinuity in the corresponding point on the boundary of the Brillouin zone; the origin of surface states was also discussed from the aspect of the band spectrum of an unlimited crystal.

REFERENCES

1. SHOCKLEY W., *Phys. Rev.* **56,** 317 (1939).
2. MAUE A. W., *Z. Phys.* **94,** 717 (1935).
3. GOODWIN E. T., *Proc. Camb. Phil. Soc.* **35,** 205 (1935).
4. GOODWIN E. T., *Proc. Camb. Phil. Soc.* **35,** 221, 232 (1935).
5. STATZ H., *Z. Naturf.* **5a,** 534 (1950).
6. LIPPMANN B. A., *Ann. Phys. New York* **2,** 16 (1957).
7. ARTMANN K., *Z. Phys.* **131,** 244 (1952).
8. KOUTECKÝ J. and TOMÁŠEK M., *Phys. Rev.* **120,** 1212 (1960).
9. ANTONČÍK E., *Czech. J. Phys.* **4,** 118 (1954).
10. ANTONČÍK E., *J. Phys. Chem. Solids* **10,** 314 (1959).
11. BOUCKAERT L. P., SMOLUCHOWSKI R. and WIGNER E., *Phys. Rev.* **50,** 58 (1936).
12. ANTONČÍK E., *Czech. J. Phys.* **9,** 291 (1959).
13. SOMMERFELD A. and BETHE H., *Handbuch der Physik* (2nd Ed.) Vol. XXIV, p. 489. Springer, Berlin (1933).
14. MOTT N. F. and JONES H., *The Theory of the Properties of Metals*, p. 159. Oxford University Press, London (1936).
15. Diamond: HERMAN F., *Phys. Rev.* **88,** 1210 (1952). Silicon: KLEINMAN L. and PHILLIPS J. C., *Phys. Rev.* **117,** 432 (1960). Germanium: HERMAN F., *Semiconductor Conference, Prague* 1960, in press.
16. JONES H. *The Theory of Brillouin Zones*, p. 157. North-Holland Publishing Co., Amsterdam (1960).

Vol. 21
1961

J. Phys. Chem. Solids Pergamon Press 1961. Vol. 21, Nos. 3/4, pp. 146–155. Printed in Great Britain.

TEMPERATURE DEPENDENCE OF THE X-RAY DIFFUSE SCATTERING OF MOLECULAR CRYSTALS: NAPHTHALENE*

M. L. CANUT and J. L. AMORÓS

Section of Crystal Thermodynamics, Department of Crystal Physics, C.S.I.C. Madrid

(*Received* 10 *February* 1961; *revised* 15 *March* 1961)

Abstract—For molecular crystals a theoretical analysis has been made on the thermal dependence of the Laval functions TDS_1, TDS_2, TDS_3 and our difference Fourier transform function DFT. The temperature factor of TDS_1 has been computed for naphthalene at several temperatures ($T > \Theta_D$) by assuming constancy of Θ_D and also with the assumption that the frequencies increase 7·6 per cent in 100°K by lowering the temperature. In both cases the inversion phenomenon appears, being observable at low temperatures. The DFT form function of naphthalene has also been computed at several temperatures, in terms of Θ_E, and the isodiffusion lines corresponding to the extended regions *G* and *C* are shown at 300° and 130°K. The reciprocal space regions more temperature-sensitive according to the different diffuse scattering functions are also shown. It is emphasized that experimental work on the thermal behaviour of the diffuse scattering at low temperatures and high values of the reciprocal vector is of the most interest. Experimental tests in naphthalene have shown the inversion of TDS_1 and that the continuous diffuse regions do not correspond to a one-phonon scattering.

1. INTRODUCTION

It is a well established fact that X-ray, electron, and neutron diffraction by crystals depend upon temperature as the scattering is affected by the thermal motion of atoms and molecules in crystals. The total scattering power of a crystal, besides Compton scattering, is the sum of different contributions, namely Bragg scattering and temperature diffuse scattering of first, second, third orders, etc. All these different contributions depend upon temperature and reciprocal (diffraction) vector in different manners. This fact can be an important clue for the right interpretation of the observed diffuse scattering. In what follows we shall consider the temperature dependence of the temperature diffuse scattering of first (TDS_1), second (TDS_2), and third (TDS_3) orders[1] and of the difference Fourier transform (DFT) function.[2] The theoretical results will be discussed in terms of the experimental evidence obtained with single crystals of naphthalene.

2. ONE-PHONON SCATTERING

According to Laval[1] the intensity of the diffuse scattering of X-rays arising from the thermal motion of the atoms of a lattice can be expressed as a series of terms

$$I_{TDS} = I_{TDS_1} + I_{TDS_2} + I_{TDS_3} + \ldots \qquad (1)$$

The first term, the first-order diffuse scattering, describes the intensity of the scattering in which a single phonon is involved. The second and third terms describe the intensity of the scattering arising from processes in which two or three phonons are involved, respectively. Generally, only the first two terms contribute appreciably.

As it is well known, the intensity of the first-order diffuse scattering is a function of the frequency, which itself is a function of the wave

* This research was in part supported by the Directorate of Solid-State Sciences, Air Force Office of Scientific Research, through the European Office of the Air Research and Development Command, under Contract No. AF 61 (052)—193.

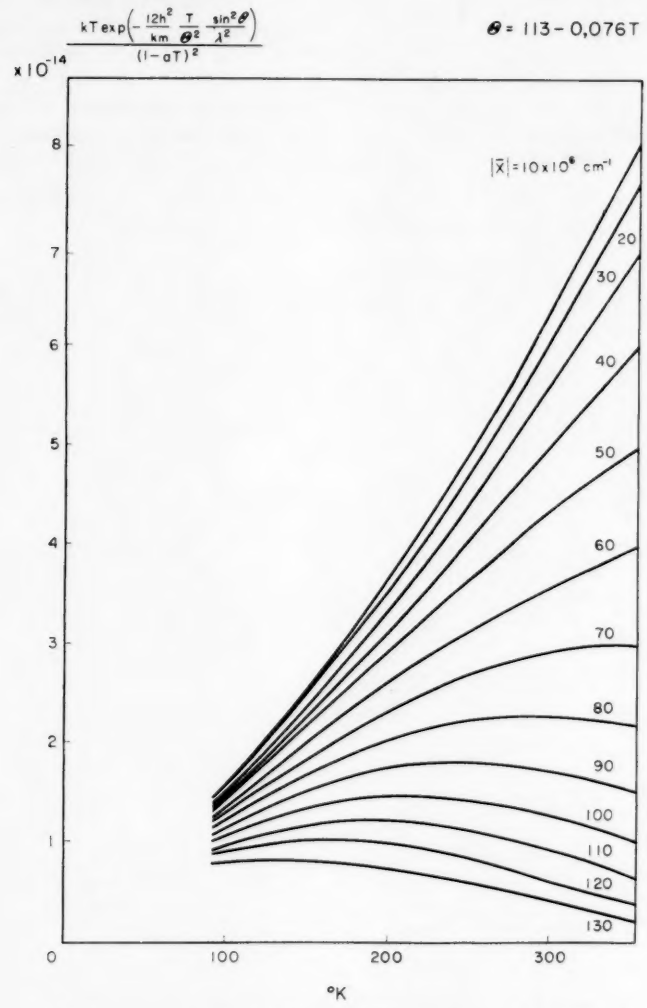

FIG. 1. Naphthalene. Temperature dependence of TDS_1 for constant values of $|\bar{X}|$ in the temperature range $\Theta_D < T < T_{mp}$. Assumption of $\Theta_D = 113\,(1-aT)$, $\nu = \nu_0\,(1-aT)$; $a = 0{\cdot}00067$.

vector of the thermal wave. The temperature dependence of TDS_1 is through the temperature factor affecting the Bragg intensities (i.e. the Debye–Waller factor) and the energy of the thermal wave; if equipartition law holds, this energy is given by kT. Second- and third-order diffuse scattering also depend upon temperature through the Debye–Waller factor, being in addition proportional, respectively, to the second and third powers of the thermal energy of the thermal waves, that is, to $(kT)^2$ and $(kT)^3$ for temperatures above the characteristic temperature of the crystal.

Thermal diffuse scattering arising from coupled harmonic oscillators is characterized by inversion temperature. CANUT and AMORÓS[3] have shown that the temperature at which the one-phonon

scattering is a maximum satisfies

$$(T_{\max})_1 = \frac{k}{3h^2} m\Theta^2 d_{hkl}^2 \qquad (2)$$

where k and h are the Boltzmann and Planck constants, respectively, m the mass of the atom or molecule, Θ the characteristic temperature and d_{hkl} the spacing of the crystal plane at which TDS_1 is associated. They also have shown that the inversion phenomenon of TDS_1 is universal, being observable in molecular crystals mainly at low temperatures.

The maxima for TDS_2 and TDS_3 for a given lattice plane of the crystal will appear at temperatures twice and three times the corresponding $(T_{\max})_1$.

In the deduction of (2), the lattice frequencies were assumed temperature independent. However, it is an experimental fact that the vibrational frequencies of the acoustic[4] and optic branches[5, 6] increase with decreasing temperature. We are lacking in experimental data about the temperature variation of the acoustical frequencies in naphthalene; however, ICHISHIMA[5] reported a linear variation of the Raman frequencies corresponding

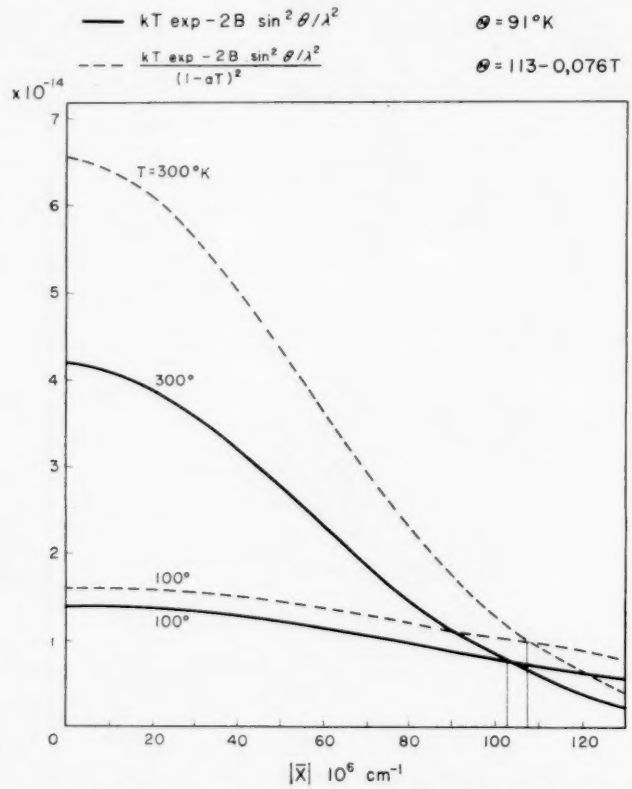

FIG. 2. Naphthalene. Temperature factors of TDS_1 at 300° and 100°K plotted vs. $|\overline{X}|$. Assumptions of constant $\Theta_D = 91$°K (continuous line), and $\Theta_D = 113\ (1-aT)$. $\nu = \nu_0\ (1-aT)$; $a = 0{\cdot}076$ (broken line). Both sets of curves show the inversion point for $|\overline{X}|$ values in the range $100 < |\overline{X}| < 110 \times 10^6$ cm^{-1}.

to the librations of the molecules in the temperature range 90–300°K. Following CRUICKSHANK[7], we can also assume that the frequencies of the translational branch depend upon temperature in the same manner. If we express the ν librational measured by ICHISHIMA in the form $\nu = \nu_0 (1-aT)$ the mean value of a becomes $a = 0{\cdot}00067$ and the corresponding variation of Θ_M must be

$$I_{\mathrm{TDS}_1}(\bar{g}) = \frac{|F_0|^2 |\bar{X}|^2}{m|\bar{g}|^2} \frac{\exp\left[-\dfrac{3h^2}{km\Theta_0^2}|\bar{X}|^2 \dfrac{T}{(1-aT)^2}\right] kT}{(1-aT)^2} \times \sum_i \frac{\cos^2\alpha_{xj}}{\nu^2_{\theta_{gj}}} \qquad (3)$$

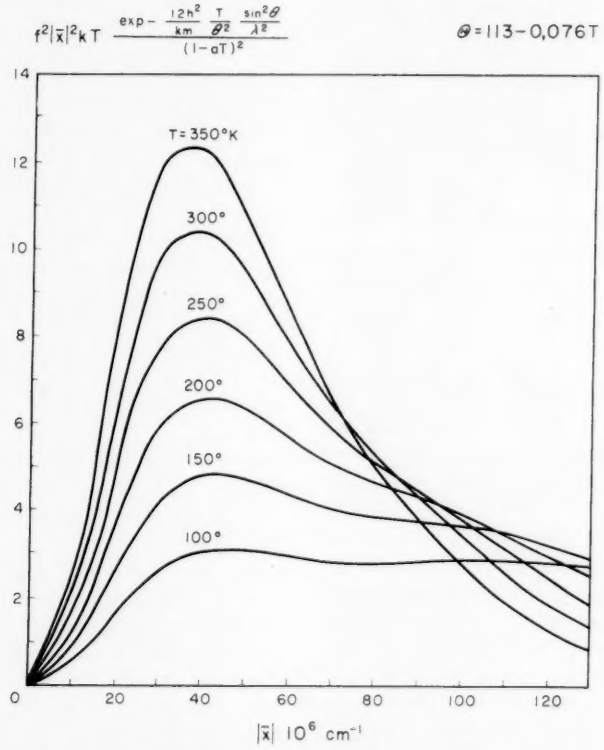

FIG. 3. Naphthalene. Curves of the form factor of TDS_1 at different absolute temperatures vs. the modulus of the diffraction vector. Assumption: $\Theta = 113\ (1-aT)$, $\nu = \nu_0\ (1-aT)$; $a = 0{\cdot}00067$.

$\Theta_M = 113\ (1-aT)$ to give the X-ray value of $\Theta_M = 91$°K at 293°K.

This linear temperature dependence of the vibrational frequencies can be easily introduced in the expression for the first-order scattering in electron units per atom for a crystal:

$I_{\mathrm{TDS}_1}(g)$ is the intensity, due to thermal elastic waves, at a point in reciprocal space a vector distance $\bar{g}$, the wave vector, from the nearest reciprocal lattice point. F_0 is the structure factor at rest corresponding to that reciprocal point; $\bar{X}$ is the diffraction vector, the difference between

Vol. 21
1961

the wave vectors of the diffracted and incident X-rays, being $|\overline{X}| = 2 \sin\theta/\lambda$. The sum over j is taken over the three independent elastic waves having the same vector $\overline{g}$ but different directions of vibration; α_{Xj} is the angle between the eigenvector of the jth wave and $\overline{X}$. If, for simplicity, we assume that the linear relation $\nu = \nu_0 (1-aT)$ holds down to 0°K, $\nu_{0_{gj}}$ would be the value of the vibrational frequency of the jth wave at 0°K. The remaining term of (3) is the temperature factor when the Debye–Waller factor contains explicitly the absolute temperature[8] and, in addition, the linear temperature variation of the frequencies is introduced. Expression (3) holds for $T > \Theta$.

The variation of the temperature factor of TDS_1 for naphthalene with temperature for constant values of the reciprocal lattice vector, $|\overline{X}|$, is shown in Fig. 1. The general shape of this set of curves is very similar to those obtained with the assumption of $\nu = \text{const}$. Comparison between both assumptions for naphthalene is given in Fig. 2, where the two temperature factors of TDS_1 have been plotted versus $|\overline{X}|$ for $T = 300$°K and 100°K. Full line corresponds to $\Theta = 90$°K; broken line corresponds to $\Theta = 113\ (1-aT)$ and $\nu = \nu_0\ (1-aT)$. The inversion is shown for $100 < |\overline{X}| < 110 \times 10^6\ \text{cm}^{-1}$. Fig. 2 shows that the variation of ν with temperature produces a small shift of $(T_{\max})_1$, but it does not eliminate the inversion. This point is important in relation with the discussion of our experimental results.

In Fig. 3 the curves for naphthalene corresponding to the TDS_1 form function when the equipartition law holds and linear dependence of frequencies with temperature is assumed, are represented. The most striking feature of those curves is that TDS_1 form function shows a maximum which in naphthalene corresponds to a region of $|\overline{X}| = 0{\cdot}40 \times 10^6\ \text{cm}^{-1}$. The presence of strong diffuse scattering associated with reciprocal lattice points in this region has been shown experimentally by DE ACHA *et al.*[9] The second interesting feature shown in Fig. 3 is the inversion of the variation of intensity with temperature for high values of $|\overline{X}|$.

3. DIFFERENCE FOURIER TRANSFORM FUNCTION, DFT

It has been pointed out by SARGINSON[10] and BORN and SARGINSON[11] that the diffuse scattering associated with non-forbidden reciprocal lattice points does not arise from the optical branches and that these branches can only produce a smooth background. On the other hand, the optical branches have, as is well known from the diatomic linear lattice, minima of ν in the middle of the reciprocal cell. According to BORN[12] it may therefore happen that weak background spots of another type exist which are just intermediate between reciprocal lattice points.

Our experiments on molecular crystals have not detected so far such maxima in the middle of the reciprocal cell, but a smooth background forming continuous diffuse regions. In 1954, VELASCO *et al.*[13] reported in adipic acid continuous diffuse scattering sheets normal to the chain direction, instead of only discs associated to some reciprocal lattice points. Diffuse continuous regions have also been observed by us for molecular crystals of different molecular shape and structural type, whose shape and orientation in reciprocal space are correlated with the shape and orientation of the individual molecules[14–18, 9]. Such background must be the one expected for the optical branches of the vibrational spectrum in molecular crystals.

One model has been advanced by AMORÓS *et al.*[2] to explain the observed diffuse scattering regions in terms of the difference Fourier transform function. DFT has been tested at room temperature for several molecular crystals.[19–23]

In the formulation of DFT, the independent vibrations of the molecules in the crystal affecting the optical branches is supposed. Such an approximation is physically understandable. At temperatures near the melting point (and this is the case for molecular (organic) crystals at room temperature) all the frequencies are excited, with random phases, and it is not too difficult to think of neighbouring molecules vibrating in their mean positions with some independence and with only the mutual mean interaction to keep the molecules in their position. At this point, it seems reasonable to remember that Einstein's model of independent vibrations must not be disregarded at high temperatures.[24] Accordingly, an Einstein characteristic temperature seems more appropriated for DFT. Taking $\Theta_E = 3\Theta_{D/4}$[25], Θ_E for naphthalene becomes 63°K at room temperature.

The form function of DFT is given by

$$f_c^2\left\{1-\exp\left[-\frac{3h^2}{km\Theta^2}|\overline{X}|^2T\right]\right\}. \qquad (4)$$

Such distribution is isotropic and centered in reciprocal space.

The general aspect of the curves of Fig. 4 is very similar to those obtained in terms of Θ_D, the main difference being that the maxima is higher with Θ_E.

Before any discussion of the diffuse scattering phenomenon can proceed it is essential to determine from the experiment as much as possible about the nature of the scattering itself. In the following, we shall describe the experimental work done with single crystals of naphthalene at room and at low temperatures.

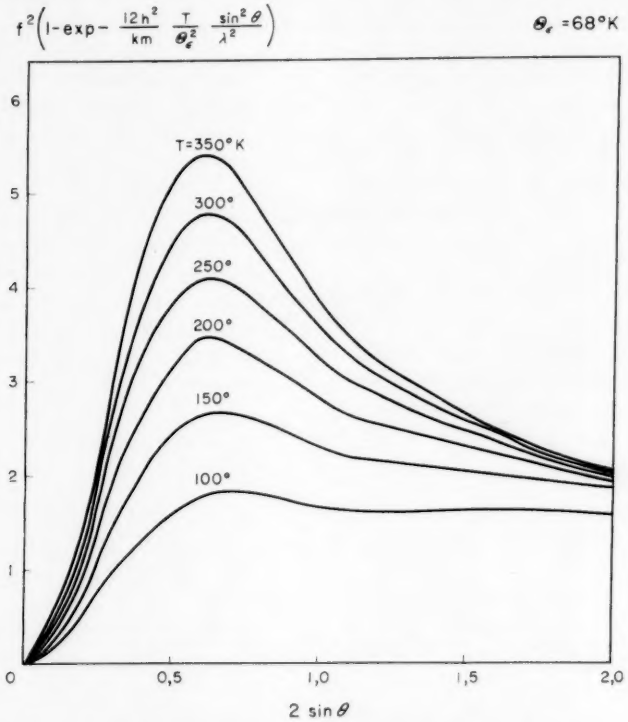

FIG. 4. Naphthalene. Forms functions of DFT at different temperatures computed in terms of $\Theta_E = 68°K$.

Fig. 4 corresponds to the DFT form function of naphthalene calculated with (4) for the absolute temperatures 100°, 150° ... 350°K in terms of Θ_E. DFT has a value zero at the origin of the reciprocal space and shows its maximum value for naphthalene in the region $|\overline{X}| = 0{\cdot}40\times10^6$ cm^{-1} for all temperatures, decreasing with increasing $|\overline{X}|$, but never vanishes. Another important feature is that DFT does not show inversion with temperature; on the contrary, it increases smoothly and steadily with temperature.

5. EXPERIMENTAL AND COMPUTATIONS

Single crystals of naphthalene were obtained by slow evaporation in an ethyl alcohol solution at room temperature. As naphthalene sublimes at room temperature, the crystals to be used in the experiment were covered with a cellulose acetate

solution in acetone and mounted in the goniometer head with dental cement. The crystals used were $1{\cdot}5\times1{\cdot}5\times2$ mm^3, the largest dimension being along [010]. The crystals were mounted along [010] and cylindrical Laue photographs were taken at room temperature, at 130°K and again at room, in order to test reversibility. The X-ray photographs were taken in a vertical Weissenberg camera ($R = 30$ mm) built in our department.[26] The camera is provided with a low temperature device, that blows on the crystal a stream of cooled dried nitrogen gas, which has been cooled previously by passing through two copper spiral tubes, the first one immersed in a mixture of dry ice and alcohol plus acetone, and the other one immersed in liquid nitrogen. X-ray Cu-filtered radiation was used from a Phillips tube running at 20 mA, 40 kV, stabilized. The Laue photographs were taken during two hours.

As the diffuse scattering of naphthalene at room temperature was previously recorded in our laboratory,[9] several cylindrical Laue photographs were selected in order to compare the diffuse scattering at room and at low temperature. The selection was made in such a way that it was possible to follow the temperature dependence of the most important continuous regions *G* and *C* [see Ref. (2)] and also to make the inversion phenomenon of TDS_1 observable, if possible.

Two of the Laue photographs taken at 300° and 130°K are shown in Fig. 5. The Laue photograph at 300°K (Fig. 5a) shows the typical Laue pattern of a molecular crystal: Laue spots, strong diffuse spots associated to non-forbidden reciprocal lattice points and diffuse continuous regions, namely *G* and *C*. In the Laue photograph taken at 130°K (Fig. 5b) the Laue spots have increased both in intensity and number. In addition, the diffuse spots associated to reciprocal lattice points with $|\overline{X}|$ values between 0 and 70×10^6 cm^{-1} have disappeared. These results were found by LONSDALE and SMITH[27] in benzil, α-resorcinol and sorbic acid. However, in those experiments, flat photographic plates in the X-ray reflection region were used and hence the diffraction space above $|\overline{X}| = 0{\cdot}80\times10^6$ cm^{-1} was not investigated.

Two new results we have obtained in our experiments:

(a) The diffuse spot associated with the reciprocal

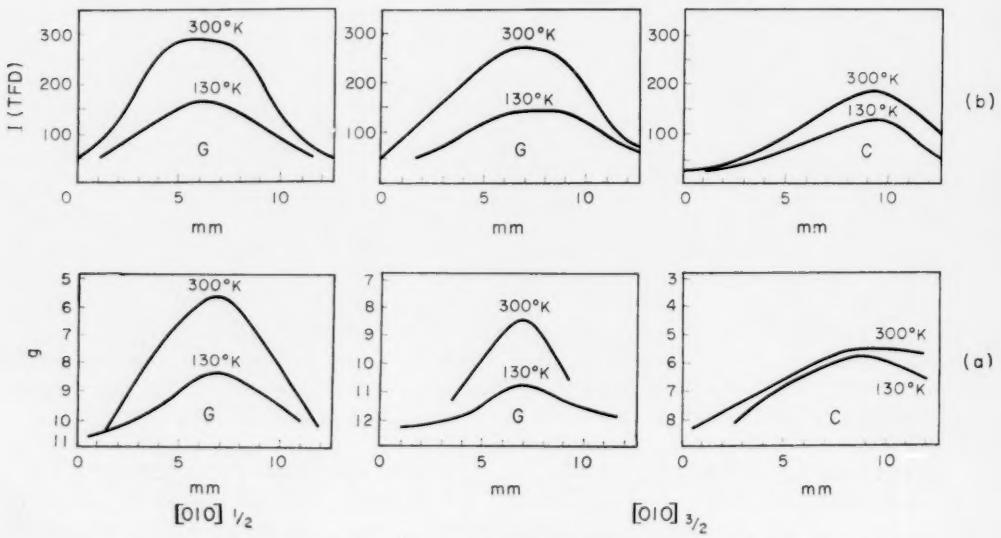

FIG. 6. Naphthalene. Sections of the *G* and *C* regions with the Ewald sphere for the Laue photographs of Fig. 5.
(a) Theoretical values in terms of DFT (Θ_E). (b) Observed values.

Vol. 21
1961

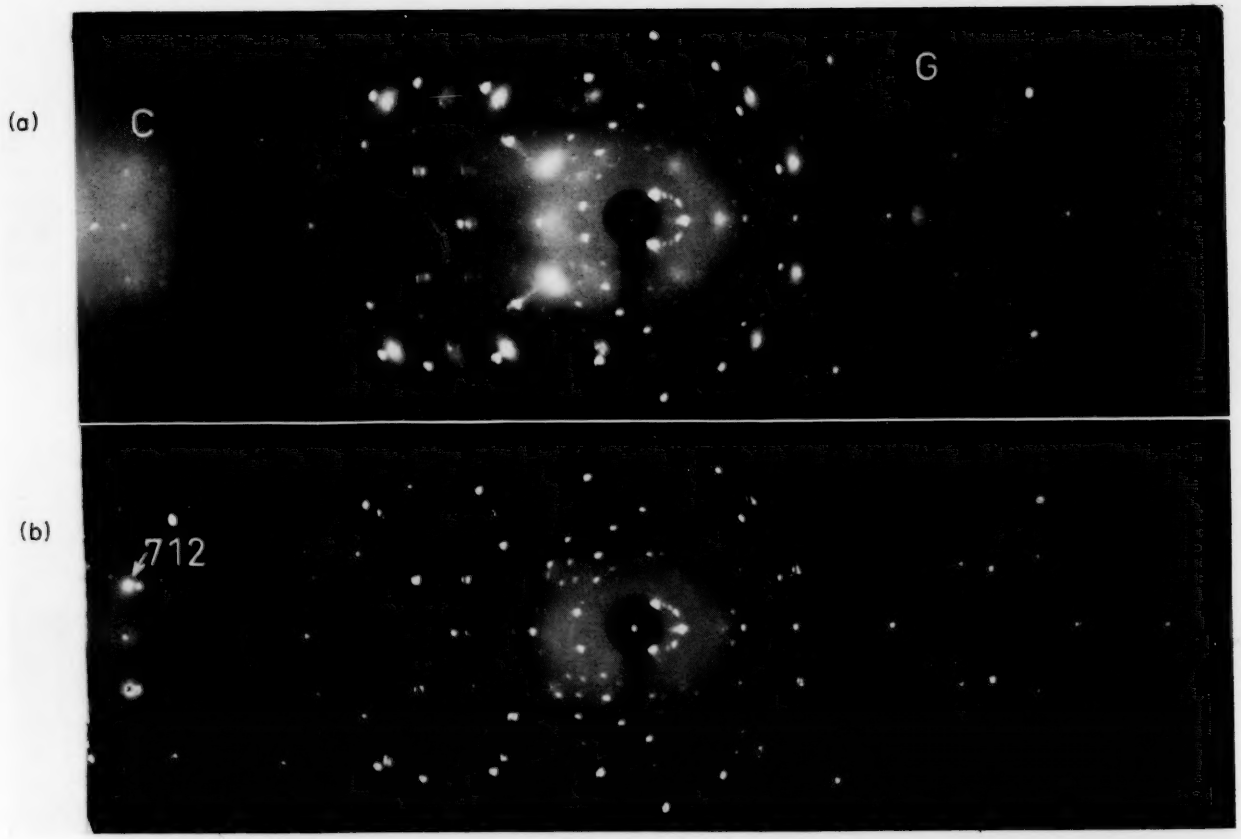

FIG. 5. Naphthalene. Laue photographs. Vertical axis, [010]. X-ray beam at 30° of a^* in the region of β^* positive. X-ray Cu-filtered radiation, 40 kV, 20 mA, 2hr.

(a) Temp: 300°K. (b) Temp: 130°K.

[facing p. 152

BLANK
PAGE

Vol.
196

lattice point 712 ($|\overline{X}| = 120 \times 10^6$ cm^{-1}) is stronger at the lowest temperature, that is, the inversion phenomenon has been detected in a molecular crystal such as naphthalene by lowering the temperature.

(b) The continuous diffuse regions decrease with decreasing temperature, even in the back reflection region, and do not show the inversion phenomenon.

The thermal dependence of the different kinds of diffuse scattering is reversible with temperature.

Fig. 6(a) shows the measurements made with a Hilger microdensitometer on films both in the regions G and C at the reciprocal lattice levels $[010]_{1/2}$ and $[010]_{3/2}$, values that follow pretty closely with the theoretical ones (Fig. 6b). To obtain these values, we had first to calculate the sections of the diffuse regions G and C with the reciprocal levels $[010]_0$, $[010]_{1/2}$ and $[010]_{3/2}$ at the temperatures 300° and 130°K. In the temperature factor of TFD an Einstein characteristic temperature $\Theta_E = 67$°K was applied.

The values of $\sum(A_p^2+B_p^2)$ for the points h, $1/2$, l and h, $3/2$, l were taken from Ref. (2). To have more accuracy in the isodiffusion contours we have computed for this work the values of $\sum(A_p^2+B_p^2)$ at the intermediate points $h/2$, $1/2$ $l/2$ and $h/2$, $3/2$, $l/2$. Naphthalene has two molecules p, q in the unit cell. As the molecule is centrosymmetric and the center of symmetry of the molecule p lies in the origin of the unit cell, only the real part of the transform contributes for any value of hkl, integer or fractional. Hence, only the real term of the asymmetric part of the molecule A_p' must be calculated and be multiplied by 2 to get the total contribution (A_p) of this molecule. On the other hand, for the molecule q we must consider also the imaginary part B_q of the transform.

Taking into account the space group relationships of the atomic coordinates of the molecules p and q we have

$$\begin{aligned}\textstyle\sum_p(A_p^2+B_p^2) &= 2A_p^2 \text{ for } h0l \text{ and } h/2, 0, l/2\\ &= A_p^2+B_q^2 \text{ for } h, k/2, l\\ &= A_p^2+B_q^2 \text{ for } h/2, k/2, l/2\end{aligned}$$

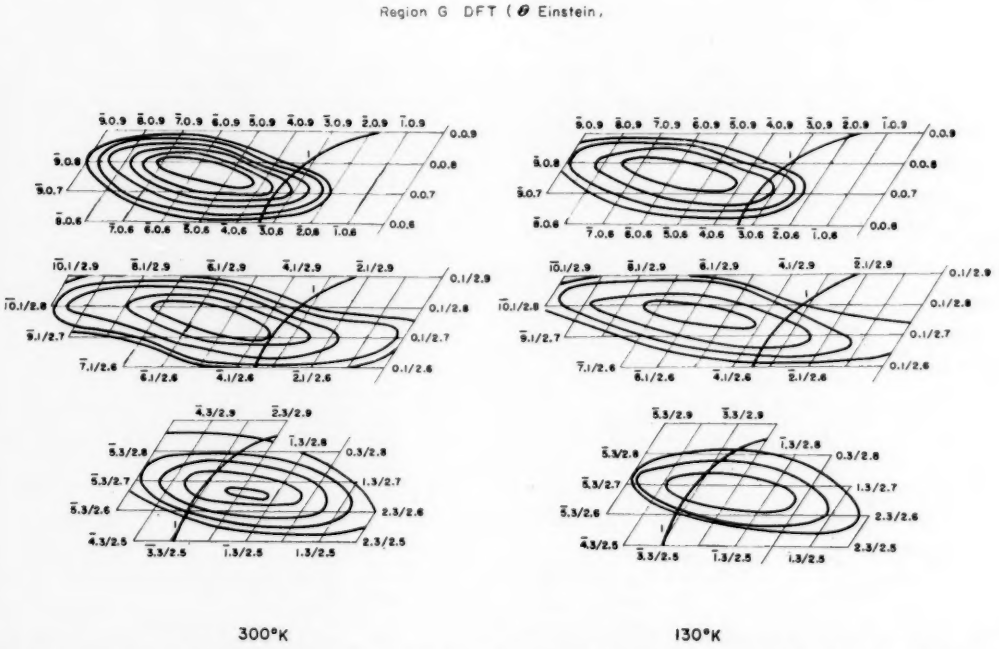

FIG. 7. Naphthalene. Theoretical isodiffusion lines of the G region at the reciprocal levels $[010]_0$, $[010]_{1/2}$ and $[010]_{3/2}$. Arbitrary values of 25, 50, 100, 200, ... The arc 1 is the section of the Ewald sphere for the Laues of Fig. 5.

Vol. 21
1961

The isodiffusion lines corresponding to the *G* and *C* regions of naphthalene at the temperatures 300° and 130°K are shown in Figs. 7 and 8. The contours have been plotted at arbitrary values of 25, 50, 100, 200, and so on. The arc marked with 1 is the trace of the Ewald sphere at the crystal setting corresponding to the Laue photographs of Fig. 5, and the values along such an arc are the theoretical values plotted in Fig. 6(b).

shows that at moderate low temperatures, long range order forces are important in molecular crystals like the one considered here.

The different nature of the continuous diffuse extended regions and of the diffuse scattering associated to reciprocal lattice points is patent through our experiments. The continuous region *C* decreases with decreasing temperature at the same time that the diffuse scattering associated

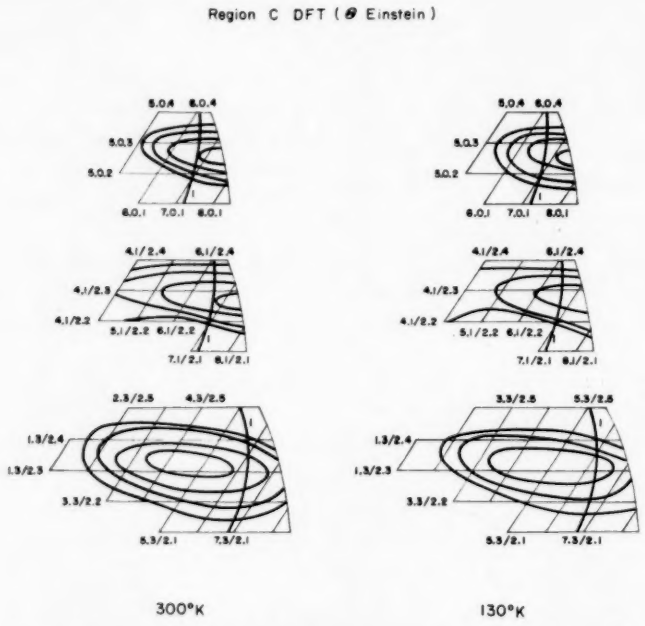

FIG. 8. Naphthalene. Theoretical isodiffusion lines of the *C* region at the reciprocal levels $[010]_0$, $[010]_{1/2}$ and $[010]_{3/2}$. Arbitrary values of 25, 50, 100, 200. The arc 1 is the section of the Ewald sphere for the Laues of Fig. 5.

DISCUSSION

Experimental detection in naphthalene of the inversion with temperature of the intensity of diffuse scattering associated with reciprocal lattice points confirms the theoretical prediction given by CANUT and AMORÓS[3]. The fact that at low temperature the diffuse scattering concentrates in the proximity of reciprocal lattice points shows that even at 130°K, a temperature higher than the Debye characteristic temperature of naphthalene, mainly long thermal waves are excited. This

to the 712 reciprocal lattice point increases. It must be emphasized that both the *C* region and the 712 reciprocal lattice point lie at the same $|\overline{X}|$ value. Thermal dependence of both kinds of diffuse scattering is different and, therefore, the diffuse scattering of the extended continuous regions cannot be certainly explained as a first order diffuse scattering (TDS_1) even if the observed increasing of vibrational frequencies with decreasing temperature is introduced. Such continuous regions show a thermal dependence of

the type $1-\exp(-2M)$ instead of $kT\exp(-2M)$, showing that they are the consequence of thermal disorder with no correlation between molecules or correlations only at small distances.

Therefore the following image of the lattice dynamics of a molecular crystal can be sought: long range order forces are important in molecular crystals as they give the possibility of long elastic waves that are observed to be present at moderate temperatures. When temperature increases, with long waves ever present, thermal movement is becoming more and more disordered, and as a consequence of it short range order is increasingly important. Coexistence of long waves and complete disordered thermal motion can only happen in the liquid phase, for instance, the waves in the surface of water.

Acknowledgements—We wish to thank Miss MARY CARMEN MORENO for performing all the computations and Miss LUCIA BLANCO for taking the Laue photographs.

Vol. 21
1961

REFERENCES

1. LAVAL J., *Bull. Soc. franç. Minér.* **64,** 1 (1941).
2. AMORÓS J. L., CANUT M. L. and DE ACHA A., *Z. Kristallogr.* **114,** 39 (1960).
3. CANUT M. L. and AMORÓS J. L., *Proc. Phys. Soc. Lond.*, **77,** 712 (1951).
4. DURAND A., *Phys. Rev.* **50,** 449 (1936).
5. ICHISHIMA I., *J. Chem. Soc. Japan* **71,** 607 (1950).
6. ICHISHIMA I. and MIZUSHIMA S. J., *J. Chem. Phys.* **18,** 1686 (1950).
7. CRUICKSHANK D. W. J., *Acta Cryst.*, **9,** 1005 (1956).
8. JAMES R. W., *The Optical Principles of the Diffraction of X-rays*, p. 642. Bell, London (1954).
9. ACHA A. DE, AMORÓS J. L. and CANUT M. L., *Bol. Soc. Esp. Hist. Nat.* **56,** 405 (1958).
10. SARGINSON K., *Proc. Roy. Soc.* **A180,** 305 (1942).
11. BORN M. and SARGINSON K., *Proc. Roy. Soc.* **A179,** 69 (1941).
12. BORN M., *Proc. Roy. Soc.* **A180,** 397 (1942).
13. VELASCO M., CANUT M. L. and AMORÓS J. L., *Publ. Dep. Crist. Min.* **1,** 165 (1954).
14. CANUT M. L. and AMORÓS J. L., *Publ. Dep. Crist. Min.* **3,** 15 (1957).
15. CANUT M. L. and AMORÓS J. L., *Publ. Dep. Crist. Min.* **3,** 27 (1957).
16. AMORÓS J. L. and CANUT M. L., *Bol. Soc. Esp. Hist. Nat.* **56,** 25 (1958).
17. CANUT M. L. and AMORÓS J. L., *Bol. Soc. Esp. Hist. Nat.* **56,** 323 (1958).
18. ALONSO P., CANUT M. L. and AMORÓS J. L., *Bol. Soc. Esp. Hist. Nat.* **56,** 379 (1958).
19. AMORÓS J. L. and CANUT M. L., *Bol. Soc. Esp. Hist. Nat.* **56,** 305 (1958).
20. ANNAKA S. and AMORÓS J. L., *J. Phys. Soc. Japan* **15,** 356 (1960).
21. ANNAKA S. and AMORÓS J. L., *Z. Kristallogr.* **114,** 433 (1960).
22. AMORÓS J. L., DE ACHA A. and CANUT M. L., *Bull. Soc. franç. Minér. Crist.* **84,** 40 (1961).
23. BANERJEE R. L., CANUT M. L. and AMORÓS J. L., *Indian J. Phys.* **35,** 62 (1961).
24. ZIMAN J. M., *Electrons and Phonons*, p. 554. University Press, Oxford (1960).
25. MOTT N. F. and JONES E. H., *The Theory of the Properties of Metals and Alloys*, p. 326. Dover Publications, New York (1958).
26. AMORÓS J. L., GUIBERT M., CANUT M. L. and ARRESE F., *Rev. Cienc. Apl.* in press.
27. LONSDALE K. and SMITH H., *Proc. Roy. Soc.* **A179,** 8 (1941).

J. Phys. Chem. Solids Pergamon Press 1961. Vol. 21, Nos. 3/4, pp. 156–171. Printed in Great Britain.

IONICITÉS, CHARGES EFFECTIVES ET MOBILITÉS ÉLECTRONIQUES DANS LES COMPOSES SEMICONDUCTEURS MINERAUX*

J. P. SUCHET

Laboratoire de Magnétisme et de Physique du Solide du C.N.R.S., Bellevue (S. & O.), France

(*Received* 6 *October* 1960; *revised* 10 *March* 1961)

Resumé—L'auteur poursuit l'étude de l'influence des liaisons chimiques sur les propriétés des semiconducteurs, amorcée par la prédiction de la semiconductibilité dans les composés[1] et le calcul empirique des énergies d'activation.[4] La conception d'une résonance des liaisons entre deux schémas covalent et ionique est brièvement rappelée et on utilise la méthode de la mésomérie pour définir un nouveau paramètre d'ionicité $0 < \lambda < 1$ en fonction de la structure du réseau, des formules électroniques des atomes et de la polarité des liaisons.

Les charges effectives portées par les deux atomes d'un composé binaire sont évaluées au moyen d'une formule empirique donnant, dans le cas des III–V, des dipôles de signe conforme aux résultats des expériences de diffusion de lithium. Elles permettent pour une centaine de composés binaires le calcul de valeurs d'ionicité rendant bien compte de la transition métal–semiconducteur pour $\lambda = 0$ (InBi/InSb, Mg_2Pb/Mg_2Sn) et de l'existence de mobilités électroniques élevées pour les polarités nulles (InSb, HgTe). La variation de la mobilité avec λ est reliée aux mécanismes de dispersion acoustique et polaire.

Abstract—The author further studies the influence of chemical bonds on the properties of semiconductors, after predicting the semiconductibility in compounds[1] and computing the energy gap empirically.[4] The concept of a resonance of the bonds between a covalent scheme and an ionic one is briefly recalled and the valence-bond theory is used to define a new ionicity parameter $0 < \lambda < 1$ as a function of the lattice structure, of the electronic formulae of atoms and of the polarity of bonds.

The effective charges supported by the two atoms of a binary compound are evaluated by means of an empirical formula which gives, in the case of the III–V, dipoles whose sign agrees with the results of the diffusion experiments of lithium. This allows for a hundred binary compounds the calculation of the ionicity values, which give a good account of the transition from metallic to semiconducting behaviour at $\lambda = 0$ (InBi/InSb, Mg_2Pb/Mg_2Sn) and of the existence of high electronic mobilities for zero polarities (InSb, HgTe). The variation of mobility as a function of λ is related to the acoustic and polar scattering mechanisms.

1. INTRODUCTION

Nous sommes efforcés antérieurement de montrer que la prédiction de la semiconductibilité dans les composés pouvait être facilitée par l'emploi d'une notation covalente pure et de schémas de filiation à partir des principaux binaires, et par la considération de réseaux lacunaires et compensés.[1] Cette classification sommaire des semiconducteurs en fonction de la coordinance covalente et du type de structure ouvrait la voie à l'établissement de relations empiriques pour le calcul de leurs caractéristiques physiques dans chacun des cas envisagés. L'idée que la semiconductibilité n'est nullement liée à l'existence d'un ordre cristallin rigoureux et que les propriétés essentielles des semiconducteurs peuvent être déterminées en gros par la nature des liaisons interatomiques à courte distance a en effet été émise par Ioffe[2–3]. Après une première étude ayant permis l'évaluation des energies d'activation,[4] nous essayons ici de préciser la

* Une partie de ce travail a été incluse dans une thése d'état soutenue à Paris en 1961.

nature même des liaisons, leur ionicité et leur polarité. Les chiffres obtenus fournissent des indications sur l'ordre de grandeur des mobilités électroniques.

La semiconductibilité intrinsèque, opposée à la conductibilité métallique, revêt deux aspects différents suivant qu'elle résulte de liaisons interatomiques purement covalentes ou purement ioniques. La transparence dans l'infra-rouge et les mobilités électroniques élevées semblent caractériser le premier cas tandis que la transparence dans le visible et le proche ultra-violet et la conductibilité électrolytique aux températures élevées caractérisent le second. Des ruptures locales de ces liaisons peuvent provoquer dans les deux cas la semiconductibilité extrinsèque, mais les défauts ponctuels actifs ne sont pas les mêmes: atomes étrangers pour l'un, lacunes et intersitiels pour l'autre.[5]

On a coutume de décrire les liaisons dans les composés chimiques minéraux en se référant à des liaisons covalente et ionique idéales, dont l'existence réelle est évidemment impossible, et en leur donnant un caractère "intermédiaire". Cette habitude entraîne la nécessité d'envisager pour chaque composé un schéma covalent idéal où les paires électroniques communes sont partagées également entre les atomes liés, chacun se trouvant alors avoir la formule électronique correspondant au type d'orbitales intervenant dans la liaison (sp^2, sp^3, p^3, etc. ...), et que l'on peut écrire au moyen de "charges formelles"[6] $M^{m-}X^{m+}$. On doit envisager simultanément un schéma ionique idéal où l'atome électronégatif X complète au détriment de son partenaire l'occupation des mêmes états quantiques que dans la formule précédente, acquérant ainsi les formules électroniques s^2p^4, s^2p^6, p^6, etc. . . . et que l'on peut écrire au moyen des charges habituelles $M^{n+}X^{n-}$. La Fig. 1 explicite entre ces deux schémas la résonance qui constitue la liaison "iono-covalente". Le nombre $c = m+n$ d'électrons de valence "nomades", c'est-à-dire échangés par les partenaires lorsqu'on passe d'un schéma à l'autre, n'est autre que celui des "cases" quantiques (représentées par des cercles) participant aux orbitales de la liaison covalente, et représente également la coordinance atomique de base (liaisons diélectroniques classiques). La coordinance réelle peut être doublée si une permutation circulaire des liaisons permet de connecter un atome alternativement à $c+c$ voisins (liaisons dites "monoélectroniques"). Le Tableau 1 rappelle les différents cas possibles.[7] Le symbole R (résonance) y désigne une coordinance réelle doublée.

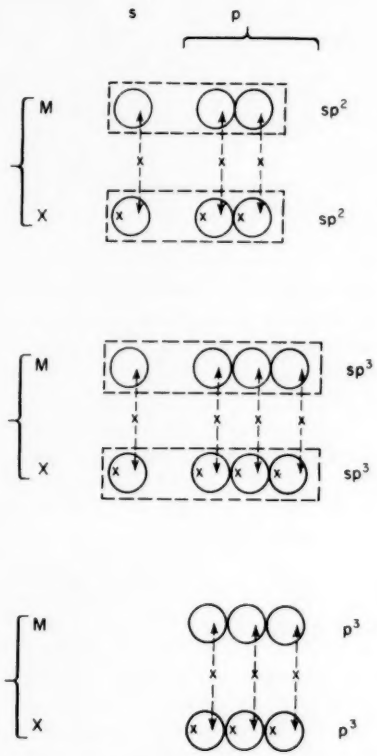

FIG. 1. Principaux schémas de liaison iono-covalents.

Le nombre c de cases quantiques intervenant dans la liaison est le seul caractère commun aux aspects covalent (orbitales et caractère directionnel) et ionique (potentiel et forces électrostatiques) d'un réseau iono-covalent. Il n'est donc pas étonnant de le voir intervenir dans la condition générale d'existence d'un tel réseau

$$n_e/n_a + b = 2c$$

où n_e est le nombre d'électrons susceptibles de participer aux liaisons covalentes compatibles avec le type de structure (éventuellement après excitation à un niveau supérieur), n_a le nombre d'atomes

Tableau 1

Orbitales utilisées dans le schéma covalent	Coordinance de base $c = m+n$	Principales structures	Désignation des liaisons	Exemples
sp^3	4	*B*3, *B*4*	tétraédrique	InSb, ZnS, $[CsSb]^{2-}$†
sp^3	4*R*	*B*2	cubique	CsCl
p^3	3	*B*29	trigonale pyramidale	SnS, $[BiTe]^+$
p^3	3*R*	*B*1	octaédrique	PbS, CaSe, NaCl
sp/sp^3	2/4*R*	*C*1	tétr./cub.	Mg_2Sn, Na_2S, $[Li_2Bi]^-$

* notations du *Strukturbericht*.
† réseau partiel, cf. Réf. (7).

y occupant les sites d'anions et b le nombre de liens que ces derniers atomes forment entre eux dans le schéma covalent. La règle que MOOSER et PEARSON[8, 9] avaient proposée pour la distinction entre la liaison metallique et une "liaison semiconductrice" correspond au cas particulier où $c = 4$ (liaison tétraédrique). Les règles de filiation à partir des composés binaires, utilisant les schémas covalents et leurs charges formelles, rendent inutile la vérification de cette condition d'existence, qui se trouve alors automatiquement remplie.[1]

2. DEFINITION D'UN PARAMETRE D'IONICITE

Nous avons trouvé précédemment que la contribution ionique à l'énergie d'activation E était beaucoup plus élevée que la contribution covalente et que le rapport E_{ion}/E dans les composés III–V, II–VI et IV–VI atteignait en moyenne 65, 75 et 90 pour cent.[4] D'autres arguments ont été récemment avancés par FOLBERTH en faveur d'un aspect ionique important dans les composés cristallisant dans les structures de la blende et de la würtzite[10, 11] et les travaux de BLOEM[12] et de SCANLON[13] sur le sulfure de plomb montrent bien que l'aspect ionique est au moins aussi important dans celle du sel gemme. GOODMAN a enfin rappelé qu'une formule chimique MX où n'intervient aucune séparation de charges entre les atomes comporte en général déjà une certaine ionicité, et insiste sur le fait que la formule neutre ZnS par exemple est également éloignée des schémas covalent $Zn^{2-}S^{2+}$ et ionique $Zn^{2+}S^{2-}$, d'où une ionicité de 50 pour cent à laquelle s'ajoute l'ionicité supplémentaire résultant d'une éventuelle séparation de charges suivant un dipôle de signe $Zn^{(+)}S^{(-)}$.[14]

En vue de définir un paramètre simple tenant compte des observations précédentes, nous proposons de considérer une unité MX arbitrairement séparée du réseau cristallin, c'est-à-dire une seule liaison M–X, abstraction faite des autres liens que peuvent former chacun des atomes M et X. Soient φ_M et φ_X les fonctions orbitales atomiques (supposées orthogonales en première approximation) qui représentent l'état des électrons sur les atomes M et X considérés comme des systèmes distincts (méthode de la mésomérie ou "valence-bond theory"). On sait que la fonction d'onde du système affecte alors la forme générale

$$\psi = a_1\varphi_M(1)\varphi_X(2)+a_2\varphi_M(2)\varphi_X(1) + a_3\varphi_M(1)\varphi_M(2)+a_4\varphi_X(1)\varphi_X(2)$$

où les deux premiers termes sont relatifs à une liaison covalente, avec permutation des deux électrons de la paire commune, tandis que les deux derniers sont relatifs à une liaison ionique, avec permutation des M et X dans les rôles de cation et d'anion. SYRKIN et DYATKINA[15], puis COULSON[16] ont montré que si l'atome X est supposé jouer le rôle d'anion, on pouvait écrire :

$$\psi = a\psi_{cov}+a'\psi_{ion}$$

où ψ_{cov} et ψ_{ion} représentent les fonctions d'onde normalisées correspondant aux schémas covalent et ionique et le rapport a'/a est une constante dont la valeur est liée au caractère ionique de la liaison. Si l'on prend pour ψ_{cov} l'expression la plus simple,

négligeant la permutation des deux électrons, il vient :

$$\psi = a\varphi_M(1)\varphi_X(2)+a'\varphi_X(1)\varphi_X(2)$$

Nous voyons que, tandis que l'électron (2) est toujours représenté par l'orbitale atomique φ_X, l'électron (1) est représenté tantôt par l'orbitale φ_M, tantôt par l'orbitale φ_X suivant que l'on considère le schéma extrême covalent ou le schéma ionique. Nous retrouvons la distinction faite à la Section 1 entre électrons "sédentaires" et "nomades" et la Fig. 2 est à rapprocher des schémas

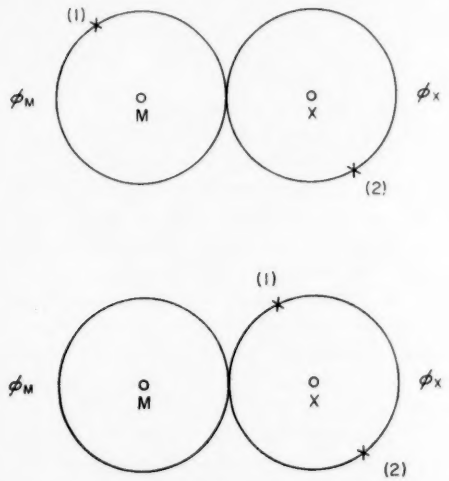

FIG. 2. Répartition des électrons de liaison sur les orbitales atomiques de M et X.

de liaisons portés sur la Fig. 1. Nous pouvons alors, en négligeant les intégrales d'échange, considérer que la résonance entre les schémas covalent et ionique n'affecte que l'un des électrons et écrire :

$$\psi = [a\varphi_M(1)+a'\varphi_X(1)]\varphi_X(2)$$

La normalisation de la fonction d'onde ψ permet de remplacer a et a' par un paramètre unique λ exprimant l'ionicité de la liaison M–X. Suivant la manière dont on l'introduit, on peut obtenir un paramètre variant entre 0 et l'infini ou seulement entre 0 et 1. Nous avons préféré cette dernière solution et obtenons

$$\psi = [(1-\lambda)^{1/2}\varphi_M+\lambda^{1/2}\varphi_X]\varphi_X$$

d'où il ressort que chacun des électrons "nomades" aura sur les atomes M et X des probabilités de présence respectivement égales à $(1-\lambda)$ et λ tandis que chaque électron "sédentaire" aura toujours sur l'atome X une probabilité de présence égale à l'unité. Si nous considérons la totalité des $2c$ électrons de valence participant aux liaisons (c électrons nomades + c électrons sédentaires), nous voyons qu'ils se répartiront en $c(1-\lambda)$ sur l'atome M et $c(1+\lambda)$ sur l'atome X.

Supposons un instant que l'unité MX ait été constituée par la simple mise en présence à grande distance des atomes isolés (neutres), dont les formules électroniques sont bien connues. Il est alors aisé de déterminer pour chaque type de composé binaire un paramètre λ_0 tel que les $2c$ électrons des c cases quantiques participant aux liaisons soient répartis entre M et X suivant $c(1-\lambda_0)$ et $c(1+\lambda_0)$. On vérifie facilement que, si m et n sont les charges définies à la Section 1, on a :

$$\lambda_0 = m/c = 1-n/c$$

Le Tableau 2 donne les valeurs ainsi obtenues et l'on remarque immédiatement qu'elles constituent une évaluation grossière de l'aspect ionique.[17]* Nous appellerons λ_0 *l'ionicité atomique* de la liaison M–X.

L'hypothèse précédente ne saurait toutefois être maintenue si nous nous plaçons dans le cas d'un réseau cristallin. Nous savons en effet que chaque atome y supporte une charge effective, c'est-à-dire que sa formule électronique diffère de celle de l'atome neutre. Soit q la charge effective (en unités électroniques) portée par l'atome M et $q' = -q$ celle portée par l'atome X : la charge q est alors positive lorsque le signe du dipôle est conforme à celui qu'il a dans le schéma ionique $M^{(+)}X^{(-)}$ et négative s'il est conforme à celui qu'il a dans le schéma covalent $M^{(-)}X^{(+)}$. Le nombre d'électrons de valence appartenant au nuage électronique de l'atome X diffère donc de la quantité $c(1+\lambda_0)$ par l'adjonction de q électrons provenant de l'atome M, de sorte que :

$$c(1+\lambda) = c(1+\lambda_0)+q$$
$$\lambda = \lambda_0+q/c \quad (\text{ou } \lambda_0-q'/c)$$

* *Note ajoutée sur épreuves.* La quantité $c\lambda_0$ constitue également une valeur approchée de la différence d'électronégativité Δx et peut être utilisée par exemple pour le calcul empirique de l'énergie d'activation dans la structure de la blende [cf. Ref. (4)].

Tableau 2

Orbitales	I	II	III	IV	V	VI	VII	λ_0
sp^3				Ge				0
sp^3			In		Sb			0,25
sp^3		Zn				S		0,50
sp^3R	Cs						Cl	0,75
p^3					As			0
p^3R				Pb		S		0,33
p^3R		Ca				Se		0,33
p^3R	Na						Cl	0,67
sp/sp^3R			Mg_2		Sn			0
sp/sp^3R	Na_2					S		0,50

Nous appellerons λ *l'ionicité cristalline* de la liaison M–X, somme de l'ionicité atomique et de la charge déplacée par liaison ou polarité.*

Dans le cas où les orbitales de liaison utilisées ne sont pas les mêmes pour les atomes M et X, la formule stoéchiométrique du cristal fait intervenir des indices simples (par exemple M_2X avec orbitales sp/sp^3R dans la structure de l'antifluorite), et il devient nécessaire de distinguer les charges m et m', n et n', les coordinances c et c' et les charges q et q'. Il est alors facile de vérifier que $m/c = m'/c'$, $n/c = n'/c'$ et $q/c = q'/c'$ de sorte que les formules ci-dessus restent valables individuellement pour chaque atome, et conduisent à des valeurs uniques ed λ_0 et λ, caractéristiques de la liaison M–X.

3. POLARITE ET CHARGES EFFECTIVES

Dans le but d'approfondir la notion de charge effective, nous allons revenir aux aspects complémentaires covalent et ionique décrits dans la Section 1. On considère souvent que l'aspect covalent d'une liaison entre deux atomes M et X provient de la déformation progressive des nuages électroniques des ions M^{n+} et X^{n-} lorsque ceux-ci approchent l'un de l'autre, sous l'influence des potentiels créés par les charges $n+$ et $n-$.[18, 19] Si nous assimilons ces ions à des sphères chargées de rayons r pour le cation et r' pour l'anion, les valeurs des potentiels à la surface des sphères sont n/r et n/r'. Supposons les deux ions au contact : on peut penser que le potentiel qui régnerait au point de contact en l'absence de déformation—soit $n/r+n/r'$—est une valeur caractéristique permettant de préjuger l'établissement de liens covalents entre atomes identiques ou différents.

Considérons d'abord des atomes identiques. Il y a toujours dans ce cas une grosse différence de rayon entre les ions X^{n+} et X^{n-} de sorte que l'on peut négliger n/r' et se borner à considérer n/r. La Fig. 3 en donne les valeurs pour les principaux éléments de la classification périodique (à l'exception des éléments de transition) en fonction des rayons ioniques de PAULING[6] en angströms. On voit immédiatement que tous les éléments dont le rapport n/r est ainsi inférieur à 7 ont une conductibilité métallique alors que pour tous ceux dont le rapport est supérieur à 7 on connait au moins une variété semiconductrice dont les atomes forment des liens covalents. Ceci peut être interprêté, par exemple pour le germanium, en disant que le potentiel qui serait créé par l'ion Ge^{4+} est suffisamment élevé pour entraîner la forte déformation du nuage électronique de Ge^{4-} constituant le lien de covalence. La charge transférée est alors égale à la charge 4 portée par les ions initiaux et l'on aboutit à un arrangement où chaque atome porte une charge effective nulle.

Considérons ensuite des atomes différents M et X. Si, reprenant la même image, nous partons de deux ions M^{n+} et X^{n-} s'approchant jusqu'au

* On remarquera que, dans le cas des hydracides, $\lambda_0 = 0$, $c = 1$ et $\lambda = q$, ce qui explique la confusion faite par de nombreux auteurs entre l'ionicité et la polarité d'une liaison.

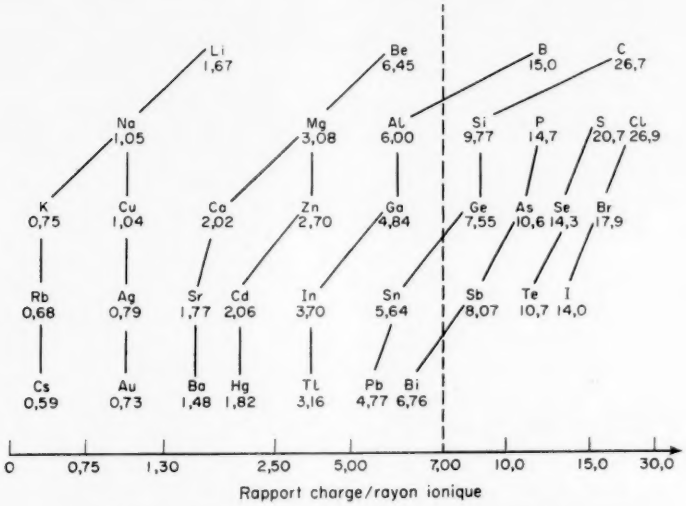

FIG. 3. Frontière entre les éléments métalliques et semiconducteurs.

contact, il est clair que la charge transférée sera ici inférieure à la charge ionique initiale, de sorte qu'il subsistera sur chaque atome une charge effective q. Nous nous étions efforcé, au cours d'une étude antérieure,[17] d'utiliser les valeurs de q figurant dans la littérature, et généralement déduites de données expérimentales au prix d'interprétations malaisées et discutables. De telles valeurs sont toutefois très peu nombreuses et, de plus, peu dignes de confiance (il a été proposé pour ZnS par exemple une dizaine de valeurs s'échelonnant entre 0,3 et 1,4.[20, 21] Nous

Tableau 3

Z'	$1/r'$					$1/r$				Z
10	C^{4-}	N^{3-}	O^{2-}	F^-	Ne	Na^+	Mg^{2+}	Al^{3+}	Si^{4+}	10
	0,385	0,585	0,715	0,736		1,053	1,539	2,0	2,44	
18	Si^{4-}	P^{3-}	S^{2-}	Cl^-	Ar	K^+	Ca^{2+}			18
	0,369	0,472	0,543	0,553		0,753	1,01			
					Ni	Cu^+	Zn^{2+}	Ga^{3+}	Ge^{4+}	28
						1,043	1,352	1,613	1,888	
36	Ge^{4-}	As^{3-}	Se^{2-}	Br^-	Kr	Rb^+	Sr^{2+}			36
	0,368	0,451	0,505	0,513		0,677	0,885			
					Pd	Ag^+	Cd^{2+}	In^{3+}	Sn^{4+}	46
						0,794	1,032	1,235	1,408	
54	Sn^{4-}	Sb^{3-}	Te^{2-}	I^-	Xe	Cs^+	Ba^{2+}			54
	0,340	0,408	0,453	0,463		0,592	0,742			
					Pt	Au^+	Hg^{2+}	Tl^{3+}	Pb^{4+}	78
						0,730	0,910	1,054	1,190	
						Tl^+	Pb^{2+}			80
						0,67	0,76			
86	Pb^{4-}	Bi^{3-}								
	0,337	0,402								

proposons ici, pour l'évaluation de ces charges, les relations empiriques suivantes :

cation

$$q = n[1-(Z/r'+Z'/r)C^{te}]$$

anion

$$q' = -n'[1-(Z/r'+Z'/r)C^{te}]$$

n et n' désignant les charges portées par les ions en présence, et la constante étant la même dans les deux cas.

Les valeurs de q et q' sont alors aisément calculées au moyen du Tableau 3 qui donne celles de Z, Z', $1/r$ et $1/r'$ pour les principaux éléments. Pour la plupart des composés semiconducteurs intéressants, la valeur de $(Z+Z')$ est comprise entre 50 et 120, de sorte que nous calculerons la constante dela formule ci-dessus à partir des liaisons Ge–Ge (64) et Sn–Sn (100). On trouve respectivement dans ces deux cas que les valeurs de 0,0128 et 0,0109 donnent des charges effectives nulles et nous adopterons la valeur moyenne 0,01185. On trouve alors une charge sensiblement nulle pour InSb, conformément aux conclusions de SLATER et KOSTER[22], des charges négatives pour AlSb et GaSb, ainsi que le laissait prévoir la formation de paires Li^+–lacunes Sb signalée par différents auteurs[23, 24], et une charge voisine de l'unité pour ZnS, ce qui n'est pas incompatible avec les travaux antérieurs.[21] Enfin, si l'on calcule l'ionicité cristalline au moyen de l'expression $\lambda = \lambda_0 + q/c$, on trouve toujours des valeurs comprises entre 0 et 1 pour les semiconducteurs connus, ce qui indique un ordre de grandeur correct.

Le Tableau 4 donne les valeurs calculées de

Tableau 4. (1°) *Structures B2 et B3/4 (coordinance de base* 4)

Composé	Charge ionique n	Ionicité atomique λ_0	Charge effective q	Ionicité cristalline λ	
AlP	3	0,25	1,55	0,64	
AlAs	3	0,25	0,28	0,32	
AlSb	3	0,25	−0,98	0,01	
AlBi	3	0,25	−3,25	−0,56	*M* (inconnu)
GaP	3	0,25	1,50	0,62	
GaAs	3	0,25	0,49	0,37	
GaSb	3	0,25	−0,49	0,13	
GaBi	3	0,25	−2,33	−0,33	*M* (inconnu)
InP	3	0,25	1,44	0,61	
InAs	3	0,25	0,69	0,42	
InSb	3	0,25	−0,04	0,24	
InBi	3	0,25	−1,43	−0,11	*M* (struct. B10)
ZnS	2	0,50	1,09	0,77	
ZnSe	2	0,50	0,51	0,63	
ZnTe	2	0,50	−0,01	0,50	
CdS	2	0,50	0,97	0,74	
CdSe	2	0,50	0,57	0,64	
CdTe	2	0,50	0,17	0,54	
HgSe	2	0,50	0,29	0,57	
HgTe	2	0,50	0,00	0,50	
MgTe	2	0,50	−0,08	0,48	
CuCl	1	0,75	0,59	0,90	
CuBr	1	0,75	0,38	0,85	
CuI	1	0,75	0,18	0,79	
AgI	1	0,75	0,23	0,81	
CsCl	1	0,75	0,52	0,88	
CsBr	1	0,75	0,42	0,85	
CsI	1	0,75	0,32	0,83	

Tableau 4 (*suite*) (2°) *Structure B*1 (*coordinance de base* 3)

Composé	Charge ionique n	Ionicité atomique λ_0	Charge effective q	Ionicité cristalline λ
GeTe	2	0,33	−0,54	0,15
SnTe	2	0,33	−0,29	0,24
PbS	2	0,33	0,65	0,55
PbSe	2	0,33	0,40	0,46
PbTe	2	0,33	0,16	0,39
CaS	2	0,33	1,34	0,78
CaSe	2	0,33	0,92	0,64
CaTe	2	0,33	0,52	0,50
SrS	2	0,33	1,16	0,72
SrSe	2	0,33	0,81	0,60
SrTe	2	0,33	0,48	0,49 (inconnu)
BaS	2	0,33	0,99	0,66
BaSe	2	0,33	0,72	0,57
BaTe	2	0,33	0,47	0,49
MgS	2	0,33	1,22	0,73
MgSe	2	0,33	0,57	0,52
AgCl	1	0,67	0,53	0,85
AgBr	1	0,67	0,38	0,80
NaCl	1	0,67	0,71	0,91
NaBr	1	0,67	0,49	0,83
NaI	1	0,67	0,27	0,76
KCl	1	0,67	0,72	0,91
KBr	1	0,67	0,57	0,86
KI	1	0,67	0,42	0,81
RbCl	1	0,67	0,62	0,87
RbBr	1	0,67	0,49	0,83
RbI	1	0,67	0,37	0,79

Tableau 4 (*suite*) (3°) *Structure C*1 (*coordinances de base* 2 *et* 4)

Composé	Charges ioniques		Ionicité atomique	Charges effectives		Ionicité cristalline
	n	n'	λ_0	q	q'	λ
Mg_2Si	2	4	0,00	1,25	−2,51	0,63
Mg_2Ge	2	4	0,00	0,60	−1,20	0,30
Mg_2Sn	2	4	0,00	−0,05	0,10	−0,02 (*M*)
Mg_2Pb	2	4	0,00	−1,13	2,26	−0,57 *M*
Na_2S	1	2	0,50	0,71	−1,42	0,86
Na_2Se	1	2	0,50	0,49	−0,98	0,74
Na_2Te	1	2	0,50	0,27	−0,55	0,64
K_2S	1	2	0,50	0,72	−1,45	0,86
K_2Se	1	2	0,50	0,57	−1,14	0,78
K_2Te	1	2	0,50	0,42	−0,84	0,71
Rb_2S	1	2	0,50	0,62	−1,25	0,81
Cu_2S	1	2	0,50	0,59	−1,19	0,80
Cu_2Se	1	2	0,50	0,39	−0,78	0,69
Cu_2Te	1	2	0,50	0,18	−0,36	0,59 (inconnu)
Ag_2S	1	2	0,50	0,54	−1,09	0,77
Ag_2Se	1	2	0,50	0,38	−0,77	0,69
Ag_2Te	1	2	0,50	0,24	−0,49	0,62

Vol. 21
1961

λ_0, q, q' (en unités électroniques) et λ pour les principaux composés binaires pour lesquels $(Z+Z')$ est au moins de l'ordre de 30. La seconde décimale a une valeur indicative. Lorsque la valeur de l'ionicité cristalline est trouvée négative, cela signifie qu'une liaison iono-covalente ne saurait exister et nous concluons à la présence de liaisons métalliques notées M. Notre calcul approché ne permet pas de conclure avec précision dans le cas où λ est sensiblement nul et nous indiquons (M)

(b) La neutralisation des charges centrales $+(n+\Delta n)$ et $-(n'+\Delta n')$ en M_2X_1 laisse subsister la charge $\Delta n-\Delta n'$ qui, faible devant les charges principales, peut en première approximation être répartie également entre les deux atomes. On obtient

$$q = n-(\Delta n+\Delta n')/2 \text{ et } q' = -[n'-(\Delta n+\Delta n')/2]$$

(c) Le moment dipolaire ainsi induit dans un cation de polarisabilité α serait de l'ordre de

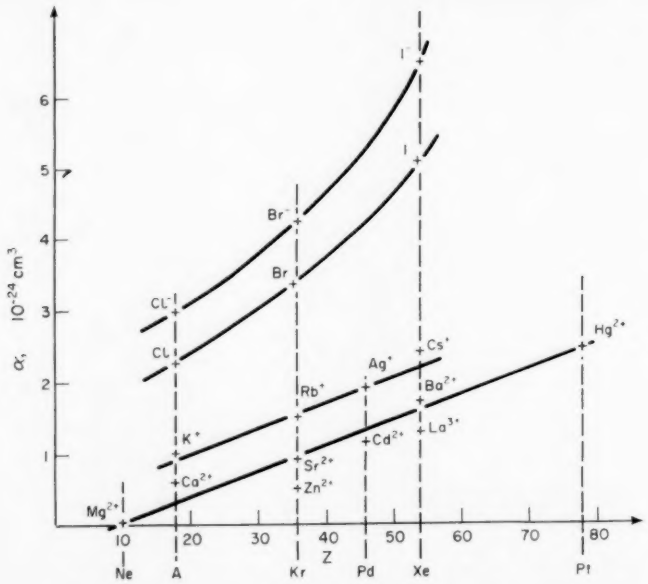

FIG. 4. Relation entre la polarisabilité et le nombre d'électrons.

qui peut s'appliquer à un métal ou à un semiconducteur de très faible énergie d'activation.

La relation empirique ci-dessus définit des charges effectives liées à la polarisation mutuelle des ions en présence dans les cristaux. Si l'on veut avoir une idée grossière de la signification de ces charges, on peut adopter l'image suivante.

(a) Chaque ion induit chez son partenaire un moment dipolaire $\delta\Delta n$ (cation) ou $\delta'\Delta n'$ (anion), où δ et δ' sont les distances M_1M_2 et X_1X_2 des centres de gravité des charges $+(n-\Delta n)$ en M_1, $+(n+\Delta n)$ en M_2, $-(n'+\Delta n')$ en X_1 et $-(n'-\Delta n')$ en X_2.

grandeur de celui que créerait un champ uniforme n'/r'^2, et réciproquement. On obtient des moments $\delta\Delta n \sim \alpha n'/r'^2$ et $\delta'\Delta n' \sim \alpha' n/r^2$.

(d) Les distances δ et δ' seraient inversement proportionnelles aux rayons ioniques r' et r, d'ou $\Delta n \sim \alpha n'/r'$ et $\Delta n' \sim \alpha' n/r$.

Nous retrouvons donc les potentiels caractéristiques n/r et $n'r'$ mentionnés plus haut, pondérés par les polarisabilités des partenaires. Celles-ci, ainsi que le montre la Fig. 4, établie d'après quelques valeurs connues,[25, 26] sont grossièrement proportionnelles au nombre total d'électrons Z ou

Z' de l'ion, si l'on excepte les atomes légers, de sorte que nous avons finalement, à un facteur constant près, $\Delta n \sim nZ/r'$ et $\Delta n' \sim nZ'/r$, et retrouvons la formule empirique proposée ci-dessus.

4. COMPOSÉS TERNAIRES ET CAS PARTICULIERS

Dans le cas d'un composé ternaire A–B–X contenant trois éléments, mais où l'atome X occupe seul les sites de cations et où aucune liaison n'existe entre les atomes A et B, il est assez simple de déterminer l'ionicité et la polarité des diverses liaisons. On suppose pour cela que les liaisons A–X et B–X sont identiques à celles de composés binaires qui cristalliseraient avec une structure de même coordinance, et l'on peut définir par rapport à l'atome X des paramètres moyens λ_0', q' et λ'. Nous prendrons comme exemples les composés ternaires $AgFeSe_2$ et $AgFeTe_2$ cristallisant dans la structure E 1 (chalcopyrite) et qui dérivent par substitution isoélectronique de la blende ZnS (Fe^{3+} : $Z = 23$, $1/r = 1{,}56$). On calcule :

	λ_0	q	q'	λ
Ag–Se	0,75	+0,77	−0,77	0,94
Fe–Se	0,25	+0,39	−0,39	0,35
$AgFeSe_2$ (moyenne)	0,50		−0,58	0,64
Ag–Te	0,75	+0,49	−0,49	0,87
Fe–Te	0,25	−0,24	+0,24	0,19
$AgFeTe_2$ (moyenne)	0,50		−0,12	0,53

Vol. 21
1961

Tableau 5

Composé	Charges ioniques		Ionicités atomiques		Charges effectives		Ionicités cristallines		
	n	n'	λ_0	λ_0' moyen	q	q'	λ	λ' moyen	
B3 ($c = 4$)									
□ Al_2S_3	3	2	0,25	0,50	1,53	−1,02	0,50	0,88	
□ Al_2Se_3	3	2	0,25	0,50	0,26	−0,17	0,31	0,54	
□ Al_2Te_3	3	2	0,25	0,50	−1,00	0,67	0,00	0,33	
□ Ga_2S_3	3	2	0,25	0,50	1,43	−0,95	0,49	0,86	
□ Ga_2Se_3	3	2	0,25	0,50	0,43	−0,29	0,36	0,57	
□ Ga_2Te_3	3	2	0,25	0,50	−0,54	0,36	0,12	0,41	
□ In_2S_3	3	2	0,25	0,50	1,32	−0,88	0,47	0,83	
□ In_2Se_3	3	2	0,25	0,50	0,60	−0,40	0,40	0,60	
□ In_2Te_3	3	2	0,25	0,50	−0,11	0,07	0,14	0,43	
D5 ($c = 2$, $c' = 4$)									
□ Zn_3P_2	2	3	0,00	0,25	1,11	−1,67	0,55	0,66	
□ Zn_3As_2	2	3	0,00	0,25	0,54	−0,82	0,27	0,45	
□ Zn_3Sb_2	2	3	0,00	0,25	0,00	0,01	0,00	0,25	(*M*)
□ Zn_3Bi_2	2	3	0,00	0,25	−0,51	1,53	−0,25	−0,13	*M*
□ Cd_3P_2	2	3	0,00	0,25	1,04	−1,57	0,52	0,64	
□ Cd_3As_2	2	3	0,00	0,25	0,63	−0,94	0,32	0,49	
□ Cd_3Sb_2	2	3	0,00	0,25	0,23	−0,35	0,12	0,34	
□ Cd_3Bi_2	2	3	0,00	0,25	−0,27	0,81	−0,13	0,05	*M*
□ Mg_3P_2	2	3	0,00	0,25	1,23	−1,85	0,61	0,71	
□ Mg_3As_2	2	3	0,00	0,25	0,59	−0,88	0,29	0,47	
□ Mg_3Sb_2	2	3	0,00	0,25	−0,06	0,09	−0,03	0,23	(*M*)
□ Mg_3Bi_2	2	3	0,00	0,25	−0,61	1,84	−0,30	−0,21	*M*

Seule la charge effective moyenne q' peut évidemment avoir une signification physique, et à la condition que les atomes Ag et Fe soient répartis dans le réseau d'une manière ordonnée de sorte que chaque atome Se ou Te forme deux liaisons avec chacun d'eux.

Nous avons expliqué au cours d'études antérieures[1, 7] en quoi l'existence d'un schéma covalent inséparable du schéma ionique conduisait aux notions de réseau "lacunaire" (où les lacunes □ supportent une charge formelle et participent aux liaisons covalentes) et de réseau "compensé" (ou coexistent un réseau partiel iono-covalent et un réseau interstitiel ionique ou moléculaire, avec d'éventuelles translocations électroniques entre ces deux réseaux). Considérons tout d'abord un composé tel que $(\square In_2)Te_3$ cristallisant dans la structure de la blende, mais où un atome sur 3 manque dans les sites de cations. Traitant la lacune comme un atome de valence zéro, nous trouvons :

□–Te	$\lambda_0 = 1$	$q = 0$	$q' = 0$	$\lambda = 1$
In–Te	0,25	−0,11	+0,11	0,14
In_2Te_3 (moyenne)	0,50		+0,07	0,43

On trouve de même, pour le composé $(\square Zn_3)P_2$ cristallisant dans la structure $D5_9$ voisine de l'antifluorite, et où un atome sur 4 manque dans les sites de cations :

□–P	$\lambda_0 = 1$	$q = 0$	$q' = 0$	$\lambda = 1$
Zn–P	0	+1,11	−2,22	0,55
Zn_3P_2 (moyenne)	0,25		−1,67	0,66

Le Tableau 5 donne les valeurs de ces paramètres pour les anions et cations de quelques composés analogues. Comme au Tableau 4, nous avons considéré que les valeurs négatives de l'ionicité cristalline indiquaient la présence de liaisons métalliques *M*.

Passons maintenant à un composé tel que Cs_3Sb cristallisant dans la structure *B*32 (NaTl) qui est un exemple typique de réseau compensé : $[CsSb]^{2-}$ constitue un réseau partiel iono-covalent à structure de blende qui emprunte les deux électrons nécessaires à ses liaisons aux ions interstitiels Cs^+. La formule habituelle

$$\lambda_0 = m/c = 1-n/c$$

donne ici 0,75 ou 0,25 suivant qu'on l'applique à Cs ou Sb, ce qui est compréhensible si nous revenons à notre définition de l'ionicité d'une liaison par rapport aux schémas extrêmes. Les formules covalentes $[Cs^3–Sb^+]$ et ionique $[Cs^+Sb^{3-}]$ sont en effet établies sans ambiguïté, mais nous ignorons comment se répartit sur la formule intermédiaire la charge globale de deux unités négatives affectée au réseau. $[Cs^{2-}Sb]$ correspondrait à $\lambda_0 = 0{,}25$ tandis que $[CsSb^{2-}]$ correspondrait à

Tableau 6

	Réseau partiel	Charges ioniques		Ionicité atomique λ_0	Charges effectives		Ionicité cristalline λ
		n	n'		q	q'	
*B*29 ($c = 3$)	$[SbTe]^+$	3	2	∼0,2	∼0,2	∼ −0,2	∼0,25
	$[BiSe]^+$	3	2	∼0,2	∼0,4	∼ −0,4	∼0,3
	$[BiTe]^+$	3	2	∼0,2	∼0,1	∼ −0,1	∼0,2
*B*3 ($c = 4$)	$[CsSb]^{2-}$	1	3	∼0,6	∼1,1	∼ −1,1	∼0,85
*C*1 ($c=2, c'=4$)	$[Cu_2Sb]^-$	1	3	∼0,4	∼0,3	∼ −0,6	∼0,5

$\lambda_0 = 0{,}75$. Tout ce que nous pouvons affirmer est que la valeur exacte est comprise entre ces deux valeurs, et plus proche de 0,75 puisque l'affinité électronique du cesium est certainement très faible devant celle de l'antimoine. Nous proposons un ordre de grandeur de 0,6. On trouve de même

5. EVALUATION DE LA MOBILITE ELECTRONIQUE

Des efforts ont été faits pour lier la mobilité des porteurs aux données structurales et atomiques dès que l'intérêt suscité par le germanium et le silicium commença à s'étendre aux composés.

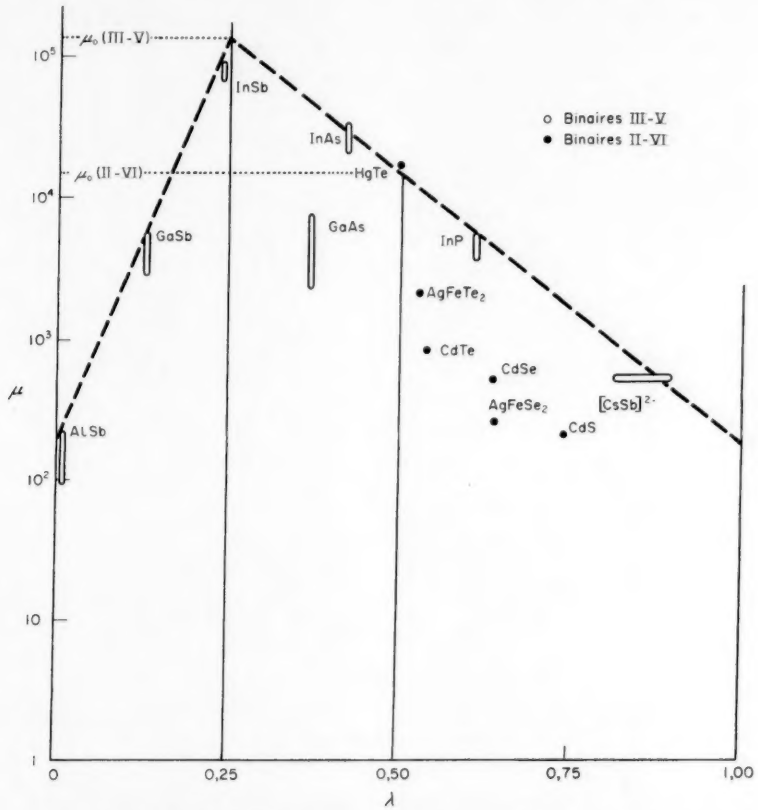

FIG. 5. Variation de la mobilité électronique avec l'ionicité cristalline (structure de la blende).

$\lambda_0 = 0$ à 0,33 avec valeur probable 0,2 pour $[BiTe]^+$ dans la structure $C33$ (Bi_2Te_3) et $\lambda_0 = 0{,}25$ à 0,50 avec valeur probable 0,4 pour $[Cu_2Sb]^-$ dans la structure $D0_3$ (Li_3Bi). Le calcul des charges effectives est également très imprécis puisque les nuages électroniques des atomes en présence sont modifiés. Le Tableau 6 donne quelques ordres de grandeur.

WELKER[27] suppose que, dans une série isoélectronique, la mobilité commence par augmenter lorsqu'on passe de l'élément IV au composé III–V, mais cette règle rencontre pour AlSb une exception flagrante. GOODMAN[28], ayant évalué approximativemement la contribution ionique à l'enérgie d'activation pour quelques composés dans la structure de la blende, montre que la

Vol. 21
1961

mobilité passe par un maximum au voisinage de InSb puis diminue de nouveau lorsque cette contribution augmente. JOUZE[29] montre que la mobilité diminue dans une structure donnée quand la chaleur de formation, c'est-à-dire la polarité de la liaison, augmente. Enfin FOLBERTH[30] introduit un "degré de modulation" indiquant la différence d'action des cuvettes de potentiel des atomes III et V sur les électrons de conduction et suppose que ce paramètre s'annule entre InSb et InAs sous l'influence de la polarisation des nuages électroniques et devient négatif pour d'autres composés. Les mobilités décroissant lorsque la valeur absolue de ce degré de modulation augmente, il devient ainsi possible d'expliquer les exceptions à la règle de WELKER.

Il est à peu près évident que le paramètre mathématique introduit par FOLBERTH s'annule en même temps que la charge effective q, telle que nous l'avons définie ci-dessus, et est de même signe. Nous devons donc trouver, grosso modo, que les mobilités élevées coincident avec des charges effectives voisines de zéro. Effectivement, la formule proposée à la Section 3 donne $q = -0{,}04$ pour InSb et 0 pour HgTe. Le classement en fonction de q ne nous a toutefois pas paru adéquat parce qu'il n'expliquait pas la décroissance inégale de la mobilité électronique pour les valeurs négatives et positives de part et d'autre du zéro. Ainsi, on trouve une mobilité électronique $\mu = 5{,}000$ cm²/V sec pour $q = +1{,}44$ (InP), mais seulement $\mu = 200$ pour $q = -1$ (AlSb). Il nous a semblé nécessaire de bien mettre en

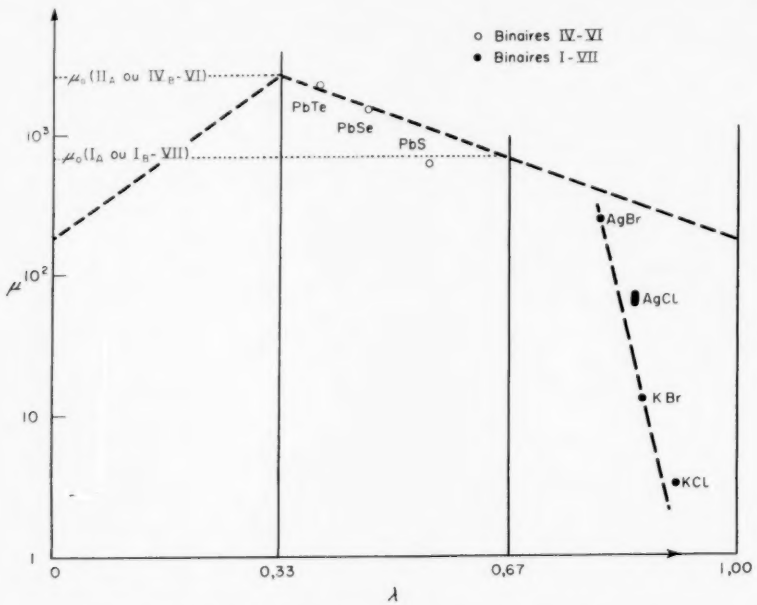

FIG. 6. Variation de la mobilité électronique avec l'ionicité cristalline (structure du sel gemme).

évidence le fait que dans le premier cas la charge effective n'atteint que la moitié de sa valeur maximale (la formule ionique $In^{3+}P^{3-}$ correspondrait au transfert de 3 électrons par rapport aux formules des atomes neutres) tandis que dans le second elle atteint cette valeur (le transfert d'un électron correspond exactement à la formule covalente $Al^{-}Sb^{+}$). Le paramètre d'ionicité λ défini à la Section 2 répond à cette préoccupation et les graphiques logarithmiques des Figs. 5 et 6 indiquent les valeurs des mobilités (d'après l'ouvrage récent de BUBE[31]) en fonction de λ, la première pour les liaisons diélectroniques par

orbitales hybrides sp^3 (structure de la blende) et la seconde pour les liaisons monoélectroniques par orbitales p^3 (structure du sel gemme).

Considérons tout d'abord les composés III–V : il apparaît nettement que le logarithme de la mobilité décroît à peu près linéairement de chaque côté de la valeur $\lambda = \lambda_0 = 0{,}25$ correspondant à une charge effective nulle. Si l'on choisit au sommet l'ordonnée $\lambda_0 = 1{,}26 \times 10^5$ cm²/V sec pour correspondre à cette abscisse, on voit que les composés InSb, GaSb, et AlSb, tous de charge effective négative, so placent sur la droite joignant ce sommet au point d'abscisse 0 et d'ordonnée 180, tandis que les composés InAs et InP, de charge effective positive, se placent sur la droite joignant le sommet au point d'abscisse 1 et de même ordonnée 180 cm²/V sec. Passons maintenant aux composés II–VI : nous pouvons nous attendre à tracer une figure triangulaire analogue à la précédente, mais dont le sommet aura ici pour abscisse $\lambda = \lambda_0 = 0{,}50$. Rien ne pouvait nous faire prévoir *a priori* que ce sommet se trouverait sur une des droites limites de la figure précédente, et il n'est d'ailleurs pas exclus qu'une révision de la mobilité de HgTe amène ultérieurement à séparer les deux figures. Toutefois, si l'on adopte pour ce composé la valeur $\mu = 16{,}000$ cm²/V sec citée par BUBE, son point représentatif se place sensiblement sur la droite limite précédemment tracée, entre InAs et InP. La Fig. 6 a été tracée par analogie avec la figure précédente. On est conduit à y adopter une valeur de μ_0 de $2{,}5 \times 10^3$.

Ces graphiques appellent deux remarques : d'une part les droites qui limitent leur partie supérieure semblent constituer une évaluation maximale de la mobilité électronique ; d'autre part les points représentatifs des principaux composés pour lesquels cette mobilité est connue avec quelque précision se répartissent immédiatement au-dessous de ces droites dans des régions aisément délimitées. Ils pourront donc constituer une aide non négligeable dans la recherche de composés à mobilité électronique élevée.

6. PREVISIONS POUR LES COMPOSES BINAIRES

Une évaluation maximale de la mobilité d'un composé donné peut ainsi être obtenue à l'aide des relations empiriques ci-dessous, correspondant aux droites limites des Figs. 5 et 6

$$(\log \mu - \log \mu_0)/(\log \mu_0 - 2{,}25) = (\lambda - \lambda_0)/(\lambda_0 - 1)$$

$$(\log \mu - \log \mu_0)/(\log \mu_0 - 2{,}25) = (\lambda - \lambda_0)/\lambda_0$$

et respectivement valables lorsque $\lambda > \lambda_0$ et $\lambda < \lambda_0$. Les valeurs de $\log \mu_0$ y sont données par la Fig. 7. Le Tableau 7 compare les mobilités ainsi calculées avec les mobilités maximales mesurées pour quelques composés.

Il est inutile de souligner le caractère approximatif des valeurs de mobilité ainsi calculées : on

Tableau 7

Structure *B*3 (blende)			Structure *B*1 (sel gemme)		
Composé	Mobilité en cm²/V sec		Composé	Mobilité cm²/V sec	
	calculée	observée		calculée	observée
AlSb	200	200	GeTe	600	
GaSb	5,000	5,000	SnTe	1,200	
InSb	95,000	80,000	PbTe	2,000	2,100
AlAs	70,000		PbSe	1,500	1,400
GaAs	45,000	6,800	PbS	1,000	600
InAs	30,000	30,000			
InP	5,000	5,000			
GaP	5,000				
AlP	4,000				
HgTe	15,000	16,000			
HgSe	7,500				

sait que cette propriété dépend de nombreux facteurs dont le raisonnement élémentaire ci-dessus ne peut tenir compte. Si l'on se borne toutefois aux deux mécanismes de dispersion les plus importants à la température ambiante—les interactions avec les vibrations acoustiques (phonons) et les interactions avec les vibrations optiques du réseau cristallin—il est possible d'expliquer qualitativement l'allure de la variation de la mobilité avec l'ionicité cristalline en supposant que c'est généralement le second, étroitement lié dans les composés au caractère polaire des liaisons, qui limite la mobilité. Nous devons retrouver dans ce cas le même ordre de grandeur de la mobilité lorsque la charge effective par liaison $q/c = \lambda - \lambda_0$ atteint sa valeur maximale, c'est-à-dire pour $\lambda = 0$ et $\lambda = 1$. Les graphiques des Figs. 5 et 6 montrent que cette mobilité semble de l'ordre de 180 cm²/V sec. Nous devons d'autre part observer des mobilités élevées en l'absence de charge effective ($\lambda = \lambda_0$) lorsque le seul mécanisme restant est la dispersion acoustique, de plus faible importance. Ce serait le cas de InSb, HgTe, PbTe et les mobilités atteintes alors semblent dépendre à la fois de la structure cristallographique, c'est-à-dire du type de liaison, et de l'ionicité atomique λ_0 (cf. Fig. 7). Indiquons que la prédominance de la dispersion polaire a justement été invoquée par EHRENREICH pour InAs et InP,[32] puis pour GaAs,[33] tandis que la prédominance de la dispersion acoustique l'était pour HgTe par TSIDIL'KOVKII[34] et RODOT[35]. On hésite encore à voir dans le cas d'InSb une dispersion polaire[36, 35] ou acoustique[37]. ANSEL'M *et al.* ont envisagé un mécanisme de dispersion par plusieurs phonons simultanés qui pourrait s'appliquer à ce dernier cas.[38] Enfin, il est probable qu'un autre mécanisme de dispersion intervient pour les halogénures alcalins (Fig. 6).

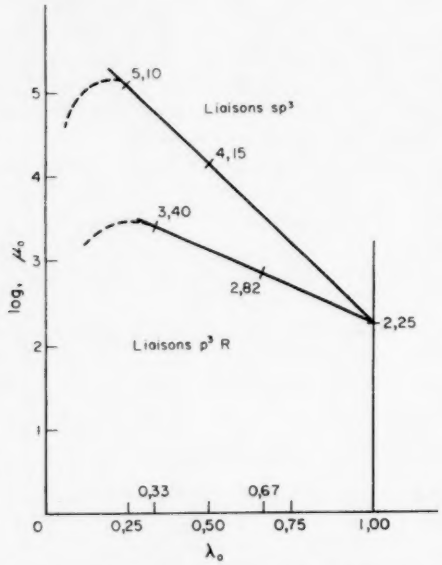

FIG. 7. Variation de log μ_0 avec l'ionicité atomique.

Tableau 8

Composé	Elément le plus volatil	Signe de la charge effective de M	Type de conductibilité	
			prédit	observé
GaP	P	+	*n*	
InP	P	+	*n*	*n*
GaAs	As	+	*n*	*n*
InAs	As	+	*n*	*n*
AlSb	Sb	−	*p*	*p*
GaSb	Sb	−	*p*	*p*
InSb	Sb	0	*n* ou *p*	*n* ou *p*
HgSe	Hg	+	*p*	*n**
HgTe	Hg	0	*n* ou *p*	*n* ou *p*
SnTe	Te	−	*p*	
PbTe	Te	+	*n*	

* type *p* inconnu.

Il est intéressant de remarquer que le signe de la charge effective permet de prédire le type de conductibilité à l'état pur d'un composé binaire MX préparé à la pression atmosphérique, si l'on connait les tensions de vapeur respectives des éléments le composant à sa température de fusion. Ainsi, pour les binaires III–V, où la tension de vapeur du métalloïde X est toujours la plus forte, on obtient vraisemblablement des défauts de SCHOTTKY relatifs à X et une formule $MX_{1-x}\square_x$ alors que les défauts inverses peuvent être prévus pour les composés $Hg_{1-x}\square_x X$ du mercure, dont la tension de vapeur est très élevée. Sachant qu'une lacune relative à un atome de charge effective positive se comportera vis-à-vis de son entourage comme une charge négative susceptible de piéger un trou (centre accepteur), et inversement, nous pouvons faire quelques prévisions que le Tableau 8 compare aux résultats expérimentaux. Il est possible d'expliquer l'exception flagrante de HgSe en remarquant que c'est un des rares composés où la charge effective reste faible (0,3) pour une différence des rayons *covalents* importante (1,48 et 1,14), de sorte que le mécanisme d'anti-structure rappelé récemment par KRÖGER[39] y est possible, des lacunes de mercure étant occupées par des atomes de sélénium.

Remerciements—C'est avec plaisir que nous mentionnons la correspondance échangée avec le Prof. C. A. COULSON et le Prof. C. KLIXBÜLL-JØRGENSEN au sujet de la conception de l'ionicité exposée au début de cet article.

BIBLIOGRAPHIE

1. SUCHET J. P., *J. Phys. Chem. Solids* **12,** 74 (1959).
2. IOFFE A. F., *Izv. akad. nauk.* (*Fiz.*) (*URSS*) **15,** 477 (1951).
3. IOFFE A. F., *Zh. tekh. fiz.* (*URSS*) **27,** 1153 (1957).
4. SUCHET J. P., *J. Phys. Chem. Solids* **16,** 265 (1960).
5. SUCHET J. P., *Chimie physique des Semiconducteurs.* Dunod, Paris (1961).
6. PAULING L., *The Nature of the Chemical Bond* (3e éd.). Cornell University Press, Ithaca (1960).
7. SUCHET J. P., *Acta Cryst.* **14,** 651 (1961).
8. MOOSER E. et PEARSON W. B., *Phys. Rev.* **101,** 1608 (1956).
9. MOOSER E. et PEARSON W. B., *Rep. Meeting Semiconductors.* Physical Society, Rugby (1956).
10. FOLBERTH O. G., *Z. Naturf.* **15a,** 425 (1960).
11. FOLBERTH O. G., *Z. Naturf.* **15a,** 431 (1960).
12. BLOEM J. *Philips Res. Rep.* **11,** 273 (1956).
13. SCANLON W. W., *Solid State Physics* (éd. par Seitz F. et Turnbull D.). Vol. IX, p. 83. Academic Press, New York (1959).
14. GOODMAN C. H. L., *Nature, Lond.* **187,** 590 (1960).
15. SYRKIN Y. K. et DYATKINA M. E., *Structure of Molecules.* Butterworth, London (1950).
16. COULSON C. A., *Valence.* Clarendon Press, Oxford (1952).
17. SUCHET J. P., *Czech. J. Phys.* (Proc. Conf. Praha 1960), 904 (1961).
18. EVANS R. C., *Crystal Chemistry.* Cambridge University Press, London (1952).
19. VAN ARKEL A. E., *Molecules and crystals in Inorganic Chemistry.* Butterworth, London (1956).
20. BIRMAN L., *Phys. Rev.* **109,** 810 (1958).
21. CURIE D., *Luminescence crystalline.* Dunod, Paris (1960).
22. SLATER J. C. et KOSTER G. F., *Phys. Rev.* **94,** 1498 (1954).
23. KOVER F. et QUILLIET A., *C.R. Acad. Sci., Paris* **244,** 1739 (1957).
24. HROSTOWSKI H. J. et FULLER C. S., *J. Phys. Chem. Solids* **4,** 155 (1958).
25. BÖTTCHER C. J. F., *Rec. Trav. Chim.* **65,** 19 (1946).
26. KETELAAR J. A. A., *Chemical Constitution.* Elsevier, Amsterdam (1958).
27. WELKER H., *Z. Naturf.* **7a,** 744 (1952).
28. GOODMAN C. H. L., *J. Electronics* **1,** 115 (1955).
29. JOUZE V. P., *Zh. tekh. fiz.* (*URSS*) **25,** 2079 (1955).
30. FOLBERTH O. G., *Z. Naturf.* **13a,** 856 (1958).
31. BUBE R. H., *Photoconductivity.* Wiley, New York (1960).
32. EHRENREICH H., *J. Phys. Chem. Solids* **12,** 97 (1959).
33. EHRENREICH H., *Czech. J. Phys.* (Proc. Conf. Praha 1960) 67 (1961).
34. TSIDIL'KOVSKII I. M., *Zh. tekh. fiz.* (*URSS*) **27.** 1744 (1957).
35. RODOT M., Thèse d'état, Paris (1960).
36. EHRENREICH H., *J. Phys. Chem. Solids* **2,** 131 (1957).
37. JOUZE V. P. et TSIDIL'KOVSKII I. M., *Zh. tekh. fiz.* (*URSS*) **28,** 2372 (1958).
38. ANSEL'M A. I. et LANG I. G., *Fiz. Tv. Tela* (*URSS*) **1,** 683 (1959).
39. KRÖGER F. A., *J. Phys. Chem. Solids* **7,** 276 (1958).

J. Phys. Chem. Solids Pergamon Press 1961. Vol. 21, Nos. 3/4, pp. 172–178. Printed in Great Britain.

CATION VALENCIES AND DISTRIBUTIONS IN SPINEL STRUCTURES CONTAINING MANGANESE

M. O'KEEFFE*

Mullard Research Laboratories, Salfords, Nr. Redhill, Surrey, England

(*Received* 3 *March* 1961; *revised* 10 *May* 1961)

Abstract—The amount of Mn^{3+} on octahedral sites required to produce tetragonal distortion in spinels is shown to depend on the nature of the other ions present. The influence of the electronic structure of these other ions is considered from the viewpoint of simple crystal field theory. Crystallographic and magnetic results are reported for spinels in which the A-sites are occupied solely by Zn^{2+} or $Zn^{2+}+Ge^{4+}$. By this means it is shown that $Mn^{3+}+Fe^{2+}$ rather than $Mn^{2+}+Fe^{3+}$ is the stable configuration on octahedral sites of spinels. The discussion is extended to prediction of the valencies and distributions in $FeMn_2O_4$, $CuMn_2O_4$ and the system $x\,Mn_3O_4+(1-x)\,NiMn_2O_4$. The proposed structures are $Mn^{2+}[Fe^{3+}Mn^{3+}]O_4$, $Cu^{2+}[Mn_2^{3+}]O_4$ and $Mn_x^{2+}Mn_{1-x}^{3+}[Ni_{1-x}^{2+}Mn_{1+x}^{3+}]O_4$ respectively.

1. INTRODUCTION

A KNOWLEDGE of the distribution and valencies of transition metal ions in spinels is of great importance in the interpretation of the magnetic, electrical and crystallographic properties of these materials. In particular, spinels containing manganese have given rise to much discussion as to the valence states and the distribution of manganese ions between the available octahedral and tetrahedral sites.[1–6]

In certain cases a study of the crystal symmetry of spinels can yield direct information on the valence states present, as a macroscopic distortion of the normally cubic symmetry due to the Jahn–Teller effect is detectable for octahedrally coordinated ions having the configuration d^4 or d^9.[7] If these ions are present in excess of a certain critical concentration, ordering of the c-axes of the individual tetragonally-distorted octahedra occurs. On octahedral sites this effect will be confined to Mn^{3+} and Cu^{2+} (and Cr^{2+} if this ion occurs in spinels) so that the occurrence of tetragonal distortion can be used to identify these ions.

Zn^{2+} and Ge^{4+} have one well defined valency and a marked preference for tetrahedral coordination so that spinels with the general formula $Zn^{2+}[Mn_x^{3+}A_{2-x}^{3+}]O_4$ and $Zn_{1-x/2}^{2}Ge_{x/2}^{4+}[Mn_x^{3+}B_{2-x}^{2+}]O_4$ can be utilized to find the critical amount, x_c, of Mn^{3+} required to produce macroscopic tetragonal distortion in the presence on octahedral sites of A^{3+} and B^{2+} respectively. It is convenient at this stage to introduce the notation $m(M)$ to be the amount of ion M (A or B in the above formulae) present at the critical composition. Using this procedure WICKHAM and CROFT[3] have found $m(Mn^{2+}) = 0{\cdot}80$ and $m(Co^{2+}) = 0{\cdot}70$. MILLER[8] has described an application of this technique to spinels containing manganese and iron; this work is referred to further below. IRANI *et al.*[9] have collected some of this data and reported results for spinel systems in which Mn^{3+}, Al^{2+} and Mg^{2+} are on octahedral sites. Measurements are described below, from which $m(Fe^{2+})$ and $m(Fe^{3+})$ are determined.

As illustrated by the work of BONGERS,[5] in many cases measurements of the magnetic susceptibility of paramagnetic spinels can prove a powerful method of determining ion valencies. Measurements are also described below where this method is used to distinguish between $Mn^{2+}+Fe^{3+}$ and $Mn^{3+}+Fe^{2+}$.

2. EXPERIMENTAL RESULTS

2.1 *Crystallographic measurements*

2.1.1. $Zn^{2+}[Mn_x^{3+}Fe_{2-x}^{3+}]O_4$. This system is

* Present Address: Department of Chemistry, Indiana University, Bloomington, Indiana.

simple, as any formulations other than that given above can be excluded as energetically unfavorable. Selected compositions were prepared from ZnO, Mn_3O_4 and Fe_2O_3 of at least "Analar" purity by conventional ceramic methods. The oxide mix was prefired at 1000°C for 16–24 hr in air and the final firing was carried out at 1175–1200°C for at least 16 hr in O_2. Cooling was at 50–100°C/hr. Crystallographic data for this system are recorded in Table 1. From these results it can be seen that $m(Fe^{3+}) = 1{\cdot}25$.

Table 1. *Lattice constants for the system* $ZnMn_xFe_{2-x}O_4$

x	a	c	c/a
0	8·443		cubic
0·60	8·443		cubic
0·75	8·44	8·44	just > 1
0·80	8·34	8·69	1·04
1·00	8·28	8·78	1·06
1·20	8·25	8·90	1·08
2·00	8·09	9·24	1·14

2.1.2. $Zn_{x/2}Ge_{1-x/2}[Mn_xFe_{2-x}]O_4$. In this system the ions on octahedral sites are either

$$[Mn_x^{3+}\,Fe_{2-x}^{2+}] \qquad \text{A}$$

or

$$\left.\begin{array}{ll}[Mn_{2x-2}^{3+}Mn_{2-x}^{2+}Fe_{2-x}^{3+}] & x > 1\\ [Mn_x^{2+}Fe_{2-2x}^{2+}Fe_x^{3+}] & x < 1\end{array}\right\} \qquad \text{B}$$

The preparation of samples in this system was as described in Section 2.1.1. except that GeO_2 was an additional raw material and the final firing was carried out in oxygen-free nitrogen for times in excess of 20 hr. The composition of selected samples was checked by chemical analysis. Two phases were always obtained for $x < 1$; a cubic spinel phase and what was presumably an olivine phase. Crystallographic data are recorded in Table 2. From these results it can be concluded that if formula A is correct then $m(Fe^{2+}) \approx 0{\cdot}55$. We must however see if the results are consistent with formulation B.

It is assumed that tetragonal distortion occurs for a definite critical amount of Mn^{3+} on octahedral sites in the presence of one other given cation.

Table 2. *Lattice constants for the system* $Zn_{x/2}Ge_{1-x/2}Mn_xFe_{2-x}O_4$

x	a	c	c/a
1·00	8·498		cubic
1·30	8·486		cubic
1·35	8·481		cubic
1·40	8·475		cubic
1·45	8·474		cubic
1·50	8·35	8·69	1·04
2·00	8·09	9·24	1·14

When there are two cations M′ and M″ with values of m, m_1 and m_2, as well as Mn^{3+} on octahedral sites, the general formula will be $[Mn_t^{3+}M'_yM''_{2-t-y}]$. To find the critical value, t_c, of t we must use a mean m given by

$$m(M', M'') = [ym_1+(2-t_c-y)m_2]/(2-t_c) \quad (1)$$

so that t_c is given by

$$t_c = 2-m(M', M'')$$
$$= \tfrac{1}{2}\{4-m_2-[m_2^2+4y(m_1+m_2)]^{1/2}\} \qquad (2)$$

Alternatively if it is assumed that rather than a critical amount of Mn^{3+} on octahedral sites being necessary for tetragonal distortion the significant quantity is the *ratio* of Mn^{3+} to the other ion, then for the case of two "other" ions we have at the critical composition:

$$\frac{[Mn^{3+}]}{[M']+[M'']} = \frac{t_c}{2-t_c}$$

$$= \left[y\left(\frac{2-m_1}{m_1}\right)+(2-t_c-y)\left(\frac{2-m_2}{m_2}\right)\right]\Big/(2-t_c)$$

$$t_c = y(m_1/m_2-1)+(2-m_2) \qquad (3)$$

Arguments for prefering this equation to equation (2) are given below (see Section 3).

If $m_1 = m(Mn^{2+}) = 0{\cdot}80$ and $m_2 = m(Fe^{3+}) = 1{\cdot}25$ then for formula B we find from equation (2) $x_c = 1{\cdot}49$ and from equation (3) $x_c = 1{\cdot}51$. Both these values are larger than the experimental value ($x_c = 1{\cdot}45$) so that formula A is preferred. For the same system MILLER[8] came to the same conclusion as to the valencies present, but it is

pointed out that MILLER's data are in disagreement with those presented here; in particular a value of $x_c \approx 1{\cdot}2$ was found.

2.1.3. *Other paramagnetic spinels.* In order to determine whether the low value found for $m(Fe^{2+})$ is reasonable, an attempt to find values of m for other d^1 or d^6 ions was made. The choice is restricted to Ti^{3+} and Co^{3+}. Mn^{3+} will almost certainly oxidize Ti^{3+}. In fact attempts to prepare $Zn[Mn_xTi_{2-x}]O_4$ always resulted in some $MnTiO_3$ being formed.

In octahedral coordination Co^{3+} is expected to be in a t_{2g}^6 configuration,[10] whereas to be comparable to Fe^{2+} the "high-spin" state $t_{2g}^4e_g^2$ is required. BONGERS[5] has prepared $ZnCoMnO_4$ which is a cubic spinel, and his susceptibility measurements point to a formula $Zn^{2+}[Co^{2+}Mn^{4+}]O_4$. This is very reasonable as it will be shown below that $Zn^{2+}[Co^{3+}Mn^{3+}]$ would be expected to be tetragonal.* It was not found possible to obtain good X-ray diffraction patterns for $ZnCo_{0{\cdot}5}Mn_{1{\cdot}5}O_4$. A tetragonal spinel pattern with c/a just greater than 1 and extra unidentified reflections was obtained.

Other spinels with the general formula $Zn[Mn^{3+}M^{3+}]O_4$ were prepared with the results recorded in Table 3. Comparison with results for M = Fe shows that $m(Ga^{3+}) \approx m(Cr^{3+}) \approx m(Fe^{3+}) = 1{\cdot}25$, whereas $m(Mg^{2+}_{0.5}Ti^{4+}_{0.5}) < 1$ clearly illustrating the influence of cation size and charge on its value of m.

Table 3. *Lattice constants for the spinels* $ZnMnMO_4$

M	a	c	c/a
Ge	$8{\cdot}23_2$	$8{\cdot}64_4$	$1{\cdot}05_0$
Al	very poor X-ray pattern		
Cr	8·25	8·63	$1{\cdot}04_5$
$(Mg_{0{\cdot}5}Ti_{0{\cdot}5})$	8·397		cubic

2.2 *Susceptibility measurements.* In favorable cases susceptibility measurements can give direct information on valency states occurring in mixed oxides. However, it was found that the susceptibility of paramagnetic spinels containing iron was dependent on the thermal history. Table 4 records the Curie constant per mole, C_M, and the constant θ in the Curie–Weiss equation

$$\chi_M = C_M/(T-\theta)$$

for a number of spinels. Measurements were made by the Gouy method from room temperature up to about 900°C.

The Curie constant of $ZnMn_2O_4$ was in good agreement with that found by BONGERS[5] and is in fair agreement with that calculated for a

Table 4. *Preparative details and the results of susceptibility measurements for a number of spinels*

Material	Firing temp.	Atmos.	Cooling	C_M	$\theta°$
$Zn_{1/2}Ge_{1/2}MnFeO_4$	1200°C	N_2	50°/hr	5·82	−225
$ZnFe_2O_4$	1175°C	O_2	50°/hr	7·30	+100
	1200°C	O_2	50°/hr	6·15	+250
$ZnFe_2O_4$+0·03ZnO	1125°C anneal at 850°C	O_2	50°/hr	7·6	0
$ZnMnFeO_4$	1200°C	O_2	50°/hr	5·94	−125
	1200°C	O_2	quenched	4·69	+175
$ZnMn_2O_4$	1175°C	O_2	50°/hr	5·59	−570

The susceptibility per mole is given by $\chi_M = C_M/(T-\theta)$.
Values of C_M ± approximately 3 per cent.
Values of θ ± approximately 10 per cent or 20° whichever is greater.

* In Section 3.1 it is shown that $m(Co^{3+}(t_{2g}^6))$ is expected to be approximately equal to $m(Fe^{3+}) = 1{\cdot}25$.

spin only moment of $\sqrt{24}\,\mu_B(C_M = 6{\cdot}00)$. The results for the other materials can be explained if it is assumed that at high temperatures some interchange of Zn^{2+} and Fe^{3+} ions occurs leaving a slightly ferrimagnetic material. This would account for the more positive apparent values of θ and the change in slope with heat treatment of the $1/\chi$ vs. T plots, particularly for $ZnFe_2O_4$. It is equally possible that some ZnO is lost by sublimation during firing leaving an iron rich material. Very similar effects have been observed with $ZnFe_2O_4$ by ARROT and GOLDMAN[11]. In view of the large negative value of θ for $Zn_{1/2}Ge_{1/2}MnFeO_4$ it is felt that some reliability attaches to the value of C_M measured. The theoretical "spin only" value for $[Mn^{3+}Fe^{2+}]$ is $C_M = 6{\cdot}00$ and for $[Mn^{2+}Fe^{3+}]$, $C_M = 8{\cdot}75$ so that the former ion valencies are strongly indicated.

From susceptibility measurements, HEIKES and JOHNSTON[12] conclude that in $Li_7Mn_{1-x}O$ the trivalent manganese has zero moment. This is a remarkable result, as even in the low spin state, t_{2g}^4, Mn^{3+} would be expected to have two unpaired electrons. A more sensitive test of the moment of Mn^{3+} is in a rock-salt type compound with the general formula $Li_x^+Mn_x^{3+}Mg_{1-2x}^{2+}O$. This material was prepared by heating the component oxides in air at 1200°C and quenching; materials prepared at lower temperatures contain $LiMn_2O_4$. For $x = 0{\cdot}1$ a single rock salt phase was obtained with $a_0 = 4{\cdot}210$ Å. The susceptibility of this material at room temperature gave an "effective moment" per manganese ion of $5{\cdot}3\ \mu_B$ which is in reasonable agreement with the expected moment of $4{\cdot}90\ \mu_B$. Measurements were not made over a range of temperatures.

3. DISCUSSION

3.1. *The values of m*

The results discussed above indicate that in general $m(M^{3+}) > 1$, whereas $m(M^{2+}) < 1$. The effect of size and or charge is obviously important in determining m, despite assumptions to the contrary.[3,6,8] It is instructive to consider what other factors will influence m.

The ions considered in this work are all approximately the same size for a given charge, so it is supposed that electronic effects are most important in determining the variation of m among ions of the same charge.

In an octahedral field the five d orbitals are split into a lower triplet, t_{2g}, and a higher doublet, e_g; configurations with t_{2g}^1, t_{2g}^2, t_{2g}^4, t_{2g}^5, e_g^1 or e_g^3 will still be orbitally degenerate so that there will be a distortion of the octahedral field. In the case of e^1 or e_g^3 the distortion will be tetragonal, and ÖPIK and PRYCE[13] have shown that in an octahedral field the stable distortion is with $c/a > 1$.

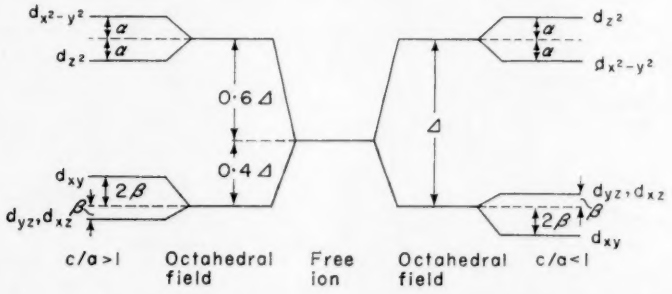

FIG. 1. Splitting of d levels in a tetragonally distorted octahedral field.

The splitting of levels with $c/a > 1$ and < 1 is shown in Fig. 1. With reference to this diagram it should be noted that normally β is 10–100 cm^{-1} and α is of the order of 1000 cm^{-1} whereas $\Delta = 10\,Dq$ is commonly of the order of 20,000 cm^{-1}.[14,15] The stabilization in terms of α, β and Δ, of possible electronic configurations for $c/a > 1$ and < 1 are listed in Table 5.

From Table 5 it can be seen that the preferred *tetragonal* distortion for d^1 and d^6 cations in the "high-spin" state will be with $c/a < 1$. These ions, when present with Mn^{3+} on octahedral sites, will therefore oppose the tendency for the lattice to adopt tetragonal symmetry with $c/a > 1$. Consequently the values of m for these cations will be reduced. Conversely, "high-spin" cations with the configuration d^2 or d^7 will favor distortion with

Table 5. Stabilization of transition metal ions in a tetragonally distorted octahedral field

Electrons	3^+	2^+	$c/a > 1$	$c/a < 1$	favors
0, 10	Sc, Ge	Ca, Zn	—	—	C
1 (t_{2g}^1)	Ti	(Sc)	$0{\cdot}4\Delta+\beta$	$0{\cdot}4\Delta+2\beta$	P
2 (t_{2g}^2)	V	Ti	$0{\cdot}8\Delta+2\beta$	$0{\cdot}8\Delta+\beta$	Q
3 (t_{2g}^3)	Cr	V	$1{\cdot}2\Delta$	$1{\cdot}2\Delta$	C
4 $\left\{ \begin{matrix} t_{2g}^3e_g^1 \\ t_{2g}^4 \end{matrix} \right\}$	Mn	Cr	$0{\cdot}6\Delta+\alpha$ $0{\cdot}6\Delta+E+\beta$	$0{\cdot}6\Delta+\alpha$ $0{\cdot}6\Delta+E+2\beta$	T P
5 $\left\{ \begin{matrix} t_{2g}^3e_g^2 \\ t_{2g}^4e_g^1 \\ t_{2g}^5 \end{matrix} \right\}$	Fe	Mn	— $E+\alpha+\beta$ $2E+2\beta$	— $E+2\beta+\alpha$ $2E+\alpha$	C T Q
6 $\left\{ \begin{matrix} t_{2g}^4e_g^2 \\ t_{2g}^5e_g^1 \\ t_{2g}^6 \end{matrix} \right\}$	Co	Fe	$0{\cdot}4\Delta+\beta$ $0{\cdot}4\Delta+E+2\beta+\alpha$ $0{\cdot}4\Delta+2E$	$0{\cdot}4\Delta+2\beta$ $0{\cdot}4\Delta+E+\beta+\alpha$ $0{\cdot}4\Delta+2E$	P T C
7 $\left\{ \begin{matrix} t_{2g}^5e_g^2 \\ t_{2g}^6e_g^1 \end{matrix} \right\}$	Ni	Co	$0{\cdot}8\Delta+2\beta$ $0{\cdot}8\Delta+E+\alpha$	$0{\cdot}8\Delta+\beta$ $0{\cdot}8\Delta+E+\alpha$	Q T
8 $t_{2g}^6e_g^2$	(Cu)	Ni	$1{\cdot}2\Delta$	$1{\cdot}2\Delta$	C
9 $t_{2g}^6e_g^3$		Cu	$0{\cdot}6\Delta+\alpha$	$0{\cdot}6\Delta+\alpha$	T

Key to Symbols

$E = \Delta - \pi$ where π = energy required to pair two unpaired electrons. If E is positive then "low spin" states obtained (for d^4, d^5, d^6, d^7).
C = cubic, T large tetragonal distortion $c/a > 1$.
P = favors tetragonal distortion $c/a < 1$.
Q = favors tetragonal distortion $c/a > 1$.

$c/a > 1$ and will have enhanced values of m; d^3, d^5 and d^8 cations exhibit no preference, so for m we expect the sequence d^2, $d^7 > d^3$, d^5, $d^8 > d^1$, d^6. Specifically, for divalent ions the theory predicts the sequence $m(Co^{2+}) > m(Mn^{2+}) \approx m(Ni^{2+}) \approx m(Mg^{2+}) > m(Fe^{2+})$.

In fact $m(Mn^{2+}) > m(Co^{2+})$, but this is thought to constitute a special case as Mn^{2+} and Mn^{3+} ions can change places simply by electron transfer which should greatly facilitate the ordering of distorted octahedra. Otherwise the observed values are consistent with the theory. To test the theory more thoroughly the value of $m(Ni^{2+})$ should be found. The predicted value is about 0·63 (i.e. $\frac{1}{2}[m(Co^{2+})+m(Fe^{2+})]$).

The only existing data for manganites containing Ni^{2+} that are of value in this connection are those of FINCH *et al.*[16] for the system Mn_3O_4–$NiFe_2O_4$. According to these authors tetragonal distortion occurs at a composition $Fe^{3+}_{0{\cdot}375}Mn^{2+}_{0{\cdot}625}[Ni^{2+}_{0{\cdot}375}Mn^{3+}_{1{\cdot}250}Fe^{3+}_{0{\cdot}375}]$. Using this result we obtain from equation (2) $m(Ni^{2+}) = 0{\cdot}25$ and from equation (3) $m(Ni^{2+}) = 0{\cdot}54$. The second value is eminently more reasonable so it may be concluded that the method of calculating critical concentrations of Mn^{3+} from equation (3) is the more appropriate.

It should be emphasized that strictly m will depend on a number of variables which have not been considered here. In particular m will depend on T/T_0 where T_0 is the tetragonal to cubic transition temperature for the spinel with only Mn^{3+} on octahedral sites. However, this temperature dependence will be very slight for T/T_0 less than about 0·7,[16] so that this effect will not be important for the spinels considered. It should also be pointed out that spin–orbit interactions have been neglected in this simple treatment. In the absence of Néel coupling this will not be serious for the first transition series ions, though for the second and third series these effects become significant[17] and the predicted sequence for m will no longer hold. For the spinels considered here the Néel temperature is well below room temperature and in the case of spinels with magnetic ions on octahedral sites only, typically about 10°K, whereas the crystallographic data and hence m refer specifically to room temperature.

It is relevant that in the fluorides of the divalent transition metals with the tetragonal rutile structure, the cation is surrounded by a tetragonally distorted octahedron of fluorine ions. For MnF_2, CoF_2 and NiF_2, c/a is $0{\cdot}99 \pm 0{\cdot}01$, whereas for FeF_2, $c/a =$

$0{\cdot}94 \pm 0{\cdot}01$.[18] The lower value of c/a for Fe^{2+} is in accord with the predictions made above.

3.2. Mn_3O_4–$NiMn_2O_4$

The system Mn_3O_4–$NiMn_2O_4$ has been studied by LARSON[19]. There is some doubt as to whether $NiMn_2O_4$ (which is an inverse cubic spinel) is

$$Mn^{2+}[Ni^{2+}Mn^{4+}]O_4 \qquad (A)$$

or

$$Mn^{3+}[Ni^{2+}Mn^{3+}]O_4 \qquad (B)$$

Formula (A) is less likely than (B) as $Mn^{2+}+Mn^{4+}$ is very unstable with respect to $2Mn^{3+}$ (the third and fourth ionization potentials of Mn are 33·7 eV and 50·7 eV respectively). BONGERS'[5] susceptibility measurements are equally consistent with either formula, but BALTZER and WHITE[20] prefer formula (A) on the basis of saturation magnetization studies. According to which formula is adopted the mixed crystals $x Mn_3O_4+(1-x)\ NiMn_2O_4$ can be written as

$$Mn^{2+}[Ni^{2+}_{1-x}Mn^{3+}_{2x}Mn^{4+}_{1-x}]O_4 \qquad (A')$$

or

$$Mn^{2+}_{x}Mn^{3+}_{1-x}[Ni^{2+}_{1-x}Mn^{3+}_{1+x}]O_4 \qquad (B')$$

The critical value of x, x_c, for tetragonal distortion to occur is 0·42. However, even with the information that $m(Mn^{4+}) < 1$[cf. $Li^+(Mn^{3+}Mn^{4+})O_4$ which is cubic[3]] and $m(Ni^{2+}) \approx 0{\cdot}55$ it is not possible to distinguish between (A′) and (B′), the calculated value of x_c being close to the observed value in both cases. Nevertheless (B′) is preferred to (A′) for the same reason as (B) is preferred to (A).

It should be noted that $ZnNiMnO_4$ is cubic[5] so that the reasonable formula is $Zn[Ni^{2+}Mn^{4+}]O_4$. $Zn[Ni^{3+}Mn^{3+}]O_4$ would be expected to be tetragonal.* It is for this reason that formulae containing Ni^{3+} were ruled out for $NiMn_2O_4$.

The resistivity in the system Mn_3O_4–$NiMn_2O_4$ is relatively low, suggesting that one element is occurring on crystallographically equivalent sites in more than one valency state,[21] and this has been used[20] as an argument in favor of the distribution (A′). If, however, it is admitted that electron transfer will be easy for an ion with two valencies on tetrahedral sites, there is no objection to (B′).

To confirm that conduction could occur between ions on tetrahedral sites, $FeNi_{1/2}Cr_{3/2}O_4$ was prepared. Owing to the very strong preference of Ni^{2+} and Cr^{3+} for octahedral sites all the iron will be on tetrahedral sites, i.e. $Fe^{3+}_{1/2}Fe^{2+}_{1/2}[Ni^{2+}_{1/2}Cr^{3+}_{3/2}]O_4$. This material was prepared from an appropriate mixture of Fe powder, Fe_2O_3, NiO and Cr_2O_3 subjected to prolonged firings at 1150°C in an evacuated silica vessel. X-ray analysis showed a spinel phase with $a_0 = 8{\cdot}336$ Å. The material was not very well sintered so that reliable resistivity measurements could not be made, but an upper limit is 100 Ω cm. The magnetic moment per formula unit was 0·26 μ_B at 295°K and 0·71 μ_B at 77°K (cf. Néel moment of 1·1 μ_B for the proposed formula).

3.3. $CuMn_2O_4$

$CuMn_2O_4$ is another cubic manganite which has given rise to doubts as to the valencies occurring. X-ray analysis by SINHA *et al.*[6] has shown that the structure is normal. SINHA *et al.*[6] and GOODENOUGH[23] propose $Cu^+[Mn^{3+}Mn^{4+}]O_4$ (C) and BONGERS[5] $Cu^{2+}[Mn^{2+}Mn^{4+}]O_4$ (D). A third possibility is $Cu^{2+}[Mn^{3+}_2]O_4$ (E).

There are two objections to structure (C). (a) The lattice constant ($a_0 = 8{\cdot}28$ Å)[6] is much smaller than expected for this structure; on the basis of $a_0 = 8{\cdot}25$ Å for $LiMn_2O_4$[3] a value of $a_0 \approx 8{\cdot}4$ Å would be predicted using Goldschmidt radii for Li^+ and Cu^+; (b) To produce $Mn^{4+}+Cu^+$ from $Mn^{3+}+Cu^{2+}$ requires an energy of about 30·5 eV which is far greater than could be gained from ordering energy, etc.

Structure (D) with Cu^{2+} on tetrahedral sites would be expected to be tetragonal with $c/a < 1$[7] (cf. $CuCr_2O_4$ $c/a = 0{\cdot}91$[22]). Further, about 17 eV is required to produce $Mn^{2+}+Mn^{4+}$ from $2\ Mn^{3+}$ whereas the energy gained back from ordering is only about 7 eV.[24] This structure can, therefore, also be eliminated.

Structure (E) is left and this has the expected valencies. Although with all Mn^{3+} on octahedral sites it might be expected to be tetragonal, it is suggested that the tendency for Cu^{2+} on tetrahedral sites to produce a tetragonal distortion in the opposite sense ($c/a < 1$) will result in a macroscopic cubic symmetry. The conclusion, therefore, is that (E) is the correct formula.

* It is interesting that if Ni^{3+} were in a low spin state $t^6_{2g}\ e_g$, then it would be expected to produce a macroscopic tetragonal distortion in its own right (see Table 5).

3.4. Fe_3O_4–Mn_3O_4

In view of the great interest in manganese ferrites the ionic distribution in the Mn_3O_4–Fe_3O_4 system is of some importance. The critical composition for tetragonal distortion is $Fe_{1\cdot2}Mn_{1\cdot8}O_4$.[4,16] As $m(Fe^{3+}) = 1\cdot25$ a formula $Mn^{2+}[Mn^{3+}_{0\cdot8}Fe^{3+}_{1\cdot2}]$ is immediately suggested. Further, for Mn_2FeO_4, $c/a = 1\cdot05$, the same value as for $Zn^{2+}[Mn^{3+}Fe^{3+}]O_4$ so that Mn_2FeO_4 is expected to be $Mn^{2+}[Mn^{3+}Fe^{3+}]O_4$ rather than the "mixed" structure proposed by FINCH *et al.*[16]

Acknowledgements—The crystallographic measurements were carried out by Mrs. S. RIDLEY and chemical analyses by Mr. E. MILLET. It is a pleasure to thank Dr. F. W. HARRISON for helpful advice and discussions and the Management of Mullard Research Laboratories for permission to publish this paper.

REFERENCES

1. GOODENOUGH J. B. and LOEB A. L., *Phys. Rev.* **98,** 391 (1955).
2. HARRISON F. W., OSMOND W. F. and TEALE R. W., *Phys. Rev.* **106,** 856 (1957).
3. WICKHAM D. G. and CROFT W. J., *J. Phys. Chem. Solids* **7,** 351 (1958).
4. ESCHENFELDER A., *J. Appl. Phys.* **29,** 378 (1958).
5. BONGERS P. F., thesis, Leiden (1957).
6. SINHA A. P. B., SANJANA N. R. and BISWAS A. B., *Acta Cryst.* **10,** 439 (1957).
7. DUNITZ J. D. and ORGEL L. E., *J. Phys. Chem. Solids* **3,** 20, 318 (1957).
8. MILLER A. J., *Phys. Rev.* **116,** 1481 (1959).
9. IRANI K. S., SINHA A. P. B. and BISWAS A. B., *J. Phys. Chem. Solids* **17,** 101 (1960).
10. COSSEE P., *J. Inorg. Nucl. Chem.* **8,** 483 (1958).
11. ARROT A. and GOLDMAN J. E., *Proc. A.I.E.E. Conf. Magnetism* 1956, p. 516.
12. HEIKES W. D. and JOHNSON R. R., *J. Amer. Chem. Soc.* **78,** 3255 (1956).
13. ÖPIK U. and PRYCE M. H. L., *Proc. Roy. Soc.* **A238,** 425 (1957).
14. VAN VLECK J. H., *J. Chem. Phys.* **7,** 61, 72 (1939).
15. MCCLURE D. S., *Solid State Physics* (edited by Seitz F. and Turnbull D.) Vol. IX, p. 399. Academic Press, New York (1959).
16. FINCH G. I., SINHA A. P. B. and SINHA K. P., *Proc. Roy. Soc.* **A242,** 28 (1957).
17. See for example LIEHR A. D., *Bell Syst. Tech. J.* **39,** 1617 (1960).
18. BAUR W. H., *Acta Cryst.* **11,** 488 (1958).
19. LARSON E. G., *Lincoln Lab. Quart. Rep.* p. 96, January 1959.
20. BALTZER P. K. and WHITE J. G., *J. Appl. Phys.* **29,** 445 (1958).
21. VERWEY E. J. W., HAAYMAN P. W., ROMEIJN F. C. and VAN OOSTERHOUT G. W., *Philips Res. Rep.* **5,** 173 (1950).
22. BERTAUT F. and DELORME C., *C.R. Acad. Sci., Paris* **239,** 504 (1954).
23. GOODENOUGH J. B., *J. Phys. Radium* **20,** 155 (1959).
24. GORTER E. W., *Philips Res. Rep.* **9,** 295 (1954).

J. Phys. Chem. Solids Pergamon Press 1961. Vol. 21, Nos. 3/4, pp. 179–198. Printed in Great Britain.

OPTICAL ABSORPTION SPECTRUM OF HYDROGENIC ATOMS IN A STRONG MAGNETIC FIELD*

H. HASEGAWA

Department of Physics, University of California, La Jolla, California

and

R. E. HOWARD

National Bureau of Standards, Washington 25, D.C.

(*Received* 30 *June* 1960; *revised* 3 *May* 1961)

Abstract—Energy levels, wave functions, and oscillator strengths are calculated for a hydrogenic atom in a uniform, static magnetic field. The results are exact in the strong field limit. The intensity of optical transitions from the ground state to states in the energy continuum is obtained as an explicit function of the energy. The results are applied to a discussion of the magneto-optical absorption spectrum of excitons in semiconductors.

1. INTRODUCTION

MAGNETO-OPTICAL absorption in semiconductors has been treated theoretically by means of a hydrogenic effective mass equation of the form:[1–3]

$$\mathscr{H}\Psi = E\Psi, \tag{1.1}$$

where

$$\mathscr{H} = \frac{1}{2m^*}\left(\boldsymbol{p}+\frac{e}{2c}\boldsymbol{H}\times\boldsymbol{r}\right)^2 - \frac{e^2}{\kappa r}. \tag{1.2}$$

Here κ is the dielectric constant, and the other symbols have their customary meaning. YAFET, *et al.*[1] investigated the ground state solution of this Schrodinger equation using a variational method. WALLIS and BOWLDEN[2] made a similar calculation, and discussed impurity absorption spectra. Recently, ELLIOTT and LOUDON[3] gave a theory of the exciton absorption spectrum in semiconductors based on a refined approximation to solutions of this equation.

The purpose of the present paper is to determine the absorption spectrum of a hydrogenic atom in terms of solutions of equation (1.1) that become exact as the strength of the magnetic field H goes to infinity. It has already been recognized that solutions for strong magnetic fields can be obtained by considering the Coulomb potential $-e^2/\kappa r$ in the Hamiltonian (1.1) as a small perturbation on the magnetic energy levels. The problem is then reduced to solving a one-dimensional Schrodinger equation of the form:

$$-\frac{\hbar^2}{2m^*}\frac{d^2F(z)}{dz^2}+V(z)F(z) = \epsilon F(z), \tag{1.3}$$

where $V(z)$ is an averaged value of the Coulomb potential. This approximation is valid if the field strength is so strong that

$$\frac{\hbar eH}{2m^*c} \gg R = \frac{m^*e^4}{2\kappa^2\hbar^2}. \tag{1.4}$$

Here R is the effective Rydberg constant of the hydrogenic atom. This condition for strong fields can also be written as

$$a^2/\lambda^2 \gg 1, \tag{1.5}$$

where a, the effective Bohr radius, and λ, the radius of the cyclotron orbit, are given by

$$a = \frac{\kappa\hbar^2}{m^*e^2}, \qquad \lambda = \left(\frac{c\hbar}{eH}\right)^{1/2}. \tag{1.6}$$

In the present paper it is shown that for

* A preliminary report on this work is presented in the *Bull. Amer. Phys. Soc.* (ser. 2) **5**, 178 (1960).

$a^2/\lambda^2 \gg 1$, ELLIOTT and LOUDON's analysis of equation (1.3) can be put in a rigorous form. The energy of any eigenstate of equation (1.3) is expressed in terms of dimensionless parameters a/λ and $\log(a/\lambda)+b$, where b, a numerical constant independent of λ, will be determined exactly. It is then possible to express physical quantities derived from the Hamiltonian (1.2) in terms of these two parameters. These expressions are exact in the limit as $H \to \infty$. Subsequently, we classify all absorption peaks arising from dipole transitions between the eigenstates of equation (1.1) as follows:

A. the intensity tends to a finite value for $a/\lambda \to \infty$
B. the intensity vanishes as $(\log a/\lambda)^{-5}$
C. the intensity vanishes as

$$(a/\lambda)^{-r}(\log a/\lambda)^{1-r'}, \quad r \geqslant 2, \quad r' \geqslant 0.$$

We have investigated the absorption spectrum for radiation polarized perpendicular to the static magnetic field, and have found that only one absorption line belongs to Class A. This absorption line is associated with the transition from the ground state to a certain excited bound state, and is allowed only for left circularly polarized radiation. The transitions to all other excited states belong to either Class B or Class C, so that their intensities vanish as $H \to \infty$. For right circular polarization, all transitions from the ground state belong to Class C.

We have given special attention to intensity as a function of photon energy for absorption from the ground state to states near the continuum edge. This problem is of particular interest since a previous theory[2] has indicated a sharp absorption peak at the energy $\hbar eH/2m^*c+I$, where I is the ionization energy (binding energy) of the ground state. This sharp absorption peak was expected as a consequence of the coalescence of free electron states. The density of these states varies with the energy ϵ, measured from the edge, as $\epsilon^{-1/2}$. It will be shown, however, that no singularity of this nature appears in the intensity curve. Rather the intensity at the continuum edge vanishes uniformly as $H \to \infty$. This is consistent with ELLIOTT and LOUDON's theory of the absorption edge in a high magnetic field, and also with recent experimental work on magneto-optic absorption by excitons[4] and donor states[5] in Ge.

2. SUM RULES FOR OSCILLATOR STRENGTHS

We shall denote a normalized eigenfunction and the corresponding energy of the Hamiltonian in equation (1.1) by Ψ_i and E_i respectively, where i is a suitably chosen quantum number. For plane polarized radiation, the intensity of a dipole transition from a state Ψ_i to another state Ψ_j is proportional to the cross section $\sigma_{i\to j}(\omega)$, (the transition probability per unit photon flux), defined by

$$\sigma_{i\to j}(\omega) = \frac{4\pi^2 e^2}{c}\,\omega|\Psi_j, r_\alpha \Psi_i)|^2 \delta(E_j - E_i - \hbar\omega). \quad (2.1)$$

Here ω is the circular frequency of the radiation, and r_α the electron dipole-moment in the direction α of the polarization.

This formula is based on the elementary theory of interactions between atoms and a radiation field. When applying this formula to a solid, assumptions must be made about the dielectric constant, refractive index, and effective mass. We simply assume that these are constants independent of the frequency ω in the energy range over which equation (1.2) applies. Thus, we assume that the intensity of the transition $i \to j$ is proportional to the quantity given by equation (2.1) or, more conveniently, to the oscillator strength, defined by

$$f_{i\to j} = \frac{2m^*}{\hbar^2}(E_j - E_i)|(\Psi_j, r_\alpha \Psi_i)|^2. \quad (2.2)$$

As is well known the $f_{i\to j}$ satisfy the relation

$$\sum_j f_{i\to j} = 1. \quad (2.3)$$

We now show that for circularly polarized radiation with the polarization vector perpendicular to the static magnetic field $\boldsymbol{H}$ alternate sum rules can be written. We introduce complex dipole moments

$$r_\pm = \tfrac{1}{2}(x \pm iy) \quad (2.4)$$

where the xy-plane is taken perpendicular to the magnetic field $\boldsymbol{H}$, and define the oscillator strengths $f^{\pm}_{i\to j}$ as

$$f^{\pm}_{i\to j} = \frac{2m^*}{\hbar^2}(E_j - E_i)|(\Psi_j, r_\pm \Psi_i)|^2. \quad (2.5)$$

Here + and − refer to left circular polarization (l.c.p.) and right circular polarization (r.c.p.), respectively. Using the relation

$$\frac{m^*i}{\hbar}[\mathcal{H},r_\alpha]=\left(\boldsymbol{p}+\frac{e}{2c}\boldsymbol{H}\times\boldsymbol{r}\right)_\alpha\equiv\pi_\alpha, \quad (2.6)$$

we can write

$$f^{\pm}_{i\to j}=\frac{1}{i\hbar}\{(\Psi_i,r_\mp\Psi_j)(\Psi_j,\pi_\pm\Psi_i)-\text{c.c.}\}, \quad (2.7)$$

where

$$\pi_\pm=\tfrac{1}{2}(\pi_x\pm i\pi_y). \quad (2.8)$$

The completeness of the set $\{\Psi_j(\boldsymbol{r})\}$ then provides the following relations:

$$\sum_j f^{\pm}_{i\to j}=\frac{1}{i\hbar}(\Psi_i,(r_\mp\pi_\pm-\pi_\mp r_\pm)\Psi_i)$$

$$=\frac{1}{2}\pm\frac{1}{2}\left(\Psi_i,\frac{1}{\hbar}(xp_y-yp_x)\right)\Psi_i\pm\frac{1}{4\lambda^2}\{\Psi_i,(x^2+y^2)\Psi_i\}. \quad (2.9)$$

Thus, the sums of the oscillator strengths are different for the two polarizations. This difference is, of course, not significant for weak fields. It is important, however, for strong fields, as is seen below.

Let us evaluate equation (2.9) using the ground state function of equation (1.1) given by YAFET *et al.* They made a variational calculation for the ground state energy, assuming the function

$$\Psi_0(\boldsymbol{r})=c\exp\left(-\frac{x^2+y^2}{4a_\perp^2}-\frac{z^2}{4a_\parallel^2}\right),$$

where c is the normalization constant, and the constants $a_\perp$ and $a_\parallel$ are determined by minimizing the energy. Substituting this expression for $\Psi_0(\boldsymbol{r})$ into equation (2.9) we find that

$$\sum_j f^{\pm}_{0\to j}=\frac{1}{2}\pm\frac{a_\perp^2}{2\lambda^2}.$$

For any value of λ, $a_\perp(\lambda)<\lambda$, but $a_\perp(\lambda)$ approaches λ as a^2/λ^2 tends to infinity ($H\to\infty$). Thus, we have

$$\lim_{\lambda\to 0}\sum_j f^{+}_{0\to j}=1, \quad \text{l.c.p.}, \quad (2.10)$$

while

$$\lim_{\lambda\to 0}\sum_j f^{-}_{0\to j}=0, \quad \text{r.c.p.}. \quad (2.11)$$

Since every oscillator strength $f_{0\to j}$ must be positive, [$\Psi_0(\boldsymbol{r})$ is the ground state], equation (2.11) shows that all transitions from the ground state become prohibited for right circular polarization as H tends to infinity. This may be interpreted in the following way. In a very strong magnetic field the effect of the Coulomb potential in the Hamiltonian of equation (1.2) is a weak perturbation on the levels determined by the rest of the Hamiltonian. In the absence of the Coulomb potential, the spectrum is the well known cyclotron resonance spectrum for which a single absorption peak is allowed at the frequency

$$\omega_c=eH/m^*c=\hbar/m^*\lambda^2.$$

Any deviation from this ideal spectrum as a result of the weak perturbation is, therefore, expected to be small, and will vanish when $\boldsymbol{H}\to\infty$. The deviation consists of first, a change of the resonance frequency which causes a shift of the main absorption, and, second, an appearance of new absorption lines (satellites), which are compensated for by a decrease in the main absorption intensity. Thus, equation (2.11) shows that for right circular polarization all absorption peaks must be regarded as weak satellites.*

3. OSCILLATOR STRENGTHS FOR STRONG FIELDS

For $a^2/\lambda^2\gg 1$, an eigenfunction $\Psi(\boldsymbol{r})$ of equation (1.1) can be written in the approximate form

$$\Psi(\boldsymbol{r})=\Phi(x,y)F(z). \quad (3.1)$$

Here $\Phi(x,y)$ represents the motion of the electron in a plane perpendicular to the field $\boldsymbol{H}$, and satisfies the equation

$$\frac{1}{2m^*}(\pi_x^2+\pi_y^2)\Phi=E^{(0)}\Phi. \quad (3.2)$$

$F(z)$ represents the motion of the electron in the z-direction, (the direction of $\boldsymbol{H}$), in a potential $V(z)$, which is the Coulomb potential averaged over the state $\Phi(x,y)$:

$$V(z)=\int|\Phi(x,y)|^2(-e^2/\kappa r)\,dx\,dy. \quad (3.3)$$

* It has, in fact, been shown that for cyclotron resonance of electrons in a parabolic band, the ratio of the intensity for circular polarization of one sense to that of the opposite sense depends on an anisotropy of the effective mass.[6]

Vol. 21
1961

Thus,

$$\left(\frac{p_z^2}{2m^*}+V(z)\right)F(z)=\epsilon F(z). \tag{3.4}$$

The total energy is given by

$$E=E^{(0)}+\epsilon. \tag{3.5}$$

We shall use JOHNSON and LIPPMAN'S method[7] of treating equation (3.2) to determine energy levels and selection rules. The operators π_x, and π_y, defined in equation (2.6), satisfy the commutation relation

$$[\pi_x,\pi_y]=\hbar^2/i\lambda^2, \tag{3.6}$$

and hence, form a canonically conjugate set. We may then introduce another set which, together with $\{\pi_x,\pi_y\}$, describes the system.

We choose the set $\{X,Y\}$ defined by

$$X=x-\frac{\lambda^2}{\hbar}\pi_y, \quad Y=y+\frac{\lambda^2}{\hbar}\pi_x. \tag{3.7}$$

The quantities X, Y are the coordinates of the center of the cyclotron orbit in the x-y plane, and satisfy the commutation relation

$$[X,Y]=i\lambda^2. \tag{3.8}$$

Also,

$$[\pi_x,X]=[\pi_y,X]=[\pi_x,Y]=[\pi_y,Y]=0. \tag{3.9}$$

Hence, in the absence of additional perturbation potentials, the set $\{X, Y\}$ is a constant of motion of the Hamiltonian given by equation (3.2). This gives rise to a high degeneracy of states with a common energy $E^{(0)}$. In the presence of the Coulomb potential $-e^2/\kappa r$, this degeneracy is lifted. However, because of the spherical symmetry of the potential, we still have another constant of motion, namely the angular momentum M, defined by

$$M=\frac{1}{\hbar}(xp_y-yp_x)$$

$$=\frac{\lambda^2}{2\hbar^2}(\pi_x^2+\pi_y^2)-\frac{1}{2\lambda^2}(X^2+Y^2). \tag{3.10}$$

Equations (3.6) and (3.8) imply that (in analogy to the well known rule for harmonic oscillators) we can write

$$\frac{\lambda^2}{2\hbar^2}(\pi_x^2+\pi_y^2)=N+\tfrac{1}{2}, \quad \frac{1}{2\lambda^2}(X^2+Y^2)=\bar{N}+\tfrac{1}{2}, \tag{3.11}$$

where N and $\bar{N}$ may be 0 or positive integers. Thus,

$$M=N-\bar{N} \tag{3.12}$$

and

$$E^{(0)}=\frac{\hbar^2}{m^*\lambda^2}(N+\tfrac{1}{2}), \quad N,\bar{N}=0,1,2\ldots. \tag{3.13}$$

We choose (N, M) as the set of quantum numbers that specifies the eigenstates of equation (1.2) and write each eigenstate as Φ_{NM} or simply as NM. The set (l, m) used by WALLIS and BOWLDEN[2] is related to the set (N, M) as follows:

$$N=l+\tfrac{1}{2}(|m|+m),$$

and

$$m=M=N-\bar{N}. \tag{3.14}$$

Selection rules for the complex dipole moments $r_\pm$ defined by equation (2.4) will now be determined. From equation (3.7)

$$r_\pm=R_\pm\mp\frac{i\lambda^2}{\hbar}\pi_\pm, \tag{3.15}$$

where

$$R_\pm=\tfrac{1}{2}(X\pm iY). \tag{3.16}$$

Now,

$$\pi_+\Phi_{NM}=\frac{\hbar}{\lambda}\sqrt{\frac{N+1}{2}}\,e^{i\theta}\Phi_{N+1\,M+1},$$

$$\pi_-\Phi_{NM}=\frac{\hbar}{\lambda}\sqrt{\frac{N}{2}}\,e^{-i\theta}\Phi_{N-1,M-1}, \tag{3.17}$$

and

$$R_+\Phi_{NM}=\lambda\sqrt{\frac{N-M}{2}}\,e^{i\theta'}\Phi_{N,M+1},$$

$$R_-\Phi_{NM}=\lambda\sqrt{\frac{N+1-M}{2}}\,e^{-i\theta'}\Phi_{N,M-1}, \tag{3.18}$$

where $e^{i\theta}$ and $e^{i\theta'}$ are arbitrary phase factors. Thus, the allowed transitions are

$NM\rightarrow N+1, M+1,$ or $N, M+1$ for l.c.p.,
$NM\rightarrow N-1, M-1,$ or $N, M-1$ for r.c.p..

In particular

$00 \to 11$ for l.c.p. and $00 \to 0,-1$ for r.c.p..

The eigenstates of equation (3.4), the Schrodinger equation for the motion along the field H, can be specified by the letter n. We denote the lowest eigenstate by $n = 0$. Since the potential $V(z)$ is different for each unperturbed state, we can write

$$\left(-\frac{\hbar^2}{2m^*}\frac{d^2}{dz^2}+V_{NM}(z)\right)F_{NMn}(z) = \epsilon_{NMn}\,F_{NMn}\,(z), \tag{3.19}$$

where

$$V_{NM}(z) = \int |\Phi_{NM}(x,y)|^2\left(-\frac{e^2}{\kappa r}\right)dxdy. \tag{3.20}$$

The potential $V_{NM}(z)$ satisfies the relation

$$V_{NM}(z) = V_{N-M,-M}(z), \tag{3.21}$$

so that the eigenvalues and eigenfunctions of equation (3.19) for two unperturbed states NM and $N-M$, $-M$ are identical, and thus

$$F_{NMn}(z) = F_{N-M,-M,n}(z), \text{ and } \epsilon_{NMn} = \epsilon_{N-M,-M,n}. \tag{3.22}$$

The problem of solving equation (3.19) will be considered later.

We now deal with the error involved in writing $\Psi(r)$ in the form of equation (3.1). Using standard perturbation theory, and noting that there is no matrix element of $-e^2/\kappa r$ between two states with different M, we can write the wave function to the first order in the perturbation as

$$\Psi_{NMn} = \Phi_{NM}F_{NMn} + \sum_{N'\neq N}\sum_{n'}\Phi_{N'M}F_{N'Mn'}\frac{(NMn|-e^2/\kappa r|N'Mn')}{E_{NMn}-E_{N'Mn'}}. \tag{3.23}$$

The matrix elements on the right-hand side are taken between two unperturbed states of the form

$$\Phi_{NM}(x,y)F_{NMn}(z).$$

Turning to the ground state $N = 0$, $M = 0$, $n = 0$, we calculate the oscillator strength

$$f_{0\to N,\pm 1,n}.$$

From the expressions for $f_{i\to j}$ given by equation (2.7) and the creation and destruction relations given by equations (3.17) and (3.18), we can see that

(1) the matrix elements

$$(\Psi_{11n},\pi_+\Psi_0) \text{ and } (\Psi_0,R_-\Psi_{0,-1,n})$$

contain non-vanishing terms of zeroth order,

(2) the matrix elements

$$(\Psi_{N1n},\pi_+\Psi_0)\ \ (N\geqslant 2),\ \ (\Psi_{N,-1,n},\pi_-\Psi_0)\ \ (N\geqslant 0),$$

and

$$(\Psi_0,R_\pm\Psi_{N,\mp 1,n})\ \ (N\geqslant 1)$$

contain non-vanishing terms of first order, but none of zeroth, and therefore,

(3) $f^+_{\to N1n}$ for $N \geqslant 2$, and $f^-_{0\to n,-1,N}$ for $N \geqslant 1$ are of higher than the first order in the perturbation expansion.

Using equations (2.7) and (3.23), we have

$$f^+_{0\to 11n} = \frac{2\lambda^2}{\hbar^2}|(11n|\pi_+|000)|^2 + \frac{1}{i\hbar}\sum_{n'}\frac{1}{E_{000}-E_{10n'}}\left\{\left(000|-\frac{e^2}{\kappa r}|10n'\right)(10n'|R_-|11n)(11n|\pi_+|000)-\text{c.c.}\right\} \tag{3.24a}$$

$$f^+_{0\to N1n} = 0(V/\Delta E)^2, \quad N > 1. \tag{3.24b}$$

$$f^-_{0\to 0,-1,n} = \frac{1}{i\hbar}\sum_{n'}\frac{1}{E_{000}-E_{10n'}}\left\{\left(000|-\frac{e^2}{\kappa r}|10n'\right)(10n'|\pi_+|0,-1,n)(0,-1,n|R_-|000)-\text{c.c.}\right\} \tag{3.25a}$$

Vol. 21 1961

and

$$f^{-}_{0\to N,-1,n} = 0(V/\Delta E)^2, \quad N \geqslant 1, \quad (3.25b)$$

where $0(V/\Delta E)^2$ means that the expression is of higher than the first order in the perturbation expansion. Since the energy denominators are of the same order of magnitude as $\Delta E = \hbar^2/m^*\lambda^2$, the perturbation expansion is valid, provided that the matrix elements V of the perturbation potential are smaller than ΔE. We shall, in fact, show in Section 4 that $V/\Delta E \to 0$, as $\lambda \to 0$. We have thus shown that the transitions from the ground state to the excited states with $N \geqslant 2$ for l.c.p. and with $N \geqslant 1$ for r.c.p. are all of higher order than those described by equations (3.24a) and (3.25a).

To calculate $f^{-}_{0\to 0,-1,n}$ to lowest order we can instead of equation (3.25a), use a simpler formula:

$$f^{-}_{0\to 0,-1,n} = \frac{2m^*}{\hbar^2}(\epsilon_{0,-1,n}-\epsilon_{000})|(0,-1,n|R_-|000)|^2. \quad (3.26)$$

This equation can be derived directly from equation (2.5) by using the unperturbed wave functions for Ψ_i and Ψ_j, since (E_j-E_i) is already of the first order in the perturbation. Taking the matrix elements of the operators π_+, and R_-, and using equations (3.17), (3.21) and (3.22), we can write the oscillator strengths as

$$f^{+}_{0\to 11n} = (F_{11n},F_{000})^2 - \frac{m^*\lambda^2}{\hbar^2}(\epsilon_{11n}-\epsilon_{000})(F_{11n},F_{000})^2, \quad \text{l.c.p.,} \quad (3.27)$$

and

$$f^{-}_{0\to 0,-1,n} = \frac{m^*\lambda^2}{\hbar^2}(\epsilon_{11n}-\epsilon_{000})(F_{11n},F_{000})^2, \quad \text{r.c.p.,} \quad (3.28)$$

where (F_{11n}, F_{000}) is the inner product of $F_{11n}(z)$, and $F_{000}(z)$.

The results obtained in this Section are: For $a^2/\lambda^2 \gg 1$ there are two series of absorptions from the ground state, first, for left circularly polarized radiation, to the states $N = 1$, $M = 1$, n, and second, for right circularly polarized radiation, to $N = 0$, $M = -1$, n. The positions of these absorptions are given by

$$\hbar\omega = \frac{\hbar^2}{m^*\lambda^2}+\epsilon_{11n}-\epsilon_{000}, \quad \text{l.c.p.,} \quad (3.29)$$

and

$$\hbar\omega = \epsilon_{11n}-\epsilon_{000} \quad \text{r.c.p.,} \quad (3.30)$$

respectively. The relative intensities of these absorptions can be calculated by solving the Schrodinger equation (3.19) and by using equations (3.27) and (3.28).

4. THE MAIN ABSORPTION

In the present section we shall consider the transition $0 \to N = 1$, $M = 1$, $n = 0$, i.e. the transition from the ground state to the lowest bound state of equation (3.19) with $N = 1$, $M = 1$. As we shall see, this is the only transition that survives when $H \to \infty$. In this limit the sum of the oscillator strength is exhausted by the single term $f^{+}_{0\to 110}$, so that

$$\lim_{\lambda\to 0} f^{+}_{0\to 110} = 1, \quad (4.1)$$

and, for all other excitations

$$\lim_{\lambda\to 0} f^{\pm}_{0\to j} = 0. \quad (4.2)$$

This result is a consequence of the fact that the Schrodinger equation (3.19) has, for each (N, M), only one bound eigenstate whose binding energy tends to infinity as $H \to \infty$, namely, the lowest eigenstate $n = 0$. Accordingly, the wave function $F_{Nmn}(z)$ with $n = 0$ is entirely localized at the origin irrespective of the quantum numbers N and M. Hence the inner product (F_{000}, F_{11n}) tends to 1 or 0, as $n = 0$ or $n \neq 0$, respectively. The increase of the binding energy is, however, slower than the increase of the unperturbed energy $\Delta E = \hbar^2/m^*\lambda^2$. We will show that

$$\lim_{\lambda\to 0} \epsilon_{NM0}/\Delta E = 0. \quad (4.3)$$

To establish these results, we must find the ground

state of the differential equation

$$-\frac{\hbar^2}{2m^*}\frac{d^2F(z)}{dz^2}+V_i(z)F(z)=\epsilon F(z), \quad (4.4)$$

with an appropriate boundary condition at $|z|=\infty$. Here, we have used the letter i in place of the quantum numbers (N, M) for the unperturbed states. In the Appendix, the potential function $V_i(z)$ is shown to have the following properties:

(I) $$V_i(z)=\frac{-e^2}{\kappa\lambda}v_i\left(\frac{|z|}{\lambda}\right) \quad (4.5)$$

where $v_i(t)$ is analytic for $|t|<\infty$, so that it can be expanded as a power series in t. When $t\to\infty$, $v_i(t)$ has the asymptotic form

$$v_i(t)=\frac{1}{t}+0(1/t^3). \quad (4.6)$$

Therefore,

(II) $$V_i(z)=-\frac{e^2}{\kappa|z|}+0(\lambda^2/z^3), \quad z\to\infty. \quad (4.7)$$

This shows that the potential $V_i(z)$ converges uniformly to the pure Coulomb potential $-e^2/\kappa|z|$ provided that $z\neq 0$.

The problem of solving a one-dimensional Schrodinger equation with a Coulomb-like potential has been discussed by LOUDON[8]. He has shown that the lowest eigenstate may have an infinite binding energy, and that the energy spectrum for all other states tends to the Balmer series as the potential becomes pure Coulomb. Here we shall extend LOUDON's treatment to the case where conditions I and II are satisfied. In the Appendix we have treated this problem with explicit expressions for $V_{00}(z)$, and $V_{11}(z)$.

We shall now solve equation (4.4) both inwards from $|z|=\infty$, and outwards from $z=0$, matching the two solutions at the points $z=\pm z_0$. For bound states this procedure will determine the discrete energy spectrum ϵ_{in}; for unbound states it will determine the phase shifts of the wave functions depending on the continuous parameter. We shall thus determine our eigenfunctions, energies, etc., to the lowest order in λ.

For the exterior region $|z|>z_0$ we shall use the pure Coulomb solution which satisfies

$$-\frac{\hbar^2}{2m^*}\frac{d^2F(z)}{dz^2}-\frac{e^2}{\kappa|z|}F(z)=\epsilon F(z). \quad (4.8)$$

This will then give the solution to zeroth order in λ. For the interior region $|z|<z_0$ we shall solve equation (4.4) to first order in λ. We must then choose the matching point z_0. We choose z_0 as small as

$$z_0=C\lambda^{1-\rho},\ \tfrac{1}{3}<\rho<1, \quad (4.9)$$

where C and ρ are constants, independent of z and λ. Then for

$$|z|>z_0=C\lambda^{1-\rho},$$

$V_i(z)$ can be approximated as closely as desired by the pure Coulomb potential $-e^2/\kappa|z|$. The constants C and ρ are quite arbitrary, and our final results do not depend on them.

We shall denote the logarithmic derivative of the solution $F(\epsilon,z)$ by $\eta(\epsilon,z)$:

$$\eta(\epsilon,z)=\frac{\partial}{\partial z}\log F(\epsilon,z)=\frac{\partial F(\epsilon,z)}{\partial z}\Big/F(\epsilon,z). \quad (4.10)$$

The matching condition is then written as

$$\eta(\epsilon,z)_{\text{int}}=\eta(\epsilon,z)_{\text{ext}}, \quad z=\pm z_0 \quad (4.11)$$

Since the potential $V(z)$ is an even function of z, our solutions will be either even or odd, so that (apart from the sign) the matching equation (4.11) is the same for z_0 and for $-z_0$. From now on we shall confine our discussion to the positive half of z-axis. In the exterior region $z>z_0$ we can evaluate the overlap integral of two solutions $F(\epsilon,z)$ and $F(\epsilon',z)$ in terms of $\eta(\epsilon,z)$ and $\eta(\epsilon',z)$ by means of the following formula:

$$\int_{z_0}^{\infty}F(\epsilon,z)F(\epsilon'z)\,dz$$

$$=\frac{\hbar^2}{2m^*}F(\epsilon,z)F(\epsilon',z)\left(\frac{\eta(\epsilon,z)-\eta(\epsilon',z)}{\epsilon-\epsilon'}\right)_{z=z_0}. \quad (4.12)$$

This is derived from the identity

$$-\frac{\hbar^2}{2m^*}\left(F(\epsilon',z)\frac{\partial^2}{\partial z^2}F(\epsilon,z)-F(\epsilon,z)\frac{\partial^2}{\partial z^2}F(\epsilon',z)\right)$$

$$=(\epsilon-\epsilon')F(\epsilon,z)F(\epsilon',z),$$

Vol. 21 1961

and the assumption that either $F(\epsilon,z)$ or $F(\epsilon',z)$ has the property

$$F(\epsilon,z), \frac{\partial}{\partial z}F(\epsilon,z) \to 0, \quad z \to \infty. \tag{4.13}$$

Letting $\epsilon \to \epsilon'$ in equation (4.12), we obtain

$$\int_{z_0}^{\infty} F^2(\epsilon,z)\,dz = \frac{\hbar^2}{2m^*}\left(F^2(\epsilon,z)\frac{\partial}{\partial\epsilon}\eta(\epsilon,z)\right)_{z=z_0}. \tag{4.14}$$

Therefore, for two bound solutions $F(\epsilon,z)$ and $F(\epsilon',z)$, we have

$$\frac{\left(\int_{z_0}^{\infty} F(\epsilon,z)F(\epsilon',z)\,dz\right)^2}{\int_{z_0}^{\infty} F^2(\epsilon,z)\,dz \int_{z_0}^{\infty} F^2(\epsilon',z)\,dz}$$

$$= \frac{1}{\dfrac{\partial\eta(\epsilon,z_0)}{\partial\epsilon} \times \dfrac{\partial\eta(\epsilon',z_0)}{\partial\epsilon'}}\left(\frac{\eta(\epsilon,z)-\eta(\epsilon',z)}{\epsilon-\epsilon'}\right)^2_{z=z_0}. \tag{4.15}$$

The exterior solution, i.e. the solution of equation (4.8) can be written as $W_{n,1/2}(2z/na)$, where $W_{n,1/2}(\zeta)$ is the well-known Whittaker function.[9] The parameter n is related to the energy ϵ by

$$\epsilon = -\frac{\hbar^2}{2m^*a^2n^2} \tag{4.16}$$

and a is defined by equation (1.6). The function $W_{n,1/2}(2z/na)$ with n positive and non-integral satisfies the boundary condition (4.13) at $z = +\infty$, and is therefore an appropriate exterior solution. For the purpose of matching this to the interior solution, we need only use the leading terms in the expansion of $W_{n,1/2}(\zeta)$. To first order in z and for $0 < n \ll 1$, we can write

$$W_{n,1/2}\left(\frac{2z}{na}\right) = -1 + \frac{2z}{a}\left(\log\frac{2z}{na} + \frac{1}{2n} + \gamma - 1\right), \tag{4.17}$$

where γ is the Euler constant ($\gamma = 0{\cdot}5772\ldots$).

We thus obtain

$$\eta(\epsilon,z)_{\text{ext.}} = \frac{\partial}{\partial z}\log W_{n,1/2}\left(\frac{2z}{na}\right) = -\frac{1}{na} - \frac{2}{a}\left(\log\frac{2z}{na} + \gamma\right) + 0(z/a). \tag{4.18}$$

We shall next determine $\eta(\epsilon,z)$ for the interior solution. For this purpose we make the transformation

$$z = \lambda t. \tag{4.19}$$

Using equation (4.5), we rewrite equation (3.19) as

$$\frac{d^2F}{dt^2} + \left(\frac{2\lambda}{a}v_i(t) - \frac{\lambda^2}{n^2a^2}\right)F = 0. \tag{4.20}$$

Since $z_0 = C\lambda^{1-\rho}$, equation (4.20) can (for $t \gg 1$), be regarded as a second order differential equation with small perturbing terms that vanish as $\lambda \to 0$. For $\lambda = 0$ equation (4.20) has the solutions,

$$F^0(t) = \text{const.}, \quad F^0(t) = \text{const.} \times t. \tag{4.21}$$

For $\lambda \neq 0$, solutions of equation (4.20) to first order in λ can be obtained from the equation

$$\frac{d^2F}{dt^2} + \frac{2\lambda}{a}v_i(t)F^0(t) = 0.$$

By taking $F^0(t)$ equal to a constant, we can obtain the even solution that is finite and non-vanishing at $t = 0$. This solution is given by

$$F(t) = \text{const.}\left(1 - \frac{2\lambda}{a}\int_0^t dt_1 \int_0^{t_1} dt_2 v_i(t_2)\right), \quad t = z/\lambda. \tag{4.22}$$

Differentiating with respect to z, we can write $\eta(\epsilon,z)_{\text{int}}$ to the lowest order in λ as

$$\eta(\epsilon,z)_{\text{int}} = -\frac{2}{a}\int_0^{z/\lambda} v_i(t)\,dt. \tag{4.23}$$

It should be noted that this expression is independent of ϵ. From equation (4.27) it follows that for

$$z/\lambda \to \infty,$$

$\eta(\epsilon,z)_{\text{int}}$ can be written in the asymptotic form

$$\eta(\epsilon,z)_{\text{int}} = -\frac{2}{a}(\log z/\lambda + \alpha_i) + 0(\lambda^2/z^2), \tag{4.24}$$

where α_i is a constant, independent of z and λ.

To determine the quantum condition we equate the right-hand sides of equations (4.18) and (4.24), and obtain the equation

$$\frac{1}{n}+\log\frac{1}{n^2}$$

$$=\log\left(\frac{a}{2\lambda}\right)^2-2\gamma+2\alpha_i+0(\lambda^{2\rho}/C^2)+0(C\lambda^{1-\rho}). \tag{4.25}$$

The leading terms in the right-hand side are independent of z_0, and of the arbitrary constants C and ρ. Those terms which depend on C and ρ vanish as $\lambda\to 0$. In this limit, we can write

$$\frac{1}{n}=Z_0+2(\alpha_i-\gamma) \tag{4.26}$$

where

$$Z_0=\log\frac{a^2}{4\lambda^2}-\log\left(\log\frac{a^2}{4\lambda^2}\right)^2+\ldots. \tag{4.27}$$

Here, the second term $2(\alpha_i-\gamma)$ is independent of λ, but is determined uniquely for a given form of the potential. Thus $1/n$, which is related to the energy by equation (4.16), increases logarithmically with a/λ irrespective of the quantum number i. The dependence of $1/n$ on i comes solely through the constant α_i.

We are now in a position to evaluate the right-hand side of equation (4.15) for two different eigenstates $F_{i,n=0}$, and $F_{i',n=0}$. The quantities ϵ, η and $\partial\eta/\partial\epsilon$, for each state i are written as

$$\epsilon=-\frac{\hbar^2}{2m^*}\frac{1}{a^2n^2},$$

$$\eta=-\frac{1}{na}-\frac{2}{a}\left(\log\left(\frac{2C\lambda^{1-\rho}}{na}\right)+\gamma\right)+\ldots,$$

$$\frac{\partial\eta}{\partial\epsilon}=\frac{m^*a}{\hbar^2}(n+2n^2+\ldots), \tag{4.28}$$

where $1/n$ is given by equation (4.26).

Although $\eta(\epsilon,z_0)$ and $\eta(\epsilon',z_0)$ depend on C and ρ their difference does not. To the lowest order in λ,

$$\eta(\epsilon_i,z_0)-\eta(\epsilon'_i,z_0)=\frac{2}{a}(\alpha'_i-\alpha_i). \tag{4.29}$$

Substituting equations (4.28) and (4.29) into equation (4.15), we obtain

$$(F_{i',n=0},F_{i,n=0})=1-\frac{4}{Z_0}+\ldots$$

$$=1-\frac{4}{\log\dfrac{a^2}{4\lambda^2}}+\ldots. \tag{4.30}$$

In the limit $\lambda\to 0$, $(H\to\infty)$, the second and the following terms, of course, tend to 0. For the states i $(N=0,\ M=0)$ and i' $(N=1,\ M=1)$, we have shown in the Appendix that

$$\alpha_{00}=\tfrac{1}{2}(\log 2+\gamma),\quad \alpha_{11}=\tfrac{1}{2}(\log 2-1+\gamma),$$

$$\eta(\epsilon_{11},z)-\eta(\epsilon_{00},z)=1/a. \tag{4.31}$$

Hence, substituting equations (4.30) and (4.31) in equation (3.27), we have

$$f^{+}_{0\to 110}=1-4/Z_0 \tag{4.32}$$

This proves equation (4.1).

The shift of the excitation energy is estimated as

$$\Delta\hbar\omega=\epsilon_{110}-\epsilon_{000}$$

$$=\frac{\hbar^2}{m^*a^2}\left(\log\frac{a^2}{2\lambda^2}-\gamma-\frac{1}{2}\right). \tag{4.33}$$

From this it follows that

$$\frac{\Delta\hbar\omega}{\hbar\omega}\to 0,\quad \lambda\to 0. \tag{4.34}$$

Consequently, the perturbation expansions given in Section 3 are justified.

The quantity $\Delta\hbar\omega$ is also equal to the excitation energy for the transition $0\to 0$, -1, 0, i.e. the transition to the lowest bound state with $M=-1$ for r.c.p. The intensity of this transition is, however, smaller than the main absorption by the factor λ^2/a^2 [equation (3.28)].

5. ABSORPTION SPECTRUM NEAR THE CONTINUUM EDGE

To complete our investigation we shall proceed by determining the discrete spectrum associated with the bound eigenstates, and then the continuous spectrum associated with the unbound eigenstates of equation (4.4). We shall study

the absorption intensity vs. photon energy near the continuum edge $\epsilon = 0$.

5A. *The discrete spectrum*

The exterior solution is given by the Whittaker function,

$$W_{n,1/2}\left(\frac{2z}{na}\right)$$

where n is positive and non-integral. For our purposes it is convenient to write this function[10] as

$$W_{n,1/2}\left(\frac{2z}{na}\right)$$

$$= -\Gamma(n)\left\{M_n\left(\frac{2z}{na}\right)\cos n\pi + \bar{M}_n\left(\frac{2z}{na}\right)\frac{\sin n\pi}{\pi}\right\}, \quad n > 0, \tag{5.1}$$

where $M_n(\zeta)$ and $\bar{M}_n(\zeta)$ are given by

$$M_n(\zeta) = e^{-\zeta/2}\,\zeta\left(\sum_{r=0}^{\infty}\frac{\Gamma(n+1)\,(-1)^r\zeta^r}{\Gamma(n-r)r!(r+1)!}\right), \tag{5.2}$$

and

$$\bar{M}_n(\zeta) = M_n(\zeta)\log\zeta + e^{-\zeta/2}\zeta\left\{-1/\zeta + \sum_{r=0}^{\infty}\frac{\Gamma(n+1)\,(-1)^r\zeta^r}{\Gamma(n-r)r!(r+1)!} \times [\psi(n-r)-\psi(1+r)-\psi(2+r)]\right\}. \tag{5.3}$$

Here $\Gamma(n)$ is a gamma function, and $\psi(n)$ is defined by the equation

$$\psi(n) = \frac{d}{dn}\log\Gamma(n). \tag{5.4}$$

The function $M_n(\zeta)$ is regular at $\zeta = 0$, and for small ζ

$$M_n(\zeta) = n\zeta - \frac{n^2\zeta^2}{2} + 0(\zeta^3). \tag{5.5}$$

The function $\bar{M}_n(\zeta)$ is irregular at $\zeta = 0$, and

$$\bar{M}_n(\zeta) = -1 + n\zeta\left(\log\zeta + \frac{1}{2n} + \psi(n) - \psi(1) - \psi(2)\right) + 0(\zeta^2\log\zeta). \tag{5.6}$$

Using equations (5.5) and (5.6), we can write the leading terms of the expansion of

$$W_{n,1/2}\left(\frac{2z}{na}\right)$$

as

$$W_{n,1/2}\left(\frac{2z}{na}\right) = -\Gamma(n)\left\{\begin{array}{l}\left(\dfrac{2z}{a}-\dfrac{2z^2}{a^2}\right)\cos n\pi \\ +\left[-1+\dfrac{2z}{a}\left(\log\dfrac{2z}{na}+\dfrac{1}{2n}+\psi(n)-\psi(1)-\psi(2)\right)\right]\dfrac{\sin n\pi}{\pi} \\ +0\left(\dfrac{z^2}{a^2}\log\dfrac{2z}{na}\right)\end{array}\right\}. \tag{5.7}$$

Equations (5.1) and (5.7) hold for $z > z_0 \neq 0$, and for non-integral n. As has been shown in Section 4, the matching point z_0 can be chosen as small as $C\lambda^{1-\rho}$, $(1/3 < \rho < 1)$, so that the deviation of n from a positive integer is expected to be small, (n is, of course, a positive integer for a pure Coulomb potential), and to vanish as $\lambda \to 0$. Thus in equation (5.7) we have two infinitesimals, z_0 and $1/\pi \sin n\pi$, both depending on λ. Accordingly, two possibilities may arise when $\lambda \to 0$: (a), $1/\pi \sin n\pi \to 0$ but slower than $z_0 = C\lambda^{1-\rho}$, and (b) $1/\pi \sin n\pi \to 0$ but faster than $z_0 = C\lambda^{1-\rho}$.

First we shall investigate (a). Here, as $\lambda \to 0$,

$$\frac{1}{\pi}\sin n\pi \to 0,$$

$$\text{and } z_0\pi\cot n\pi = C\lambda^{1-\rho}\pi\cot n\pi \to 0. \tag{5.8}$$

From equation (5.7) we can write

$$W_{n,1/2}\left(\frac{2z}{na}\right) = \Gamma(n)\frac{\sin n\pi}{\pi}(1+0[\lambda^{1-\rho}\cot n\pi]),$$

and

$$\eta(\epsilon,z)_{\text{ext}} = \frac{\partial}{\partial z}\log W_{n,1/2}\left(\frac{2z}{na}\right)$$
$$= -\frac{2}{a}\left(\log\frac{2z}{a}+\pi\cot n\pi+2\gamma-\Theta(n)\right), \quad (5.9)$$

where

$$\Theta(n) = \log n-\frac{1}{2n}-\psi(n)$$
$$= \log n+\frac{1}{2n}-\psi(n+1). \quad (5.10)$$

We shall equate the right-hand side of equation (5.10) to $\eta(\epsilon,z)_{\text{int}}$ to obtain the quantum condition. For the interior solution which is finite and non-vanishing at $z=0$, the quantity $\eta(\epsilon,z)_{\text{int}}$ has already been obtained [see equations (4.22) and (4.23)]. Using the asymptotic expression for $\eta(\epsilon,z)_{\text{int}}$ given by equation (4.24) we can write the matching equation as

$$\pi\cot n\pi-\Theta(n) = \log\frac{a}{2\lambda}+\alpha_l-2\gamma. \quad (5.11)$$

For $0 < n \leqslant 1$ we can expand as follows:

$$\pi\cot n\pi \sim \frac{1}{n}, \quad \Theta(n) \sim \log n+\frac{1}{2n}+\gamma. \quad (5.12)$$

Equation (5.11) then reduces to the quantum condition for the ground state as given by equation (4.25). For n bounded away from zero, the function $\Theta(n)$ is finite, and only the term $\pi\cot n\pi$ on the left-hand side of equation (5.11) can balance the term $\log a/2\lambda$. For $\lambda\to 0$, therefore, $n\to\nu$, where ν is a positive integer. We can write

$$n = \nu+\delta\nu, \quad \nu = 1, 2, 3, \ldots . \quad (5.13)$$
$$0 < \delta\nu < 1.$$

In equation (5.13) the quantum defect $\delta\nu$ satisfies the equation

$$\pi\cot\delta_\nu\pi = \log\frac{a}{2\lambda}+\alpha_l-2\gamma+\Theta(\nu). \quad (5.14)$$

Since the right-hand side of this equation diverges logarithmically as $\lambda/a\to 0$, equation (5.8) is satisfied.

Thus, our energy spectrum becomes identical to the Balmer series for $\lambda\to 0$, except that here the lowest state has a binding energy that becomes infinite in this limit. The numerical constants $\Theta(\nu)$ are, in general, very small corrections to the ν-independent terms in the expression for $\delta\nu$. For $\nu\gg 1$ we have the asymptotic representation

$$\Theta(\nu) = \sum_{r=1}^{m}\frac{B_{2r}}{2r\nu^{2r}}+0\left(\frac{1}{\nu^{2m+2}}\right), \quad (5.15)$$

where B_{2r} is a Bernoulli constant ($B_2 = 1/6$, $B_4 = -1/30, \ldots$).[7]

Differentiating equation (5.9) with respect to ϵ, we have

$$\frac{\partial}{\partial\epsilon}\eta(\epsilon,z)_{\text{ext}}$$
$$= \frac{2m^*an^3}{\hbar^2}\left(\pi^2\operatorname{cosec}^2 n\pi+\frac{d\Theta}{dn}\right)$$
$$= \frac{2m^*an^3}{\hbar^2}\left\{\left(\log\frac{a}{2\lambda}+\alpha_l-2\gamma+\Theta\right)^2+\pi^2+\frac{d\Theta}{dn}\right\}. \quad (5.16)$$

Next, we turn to (b). Here, as $\lambda\to 0$

$$\frac{1}{\pi}\sin n\pi\to 0, \text{ and } \frac{1}{\pi z_0}\tan n\pi = \frac{\lambda^{\rho-1}}{\pi C}\tan n\pi\to 0. \quad (5.17)$$

The leading terms of

$$W_{n,1/2}\left(\frac{2z}{na}\right)$$

can be written as

$$W_{n,1/2}\left(\frac{2z}{na}\right)$$
$$= -\Gamma(n)\frac{2z}{a}\cos n\pi(1+0[\lambda^{\rho-1}\tan n\pi]).$$

Accordingly, we have

$$\eta(\epsilon,z)_{\text{ext}}$$
$$= \frac{1}{z}\left\{1-\frac{2z}{a}+\frac{\tan n\pi}{\pi}\left(\log\frac{2z}{a}+2\gamma-\Theta(n)\right)\right\}. \quad (5.18)$$

This expression for $\eta(\epsilon,z)_{\rm ext}$ cannot be matched with $\eta(\epsilon,z)_{\rm int}$ as given by equation (4.24), but only with the $\eta(\epsilon,z)$ which corresponds to the other interior solution:

$$F(z) = \text{const.}\left(t-\frac{2\lambda}{a}\int_0^t dt_1\int_0^{t_1} dt_2 v_l(t_2)t_2\right),$$

$$t = z/\lambda. \qquad (5.19)$$

This solution vanishes at $z = 0$. All solutions obtained by matching this interior solution have odd parity, so that they are orthogonal to the lowest eigenfunction. Therefore, in (b), excitations from the ground state induced by circularly polarized light are prohibited. Accordingly, we shall not consider this case any further. It can be shown, however, that solutions in (b) provide an energy spectrum similar to the Balmer series with quantum defects proportional to $-\lambda/a\ [\log a/2\lambda]^{-1}$, and that no eigenstate is allowed whose binding energy tends to infinity as $a/\lambda \to \infty$.

All solutions in (a) have the same parity as the lowest eigenstate, i.e. even parity, and excitations from the ground state are allowed. We can calculate the associated oscillator strengths by making use of equation (4.15). The necessary quantities have already been obtained in equations (4.26), (4.28), (4.31) and (5.16).

For the absorption $0 \to N = 1$, $M = 1$, $n \geqslant 1$, we have

$$f^+_{0\to 11n} = \frac{\dfrac{2}{n^3}\left(\dfrac{\hbar^2}{2m^*a^2}\right)^{3/2}(-\epsilon_0)^{1/2}}{\left(Z_n^2+\pi^2+\dfrac{d\Theta}{dn}\right)(\epsilon_n-\epsilon_0)^2}, \qquad (5.20)$$

where

$$Z_n = \tfrac{1}{2}(\log a^2/2\lambda^2 - 1 - 3\gamma) + \Theta(n), \qquad (5.21)$$

and

$$\epsilon_0 = -\frac{\hbar^2}{2m^*a^2}\left(\log\frac{a^2}{2\lambda^2}-\gamma\right)^2, \quad \epsilon_n = -\frac{\hbar^2}{2m^*a^2}\frac{1}{n^2}. \qquad (5.22)$$

The function $\Theta(n)$ is given by equation (5.10). For $n \to \infty$, $\Theta(n)$ vanishes with the leading term $1/12n^2$. Therefore, $f^+_{0\to 11n}$ depends on n nearly as n^{-3}. For $n \gg 1$, however, we must take into account the fact that the energy spacing is dense, as is shown by the relation

$$(\epsilon_{n+1}-\epsilon_n)^{-1} = \frac{dn}{d\epsilon_n} = \frac{m^*a^2}{\hbar^2}\cdot n^3. \qquad (5.23)$$

We define the oscillator strength per unit energy as

$$\frac{dn}{d\epsilon}f^+_{0\to 11n} = \frac{\left(\dfrac{\hbar^2}{2m^*a^2}(-\epsilon_0)\right)^{1/2}}{\left(Z_n^2+\pi^2+\dfrac{d\Theta}{dn}\right)(\epsilon_n-\epsilon_0)^2}, \quad \text{l.c.p.}, \qquad (5.24)$$

Similarly,

$$\frac{dn}{d\epsilon}f^-_{0\to 0,-1,n} = \frac{\dfrac{m^*\lambda^2}{\hbar^2}\left(\dfrac{\hbar^2}{2m^*a^2}(-\epsilon_0)\right)^{1/2}}{\left(Z_n^2+\pi^2+\dfrac{d\Theta}{dn}\right)(\epsilon_n-\epsilon_0)}, \quad \text{r.c.p.}, \qquad (5.25)$$

5B. *The continuous spectrum*

The eigenfunction $F(\epsilon,z)$, $(\epsilon > 0)$, must have a plane wave asymptotic form, $\cos(kz+\sigma_k(z))$, for $z \to \infty$, where the phase $\sigma_k(z)$ may vary logarithmically with z. The wave number k is related to the energy ϵ by the equation

$$\epsilon = \hbar^2k^2/2m^*.$$

The phase $\sigma_k(z)$ must be determined so that $F(\epsilon,z)$ satisfies equation (4.4). For $z > z_0$ two linearly independent solutions are given by Whittaker functions with imaginary parameters. The asymptotic solutions are

$$W_{\pm in,1/2}\left(\mp\frac{2iz}{na}\right) \to e^{|n|\pi/2}\exp\pm i\left(kz+\frac{1}{ka}\log 2|k|z\right), \qquad (5.26)$$

where

$$k = 1/na.$$

For the continuum states, the orthonormality conditions are written as

$$c_k^2\int_0^\infty W_{in,1/2}\left(-\frac{2iz}{na}\right)W_{-in',1/2}\left(\frac{2iz}{n'a}\right)dz = \delta(k-k'). \qquad (5.27)$$

The integration which determines the constants

c_k is carried out by making use of the asymptotic solutions given by equation (5.26).[11]

We now write a normalized eigenfunction in the following form

$$F(\epsilon,z) = \frac{e^{-|n|\pi/2}}{\sqrt{2\pi}} \times \left\{ W_{in,1/2}\left(-\frac{2iz}{na}\right) e^{i\theta} + W_{-in,1/2}\left(\frac{2iz}{na}\right) e^{-i\theta} \right\}. \tag{5.28}$$

Here the phase factors $e^{\pm i\theta}$ are determined by the matching condition.

Since our function $F(\epsilon,z)$ is already normalized in $z_0 \leqslant z < \infty$, equation (4.15) for the overlap integral may be modified to read

$$\frac{\left(\int_0^\infty F(\epsilon,z)F(\epsilon',z)\,dz\right)^2}{\int_{z_0}^\infty F^2(\epsilon',z)\,dz} = \frac{\dfrac{\hbar^2}{2m^*}F^2(\epsilon,z)}{\dfrac{\partial}{\partial\epsilon'}\eta(\epsilon',z)} \left(\frac{\eta(\epsilon,z)-\eta(\epsilon',z)}{\epsilon-\epsilon'}\right)^2_{z=z_0}. \tag{5.29}$$

In this expression, we have assumed that $F(\epsilon',z)$ is a bound eigenfunction that satisfies equation (4.13), (e.g. the lowest state $F_0(z)$). To evaluate the right-hand side of equation (5.29), we must evaluate $F^2(\epsilon,z)_{z=z_0}$, i.e. the amplitude of the unbound eigenfunction at the matching point. The other quantities entering the formula have already been obtained.

Assuming that $z_0 = C\lambda^{1-\rho} \to 0$, we take the leading terms in the expansion of

$$W_{\pm in,1/2}\left(\mp\frac{2iz}{na}\right)$$

to match the interior solution given by equation (4.22). Using the relation

$$\Gamma(in) = \left(\frac{\pi}{n\sinh n\pi}\right)^{1/2} \exp -i\sigma_n,$$

where

$$\sigma_n = \arg\Gamma(-in) = \mathrm{Sgn}(n)\frac{\pi}{2} + \frac{1}{2i}\{\log\Gamma(1-in) - \log\Gamma(1+in)\},$$

we can write

$$F(\epsilon,z) = \frac{2e^{-|n|\pi/2}}{\sqrt{2\pi}}\left(\frac{\sinh n\pi}{n\pi}\right)^{1/2}\sin(\sigma_n-\theta), \quad z\to 0. \tag{5.30}$$

For $\eta(\epsilon,z)_{\mathrm{ext}}$ we have

$$\eta(\epsilon,z)_{\mathrm{ext}} = -\frac{2}{a}\left(\log\frac{2z}{a} + \frac{\mathrm{Sgn}(n)\pi}{1-\exp(-2\pi|n|)}\cot(\sigma_n-\theta) + 2\gamma - Re\Theta(in)\right), \tag{5.31}$$

where Θ, for an imaginary parameter, is also defined by equation (5.10). Here, we have

$$Re\Theta(in) = \log|n| - \tfrac{1}{2}\{\psi(1+in)+\psi(1-in)\} = -\log|k|a - \tfrac{1}{2}\{\psi(1+i/ka)+\psi(1-i/ka)\}. \tag{5.32}$$

From equations (4.24) and (5.31), the matching condition may be written as

$$\mathrm{Sgn}(n)\pi\cot(\sigma_n-\theta) = (1-e^{-2\pi|n|})\left(\log\frac{a}{2\lambda} + \alpha_i - 2\gamma + Re\Theta(in)\right). \tag{5.33}$$

We substitute this expression into equation (5.30) to obtain $F^2(\epsilon,z)$. The result is

$$F^2(\epsilon,z) = \frac{[1-\exp(-2\pi/|k|a)]|k|a}{\mathscr{Z}_k^2+\pi^2}, \quad z\to 0, \tag{5.34}$$

where

$$\mathscr{Z}_k = (1-e^{-2\pi/|k|a}) \times \left(\log\frac{a}{2\lambda} + \alpha_i - 2\gamma + Re\Theta(i/ka)\right). \tag{5.35}$$

In particular, for $i = (1, 1)$ we have

$$\mathscr{Z}_k = (1-e^{-2\pi/|k|a}) \times \left\{\tfrac{1}{2}\left(\log\frac{a^2}{2\lambda^2} - 1 - 3\gamma\right) + Re\Theta(i/ka)\right\}. \tag{5.36}$$

Vol. 21
1961

Finally we substitute equations (4.28), (4.31) and (5.34) into equation (5.29) to obtain the oscillator strength for the continuous spectrum. Multiplying by the density of states

$$dk/d\epsilon = m^*/\hbar^2|k|$$

we have

$$\frac{dk}{d\epsilon} f^+_{0\to 11k} = \frac{\left(\frac{\hbar^2}{2m^*a^2}(-\epsilon_0)\right)^{1/2}(1-e^{-2\pi/|k|a})}{(\mathscr{Z}_k^2+\pi^2)(\epsilon_k-\epsilon_0)^2}, \quad \text{l.c.p. (5.37)}$$

and

$$\frac{dk}{d\epsilon} f_{0\to 0,-1,k} = \frac{\frac{m^*\lambda^2}{\hbar^2}\left(\frac{\hbar^2}{2m^*a^2}(-\epsilon_0)\right)^{1/2}(1-e^{-2\pi/|k|a})}{(\mathscr{Z}_k^2+\pi^2)(\epsilon_k-\epsilon_0)}, \quad \text{r.c.p..} \tag{5.38}$$

5C. *The spectrum as a function of excited state energy*

In equations (5.24) and (5.37) for l.c.p., and equation (5.25) and (5.38) for r.c.p. the dependence of the absorption intensities on the photon energy $\hbar\omega$ can be obtained by the substitutions

$$\hbar\omega = \epsilon + \hbar^2/m^*\lambda^2 + I, \quad \text{for l.c.p.,}$$

and

$$\hbar\omega = \epsilon + I, \quad \text{for r.c.p..}$$

Here

$$I = -\epsilon_0 = -R\left(\log\frac{a^2}{2\lambda^2} - \gamma\right)^2, \tag{5.39}$$

and

$$\epsilon = \epsilon_k = R(ka)^2 \quad \text{for continuum states,}$$
$$= \epsilon_n = -R/n^2 \quad \text{for discrete states,} \tag{5.40}$$

where R is the effective Rydberg constant $\hbar^2/2m^*a^2$.

We shall investigate the absorption intensities in terms of the parameter ϵ measured in units of R.

The dependence of $dk/d\epsilon\, f^+_{0\to 11k}$ [equation (5.37)] on ϵ comes from $1-e^{-2\pi/|k|a}$ in the numerator, and $\mathscr{Z}_k$ and $(\epsilon_k+I)^2$ in the denominator. The quantity $\mathscr{Z}_k$, a complicated function of k, is given by equation (5.36), in which $Re\Theta(i/ka)$ is obtained from equation (5.32). In terms of ϵ, we have the following expansions of $Re\Theta(i\epsilon^{-1/2})$:

$$Re\Theta(i\epsilon^{-1/2}) = \gamma - \tfrac{1}{2}\log\epsilon - \sum_{r=1}^{\infty}\frac{1}{r(r^2\epsilon+1)}, \quad 0<\epsilon$$

$$= \gamma - \tfrac{1}{2}\log\epsilon - \sum_{r=1}^{\infty}(-1)^{r+1}\zeta(2r+1)\epsilon^{-r}, \quad |\epsilon|>1$$

$$= -\sum_{r=1}^{m}\frac{(-1)^{r+1}B_{2r}}{2r}\epsilon^r + 0(\epsilon^{m+1}), \quad |\epsilon|<1,$$

where $\zeta(r)$ is Riemann's ζ-function, and the B_{2r} are Bernoulli numbers.[12] We can see that, for $\epsilon\to\infty$, $Re\Theta(i\epsilon^{-1/2})$ diverges logarithmically, and that for $\epsilon\to 0$, it vanishes with the leading term $-\frac{1}{12}\epsilon$. For $\epsilon\to\infty$, however, $\mathscr{Z}_k$ vanishes with the leading term $-\pi\epsilon^{-1/2}\log\epsilon$ because of the factor $(1-e^{-2\pi/|k|a})$. Referring to the expression for $F^2(\epsilon,0)$ as given by equation (5.34), we find that

$$F^2(\epsilon,0)\to\frac{2}{\pi}, \quad \epsilon\to\infty, \tag{5.42}$$

and for states $(11k)$,

$$F^2(\epsilon,0)\simeq\frac{2}{\pi}\frac{\epsilon}{\left\{\log\left(\frac{a^2}{2\lambda^2\epsilon}\right)-(1+\gamma)\right\}^2+\epsilon}, \quad \epsilon\gg 1, \tag{5.43}$$

$$F^2(\epsilon,0) = \frac{4\epsilon^{1/2}}{\left\{\log\left(\frac{a^2}{2\lambda^2}\right)-(1+3\gamma)\right\}^2+4\pi^2} \times[1+0(\epsilon)], \quad \epsilon\to 0. \tag{5.44}$$

Equation (5.42) shows that electrons with sufficiently high energies are completely free, while

equation (5.44) shows that the Coulomb effect is significant for slow electrons whose amplitudes at the origin become zero with the leading term proportional to $\epsilon^{1/2}$. The dependence of $F^2(\epsilon,0)$ on ϵ is shown schematically in Fig. 1.

The intensities

$$\frac{dk}{d\epsilon}f^{+}_{0\to 11k} \quad \text{and} \quad \frac{dk}{d\epsilon}f^{-}_{0\to 0,-1,k}$$

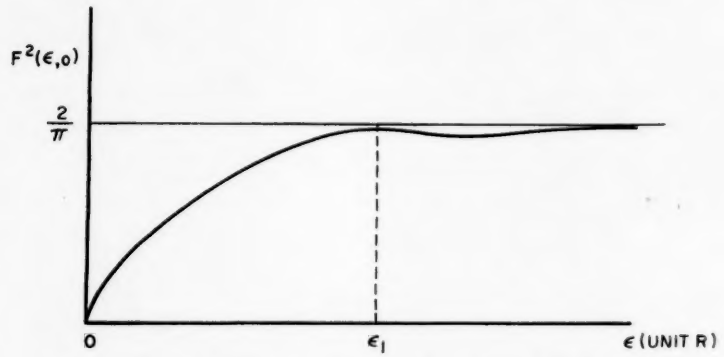

FIG. 1. Dependence of continuum wave functions at the origin on the energy ϵ [see equations (5.42)–(5.44)]. The maximum occurs at $\epsilon_1 \simeq a^2/2\lambda^2\, e^{-(1+\gamma)}$.

are given by the equations

$$\frac{dk}{d\epsilon}f^{+}_{0\to 11k} = I^{1/2}F^2(\epsilon,0)\epsilon^{-1/2}(I+\epsilon)^{-2}, \quad \text{l.c.p.,} \quad (5.45)$$

and

$$\frac{dk}{d\epsilon}f^{-}_{0\to 0,-1,k} = \frac{\lambda^2}{2a^2}I^{1/2}F^2(\epsilon,0)\epsilon^{-1/2}(I+\epsilon)^{-1}, \quad \text{r.c.p.}, \quad (5.46)$$

Because of the factor

$$\epsilon^{-1/2}(I+\epsilon)^{-\gamma}(\gamma = 1, \text{ or } 2),$$

the intensities for $\epsilon \gg 1$ vary as $\epsilon^{-5/2}$ for l.c.p., and as $\epsilon^{-3/2}$ for r.c.p., and their magnitudes at $\epsilon = 0$ are finite. For small ϵ we have

$$\frac{dk}{d\epsilon}f^{+}_{0\to 11k} = \frac{4I^{-3/2}}{\left\{\log\left(\frac{a^2}{2\lambda^2}\right)-(1+3\gamma)\right\}^2+4\pi^2} \times (1+B\epsilon+0(\epsilon^2)), \quad (5.47)$$

where

$$B = \frac{\frac{1}{3}\{\log(a^2/2\lambda^2)-(1+3\gamma)\}}{\left\{\log\left(\frac{a^2}{2\lambda^2}\right)-(1+3\gamma)\right\}^2+4\pi^2} - \frac{2}{\left\{\log\left(\frac{a^2}{2\lambda^2}\right)-\gamma\right\}^2}. \quad (5.48)$$

For $\epsilon < 0$ but close to 0,

$$\frac{dk}{d\epsilon}f^{+}_{0\to 11k}$$

is replaced by

$$\frac{dn}{d\epsilon}f^{+}_{0\to 11n}.$$

From equations (5.20), (5.21) and (5.10), we find that

$$\frac{dn}{d\epsilon}f^{+}_{0\to 11n} = \frac{4I^{-3/2}}{\left\{\log\left(\frac{a^2}{2\lambda^2}\right)-(1+3\gamma)\right\}^2+4\pi^2} \times [1+B\epsilon+0(\epsilon^{3/2})], \quad (5.49)$$

where B is also given by equation (5.48).

The transition from the continuous spectrum to the discrete spectrum in the region $\epsilon < 0$ is related to the mechanism of line broadening, and

Vol. 21
1961

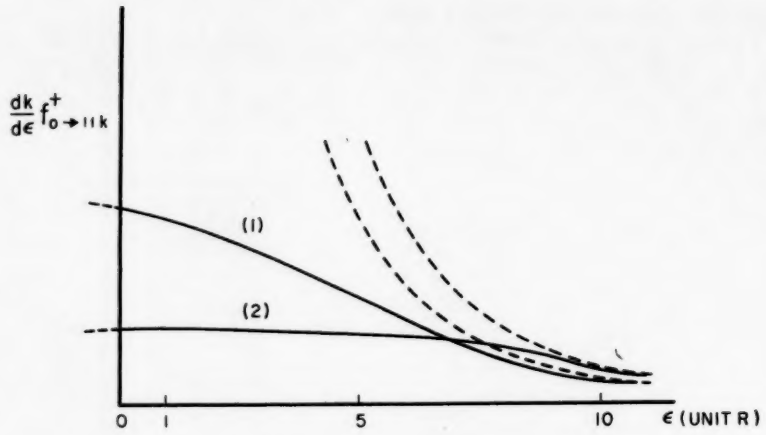

FIG. 2. Intensities of the continuous spectrum.
(1) $a^2/\lambda^2 = 20$.
(2) $a^2/\lambda^2 = 40$.
Dotted lines on the right side indicate the asymptotes.

will not be investigated here. Theoretical curves of the intensity for some values of the ratio a^2/λ^2 are shown in Fig. 2.

6. DISCUSSION AND APPLICATION TO EXCITONS

The optical excitations of a hydrogenic atom in a strong magnetic field are shown diagramatically. in Fig. 3. They are classified according to the dependence of their intensities on the ratio a^2/λ^2. The oscillator strength for the transition $0 \to N=1$, $M = 1$, $n = 0$ for l.c.p. is unity in the strong field limit $a^2/\lambda^2 \to \infty$ (Class A). The oscillator strengths (or strengths per unit energy) for the transitions $0 \to N = 1$, $M = 1$, $n > 1$ for l.c.p. vanish as $(\log a^2/\lambda^2)^{-5}$ (Class B). These absorption lines arise

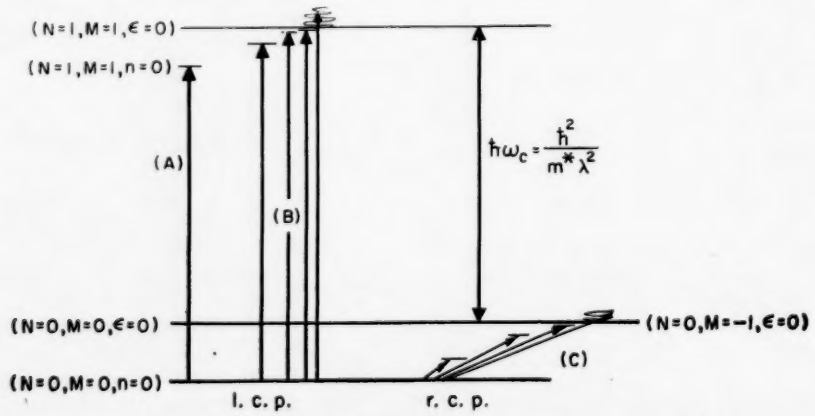

FIG. 3. Schematic diagram of optical excitation from the ground state to various excited states ($a^2/\lambda^2 = 20$).

at energies just above the fundamental cyclotron resonance energy,

$$\hbar\omega_c = \hbar eH/m^*c.$$

For r.c.p. a series of absorption lines arise on the low energy side of $\hbar\omega_c$, (Class C). These vanish as

$$\frac{\lambda^2}{a^2}(\log a^2/\lambda^2)^{1-r}, 0 \leqslant r \leqslant 4.$$

exciton is present was given by[3]

$$f_{0\to i} = \frac{2V}{mh\nu}|\xi\cdot p_{cv}(0)|^2|U_i(0)|^2 \qquad (6.1)$$

Here, V is the volume of the crystal, and $\xi\cdot p_{cv}(0)$ the matrix element of the one electron momentum in the direction of the polarization ξ between two Bloch states at $k = 0$. In the "allowed" case $\xi\cdot p_{cv} \neq 0$.

The solutions of equation (1.1) discussed in the

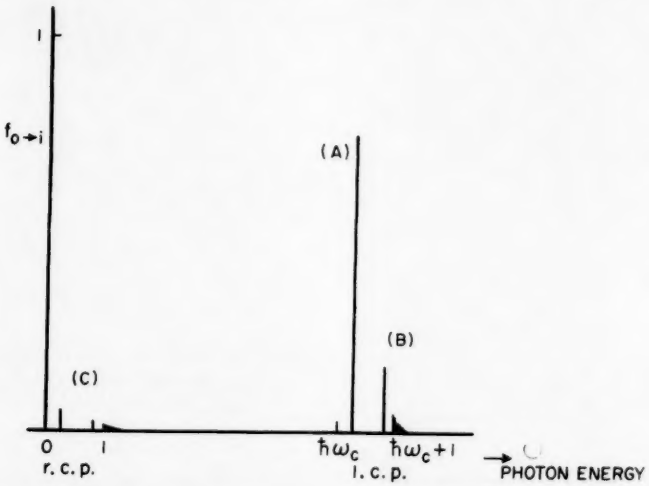

FIG. 4. Intensities of the absorption lines ($a^2/\lambda^2 = 20$).

All other absorption lines and absorption bands are weaker, and vanish at least as fast as λ^2/a^2. These features are shown schematically in Fig. 4.

In Section 5C the absorption intensity was obtained explicitly as a function of the energy of the continuum states. This calculation can be applied to the study of the absorption edge of excitons in a strong magnetic field. ELLIOTT and LOUDON[3] considered the fundamental absorption of a semiconductor with isotropic effective masses in the conduction and valence bands. The relative motion of an electron–hole pair, represented by a wave function $U(r)$, was taken to satisfy an effective mass equation identical to equation (1.1) and (1.2). The oscillator strength for the absorption from the perfect insulating state to the state where an

previous sections give the relative motion $U_i(r)$ when

$$\hbar\omega_c \gg m^*e^2/2\kappa^2\hbar^2,$$

where m^* is the reduced mass of the electron–hole pair. For excitations to the continuum states which belong to the first Landau level, the intensity given by equation (6·1) is

$$\frac{dk}{d\epsilon}f_{0\to 00k} = AV|\Phi_{00}(0)|^2F^2(\epsilon_k,0)\frac{dk}{d\epsilon}$$

$$= \frac{AV}{2\pi\lambda^2}\frac{dk}{d\epsilon}F^2(\epsilon_k,0), \qquad (6.2)$$

where

$$A = \frac{2}{mh\nu}|\xi\cdot p_{cv}(0)|^2. \qquad (6.3)$$

Since the excitation energy $h\nu$ is large compared to ϵ_k, the energy dependence of the intensity comes almost entirely from the quantity

$$\frac{V}{2\pi\lambda^2}\frac{dk}{d\epsilon}F^2(\epsilon_k,0).$$

$F^2(\epsilon_k,0)$ is readily obtained from equations (5.34), (5.35) and (4.31). We find that

$$\frac{V}{2\pi\lambda^2}\frac{dk}{d\epsilon}F^2(\epsilon_k,0)=\frac{m^*V}{2\pi\hbar^2\lambda^2}\frac{a[1-\exp(-2\pi/|k|a)]}{\mathscr{Z}_k^2+\pi^2}, \tag{6.4}$$

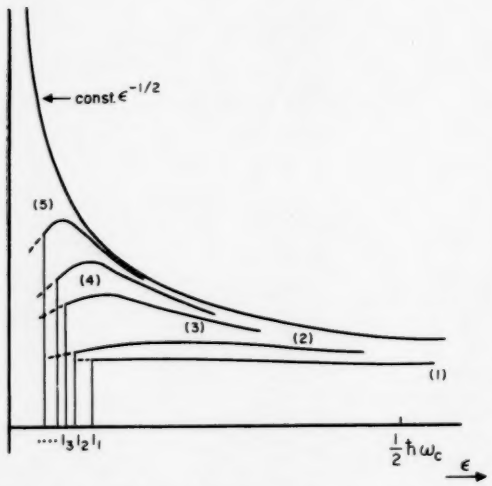

FIG. 5. Intensity of continuous spectrum for exciton magneto-absorption. I_1, I_2, ... correspond respectively to the continuum edges for
(1) $a^2/\lambda^2 = 10$ (2) $a^2/\lambda^2 = 20$ (3) $a^2/\lambda^2 = 60$
(4) $a^2/\lambda^2 = 100$ and (5) $a^2/\lambda^2 = 200$
As $a \to \infty$ (λ fixed), spectrum tends to $\epsilon^{-1/2}$.

where

$$\mathscr{Z}_k = \tfrac{1}{2}(1-e^{-2\pi/|k|a}) \times\left\{\log\frac{a^2}{2\lambda^2}-3\gamma+2Re\Theta(i/ka)\right\}. \tag{6.5}$$

The energy dependence of equation (6.4) is shown in Fig. 5. For $|k|a \gg 1$ it is equal to $\epsilon^{-1/2}$, the density of states function for one dimensional free particles, while for $|k|\,a \to 0$ it tends to a finite value. The sharp absorption peak expected from the coalescence of the Landau levels is thus removed by the effect of the Coulomb binding between the electron and the hole. This is in agreement with ELLIOTT and LOUDON. By increasing the parameter a (the effective Bohr radius) from a finite value to infinity, one can also see the continuous transition from the exciton spectrum to the spectrum of the free electron–hole pair.

Finally it may be noted that equation (6.4) predicts that for a sufficiently large value of a^2/λ^2, the slope of the intensity vs. ϵ curve is positive at $\epsilon = 0$. Hence the intensity will have a maximum at a certain point, $\epsilon > 0$. For small ϵ

$$\frac{V}{2\pi\lambda^2}\frac{dk}{d\epsilon}F^2(\epsilon,0)=\frac{mV}{2\pi\hbar^2\lambda^2}\frac{a}{\mathscr{Z}_0^2+\pi^2}(1+B\epsilon),$$

where

$$B=\frac{1}{3}\frac{\left\{\log\dfrac{a^2}{2\lambda^2}-3\gamma\right\}}{\left\{\log\left(\dfrac{a^2}{2\lambda^2}\right)-3\gamma\right\}^2+4\pi^2}. \tag{6.6}$$

Some numerical values of B are given in Table 1, and are compared with ELLIOTT and LOUDON's results.

Table 1. *Slopes of the intensity curves at* $\epsilon = 0$

	B	
$a^2/\lambda^2 = 3{\cdot}7$	$-0{\cdot}031$	$(-0{\cdot}061)$
$7{\cdot}1$	$-0{\cdot}005$	$(-0{\cdot}034)$
10	$-0{\cdot}0003$	
20	$0{\cdot}008$	
100	$0{\cdot}107$	
200	$0{\cdot}172$	

The numbers in brackets are those given in Ref. (3). [See equation (6.6)].

Acknowledgements—This investigation was started as a result of a suggestion made by Professor W. KOHN, whom the authors would like to thank. They would like also to thank Professor R. H. BOYER, Professor J. M. RADCLIFFE and Professor R. SMOLUCHOWSKI for helpful comments. A major part of this work was pursued at the Carnegie Institute of Technology, where it was supported by the Office of Naval Research.

REFERENCES

1. YAFET Y., KEYES R. W. and ADAMS E. N., *J. Phys. Chem. Solids* **1,** 137 (1956).
2. WALLIS R. F. and BOWLDEN H. J., *J. Phys. Chem. Solids* **7,** 78 (1958).
3. ELLIOTT R. J. and LOUDON R., *J. Phys. Chem. Solids* **15,** 196 (1960).
4. EDWARDS D. F. and LAZAZZERA V. J., *Phys. Rev.* **120,** 420 (1960).
5. BOYLE W. S. and HOWARD R. E., *J. Phys. Chem. Solids* **19,** 181 (1961).
6. DRESSELHAUS G., KIP A. F. and KITTEL C., *Phys. Rev.* **98,** 368 (1955).
7. JOHNSON M. H. and LIPPMANN B. A., *Phys. Rev.* **76,** 828 (1949).
8. LOUDON R., *Amer. J. Phys.* **27,** 649 (1959).
9. ERDELYI A., MAGNUS W., OBERHETTINGER F. and TRICOMI F. G., *Higher Transcendental Functions* Vol. I. McGraw-Hill, New York (1953).
10. HARTREE D. R., *Proc. Camb. Phil. Soc.* **24,** 426 (1928).
11. LANDAU L. D. and LIFSHITZ E. M., *Quantum Mechanics,* pp. 59–60. Pergamon Press, London (1958).
12. ERDELY A., MAGNUS W., OBERHETTINGER F. and TRICOMI F. G., *Higher Transcendental Functions,* Vol. II. McGraw-Hill, New York (1953).

APPENDIX

EXPRESSIONS FOR THE POTENTIALS $V_{00}(z)$, $V_{11}(z)$ AND FOR THE CONSTANTS α_{00}, α_{11}

The unperturbed solutions of equation (3.2) for $N = 0$, $M = 0$, and $N = 1$, $M = 1$ are given by

$$|\Phi_{00}(x,y)|^2\,dxdy = e^{-u}\,du, \tag{A.1}$$

$$|\Phi_{11}(x,y)|^2\,dxdy = e^{-u}u\,du,\ u = \frac{1}{2\lambda^2}(x^2+y^2). \tag{A.2}$$

The effective potentials $V_{00}(z)$ and $V_{11}(z)$ are then

$$V_{00}(z) = -\frac{e^2}{\kappa\lambda}\int_0^\infty \frac{e^{-u}}{\sqrt{(2u+t^2)}}\,du, \tag{A.3}$$

$$V_{11}(z) = -\frac{e^2}{\kappa\lambda}\int_0^\infty \frac{ue^{-u}}{\sqrt{(2u+t^2)}}\,du,\quad t = z/\lambda. \tag{A.4}$$

The integral in equation (A.3) can be written as

$$\int_0^\infty \frac{e^{-u}}{\sqrt{(2u+t^2)}}\,du = \frac{1}{\sqrt{2}}\,e^{t^2/2}\int_{t^2/2}^\infty e^{-u}u^{-1/2}\,du. \tag{A.5}$$

For real, positive t it can be expanded in a power series:

$$\int_0^\infty \frac{e^{-u}}{\sqrt{(2u+t^2)}}\,du = \sqrt{\frac{\pi}{2}}\left\{\sum_{r=0}^\infty \frac{(1)^r}{\Gamma(r/2+1)2^{r/2}}\cdot t^r\right\}. \tag{A.6}$$

This series is convergent for $|t| < \infty$, and by analytical continuation it defines a function $V_{00}(t)$, which is analytic everywhere except at $t = \infty$. The function $v_{00}(z)$ is defined by

$$V_{00}(z) = -\frac{e^2}{\kappa\lambda}v_{00}(|t|),\ -\infty < t < \infty. \tag{A.7}$$

For $t \to \infty$, the integral in equations (A.6) yields the asymptotic expansion

$$\int_0^\infty \frac{e^{-u}}{\sqrt{(2u+t^2)}}\,du = \frac{1}{t} + 0\left(\frac{1}{t^3}\right),\quad t \to \infty. \tag{A.8}$$

Similar expansions hold for the integral in equation (A.4). We have thus confirmed the validity of equations (4.5) and (4.7) for the potentials $V_{00}(z)$ and $V_{11}(z)$.

The interior solution of the Schrodinger equation (4.4) which is finite and non-vanishing at $z = 0$ is given by equation (4.22). Its logarithmic derivative is given by equation (4.23). For $N = 0$, $M = 0$

$$\eta_{\text{int}}(z) = -\frac{2}{a}\int_0^{z/\lambda} v_{00}(t)\,dt \tag{A.9}$$

Using the integral representation for $V_{00}(t)$ in equation (A.3) and changing the order of the integrations, we can write

$$\begin{aligned}\eta_{\text{int}}(z) &= -\frac{2}{a}\int_0^\infty du e^{-u}\int_0^{z/\lambda}\frac{dt}{\sqrt{(2u+t^2)}}\\ &= -\frac{2}{a}\int_0^\infty du e^{-u}\{\log[t+\sqrt{(t^2+2u)}]\\ &\qquad -\log\sqrt{2u}\}\\ &= -\frac{2}{a}\left\{\log t + \int_0^\infty e^{-u}[\log(1+\sqrt{(1+2u/t^2)}\right.\\ &\qquad \left. -\log\sqrt{2u}]\,du\right\},\quad t = z/\lambda.\end{aligned} \tag{A.10}$$

For $z/\lambda \gg 1$, therefore, one has the asymptotic representation

$$\eta_{\text{int}}(z) = -\frac{2}{a}\{\log z/\lambda + \tfrac{1}{2}\log 2 - \tfrac{1}{2}\int_0^\infty e^{-u}\log u\, du + 0(\lambda^2/z^2)\}. \quad \text{(A.11)}$$

For $i = (0,0)$, the constant α appearing in equation (4.24) is now given by

$$\alpha_{00} = \tfrac{1}{2}\log 2 - \tfrac{1}{2}\int_0^\infty e^{-u}\log u\, du. \quad \text{(A.12)}$$

A similar calculation for $i = (1,1)$ yields

$$\alpha_{11} = \tfrac{1}{2}\log 2 - \tfrac{1}{2}\int_0^\infty e^{-u}\, u\log u\, du = \tfrac{1}{2}(\log 2 - 1) - \tfrac{1}{2}\int_0^\infty e^{-u}\log u\, du. \quad \text{(A.13)}$$

Now,

$$-\int_0^\infty e^{-u}\log u\, du = \gamma \quad \text{(A.14)}$$

and therefore,

$$\alpha_{00} = \tfrac{1}{2}(\log 2 + \gamma), \quad \alpha_{11} = \tfrac{1}{2}(\log 2 - 1 + \gamma). \quad \text{(A.15)}$$

Vol. 196

J. Phys. Chem. Solids Pergamon Press 1961. Vol. 21, Nos. 3/4, pp. 199–205. Printed in Great Britain.

CRYSTAL GROWTH BY CHEMICAL TRANSPORT REACTIONS—I

BINARY, TERNARY, AND MIXED-CRYSTAL CHALCOGENIDES

R. NITSCHE, H. U. BÖLSTERLI and M. LICHTENSTEIGER

Laboratories R.C.A. Ltd., Hardturmstrasse 169, Zurich, 5, Switzerland

(*Received* 15 *May* 1961)

Abstract—The concept of chemical transport reactions (volatilization of a material via a low-volatile chemical intermediate at a temperature T_1 and back-reaction of the mixture at a temperature T_2, using the temperature dependence of the chemical equilibrium involved) is a valuable tool for growing single crystals of many materials which cannot be easily obtained from the melt. The main advantage is the use of growth temperatures well below the melting or sublimation point. The method was used to grow crystals of the binary chalcogenides: ZnS, ZnSe, CdS, CdSe, MnS, SnS, SnS_2, In_2S_3, Ga_2S_3, GaS and GaSe. Ternary chalcogenides of the type AB_2X_4 (A = Zn, Cd, Hg; B = Ga, In; X = S, Se) were obtained for the first time as single crystals. Mixed crystals of ZnS·MnS were prepared over a wide range of composition.

Vol. 21
1961

INTRODUCTION

CRYSTAL growth from the melt by the classical methods of Kyropoulos and Bridgman becomes exceedingly difficult if applied to materials having high melting points. Additional difficulties arise if compounds are to be grown which show appreciable dissociation at the melting point or which melt only under elevated pressure. To obtain single crystals of such materials usually vapor phase methods are used. The polycrystalline starting material is sublimed either *in vacuo* or in a stream of a carrier gas or the vapors of its constituents are reacted in a crystallization chamber. The temperatures required for these processes are high—in the vicinity of the sublimation point—and they have to be closely controlled in order to avoid polynucleation by surpassing the usually small supersaturation range. If the process is carried out in a closed system because oxygen has to be excluded, the limiting temperature is usually given by the softening point of quartz. If inert carrier gases are used the control of their flow and the geometry of the arrangement pose additional problems.

It therefore is highly desirable to devise methods for growing crystals from the vapor phase which will work well below the sublimation point of the material involved without increasing the difference in free energy between vapor and growing seeds to a degree which would lead to nucleation. This can be achieved by utilizing the concept of chemical transport reactions, a term first introduced by SCHÄFER[1]. Instead of vaporizing a solid directly at high temperatures it may be vaporized at much lower temperatures by forming highly volatile chemical intermediates and reacting back the resulting gas mixture at a different temperature utilizing the temperature dependence of the chemical equilibrium involved. By properly adjusting the two temperatures the departure from chemical equilibrium in the vicinity of the growing seeds can be made small enough to avoid nucleation but large enough to make the seeds grow, i.e. the proper supersaturation can be maintained.

In a recent note[2] a brief description was given on the growth of a few chalcogenides by this method. This paper discusses the method in detail and gives a survey of the growth conditions of a large number of chalcogenides.

Part I will deal with the physical chemistry of transport reactions in general, in Part II the requirements for growing crystals by chemical

transport reactions will be discussed, and in Part III the binary and ternary chalcogenides will be described of which crystals have been grown by the outlined principles.

1. PHYSICAL CHEMISTRY OF CHEMICAL TRANSPORT REACTIONS

Consider a closed system containing $n+1$ components all of which are in chemical equilibrium with each other. The temperature is chosen such that only one component is solid, the other n components gaseous. If there were a local perturbation of the equilibrium such that the solid component would have a smaller free energy at the perturbed area, it would migrate via the gas phase to this area until equilibrium is established again. The simplest way to bring about such a perturbation is a local change in temperature; that is, imposing a temperature gradient on the system. For $n = 1$ the trivial case of sublimation of a solid via its gaseous atoms or molecules results. In the following, the case $n = 3$ is considered which applies to the transport of metal chalcogenides by halogens. The equilibria involved are: $MeCh + Hal \rightleftharpoons MeHal + Ch$; a specific example is $ZnS + I_2 \rightleftharpoons ZnI_2 + \frac{1}{2} S_2$. The simplest experimental arrangement for a transport experiment is a closed horizontal tube. One end, the vaporization chamber, contains some polycrystalline feed material, e.g. ZnS and a small amount of iodine, the transporter. If the vaporization chamber is held at 1000°C and the other end, the crystallization chamber, at 750°C, ZnS will be transported via the vapor phase and deposit in crystals in the crystallization chamber because of the temperature dependence of the above equilibrium. The elegant feature of the method is that already tiny amounts of the transporter are sufficient to transport practically unlimited amounts of the solid, because the transporter set free during crystallization diffuses back to pick up more solid, etc.

Now the question arises which parameters govern such a transport reaction, and is it possible to make predictions of what kind of transporter would yield optimal transport in a given system? The yield of a transport reaction can be characterized by the quantity $\dot{m}$, i.e. the amount of material transported per unit time from the vaporization to the crystallization chamber. In a similar way as the current flowing through a resistor is given by the product of the potential difference Δp at its ends and its conductance L, $\dot{m}$ can be written as the product of two functions, Δp and L. The function Δp characterizes the "chemical potential difference" between vaporization and crystallization chamber and is proportional to the difference in vapor pressure of the transporter in the two chambers. Δp is a function of the "chemical parameters" of the system: the temperature T_1 of the vaporization chamber, the temperature T_2 of the crystallization chamber, the change in free energy ΔG for the reaction involved and the concentration of the transporter c_T. $\Delta p = \Delta p(T_1, T_2 \cdot \Delta G, c_T) \cdot L$, on the other hand, characterizing the "conductance" of the system in respect to the vapor transport between the two chambers, is a function of the "geometrical parameters" of the system; the length l of the tube, its cross-section q and a "specific conductance" σ which characterizes the physical nature of the transport mechanism: diffusion, convection or laminar flow. Thus $\dot{m} \cong \Delta p(T_1, T_2, \Delta G, c_T) \cdot L(l, q, 2\sigma)$.

To predict $\dot{m}$ for a chosen system it thus is necessary to derive the functions Δp and L explicitly. For Δp this is possible if the types of reaction taking part in the transport and their free energy changes in the operating temperature range, i.e. the specific heats of the reaction components, are known. By forming the expression $\Delta G = \Delta H - T\Delta S = -RT \cdot \ln K$ at the two temperatures T_1 and T_2 and observing the conditions imposed by c_T on the partial pressures of the components occuring in the explicit expression for K, one can solve for Δp of the transporter. Important information can already be gained, however, if only the sign of the heat of reaction ΔH is known, because the expression $d \ln K/dT = \Delta H/RT^2$ indicates whether transport is to be expected from hot to cold, or vice versa. Unlike ordinary sublimation not all reactions transport from hot to cold. Only if $\Delta H > 0$, i.e. for endothermic reactions where K increases with temperature, will transport occur from hot to cold. If $\Delta H < 0$ the reaction will transport from cold to hot. Examples are known for both cases. Transport of metal chalcogenides with iodine as transporter, however, occurs always from hot to cold. A good qualitative insight on the connection between Δp and ΔG is gained by the method of SCHÄFER[1] who plots Δp vs. ΔH curves

with the entropy change ΔS as parameter. Such curves are particularly useful for estimating the relative magnitude of $\dot{m}$ for various substances transported by the same mechanism. The essential conclusion is that transport can only occur if K is of the order of unity, i.e. if the equilibrium is not extreme.

It is much more difficult to derive an explicit expression for L because transport of the vapor can be effected in three ways.

1. By diffusion between the two chambers, if narrow tubes are used, and if the total pressure in the system is small. Several cases have been treated theoretically by SCHÄFER and are in good agreement with experimental data. Transport by diffusion only, however, is slow and all the experiments described below were well in the pressure range (of the order of 1 atm) above pure diffusion.
2. By convection. This takes over at higher pressures, in wider tubes, and in tubes inclined against the horizontal.
3. By laminar flow, if the reaction involves a change in mole numbers, and if the reaction velocity on both sides is high enough to maintain a constant pressure difference.

Which mechanism prevails depends largely on the transporter concentration c_T, determining the total pressure, and on the geometry of the system. Since there is usually an overlap between several of these mechanisms and the exact temperature distribution along the tube plays a role also, it is difficult to arrive at an analytical expression for L. Qualitative estimates of $\dot{m}$ however, can usually be obtained by estimating ΔP, especially since L will not vary very much if related reactions are compared.

2. CRYSTAL GROWTH BY TRANSPORT REACTIONS

In general, transport reactions yield polycrystaline material consisting of intergrown crystallites. Attempts were made to investigate the influence the forementioned parameters have on the growth of well developed single crystals and to arrive at reproducible experimental conditions.

Basically one can say that if transport reactions are to be used for crystal growth, $\dot{m}$, the amount of material arriving in the growing chamber per unit time has to be carefully controlled. $\dot{m}$ should not exceed a certain maximum value because otherwise the growing seeds cannot digest the arriving materials and supersaturation will increase until additional nucleation takes place. $\dot{m}$ can be controlled by Δp (variation of $\Delta T = T_1 - T_2$) as well as by L (variation of geometry). To obtain optimal velocity of growth $\dot{m}$ should be raised during the experiment since a growing crystal can increase its intake as its surface increases.

ZnS was chosen as a model substance to study the influence of the various parameters on its growth but the results apply to the other chalcogenides mentioned below as well. It was tried to vary only one parameter at a time.

First the role of the chemical parameters will be considered. Having found a strong transport effect with iodine, bromine and chlorine also were studied as transporters. Br gave much smaller $\dot{m}$ values and Cl showed practically no transport at all. This is in qualitative agreement with an estimate of the ΔG values at room temperatures from literature data. They showed that the iodine reaction had the lowest ΔG value and thus the least extreme equilibrium position as required for a reasonable transport effect. Iodine was used as transporter in all other systems, although this may not necessarily mean optimal transport.

The experimental technique was as follows. Approximately 3 g of pure, polycrystalline ZnS was placed into one end of a quartz ampule (length 15 cm, internal diameter 8 mm). It was degassed in high vacuum at 800°C, iodine condensed in with liquid air and the ampule drawn off. The ampule was then placed horizontally into a tubular two-zone furnace. The usual reaction time was 16 hr.

Since SCHÄFER[1] had previously described the transport of iron oxide with HCl gas according to: $Fe_2O_3 + 6HCl \rightleftharpoons 2FeCl_3 + H_2O$ one had to think about the analogous reaction: $ZnS + 2HI \rightleftharpoons ZnI_2 + H_2S$. However, by adding various amounts of hydrogen up to the equivalent to HI, no differences in $\dot{m}$ or in crystal habit were found as compared to pure iodine.

The role of c_T: $\dot{m}$ increased stronger than linear with c_T up to a value of $c_T = 15$ mg I/cm³ which could not be exceeded for safety reasons. A strong dependence of the size and the quality of the resulting crystals on c_T however was noted. At $c_T = 1$ mg I/cm³ growth was very slow although

Vol. 21
1961

well developed individual crystals resulted. Best results were obtained at $c_T = 5$ mg I/cm³ ($\dot{m} = 20$ mg ZnS/hr). Clear crystals with well developed faces formed which after 40 hr had sizes up to 5×5 mm. At higher iodine concentrations, e.g. $c_T = 15$ mg I/cm³, $\dot{m}$ was so large (80 mg ZnS/hr) that polynucleation occured and layers of intergrown crystallites resulted.

The role of T_1 and T_2. The absolute values of these temperatures can be varied over a relatively wide range if one considers only $\dot{m}$ and not the quality of the crystals. For a c_T of 5 mg I/cm³ not too different $\dot{m}$ values were obtained for 1300–1100°C as well as for 900–600°C. The range of permissible supersaturation, however, decreases with temperature. At $T_2 = 600$°C only a microcrystalline cake is formed because of polynucleation. A minimum T_2 of 700°C was required to obtain individual, well developed crystals. The difference ΔT between T_1 and T_2 was found to be of minor importance since at the geometry employed the "conductance" L rather than the partial pressure difference Δp appeared to be the rate determining step in the growth process. The optimal growth temperature T_2 has to be evaluated empirically for a given substance. The proper choice of T_2 depends also on the physical properties required from the crystal such as the amount of transporter dissolved in the crystal, the number of imperfections etc. If polymorphism exists, T_2 has to be chosen according to the stability range of the modification desired.

Now the influence of the geometrical parameters will be discussed. $\dot{m}$ decreases approximately linearly with the tube length l because of the increasing flow resistance. The obvious conclusion to use very short tubes, however, is not quite correct since one has to consider that if several seeds are to form and grow in one experiment the crystallization chamber should not be too small in order to avoid intergrowth between the crystals. A good compromise between these requirements is to heat the tube not symmetrically but asymmetrically in such a way that the vaporization chamber is small but the crystallization chamber is large.

The temperature distribution in the crystallization chamber should be as uniform as possible in order to avoid re-evaporation of crystals from warmer parts in the course of an experiment. For orientating experiments, on the other hand, it is quite useful to have a sloping temperature distribution along the crystallization chamber in order to find the temperature of optimal crystal growth.

The temperature drop between the two chambers should not be too abrupt in order to avoid a clogging up of the tube in this region.

The most important geometrical parameter is the tube cross section q which influences $\dot{m}$ decisively. For $c_T = 5$ mg I/cm³ and $T_1 = 1000$°C, $T_2 = 750$°C, $\dot{m}$ was 20 mg ZnS/hr for a tube with 8 mm diameter but 300 mg/hr for a tube with 20 mm diameter.

This large influence of q on m is probably due to the relative decrease of the friction of the moving gases along the walls of the tube and to a partial transition from diffusion to convection with increasing q. The latter is also substantiated by the fact that in large diameter tubes the crystals are always found at the bottom of the tube (according to the direction of the gas flow) whereas in smaller tubes they are found all around the circumference of the tube.

Concluding, the following requirements have to be observed if transport reactions are to be used for the growth of single crystals.

1. The rate of transport $\dot{m}$ is not to exceed the rate of growth of the seeds.
2. The optimal crystallization temperature has to be evaluated empirically for each system taking into account the possibility of polymorphism.
3. The crystallization chamber should be large in order to prevent intergrowth between adjacent seeds. Asymmetric heating is useful.
4. The temperature distribution in the crystallization chamber should be as uniform as possible to avoid partial re-evaporation of already grown crystals.
5. Well developed crystals form easier in large diameter tubes where convection determines the rate of transport.
6. The temperature difference between the two chambers can be made smaller if wider tubes are used (thus facilitating an even temperature distribution along the crystallization chamber) since the gas flow is here the rate determining step.

3. CHALCOGENIDE CRYSTALS GROWN BY THE TRANSPORT METHOD

If a simple binary chalcogenide is transported,

the structure of the crystals formed corresponds to the phase stable at the growing temperature. If the chalcogenide exists in various valency states, the resulting crystals are not necessarily identical with the valency state of the starting material. Depending on temperature, the transported crystals can have a different composition, e.g. if SnS is transported at 650–500°C pure SnS is obtained. At 950–600°C however, SnS_2 is formed in the crystallization chamber.

If a mixture of two binary chalcogenides is transported the following cases are possible.

(a) Formation of mixed crystals of the two binaries.

(b) Formation of a ternary chalcogenide.

(c) Separate transport of the two binaries if complete immiscibility exists.

In most cases it is not necessary to start with well defined binary chalcogenides or mixtures thereof. Often it is sufficient to react a stoichiometric mixture of the elements at high temperatures and subject this resulting product to the transport reaction.

A. *Binary chalcogenides*

The binary chalcogenides prepared are listed in Table 1.

An interesting case is ZnS because it exhibits polymorphism. Crystals grown previously by reacting zinc vapor with hydrogen sulfide are always mixtures of the cubic and the hexagonal phase, the boundaries of which are visible as "striations". The transport method allows a separation of the phases by varying the growth temperature. At temperatures below 1000°C the pure cubic modification—as checked by X-rays and optical inspection—is obtained. Around 1150° mainly hexagonal crystals form containing only very few striations. By admixing small amounts of silver or copper these crystals can be made to luminesce blue or green respectively.

In the case of CdS the amount of iodine incorporated in the crystals was determined quantitatively by using radioactive I^{131} as a tracer in the transporting iodine. The iodine content was found to be 10^{-2} weight per cent. It is evenly distributed throughout the crystals, as found by partial etching.

Table 1. Properties and growth conditions of binary chalcogenides

Compound	Color	Crystal shape	Size (mm)	Structure	T_1°C	T_2°C	c_T (mgI/cm³)
ZnS	white	polyhedra	6 × 6 × 2	cubic sphalerite	1000	750	5
ZnS	white	hexagonal columns	6 × 4 × 4	predominantly hexagonal, wurtzite	1300	1150	5
ZnSe	yellow-orange	polyhedra	4 × 4 × 3	cubic, sphalerite	1050	800	5
CdS	orange	hexagonal columns	6 × 6 × 8	hexagonal, wurtzite	850	650	5
CdSe	black	hexagonal needles	8 × 2 × 2	hexagonal, wurtzite	1000	500	5
MnS	dark green	plates	5 × 5 × 0·1	cubic NaCl structure,	1000	550	5
SnS	black	needles	5 × 0·2 × 0·2	rhombohedral	650	500	5
SnS	yellow	plates	5 × 5 × 1	hexagonal	950	600	5
GaS_2	yellow	plates	5 × 5 × 0·01	hexagonal	925	850	5
Ga_2S_3	white	hexagonal columns	4 × 1 × 1	rhombohedral	1000	800	5
GaSe	dark red	plates	4 × 4 × 0·01	hexagonal	870	750	5
In_2S_3	dark red	octahedra	4 × 4 × 4	cubic	950	450	5

B. *Mixed crystals of binary chalcogenides*

The system ZnS–MnS was found to be a good example of mixed crystal formation by chemical transport reactions. If a mixture of polycrystalline ZnS and MnS is transported in a sloping temperature gradient ($T_1 = 1050°C$, $T_2 = 950–750°C$) and one collects the crystals formed at various temperatures, one finds crystals grown at 750°C are slightly orange colored, have the cubic sphalerite structure and contain 2 per cent by weight of Mn. With increasing T_2 the manganese content increases and the crystals remain cubic up to 850°C. Between 860° and 880°C a mixture between the cubic and the hexagonal wurtzite phase forms and above 900°C the crystals are purely hexagonal and contain around 10 per cent of Mn.

This is very surprising since both pure ZnS and pure MnS (NaCl structure) grow in the cubic form at 900°C, the mixture however prefers the hexagonal structure. The phenomenon was used to "construct" crystals with built-in phase changes. A mixture of ZnS and MnS was transported and the temperature T_2 of the growing chamber oscillated periodically during the growth process between 750° and 950°C. The crystals obtained showed indeed striations corresponding to the number of temperature cycles during the growth period.

C. *Ternary chalcogenides*

The transport method proved to be capable of yielding a large variety of ternary chalcogenide crystals of the general formula AB_2X_4, where A = Zn, Cd, Hg; B = In, Ga and X = S, Se. They are listed in Table 2. These materials, known so far only in the microcrystalline state, show interesting photoelectric properties which have been reported elsewhere.[3] HAHN[4] and coworkers obtained polycrystalline samples of these ternaries by sintering together the binary constituents at high temperatures. Our X-ray data obtained so far are in agreement with the structures these authors propose.

Table 2. Properties and growth conditions of ternary chalcogenides

Compound	Color	Crystal shape	Size (mm)	Structure	T_1 °C	T_2 °C	c_T (mg I/cm³)
$ZnIn_2S_4$	yellow	platelets	10 × 10 × 0·1	rhombohedral	750	700	5
$CdIn_2S_4$	red	octahedra	5 × 5 × 5	cubic, thiospinel	850	750	5
$HgIn_2S_4$	black	octahedra	1 × 1 × 1	cubic, thiospinel	950	650	5
$ZnIn_2Se_4$	dark red	columns	1 × 1 × 5	tetragonal	700	650	5
$CdIn_2Se_4$	black	columns	1 × 1 × 5	tetragonal	650	600	5
$ZnGa_2S_4$	white	polyhedra	0·1 × 0·1 × 0·1	tetragonal	1100	1000	5
$CdGa_2S_4$	yellow	columns	2 × 2 × 6	tetragonal	650	600	5
$HgGa_2S_4$	yellow	needles	0·3 × 0·3 × 8	tetragonal	730	580	5
$ZnGa_2Se_4$	orange-red	polyhedra	0·5 × 0·5 × 1	tetragonal	1100	1000	5
$CdGa_2Se_4$	orange-red	columns	1 × 1 × 4	tetragonal	900	750	5
$HgGa_2S_4$	black	needles	0·5 × 0·5 × 10	tetragonal	760	700	5

4. CONCLUSIONS

The concept of chemical transport reactions is—if properly modified—a useful tool for growing single crystals of metal chalcogenides having high

melting or sublimation points. Not only simple binary, but also ternary and probably quaternary compounds as well as mixed crystals can be prepared. The method will certainly be useful for other chemical systems.

If means are found to control nucleation at will over wide ranges of temperature and composition it should be possible to prepare large single crystals as well as thin microcrystalline layers.

A disadvantage is the possibility of incorporation of the transporter in the crystals formed. On the other hand, being a complicated distillation a transport reaction might also prove to be a means of purification for certain compounds.

REFERENCES

1. SCHÄFER H., *Z. anorg. Chem.* **286,** 27, 42 (1956); **290,** 279 (1957); **291,** 221, 254 (1957).
2. NITSCHE R., *J. Phys. Chem. Solids* **17,** 163 (1960).
3. BEUN J. A., NITSCHE R. and LICHTENSTEIGER M., *Physica* **26,** 647 (1960); *Physica*, to be published.
4. HAHN H. *et al.*, *Z. anorg. Chem.* **279,** 241 (1955).

ol. 21
961

J. Phys. Chem. Solids Pergamon Press 1961. Vol. 21, Nos. 3/4, pp. 206–209. Printed in Great Britain.

THE PARAMAGNETIC SUSCEPTIBILITIES OF SOME URANIUM–MOLYBDENUM ALLOYS BETWEEN 100°K AND 300°K

B. S. CHANDRASEKHAR and J. M. BARDEEN*

Westinghouse Research Laboratories, Pittsburgh 35, Pennsylvania

(*Received* 22 *May* 1961)

Abstract—Measurements of the paramagnetic susceptibilities of quenched γ-phase uranium–molybdenum alloys, containing 15–30 atomic per cent molybdenum, in the range 100–300°K are described. The results are shown to be consistent with a decreasing density of states at the Fermi energy with increasing Mo concentration. This is in agreement with the results of specific heat measurements, and with the resistivity and Hall effect in these alloys. The temperature variation of the susceptibility can also be understood on the same basis.

1. INTRODUCTION

URANIUM metal exhibits three allotropic modifications as a function of temperature. These are respectively α (orthorhombic) up to 935°K, β (tetragonal) from 935°K to 1042°K, and γ (body centered cubic) from 1042°K to the melting point of 1202°K. The γ-phase in certain binary alloys of uranium, notably those with 15–30 atomic per cent niobium or molybdenum, can be retained at room temperature by quenching from about 1200°K.

The quenched γ-phase alloys U–Mo and U–Nb have been shown to be superconducting, and also to have very high electrical resistivities which decrease monotonically with increasing temperature between 4°K and 300°K.[1,2] It has been suggested[1, 3] that the high values and the unusual temperature dependence of the resistivity are due to a very high density of states at the Fermi surface which decreases with increasing Mo or Nb concentration.

It is well known that the Pauli paramagnetic susceptibility χ and its temperature derivative $(d\chi/dT)$ are related to the density of states in the neighborhood of the Fermi energy. The experiments described here were undertaken to see if the susceptibility of the alloys could be described using the same model as that applied to the resistivity.

2. EXPERIMENTAL DETAILS

The uranium–molybdenum samples were the same ones that had been used in the study of the resistivity. The compositions ranged from 15·8 to 30·4 atomic per cent (a/o) of molybdenum. Their preparation has been described in a previous paper.[1] They were in the shape of cylindrical rods, 0·1–0·3 cm diameter and 5–8 cm long.

The standard Gouy method[4] was employed. The force on the sample was measured in fields up to 5000 Oe, using a helical spring which had been developed for use in gravity meters.[5] There was no ferromagnetic impurity detected in any of the samples at room temperature. The 30·4 a/o alloy showed a field-dependent susceptibility at lower temperatures, as will be described later. In all other cases, the susceptibility was independent of field down to the lowest temperatures. The susceptibility at lower temperatures was measured relative to that at 300°K, which itself was determined absolutely on a separate apparatus using a chemical micro-balance.† The overall

* Present address: Norman Bridge Laboratory of Physics, California Institute of Technology, Pasadena, California.

† The authors are grateful to R. BOWERS for making the absolute measurements.

accuracy of the latter data is estimated to be about 2 per cent, while the relative measurements as a function of temperature are more precise.

3. EXPERIMENTAL RESULTS

Figure 1 shows the molar susceptibilities of the alloys as a function of temperature. The main

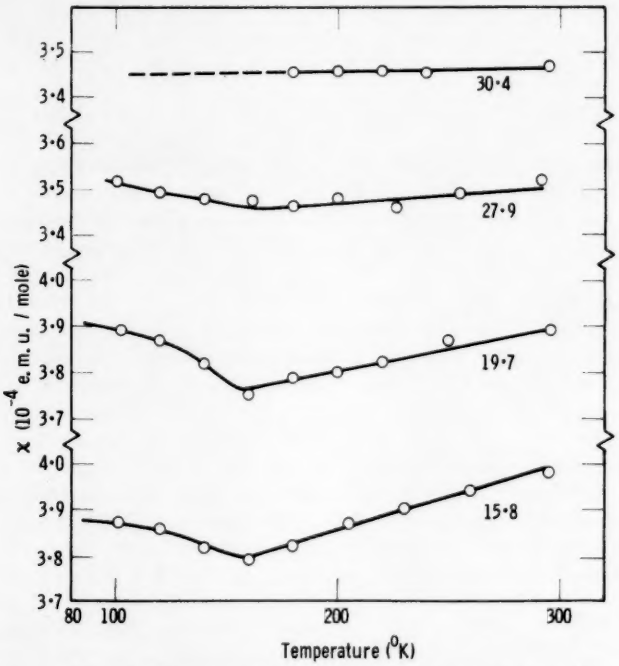

FIG. 1. Paramagnetic susceptibilities of quenched γ-phase U–Mo alloys as a function of temperature. The atomic per cent of Mo is shown against each curve. Note that each curve has its own χ-scale.

features of the results are the following.

(1) Above about 160°K, the slope of the χ vs. T curve is positive, and *decreases* with *increasing* molybdenum concentration.

(2) Below 160°K, the susceptibilities of the 15·8, 19·7 and 27·9 a/o alloys *increase* with decreasing T, but are still field-independent. The susceptibility of the 30·4 a/o alloy, on the other hand, is so strongly field-dependent that no reliable estimate of the limiting value could be obtained even using the Honda–Owen method.[4]

(3) In Table 1 are listed the extrapolated values χ_0 of the susceptibility at 0°K, and the values of $(\Delta\chi/\Delta T)$ for T between 160°K and 300°K for each alloy.

4. DISCUSSION

The high, slightly temperature dependent, susceptibilities of these alloys is characteristic of many transition metals, and is attributed mainly to the Pauli paramagnetism of the electrons at the Fermi surface. A part of the observed susceptibility is certainly due to the diamagnetism of the core electrons; while no calculation of this for uranium exists, it must be, as FRIEDEL[6] points out, less than that of radon, viz. $0{\cdot}245\times10^{-4}$ e.m.u./mol.,[7] and may therefore be neglected. The molar Pauli spin susceptibility is given by[8]

$$\chi = 2\mu^2 n(\zeta_0) + \frac{\pi^2\mu^2k^2T^2}{6}\left[n''(\zeta_0)-\frac{[n'(\zeta_0)]^2}{n(\zeta_0)}\right]+\ldots \qquad (1)$$

Table 1. *The values of* χ_0 *and* $(\Delta\chi/\Delta T)$ *for quenched* γ*-phase* U–Mo *alloys*

Composition (a/o Mo)	$\chi_0(10^{-6}$ e.m.u. mol$^{-1})$	$\Delta\chi/\Delta T$ (10^{-8} e.m.u. mol^{-1} deg^{-1})
15·8	3·57	14·5
19·7	3·61	10·0
27·9	3·40	3·64
30·4	3·45	0·62

where μ = the Bohr magneton ($e\hbar/2mc$), $n(\zeta_0)$ = molar density of states at the Fermi energy ζ_0, the primes denote differentiation with respect to energy, and the other symbols have their usual meanings. The above expression does not take account of exchange and correlation effects;[9] they are not quantitatively well understood, and furthermore the primary interest here is in the relative effects of varying the alloying concentration, where they may be expected to play only a minor role. It is also assumed that the Landau diamagnetism of the conduction electrons is negligible.

With the above assumptions, equation (1) has been used to calculate the density of states at 0°K from the extrapolated values of χ given in Table 1. The density of states, as is well known, can also be calculated from the electronic heat capacity C_e:

$$C_e = \frac{2\pi^2 k^2 T}{3} n(\zeta_0) \qquad (2)$$

GOODMAN *et al.*'s[10] specific heat data have been used in equation (2) to obtain $n(\zeta_0)$. The two sets of values of $n(\zeta_0)$ so obtained are shown in Table 2.

From Table 2, a tendency towards decreasing $n(\zeta_0)$ with increasing molybdenum concentration is shown by the susceptibility data, thus confirming the results of the specific heat measurements and lending some weight to the suggested explanation[1] of the electrical resistivity of these alloys. The value of R is nearly the same, $\approx 1{\cdot}7$, for all the alloys. The fact that it differs from unity is mainly due to the neglect of exchange and correlation effects in equation (1). FRIEDEL[6] has remarked that the inclusion of exchange should give $R \approx 3$. Since the effect of correlation, at least in the nearly free electron model, is to decrease the susceptibility,[9] the value for R of 1·7 obtained above is not unreasonable.

The decrease in $(\Delta\chi/\Delta T)$ with increasing molybdenum concentration, shown in Table 1, is interesting. BLATT[3] has obtained, from a consideration of the resistivities and Hall constants of these alloys, estimates for the derivatives of the density-of-states curve at ζ_0. These values, inserted in equation (1), predict both the positive sign of $(\Delta\chi/\Delta T)$ and its decrease with increasing concentration as experimentally observed. But the predicted magnitude of the concentration dependence

Table 2. *Values of* $n(\zeta_0)$ *in* 10^{36} erg^{-1} mole^{-1} *obtained from susceptibility and electronic heat capacity data. The last column gives the ratio* R *of* $n_{\text{susceptibility}}$ *to* $n_{\text{sp. heat}}$.

Specific heats		Susceptibilities		a/o Mo	R
a/o Mo	$n(\zeta_0)$	a/o Mo	$n(\zeta_0)$		
17·8	1·20	15·8	2·06	15·8	1·69
21·6	1·19	19·7	2·08	19·7	1·73
25·3	1·18	27·9	1·96	27·9	1·70
29·6	1·14	30·4	1·99	30·4	1·74

is an order of magnitude smaller than is actually observed.

Finally, the temperature dependence of χ for $T < 160°K$ is noteworthy. The increase in χ with decreasing T in this region has been seen in α-uranium also.[11] It is believed that this behavior is connected with the existence of small amounts of uranium hydride, which becomes ferromagnetic in this temperature region. An analysis of the alloys used in the present experiments did in fact show hydrogen to be present to the extent of ~ 50 parts per million. Presumably, if the magnetization curve for the ferromagnetic particles remains linear in the range of fields used, a field-independent susceptibility which is greater than that due to the paramagnetic alloy alone would be observed.

5. CONCLUSIONS

It has been shown that the qualitative behavior of the paramagnetic susceptibilities of the quenched γ-phase U–Mo alloys is consistent with the band structure that had been suggested on the basis of the resistivities and Hall coefficients. The quantitative discrepancies are not too serious in view of the simplified nature of the model, and the as yet unsurmounted difficulties in the theory of spin paramagnetism in the transition metals.

Note added in proof

BATES and BARNARD[12] have recently measured the susceptibilities of the metastable γ-phase U–Mo alloys above 300°K. The two sets of measurements are in reasonable agreement at 300°K.

Acknowledgement—The authors are grateful to R. REISER of the Gulf Research Laboratories for providing the helical spring used in these experiments.

REFERENCES

1. CHANDRASEKHAR B. S. and HULM J. K., *J. Phys. Chem. Solids* **7,** 259 (1958).
2. BERLINCOURT T. G., *J. Phys. Chem. Solids* **11,** 12 (1959).
3. BLATT F. J., *J. Phys. Chem. Solids* **17,** 177 (1961).
4. BATES L. F., *Modern Magnetism*, pp. 115, 134. Cambridge University Press (1951).
5. WYCKOFF R. D., *Geophysics* **6,** 13 (1941).
6. FRIEDEL J., *J. Phys. Chem. Solids* **1,** 175 (1956).
7. VAN VLECK J. H., *Electric and Magnetic Susceptibilities*. Oxford University Press (1932).
8. STONER E. C., *Proc. Roy. Soc.* A**154,** 656 (1936).
9. WILSON A. H., *The Theory of Metals*, p. 153. Cambridge University Press (1953).
10. GOODMAN B. B., HILLAIRET J., VEYSSIÉ J. J. and WEIL L., *Programme of the VIIth International Conference on Low Temperature Physics*, p. 316. University of Toronto Press (1960).
11. BATES L. F. and LOASBY R. G., *Proc. Phys. Soc. Lond.* **72,** 757 (1958).
12. BATES L. F. and BARNARD R. D., *Proc. Phys. Soc. Lond.* **77,** 691 (1961).

J. Phys. Chem. Solids Pergamon Press 1961. Vol. 21, Nos. 3/4, pp. 210–218. Printed in Great Britain.

NUCLEAR MAGNETIC RESONANCE IN GALLIUM PHOSPHIDE

M. J. WEBER

Research Division, Raytheon Company, Waltham, Massachusetts

(*Received* 1 *June* 1961)

Abstract—Pulsed and CW measurements have been made of the nuclear magnetic resonances of ^{69}Ga, ^{71}Ga, and ^{31}P in polycrystalline GaP. The resonance line shapes are approximately Gaussian with line widths $\sim$ 10 per cent greater than the calculated dipolar widths. The origin of the additional broadening is discussed and compared with line broadening observed in other III–V semiconductors. Positive frequency shifts of the gallium resonances in GaP relative to $GaCl_3$ of $\Delta\nu$ (^{69}Ga) = 0·65 $\pm$ 0·07 kc/s and $\Delta\nu$ (^{71}Ga) = 0·95 $\pm$ 0·07 kc/s are observed. The spin–lattice relaxation times T_1 have been measured using pulsed n.m.r. techniques. The phosphorus T_1 is temperature independent between 77–462°K and is attributed to spin-diffusion limited relaxation via paramagnetic impurities. The gallium relaxation arises from time-dependent quadrupole interactions and in the range 77–700°K can be fitted to Van Kranendonk's temperature dependence for a two-phonon relaxation process using a Debye temperature $\Theta \sim 400$°K. Quadrupolar relaxation in strongly covalently bonded crystals is discussed briefly.

1. INTRODUCTION

GALLIUM phosphide is one of the group III–group V intermetallic compound semiconductors. The techniques of nuclear magnetic resonance can be used to study these compounds and thereby obtain information about the nuclear environment, band structure, and spin–lattice interactions in these semiconductors. Several investigations[1–7] of this nature have been performed, however thus far they have been confined principally to the examination of III–V compounds formed from elements heavier than those present in GaP. Since the chemical bonding, electronic structure, and electron–nuclear hyperfine interactions vary from compound to compound, it is of interest to study the nuclear resonances in GaP, to compare measurements in GaP with those obtained in other III–V semiconductors, and finally to relate these results, wherever possible, to variations in the above properties.

For the purposes of magnetic resonance studies, the nuclei in GaP have several desirable properties. These are summarized in Table 1 which lists the nuclear spin, magnetic moment, electric quadrupole moment, and relative abundance of the principal nuclear isotopes. Since there are two gallium isotopes which are approximately equally abundant and which have quadrupole moments differing by a factor of 1·6, one should be able to use their resonances to identify and study quadrupole interactions and the associated crystalline electric field gradients. At the same time the spin

Table 1. *Nuclear spin, moments, and abundance of principal isotopes in* GaP

Nucleus	Spin	Magnetic moments ($e\hbar/2Mc$)	Quadrupole moments (10^{-24} cm^2)	Natural abundances (per cent)
^{69}Ga	$\frac{3}{2}$	2·0108	0·2318	60·2
^{71}Ga	$\frac{3}{2}$	2·5549	0·1461	39·8
^{31}P	$\frac{1}{2}$	1·1305	—	100

$\frac{1}{2}$ phosphorus nucleus enables one to study effects such as line broadening and spin–lattice relaxation in the absence of any quadrupole effects.

Crystals of the III–V compound semiconductors have the zinc blende lattice structure[8] with tetrahedral coordination at each nuclear lattice site. The bonding[9] is ionic-covalent where the ionic component is in the order of 25 per cent. As the constituent atoms of GaP have one of the greatest electronegativity differences[10] of the III–V semiconductors studied thus far, it should exhibit one of the largest percentages of ionic bonding. This ionicity is also reflected in the relatively large energy gap in GaP of 2·4 eV.

After a brief description of the experimental apparatus used in the present investigation, we discuss the CW measurements of the line shape, line width, and frequency shift of the resonances in GaP and compare these results with similar measurements made in other III–V semiconductors. The results of a study of the spin–lattice relaxation of these resonances as a function of temperature are then presented and the relaxation mechanisms for both phosphorus and gallium are discussed.

Vol. 21
1961

2. APPARATUS

Observations of the width, shape, frequency, and intensity of the nuclear resonance absorption lines were made using a Pound–Knight–Watkins marginal oscillator spectrometer.[11] A Varian 12 in. electromagnet provided magnetic fields to 12·5 kG which were modulated at 200 c/s. As phase sensitive signal detection was used, the derivative of absorption was recorded. The resonant frequencies were measured with a Beckman Model 7175 frequency counter. A Varian Model F–8 gaussmeter was used as an independent measure of the magnetic field strength.

Pulsed nuclear magnetic induction techniques were used to measure the spin–lattice relaxation times and the lifetimes of the free precession decay and spin-echo signals. The pulsed spectrometer was of standard design and consisted of a pulsed oscillator[12] and a low-noise preamplifier, wide band amplifier receiver combination which had greater than one microvolt sensitivity for a signal-to-noise ratio of unity. The detected signal was displayed on an oscilloscope. All timing sequencies and gating pulses were obtained from an appropriate array of Tektronix Type 162 and 163 pulse generator units. The linearity of response of the over-all receiver system was checked to insure the accuracy of the spin–lattice relaxation measurements.

Relaxation measurements at low temperatures were made by immersing the sample and receiver coil directly into a Dewar containing liquid nitrogen, toluene–dry ice solution, or Freon 12. For high temperature measurements, the sample was placed in a specially insulated Dewar containing a non-inductive heater coil in which temperatures to 900°K could be obtained and controlled electronically to within the order of ± 1°K.

3. LINE WIDTH, LINE SHAPE, AND RESONANCE FREQUENCY

Measurements have been made of the line widths, line shapes, and center frequencies of the ^{69}Ga, ^{71}Ga, and ^{31}P nuclear resonances in gallium phosphide at room temperature. The GaP sample, which was prepared by Dr. L. NEURINGER of this laboratory, was polycrystalline and had an impurity concentration of $\sim 5 \times 10^{17}$/cm.^{3} To insure adequate penetration of the r.f. field, a powdered sample was prepared and used for all measurements.

The results of the line width measurements are presented in Table 2 where the reported width δH is the full width between points of maximum slope of the absorption curve. Due precautions were taken to eliminate both modulation broadening and distortion of the resonance due to saturation effects. Because of the long spin–lattice relaxation time of phosphorus, it was not possible to completely eliminate saturation effects from the ^{31}P resonance even when using the lowest available r.f. level of the spectrometer. Therefore the line width was determined from measurements of the spin-echo signals obtained using the pulsed resonance spectrometer. The decay times T_2^* of the corresponding free precession signals of the gallium resonances were also measured and related to the line widths defined above. Good agreement was found between the pulsed and CW data.

Both the Ga and P resonances were observed to be symmetric about the center frequency. The recorded resonance curves were compared with both Gaussian and Lorentzian line shape functions

and all resonances exhibited approximately Gaussian line shapes. Fig. 1 shows a typical comparison of an observed ^{71}Ga resonance and a best-fit Gaussian and Lorentzian curve. In almost all

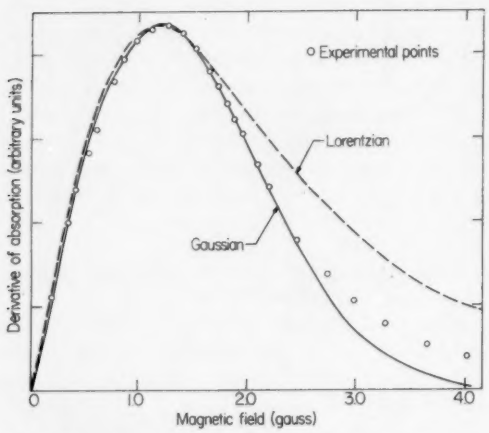

FIG. 1. Line shape of typical ^{71}Ga resonance in GaP compared to Gaussian and Lorentzian shape functions.

cases of ^{71}Ga the symmetric wings of the resonance were observed to fall off slower than that predicted by a Gaussian function. A similar departure, but less pronounced, was also noted for ^{69}Ga.

An attempt was made to determine the second moments of the experimental resonance curves dg/dH using the formula[13]

$$\langle \Delta H^2 \rangle = \int_{-\infty}^{\infty} (H-H_0)^3 \left(\frac{dg}{dH}\right) dH \Big/ 3 \times \int_{-\infty}^{\infty} (H-H_0) \left(\frac{dg}{dH}\right) dH. \quad (1)$$

As noted above, the far wings of the resonances decreased very slowly and, accordingly, made an important contribution to the second moment. Due to the sensitivity of $\langle \Delta H^2 \rangle$ to the contributions from the wings of the lines and the experimental uncertainties in the data from this region, the results obtained varied considerably from curve to curve and were not considered to be significant. Therefore the second moments were calculated from the measured line widths assuming a Gaussian line shape where $\langle \Delta H^2 \rangle = (\delta H)^2/4$ and are given in the third column of Table 2. These results are of the correct order of magnitude, however, they tend to underestimate the true second moments.

The second moments of the dipolar broadening of the resonances were calculated using VAN VLECK's theoretical expression[14]

$$\langle \Delta H^2 \rangle = \frac{3}{5}\frac{I+1}{I}\mu^2 \sum_i r_i^{-6} + \frac{4}{15}\sum_f \frac{I_f+1}{I_f}\mu_f^2 r_f^{-6} \quad (2)$$

for a powdered sample, where I and μ are the spin and magnetic moment of the resonant nuclei i and the unlike nuclei f. The results are presented in the fourth column of Table 2. The experimental second moments for ^{69}Ga, ^{71}Ga, and ^{31}P are all greater than the theoretical second moments. The differences are slightly larger than the experimental errors and, in view of our estimate of the experimental second moments, indicate the presence of an additional line broadening mechanism.

Table 2. Line widths δH and second moments $\langle \Delta H^2 \rangle$ of the nuclear resonances in GaP. *The experimental second moment is derived from the measured line width assuming a Gaussian line shape (see text)*

Nucleus	δH (G)	Experimental $\langle \Delta H^2 \rangle$ (G^2)	Dipolar $\langle \Delta H^2 \rangle$ (G^2)
^{69}Ga	2·26 ± 0·15	1·28	1·08
^{71}Ga	2·26 ± 0·15	1·28	1·09
^{31}P	2·9 ± 0·3	2·10	1·70

The additional line width of the gallium resonances may be due to first or second order quadrupole interactions. In a perfect GaP crystal, the tetrahedral symmetry of the zinc blende lattice would preclude any quadrupolar effects since the crystalline electric field gradient at each nuclear site would be zero. The existence of various crystalline imperfections, however, can destroy this symmetry and give rise to a distribution of internal field gradients and hence quadrupolar broadening. The magnitude of such broadening is proportional to the quadrupole moment Q of the resonant nucleus and the resultant line shapes for a powdered sample are, in general, asymmetric. Since $Q(^{69}\text{Ga})/Q(^{71}\text{Ga}) = 1{\cdot}6$, the ^{69}Ga resonance should exhibit the greater broadening. Although the observed line widths of the two gallium resonances are equal and the line shapes symmetric, the experimental error involved in the measurements is almost as large as the additional line widths and hence may mask the characteristics of quadrupolar broadening. Thus although some quadrupolar broadening may be present, it does not predominate and can not be well established from the present measurements. Quadrupolar broadening, of course, is absent from the spin $\frac{1}{2}$ phosphorus resonance and hence can not account for the additional ^{31}P line width.

A more probable source of the additional line width of the GaP resonances is indirect nuclear exchange broadening. This mechanism has been invoked by SHULMAN *et al.*[1, 3] to explain the large line widths observed in several III–V intermetallic compounds. Via hyperfine interactions with an intermediary electron spin, two nuclei i and j can exhibit isotropic exchange coupling of the form $A\boldsymbol{S}_i\cdot\boldsymbol{S}_j$. When i and j denote different nuclear species, this coupling can give rise to line broadening. As hyperfine interactions are, in general, stronger in heavier atoms, this broadening mechanism should be more important in III–V compounds formed from the heavier elements. This is indeed observed. For example, the exchange broadening contributions to the second moments required by SHULMAN *et al.*[3] to explain their data for GaSb were $\langle\Delta H^2\,(^{69}\text{Ga})\rangle_{ex} = 5{\cdot}3\text{G}^2$ and $\langle\Delta H^2\,(^{121}\text{Sb}\rangle_{ex} = 5{\cdot}6\text{G}^2$, whereas for GaAs they found be $\langle\Delta H^2\,(^{69}\text{Ga})\rangle_{ex} = 0{\cdot}68\text{G}^2$ and $\langle\Delta H^2\,(^{75}\text{As})\rangle_{ex} = 0{\cdot}70\text{G}^2$. As GaP contains the lightest atoms in this series of gallium compounds, the exchange broadening would be expected to be the smallest which is in qualitative agreement with the results in Table 2. Unlike quadrupolar broadening, exchange broadening in GaP is expected to be approximately the same for both gallium isotopes. Thus the magnitude of the additional broadening observed in the GaP resonances appears to be consistent with a mechanism involving indirect nuclear exchange broadening. Unfortunately the smallest of the additional broadening in GaP and the accompanying error add to the difficulties previously encountered[1, 3] in attempting quantitative agreement between line width measurements and the theory of exchange broadening and therefore no meaningful information about the energy band structure in GaP can be obtained from these measurements.

The center frequencies of the gallium resonances in GaP have been measured relative to those in a 6N solution of $GaCl_3$. An r.f. coil arrangement was used wherein the two samples could be interchanged without perturbing the spectrometer operation or the magnetic field which was held constant and periodically monitored. The ratios of the apparent gallium magnetic moments μ in the two compounds are

$$\frac{\mu(^{69}\text{GaP})}{\mu(^{69}\text{GaCl}_3)} = 1{\cdot}000063 \pm 0{\cdot}000008,$$

and

$$\frac{\mu(^{71}\text{GaP})}{\mu(^{71}\text{GaCl}_3)} = 1{\cdot}000073 \pm 0{\cdot}000007.$$

The ratio of the ^{71}Ga and ^{69}Ga magnetic moments in $GaCl_3$ was measured to be $1{\cdot}270615 \pm 0{\cdot}000010$ which, within experimental error, is in agreement with the more accurate result of RICE and POUND[15] of $\mu(^{71}\text{GaCl}_3)/\mu(^{69}\text{GaCl}_3) = 1{\cdot}27062642 \pm 0{\cdot}0000020$. No measurements were made of the phosphorus frequency in GaP due to the poor signal-to-noise of this resonance and the presence of saturation effects.

Positive frequency shifts $\Delta\nu(^{69}\text{Ga}) = \nu(^{69}\text{GaP}) - \nu(^{69}\text{GaCl}_3) = 0{\cdot}65 \pm 0{\cdot}07$ kc/s and $\Delta\nu\,(^{71}\text{Ga}) = 0{\cdot}95 \pm 0{\cdot}07$ kc/s are observed. Using the impurity concentration in our sample, the estimated Knight shift due to free charge carriers is too small to explain the above results. Second-order quadrupolar shifts are ruled out (1) based on estimates of the quadrupole coupling derived

from the line width measurements and (2) because they are negative. The shifts, therefore, appear to be chemical shifts. RAMSEY[16] has treated the problem of chemical shifts and shown that the magnetic shielding of nuclei in molecules arises from a combination of diamagnetic and second-order paramagnetic effects. These effects are dependent upon the chemical structure of the compounds and, in general, are very difficult to calculate. Preliminary measurements of the gallium resonances in GaAs also exhibit positive frequency shifts of the same order-of-magnitude as those observed in GaP. This suggests that careful measurements and interpretation of the chemical shifts in a series of III–V semiconductors, as has been done for various metal halides,[17] may yield information that would be useful in elucidating the covalency in these compounds.

IV. SPIN–LATTICE RELAXATION

The spin–lattice relaxation times T_1 in GaP have been measured using pulsed nuclear magnetic induction techniques.[18] To reduce the equilibrium magnetization M_0 to zero and to ensure complete saturation of the spin system at time $t = 0$, a series of five equally spaced 90° pulses were applied. The total series of pulses required about 1 m sec which was always very much less than T_1. The recovery of the spin system toward equilibrium was measured by varying the time interval between successive pulse series and observing the free precession signals following the first pulse of each series. Since the magnitude of this signal is proportional to the z-component of spin magnetization $M(t)$ present at the time the pulse is applied, it is a direct measure of the longitudinal relaxation recovery of the spin system during the time interval between saturation pulses. For a spin system with a well defined spin temperature, the relaxation can be described by a simple exponential recovery of the form $M(t) = M_0[1-\exp(-t/T_1)]$ with the initial condition $M(0) = 0$.

Depending upon the available signal-to-noise of the resonance being studied, data was recorded either directly from the oscilloscope presentation or from integration photographs taken using a Polaroid camera. The results given represent the average of many measurements at each temperature. The errors associated with the gallium relaxation measurements are believed to be less than 10 per cent.

A. *Phosphorus*

The relaxation time T_1 of ^{31}P has been measured in the temperature range 77–462°K and the results plotted in Fig. 2 as a function of temperature. Over the temperature range investigated the phosphorus relaxation is approximately temperature independent. Since the phosphorus T_1's were

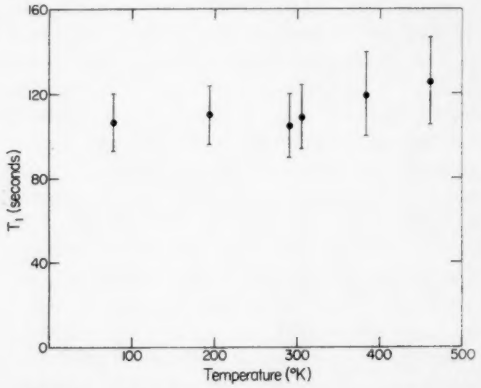

FIG. 2. Spin–lattice relaxation time T_1 of the ^{31}P resonance in GaP as a function of temperature.

in the order of 2 min, long-term drifts and instabilities in the pulse spectrometer occurring during the time required to record the complete relaxation recovery contributed to a reduction in the over-all accuracy of the measurements.

The relaxation of spin $I = \frac{1}{2}$ nuclei is usually attributed to interactions with electronic spins. For the case of semiconductors, BLOEMBERGEN[19] has considered two general sources of nuclear relaxation arising from interaction with (1) mobile charge carriers and (2) bound paramagnetic impurities. The first mechanism originates in the hyperfine interaction $\boldsymbol{I}\cdot\boldsymbol{S}$ between the nuclear spin and mobile electrons or holes. Calculations of the relaxation time of this mechanism using the estimated impurity concentration of our sample yield results more than an order of magnitude longer than the observed T_1's of ^{31}P. In addition the relaxation should be temperature dependence with a rate proportional to $T^{1/2}$ or faster. As no such temperature dependence is

Vol. 2
1961

observed, we rule out mobile charges as the operative phosphorus relaxation mechanism in our GaP sample.

The relaxation rate of the second mechanism[20] based upon the interaction of the nuclear spins with bound paramagnetic impurities may be limited by either the time required for (i) the spin energy to diffuse to the paramagnetic impurity or (ii) the impurity relaxation to the lattice. In the latter case the nuclear relaxation would reflect the temperature dependence of the impurity spin–lattice relaxation. This, however, is not observed. If, on the other hand, the phosphorus relaxation was limited by spin-diffusion, the T_1 would be temperature independent. Although we do not know the exact nature or spacial distribution of the impurities present in our sample, estimates of the spin-diffusion time required to explain the observed T_1's are not unreasonable. Thus we conclude that the temperature independent T_1 of phosphorus is due to spin-diffusion limited relaxation via bound paramagnetic impurities.

As BLOEMBERGEN has pointed out, if at high temperatures the bound paramagnetic impurity centers become ionized, the associated electrons will become less effective relaxers and the nuclear T_1 will increase. No distinct evidence of such behavior is observed in our GaP samples for temperatures up to 460°K. To study spin–lattice relaxation mechanisms in semiconductors further, it would be of interest to measure the ^{31}P relaxation in various III–V phosphorus compounds as a function of both temperature and paramagnetic impurity concentration.

B. *Gallium*

Measurements of the spin–lattice relaxation of the ^{69}Ga and ^{71}Ga resonances have been made in the temperature range of 77–700°K. All data could be fitted to a simple exponential recovery of the spin system toward equilibrium. The results are shown in Fig. 3.

Since both gallium isotopes have spin $I = \frac{3}{2}$ and, therefore, have nuclear quadrupole moments, the most probable source of spin–lattice coupling in the absence of large quantities of paramagnetic impurities is electric quadrupole interactions. Although the gallium nuclei in the zinc blende lattice of GaP are located in sites of tetrahedral symmetry, which for point electronic charges would have zero electric field gradient, thermal lattice vibrations destroy this symmetry and give rise to time-dependent field gradients capable of inducing quadrupole relaxation transitions.

We can test the hypothesis of quadrupolar relaxation by noting that for this case the relaxation transition probabilities will be proportional to the square of the quadrupole moment Q of the nucleus of interest. Since the electronic structure and lattice environment of the two gallium isotopes are identical, the ratio T_1 (^{71}Ga)/T_1 (^{69}Ga) should be equal to $[Q(^{69}\text{Ga})/Q\ (^{71}\text{Ga})]^2$. From measurements at room temperature T_1 (^{71}Ga)/T_1 (^{69}Ga) = 2·65 ± 0·2 which is in good agreement with $[Q(^{69}\text{Ga})/Q(^{71}\text{Ga})]^2 = 2{\cdot}52$ obtained from the values of the quadrupole moments given in Table 1. Within the experimental error of the data in Fig. 3, the T_1 (^{71}Ga)/T_1 (^{69}Ga) ratio indicates that the gallium relaxation is predominantly quadrupolar over the entire temperature range investigated. Measurements by other investigators[5, 7] of

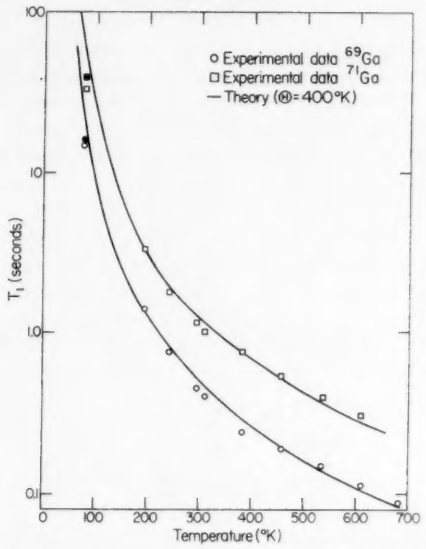

FIG. 3. Spin–lattice relaxation time T_1 of the ^{69}Ga and ^{71}Ga resonances in GaP. VAN KRANENDONK's theoretical temperature dependence for a two-phonon relaxation process is shown for a Debye temperature $\Theta = 400$°K. The points ● and ■ are the T_1's for quadrupolar relaxation after correcting for paramagnetic impurity relaxation.

T_1 and its temperature dependence in several different III–V semiconductors have also established the presence of quadrupolar spin–lattice relaxation.

Several authors have developed detailed theories of quadrupolar spin–lattice relaxation in solids. These theories differ principally in the models used to describe the source of the fluctuating electric field gradient at the nucleus and include treatment of a point charge ionic model,[21] the presence of a small admixture of covalent bonding,[17] and charge overlap between neighboring ions.[22] Since III–V semiconducting compounds are strongly covalently bonded crystals, none of the above relaxation theories is strictly applicable to GaP.

MIEHER[7], to interpret his measurements of T_1 in various III–V semiconductors, has extended VAN KRANENDONK's treatment[21] of quadrupolar relaxation in the NaCl lattice to the zinc blende lattice assuming a simple point charge ionic model of the field gradient. For temperatures $T > 0{\cdot}02\,\Theta$, where Θ is the Debye temperature, MIEHER finds a spatially isotropic T_1 given by

$$\frac{1}{T_1} = 51\,\frac{2I+3}{I^2(2I-1)}\,\frac{(e^2\gamma Q)^2}{d^2v^3r^{13}}\left(\frac{T}{\Theta}\right)^2 E(T/\Theta), \quad (3)$$

where the concept of a spin temperature was used to relate the calculated transition probabilities to the observable T_1. In equation (3) r is the nearest neighbor internuclear distance, v is an average phonon velocity, and d is the mass density of the crystal. The function $E(T/\Theta)$ is a complicated integral over a Debye spectrum of lattice vibrations and has been evaluated numerically by VAN KRANENDONK[21]. γ is a dimensionless multiplicative factor which is introduced to take into account antishielding of the nucleus due to distortions in the surrounding electronic charge cloud and possibly other deviations from an ideal point charge model.

The functional temperature dependence in (3) is identical to that derived by VAN KRANENDONK for the cubic NaCl lattice. Using this result MIEHER has found good agreement between theory and experiment for the ^{115}In relaxation in InP. In the temperature range considered, $T > 70°$K, Raman type relaxation processes involving the inelastic scattering of two lattice phonons accompanied by a spin transition are dominant. Since this mechanism utilizes an integrated effect of the entire lattice frequency spectrum, the resulting form of the temperature dependence is not sensitive to the details of the lattice or its vibration spectrum. This probably accounts for the general success and applicability of VAN KRANENDONK's theoretical temperature dependence.

The temperature dependence $(T/\Theta)^2E(T/\Theta)$ given in (3) has been applied to the data for GaP. The most satisfactory over-all fit to the data is obtained using a Debye temperature Θ of 400°K. The results are illustrated in Fig. 3 as a solid curve. The value $\Theta \sim 400°$K is in reasonable agreement with estimates[23] of the Debye temperature for GaP based upon knowledge of the reststrahlen frequencies and elastic constants of similar III–V compounds. In the region $T > \Theta$, $E(T/\Theta)$ approaches unity and a familiar $1/T^2$ dependence of the relaxation at high temperatures is observed.

The data at 77°K produces the poorest fit between experiment and the theoretical temperature dependence. Also, the ratio $T_1(^{71}\text{Ga})/T_1(^{69}\text{Ga}) = 2{\cdot}28$ which, with an estimated error of $\pm\ 0{\cdot}2$, falls beyond the predicted value of 2·52 for quadrupolar relaxation. Since quadrupolar relaxation becomes very slow at low temperatures, relaxation due to paramagnetic impurities[20] may no longer be negligible and may account for the above discrepancies. Since the relaxation of phosphorus in our sample of GaP is due to the presence of paramagnetic impurities and since at all temperatures investigated $T_1(\text{Ga}) < \frac{1}{3}T_1(\text{P})$, an impurity mechanism can add at most a small contribution to the observed gallium relaxation rate at 77°K. Using the measured spin-diffusion limited phosphorus T_1 and introducing the gyromagnetic ratio, spin, line width, and concentration appropriate for ^{69}Ga and ^{71}Ga into the spin diffusion constant, we have estimated the rate of gallium relaxation via paramagnetic impurities. These results, which in the case of ^{71}Ga amounted to more than 15 per cent of the observed relaxation rate, were subtracted from the measured gallium T_1's. The remaining relaxation is attributed to quadrupole interactions and the associated T_1's at 77°K are plotted in Fig. 3. The corrected T_1's are in better agreement with the theoretical temperature dependence (although the differences are still greater

than the experimental error) and the ratio of the quadrupolar relaxation for ^{71}Ga and ^{69}Ga is now 2·6.

The magnitude of the gallium T_1's in GaP have been calculated using equation (3). If a purely ionic model is assumed, γ can be related to the Sternheimer antishielding factor[24] γ_∞ by $\gamma = 1-\gamma_\infty$. The γ_∞ for the free ion Ga^{3+} has been calculated recently[25] using contracted wave functions and a value of $\gamma_\infty = -6{\cdot}94$ was obtained. Substituting this result into equation (3), we find T_1's several orders of magnitude longer than observed. To obtain agreement between theory and experiment, an enhancement factor $\gamma \approx 180$ is required. Using MIEHER's T_1 data and equation (3) a similar value is found for gallium in GaAs, while in GaSb a gallium $\gamma \sim 250$ is required. This latter result is in reasonable agreement with the γ's obtained by OLIVER[6] from a study of the reduction of the gallium resonance intensity in GaSb due to the addition of impurities.

Although only the order-of-magnitude of the γ's determined from T_1 measurements is meaningful, due to the numerous assumptions and approximations made in carrying out a detailed calculation of the relaxation transition probabilities, the large difference between these results and the calculated γ_∞ is significant. As noted earlier, the treatment of a point charge ionic model is not a physically correct description of the III–V semiconductors. The presence of covalent bonding in these compounds is expected to give rise to large fluctuating electric field gradients at the nuclei and thereby increase the rate of quadrupolar relaxation above that predicted by a simple ionic model. The large discrepancy between the observed enhancement factor γ and the calculated γ_∞ is an indication of the importance of covalent bonding for the retaxation.

A careful study of the spin–lattice relaxation of a series of ionic-covalent crystals such as the III–V compounds may contribute to the understanding of quadrupolar relaxation in strongly covalent crystals. Consider, for example, the series of gallium compounds of P, As, and Sb. Since the degree of ionicity increases, in general, with increasing electronegativity difference between the constituent atoms, GaP is expected to exhibit the smallest percentage of covalent bonding of the series. The larger enhancement factor γ required for gallium in GaSb relative to that required in GaP may therefore be attributable to greater covalency in the former compound. The suggestion has also been made[4] that the effective antishielding factor γ may be ascribed to distortions of the valence band wavefunctions in the III–V semiconductors. Since such distortions would be more probable in compounds having small energy gaps E_g, the gallium in GaSb is again predicted to have the largest effective $\gamma[E_g(\text{GaSb}) = 0{\cdot}80\text{ eV}$, E_g (GaAs) $= 1{\cdot}53$ eV, E_g (GaP) $= 2{\cdot}4$ eV]. Although it is not felt possible to extract any quantitative information regarding these points from the present data, the results do indicate that a systematic study as suggested above and a detailed treatment of quadrupolar relaxation in solids having predominantly covalent bonding would be of considerable interest.

V. SUMMARY

The investigation and measurements of the nuclear resonances in GaP have shown the following.

1. Dipolar broadening alone is insufficient to account for the observed line widths. The additional line width is probably due to indirect nuclear exchange broadening.
2. The gallium resonances in GaP exhibit a positive frequency shift relative to the resonances in 6N $GaCl_3$.
3. The spin–lattice relaxation of phosphorus nuclei arises from interactions with bound paramagnetic impurities present in the sample used and the temperature independence of T_1 indicates that the relaxation rate is limited by spin-diffusion.
4. Quadrupole interactions are the source of the gallium spin–lattice relaxation. Fitting VAN KRANENDONK's theoretical temperature dependence to the experimental T_1's yields a characteristic Debye temperature for GaP of $\Theta \sim 400°$K. A simple ionic model and Sternheimer antishielding factor do not provide an adequate description of the spin–lattice coupling.

The results of these measurements when combined with results obtained in other III–V semiconductors indicate that a careful and symmetric study of the chemical shifts, quadrupolar relaxation, and

Vol. 21
1961

exchange broadening should contribute to a better understanding of the nature and variation of the covalent bonding and band structure of these compounds.

Acknowledgements—The author wishes to thank Dr. L. RIMAI for many helpful discussions and suggestions during the course of this work and Dr. L. NEURINGER for providing the GaP sample and discussions of the properties of III–V semiconductors. The author would also like to express his thanks and appreciation to Mr. R. ALLEN for measurements of the relaxation times and Messrs. J. BLODGETT and J. HOWLEY for measurements of the CW resonances.

REFERENCES

1. SHULMAN R. G., MAYS J. M. and MCCALL D. W., *Phys. Rev.* **100,** 692 (1955).
2. SHULMAN R. G., WYLUDA B. J. and ANDERSON P. W., *Phys. Rev.* **107,** 953 (1957).
3. SHULMAN R. G., WYLUDA B. J. and HROSTOWSKI H. J., *Phys. Rev.* **109,** 808 (1958).
4. RHODERICK E. H., *Phil. Mag.* **3,** 545 (1958).
5. KRAUS O., *J. Phys. Chem. Solids* **8,** 504 (1959).
6. OLIVER D. J., *J. Phys. Chem. Solids* **11,** 257 (1959).
7. MIEHER R. L., *Phys. Rev. Letters* **4,** 57 (1960); Thesis, University of Illinois (1960), unpublished.
8. WYCKOFF R. W. G., *Crystal Structures*. Interscience, New York (1957).
9. GOODMAN C. H. L., *Nature, Lond.* **187,** 590 (1960).
10. PAULING L., *The Nature of the Chemical Bond* (3rd Ed.). Cornell University Press, Ithaca, New York (1960).
11. POUND R. V. and KNIGHT W. D., *Rev. Sci. Instrum.* **21,** 219 (1950); WATKINS G. D., Thesis, Harvard University (1952), unpublished.
12. DAS T. P. and HAHN E. L., *Nuclear Quadrupole Resonance Spectroscopy, Solid State Physics, Supplement* 1. Academic Press, New York (1958).
13. PAKE G. E. and PURCELL E. M., *Phys. Rev.* **74,** 1184 (1948).
14. VAN VLECK J. H., *Phys. Rev.* **74,** 1168 (1948).
15. RICE M. and POUND R. V., *Phys. Rev.* **99,** 1036 (1955).
16. RAMSEY N. F., *Phys. Rev.* **78,** 699 (1950).
17. YOSIDA K. and MORIYA T., *J. Phys. Soc. Japan* **11,** 33 (1956).
18. HAHN E. L., *Phys. Rev.* **80,** 580 (1950); PAKE G. E. *Nuclear Magnetic Resonance, Solid State Physics* Vol. II. Academic Press, New York (1956).
19. BLOEMBERGEN N., *Physica* **20,** 1130 (1954).
20. BLOEMBERGEN N., *Physica* **15,** 386 (1949).
21. VAN KRANENDONK J., *Physica* **20,** 781 (1954).
22. KONDO J. and YAMASHITA J., *J. Phys. Chem. Solids* **10,** 285 (1959).
23. NEURINGER L., private communication.
24. FOLEY H. M., STERNHEIMER R. M. and TYCKO D., *Phys. Rev.* **93,** 734 (1954); STEINHEIMER R. M., *Phys. Rev.* **102,** 731 (1956).
25. BURNS G. and WIKNER E. G., *Phys. Rev.* **121,** 155 (1961).

J. Phys. Chem. Solids Pergamon Press 1961. Vol. 21, Nos. 3/4, pp. 219–227. Printed in Great Britain.

HYDROGEN–DEUTERIUM EXCHANGE ON CLEAN NICKEL SURFACES*

D. SHOOTER and H. E. FARNSWORTH

Barus Physics Laboratory, Brown University, Providence, R.I.

(*Received* 7 *June* 1961)

Abstract—A reaction chamber has been developed for measuring the catalytic activity of small samples cleaned by argon ion bombardment. It has two compartments. Cleaning of the catalyst takes place in the lower compartment and it is then transferred to the upper compartment which contains no other active materials. Activity measurements were made with the two compartments isolated from each other by a ground glass valve. Hydrogen–deuterium exchange was studied on a solid polycrystalline nickel catalyst. Gas mixtures were analyzed with an omegatron mass spectrometer. The rate of reaction on the clean surface was $8{\cdot}8 \times 10^{16}$ molecules cm^{-2} sec^{-1} (p = 1mmHg, T = 293°K). Measurements were made of the activity as a function of pressure, contamination, and conditions of ion bombardment.

Vol. 21
1961

1. INTRODUCTION

ONE OF the major problems in heterogeneous catalysis at present is that of adequately defining the nature of the catalyst surface being studied. This involves the effective removal of surface contamination and reduction of the concentration of contaminants in the gas phase so that the surface does not become recontaminated before completion of the measurements. Present vacuum techniques result in pressures of 10^{-9} mm Hg and below, thus minimizing contamination from the ambient. Cleaning the surface of its initial oxide or other contaminating layers is more difficult except in the case of high melting point metals which can be cleaned by heating *in vacuo*. FARNSWORTH *et al.*[1, 2] have demonstrated that the technique of argon ion bombardment is effective in cleaning the surface of a wide variety of single crystal and polycrystalline materials. Using these techniques they have obtained the activity of nickel and nickel alloys in ethylene hydrogenation.[3, 4] In the present work the activity of nickel in hydrogen–deuterium exchange was studied on surfaces cleaned by ion bombardment, the reaction rate being measured with an omegatron mass spectrometer.[5] The technique of ion bombardment in catalytic experiments introduces a problem since the electron gun and the sputtered film of catalytic material formed during the bombardment may have an activity comparable to the sample being studied. For the experiments on ethylene hydrogenation,[3, 4] this problem was solved by cooling these parts to −80°C, thus suppressing the activity. It was not expected that this method would be capable of suppressing the activity for hydrogen deuterium exchange so a different design of reaction chamber was used.

* This work was supported by the U.S. Army Signal Corps.

2. EXPERIMENTAL

2:1 *Apparatus*

A block diagram of the apparatus is given in Fig. 1. The reaction chamber, which has two compartments separated by a ground glass valve, is connected to the rest of the apparatus by three metal valves. Two of these valves connect the top compartment to the gas storage line and the omegatron respectively, and the third connects the bottom compartment to the main pumping line. The reaction vessel and metal valves are further isolated by liquid nitrogen traps. During reaction runs the omegatron must be continuously pumped and so has its own evacuation system. A mercury diffusion pump is essential for the omegatron, because with an oil diffusion pump

copious amounts of hydrogen and some higher hydrocarbon fractions are observed in the omegatron. This is presumably due to breakdown of the pump oil and has been observed by other workers.[6, 7]

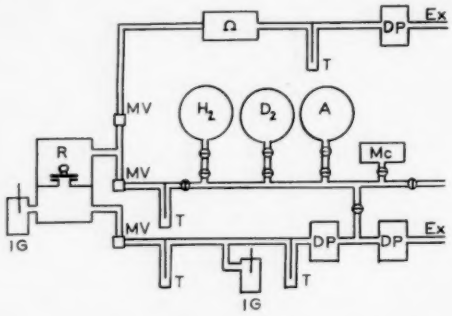

FIG. 1. Block diagram of the apparatus. DP—Mercury diffusion pumps, McLeod gauge, R—reaction chamber, I. G.—Ion gauge, MV—metal valves, Ω—omegatron, T—cold trap.

2 : 2 *Reaction chamber and catalyst*

Details of the reaction chamber are shown in Fig. 2. Reaction rates are studied in the top compartment which has no exposed metal surfaces. It is separated from the lower cleaning compartment by the non-lubricated ground glass valve. The electron gun in this compartment is used for electron bombardment and ion bombardment, and is contructed with a filament shield which prevents evaporation of tungsten from the gun filament onto the crystal and minimizes ion bombardment of the filament. Also attached to this compartment is an ion gauge (Westinghouse WL 5966) to monitor the pressure. Because of the relative positions of the crystal and filament, it is necessary to direct the electron beam onto the crystal by means of a small external magnet.

A polycrystalline nickel sample was used with a geometrical surface area of 6 cm^2. It was cut to a "T" shape (see Fig. 1) so that it would hang in the upper crystal support. Before placing it in the reaction chamber, it was electropolished and given a final etch for five minutes at room temperature in a solution of 70 per cent glacial acetic acid, 20 per cent fuming nitric acid and 10 per cent concentrated hydrochloric acid.

The catalyst is held in the upper end of a quartz tube for cleaning purposes. In its lower position the catalyst is then opposite the electron gun. After cleaning, the tube and crystal are moved magnetically through the opened glass valve and the catalyst is transferred to the upper quartz support. On retracting the tube and closing the glass valve, the reaction can be conducted.

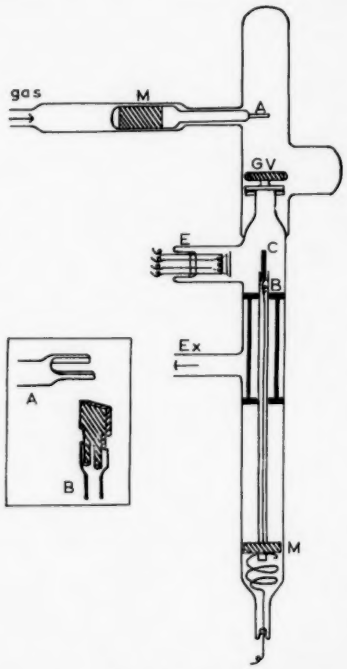

FIG. 2. Reaction chamber. M—magnetic controls, GV—glass valve, C—catalyst, E—electron gun, A and B—upper and lower catalyst supports, respectively. Inset shows detail of catalyst supports.

2 : 3 *The omegatron*

The omegatron mass spectrometer used in this work is similar to ALPERT's design[8] without guard rings. It is constructed from molybdenum with a box 2 × 2 × 1·5 cm^3. A tantalum filament coated with lanthanum boride[9] is used as a source of ionizing electrons. This filament* which operates at a much lower temperature (1100°K) than ordinary filaments does not dissociate hydrogen to any appreciable extent.[10] It is found that

* The filament was supplied by the Raytheon Company, Waltham, Mass.

compared to a conventional tungsten filament the amounts of HD and H_2O produced by reaction in the omegatron are greatly reduced. The r.f. field is provided by a Hewlett–Packard oscillator model 650 A. Ion currents are measured with a vibrating reed electrometer (Applied Physics Corporation) connected to a Varian Recorder.

A permanent magnet of 2000 G is used in this work, which is adequate to completely resolve masses 2, 3 and 4. When measuring the exchange reaction it is normally operated for maximum sensitivity.

Values obtained for the sensitivity and resolution* are given in Table 1.

Table 1. *Sensitivity and resolution of the omegatron. Electron accelerating voltage* 100, *electron beam current* 6 μA, *r.f. voltage* 3 V (r.m.s.), *trapping voltage on box* +1·6

	Sensitivity	Resolution
Hydrogen	$1{\cdot}0\times10^{-9}$ mm Hg	220
Hydrogen deuteride	$6{\cdot}7\times10^{-10}$ mm Hg	100
Deuterium	$5{\cdot}2\times10^{-10}$ mm Hg	94

The sensitivities given are not absolute values since they were measured with a conventional ion gauge and no correction was made for the dissociation of hydrogen. However, the three species H_2, HD, and D_2 are identical chemically so that the relative sensitivities should be correct. It was found that the peak height varied linearly with pressure in the range 10^{-7} to 10^{-6} mm Hg; hence, the reaction was normally studied with the omegatron operating in this range. Since it is not possible to obtain pure HD, the sensitivity of an equilibrium mixture of HD, H_2 and D_2 was determined and the sensitivity for HD was calculated. The resolution decreases with increasing mass number and consecutive masses above 18 could not be resolved completely with the present magnet. Resolution could be improved somewhat by decreasing the r.f. voltage but only at the expense of the sensitivity.

* The sensitivity is defined[7] as the gas pressure giving an ion current of 10^{-14} A. The resolution is calculated with ΔM measured at half-peak height.

Reactions were studied at about 1 mm pressure and the metal valve to the omegatron was used as a leak which kept the pressure in the omegatron below 10^{-6} mm Hg. The contents of the reaction vessel were monitored continuously but because of the large pressure drop across the valve the concentration of the reactants in the reaction compartment was not sensibly altered. No preferential diffusion of the lighter species through the metal valve was observed. The omegatron can also be used to monitor the vacuum conditions if the pressure is not too low.

2 : 4 *Cleaning of the catalyst*

After baking the system and outgassing the metal parts, the sample was outgassed at red heat by electron bombardment. Between experimental runs, the reaction chamber was pumped to a pressure of 10^{-8} mm. Most of this residual gas was argon. The rate of contamination of the nickel indicates that the pressure of adsorbable gases was below 10^{-10} mm Hg.

No attempt was made to measure the exchange reaction until the sample had been outgassed for 117 hr at red heat and had received 20 min of ion bombardment. The standard conditions of ion bombardment were 100 μA at 500 V for ten minutes on each of the two major surfaces of the catalyst; this was later reduced to five minutes on each side. Alternate ion bombardment and heating treatments were given to the crystal, the activity being periodically examined. At the conclusion of the experiments the crystal had received a total of 220 hr of heating at red heat and 225 min of ion bombardment.

2 : 5 *Gases*

Hydrogen (99·99 per cent) and argon (99·999 per cent) used in these experiments were mass spectrographically pure and were used as received. The best deuterium available was less pure (average 99·66 per cent D_2) and was said to contain HD and D_2O. Both the hydrogen and deuterium were analyzed in the omegatron and found to contain, besides HD, some impurity of mass 28. This mass 28 was associated with masses 14 and 7. No mass 16 or mass 12 was observed which suggests that the impurity is nitrogen. Since the omegatron was not calibrated for nitrogen, no quantitative estimate was made. An attempt was

made to further purify the deuterium by allowing it to remain in contact with a freshly evaporated molybdenum film for twelve hours. When this gas was examined in the omegatron the mass spectrum was the same as before.

3. RESULTS

Hydrogen–deuterium exchange is a reversible reaction which occurs on the catalyst surface. Under the conditions of these experiments the weight of evidence[21] seems to favor the mechanism originally proposed by BONHOEFFER and FARKAS[22]. This mechanism involves dissociation and chemisorption of the hydrogen and deuterium as atoms on the surface. Adjacent hydrogen and deuterium atoms can then evaporate as HD. Proportions of HD, H_2 and D_2 leaving the surface are the equilibrium proportions for the mixture. The rate of approach to equilibrium, in agreement with all other experiments, followed a first order law with an experimental rate constant

$$k_e=\frac{2{\cdot}3}{t}\log\frac{(\mathrm{HD})_e-(\mathrm{HD})_0}{(\mathrm{HD})_e-(\mathrm{HD})_t}\ \mathrm{min}^{-1}\ (\text{constant } p,\ T), \tag{1}$$

where the subscripts e, 0, t refer to concentrations at equilibrium, time zero, and time t, respectively. k_e is usually corrected for the volume of the reaction chamber and the surface area of the catalyst, giving $k_0 = k_eV/A$. The experimental rate constant is related to the half life by the equation $\tau = 0{\cdot}69/k_e$. An approximately 50/50 mixture was used which gives the maximum concentration of HD at equilibrium. In experiments which went to equilibrium, good agreement was obtained between observed and calculated equilibrium constants.

3 : 1 *Activity of the metal valves*

The upper compartment of the reaction chamber is not completely free of metal, the reacting gases unavoidably come in contact with a small area of metal on one side of the metal valves. In preliminary experiments before the reaction chamber was attached, the activity of this metal was measured. When freshly baked, the valves had a half life of 10^4 min. This activity could not be reduced by cooling the valve in dry ice but it decayed over a period of days to a much smaller value. Since the original activity is immeasurably small compared to the activity of the sample, activity from this source was neglected.

3 : 2 *Conductance of the ground glass valve*

Successful operation of this apparatus depends on the effectiveness of the ground glass valve. It has a central hole of 1·5 cm diameter with an over-all diameter of 3 cm, and was polished in the laboratory to something approaching optical flatness. For hydrogen at about 1 mm pressure, the measured conductance was about 1 per cent per minute. When the reaction was conducted with the glass valve closed and the bottom compartment closed off from the pumps, an activity was measured

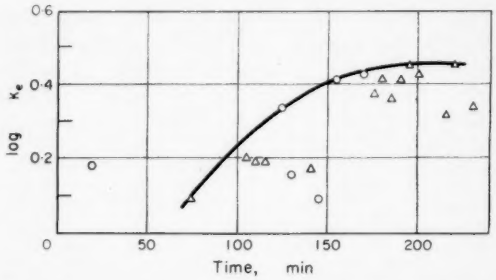

FIG. 3. Increase in catalytic activity with total bombardment time. △—Ion bombarded surfaces. ○—Annealed surfaces. Curve is drawn through the maximum values.

due to diffusion through the valve, exchange on the metal parts, and diffusion back again. When the lower compartment was pumped continuously during experiments, no activity was detected even in the presence of hot filaments in the lower compartment. Some separation of the gases due to molecular diffusion through the glass valve was observed. These limitations placed a lower limit on the observable reaction velocity which corresponds to a velocity constant, $k_e = 3\times10^{-4}$ min^{-1} (half life $2{\cdot}3\times10^3$ min). Since the activity of nickel is much higher than this, these measurements were not affected.

3 : 3 *Activity of ion bombarded and annealed surfaces*

No difference in activity between ion bombarded and heated surfaces was observed which can be attributed to different surface treatments. The heated surface was produced by heating it to red

Vol. 2
1961

heat for about twenty minutes and then allowing it to cool to room temperature. These results are in agreement with the preliminary findings of FARNSWORTH and WOODCOCK[3] using a different apparatus. A very high activity was obtained after only twenty minutes of ion bombardment; however, this activity decayed very rapidly. After 100 min of ion bombardment with intermittent annealing, the results became more reproducible and, with further ion bombardment, the activity gradually increased until it was nearly twice that in the earlier experiments. (Fig. 3). The final result obtained was $k_e = 2{\cdot}9\ \text{min}^{-1}$. Corrected for the surface area and volume of the reaction chamber (337 cm^2), this gives $k_0 = 1{\cdot}6 \times 10^2\ \text{cm min}^{-1}$.

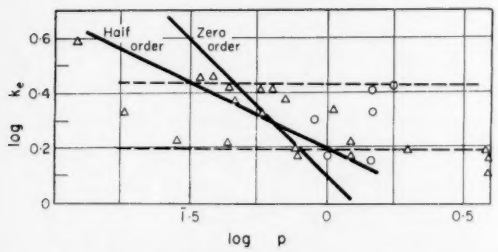

FIG. 4. Pressure dependence of the activity. △—Ion bombarded surfaces. ○—Annealed surfaces.

This extremely high activity prevented measurements of the activation energy because the reaction was too fast to follow above room temperature. The construction of the apparatus prevented measurements below room temperature.

3 : 4 *Variation of activity with pressure*

The pressure was varied from 0·15 mm to 4 mm. In this range no significant variation of the velocity constant k_e was observed, except that which can be attributed to contamination. Fig. 4 shows the results obtained. Since the absolute rate is proportional to $k_e p$, the reaction shows first order behavior. The slopes required for a zero order and a half order reaction are shown on Fig. 4 for comparison.

3 : 5 *Variation of activity with contamination*

It was found that the activity decayed with time even after 200 min of ion bombardment, showing that contamination of the surface was still occurring. A typical sequence of runs is shown in Fig. 5. Results from the ion bombarded surface were more reproducible than those from the heated surface and the clean surface value could be maintained for a longer time.

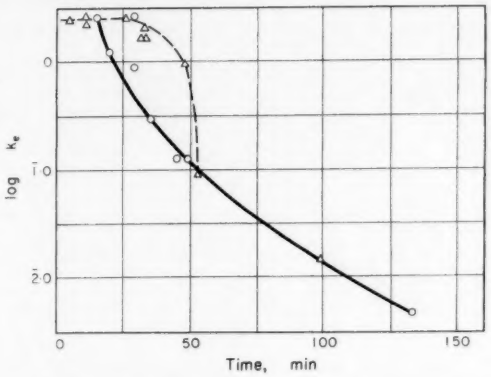

FIG. 5. Decay of activity with time due to contamination. △—Ion bombarded surfaces. ○—Annealed surfaces.

A second run on an ion bombarded surface, without further cleaning, gave the same activity as the first if it was started within about thirty minutes. Subsequent contamination of the ion bombarded surface seemed to take place more rapidly. The point for a heated surface which is farthest from the general curve was the result of several consecutive ion bombardments followed by a very short heat treatment. After only 130 min the activity had dropped to 0·2 per cent of the clean surface value, but it dropped only a little further in the next twenty hours.

Contamination of the nickel from the hydrogen and deuterium used for exchange did not occur, because a decay in activity during a run was rarely observed and a second run often gave the same activity as the first without further cleaning of the surface. Some activity measurements were also made on the tungsten filament of the electron gun. Results were reproducible only if the filament was cleaned before each run indicating that contamination from the hydrogen and deuterium was occurring. This is further evidence (see Section 2 : 5) that the impurity in the hydrogen and deuterium is nitrogen and not carbon monoxide, since nitrogen adsorbs on tungsten but does not adsorb on nickel at room temperature.[11, 12]

3 : 6 *Variation of activity with ion bombardment*

The energy of the bombarding argon ions was varied to determine if minimum conditions existed for cleaning the crystal. Fig. 6 shows that for a current of 100 μA for 5 min the same activity is obtained down to 150 V. Below this the activity decreases very sharply. 100 V ions were also used

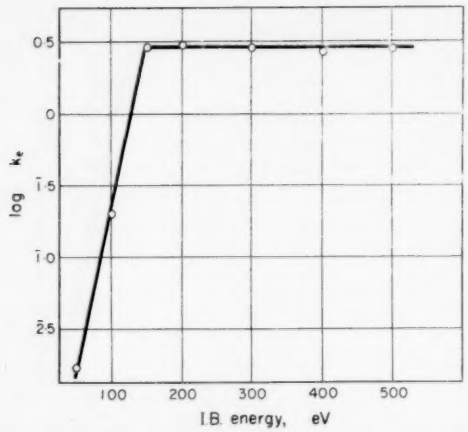

FIG. 6. Variation of activity with ion bombardment energy, for 5 min at 100 μA.

to bombard the crystal for varying times and current densities. At 100 V and 100 μA no cleaning was observed even for bombarding times up to

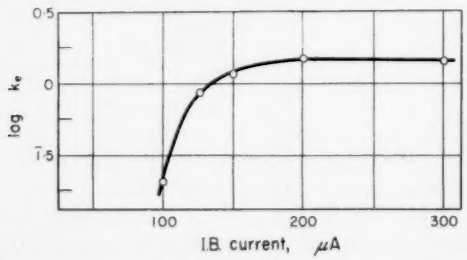

FIG. 7. Variation of activity with ion bombardment current, for 5 min at 100 V.

20 min on each side. For 100 V × 5 min, a partial recovery of the activity occurred as the current density was increased. (Fig. 7). Only 50 per cent of the clean surface activity could be obtained by this treatment. The effect of shorter bombarding times above 150 V was not investigated.

It may be concluded from these results that a minimum bombarding energy of 150 eV is necessary to obtain a reproducible surface. Since the standard bombarding energy used was 500 eV, the results should be characteristic of the clean surface.

3 : 7 *Activity of an evaporated film*

In connection with this work some earlier results obtained by one of the authors (D.S.) are of interest.* The work was done on a nickel film evaporated in a vacuum system similar to one previously described.[13] A liquid nitrogen trap and mercury cut-off were used to protect the film from

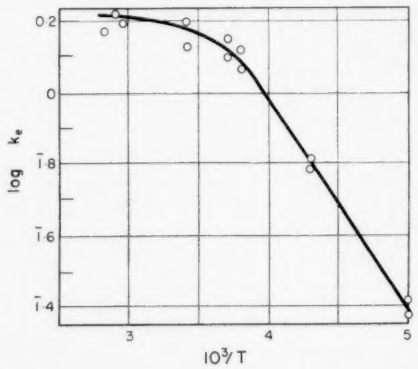

FIG. 8. Temperature dependence of activity on the evaporated nickel film.

contamination. The baking and outgassing procedures were similar to those used in the present work. A McLeod gauge situated some distance from the reaction chamber was the only pressure measuring device; this had a lower limit of 10^{-6} mm Hg. Rate measurements were made with a micro Pirani gauge.[14] The film was deposited at room temperature and had a geometrical area of 30 cm^2. Its activity for hydrogen–deuterium exchange was very high with a velocity constant $k_0 = 17{\cdot}3$ cm min^{-1} (293°K). Para-hydrogen conversion was also measured on this film and found to proceed at the same rate. The temperature dependence of the rate constant was studied over the range 200–450°K. Fig. 8 shows the Arrhenius

* Performed with D. D. ELEY at the University of Nottingham, England.

plot. The constants calculated from the equation $k_0 = B_0 \exp -E/RT$ are (for the range 200–300°K), $E = 2{\cdot}4$ kcal mole^{-1}, $B_0 = 1{\cdot}3 \times 10^3$ cm min^{-1}. The decrease in the activity above room temperature was reversible and was also observed for the para-hydrogen conversion. It cannot therefore be attributed to contamination in the usual sense.

4. DISCUSSION

The velocity constant k_0 can be converted into an absolute rate in molecules cm^{-2} sec^{-1} given by $k_m = k_0 p/60\,kT$. Values of k_m obtained in this work, calculated for $p = 1$ mm Hg and $T = 293$°K, are given in Table 2. Results obtained by other workers and values of the activation energy are included for comparison.

Table 2. Activity of nickel in hydrogen–deuterium exchange

	k_m (molecules cm^{-2} sec^{-1})	E (kcal mole^{-1})
This work (solid nickel)	$8{\cdot}8 \times 10^{16}$	—
(evaporated film)	$9{\cdot}5 \times 10^{15}$	2·4
HULATT[16] (wire)	$8{\cdot}4 \times 10^{17}$	2·6
SCHUIT *et al.*[17] (supported on $SiO)_2$	$1{\cdot}6 \times 10^{11}$	3·0

HULATT's result was for the para-hydrogen conversion. However, besides this work, other studies[18, 19] have shown that nickel has the same activity in both conversion and exchange so the result is comparable. The velocity constant for the solid sample falls between values for the wire and the evaporated film. The activation energy appears to be the same for all types of catalyst so that the difference in the activity is due to a changing pre-exponential factor. Similar variations in activity with type of catalyst preparation have been observed by other workers.[20] It has been suggested that this difference may simply be due to changes in the relative abundance of the crystal planes exposed at the surface.[15] This could be subjected to test in the present apparatus.

One difference observed between the experiments on the solid sample and those on the evaporated film was the rate of contamination. For the film, the high activity was maintained for several days without decay. The solid sample was maintained in an apparently better vacuum and yet the activity began to decay in only half an hour. If it is assumed that the film was almost completely contaminated when it was deposited, then one must assume that the true area of the film was greater than the geometrical area by a factor of at least 100 and even so it should have exhibited some decay over the period of time involved. An alternative explanation is that some contaminant was present in the present high vacuum system which was not present in the earlier system. The O_2 concentration is extremely small in a high vacuum system due to its rapid adsorption and conversion into CO by hot filaments.[23] In the present work no mass 32 was ever found in the omegatron, indicating a partial pressure below 5×10^{-11} mm Hg. The main constituent of the residual ambient was mass 28. Nitrogen does not adsorb on nickel under these conditions[11, 12] so unless the contamination is coming from the interior of the crystal it should be CO. The absence of hot filaments in the system containing the evaporated film together with the gettering action provided by the evaporating film could make the CO concentration much smaller there.

It was noted that an activity corresponding to approximately 50 per cent of the clean surface value appeared under a variety of conditions.

(a) 50 per cent activity appeared after only 100 min of ion bombardment. Nearly 200 min were required to obtain the clean surface value.

(b) When the full activity had been obtained, a second run conducted without cleaning the surface often gave 50 per cent activity.

(c) As shown in Fig. 7, when the surface was bombarded with 100 V ions, 50 per cent was the

maximum activity that could be obtained on increasing the current density.

This suggests that the surface could be divided energetically into at least two parts. That half having the most strongly bound contaminant (probably NiO) was difficult to clean initially even with 500 V ions. When recontaminated (probably CO) it could be cleaned by 150 V ions but not by 100 V ions.

No recent results of the pressure dependence of exchange on nickel are available to compare with the present work. It is of interest because it has been used to decide between the two proposed mechanisms for para-hydrogen conversion and hydrogen deuterium exchange. These are the exchange mechanism (BONHOEFFER–FARKAS[22]),

$$H_2+D_2+M \rightleftharpoons MH+MD \rightleftharpoons HD+M \qquad (1)$$

and the interchange mechanism (ELEY–RIDEAL[13])

$$D_2+MH \rightleftharpoons MH(D_2) \rightleftharpoons MD+HD \qquad (2)$$

where M represents a metal atom. Calculations of the kinetics of the para-hydrogen conversion[24] lead one to expect a zero order reaction for mechanism (1) and a first order reaction for mechanism (2). Most of the experimental determinations for the para-hydrogen conversion show zero order or nearly zero order kinetics and this has been used as evidence in favor of mechanism (1). Fig. 4 shows that the results obtained here are definitely not zero order or even half order. As originally proposed, mechanism (2) involved reaction between an adsorbed atom and a molecule in a van der Waals layer, and such a layer would be expected to be very dilute at room temperature and 1 mm pressure. Recent experiments on nickel[24, 25] have indicated a molecular adsorption of hydrogen when the surface is nearly completely covered by hydrogen atoms. Clearly this removes the above objection to mechanism (2) but it also blurs the distinction between the two mechanisms.

5. CONCLUSION

It may be concluded that reliable activity measurements can be obtained using the apparatus described in this paper. The ground glass valve used in these experiments was satisfactory for reasonably fast reactions and so would be equally suitable for other transition metals which show the same activity.[15] Another ground glass valve tested later in the laboratory showed only $\frac{1}{3}$ of the conductance of the first one. If a reaction were being studied involving gases of higher molecular weight, diffusion through the valve could probably be neglected. Analysis with the omegatron is also equally applicable to other reactions. Since the activity found for nickel was high, the reactivity of single crystal faces only one cm^2 or less in area can be measured easily. Use of a smaller sample would also make it possible to study the temperature dependence.

It has been demonstrated that cleaning conditions similar to those used here were able to give an electron diffraction pattern characteristic of a clean nickel surface.[2] The final result obtained should therefore be characteristic of the clean surface. The equivalence of results from ion bombarded and annealed surfaces shows that defects are not important in exchange, unlike ethylene hydrogenation.[3, 4] This had previously been inferred from the characteristics of hydrogen adsorption and the magnitude of the rate.

REFERENCES

1. SCHLIER R. E. and FARNSWORTH H. E., *J. Phys. Chem. Solids* **6**, 271 (1958).
2. FARNSWORTH H. E., SCHLIER R. E., GEORGE T. H. and BURGER R. M., *J. Appl. Phys.* **29**, 1150 (1958).
3. FARNSWORTH H. E. and WOODCOCK R. F., *Advanc. Catalys.* **9**, 123 (1957).
4. TUUL J. and FARNSWORTH H. E., *J. Amer. Chem. Soc.*, in press.
5. SOMMER H., THOMAS H. S. and HIPPLE J. A., *Phys. Rev.* **82**, 697 (1951).
6. WOLSKY S. P., ZDANUK E., BIERIG R. and RUBIN L. G., 19*th Annual Conference on Physical Electronics*, p. 162. Massachusetts Institute of Technology (1959).
7. KORNELSEN E. V., 19*th Annual Conference on Physical Electronics*, p. 156. Massachusetts Institute of Technology (1959).
8. ALPERT D. and BURITZ R. S., *J. Appl. Phys.* **25**, 202 (1954).
9. LAFFERTY J. M., *J. Appl. Phys.* **22**, 299 (1951).
10. HICKMOTT T. W., *J. Chem. Phys.* **32**, 810 (1960).
11. TRAPNELL B. M. W., *Proc. Roy. Soc.* **A218**, 566 (1953).
12. MADDEN H. H. and FARNSWORTH H. E., *J. Chem. Phys.* **34**, 1186 (1961).
13. COUPER A. and ELEY D. D., *Disc. Faraday Soc.* **8**, 172 (1950).
14. BOLLAND J. L. and MELVILLE H. W., *Trans. Faraday Soc.* **33**, 1316 (1937).

15. ELEY D. D. and SHOOTER D., *Proc. Chem. Soc.* 315 (1959).
16. COUPER A., ELEY D. D., HULATT M. J. and ROSSINGTON D. R., *Bull. Soc. Chim. Belg.* **67,** 343 (1958).
17. SCHUIT G. C. A., DE BOER N. H., DORGELO G. J. H. and VAN REIJEN L. L., *Chemisorption* (edited by GARNER W. E.) p. 39. Butterworth, London (1957).
18. FAJANS E., *Z. Phys. Chem.* B**38,** 239, 252 (1935).
19. FARKAS A. and FARKAS L., *J. Amer. Chem. Soc.* **64,** 1594 (1942).
20. ELEY D. D. and ROSSINGTON D. R., *Chemisorption* (edited by GARNER W. E.) p. 137. Butterworths, London (1957).
21. TRAPNELL B. M. W., *Catalysis*, Vol. III, (edited by EMMETT P. H.). Reinhold, New York (1955).
22. BONHOEFFER K. F. and FARKAS A., *Z. Phys. Chem.* B**12,** 231 (1931).
23. SCHLIER R. E., *J. Appl. Phys.* **29,** 1162 (1958).
24. SACHTLER W. M. H. and DORGELO G. J. H., *Bull. Soc. Chim. Belg.* **67,** 465 (1958).
25. SACHTLER W. M. H. and DORGELO G. J. H., *Vierte Internationale Kongress Electronenmikroskopie, Berlin* (1958) Verh. **1,** 801 (1960).

Vol. 21
1961

J. Phys. Chem. Solids Pergamon Press 1961. Vol. 21, Nos. 3/4, pp. 228–233. Printed in Great Britain.

ON THE FEASIBILITY OF PHONON DIFFRACTION IN LIQUID HELIUM

E. T. KORNHAUSER*

H. H. Wills Physics Laboratory, University of Bristol

(*Received* 13 *October* 1960; *revised* 15 *June* 1961)

Abstract—The feasibility of diffracting the phonon radiation from a heat source in a liquid helium bath at about 0·3°K is examined, and a proposed experiment is described in some detail. The performance of ordinary optical diffraction gratings at the very short wavelengths involved is analyzed and found to be adequate for the purpose.

I. INTRODUCTION

THE NEED to investigate the various interactions of phonons of higher frequency than is obtainable by transduction of electromagnetic energy from conventional microwave sources[1–4] suggests the analysis by spectroscopic means of the thermal phonon radiation in solids and liquids. The primary requirement for such a phonon spectroscope is a medium of propagation in which the phonon mean free path is of the order of or larger than the size of the apparatus. Experiments on heat conductivity at low temperature indicate that such long mean free paths do exist in some dielectric crystals at liquid helium temperature[5–7] and in liquid helium itself at a few tenths of a degree.[8–11] Furthermore, these experiments demonstrate the occurrence of a high percentage of specular reflection at smooth surfaces.[7, 8, 10]

The use of conventional spectroscopic techniques in crystals presents some rather formidable difficulties due principally to the inherent anisotropy of the medium, and this approach will not be discussed here. A liquid helium bath, however, has the immediately obvious advantages that it is a liquid and is isotropic. Its relevant properties will be discussed in Section II.

If phonon spectroscopy does in fact prove feasible, it would be possible to use such a spectroscope in conjunction with a heat source as a monochromator to obtain phonon radiation in a given wavelength range in order to investigate in more detail their interaction with electrons, photons, other phonons, or crystal imperfections. Another exciting prospect would be the direct measurement of the excitation spectra of solids.

II. PHONON PROPAGATION IN LIQUID HELIUM II

At temperatures below about 0·6°K the roton spectrum of liquid helium is not excited and the thermal spectrum consists entirely of longitudinal phonons, whose mean free path increases rapidly with decreasing temperature. According to the theory of Landau and Khalatnikov the mean free path is given by $l = 4{\cdot}7 \times 10^{-4} T^{-9}$ cm.[8] The experimental values of l seem somewhat less[8,10,11] than that, but are generally agreed to be of the order of centimeters at about 0·3°K. One cause of a reduced value of l is the presence of ^{3}He impurities, which scatter strongly because of their large relative mass difference from ^{4}He.

It should be pointed out that the mean free path inferred from heat conduction experiments is with reference only to processes in which phonon momentum is not conserved. It may be that phonon–phonon scattering events which conserve momentum may be taking place more frequently, tending to establish a local thermal equilibrium, as has been suggested by WHITWORTH[8]. However, the fact that second sound propagation of heat pulses loses its character at these very low

* On leave from Brown University, Providence 12, Rhode Island, U.S.A.

temperatures[11] seems to imply that this is not so. In any case, if the proposed experiment can be successfully performed, the dependence of the measured spectra on source temperature should indicate to what extent the spectrum is being modified in its flow through the helium.

Thus the advantages of performing a diffraction experiment in a liquid helium bath, as opposed to a crystalline medium, may be summarized as follows: (1) the medium is isotropic, (2) only longitudinal phonons exist, (3) the medium is a liquid, permitting simple adjustment of apparatus, and (4) the grating may be an ordinary optical one ruled on metal or glass, or even a plastic replica. Arrayed against this are two principal disadvantages. First, lower temperatures are required than in crystals to obtain a sufficiently short mean free path, necessitating the use of adiabatic demagnetization. Second, the phonon velocity in helium II ($2{\cdot}4\times10^4$ cm/sec) is an order of magnitude smaller, giving a corresponding decrease in the already extremely short wavelengths. However, neither of these difficulties is insuperable.

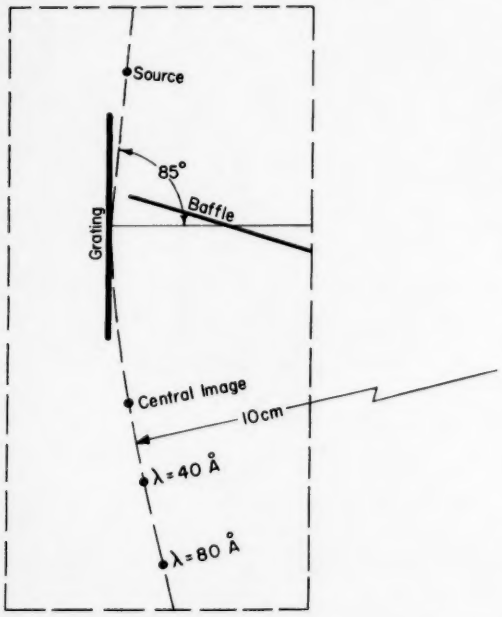

FIG. 1. Liquid helium phonon spectrometer.

III. DESIGN OF A SPECIFIC EXPERIMENT

It seems feasible, then, to perform a diffraction experiment in liquid helium at a temperature of about 0·3°K. Probably the simplest arrangement would be to use a concave grating of conventional optical spacing, with a large angle of incidence, as shown schematically in Fig. 1.

The grating has a spacing of 10^4 lines/cm and is curved to a radius of 20 cm. The angle of incidence is 85°, and the points on the Rowland circle (radius, 10 cm) corresponding to wavelengths of 40 Å and 80 Å in the first order have diffraction angles of 82·36° and 79·72° respectively, giving a total linear dispersion of the spectrum between 0 and 80 Å of 1·83 cm. The baffle serves to prevent the source radiation from falling directly on the receiving surface, while unwanted reflections from the walls are eliminated by pulsing the source with pulses of 50–100μ sec in length and using heat receivers whose time constant is considerably shorter than this. The walls of the container should be rough to diffuse the unwanted reflections as much as possible.

The source consists of a fine wire through which a pulse of current is sent to produce a slight increase in temperature. At these low temperatures, the phonon spectrum should be a simple black body curve, which at 0·3°K gives the spectra shown in Fig. 2 for the first three orders. The receivers can be separate resistance strips of aquadag painted on a paper strip spaced about one every millimeter and oriented parallel to the source wire. Since such heat receivers are incapable of discriminating wavelengths, the various orders of spectra will add, and the spectrum one would expect to observe from the receivers is as shown in Fig. 3. The sharp peak in the center is, of course, the geometrical image, which is surrounded on either side by a relatively low intensity region. At about one centimeter displacement, corresponding to about 40 Å wavelength in first order, the spectrum should rise rapidly, and by the time the first order reaches its peak around 80 Å, the second order becomes significant. When the power input to the source is increased, raising its temperature to a higher value, the spectrum should shift toward the central maximum, since more short wavelength energy is present.

The heat flow across a boundary into liquid helium has been measured by FAIRBANK and

Vol. 21
1961

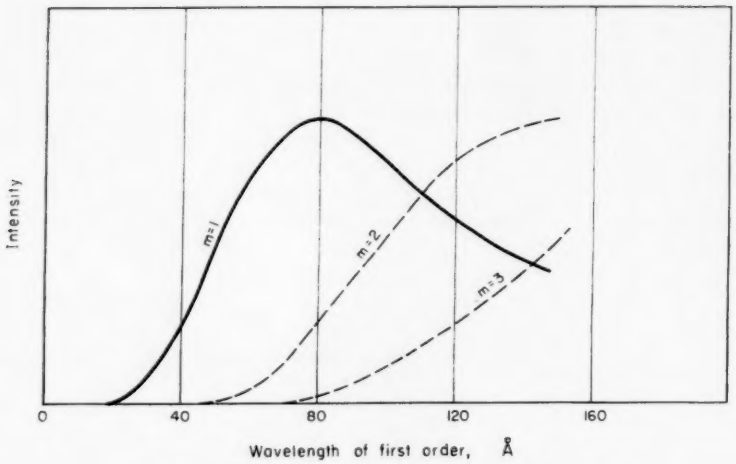

FIG. 2. First three orders of phonon spectra at 0·3°K.

WILKS[12] as $2{\cdot}22\times10^{-2}\,T^2$ W/cm²/deg. At 0·3°K this gives 2×10^{-3} W/cm²/deg. If the source wire has a diameter of about 2×10^{-2} cm and a length of about 1 cm, the surface area is 5×10^{-2} cm² and the heat flow is 10^{-4} W per degree of temperature difference. If the source were heated up about 1°K for a pulse time of 100μsec (corresponding to propagation over a distance of 2·4 cm), the total energy emitted during the pulse would be 10^{-1} erg. This may, in fact, prove too small an energy for the sensitivity of the receivers, although energies of this order of magnitude were used by KRAMERS *et al.*[11] in tube experiments and detected with carbon thermometers. Larger source temperatures may, of course, be used, but one would then expect the spectrum to shift farther toward the central maximum and the helium bath to be heated up more quickly. Alternatively, a larger diameter source may be used to avoid higher temperatures, since the receiving surface will have a graininess of about 1 mm.

As suggested in Fig. 1, the whole apparatus can

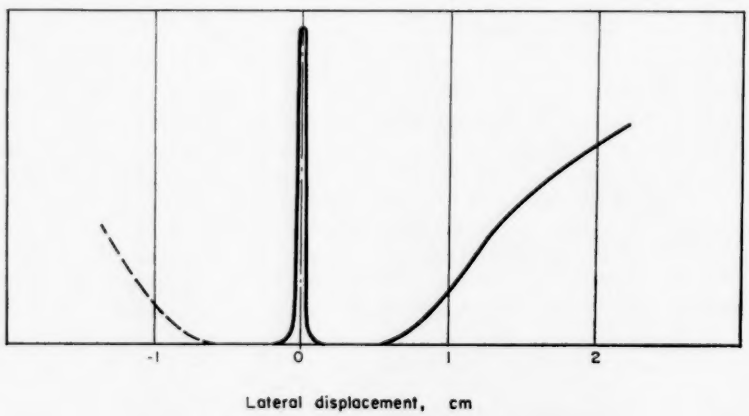

FIG. 3. Anticipated measured phonon spectrum.

Vol. 2
1961

be contained in a volume of about 50 cm^3, giving a mass of 7 g of helium. Since at 0·3°K the specific heat of He II is about $6{\cdot}4 \times 10^{-4}$ J/gm/deg[13], the total heat capacity of the helium bath (excluding the container and apparatus) is $4{\cdot}5 \times 10^4$ ergs/deg. This would mean that at least 10^4 pulses of the magnitude given above could be used before the bath would be heated up to a point where recooling would be required. Since this is many more pulses than required, considerable leeway exists for the use of higher energy pulses if required.

The remaining practical question is that of the grating itself. In high-resolution optical spectroscopy the criterion usually applied to gratings is that the tolerance in their surface conformation should not exceed a quarter wavelength. For the extremely short wavelengths involved in this experiment such tolerances are, of course, not possible, nor are they required, since resolving power is not the goal. The spectrum is a continuous one, and since the receivers will integrate the energy over a spacing of about 1 mm, resolution of a given wavelength component to a spread of this amount on the receiving surface would be adequate. Nevertheless, it is of interest to examine the behavior of gratings whose error may be hundreds or even thousands of wavelengths to see if the requisite behavior is obtained and if, in fact, a diffracted spectrum may be observed at all. This question is discussed in the Appendix, where it is shown that the necessary resolution should be easily obtainable.

Acknowledgements—The author is indebted to Professors F. C. Frank and M. H. L. Pryce for suggesting this problem and for many enlightening discussions and to the National Science Foundation for the award of a N.A.T.O. fellowship.

REFERENCES

1. Jacobsen E. H., *Phys. Rev. Letters* **2,** 249 (1959).
2. Bömmel H. E. and Dransfeld K., *Phys. Rev. Letters* **2,** 298 (1959).
3. Bömmel H. E. and Dransfeld K., *Phys. Rev. Letters* **3,** 83 (1959).
4. Bömmel H. E. and Dransfeld K., *Phys. Rev.* **117,** 1245 (1960).
5. Berman R., *Proc. Roy. Soc.* **A208,** 90 (1951).
6. Berman R., *Advanc. Phys.* **2,** 103 (1953).
7. Berman R., Foster E. L. and Ziman J. M., *Proc. Roy. Soc.* **A231,** 130 (1955).
8. Whitworth R. W., *Proc. Roy. Soc.* **A246,** 390 (1958).
9. Wilks J., *Rep. Progr. Phys.* **20,** 38 (1937).
10. Osborne D. V., *Phil. Mag.* **1,** 301 (1956).
11. Kramers H. C., van Peski-Tinbergen T., Wiebs J., van der Burg F. A. W. and Gorter C. J., *Physica* **20,** 743 (1954).
12. Fairbank H. A. and Wilks J., *Proc. Roy. Soc.* **A231,** 545 (1955).
13. Kramers H. C., Wasscher J. D. and Gorter C. J., *Physica* **18,** 329 (1952).
14. Cornu A., *C.R. Acad. Sci. Paris* **116,** 1215 (1893).
15. Sparrow C. M., *Astrophys. J.* **49,** 65 (1919).
16. Kornhauser E. T., *Quart. Appl. Math.* **19,** 153 (1961).
17. Michelson A. A., *Astrophys. J.* **18,** 278 (1903).

APPENDIX

Behavior of Highly Imperfect Gratings

The analysis of the effect of various types of imperfections in diffraction gratings by the method of the Cornu vector curve[14] has been given by Sparrow[15]. The application, however, was to calculate the decrease in the intensity of the maximum of a line spectrum for errors of spacing of the order of one wavelength. In the experiment described in Section III, the "plate" of the spectrograph consists of a coarse grating of thermometers which integrate the total energy falling on them. Thus the interesting questions are whether, for a given wavelength component, the spread given to the various orders by the aberrations of the system exceeds the graininess of the plate, and how the total energy contained within this spread-out line depends on the magnitude of the error.

The dominant term in the grating error is what Sparrow[15] calls the linear error of spacing. This term may, in fact, be due to curvature of the incident wavefront, improper curvature of the grating, a progressive error in the spacing of the grating, or improper focus of the diffracted wave. The analysis applies equally well to plane or concave gratings, although the physical cause of the error will be slightly different. In the notation of Sparrow the analytical expression for the Cornu vector curve including only this dominant error term is

$$\phi = c_0 s + \tfrac{1}{2}\beta s^2, \qquad (1)$$

where ϕ and s are the angle and arc length along the vector curve, β is a constant specifying the magnitude of the error, and c_0 is the curvature of the vector curve in the absence of error, given by

$$c_0 = (2\pi/\Delta s)\,[(a/\lambda)\sin\theta - m]. \qquad (2)$$

In equation (2), Δs is the amplitude of the wave from each line of the grating, a the grating spacing, λ the wavelength, θ the diffraction angle, and m the order of the spectrum. The total amplitude of the received

radiation in a given direction θ is

$$A = \int_{-N\Delta s}^{N\Delta s} e^{i\phi}\, ds, \tag{3}$$

where $2N$ is the total number of lines in the grating. A change of variable, $z = (\beta/2)^{1/2}\ (s+c_0/\beta)$, converts equation (3) into the form

$$\begin{aligned} A &= (2/\beta)^{1/2}\, e^{ix^2} \int_{x-\alpha}^{x+\alpha} e^{iz^2}\, dz \\ &= (2/\beta)^{1/2}\, e^{ix^2} \{[C(x-\alpha)-C(x+\alpha)] \\ &\qquad +i[S(x-\alpha)-S(x+\alpha)]\}, \end{aligned} \tag{4}$$

where $x = c_0/(2\beta)^{1/2}$, $\alpha = (\beta/2)^{1/2}\ N\Delta s$, and C and S are Fresnel integrals defined by $C(x) = \int_x^\infty \cos u^2\, du$, $S(x) = \int_x^\infty \sin u^2\, du$. The intensity I is given by $|A|^2$, and so has the value

$$\begin{aligned} I = (2/\beta)\, \{&[C(x+\alpha)-C(x-\alpha)]^2 \\ &+[S(x+\alpha)-S(x-\alpha)]^2\}. \end{aligned} \tag{5}$$

To find the total energy at the wavelength λ incident on the plate in a given spectral order m, one should integrate I over θ from $\theta_m-\epsilon$ to $\theta_m+\epsilon$, where θ_m is the angle of the unperturbed maximum of the m'th order, i.e. $\sin\theta_m = m\lambda/a$, and ϵ is large enough to encompass all significant energy in the line. If N is very large, then ϵ is relatively small, and the integral over θ is equivalent to an integral over c_0 from $-\infty$ to ∞. The total power

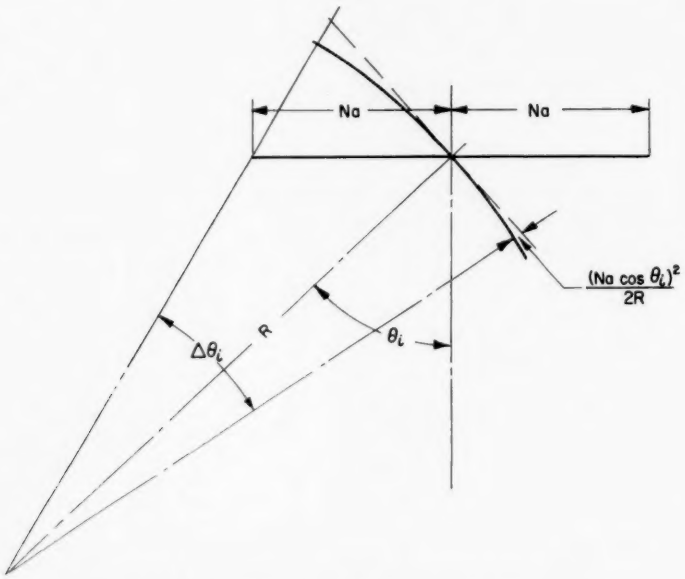

FIG. 4. Phase error produced by curvature of wavefront.

then in the m'th spectral line is

$$\begin{aligned} P = \int_{\theta_m-\epsilon}^{\theta_m+\epsilon} I\, d\theta &= (\lambda\Delta s/2\pi a\cos\theta_m)\int_{-\infty}^{\infty} I\, dc_0 \\ &= (2/\beta)^{1/2}(\lambda\Delta s/\pi a\cos\theta_m)\int_{-\infty}^{\infty} \{[C(x+\alpha)-C(x-\alpha)]^2 \\ &\qquad +[S(x+\alpha)-S(x-\alpha)]^2\}\, dx. \end{aligned} \tag{6}$$

The integral in equation (6) is evaluated elsewhere,[16] where it is shown to have the value $2\pi\alpha$, so that

$$P = 2\lambda N(\Delta s)^2/a\cos\theta_m, \tag{7}$$

about which the most significant point is that it is independent of β. Thus the total energy scattered into a given spectral order is independent of the magnitude of the error term, but as β increases it is spread out over

Vol. 2
1961

a broader area. The amount by which it is broadened can be estimated from the way in which the intensity curve in equation (5) approaches the unperturbed distribution, $2\sin(c_0N\Delta s)/c_0$, as β gets smaller.

So long as $c_0 \gg (2\beta)^{1/2}$, one may use in equation (5) the asymptotic form of the Fresnal integrals for large argument, so that equation (5) becomes

$$I \doteqdot (4/c_0^2)\,[1-(\beta N\Delta s/c_0)^2]^{-2}[\sin^2(c_0N\Delta s) + (\beta N\Delta s/c_0)^2\cos^2(c_0N\Delta s)]. \quad (8)$$

Thus the curve begins to approximate well the unperturbed one for $|c_0| > \beta N\Delta s$, which corresponds to an angular spread of the diffracted wave of

$$\Delta\theta_m = (\lambda\Delta s/2\pi a\cos\theta_m)\Delta c_0 = \lambda\beta N(\Delta s)^2/\pi a\cos\theta_m. \quad (9)$$

For angles outside this range the amount of energy is certainly negligible, since in the unperturbed curve more than 90 per cent of the energy lies within the central peak, which is extremely narrow for large N.

Now, as shown in Fig. 4, an angular spread $\Delta\theta_i$ of a wave incident on a plane grating at angle θ_i, corresponding to a radius of curvature of the wavefront R, produces a maximum phase error of

$$\Delta\phi = \tfrac{1}{2}\beta(N\Delta s)^2 = (2\pi/\lambda)\,[(Na\cos\theta_i)^2/2R], \quad (10)$$

and hence

$$\Delta\theta_i = 2Na\cos\theta_i/R = \lambda\beta N(\Delta s)^2/\pi a\cos\theta_i. \quad (11)$$

Finally, then

$$\Delta\theta_m = (\cos\theta_i/\cos\theta_m)\Delta\theta_i, \quad (12)$$

which indicates that when the angle of the diffracted spectrum differs by only a small amount from that of the specular reflection, the angular spread of the diffracted line is comparable to that of the central image. Hence the practical criterion to be applied is that if the optical system is good enough to focus the central image sufficiently sharply, the lower order spectra will also have adequate resolution.

The analytical method used in the preceding paragraphs of replacing the vector polygon by a continuous curve is valid when the radius of curvature of that curve is large compared to Δs, or $c_0\,\Delta s \ll 1$. From equation (2) this means that the limit of angular spread over which it may be applied is

$$\Delta\theta \ll \lambda/\pi a\cos\theta_m = [N/\beta(N\Delta s)^2]\Delta\theta_m = (N/2\Delta\phi)\Delta\theta_m. \quad (13)$$

Thus if it is to be used in the entire range over which the spectral line is spread out, one must have $\Delta\phi \ll N$, which is to say that the total phase error at the ends of the grating should be considerably smaller than the number of lines in the grating. In a grating of 10^4 lines/cm this should not be a difficult criterion to meet. Also, only the dominant term in the expansion of the phase error has been included, it having been assumed that the higher order terms will contribute less to the spread of the diffracted spectrum. There is, however, one other type of imperfection whose effect can be rigorously found analytically, the discontinuous jump in phase,[17] which leads to a cusp in the vector curve. The result of such analysis leads to the same conclusions which were drawn for the progressive error.

Finally, it was implied in Section III that a grating bent to cylindrical form could be used instead of a spherically concave grating. Since reflection in the direction parallel to the rulings of the grating is specular in nature, this is true provided the geometrical focusing is still sufficiently sharp over the length of the receivers and provided one is willing to accept the decrease in intensity caused by the complete absence of focusing in this direction. If a cylindrical surface is used, it would be advisable to make the source wire shorter than the length of the rulings of the grating and the receivers longer, so as to intercept as much of the emitted energy as possible.

J. Phys. Chem. Solids Pergamon Press 1961. Vol. 21, Nos. 3/4, pp. 234–251. Printed in Great Britain.

ETUDE DE NIOBATES ET TANTALATES DE METAUX DE TRANSITION BIVALENTS

E. F. BERTAUT, L. CORLISS* et F. FORRAT

Centre d'Etudes Nucléaires de Grenoble

et

R. ALEONARD et R. PAUTHENET

Laboratoire d'Electrostatique et de Physique du Métal, Grenoble

(*Received* 10 *April* 1961)

Résumé—La structure de $A_2M_4O_9$ (A = Nb, Ta ; M = Mn, Fe, Co, Mg) a été étudiée aux rayons X. Elle dérive de la structure du corindon $Al_2O_3-\alpha$ par un ordre des cations A et M. Le groupe d'espace le plus probable est $P\bar{3}c1$. Les mesures magnétiques et la diffraction neutronique montrent la nature antiferromagnétique de $Nb_2Mn_4O_9$ et de $Nb_2Co_4O_9$. Les spins forment des chaînes selon les droites $\frac{1}{3}\,\frac{2}{3}\,z$ (spins +) et $\frac{2}{3}\,\frac{1}{3}\,z$ (spins −).

Abstract—The structure of $A_2M_4O_9$ (A = Nb, Ta ; M = Mn, Fe, Co, Mg) has been studied by X-rays. It derives from the corundum type structure ($\alpha-Al_2O_3$) by an ordering of the cations A and M. The most probable space group is $P\bar{3}c1$. Magnetic measurements and neutron diffraction show up the antiferromagnetic nature of $Nb_2Mn_4O_9$ and $Nb_2Co_4O_9$. The spins form chains along the lines $\frac{1}{3}\,\frac{2}{3}\,z$ (+spins) and $\frac{2}{3}\,\frac{1}{3}\,z$ (−spins).

Vol. 2
1961

INTRODUCTION

Les combinaisons du type niobate et tantalate[1] A_2MO_6 où A = Nb, Ta ; M = métal de transition bivalent et Mg sont bien connues. Nous les complétons par l'étude des composés $A_2M_4O_9$ où M = Mn, Fe, Co, Ni, Mg.†

Le présent travail rentre dans le cadre d'un programme d'études plus général, celui de la "substitution isomorphe", c'est-à-dire de la substitution des ions présents dans une structure ionique connue par d'autres ions, de rayons comparables et de valences en général différentes, tout en conservant le type de structure. Citons comme exemple la substitution

$$Ca^{2+}+Si^{4+}\rightarrow T^{3+}+Fe^{3+}\ (T = \text{terre rare})$$

qui a abouti à la découverte des grenats ferrimagnétiques.[2] Dans le cas actuel, la substitution

$$A^{5+}+2M^{2+}\rightarrow 3\ Fe^{3+}\text{ ou }Al^{3+}$$

relie directement les structures $A_2M_4O_9$ au type corindon Al_2O_3 et à l'hématite Fe_2O_3 comme nous allons le montrer dans l'étude cristallographique de la première partie.

En dehors de l'intérêt purement cristallographique de la structure et des paramètres qui la définissent, on peut se demander comment la configuration des spins varie dans les composés dérivant du type corindon tels que Cr_2O_3 ; $Fe_2O_3-\alpha$; les ilménites $TiMO_3$ et enfin les niobates (et tantalates) $A_2M_4O_9$. C'est pourquoi nous avons entrepris au Centre d'Etudes Nucléaires de Grenoble, une étude par diffraction neutronique des composés $Nb_2Mn_4O_9$ et $Nb_2Co_4O_9$. Cette étude fait l'objet de la deuxième partie.

La troisième partie est consacrée aux mesures magnétiques et à leur discussion. Les mesures de

* Adresse actuelle : Brookhaven National Laboratories Upton, Long Island, N.Y. (USA).

† Nous n'avons pas encore réussi à préparer les composés avec M = Cu.

susceptibilité en fonction de la température permettent de déterminer des températures antiferromagnétique et de Curie–Néel, ainsi que des valeurs des moments magnétiques et de certaines intégrales d'échange. L'interprétation de la structure magnétique, trouvée par diffraction neutronique s'en trouve grandement facilitée.

Dans une quatrième partie, nous examinons, par un calcul matriciel toutes les structures magnétiques qui conservent la maille cristallographique et nous établissons les critères de stabilité de la structure observée.

Enfin, nous résumons dans les conclusions, les principaux résultats obtenus.

PREMIERE PARTIE

Préparation

Les niobates et tantalates ont été préparés à partir du mélange des oxydes constituants dans des conditions de température et d'atmosphère variant selon l'ion M comme il suit :

Mn (1.250°C sous H_2) ; Mg (1.400°C à l'air) ; Ni et Co (1.300°C à l'air) Fe (1.200°C sous argon). Après un chauffage de 10 heures, les produits sont homogénéisés par broyage et finalement recuits dans les mêmes conditions.

Etude cristallographique aux rayons X

La méthode des poudres a été employée en

Tableau 1. *Comparaison d'un diffractogramme de* $Nb_2Co_4O_9$ *et de* $Fe_2O_3-\alpha$ *sous radiation* $K\alpha$ *du cobalt*

Indice *h k l*	$Nb_2Co_4O_9$		$Fe_2O_3-\alpha$	
	d	I_{obs}	*d*	I_{obs}
0 0 2	7,07	1	—	—
1 0 0	4,48	17	—	—
1 0 2	3,78	23	3,68	18
0 0 4	3,54	4	—	—
1 0 4	2,77	100	2,69	100
1 1 0	2,58	57	2,51	75
0 0 6	2,36	5	—	—
1 1 3	2,27	20	2,20	18
2 0 0	2,24	3	—	—
2 0 2	2,13	2	—	—
1 0 6, 1 1 4	2,09	5	—	—
2 0 4	1,891	28	1,84	63
0 0 8	1,768	5	—	—
1 1 6	1,741	43	1,69	63
2 1 0	1,692	3	—	—
1 0 8, 2 1 2	1,645	15	1,60	13
2 0 6	1,623	1	—	—
2 1 4	1,526	38	1,485	50
3 0 0	1,492	28	1,452	50
3 0 2, 1 1 8	1,459	4	—	—
2 0 8	1,387	7	1,351	3
3 0 4, 2 1 6	1,374	3	—	—
1, 0, 10	1,348	13	1,308	18
2 2 0	1,292	7	1,259	13
3 0 6	1,261	3	1,230	3
1, 1, 10 ; 3, 1, 0	1,241	2	—	—
3, 1, 2 ; 2, 1, 8	1,222	19	1,190	8
2, 0, 10	1,195	15	1,195	5
3 1 4	1,171	17	1,140	13
3 0 8	1,140	2	—	—
2 2 6	1,133	15	1,104	10
2, 1, 11	1,085	21	1,056	8

utilisant, soit une chambre Debye–Scherrer et la radiation filtrée Kα du fer, soit un diffractographe enregistreur et la radiation Kα_1 du cobalt, monochromatisée par la technique de Guinier.

L'analogie des diagrammes avec ceux de $Fe_2O_3-\alpha$ est frappante comme le montre le Tableau 1. Nous y avons représenté les données de diffraction (indices $h\ k\ l$, distances réticulaires d et intensités observées) de $Nb_2Co_4O_9$ et à titre de comparaison celles de $Fe_2O_3-\alpha$ en notation hexagonale. Toutes les positions de raies fortes et moyennes dont les indices obéissent à la règle $-h+k+l=3n$ coïncident pratiquement.

charges élevées se trouvent aussi loin que possible les uns des autres. Remarquons cependant que la structure de $Al_2O_3-\alpha$ (et de $Fe_2O_3-\alpha$) élucidée par PAULING et HENDRICKS[3] constitue une exception à une des règles de Pauling. En effet, dans le type corindon, les octaèdres d'oxygène de coordination sont groupés par paires *ayant une face en commun.*

La surstructure la plus simple que l'on puisse concevoir placerait une seule sorte d'ions A^{5+} ou M^{2+} sur chacun des trois sous-réseaux rhomboédriques du corindon qui correspondent aux translations 0 0 0 ; $\frac{2}{3}\ \frac{1}{3}\ \frac{1}{3}$; $\frac{1}{3}\ \frac{2}{3}\ \frac{2}{3}$. Dans le groupe

Tableau 2. Paramètres cristallins

Formule	Systeme	Maille (Å)		DX (g/cm³)
		a	c	
$Nb_2Co_4O_9$	Hexagonal	5,177	14,168	5,72
$Nb_2Fe_4O_9$	,,	5,233	14,236	5,44
$Nb_2Mn_4O_9$	,,	5,335	14,320	5,19
$Nb_2Mg_4O_9$	,,	5,171	14,173	4,32
$Ta_2Co_4O_9$	,,	5,181	14,174	7,47
$Ta_2Mn_4O_9$	,,	5,337	14,333	6,81
$Ta_2Mg_4O_9$	,,	5,170	14,143	6,12
$Nb_2Ni_4O_9$	Orthorhombique	$a=10,144$ $b=17,468$	$c=14,318$	

Le Tableau 2 résume les paramètres en Å et les densités en g/cm³ des mailles hexagonales. Nous y avons également inclus les paramètres de $Nb_2Ni_4O_9$, composé orthorhombique, dont nous nous réservons l'étude.

De nombreuses raies de surstructure indiquent clairement que les ions A^{5+} et M^{2+} s'ordonnent, abaissant la symétrie rhomboédrique à celle hexagonale. Les règles d'extinction $h\ k\ i\ l$ existe à tous les ordres, $h\ o\ \bar{h}\ l$ n'existe qu'avec $l=2n$, ainsi que l'absence de tout effet piézoélectrique que nous avons cherché selon la méthode de GIEBE et SCHEIBE font apparaître le groupe d'espace $P\ \bar{3}\ c\ 1$ comme étant le plus probable.

Selon les règles de Pauling, basées sur des raisonnements d'énergie électrostatique, il semble naturel de constuire un modèle où les ions A^{5+} de $P\ \bar{3}\ c\ 1$ on a sa disposition un site (4*c*) : $\pm 00z$; $00, \frac{1}{2}+z$) et deux sites (4*d*) $\pm$ ($\frac{1}{3}, \frac{2}{3}, z$; $\frac{1}{3}, \frac{2}{3}, \frac{1}{2}+z$) pour placer les cations tandis que le paquetage compact des atomes d'oxygène peut être réalisé dans les positions

(12g) $\pm$ ($x\ y\ z$; $\bar{y}, x-y, z$; $y-x, \bar{x}, z$; $\bar{y}, \bar{x}, \frac{1}{2}+z$; $x, x-y, \frac{1}{2}+z$; $y-x, y, \frac{1}{2}+z$) et
(6*f*) $\pm$ ($x, 0, \frac{1}{4}$; $0, x, \frac{1}{4}$; $\bar{x}, \bar{x}, \frac{1}{4}$)

Selon notre première hypothèse, les ions A^{5+} seraient les plus éloignés les uns des autres dans une position (4d) tandis que dans une position (4c), deuxième hypothèse à envisager, ils seraient couplés par paires dont les octaèdres d'oxygène de coordination auraient une face en commun. *Fait inattendu, c'est la deuxième hypothèse qui se trouve réalisée.* Ceci est clairement démontré par

Tableau 3. *Correspondance entre les positions atomiques dans* $Fe_2O_3-\alpha$ *et dans* $Nb_2Co_4O_9$

$Fe_2O_3-\alpha$ Description hexagonale	Translations rhomboédriques	$Nb_2Co_4O_9$
$R\bar{3}c1$		$P\bar{3}c1$
Fe en [12(*c*)] $\pm$ (00z ; 00 $\frac{1}{2}+z$)+	0 0 0 $\frac{2}{3}$ $\frac{1}{3}$ $\frac{1}{3}$ $\frac{1}{3}$ $\frac{2}{3}$ $\frac{2}{3}$	Nb en [4(*c*)] $\pm$ (00z ; 00$\frac{1}{2}+z$) Co_I en [4(*d*)] $\pm$ ($\frac{1}{3}$ $\frac{2}{3}$ z ; $\frac{1}{3}$ $\frac{2}{3}$ $\frac{1}{2}+z$) Co_{II} en [4(*d*)]
O en [18(*e*)] $\pm$ (xO $\frac{1}{4}$; Ox $\frac{1}{4}$; $\bar{x}\bar{x}\frac{1}{4}$)	0 0 0 $\frac{2}{3}$ $\frac{1}{3}$ $\frac{1}{3}$ $\frac{1}{3}$ $\frac{2}{3}$ $\frac{2}{3}$	O_I en (6*f*) $\pm$ (xO $\frac{1}{4}$; Ox $\frac{1}{4}$; $\bar{x}\bar{x}$ $\frac{1}{4}$) O_{II} en (12*g*) position générale

La description hexagonale de $Fe_2O_3-\alpha$, conformément aux *Tables Internationales*[4] est rapportée au centre de symétrie à l'origine ($z = 0{,}105+0{,}250 = 0{,}355$; $x = 0{,}292$). Elle diffère de la description de PAULING[3] par une translation de $\frac{1}{4}$ selon Oz.

la mesure de l'intensité de la raie (100) qui dans la première hypothèse est observée quatre fois trop forte, alors que l'accord avec la deuxième hypothèse est bon.

La correspondance entre les positions atomiques dans $Fe_2O_3-\alpha$ et $Nb_2Mn_4O_9$ est illustrée par le Tableau 3. Remarquons que dans la description de PAULING, les centres de symétrie sont en $\pm$ (00z) avec $z = \pm\frac{1}{4}$ tandis que dans notre description, en conformité avec les *Nouvelles Tables Internationales*,[4] les centres de symétrie se trouvent à l'origine et en (00$\frac{1}{2}$).

Alors que les rayons X permettent de fixer les positions des atomes avec une assez bonne précision, nous remettons la détermination des paramètres d'oxygène et la description de la structure au chapitre suivant, car la section efficace relativement élevée de l'oxygène en diffraction neutronique permet d'obtenir une précision meilleure qu'aux rayons X.

DEUXIEME PARTIE

Etude de $Nb_2Co_4O_9$ *et* $Nb_2Mn_4O_9$ *par diffraction neutronique*

Des diagrammes de diffraction ont été réalisés à la température ordinaire et à celles de l'azote et de l'hélium liquide au diffractomètre à neutrons du Centre d'Etudes Nucléaires de Grenoble. Un système à moniteur automatisé assure une indépendance complète des fluctuations de la pile et une bonne reproductibilité des mesures d'intensité. Les intensités de diffraction sont enregistrées "point par point" avec des intervalles angulaires de $\Delta\,\Theta = 3'$. Un monocristal de cuivre produit un faisceau monocinétique de longueur d'onde $\lambda = 1.198$ Å. La composante $\lambda/2$ est de 2,5 pour cent. On en corrige les intensités observées de la manière habituelle.

Etude à température ordinaire

La Fig. 1 représente les enregistrements à température ordinaire. Les raies dues au porte-échantillon en aluminium sont marquées Al. A cause de nombreuses superpositions de raies, la méthode des moindres carrés a été appliquée, non pas aux facteurs de structure, mais aux intensités.

Comme valeurs de départ des paramètres de positions, on a utilisé les valeurs de z des atomes lourds, connus approximativement par l'étude aux rayons X et les paramètres des atomes d'oxygène dans $Fe_2O_3-\alpha$. légèrement corrigés par des considérations stériques. Les intensités ont été calculées comme

$$I_c = pF^2/(\sin\Theta \sin 2\Theta)$$

où F est le facteur de structure ordinaire, p la multiplicité des plans de réflexion. Dans le calcul d'intensité, on doit tenir compte du fait qu'à toute raie "rhomboédrique" $h\,k\,i\,l$ se trouve superposée une raie de structure $k\,h\,i\,l$ pour $l \neq 3n$. [Exemple :

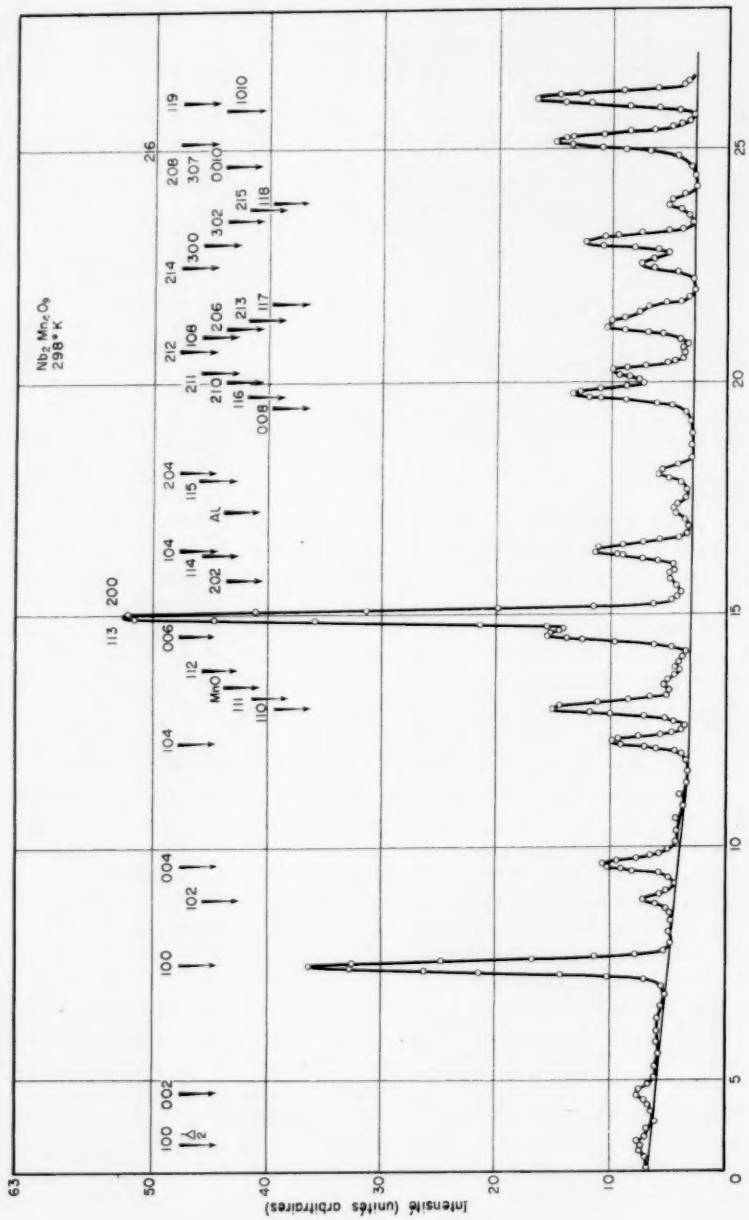

FIG. 1(a). Diagramme à température ordinaire de $Nb_2Mn_4O_9$.

Vol. 2
196

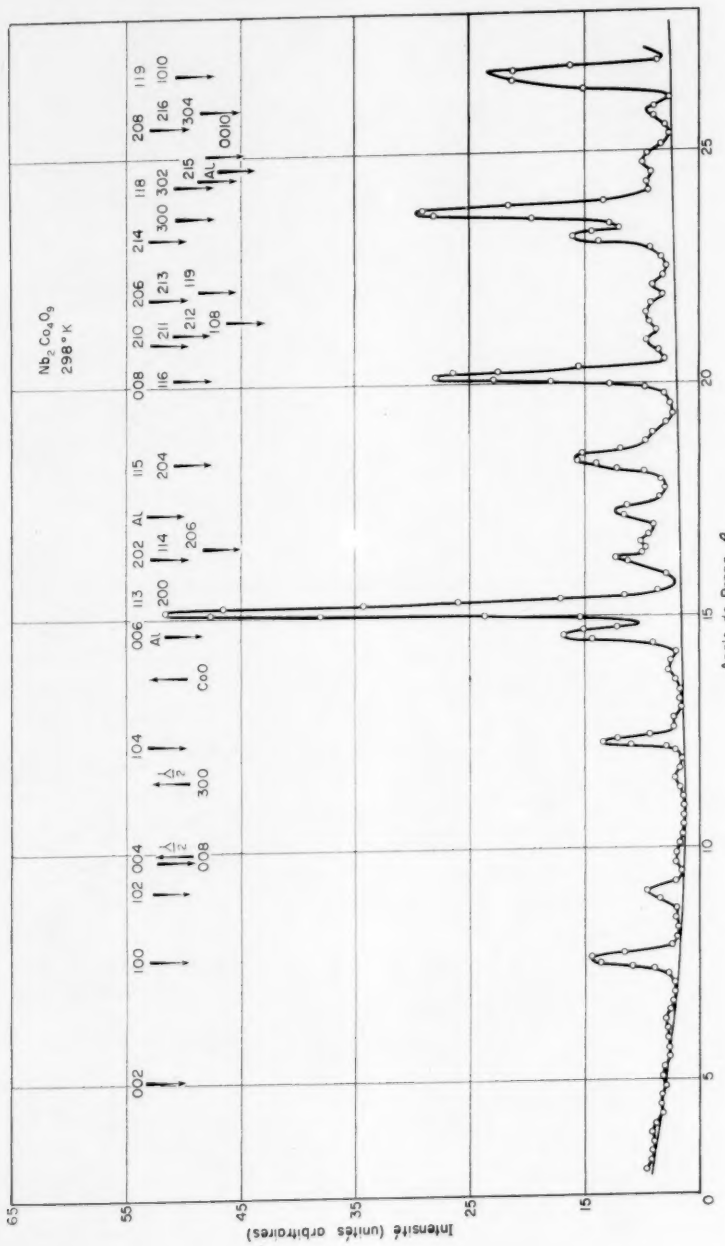

FIG. 1(b). Diagramme à température ordinaire de $Nb_2Co_4O_9$.

Tableau 4. *Paramètres de position, groupe* $P\,\bar{3}\,c\,1$

		$Nb_2Mn_4O_9$	$Nb_2Co_4O_9$
Nb	4*c*	$z = 0{,}3575$	$z = 0{,}360$
M_I	4*d*	$z = 0{,}0181$	$z = 0{,}027$
M_{II}	4*d*	$z = 0{,}297$	$z = 0{,}307$
O_I	6*f*	$x = 0{,}300$	$x = 0{,}305$
O_{II}	12*g*	$x = 0{,}334$	$x = 0{,}333$
		$y = 0{,}295$	$y = 0{,}295$
		$z = 0{,}0884$	$z = 0{,}0833$

Tableau 5. *Intensités observées et calculées (Température ordinaire)*

h k l	$Nb_2Mn_4O_9$		$Nb_2Co_4O_9$	
	I_c	I_0	I_c	I_0
002	20	21	0	2
100	472	443	127	128
102	16	26	49	40
004	93	106	6	10
104	102	88	101	131
110, 111	162	179	0	0
112	4	3	0	1
006, *113*, 200	877	875	738	751
202	38	35	34	32
114, 106	162	141		
204, 115	22	42	140	132
008, *116*	159	156	357	343
210, 211	114	127	104	104
212,	2	9		
108, *206*	162	185		
213, 117			27	43
214	59	68	31	23
300	159	143	453	426
302, *118*	26	36	39	32
215				
0010, *208*	198	201	47	43
304, *216*				
1010 *119*	248	223	284	299
	$R = 0{,}07$		$R = 0{,}065$	

Vol. 2
196

(0 1 2) raie "rhomboédrique" et (1 0 2) raie de surstructure sont superposées.]

Les longueurs de FERMI $\times 10^{12}$ suivantes ont été utilisées : $b(\mathrm{Mn}) = -0{,}37$; $b(\mathrm{Co}) = 0{,}25$; $b(\mathrm{Nb}) = 0{,}69$; $b(\mathrm{O}) = 0{,}58$.

Par deux itérations de la méthode de moindres carrés, nous avons déduit les sept paramètres de position de $Nb_2Mn_4O_9$ et $Nb_2Co_4O_9$ figurant dans le Tableau 4. L'accord entre intensités observées et calculées, résumées dans le Tableau 5 est satisfaisant, les facteurs

$$R = \sum|I_{obs} - I_{calc}| / \sum I_{calc}$$

étant voisins de 0,07 pour les deux composés. Des corrections de vibrations thermiques n'ont pas été appliquées.

des atomes de Nb est commun à deux octaèdres. La répulsion coulombienne déplace les atomes Nb vers les plus grands triangles, de sorte que Nb se trouve bien écarté du centre de l'octaèdre. La différence entre les deux distances $Nb–O_I$ = 2,23 Å et $Nb–O_{II}$ = 1,85 Å est exceptionnellement large (0,38 Å) comparée aux différences correspondantes dans $Al_2O_3-\alpha$ (0,145 Å) et dans $Fe_2O_3-\alpha$ (0,075 Å).[3] Les octaèdres autour des M ont un grand triangle en commun, fourni par les O_{II}. Alors que les distances $Mn_I–O_{II}$ (3 O_{II} à 2,27 Å, 3 O_{II} à 2,22 Å) oscillent peu autour de la valeur normale de 2,23 Å, les distances $Mn_{II}–O_{II}$ (2,35 Å) et $Mn_{II}–O_I$ (1,99 Å) sont bien différentes, la dernière étant anormalement courte. Il se peut que les atomes O_I ne soient pas tout à fait dans

Tableau 6. Distances interatomiques

	$Nb_2Co_4O_9$	$Nb_2Mn_4O_9$
Nb–Nb	3,12	3,08
M_I–M_I	3,09	3,12
M_I–M_{II}	3,12	3,17
Nb–O_I	2,21	2,22
Nb–O_{II}	1,82	1,85
M_{II}–O_I	1,98	1,99
M_{II}–O_{II}	2,25	2,35
M_I–O_{II}	2,26	2,27
M_I–O'_{II}	2,08	2,22
O_I–O_I	2,73	2,77
O_{II}–O_{II}	2,93	2,92
O_I–O_{II}	2,90	2,91

Description de la structure. La Fig. 2 répresente la structure des niobates et tantalates de formule $A_2M_4O_9$. La structure peut être décrite par des chaînes d'octaèdres selon c ne contenant qu'une sorte de cations; A selon $00z$, M selon $\frac{1}{3}\ \frac{2}{3}\ z$ et $\frac{2}{3}\ \frac{1}{3}\ z$. Sur trois octaèdres d'une chaîne, deux sont occupés par les cations. Le Tableau 6 résume les principales distances interatomiques dans $Nb_2Mn_4O_9$. On remarque la grande déformation des octaèdres d'oxygène autour des atomes de Nb (Fig. 3). Chaque octaèdre est formé par deux triangles équilatéraux dont le plan est perpendiculaire à l'axe ternaire. Les côtés des triangles sont respectivement 2,77 Å (O_I-O_I) et 2,92 Å (O_I-O_{II}). Le plus petit triangle qui écrante l'action répulsive le plan $z = \frac{1}{4}$ imposé par le choix du groupe $P\bar{3}c1$. Dans le groupe non centrosymétrique $P3c1$ le paramètre z est à nouveau libre. Mais comme alors le nombre de paramètres devient prohibitif, nous n'avons pas approfondi ce point pour l'instant, quitte à le reprendre plus tard.

Les différences entre les distances interatomiques dans les niobates de Co et de Mn (Tableau 6) s'expliquent principalement par la différence entre les rayons ioniques de ces cations.

Etude aux basses températures

$Nb_2Mn_4O_9$. Déjà, à la température de l'azote liquide, on observe une variation très notable des intensités, encore accentuée à celle de l'hélium

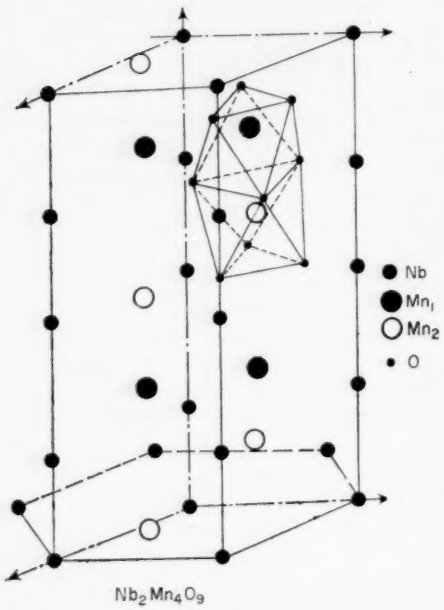

FIG. 2. Structure cristallographique des niobates et tantalates $A_2M_4O_9$ (A = Nb, Ta ; M = Mn, Fe, Co, Mg).

liquide. On remarque notamment sur la Fig. 4 que le rapport des intensités I (1 1 3)/I (1 0 0) est inversé. Comme le cryostat utilisé possède un porte-échantillon en laiton, deux diagrammes, l'un avec, l'autre sans la substance, ont été enregistrés. Ce dernier montre la présence de raies faibles dues au laiton et produites par la composante $\lambda/2$ de raies fortes du laiton. Elles sont repérées par les flèches ↑ sur la figure. Les intensités totales sont calculées à partir du diagramme différence des deux diagrammes précédents. La raie (1 1 3) étant une raie d'oxygène, sert d'étalon interne, compte tenu des composantes non résolues (mais considérablement plus faibles) de (2 0 0) et (1 1 2). En admettant que les paramètres atomiques soient aux basses températures les mêmes que ceux déterminés à l'ambiante, on remarque que les raies (0 0 2) n'ont pas de composante magnétique, tandis que la variation d'intensité est maximum pour la raie (1 0 0). On en déduit que la direction des spins est selon l'axe c.

Comme il n'y a pas apparation de raies nouvelles, nous pouvons conclure que l'ordre antiferromagnétique s'installant aux basses températures, conserve la maille cristallographique. Dans ces conditions, il est alors relativement simple d'énumérer les configurations différentes possibles dont le nombre maximum est égal au nombre de réseaux de Bravais occupés par des ions magnétiques, soit à huit dans le cas présent. La Fig. 5 illustre les huit configurations possibles. Le calcul permettant de les établir selon la méthode exposée par l'un de nous[5, 6] est donnée dans la quatrième partie.

Parmi les modèles possibles, c'est le mode 3 (Fig. 5) qui fournit le meilleur accord avec les intensités observées. La configuration magnétique est décrite par deux chaînes de spins, l'une, le long de la droite $\frac{1}{3}\ \frac{2}{3}\ z$ constitue le sous-réseau magnétique M_1, l'autre, le long de la droite $\frac{2}{3}\ \frac{1}{3}\ z$ antiparallèle à la précédente constitue le sous-réseau M_2. Le groupe magnétique de SHUBNIKOV est $P\bar{3}'c'1$. La Fig. 6 distingue les positions cristallographiques (Mn_I○ et Mn_{II}●) et montre en même temps la direction des spins.

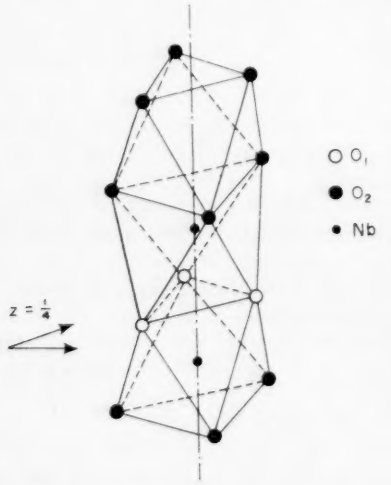

FIG. 3. Coordinations de Nb.

Le Tableau 7 résume les indices de $h\,k\,l$, les intensités nucléaires déjà calculées (cf. Tableau 5), les intensités magnétiques calculées dans l'hypothèse de spins $S = \frac{5}{2}$ alignés selon c et totalement saturés (3ème colonne) en utilisant le facteur de forme de Mn^{2+}[7], la somme I_{tot} des intensités calculées (4ème colonne) et enfin à titre de comparaison (5ème colonne) l'intensité observée corrigée de la contribution du cryostat. L'accord

Vol. 2
196

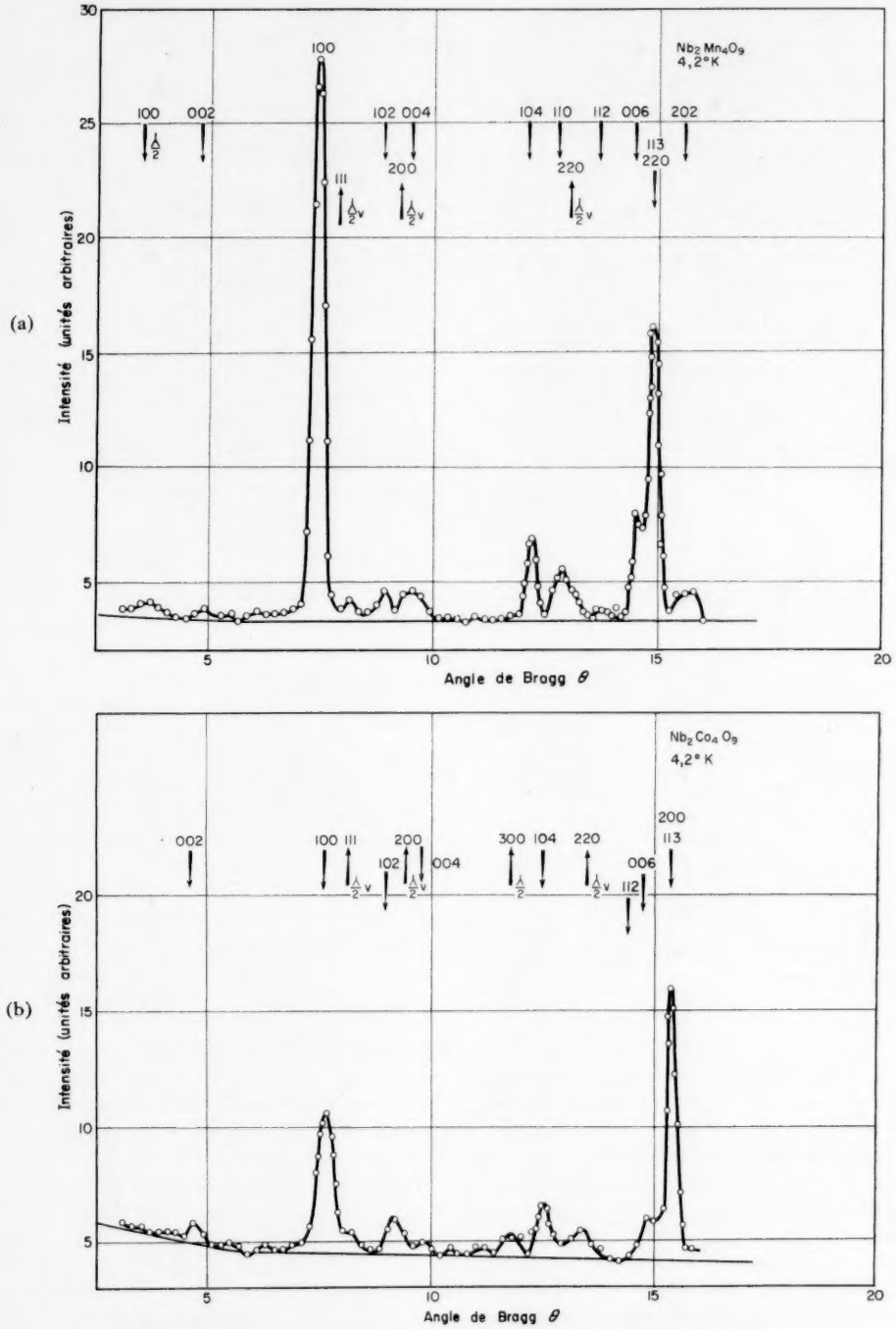

FIG. 4. Diagrammes à 4,2°K de $Nb_2Mn_4O_9$ (a) et de$Nb_2Co_4O_9$ (b).

Vol. 21
1961

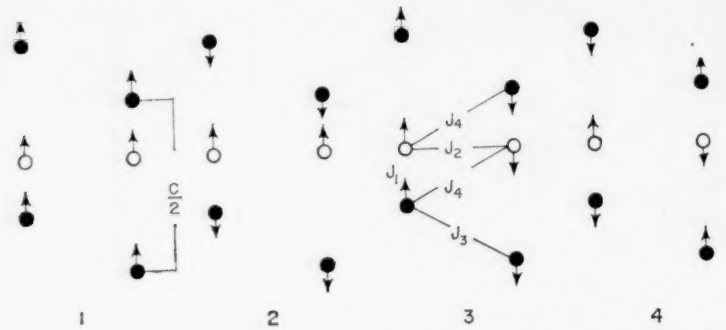

FIG. 5. Modèles magnétiques. Quatre autres motifs se déduisent de ceux dessinés en conservant le motif central (constitué par 4 atomes) et en renversant l'orientation des spins après une translation $c/2$.

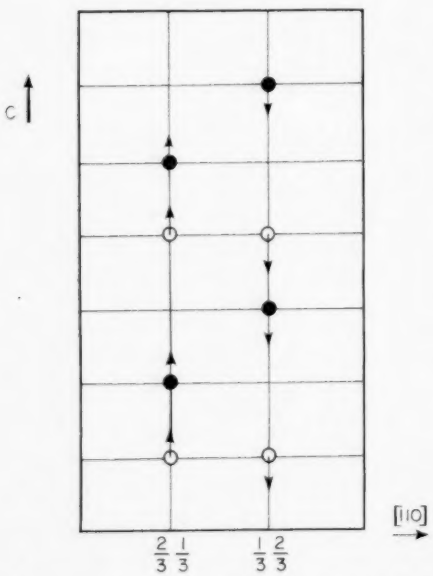

FIG. 6. Structure magnétique de $Nb_2Co_4O_9$ et $Nb_2Mn_4O_9$.

est jugé satisfaisant, compte tenu de la précision plus faible de nos mesures d'intensités aux basses températures.

Signe des interactions. Les voisins Mn^{2+} les plus proches ($d = 3{,}166$ Å) ayant leurs octaèdres de coordination accolés par une face, ont leurs spins parallèles, ce qui suggère la présence d'interactions directes positives. Cependant, les mesures magnétiques (3ème partie) montrent d'une manière convaincante que toutes les interactions aussi bien dans une chaîne, qu'entre les chaînes, sont négatives (cf. 4ème partie) en confirmation de la prédiction théorique de GOODENOUGH[8] selon laquelle les interactions directes $Mn^{2+} - Mn^{2+}$ sont négatives.

$Nb_2Co_4O_9$. Nous n'avons pas noté de variation sensible des intensités dans les diagrammes à la température ordinaire et à celle de l'azote liquide. A la température de l'hélium liquide, la contribution magnétique est nette et qualitativement analogue à celle dans $Nb_2Mn_4O_9$ quoique moins spectaculaire, comme le montre l'accroissement notable du rapport $I(100)/I(113)$.

Alors que l'existence d'un ordre antiferromagnétique est clairement révélée aux neutrons, il serait difficile d'inférer ce résultat sur la seule base de la mesure de susceptibilité magnétique. En effet, $1/\chi$ ne montre pas de minimum net comme dans $Nb_2Mn_4O_9$ (cf. Fig. 8).

Le seul modèle compatible avec les intensités observées (et corrigées comme plus haut) est le modèle 3 (Figs. 5 et 6). Pour ajuster les intensités magnétiques, on dispose de deux paramètres, la direction et la valeur des moments magnétiques, la contribution du moment orbital dans Co^{2+} étant en général non négligeable.

Comme les intensités des raies (004) et (006) n'ont pas varié, nous supposons les moments parallèles à l'axe c. On obtient alors un bon accord entre raies fortes (100) et moyennes (104) observées et calculées en prenant $S\sigma/\sigma_0 = \frac{3}{2}$. Ici σ/σ_0 est le rapport des saturations à 4,2 K° et au zéro absolu. Dans le calcul de l'intensité magnétique, on a

Tableau 7. Intensités aux basses températures (4,2°K)

$Nb_2Mn_4O_9$

h k l	I_{calc}			I_{obs}
	I_{nuc}	I_{mag}	I_{tot}	
0 0 2	20	0	20	17
1 0 0	472	1132	1604	1550
1 0 2	16	15	31	49
0 0 4	93	0	93	78
1 0 4	102	122	224	209
110, 111	162	0	162	178
006, 113, 200	877	137	1014	1014

$Nb_2Co_4O_9$

h k l	I_{calc}			I_{obs}
	I_{nuc}	I_{mag}	I_{tot}	
0 0 2	2	0	2	15
1 0 0	128	422	550	542
1 0 2	40	7	47	62
0 0 4	10	0	10	26
1 0 4	131	34	165	156
112, 006	862	51	913	913
113, 200				

Vol. 21
1961

encore utilisé le facteur de forme de Mn^{2+}[7]. Dans l'hypothèse d'une saturation pratiquement totale* ($\sigma/\sigma_0 \sim 1$), la valeur du moment correspondrait au spin seul de Co^{2+}, c'est-à-dire à un moment orbital complètement bloqué à 4,2°K.

Nous avons repris les calculs, tenant compte d'une contribution orbitale en supposant que $S\sigma/\sigma_0 = \frac{4}{2}$. Pour accorder les intensités observées et calculées de la raie (1 0 0), il est alors nécessaire de supposer les spins parallèles au plan (0 0 2). Mais alors, l'intensité calculée de la raie (1 0 4) est deux fois plus grande que celle observée, ce qui est certainement en dehors de l'erreur de mesure possible.

En résumé, les intensités des raies fortes (1 0 0) et moyennes (1 0 4) sont en acc d, avec une valeur de spin seul ($S = \frac{3}{2}$) les spins étant parallèles à l'axe *c*. Elles sont en désaccord avec une valeur $S = \frac{4}{2}$.

* Cela est rendu vraisembable par l'estimation de la temperature Θ_N basée sur les mesures de susceptibilité.

TROISIEME PARTIE

Propriétés magnétiques du niobate de manganèse et du niobate de cobalt

L'étude des propriétés magnétiques du niobate de cobalt $Nb_2O_5 \cdot 4CoO$ et du niobate de manganèse $Nb_2O_5 \cdot 4MnO$ à été faite sur des échantillons polycristallins. A une température donnée *T* comprise entre 2,5°K et l'ambiante, on a mesuré, par la méthode d'extraction axiale la variation de l'aimantation spécifique σ en fonction du champ magnétique interne H_i ; au-dessus de la température ambiante, on a déterminé directement la susceptibilité au moyen d'une balance de translation. Les résultats se résument ainsi :

$Nb_2O_5 \cdot 4MnO$ est antiferromagnétique (Fig. 7) avec une température de Neél Θ_N à 125°K et une

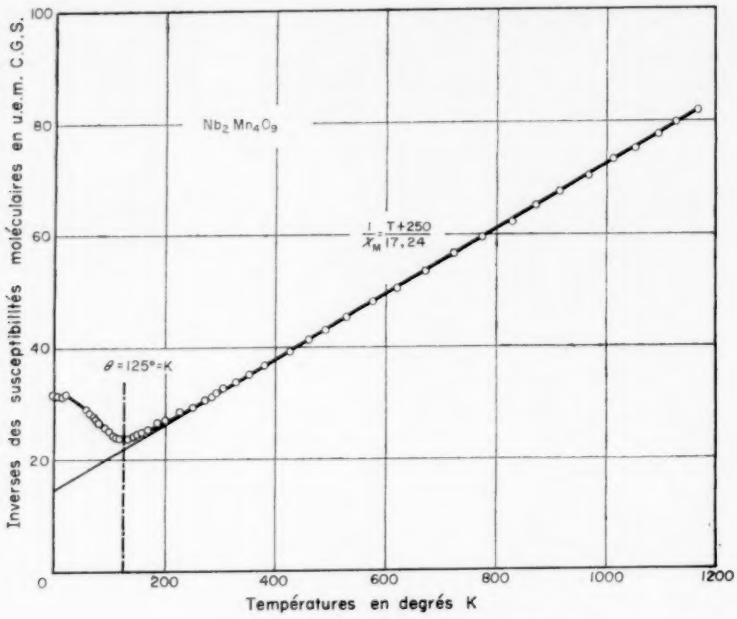

FIG. 7. $1/\chi_m(T)$ pour $Nb_2O_5 \cdot 4MnO$.

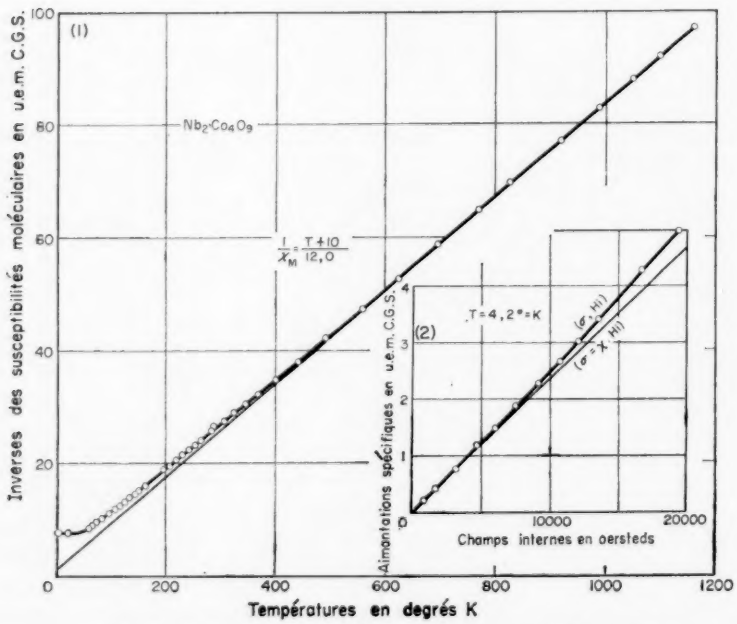

FIG. 8. (a) $1/\chi_m(T)$ pour $Nb_2O_5 \cdot 4CoO$ (b) $\sigma(H)$ à $T = 4,2°K$.

température de Curie Θ_P à $-250°K$. Les isothermes (σ_i, H_i) tracées jusqu'à environ 20.000 Oe sont linéaires, même aux très basses températures ; le coefficient angulaire des droites correspondantes définit la valeur de la susceptibilité. Aux températures supérieures à Θ_N la courbe ($1/\chi_m$, T) définit une constante de Curie C égale à 17,24 soit 4,31 par ion Mn^{2+} en bon accord avec la valeur 4,39 calculée par cation considéré dans l'état ^6S. Si l'on désigne par n et n' les coefficients de champ moléculaire représentant respectivement les interactions entre ions sur deux sous-réseaux différents et celles entre ions sur un même sous-réseau, on peut, à partir des valeurs numériques de Θ_N et Θ_P et de leurs expressions[9]

$$\Theta_N = C/2\,(n'-n) \text{ et } \Theta_P = C/2\,(n'+n)$$

en fonction de n et n', calculer $n = -21{,}6$ et $n' = -7{,}3$. On remarque que $n = +3n'$ et que la susceptibilité au zéro absolu est de l'ordre de 2/3 de la susceptibilité à la température de transition Θ_N.

Des résultats sur $Nb_2O_5 \cdot 4CoO$ (Fig. 8), il est plus difficile de déduire l'existence de l'antiferromagnétisme. Aux températures supérieures à 30°K ($1/\chi_m$,T) suit une loi de Curie Weiss avec $\Theta_P = -10°$ et $C = 12{,}0$, soit 3,0 par ion Co^{2+}. Cette constante de Curie est comprise entre les valeurs 1,88 et 5,61 calculées pour cet ion respectivement avec $S = 3/2$ et $J = L+S = 9/2$; elle est en accord avec la plupart des constantes de Curie expérimentales relatives à cet ion[10, 11, 12] et plus particulièrement avec les valeurs 3,07 dans CoO[13] et 3,02 dans $Fe_2O_3 \cdot CoO$[14]. Il semble que, dans ces deux dernières substances et dans le niobate de cobalt, l'amplitude du blocage du moment, sous l'effet du champ cristallin, soit du même ordre de grandeur ; on fera remarquer que dans ces composés, chaque ion Co^{2+} est entouré d'un octaèdre d'ions oxygène. Aux températures inférieures à 30°K, les courbes (σ, H_i) présentent une courbure dont la concavité est tournée vers l'axe des σ (Fig. 8), la susceptibilité représentée par le rapport σ/H_i croît avec le champ ; pour tracer la courbe ($1/\chi_m$, T) on a convenu de prendre pour la valeur de la susceptibilité celle qui correspond au coefficient angulaire de la tangente à l'origine de la courbe. Un résultat semblable a déjà été observé sur MnO et MnF_2[12] ; il peut être expliqué par l'augmentation de susceptibilité due au fait que, sous l'action du champ magnétique, la direction d'antiferromagnétisme tend à se rapprocher du plan perpendiculaire à ce champ.[15, 16] Dans le cas d'un cristal uniaxe, si l'on représente l'énergie de couplage de la direction d'antiferromagnétisme avec cet axe par une expression de la forme $K_1 \sin^2\Theta$ dans laquelle Θ représente l'angle de cette direction avec l'axe du cristal, la susceptibilité d'une poudre dans un champ H s'exprime par la relation

$$\chi = \frac{1}{3}\chi_{\parallel} + \frac{2}{3}\chi_{\perp} + \frac{2}{15}\cdot\left(\frac{\chi_{\parallel}-\chi_{\perp}}{K_1}\right)^2 \cdot H^2$$

où $\chi_{\parallel}$ et $\chi_{\perp}$ repésentent respectivement les susceptibilitiés suivant les directions d'antiferromagnétisme et une direction perpendiculaire. A 4,2°K, $\chi_{\parallel}$ est très faible ; on le suppose nul ; on déduit K_1 de l'ordre de $1{,}3 \cdot 10^6$ ergs/cm^3, ce qui est grand, mais d'un ordre de grandeur admissible. En prenant $\Theta_N = 30°K$, on trouve $n = -3{,}34$ et $n' = +1{,}67$.

Pour ces deux niobates, dans un intervalle de température de l'ordre de 300° au-dessus de Θ_N, on a remarqué qu'aux erreurs d'expérience près, la susceptibilité est indépendante du champ appliqué (jusqu'à 20.000 Oe) et que la courbe ($1/\chi_m$, T) est au-dessus et s'écarte d'autant plus de la droite de paramagnétisme à haute température que l'on s'approche de Θ_N. Cette allure de courbe, observée sur d'autres antiferromagnétiques[21, 13] est à rapprocher de celle mesurée sur les ferromagnétiques dans la zone paramagnétique; comme pour ces derniers, elle est peut être due aux fluctuations du champ moléculaire.[17]

QUATRIEME PARTIE

Configurations magnétiques

Les configurations d'équilibre des spins sont solution d'une équation matricielle[5, 6] de la forme

$$(\zeta-\lambda)\boldsymbol{T}(\boldsymbol{k}) = 0 \qquad (1)$$

La dimension de la matrice (ζ) est égale au nombre n de réseaux de Bravais, occupés par des atomes magnétiques. (λ) est une matrice diagonale d'éléments $\lambda_{ii}\,\delta_{ij}$ ($j = 1, \ldots, n$). Les paramètres λ_{ii} sont égaux pour des sous-réseaux équivalents (c'est-à-dire reliés par des opérations de symétrie du groupe). Leur connaissance permet d'évaluer l'énergie d'échange (2). Les vecteurs $\boldsymbol{T}(\boldsymbol{k})$ à n

Vol. 21
1961

composantes $\boldsymbol{T_j(k)}$ $(j = 1, \ldots, n)$ sont liés aux vecteurs spins par (3).

$$H = -2\sum\lambda_{ij} \tag{2}$$

$$\boldsymbol{\sigma_j(R)} = \sum_k \boldsymbol{T_j(k)}\text{ixp}-(\boldsymbol{k}\cdot\boldsymbol{R})^* \tag{3}$$

Ici $\boldsymbol{\sigma_j}$ est un vecteur unitaire de même direction que le spin $\boldsymbol{S_j}$ $(\boldsymbol{\sigma_j} = \boldsymbol{S_j}/S_j)$. Les éléments de la matrice (ζ) sont

$$\zeta_{ij} = \sum_j C_{ij}\,\text{ixp}\,\boldsymbol{k}.(\boldsymbol{R_i}-\boldsymbol{R_j}) \tag{4}$$

où

$$C_{ij} = S_i J_{ij} S_j \tag{5}$$

J_{ij} est l'intégrale d'échange. Lorsque les mailles cristallographiques et magnétiques coïncident, on trouve toutes les configurations fondamentales possibles en posant $\boldsymbol{k} = 0$. $\boldsymbol{\sigma_j(R)}$ et $\boldsymbol{T_j}$ (0) s'identifient alors.

La méthode générale $(\boldsymbol{k} \neq 0)$ reste cependant valable. On peut montrer qu'il suffit d'étudier une seule solution exprimée en fonction de $\boldsymbol{k}$ pour trouver tous les modes possibles.[19]

Dans les niobates de Co et Mn, les mailles cristallographiques et magnétiques coïncident, de sorte qu'en posant $\boldsymbol{k} = 0$, on aura à résoudre un système de dimension 8 (car il y a 4 atomes M_I et 4 atomes M_{II}). De même, il y aura dans la matrice (λ) 8 termes diagonaux, dont 4 égaux à λ_I et 4 à λ_{II}. Profitant de la remarque faite plus haut, nous allons étudier le système (1) non pas pour $\boldsymbol{k} = 0$, mais pour $\boldsymbol{k} = (00l)$. Cela nous permet de ramener la dimension de la matrice à 4. Posant successivement $l = 0$ et $l = 1$, nous trouverons en tout 8 modes (Fig. 5).

Mise en équation :

Nous considérons les cations magnétiques

$$\text{I}(\tfrac{1}{3}\ \tfrac{2}{3}\ z_\text{I}),\ \text{II}\ (\tfrac{1}{3}\ \tfrac{2}{3}\ z_\text{II}),$$

$$\text{I}_-(\tfrac{2}{3}\ \tfrac{1}{3}, -z_\text{I})\ \text{et}\ \text{II}_-(\tfrac{2}{3}\ \tfrac{1}{6}, -z_\text{II}).$$

Nous tabulons en partie la mise en équation du problème. Du Tableau 8 et à l'aide de (1) et (4), on déduit :

$$\begin{aligned}\lambda_\text{I}\boldsymbol{T_I(k)} = {} & AJ_2\,\text{ixp}\,2lz_\text{I}\boldsymbol{T_{I_-}(k)} \\ & + J_1\,\text{ixp}\,l(z_\text{I}-z_\text{II})\boldsymbol{T_{II}(k)} \\ & + AJ_4\,\text{ixp}\,l(z_\text{I}+z_\text{II})\boldsymbol{T_{II_-}(k)}\end{aligned} \tag{6}$$

$$\begin{aligned}\lambda_\text{II}\boldsymbol{T_{II}(k)} = {} & A\,J_3\,\text{ixp}\,l\,z_\text{II}\,\text{ixp}\,l/2\,\boldsymbol{T_{II_-}(k)} \\ & + J_1\,\text{ixp}\,l(z_\text{II}-z_\text{I})\boldsymbol{T_I(k)} \\ & + AJ_4\,\text{ixp}\,l(z_\text{I}+z_\text{II})\,\boldsymbol{T_{I_-}^*(k)}\end{aligned} \tag{7}$$

Ici, on a abrégé

$$\begin{aligned}A = {} & \text{ixp}(-h+k)/3+\text{ixp}(2h+k)/3 \\ & +\text{ixp}-(h+2k)/3\end{aligned} \tag{8}$$

La signification des intégrales d'échange est illustrée par le Tableau 8 et la Fig. 5. Complétant les équations écrites par celles relatives

* On utilise la notation de WANNIER[18] $\text{ixp}\alpha = \exp 2\pi i\alpha$.

Tableau 8. *Voisinages et intégrales d'échange* ($Nb_2Mn_0O_9$)

Atome	Voisins	Distance (Å)	Intégrale d'échange
I($\frac{1}{3}\ \frac{2}{3}\ z_\text{I}$)	1 voisin II en ($\frac{1}{3}\ \frac{2}{3}\ z_\text{II}$)	3,17	y_1
	3 voisins I$-$en ($\frac{2}{3}\ \frac{1}{3}\ \bar{z}_\text{I}$; $\bar{\frac{1}{3}}\ \frac{1}{3}\ \bar{z}_\text{I}$; $\frac{2}{3}\ \frac{4}{3}\ \bar{z}_\text{I}$)	3,12	y_2
	3 voisins II$-$en ($\frac{2}{3}\ \frac{1}{3}\ \bar{z}_\text{II}$; etc.)	4,06	y_4
II($\frac{1}{3}\ \frac{2}{3}\ z_\text{II}$)	1 voisin I en ($\frac{1}{3}\ \frac{2}{3}\ z_\text{I}$)	3,17	y_1
	3 voisins II$-$en ($\frac{2}{3}\ \frac{1}{3}\ \bar{z}_\text{II}-\frac{1}{2}$; etc.)	3,36	y_3
	3 voisins I$-$en ($\frac{2}{3}\ \frac{1}{3}\ \bar{z}_\text{I}$; etc. . .)	4,06	y_4

* Les valeurs $z_\text{I} = 0{,}0181$; $z_\text{II} = -0{,}203$ ont été utilisées.

aux atomes I− et II− et posant

$$\boldsymbol{Q}_j(\boldsymbol{k}) = \boldsymbol{T}_j(\boldsymbol{k})\exp -lz_j \text{ pour } j = \text{I, II, I}_-\text{, II}_- \quad (9)$$

le système (I) prend la forme (10) où $M(\boldsymbol{k})$ est la matrice (11) dont les lignes se rapportent respectivement aux sous-réseaux I, I−, II, II−

$$M(\boldsymbol{k})\,\boldsymbol{Q}(\boldsymbol{k}) = 0 \quad (10)$$

$$M(\boldsymbol{k}) = \begin{pmatrix} -\lambda_{\mathrm{I}} & AJ_2 & J_1 & AJ_4 \\ A^*J_2 & -\lambda_{\mathrm{I}} & A^*J_4 & J_1 \\ J_1 & AJ_4 & -\lambda_{\mathrm{II}} & AJ_3 \exp \tfrac{1}{2}l \\ A^*J_4 & J_1 & A^*J_3 \exp -\tfrac{1}{2}l & -\lambda_{\mathrm{II}} \end{pmatrix} \quad (11)$$

Lorsque $\boldsymbol{k} = (00l)$, $A = 3$. Faisons d'abord $h = k = l = 0$. Transformant $M(0)$ par la matrice U (12), on obtient une diagonalisation partielle de $M(0)$ en deux sous-matrices M_1' et M_2' (15)

$$U = \begin{pmatrix} 1 & . & -1 & . \\ 1 & . & 1 & . \\ . & 1 & . & -1 \\ . & 1 & . & 1 \end{pmatrix} \Big/ \sqrt{2} \quad (12)$$

On a

$$\boldsymbol{Q} = U\,\boldsymbol{Q}' \;;\; M'\,\boldsymbol{Q}' = 0 \text{ avec} \quad (13)$$

$$M' = U^{-1}\,M\,U = \begin{pmatrix} M_1' & . \\ . & M_2' \end{pmatrix} \quad (14)$$

$$M_1' = \begin{pmatrix} -\lambda_{\mathrm{I}}+3J_2 & J_1+3J_4 \\ J_1+3J_4 & -\lambda_{\mathrm{II}}+3J_3 \end{pmatrix};$$

$$M_2' = \begin{pmatrix} -\lambda_{\mathrm{I}}-3J_2 & J_1-3J_4 \\ J_1-3J_4 & -\lambda_{\mathrm{II}}-3J_3 \end{pmatrix} \quad (15)$$

Posons

$$Q_1' = 1 \;;\; Q_2' = \exp i\phi \quad (16)$$

On obtient

$$\lambda_{\mathrm{I}} = 3J_2+(J_1+3J_4)\exp i\phi$$
$$\lambda_{\mathrm{II}} = 3J_3+(J_1+3J_4)\exp -i\phi \quad (17)$$

D'où

$$\lambda_{\mathrm{I}}+\lambda_{\mathrm{II}} = 3(J_2+J_3)+2(J_1+3J_4)\cos\phi \quad (18)$$

$\lambda_{\mathrm{I}}+\lambda_{\mathrm{II}}$ doit être maximum. On doit distinguer deux cas

(1) $J_1+3J_4 > 0$. Alors $\phi = 0$; $Q_1' = Q_2' = 1$ (19)

(2) $J_1+3J_4 < 0$. Alors $\phi = \pi$; $Q_1' = -Q_2'$ (20)

Discutant de la même manière la sous-matrice M_2' (15), on a

(3) $J_1-3J_4 > 0$ avec $Q_3' = Q_4' = 1$ (21)

(4) $J_1-3J_4 < 0$ avec $Q_3' = -Q_4'$ (22)

On a alors

$$\lambda_{\mathrm{I}}+\lambda_{\mathrm{II}} = -3(J_2+J_3) \pm (J_1-3J_4) \quad (23)$$

où le signe + correspond au cas (3), − au cas (4).

Les modes des atomes I, I−, II, II− sont représentés grâce à (12)–(21) par les colonnes de la matrice (Q) (24)

Faisant $h = k = 0$ et $l = 1$ dans (11) on trouve quatre modes supplémentaires qui se déduisent des quatre modes précédents par un changement de signe de l'interaction J_3. Nous ne les discuterons pas davantage. C'est le cas (3) (21) qui est observé

$$(Q) = \begin{pmatrix} 1 & 1 & -1 & -1 \\ 1 & -1 & 1 & -1 \\ 1 & -1 & -1 & 1 \\ 1 & 1 & 1 & 1 \end{pmatrix} \quad (24)$$

Conditions de stabilité. Ecrivons que la matrice $[\lambda_0-\zeta(\boldsymbol{k}_0+\boldsymbol{dk})]$ a des racines positives pour $\boldsymbol{dk}$ petit, $\boldsymbol{k}_0$ (= 0) étant le vecteur $\boldsymbol{k}$ d'équilibre, (λ_0) étant la matrice dont les éléments diagonaux sont

$$\lambda_I = -3J_2+J_1-3J_4 \;;\; \lambda_{\mathrm{II}} = -3J_3+J_1-3J_4 \quad (25)$$

En dehors de $\lambda_{\mathrm{I}} > 0$ et $\lambda_{\mathrm{II}} > 0$ et de la condition (21) on trouve les conditions de stabilité suivantes

$$J_3 < 0 \;;\; J_2+J_3+2J_4 < 0 \;;\; 2(3J_2J_3-J_1J_4) - (J_2+J_3)(J_1-3J_4) > 0$$
$$[6J_2-(J_1+3J_4) < 0 \;;\; 6J_3-(J_1+3J_4) < 0] \quad (26)$$

(Les conditions les moins restrictives sont écrites entre crochets.) Avec les notations de la troisième partie, on a, à une constante de proportionnalité près :

$$n = 3(J_2+J_3+2J_4) \;;\; n' = J_1 \quad (27)$$

Le mode (3) (Fig. 5) et (25) est favorisé par des interactions J_2, J_3, J_4 négatives et J_1 positive. Dans le cas de $Nb_2Co_4O_9$, on a n négatif et n' positif. Par contre, dans $Nb_2Mn_4O_9$, n' (donc J_1) coefficient d'interaction dans un même sous-réseau de Néel est négatif, contrairement à ce que suggérerait la structure.

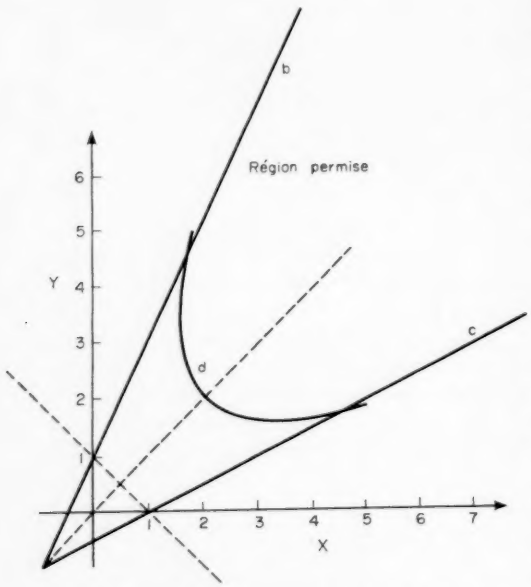

FIG. 9. Domaine de stabilité dans $Nb_2Mn_4O_9$
$x = J_2/J_4 \quad y = J_3/J_4$

Cas de $Nb_2Mn_4O_9$. De la relation trouvée expérimentalement $n = 3n'$, on déduit que

$$J_1 = J_2 + J_3 + 2J_4 \qquad (28)$$

J_1 étant négatif, J_4 *doit* être différent de zéro et certainement négatif d'après (21). Posant

$$x = J_2/J_4 \; ; \; y = J_3/J_4 \qquad (29)$$

les inégalités significatives deviennent après substitution de (28) et (29)

$$y > 0 \,(a); -2x+y-1 < 0 \,(b) \; ; \; x-2y-1 < 0 \,(c) \; ;$$
$$x^2+y^2-4xy+4+x+y < 0 \;\; (d) \qquad (30)$$

Elles délimitent le domaine de stabilité compris entre les droites (b) et (c) et la branche positive de l'hyperbole (d) (Fig. 9). On en déduit que x et y ne peuvent tomber au-dessous d'une valeur minimum de $\frac{1}{2}(1+\sqrt{6}) = 1{,}73$. En admettant $J_2 \sim J_3$, x et y seraient au moins supérieures à $+2$.

En résumé, dans $Nb_2Mn_4O_9$ toutes les interactions J_j ($j = 1, 2, 3, 4$) sont négatives et non nulles, et en admettant $J_2 \sim J_3$ les interactions J_2 et J_3 seraient au moins deux fois plus intenses que J_4, tandis que J_1 serait, selon (28) au moins six fois plus fort que J_4.

Enfin, on peut montrer, soit par la méthode de DZYALOSHINSKI,[20] soit par une méthode matricielle[21] que lorsque les spins sont dirigés selon l'axe c, les composés hexagonaux étudiés doivent être des antiferromagnétiques sans ferromagnétisme faible "parasitique". Celui-ci, effectivement, n'est pas observé.

CONCLUSIONS

La structure de $A_2M_4O_9$ (A = Nb, Ta ; M = Mn, Fe, Co, Mg) constitue un nouveau type de surstructure du corindon au même titre que les ilménites. Mais alors que dans les ilménites le rapport des cations est 1 : 1, il est ici 1 : 2. Le groupe d'espace le plus probable est $P\,\bar{3}\,c\,1$. Fait assez surprenant, les octaèdres de coordination du niobium pentavalent ont une face commune. En conséquence, la répulsion coulombienne déplace les atomes Nb voisins proches très notablement des centres de l'octaèdre.

Les substance $Nb_2Co_4O_9$ et $Nb_2Mn_4O_9$ ont une structure antiferromagnétique en chaînes. La droite $\frac{1}{3}\;\frac{2}{3}\;z$ porte des spins orientés selon c, la droite $\frac{2}{3}\;\frac{1}{3}\;z$ porte des spins orientés en sens inverse.

Mn^{2+} est dans un état ^6S. La situation dans Co^{2+} est plus délicate. Les mesures de susceptibilité dans la région paramagnétique ($T > 40°K$) indiquent un moment de $S = \frac{4}{2}$, c'est-à-dire une contribution orbitale tandis que les mesures par diffraction neutronique dans la région antiferromagnétique ($T = 4{,}2°K$) indiquent un moment de $S = \frac{3}{2}$, c'est-à-dire de la valeur de spin seul. Il est donc probable qu'aux très basses températures, le moment orbital de Co soit complètement bloqué.

REFERENCES

1. *Strukturbericht*, Vol. II, p. 55. (1928–1932). Akad. Verlagsges.

2. BERTAUT E. F. et FORRAT F., *C.R. Acad. Sci., Paris* **242,** 382 (1956).
3. PAULING L. et HENDRICKS S. B., *J. Amer. Chem. Soc.* **47,** 781 (1925).
4. *International Tables for X-ray Crystallography*. The Kynoch Press, Birmingham (1952).
5. BERTAUT E. F., *C.R. Acad. Sci., Paris* **250,** 85 (1960).
6. BERTAUT E. F., *C.R. Acad. Sci., Paris* **252,** 76 (1961).
7. HASTINGS J. M., ELLIOT N. et CORLISS L. M., *Phys. Rev.* **115,** 13 (1959).
8. GOODENOUGH J. B., *Phys. Rev.* **117,** 1442 (1960).
9. NEEL L., *Ann. Phys., Paris* **3,** 137 (1948).
10. BENOIT R., *C.R. Acad. Sci., Paris* **231,** 1216 (1950).
11. SERRES A., *Ann. Phys. Paris* **17,** 5 (1932).
12. BIZETTE H., *Ann. Phys., Paris* **1,** 233 (1946).
13. TROMBE F., *J. Phys. Radium* **12,** 171 (1951).
14. FALLOT M. et MARONI P., *J. Phys. Radium* **12,** 257 (1951).
15. NEEL L., *Proc. Intern. Conf. Théor. Phys. Kyoto.* (1953).
16. NAGAMIYA T., *Proc. Theor. Phys.* **4,** 342 (1951).
17. NEEL L., *Ann. Phys. Paris,* **17,** 5 (1932).
18. WANNIER G. H., *Elements of Solid State Theory,* University Press, Cambridge (1959).
19. BERTAUT E. F., *C.R. Acad. Sci., Paris* **252,** 252 (1961).
20. DZYALOSHINSKI I., *J. Phys. Chem. Solids* **4,** 241 (1958).
21. BERTAUT E. F., *C.R. Acad. Sci., Paris* **252,** 2078 (1961).

ol. 21
1961

J. Phys. Chem. Solids Pergamon Press 1961. Vol. 21, Nos. 3/4, pp. 252–255. Printed in Great Britain.

SUPERCONDUCTING TITANIUM–MOLYBDENUM ALLOYS

R. D. BLAUGHER, B. S. CHANDRASEKHAR and J. K. HULM

Westinghouse Research Laboratories, Pittsburgh 35, Pennsylvania

and

E. CORENZWIT and B. T. MATTHIAS

Bell Telephone Laboratories, Murray Hill, New Jersey

(*Received* 11 *May* 1961)

Abstract—Alloys in the titanium–molybdenum system were tested for superconductivity down to 1·0°K. Both the hexagonal titanium rich and the cubic molybdenum rich phases showed superconductivity. The transition temperature of the cubic alloys rose to a maximum value of 3·7°K at about 16 atomic per cent molybdenum. This maximum is discussed in terms of density of states and the BCS theory.

INTRODUCTION

THE superconductivity of compounds and alloys of the transition metals has received an increasing amount of attention in the past few years.[1–6] One of the attractive features of alloys in this part of the periodic system is the occurrence of very wide range solid solutions. This is true not only for alloys of neighboring elements but even for elements separated by two or more groups. Such alloys permit us to study the effect upon superconductivity of quite substantial changes of electronic structure, while at the same time keeping the atomic arrangement fixed. In pursuit of this objective, we investigated the system titanium–molybdenum, for which a body-centered cubic solid solution exists over the range from pure molybdenum to 94 atomic per cent of titanium. This gave us the possibility of varying the average number of valence electrons per atom smoothly over the range from 4·12 up to 6·0.

From previous work,[7] it was anticipated that the superconducting transition temperature would exhibit a maximum in the neighborhood of 5·0 valence electrons per atom. This maximum was indeed found, although at a somewhat lower valence number, 4·32 electrons per atom. The significance of this behavior is discussed in terms of the electronic structure of the titanium–molybdenum alloys and the Bardeen–Cooper–Schrieffer theory of superconductivity.[8]

EXPERIMENTAL DETAILS

The phase diagram of the titanium rich end of the titanium–molybdenum alloy system as determined by HANSEN *et al.*[9] is shown schematically in Fig. 1. Superimposed on this diagram is the martensitic transformation curve (M_s curve) obtained by DUWEZ.[10] The M_s curve indicates for a given composition the point at which, with decreasing temperature, body-centered cubic or β-material begins to transform martensitically into hexagonal material α', of the same composition. This must be distinguished from the separation of non-martensitic hexagonal material, α, which would have a much lower molybdenum content. The relative yields of the β-, α-, and α'-phases depend not only on the initial composition of the alloy, but also upon the rate of cooling. Apparently, the separation of α is inhibited by rapid quenching, and using this technique one may either obtain pure β or $\beta+\alpha'$ in which each phase has a composition close to nominal. The occurrence of β or $\beta+\alpha'$ depends on whether the molybdenum content lies above or below 6 atomic per cent, respectively. Thus, in order to produce phases of known composition, quenching was preferred to slow cooling in the terminal heat treatment stage of the present work.

The initial mixing of the titanium–molybdenum alloys was accomplished by levitation melting[11] followed by casting into rods of about 4 mm

diameter and 6 cm length. These samples were annealed by electron bombardment for about 30 hr at 1100°C and then quenched in water. For molybdenum contents in excess of 6 atomic per cent, it is believed that the samples were almost entirely cubic, although a slight amount of α may have been present at the titanium rich end.

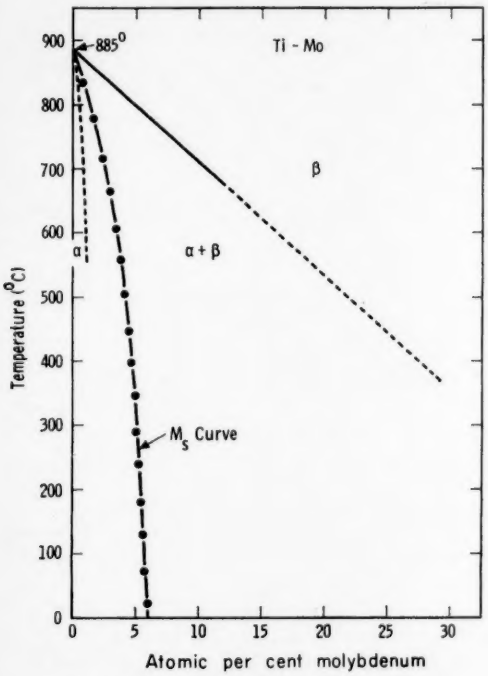

FIG. 1. Titanium–molybdenum phase diagram.

Similarly, below 6 atomic per cent molybdenum, the samples were predominantly $\beta+\alpha'$, with again the possibility of a trace of α-phase.

The alloys were tested for superconductivity using a ballistic method in which the variation of the low field strength magnetic susceptibility with temperature is determined. The essentials of this technique are described elsewhere.[6,12] The transition temperature was taken from the midpoint of the transition curve, that is, the temperature at which the susceptibility lies halfway between the normal and the ultimate superconduting values. The total width of the transition was determined in each case, since this is a valuable guide to the metallurgical state of the specimen.

RESULTS AND DISCUSSION

Figure 2 shows the observed dependence of the superconducting transition temperature, T_c, upon alloy concentration for the titanium–molybdenum system. Quite sharp superconducting transitions were obtained for all the compositions studied, even in the region below 6 atomic per cent molybdenum, where a phase mixture, $\beta+\alpha'$, is almost certainly present. The total width from commencement to completion of the transition varied from about 0·2°K up to about 0·6°K, with average values around 0·4°K. The widest transitions

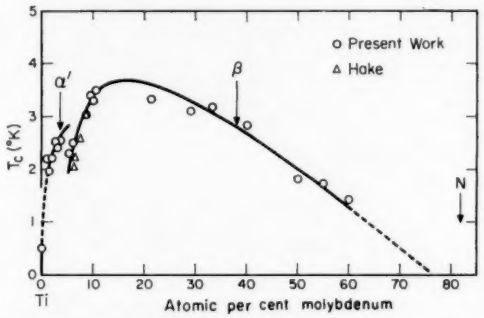

FIG. 2. Superconducting transition temperature vs. composition, titanium–molybdenum system.

occurred in the range 3–6 atomic per cent molybdenum which suggests that the transformation of β to α' was only partially complete in this range, in good agreement with the phase diagram.

Figure 2 also shows data by HAKE[5] for alloys at the lower end of the β-region. These data are in fair agreement with our results for cubic alloys in the same region.

The discontinuity of T_c observed at about 6 atomic per cent molybdenum was not surprising in view of the change of crystal structure which occurs in this composition. To the left of the discontinuity, T_c increases with increasing molybdenum content for the α' hexagonal phase. This is in accord with the empirical rule[7] that T_c increases as the average number of valence electrons per atom increases from 4 towards 5. If the α'-phase could be preserved at higher molybdenum contents (which it cannot for metallurgical reasons), we would expect a maximum in T_c. Such a maximum has been observed for other hexagonal solid solutions.[13] It is also interesting

to note that the α'-curve can be reasonably extrapolated to $T_c = 0{\cdot}49°K$ for pure titanium.[14]

The transition temperature of the β-phase attains a well-defined maximum in the vicinity of 16 atomic per cent molybdenum. The existence of this maximum is also in general agreement with a suggestion of MATTHIAS.[7] However, the occurrence of the maximum at 4·32 valence electrons per atom was surprising to us since values between 4·6 and 4·7 valence electrons per atom seem to be typical for other body-centered cubic solid solutions.[6]

compositions considered. This, in contrast to the nearly 20 per cent change of $N(0)$ over the same range, indicates that the interaction parameter is approximately constant for these alloys. The value of $N(0)V/\gamma$ for the body-centered cubic Ti–Mo alloys lies close to 39 mol deg^2 mJ^{-1}, which differs considerably from the value of 16 mol deg^2 mJ^{-1} obtained for b.c.c. U–Mo alloys.[15] It appears, therefore, that the constancy of V conjectured by PINES[16] applies approximately for a given alloy series, but does not hold for alloys based on different transition metals.

Table 1

Atom per cent Mo	T_c* (°K)	Θ* (°K)	γ* (mJ mol^{-1} deg^{-2})	$N(0)V$	$N(0)V/\gamma$ (mol deg^2 mJ^{-1})
6·25	2·04	364	4·90	0·199	40·6
6·50	2·23	354	5·06	0·204	40·3
7·54	2·60	337	5·56	0·212	38·2
8·60	3·09	310	5·88	0·225	38·2

* Experimental values due to HAKE.[5]

Since T_c is thought to be a monotomic function of $N(0)$, the density of states at the Fermi surface, the cubic phase of Mo–Ti ought to exhibit a peak in density of states in the vicinity of 15 atomic per cent molybdenum. Unfortunately, we have no data on the electronic heat capacity over the range of interest, although HAKE[5] has given such data for 6 to 9 per cent molybdenum (Table 1).

According to the BCS theory[8] in the form used by GOODMAN *et al.*[15] the superconducting transition temperature is given by

$$\frac{T_c}{\Theta} = 0{\cdot}855 \exp\left[-\frac{1}{N(0)V}\right] \qquad (1)$$

where Θ is the Debye temperature and V is the interaction parameter responsible for the occurrence of superconductivity. From the experimental values of T_c, Θ, and γ shown in Table 1, we have calculated the values of $N(0)V$ and $N(0)V/\gamma[= 3V/2\pi^2k^2]$ given in the last two columns. The last column, which is thus proportional to the interaction parameter, V, only changes by about 5 per cent over the range of

Acknowledgements—We wish to thank G. COMENETZ, J. W. SALATKA, and W. PETRAS for assistance in levitation melting.

REFERENCES

1. CHANDRASEKHAR B. S. and HULM J. K., *J. Phys. Chem. Solids* **7**, 259 (1958).
2. CALVERLEY A. and ROSE-INNES A. C., *Proc. Roy. Soc.* **A255**, 267 (1960).
3. MÜLLER J., *Helv. Phys. Acta.* **32**, 141 (1959).
4. BERLINCOURT T. G., *J. Phys. Chem. Solids* **11**, 12 (1959).
5. HAKE R. R., *Proceedings of the Seventh International Conference on Low Temperature Physics.* University of Toronto Press, Toronto (1960).
6. BLAUGHER R. D. and HULM J. K., *Superconducting Solid Solution Alloys of the Transition Elements*, to be published.
7. MATTHIAS B. T., *Progress in Low Temperature Physics*, Vol. II. North-Holland Publishing Company, Amsterdam (1957).
8. BARDEEN J., COOPER L. N. and SCHRIEFFER J. R., *Phys. Rev.* **108**, 1175 (1957).
9. HANSEN M., KAMEN E. L., KESSLER H. D. and MCPHERSON D. J., *Trans. Amer. Inst. Min. (Metall.) Engrs.* **191**, 881 (1951).
10. DUWEZ P., *Trans. Amer. Soc. Metals* **45**, 934 (1953).

11. WROUGHTON D. M., OKRESS E. C., BRACE P. H., COMENETZ G. and KELLEY J. C. R., *J. Elektrochem. Soc.* **99,** 205 (1956).
12. HARDY G. F. and HULM J. K., *Phys. Rev.* **93,** 1004 (1954).
13. MATTHIAS B. T., COMPTON V. B., SUHL H. and CORENZWIT E., *Phys. Rev.* **115,** 1597 (1959).
14. STEELE M. C. and HEIN R. A., *Phys. Rev.* **92,** 243 (1953).
15. GOODMAN B. B., HILLAIRET J., VEYSSIÉ J. J. and WEIL L., *Proceedings of the Seventh International Conference on Low Temperature Physics.* University of Toronto Press, Toronto (1960).
16. PINES D., *Phys. Rev.* **109,** 280 (1958).

Vol. 21
1961

J. Phys. Chem. Solids Pergamon Press 1961. Vol. 21, Nos. 3/4, pp. 256–279. Printed in Great Britain.

CONFIGURATIONS MAGNÉTIQUES. MÉTHODE DE FOURIER

E. F. BERTAUT

Laboratoire d'Electrostatique et de Physique du Métal et Centre d'Etudes Nucléaires, Grenoble, France

(*Received* 5 *July* 1960; *revised* 15 *May* 1961)

Résumé—Les configurations magnétiques sont directement reliées aux vecteurs propres d'une matrice. Tout réseau de Bravais j, occupé par des ions magnétiques fournit à l'énergie d'échange une contribution $-2\lambda_j$. Les paramètres scalaires λ_j sont invariants dans les opérations de symétrie du groupe cristallographique.

Lorsque les ions magnétiques n'occupent qu'un seul réseau de Bravais ($j = 1$), λ_1 s'identifie avec la transformée de Fourier de l'intégrale d'échange et la méthode matricielle se réduit à celle de Villain.

Dans le cas d'un ensemble $\{A\}$ de n atomes équivalents, la recherche des λ_j est ramenée à celle des valeurs propres d'une matrice. Quand la maille chimique est conservée, les vecteurs propres qui décrivent les configurations des spins forment la base de représentations irréductibles ce qui relie la méthode matricielle à celle de DZYALOSHINSKY et TUROV. Un mode trivial est le mode ferromagnétique correspondant à la représentation identité.

Dans les sytèmes couplés $\{AB\}$ les vecteurs propres du problème matriciel sont des combinaisons linéaires des vecteurs propres de $\{A\}$ et de $\{B\}$. Le ferrimagnétisme de Néel apparaît comme le résultat du couplage de deux modes "triviaux" ferromagnétiques de $\{A\}$ et de $\{B\}$.

La stabilité des solutions s'exprime par des conditions d'inégalité entre intégrales d'échange. L'étude se limite à la détermination de modes fondamentaux, c'est-à-dire de modes complets à un seul vecteur de propagation.

Les applications suivantes sont étudiées :

(a) le cube centré (exemple d'un réseau de Bravais)
(b) les structures apparentées au corindon telles que Fe_2O_3-α, Cr_2O_3, les ilménites (exemple de n réseaux de Bravais équivalents)
(c) les spinelles cubiques et (d) les grenats (exemples de systèmes couplés).

Abstract—Spin configurations are directly related to the eigenvectors of a matrix. Each Bravais lattice j, occupied by magnetic ions, contributes to the exchange energy a value $-2\lambda_j$. The scalar parameters λ_j are invariant in the symmetry operations of the crystallographic group.

If the magnetic ions only occupy one Bravais lattice ($j = 1$), λ_1 is the fourier transform of the exchange integral and the matrix method is reduced to the Villain method.

In the case of a set $\{A\}$ of n equivalent atoms, the λ_j are the eigenvalues of a matrix. When the chemical unit cell is conserved, the eigenvectors which describe the spin configurations form the basis of irreducible representations which fact relates the matrix method to the group theoretical method of DZYALOSHINSKY and TUROV. A trivial mode is the ferromagnetic one which corresponds to the identity representation.

In coupled systems $\{AB\}$ the eigenvectors are linear combinations of the eigenvectors of $\{A\}$ and $\{B\}$. Néel's ferrimagnetism appears as the result of the coupling of the "trivial" ferromagnetic modes of $\{A\}$ and $\{B\}$.

Stability conditions of the solutions are expressed by inequalities between exchange integrals.

The study is limited to the determination of "fundamental modes", i.e. complete modes with a single propagation vector $\boldsymbol{k}$.

The following applications of the matrix method are studied:

(a) the body-centered cube (example of one Bravais-lattice)
(b) structures related to the corundum type as Fe_2O_3, Cr_2O_3, ilmenites (example of n equivalent Bravais-lattices).
(c) cubic spinels and (d) garnets (examples of coupled systems).

1. INTRODUCTION

Sur une simple hypothèse de travail

Soit $H(1\text{–}1)$ l'énergie d'échange de Heisenberg–Néel.

$$\begin{aligned} H &= -2\sum_{RR'} J_{RR'}\boldsymbol{S}_R \cdot \boldsymbol{S}_{R'} \\ &= -2\sum_{RR'} C_{RR'}\boldsymbol{\sigma}_R \cdot \boldsymbol{\sigma}_{R'} \\ &= -2\sum_{RR'} C_{RR'} \cos \Theta(\boldsymbol{R},\boldsymbol{R}') \end{aligned} \qquad (1\text{–}1)$$

Ici $\boldsymbol{S}_R$ est le spin au point $\boldsymbol{R}$. $J_{RR'}$ est l'intégrale d'échange.

$$C_{RR'} = S_R J_{RR'} S_{R'} \qquad (1\text{–}2)$$

$\boldsymbol{\sigma}_R$ est un vecteur unitaire de même direction que le spin $\boldsymbol{S}_R$. $\Theta(\boldsymbol{R},\boldsymbol{R}')$ est l'angle entre les spins en $\boldsymbol{R}$ et $\boldsymbol{R}'$. L'hypothèse la plus simple que l'on puisse faire est que l'angle $\Theta(\boldsymbol{R},\boldsymbol{R}')$ ne dépende que de $\boldsymbol{R}-\boldsymbol{R}'$. La quantité invariante la plus simple qui puisse définir $\Theta(\boldsymbol{R},\boldsymbol{R}')$, grandeur sans dimension, est le produit scalaire (1–3) de $\boldsymbol{R}-\boldsymbol{R}'$ avec un vecteur $\boldsymbol{k}$ de l'espace réciproque, ayant la dimension de l'inverse d'une longueur.

$$\Theta_{RR'} = 2\pi \boldsymbol{k} \cdot (\boldsymbol{R}-\boldsymbol{R}') \qquad (1\text{–}3)$$

Posons plus généralement

$$\Theta_{R_iR_j} = 2\pi \boldsymbol{k} \cdot (\boldsymbol{R}_i-\boldsymbol{R}_j)+\phi_{ij} \qquad (1\text{–}4)$$

où $\phi_{ij} = \phi_i - \phi_j$ est une différence de phases constante, ne dépendant que des sousréseaux i et j sur lesquels se trouvent $\boldsymbol{S}_{R_i}$ et $\boldsymbol{S}_{R_j}$ respectivement. Quelle est la signification physique de la relation (1–4)? Elle impose à toute configuration de spins d'avoir un vecteur de propagation $\boldsymbol{k}$. En d'autres termes les spins seraient en phase dans des plans perpendiculaires à un vecteur $\boldsymbol{k}$. En effet, soit $\boldsymbol{R}_i$ un vecteur variable, $\boldsymbol{R}_j$ et $\boldsymbol{k}$ des vecteurs constants. L'équation (1–4) avec $\Theta_{R_iR_j} =$ constant est l'équation du plan décrit par $\boldsymbol{R}_i$. La "longueur d'onde" de propagation est $|\boldsymbol{k}|^{-1}$. Lorsque $\boldsymbol{k}$ est un vecteur entier de l'espace réciproque, $|\boldsymbol{k}|^{-1} = d(hkl)$ est la distance réticulaire des plans (hkl). Une telle hypothèse peut être étayée sur un fait d'expérience bien connu, à savoir que dans un très grand nombre de structures déterminées aux neutrons les spins sont en phase dans des plans réticulaires bien déterminés.

On doit alors déterminer le vecteur $\boldsymbol{k}$ par la condition que l'énergie d'échange est minimum. En particularisant notre hypothèse pour un réseau de Bravais ($S_i = S_j = S_0$), l'énergie d'échange (1–1) se réduit à

$$H = 2S_0^2\, \zeta(\boldsymbol{k}) \qquad (1\text{–}5)$$

où

$$\zeta(\boldsymbol{k}) = \sum J_{ij} \cos 2\pi \boldsymbol{k} \cdot (\boldsymbol{R}_i-\boldsymbol{R}_j) \qquad (1\text{–}6)$$

En d'autres termes la "transformée de Fourier" $\zeta(\boldsymbol{k})$ de l'intégrale d'échange doit être maximum. Or c'est exactement le résultat démontré par Villain[1] pour les réseaux de Bravais. L'hypothèse de l'existence d'un vecteur de propagation unique que nous appellerons "hypothèse U" constitue donc une extension naturelle du travail de Villain.

Dans la section suivante nous décrivons une version matricielle qui justifiera le titre de "méthode de Fourier" donné au mémoire (malgré la restriction de l'hypothèse U à un vecteur $\boldsymbol{k}$) et, d'autre part limitera la validité des solutions que la minimisation naïve de (1–1) (1–4) permet de trouver. La méthode matricielle contient le résultat de Villain comme cas particulier. En même temps elle fournit une liaison simple aussi bien avec les méthodes de Kaplan[2] et Yoshimori[3] qu'avec celles de Dzyaloshinsky[4] et Turov[5]. Nous appliquons les enseignements de la partie théorique (Section 2) à l'étude du cube centré (Section 3), des structures du type corindon telles que Fe_2O_3-α, Cr_2O_3, ilménites (Section 4), aux spinelles cubiques (Section 5) et aux grenats (Section 6).

Notre méthode est directement basée sur les équations de mouvement de spins. Les vecteurs propres d'une certaine matrice sont directement liés aux configurations de spins et les valeurs propres sont liées à l'énergie d'échange.

2. METHODE DE FOURIER

L'équation de mouvement de spins est selon (1–1)

$$\hbar \frac{d\boldsymbol{S}_R}{dt} = 2\sum_{R'} J_{RR'}\boldsymbol{S}_{R'} \cdot \boldsymbol{S}_R \qquad (2\text{–}1)$$

Dans une configuration stable le premier membre de (2–1) est nul. $\boldsymbol{S}_R$ est parallèle à

$$\sum_{R'} J_{RR'}\boldsymbol{S}_{R'}$$

(champ moléculaire) ce que nous écrivons en termes de spins unitaires

$$\lambda_R \boldsymbol{\sigma}_R = \sum_{R'} C_{RR'} \boldsymbol{\sigma}_{R'} \qquad (2\text{–}2)$$

Ici λ_R est une constante de proportionnalité, définie positive, ayant les dimensions d'une énergie. La substitution de (2–2) dans (1–1) fournit

$$H = -2 \sum_R \lambda_R \qquad (2\text{–}3)$$

L'hamiltonien H doit être invariant par rapport aux translations du réseau cristallographique. Or à tout spin $\boldsymbol{\sigma}_{R+L}$ appartenant à un même réseau de Bravais ($\boldsymbol{L} = l_1\boldsymbol{a}_1 + l_2\boldsymbol{a}_2 + l_3\boldsymbol{a}_3$; l_j entier, $\boldsymbol{a}_j$ translations du réseau, $j = 1,2,3$) correspond le même scalaire λ_R. Plus généralement l'invariance de l'hamiltonien par rapport aux opérations de symétrie du groupe cristallographique est due à ce qu'à tous les points cristallographiquement équivalents, c'est à dire reliés par les opérations du groupe correspond le même scalaire λ_R.

On écrira autant d'équations (2–3) qu'il y a de réseaux de Bravais, porteurs de spins dans la structure (par exemple 4 dans Fe_2O_3-α, 6 dans les spinelles cubiques, 20 dans le grenat d'yttrium et de fer, 32 dans les grenats des terres rares). Numérotons les n réseaux de Bravais par les indices i et j ($i, j = 1, \ldots, n$) (au lieu de R et R'), multiplions (2–2) par $\exp 2\pi i\boldsymbol{k} \cdot \boldsymbol{R}_l$ et sommons sur tous les $\boldsymbol{R}_l$ d'un même réseau de Bravais. Grâce au fait que $C_{RR'}$ ne dépend que de $\boldsymbol{R}-\boldsymbol{R}'$ le résultat est (cf. Appendice A.2. pour une autre version, indépendante de coordonnées)

$$\lambda_i \boldsymbol{T}_i(\boldsymbol{k}) = \sum_j \zeta_{ij}(\boldsymbol{k}) \boldsymbol{T}_j(\boldsymbol{k}) \qquad (2\text{–}4)$$

Ici $\boldsymbol{T}_i(\boldsymbol{k})$ est la transformée de Fourier de $\boldsymbol{\sigma}_i(\boldsymbol{R})$. Sous forme matricielle on peut écrire

$$M(\boldsymbol{k})\boldsymbol{T}(\boldsymbol{k}) = (\zeta(\boldsymbol{k}) - \lambda)\boldsymbol{T}(\boldsymbol{k}) = 0 \qquad (2\text{–}5)$$

Ici $\boldsymbol{T}(\boldsymbol{k})$ est un vecteur à n composantes, (λ) la matrice diagonale dont les éléments sont $\lambda_i\delta_{ij}$ et $\zeta(\boldsymbol{k})$ la matrice d'éléments

$$\zeta_{ij} = \sum_{R_j} C_{ij} \exp\, 2\pi i\boldsymbol{k} \cdot (\boldsymbol{R}_i - \boldsymbol{R}_j) \qquad (2\text{–}6)$$

Cette dernière relation contient en réalité deux sommations, une première sur tous les points équivalents $\boldsymbol{R}_j$ appartenant à une même intégrale d'échange C_{ij} (par exemple tous les points équivalents du premier voisinage de $\boldsymbol{R}_i$) et une seconde sommation sur les divers voisinages (premiers, seconds etc.) *dans le réseau j*. La dimension des matrices $\zeta(\boldsymbol{k})$ et (λ) est n. $\boldsymbol{\sigma}_i(\boldsymbol{R})$ et $\boldsymbol{T}_i(\boldsymbol{k})$ sont liés par

$$\boldsymbol{\sigma}_i(\boldsymbol{R}) = \sum_k \boldsymbol{T}_i(\boldsymbol{k}) \exp -2\pi i\boldsymbol{k} \cdot \boldsymbol{R} \qquad (2\text{–}7)$$

On démontre aisément que (cf. Appendice A.1)

$$\sum_k |\boldsymbol{T}_i(\boldsymbol{k})|^2 = 1 \; ; \qquad (2\text{–}8)$$

$$\sum_{k \neq k'} \boldsymbol{T}_i^*(\boldsymbol{k}) \boldsymbol{T}_i(\boldsymbol{k}') \exp -2\pi i(\boldsymbol{k}-\boldsymbol{k}') \cdot \boldsymbol{R} = 0 \qquad (2\text{–}8a)$$

En particulier lorsqu'on ramène le spin $\boldsymbol{\sigma}_i(\boldsymbol{R})$ à l'origine, (2–8a) se réduit à

$$\sum_{k \neq k'} \boldsymbol{T}_i^*(\boldsymbol{k}) \boldsymbol{T}_i(\boldsymbol{k}') = 0 \qquad (2\text{–}8b)$$

La substitution de (2–7) dans (1–1) fournit

$$H = -2 \sum_{i,j,k} \boldsymbol{T}_i^*(\boldsymbol{k}) \zeta_{ij}(\boldsymbol{k}) \boldsymbol{T}_j(\boldsymbol{k})$$

$$= -2 \sum_i \lambda_i \sum_k |\boldsymbol{T}_i(\boldsymbol{k})|^2 = -2 \sum_i \lambda_i \qquad (2\text{–}9)$$

Nous supposons (hypothèse U) qu'il existe une solution $\boldsymbol{k} = \boldsymbol{k}_o$ de (2–5). A cause de la nature hermitique de la matrice $\zeta(\boldsymbol{k})$ il est immédiat que $\boldsymbol{k} = -\boldsymbol{k}_o$ est aussi solution. Nous appellerons "mode fondamental "un mode caractérisé par la solution $\pm\ \boldsymbol{k}_o$ par opposition aux "modes composés", resultant de la superposition de plusieurs modes $\boldsymbol{k}_1, \boldsymbol{k}_2$ etc. que nous n'étudions pas dans ce mémoire. Dans ces conditions les relations (2–8) (2–8b) se réduisent à

$$|\boldsymbol{T}_j(\boldsymbol{k})|^2 + |\boldsymbol{T}_j(-\boldsymbol{k})|^2 = 1 \; ; \; \boldsymbol{T}_j^2(\boldsymbol{k}) + \boldsymbol{T}_j^2(-\boldsymbol{k}) = 0 \qquad (2\text{–}10)$$

Le vecteur $\boldsymbol{T}_i(\boldsymbol{k})$ est nécessairement complexe ($\boldsymbol{k} \neq 0$). Une solution simple est

$$\boldsymbol{T}_j(\boldsymbol{k}) = (\boldsymbol{x} + i\boldsymbol{y}) \exp\, i\phi_j/2 \qquad (2\text{–}11)$$

où $\boldsymbol{x}$ et $\boldsymbol{y}$ sont des vecteurs unitaires et orthogonaux. On a alors

$$\boldsymbol{\sigma}_j(\boldsymbol{R}) = \boldsymbol{x} \cos(2\pi\boldsymbol{k} \cdot \boldsymbol{R}_j + \phi_j) + \boldsymbol{y} \sin(2\pi\boldsymbol{k} \cdot \boldsymbol{R}_j + \phi_j) \qquad (2\text{–}12)$$

L'angle Θ_{ij} entre les spins en $\boldsymbol{R}_i$ et $\boldsymbol{R}_j$ sera selon (2–12) donné par (1–4).

Soit alors un vecteur propre $\boldsymbol{T}(\boldsymbol{k})$ à n composantes (2–11), solution de (2–5). Comme un vecteur propre n'est déterminé qu'à un facteur constant près, l'ensemble des $\exp i\phi_j$ ($j=1, \ldots, n$) sera encore solution de (2–5). Le nombre de vecteurs propres possibles est égal à la dimension de la matrice $\zeta(\boldsymbol{k})$, soit égal à n. Notons-les $\boldsymbol{T}^p(\boldsymbol{k})$ où p n'est pas un exposant, mais un indice ($p = 1, \ldots, n$) qui numérote un mode p.

Supposons que tous les vecteurs propres $\boldsymbol{T}^p(\boldsymbol{k})$ aient des composantes $\boldsymbol{T}_j^p(\boldsymbol{k})$ telles que (2–11)*. Avec l'ensemble des $\exp i\phi_j^p$ nous pouvons construire une "matrice de phases" Φ ($\Phi_{jp} = \exp i\phi^p$) Soit $\tilde{\Phi}$ la matrice conjuguée et transposée. On aura

$$\tilde{\Phi}\,\zeta(\boldsymbol{k})\Phi = \begin{pmatrix} \sum_j n_j \lambda_j^1 & \cdots & \\ \vdots & \ddots & \\ & & \sum_j n_j \lambda_j^p \end{pmatrix} \qquad (2\text{–}13)$$

Ici n_j est le nombre d'atomes équivalents de l'espèce j dans la maille. On a $\sum_j n_j = n$. Les termes diagonaux représentent au facteur -2 près l'énergie d'un mode p. Nous sommes maintenant en mesure de discuter quelques points particuliers.

2.1. *Réseaux de Bravais*

Dans ce cas (2–4) se réduit au résultat de VILLAIN[1]. La minimisation de (1–1) fournira toujours le résultat correct (cf. cube centré. 3).

2.2 *Réseaux à n atomes magnétiques équivalents*

Les termes λ_i de la matrice (λ) sont tous égaux. Le problème est ramené à celui de la recherche des valeurs et vecteurs propres d'une matrice d'ordre n (exemple Fe_2O_3-α ; Cr_2O_3·4)

2.3. *Mailles magnétiques et chimiques identiques*

Dans ce cas on peut poser $\boldsymbol{k} = 0$. Les relations (2–12) et (1–4) montrent alors que le problème de la recherche d'un vecteur propre est ramené à celui de la recherche de $n-1$ phases ϕ_j. $\boldsymbol{\sigma}_j$ et $\boldsymbol{T}_j(0)$ s'identifient alors (2–7). *Le nombre de modes possibles conservant la maille est egal à n, nombre de réseaux de Bravais.*

Remarque : Il est encore possible de résoudre le même problème avec un vecteur $\boldsymbol{k} \neq 0$, vecteur entier de l'espace réciproque (vecteur non réduit à la première zone de Brillouin). On perd alors l'avantage de la relation $\boldsymbol{\sigma}_j = \boldsymbol{T}_j(0)$, mais l'intuition géométrique y gagne en ce que les composantes entières [*hkl*] du vecteur $\boldsymbol{k}$ indiquent dans quels plans réticulaires (*hkl*) les spins sont en phase. Exemple : Dans les spinelles le mode ferrimagnétique classique des spins sur les réseaux $a_1, a_2, b_1, b_2, b_3, b_4$, peut être décrit par le vecteur $\boldsymbol{T}(0) = (-1, -1\ ;\ 1,\ 1,\ 1,\ 1)$, mais aussi par $\boldsymbol{k} = [400]$ ou $[444]$ et $\boldsymbol{T}(\boldsymbol{k}) = (1, 1\ ;\ 1, 1, 1, 1)$ ce qui indique que les spins dans les plans (400) et (444) sont en phase. Les deux descriptions sont naturellement équivalentes.

Cette grande flexibilité de la méthode permet d'employer deux variantes, soit la recherche de n racines et vecteurs propres $\boldsymbol{T}(0)$ par la diagonalisation complète de la matrice réelle $\zeta(0)$, soit la recherche (sans diagonalisation) d'une *seule* racine $\lambda(\boldsymbol{k})$, les différents modes étant trouvés en différentiant $\lambda(\boldsymbol{k})$ par rapport à $\boldsymbol{k}$ (cf. Fe_2O_3-α · 4).

2.4. *Relation avec la théorie des groupes*

On considère le cas 2.2. avec $\boldsymbol{k} = 0$. Le coefficient C_{ij} dans (1–1) connecte un spin $\boldsymbol{\sigma}_i$ avec un spin $\boldsymbol{\sigma}_j$. Ces spins sont reliés par une opération de symétrie C telle que $\boldsymbol{\sigma}_j = C\boldsymbol{\sigma}_i$. Dans le système matriciel (2–5) (2–6) le coefficient de C_{ij} (c'est à dire d'une même intégrale d'échange) est précisément la matrice représentative de l'opérateur C appliqué aux n spins équivalents (cf. Fe_2O_3-α · 4) Réciproquement (et cela peut être considéré comme une définition), tous les spins $\boldsymbol{\sigma}_i$ et $\boldsymbol{\sigma}_j$ reliés par une même distance et même opération ou suite d'opérations de symétrie appartiennent à la même intégrale d'échange, au même coefficient C_{ij}.

Les vecteurs propres de la matrice $\zeta(0)$ sont les combinaisons linéaires de spins décrivant une configuration. Lorsque les racines de $\zeta(0)$ sont toutes distinctes, les vecteurs propres de $\zeta(0)$ restent invariants dans toutes les opérations de symétrie considérées (cf. Fe_2O_3-α · 4). Lorsqu'une racine est q fois dégénérée, les q vecteurs propres correspondants forment un sousespace invariant

* Nous verrons (cf. spinelles, modes {B}) que cela n'est pas toujours possible dans certains modes que nous appellerons "modes incomplets".

ol. 21
1961

de dimension q; les opérateurs C du groupe transforment les q vecteurs en eux et entre eux. Ces remarques relient immédiatement la méthode de DZYALOSHINSKI[4] et TUROV[5] à la nôtre. En effet, il revient au même de dire que les n spins forment une base réductible et que l'on cherche la base des représentations irréductibles. En un mot, la théorie des groupes permet de connaître *a priori* les combinaisons irréductibles de spins, leurs sousespaces invariants, c'est à dire (sans resoudre $\zeta(0)$) les vecteurs propres de $\zeta(0)$ et le degré de dégénérescence de ses racines.

D'une manière concise, on peut énoncer la proposition suivante :

Si pour une valeur propre λ et un vecteur propre correspondant $\boldsymbol{T}(0)$, $\zeta(0)$ reste invariant dans une opération de symétrie C $[C^{-1}\,\zeta(0)\;C = \zeta(0)]$, alors $\boldsymbol{CT}(0)$ est aussi un vecteur propre de même valeur propre λ [Réciproquement, si λ est une racine non dégénérée, $\boldsymbol{T}(0)$ est invariant dans toutes les opérations de symétrie considérées qui entrent dans la matrice $\zeta(0)$].

Remarque : Un mode trivial, correspondant à la representation identité, existant toujours pour $\boldsymbol{k} = 0$, est le mode ferromagnétique. Inversement, dans des réseaux de spins ordonnés, il n'y a pas de ferromagnétisme quand la maille chimique et magnétique ne coincident pas (Si $\boldsymbol{k}$ est un vecteur réduit et $\boldsymbol{k} \neq 0$ on a

$$\sum_R \boldsymbol{\sigma}_R = 0).$$

2.5. *Couplage de systèmes*

Considérons un ensemble $\{A\}$ de n_A spins équivalents, couplé à un ensemble $\{B\}$ de n_B spins équivalents par des intégrales d'échange. La matrice $\zeta(\boldsymbol{k})$ du système couplé $\{AB\}$ aura la forme

$$\zeta(\boldsymbol{k}) = \left(\begin{array}{c|c} \zeta_A & \zeta_{AB} \\ \hline \zeta_{BA} & \zeta_{\ B} \end{array}\right) \qquad (2\text{–}14)$$

où ζ_{AB} est une matrice $n_A \times n_B$ de couplage.

Supposons connus les n_A vecteurs propres $\boldsymbol{A_j}$ $(j = 1, \ldots, n_A)$ de ζ_A et les n_B vecteurs propres $\boldsymbol{B_j}$ $(j = 1, \ldots, n_B)$ de ζ_B. L'ensemble des n_A+n_B vecteurs propres constitue un système complet. Donc les n_A+n_B vecteurs propres du système couplé $\{AB\}$ doivent être des combinaisons linéaires des vecteurs $\boldsymbol{A_j}$ et $\boldsymbol{B_j}$. Les combinaisons linéaires correctes sont celles qui diagonalisent la matrice de perturbation (p) (voir sous spinelles et grenats 5 et 6).

$$(p) = \left(\begin{array}{c|c} 0 & \zeta_{AB} \\ \hline \tilde{\zeta}_{AB} & 0 \end{array}\right) \qquad (2\text{–}15)$$

Des systèmes plus complexes $\{ABC\}$ peuvent être étudiés de la même façon, en réduisant d'abord $\{AB\}$ et en couplant ensuite avec $\{C\}$.

Considérons $\boldsymbol{k} = 0$ et soient $\boldsymbol{A}_1(0)$ et $\boldsymbol{B}_1(0)$ les modes ferromagnétiques de $\{A\}$ et de $\{B\}$. C'est parce que ces modes ferromagnétiques sont toujours vecteurs propres de $\zeta_A(0)$ et de $\zeta_B(0)$ respectivement que les modes $\boldsymbol{A}_1(0)+\boldsymbol{B}_1(0)$ et $\boldsymbol{A}_1(0)-\boldsymbol{B}_1(0)$ peuvent être vecteurs propres de $\zeta(0)$ (2–14). C'est à cette circonstance que le ferrimagnétisme de Néel doit sa généralité.

A partir des équations (2–2) ou (2–4) on démontre facilement que l'énergie de couplage H_{AB} se partage également entre $\{A\}$ et $\{B\}$ en d'autres termes dans les expressions de $n_A\lambda_A$ et $n_B\lambda_B$ d'un mode déterminé de vecteur $\boldsymbol{k}$ les $C_{A_iB_j}$ ont les mêmes coefficients numériques.

2.6. *Mélange de configuration*

On explorera dans ce mémoire uniquement les conséquences de l'hypothèse U, c'est à dire on étudiera les modes fondamentaux correspondant à un vecteur de propagation $\boldsymbol{k}$. Nous laissons donc de côté des superpositions de modes $\boldsymbol{k}_1$, $\boldsymbol{k}_2$ etc. traités dans les spinelles par KAPLAN[2]. Aussi longtemps que nous nous limitons aux interactions isotropes des intégrales d'échange et en absence de dégénérescence nous ne rencontrerons pas de mélanges de configurations pour $\boldsymbol{k}$ fixé tels que par exemple un mode antiferromagnétique associé à un mode ferromagnétique (ferromagnétisme parasite de Fe_2O_3-α). L'auteur a considéré ailleurs l'influence d'interactions anisotropes.[6]

La seule exception est celle de la dég nérescence accidentelle qui donne lieu au couplage de YAFET et KITTEL[7] (voir spinelles et grenats).

2.7. *Recherche d'une solution par minimisation directe de H* (1–1)

On peut se demander dans quelle mesure une solution trouvée p r la minimisation de (1–1) compte tenu de (1–3, 4) est valable dans le cas général. La résponse est simple. Il faut que la

Vol. 2
1961

solution vérifie les équations générales d'équilibre (2–2) à (2–4). Il faut en particulier vérifier que les paramètres λ_j appartenant à des points équivalents soient égaux (Exemple : Sur les 4 sous-réseaux b_j ($j = 1, ..., 4$) des sites octaédriques d'un spinelle cubique on doit avoir une même valeur λ_b).

2.8. *Comparaison avec d'autres méthodes*

On obtient les mêmes équations (2–2) en minimisant l'hamiltonien (1–1) sous les "conditions fortes" (strong conditions de LUTTINGER et TISZA[8]) S_j^2 = constant et en introduisant des paramètres de Lagrange λ_j. D'autres auteurs[3] se contentent des "conditions faibles" (weak conditions[8]) en posant $\sum S_j^2$ constant et cherchent ensuite si la solution trouvée vérifie aussi la condition forte.

KAPLAN[2], LYONS et KAPLAN[9], dans le cas de systèmes couplés $\{AB\}$ cherchent à relier directement les modes aux racines de la matrice du système couplé alors que nous considérons séparément les modes de $\{A\}$ et de $\{B\}$ (Les racines de $\zeta(\boldsymbol{k})$ (2–14) n'interviennent pas dans nos considérations).

Notre méthode, basée sur les équations de mouvement (2–1) a l'avantage de respecter les conditions fortes[8] dans tous les cas et de donner une interprétation directe des paramètres scalaires λ_j, mettant bien en évidence leur caractère d'invariance dans les opérations de symétrie.

2.9. *Stabilité des modes*

Pour que $(\lambda)_s$ caractérise un mode stable il faut et il suffit que la matrice

$$M(\boldsymbol{dk}) = (\lambda)_s - \zeta(\boldsymbol{k}_o + \boldsymbol{dk}) \qquad (2\text{–}16)$$

ait des racines toutes positives pour des variations arbitraires $\boldsymbol{dk}$. Nous n'envisageons que le cas de très petites variations $\boldsymbol{dk}$. Pour simplifier davantage, considérons le cas 2.2. On a alors pour des modes complets et faisant tendre $\boldsymbol{dk}$ vers zero

$$\tilde{\Phi}(\lambda_s - \zeta(\boldsymbol{k}_o)\Phi = n \begin{pmatrix} \lambda_s-\lambda_1 & & \\ & \ddots & \\ & & \lambda_s-\lambda_n \end{pmatrix} \qquad (2\text{–}17)$$

Pour que l'état s soit stable il faut que

$$\lambda_s - \lambda_p > 0 \qquad (2\text{–}18)$$

quelque soit p. Cela revient simplement à comparer les énergies des modes.

Supposons que l'on sache diagonaliser $M(\boldsymbol{dk})$ (2–16) au moins partiellement en sous-matrices. Chaque sousmatrice doit avoir un déterminant positif ou nul quand $\boldsymbol{dk}$ tend vers zero. Soit alors $m(\boldsymbol{dk})$ la plus petite sousmatrice dont le déterminant s'annulle quand $\boldsymbol{dk} = 0$. Il est toujours possible de définir $m(\boldsymbol{dk})$ en fonction d'une variable q, définie positive, telle que $q \to 0$ quand $\boldsymbol{dk} \to 0$ et telle que

$$|m(\boldsymbol{dk})| = qf(q) \qquad (2\text{–}19)$$

Il faut alors que $|m(\boldsymbol{dk})|$ croisse pour $\boldsymbol{dk} \neq 0$, c'est à dire que

$$\left(\frac{d|m|}{dq}\right)_{q=0} > 0 \quad \text{ou} \quad f(0) > 0 \qquad (2\text{–}20)$$

Les conditions obtenues s'expriment par des relations d'inégalites entre intégrales d'échange (cf. Fe_2O_3 • 4.)

3. CUBE CENTRE

La description suivante est plus détaillée que celle donnée par KAPLAN[15], l'auteur[10] et par COOPER[11].

Nous tiendrons compte des 8 premiers voisins ($\pm\frac{1}{2}$, $\pm\frac{1}{2}$, $\pm\frac{1}{2}$), des 6 voisins seconds [(± 1, 0, 0)+ ⟩] et des 12 troisièmes voisins [(± 1, ± 1, 0)+ ⟩]. L'énergie d'échange sera

$$H = -2S^2[8J_1(\cos X \cos Y \cos Z) + 2J_2 \times (\cos 2X + \cos 2Y + \cos 2Z) + 4J_3(\cos 2X \cos 2Y + \cos 2Y \cos 2Z + \cos 2Z \cos 2X)] \qquad (3\text{–}1)$$

$$\text{où } X = \pi h \; ; \quad Y = \pi k \; ; \quad Z = \pi l \qquad (3\text{–}2)$$

Les différents modes et conditions de stabilité sont obtenus par minimisation de H.

3.1. *Modes colineaires*

Mode [000]. C'est le mode ferromagnétique classique.

$$J_1 + J_2 + 4J_3 > 0 \qquad (3\text{–}3)$$

$$H[000] = -4S^2(4J_1 + 3J_2 + 6J_3) \qquad (3\text{–}4)$$

Mode [111]. C'est le mode antiferromagnétique classique du type CsCl.

$$-J_1+J_2+4J_3 > 0 \qquad (3\text{–}5)$$

$$H[111] = -4S^2(-4J_1+3J_2+6J_3) \qquad (3\text{–}6)$$

Mode $[\frac{1}{2}, \frac{1}{2}, 0]$. Dans ce mode antiferromagnétique, la maille est à doubler selon a et b. Tout mode $[p/2, q/2, r]$ a ec $p = 2n+1$, $q = 2+1$ et r entier ainsi que ceux formés par la permutation de ces nombres, est équivalent. Les conditions de stabilité sont

$$J_2 < 0\,; \quad J_2-4J_3 > 0\,; \quad (J_2+J_1)(J_2-J_1) > 0 \qquad (3\text{–}7)$$

l'énergie de ce mode est indépendante de J_1. On vérifie effectivement par (2–7) qu'à tout voisin proche correspond un autre voisin proche de direction opposée. On a :

$$H\,[\tfrac{1}{2}\tfrac{1}{2}0] = 4S^2(J_2+2J_3) \qquad (3\text{–}8)$$

Mode $[\frac{1}{2}\,\frac{1}{2}\,\frac{1}{2}]$. Dans ce mode antiferromagnétique, la maille est à doubler dans les trois sens. L'énergie est indépendante de J_1. La seule condition de stabilité est

$$J_2-2J_3 < 0 \qquad (3\text{–}9)$$

$$H\,[\tfrac{1}{2}\tfrac{1}{2}\tfrac{1}{2}] = 12S^2(J_2-2J_3) \qquad (3\text{–}10)$$

Les 4 modes ont déjà été décrits par SMART[12] et numérotés 1, 3, 4, 8 par GERSCH et KOEHLER[13].

Ce sont les seuls modes stables colinéaires que (3–1) permet de trouver. Il est très instructif de distinguer deux cas selon que $J_3 > 0$ ou < 0.

(a) $J_3 > 0$. Le mode $[\frac{1}{2}\,\frac{1}{2}\,0]$ n'est pas stable. Faisant abstraction de l'existence possible de modes spiralés, nous déterminons les domaines d'existence dans un diagramme de variables

$$x = J_1/J_3\,; \quad y = J_2/J_3 \qquad (3\text{–}11)$$

en utilisant les critères de stabilité, de comparaison et de négativité des énergies des seuls modes colinéaires. On trouve alors que les régions de stabilité des modes [000] [111] et $[\frac{1}{2}\frac{1}{2}\frac{1}{2}]$ et *remplissent tout le plan* (Fig. 1). Il en est tout autrement dans le cas où.

(b) $J_3 < 0$. Avec la même représentation (xy). *on remarque que les* 4 *régions délimitées ne couvrent pas tout le plan.* (cf. Fig. 2a). Cela est un indice sérieux en faveur de l'existence de modes non colinéaires, comblant les régions vides.

3.2. *Modes spirales*

Nous considérons les modes [*h*00], [*hh*0], [*hh*1] et [*hhh*].

Mode [*h*00].

$$\cos X = -x/(y+4)\,;$$

$$H[h\,0\,0] = 4S^2J_3[2-y+2x^2/(y+4)] \qquad (3\text{–}12)$$

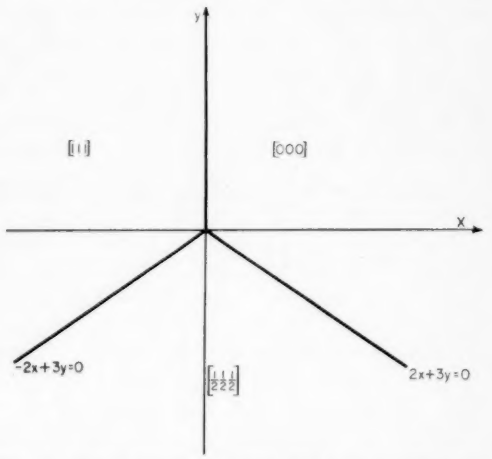

FIG. 1. Cube centré. Stabilité des modes colinéaires $J_3 > 0$.

L'existence de cos X et les conditions de stabilité imposent les inégalités

$$H(x+y+4)\,(Y-x+y+4) > 0 \qquad (3\text{–}13)$$

$$y < 0\,; \quad y+4 > 0 \qquad (3\text{–}14)$$

qui délimitent justement une région du plan (x,y) laissée vide par les modes colinéaires. C'est ce mode qui a été préconisé par KAPLAN[15] pour expliquer le diagramme de diffraction de Cr obtenu par CORLISS *et al.*[14]. La différence d'énergies des modes [*h*00] et [111] est

$$H[h00]-H[111] = 8S^2(J_2+4J_3)(1+\cos X)^2 \qquad (3\text{–}15)$$

CORLISS *et al.* ont observé une périodicité d'environ 28 mailles cristallographiques. Cela correspond à un angle $X = \pi+\eta$ tel que $2\pi 28h = 56\ X = 360+2n\pi$. On en déduit $\eta = 6°25'$.

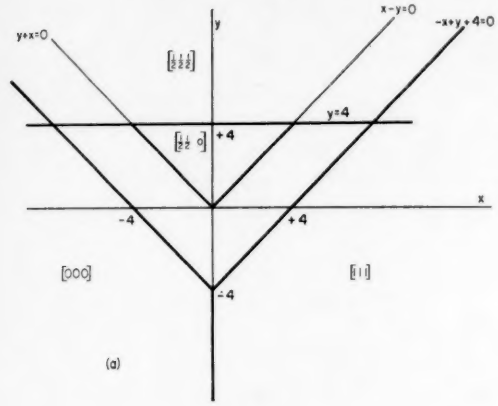

(a)

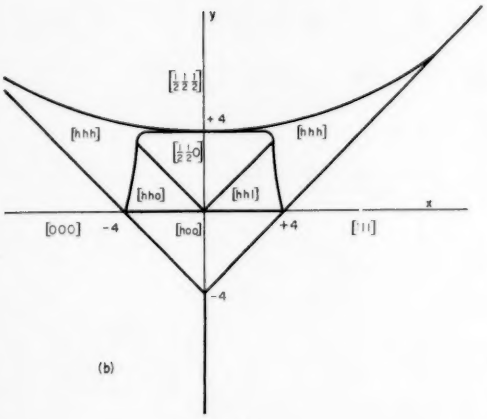

(b)

FIG. 2. Cube centré. Stabilité des modes pour $J_3 < 0$.
(a) modes colinéaires, non compte tenu de l'existence de modes spirales
(b) diagramme complet.

$\cos X = -0{,}9937$ est donc très voisin de -1 de sorte que

$$\Delta H/H < 2(1+\cos X)^2 \sim 0{,}8 \cdot 10^{-4} \quad (3\text{–}16)$$

en accord avec l'estimation de KAPLAN[15]. La très faible différence d'énergie explique peut-être la grande sensibilité de la structure aux impuretés et l'intervention probable d'autres facteurs.

Mode [*hh*0].

$$\cos 2X = -1-(x+y)/4 \quad (3\text{–}17)$$

$$H[hh0] = 2S^2J_3[2y+4+(x+y)^2] \quad (3\text{–}18)$$

Les conditions de stabilité sont

$$x < 0 \; ; \quad y > 0 \quad (3\text{–}19)$$

et

$$(x+y)(x+y+4) < 0 \; ; \quad (x+4)(x+y+4) > 0 \quad (3\text{–}20)$$

Mode [*hh*1].

$$\cos 2X = -1-(-J_1+J_2)/2J_3 \quad (3\text{–}21)$$

$$H[hh1] = 2S^2J_3[2y+4+(y-x)^2] \quad (3\text{–}22)$$

Ce mode dérive du précédent par le changement de J_1 en $-J_1$. Le domaine d'existence (Fig. 2b) est donc symétrique de celui de [*hh*0] par rapport à l'axe des y.

Mode [*hhh*]. En dérivant (3–1) par rapport à X, Y, Z, et en posant $X = Y = Z$ on obtient une équation quadratique en cos X dont les solutions sont

$$\cos X_1 = -(x/16)-\Delta^{1/2} \; ; \; \cos X_2 = -x/16+\Delta^{1/2} \quad (3\text{–}23)$$

où

$$\Delta = (x/16)^2+\tfrac{1}{2}-y/8 \quad (3\text{–}24)$$

Les racines cos X_1 avec $x > 0$, et cos X_2 avec $x < 0$ existent dans la region délimitée par la parabole (3–24) ($\Delta > 0$; côté origine) et par l'inégalité

$$(y-x+4)(y+x+4) > 0 \quad (3\text{–}25)$$

L'énergie prend les valeurs

$$H = \tfrac{1}{2}S^2J_3[\Delta(16\sqrt{(\Delta)} \pm x)^2-(y-8)^2+8y] \quad (3\text{–}26)$$

où le signe + correspond à cos X_1, le signe − à cos X_2. Les critères de stabilité sont toujours vérifiés pour $J_3 < 0$ et les racines étudiées. L'analyse des racines cos X_1 avec $x < 0$ et cos X_2 avec $x > 0$ montre que dans notre diagramme $J_3 < 0$ elles n'ont aucun domaine de stabilité.

Nous n'avons pas étudié la possibilité d'existence de modes d'ordre plus élevé.

En conclusion, les modes spirales étudiés comblent exactement des regions laissées vides par les modes colinéaires dans le diagramme de la Fig. 2(a).

Vol. 21
1961

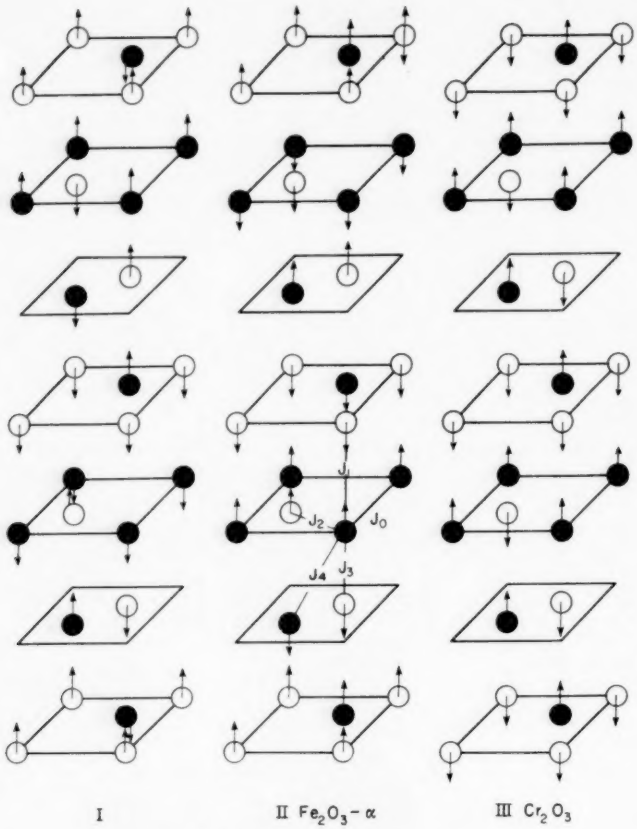

FIG. 3. Structures du type corindon
○ atomes en $z(1)$ et $\frac{1}{2}+z(2)$
● atomes en $\bar{z}(3)$ et $\frac{1}{2}-z(4)$

Le mode IV ferromagnétique n'est pas présenté.

Les mêmes figures sont valables pour les ilménites $TiMO_3$ (M = métal de transition bivalent). Mode II ($TiNiO_3$). Mode III ($TiMnO_3$).

4. STRUCTURES DU TYPE CORINDON

Fe_2O_3-α et Cr_2O_3 bien que isotypes de Al_2O_3-α ont des arrangements de spin différents[16, 17] (Fig. 3). Nous allons retrouver leurs modes comme solutions d'une même matrice. L'étude des conditions de stabilité révèlera les interactions responsables de la différence des structures. Les cations occupent les positions (en notation hexagonale) $00z$ (1), $00,z+\frac{1}{2}$ (2), $00\bar{z}$(3) et $00,\bar{z}+\frac{1}{2}$ (4). Les nombres entre parenthèses numérotent les réseaux de Bravais. Dans la description de PAULING et HENDRICKS[18] $z = 0{,}105$ pour Fe_2O_3-α ; les centres de symétrie ne sont pas à l'origine, mais en $(0\frac{1}{4}$ et $00\frac{3}{4}$. Les voisins de l'atome (1), leurs distances et appartenances aux sousréseaux 1 à 4 ainsi que leurs intégrales d'échange sont spécifiés dans le Tableau 1 qui permet d'écrire la première des équations du système matriciel (4–1). On construit des tableaux analogues pour (2) (3) et (4). Le système

Tableau 1. *Voisinage de* 00z

Nombre	Coordonnées	Distance	Intégrale d'échange	Réseau
6	$1, 0, z$; $\bar{1}, 0, z$; $0, 1, z$; $0, \bar{1}, z$; $1, 1, z$; $\bar{1}, \bar{1}, z$.	5,023	J_0	1
3	$\frac{1}{3}, \frac{2}{3}, z+\frac{1}{6}$; $\frac{1}{3}, \overline{\frac{1}{3}}, z+\frac{1}{6}$; $\overline{\frac{2}{3}}, \overline{\frac{1}{3}}, z+\frac{1}{6}$	3,693	J_4	2
3	$\overline{\frac{1}{3}}, \overline{\frac{2}{3}}, z-\frac{1}{6}$; $\overline{\frac{1}{3}}, \frac{1}{3}, z-\frac{1}{6}$; $\frac{2}{3}, \frac{1}{3}, z-\frac{1}{6}$			
1	$0, 0, \bar{z}$.	2,88	J_1	3
3	$\overline{\frac{1}{3}}, \overline{\frac{2}{3}}, \frac{1}{3}-z$; $\overline{\frac{1}{3}}, \frac{1}{3}, \frac{1}{3}-z$; $\frac{2}{3}, \frac{1}{3}, \frac{1}{3}-z$.	3,36	J_3	3
3	$\frac{1}{3}, \frac{2}{3}, \frac{1}{6}-z$; $\frac{1}{3}, \overline{\frac{1}{3}}, \frac{1}{6}-z$; $\overline{\frac{2}{3}}, \overline{\frac{1}{3}}, \frac{1}{6}-z$.	2,96	J_4	4

(2–5) prend la forme

$$M(\boldsymbol{k})\boldsymbol{T}(\boldsymbol{k}) = \begin{pmatrix} A-\lambda & B & C & D \\ B & A-\lambda & D & C \\ C^* & D^* & A-\lambda & B \\ D^* & C^* & B & A-\lambda \end{pmatrix} \begin{pmatrix} \boldsymbol{T}_1 \\ \boldsymbol{T}_2 \\ \boldsymbol{T}_3 \\ \boldsymbol{T}_4 \end{pmatrix} = 0 \qquad (4\text{–}1)$$

Ici, A, B (réels), C et D (complexes) sont des expressions, linéaires dans les intégrales d'échange, données dans l'Appendice A.3.

4.1. *Première méthode*

Transformant $M(\boldsymbol{k})$ par la matrice

$$U = \begin{pmatrix} 1 & . & -1 & . \\ 1 & . & 1 & . \\ . & 1 & . & -1 \\ . & 1 & . & 1 \end{pmatrix} \Big/ \sqrt{(2)} \qquad (4\text{–}2)$$

on obtient une diagonalisation partielle

$$M' = U^{-1}MU = \begin{pmatrix} M_1 & . \\ . & M_2 \end{pmatrix} \qquad (4\text{–}3)$$

où

$$M_{1,2} = \begin{pmatrix} A \pm B-\lambda & C \pm D \\ C^* \pm D^* & A \pm B-\lambda \end{pmatrix} \qquad (4\text{–}4)$$

le signe + tenant pour M_1, et − pour M_2. De $|M_1| = 0$ on déduit une racine

$$\lambda = A+B+(C\,C^*+D\,D^*+C\,D^*+D\,C^*)^{1/2} \qquad (4\text{–}5)$$

L'inspection de (4–1) montre d'ailleurs que $\boldsymbol{T}_1 = \boldsymbol{T}_2$; $\boldsymbol{T}_3 = \boldsymbol{T}_4$ est certainement une solution ce qui aurait donné lieu à (4–5) d'une façon plus immédiate.

Il suffit de différentier (4–5) par rapport à $\boldsymbol{k}$ pour trouver les solutions possibles. Le Tableau 2 résume les 4 modes colinéaires ainsi trouvés. L'étude de M_2 n'apporte rien de nouveau à ce point de vue (ce que le lecteur pourra prouver à titre d'exercice). De même les conditions de stabilité du Tableau 3 peuvent être trouvées en écrivant que la forme quadratique formée par les dérivées secondes de $-\lambda$ par rapport aux composantes de $\boldsymbol{k}$ est définie positive.

Montrons cependant sur le mode II du Tableau 2 que la méthode matricielle de recherche de conditions de stabilite conduit aux mêmes résultats. On a

$$\lambda_{II} = 6J_0+3J_2-(J_1+3J_3+6J_4) \qquad (4\text{–}6)$$

Cette racine annulle le déterminant M_1 pour $\boldsymbol{k} = [003]$ de sorte que la méthode decrite sous 2–9 devient applicable. Avec les notations de l'Appendice A.3 on trouve alors

$$|m| = |M_1| = (\lambda-A-B)^2-|C+D|^2$$
$$= 6q[6J_4^2q-6J_2J_4+(J_1+3J_3)(2J_4-J_2)$$
$$+2(2-q)J_1J_3] \qquad (4\text{–}7)$$

Tableau 2. *Solutions colinéaires appartenant à* $\lambda(\boldsymbol{k})$ (4–5)

Valeur propre	Coefficients de Néel		Vecteur de propagation	Vecteur propre		Structure
	n'	n		$T_1 = T_2$;	$T_3 = T_4$	
$\lambda_{\mathrm{I}} =$	$6J_0+J_1+3J_3$	$-(3J_2+6J_4)$	[003]	α	α^*	—
$\lambda_{\mathrm{II}} =$	$6J_0+3J_2$	$-(J_1+3J_3+6J_4)$	[003]	α	$-\alpha^*$	Fe_2O_3-α
$\lambda_{\mathrm{III}} =$	$6J_0+6J_4$	$-(J_1+3J_2+3J_3)$	[000]	1	−1	Cr_2O_3
$\lambda_{\mathrm{IV}} =$	$6J_0+6J_4$	$+(J_1+3J_2+3J_3)$	[000]	1	1	—

$\alpha = \exp(-2\pi i l z)$

Tableau 3. *Conditions de stabilité*

Mode			
I	$J_1+3(J_3-J_2)>0$;	$-6J_0+2J_4+J_2-J_3<0$;	$2J_4(J_1+3J_3-3J_2)+J_2(J_1+3J_3)-4J_1J_3<0$
II	$J_1+3(J_3-J_2)<0$;	$-6J_0+2J_4-J_2+J_3<0$;	$-2J_4(J_1+3J_3-3J_2)+J_2(J_1+3J_3)-4J_1J_3<0$
III	$J_1+3(J_3+J_2)<0$;	$-6J_0-2J_4+J_2+J_3<0$;	$2J_4(J_1+3J_3+3J_2)-J_2(J_1+3J_3)-4J_1J_3<0$
IV	$J_1+3(J_3+J_2)>0$;	$6J_0+2J_4+J_2+J_3>0$;	$2J_4(J_1+3J_3+3J_2)+J_2(J_1+3J_3)+4J_1J_3>0$

où l'on a posé

$$q = 1+\cos \pi l/3 \qquad (4\text{–}8)$$

q tend vers zéro quand l tend vers 3 et est défini positif partout ailleurs. On vérifie que la condition

$$\left(\frac{d|m|}{dq}\right)_{q=0} > 0 \qquad (2\text{–}20)$$

reproduit l'inégalité d'ordre deux figurant au Tableau 3, mode II.

4.2. *Deuxième méthode*

On peut diagonaliser la matrice réelle $\zeta(0)$ par la matrice de phases

$$\Phi = \begin{pmatrix} 1 & 1 & 1 & 1 \\ 1 & -1 & 1 & -1 \\ 1 & 1 & -1 & -1 \\ 1 & -1 & -1 & 1 \end{pmatrix} \qquad (4\text{–}9)$$

dont les vecteurs colonnes sont les modes $\boldsymbol{T}(0)$ fournissant directement la configuration des spins. L'ordre des colonnes correspond aux modes IV (ferromagnétiques), I, III et II du Tableau 2.

Si nous désignons les matrices, coefficients de A, B, C, D dans $\zeta(0)$ par les mêmes lettres on verifie immédiatement leur nature binaire pour (B), (C) et (D), car $(B)^2 = (C)^2 = (D)^2 = (1)$. Le coefficient de D (4–10) est la matrice représentative de l'inversion $(\bar{\boldsymbol{1}})$ qui réalise la substitution $1 \rightleftarrows 4$, $2 \rightleftarrows 3$.

$$(D) = \begin{pmatrix} . & . & . & 1 \\ . & . & 1 & . \\ . & 1 & . & . \\ 1 & . & . & . \end{pmatrix} \qquad (4\text{–}10)$$

De même (C) représente l'axe d'ordre **2** passant par l'origine. On vérifie que $(B) = (C)\,(D)$. On aurait pu aussi bien trouver *a priori* les vecteurs

propres en cherchant les combinaisons linéaires de spins invariantes dans les opérations $(\bar{I})$ et **2**.

4.3. *Discussion des modes. Stabilité du mode de* Fe_2O_3

Le mode I n'a pas encore été observé. Le mode II est celui de Fe_2O_3-α, le mode III celui de Cr_2O_3. On passe du mode II au mode III par la substitution $J_2 \to -J_2$, $J_4 \to -J_4$.

Ce qui distingue principalement les structures est le signe de la quantité J_2-2J_4, positive dans Fe_2O_3-α, négative dans Cr_2O_3. L'expérience[19] fournit les combinaisons $n = -687$ et $n' = -183$ des intégrales d'échange où n est le coefficient de champ moléculaire[20] *entre* les sousréseaux de Néel et n' est le coefficient *dans* un sousréseaux de Néel. Les sousréseaux de Néel sont les sommes des réseaux de Bravais ayant la même orientation de spins. Si nous exprimons les intégrales d'échange J_j dans les mêmes unités que n et n', on a (en négligeant J_0)

$$J_2 = n'/3 = -61$$

$$J_1+3J_3+6J_4 = -687 = n \qquad (4\text{–}11)$$

De plus, éliminant dans les inégalités du Tableau 3, mode II, J_2 et J_4 par exemple, on trouve que la région permise pour J_1 et $3J_3$ est délimitée par les inégalités suivantes

$$J_1 > n-n' \; ; \quad n-n' < J_1+3J_3 < n'$$

$$-(J_1-3J_3)^2+n(J_1+3J_3)-nn' > 0 \qquad (4\text{–}12)$$

Le graphique (Fig. 4) montre la région permise dans Fe_2O_3-α. On trouve de même

$$(n-n')/6 < J_4 < n'/6 \qquad (4\text{–}13)$$

En résumé toutes les interactions dans Fe_2O_3-α (J_1 à J_4) sont négatives et les conditions de stabilité permettent d'en limiter les intervalles d'existence (cf. Réfs. 21, 22).

Ilménites $MTiO_3$

Ce que nous venons de dire des structures du type corindon peut se transposer mot à mot pour les structures du type $MTiO_3$ où M est un métal de transition bivalent. Même les dessins (Fig. 3) et conditions de stabilité du Tableau 3 sont encore valables à condition de sousentendre que les plans porteurs de Ti ont été supprimés et que les intégrales J_j pour $j = 1$, 3 et 4 sont des intégrales de super-superéchange. C'est ainsi que $MnTiO_3$ a la structure de Cr_2O_3, $NiTiO_3$ celle de Fe_2O_3-α.[23]

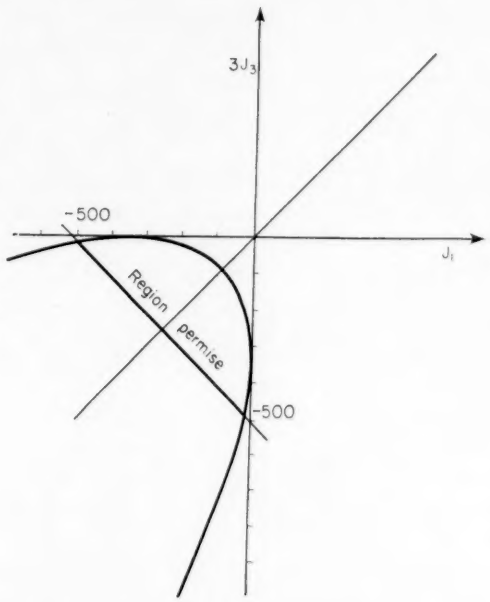

FIG. 4. Domaine d'existence des intégrales d'échange dans Fe_2O_3.

La région permise aux paramètres J_1 et $3J_3$ est limitée par une parabole et une droite.

5. SPINELLES CUBIQUES

Le problème a été considéré souvent[7, 20] et récemment par KAPLAN[2] dans le but de trouver l'état fondamental.* Notre but est plus modeste. Nous considérons ici le spinelle comme un exemple d'un couplage de deux systèmes $\{A\}$ et $\{B\}$. Nous traitons *séparément* les modes des sites tétraédriques $\{A\}$ (000 ; $\frac{111}{444}$) et des sites octaédriques $\{B\}$ [5, 5, 5 ; 5, 3, 3, ; 3, 5, 3 ; 3, 3, 5 en huitièmes ; positions abrégées b_j ($j = 1, ..., 4$)]. Nous étudions ensuite leur couplage en *modes fondamentaux complets*.

* For the English reader : To avoid confusion "état fondamental" means ground state. "Mode fondamental" means a single mode with a definite $\boldsymbol{k}$-vector.

5.1. *Modes de* $\{A\}$

La matrice $\zeta_A(\boldsymbol{k})$ a la forme

$$\zeta_A(\boldsymbol{k}) = \begin{pmatrix} . & a \\ a^* & . \end{pmatrix} \tag{5-1}$$

où

$$a = 4C_{AA}(\cos X \cos Y \cos Z + i \sin X \sin Y \sin Z) \tag{5-2}$$

$$X = \pi h/2\ ; \quad Y = \pi k/2\ ; \quad Z = \pi l/2 \tag{5-3}$$

Les vecteurs propres sont $A_1 = [\exp i(\alpha/2), \exp -i(\alpha/2)]$ et $A_2 = [\exp i(\alpha/2), -\exp -i(\alpha/2)]$, les valeurs propres correspondantes sont $+$ et $-|a|$. α est la phase de $a = |a| \exp i\alpha$. Pour les modes [000], $hh0$], [$h00$], les vecteurs propres se réduisent à (1, 1) et (1, −1).

5.2. *Modes de* $\{B\}$

La matrice $\zeta_B(\boldsymbol{k})$ a la forme

$$\zeta_B(\boldsymbol{k}) = 2C_{BB} \begin{pmatrix} . & b & c & d \\ b & . & e & f \\ c & e & . & g \\ d & f & g & . \end{pmatrix} \tag{5-4}$$

où $b = \cos(X+Y)\ ;\quad c = \cos(Z+X)\ ;$

$$d = \cos(Y+Z)$$

$$e = \cos(Y-Z)\ ;\quad f = \cos(Z-X)\ ;$$

$$g = \cos(X-Y) \tag{5-5}$$

(a) $\boldsymbol{k} = 0$. Les coefficients de la matrice (5–4) sont tous égaux à l'unité. On diagonalise au moyen de la matrice Φ (4–9) qui intervient souvent dans le problème de 4 spins équivalents. Seul le mode trivial ferromagnétique B_1 est invariant ($\lambda_f = 6C_{BB}$). Les 3 modes a.f. $B_2 = (1,-1,1,-1)$; $B_3 = (1,1,-1,-1)$; $B_4 = 1,-1,-1,1)$ ont une racine triplement dégénérée

$$\lambda_{\text{a.f.}} = -2C_{BB} \tag{5-6a}$$

En effet les opérations de l'axe ternaire **3** et $\mathbf{3}^2$ passant par le point $\frac{5}{8}\frac{5}{8}\frac{5}{8}$ transforment les vecteurs $B_{2,3,4}$ entre eux (cf. sous 2.4.) A cause de cette dégénérescence élevée on peut même construire des modèles a.f. non colinéaires. Par exemple le vecteur

$\boldsymbol{B}_t = B_2\boldsymbol{x} + B_3\boldsymbol{y} + B_4\boldsymbol{z}/\sqrt{3}$ (modèle tétraédrique)

est solution. On vérifie que les spins $\boldsymbol{\sigma}_{bj}$ sont dirigés selon les 4 diagonales du cube. On peut aussi construire des *modes incomplets* comme

$B_b = \frac{1}{2}(B_2 - B_4) = (0,0,1,-1)$ (modèle binaire)

et

$B_{\text{tr}} = \frac{1}{2}(r_1B_2 + B_3 + r_2B_4) = (0,1,r_1,r_2)$ (modèle ternaire)

où

$$r_1 = r_2^* = \exp 2\pi i/3$$

(b) *Cas général.* On montre aisément[25] que (5–4) a toujours 2 racines dégénérées (5–6a) (On vérifie simplement que la matrice $\zeta_B(\boldsymbol{k})/2C_{BB} + (1)$ a tous ses mineurs d'ordre 3 identiquement nuls). Les 2 autres racines sont

$$\lambda = 2C_{BB}[1 \pm (1 + \cos 2X \cdot \cos 2Y + \ldots)^{1/2}] \tag{5-6b}$$

(c) *Cas particuliers*

$\boldsymbol{k} = [h00]$: La matrice Φ (4–9) diagonalise encore la matrice (5–4) Les racines non dégénérées, correspondant à B_1 et B_3 sont $\lambda_{1,3} = 2C_{BB}(1 \pm 2\cos X)$. Comme les racines dégénérées $\lambda_{2,4}$ (5–6a) ne dépendent pas de h (cf. 5.2a) *toute spirale* [$h00$] (5–7) *possède la même énergie quelque soit h* (cf. ANDERSON[24]).

$$\boldsymbol{\sigma}_{b_1} = \boldsymbol{x}\cos 5\pi h/4 - \boldsymbol{y}\sin 5\pi h/4 = -\boldsymbol{\sigma}_{b_2}$$

$$\boldsymbol{\sigma}_{b_3} = -\boldsymbol{x}\cos 3\pi h/4 + \boldsymbol{y}\sin 3\pi h/4 = -\boldsymbol{\sigma}_{b_4} \tag{5-7}$$

$\boldsymbol{k} = [hh0]$ (Mode incomplet) : Les modes non dégénérées sont $B_1 = (\cos X, \cos X, 1, 1)$ et $B_3 = (-1,1,0,0)$ $\{\lambda_{1,4} = 2C_{BB}[1 \pm (1 + \cos 2X)]\}$. Les modes dégénérés sont $B_2 = (1,1,-\cos X, -\cos X)$ et $B_4 = (0,0,1,-1)$. *C'est la première fois que nous rencontrons des modes inc mplets* où les vecteurs propres ne se mettent plus sous la forme (2–11).

Remarque : On peut encore construire un mode complet $B = (1,1,-\exp -iX, -\exp iX)$ à l'aide des modes dégénérés $B_{2,4}$. Mais cela n'est pas possible pour B_1 et B_3.

$\boldsymbol{k} = [hhh]$: Mentionnons seulement que dans ses modes, également incomplets, les 2 modes dégénérés ont pour vecteurs propres $(0,1,r_1,r_2)$ et $(0,1,r_2,r_1)$ (cf. sous 5.2a). En résume, nous avons rencontré λ (5–6a) dans des modes complets

Vol. 2
1961

($\boldsymbol{k} = [000]$, $[h00]$, $[hh0]$), et incomplets ($[hh0]$, $[hhh]$). Quand $h \to 0$, on retrouve ces modes comme combinaisons linéaires des vecteurs $B_{2,3,4}$ du cas $\boldsymbol{k} = 0$.

5.3. *Couplage A-B*

La matrice de couplage ζ_{AB} (cf. 2.5.) a la forme

$$\zeta_{AB} = 3\,C_{AB} \begin{pmatrix} \zeta_1 & \zeta_2 & \zeta_3 & \zeta_4 \\ \zeta_1^* & \zeta_2^* & \zeta_3^* & \zeta_4^* \end{pmatrix} \qquad (5\text{–}8)$$

Les fonctions ζ_j ont déjà été données par KOUVEL[26], KAPLAN[2], DE GENNES et VILLAIN[27].

(a) $\boldsymbol{k} = 0$. On a $\zeta_j = 1$ pour $j = 1,2,3,4$. Avec les vecteurs propres connus de $\{A\}$ et de $\{B\}$ nous construisons la matrice

$$\Psi = \begin{pmatrix} (A) & 0 \\ 0 & (B) \end{pmatrix} \qquad (5\text{–}9)$$

Ici

$$(A) = \begin{pmatrix} 1 & 1 \\ 1 & -1 \end{pmatrix} \qquad (5\text{–}10)$$

et (B) est identique à la matrice Φ (4–9)

Ψ ne diagonalise pas encore la matrice de perturbation (p) (2–15), mais

$$(p') = \Psi\,(p)\,\Psi \qquad (5\text{–}11)$$

est relativement vide et ne contient que deux termes $p'_{13} = p'_{31} = 24\ C_{AB}$ ce qui signifie que uniquement les modes de la 1ère et 3ème colonne de Ψ, c'est-à-dire les modes ferromagnétiques A_1 et B_1 interagissent. La matrice (p') est diagonalisée par les vecteurs $\tau_1 = (1,0,1,0,0,0)$ et $\tau_2 = (1,0,-1,0,0,0)$. Les combinaisons correctes de vecteurs propres sont alors

$$T_{AB\mathrm{I}} = \Psi\tau_1 = A_1 + B_1 = (1,1,1,1,1,1)$$
$$T_{AB\mathrm{III}} = \Psi\tau_2 = A_1 - B_1 = (1,1,-1,-1,-1,-1,) \qquad (5\text{–}12)$$

tandis que les autres vecteurs de Ψ (2^e,4^e,5^e,6^e colonne) restent inchangés. Le mode $T_{AB\mathrm{III}}$ est le mode classique ferrimagnétique de Néel. On trouve

$$\lambda_A = 4C_{AA} - 12C_{AB}\ ;\ \lambda_B = 6(C_{BB} - C_{AB}) \qquad (5\text{–}13)$$

L'énergie par unité de formule est

$$H = -2\,(\lambda_A + 2\lambda_B) \qquad (5\text{–}14)$$

On remarque (cf. 2.5) que l'énergie d'intéraction se partage également entre les modes A et B (c'est-à-dire le coefficient de C_{AB} dans λ_A et 2 λ_B est le même).

(b) $\boldsymbol{k} = [h00]$. On a

$$\zeta_1 = \zeta_2 = \zeta_3^* = \zeta_4^* = \tfrac{1}{3}\,(\exp 3iX/2 + 2\exp -iX/2) \qquad (5\text{–}15)$$

Les modes de $\{A\}$ et de $\{B\}$ étant les mêmes que pour $\boldsymbol{k} = 0$, on utilisera la même matrice Ψ (5–9). Les termes non nuls de (p') sont

$$p'_{13} = p'_{31} = 8\,C_{AB}(2\cos X/2 + \cos 3X/2)$$
$$p'_{25} = p'_{52} = 8iC_{AB}(\sin 3X/2 - 2\sin X/2) \qquad (5\text{–}16)$$

(p') est diagonalisé par la matrice (τ) dont les termes non nuls sont

$$\tau_{11} = \tau_{22} = -\tau_{33} = \tau_{13} = \tau_{31} = \tau_{25} = 1$$
$$\tau_{52} = -\tau_{55} = i \qquad (5\text{–}17)$$

La matrice $\Psi\tau$ décrit les modes couplés. La "matrice de phases" du système $\{AB\}$ est finalement

$$\begin{array}{cccccc} 1 & 1 & 1 & . & 1 & . \\ 1 & -1 & 1 & . & -1 & . \\ 1 & i & -1 & 1 & -i & 1 \\ 1 & i & -1 & -1 & -i & -1 \\ 1 & -i & -1 & 1 & i & -1 \\ 1 & -i & -1 & -1 & i & 1 \end{array} \qquad (5\text{–}18)$$

Indiquons les modes par le numéro d'ordre de la colonne. On a

Modes I, III :

$$\lambda_A = 4\,C_{AA}\cos X \pm p'_{13}/2$$
$$\lambda_B = 2(1 + 2\cos X)\,C_{BB} \pm p'_{13}/4 \qquad (5\text{–}19)$$

Modes II, V :

$$\lambda_A = -4\,C_{AA}\cos X \pm p'_{25}/2i$$
$$\lambda_B = -2C_{BB}(2\cos X - 1) \pm p'_{25}/4i \qquad (5\text{–}20)$$

où devant le terme d'interaction le signe + est valable pour I et II, le signe − pour III et V. Les modes IV et VI ont les énergies $\lambda_B = -2C_{BB}$. Comme dans le cas de Fe_2O_3-α il suffit de discuter un seul des modes I, II, III, V. Dans l'ordre

indiqué on retrouve par exemple le mode ferrimagnétique avec les valeurs respectives de h égales à 4 ; 2 ; 0 et -2.

(c) *Couplage de modes antiferromagnétiques.* Les modes I et V se réduisent pour $h = 0$ à des modes a.f. des sites A et B considérés séparément. Cependant le couplage AB fournit pour de faibles variations de h une contribution qui est du premier ordre en h (tandis que les coefficients de C_{AA} et de C_{BB} ne varient qu'au second ordre). Il en est de même des modes I et III au voisinage de $h = 2$. Nous discuterons ici le mode I. En dehors de $h = 4$, $\lambda_A+2\lambda_B$ est maximum pour

$$u^2+\tfrac{1}{3}\,qu-\tfrac{1}{12} = 0 \qquad (5\text{–}21)$$

où

$$u = \cos X/2\ ;\quad q = (\tfrac{1}{2}C_{AA}+C_{BB})/C_{AB} \qquad (5\text{–}22)$$

La seule solution acceptable est la racine positive

$$u = [-q+(q^2+3)^{1/2}]/6 \qquad (5\text{–}23)$$

On trouve après quelques transformations algébriques (utilisant (5–21) à (5–23))

$$\lambda_A+2\lambda_B = -4C_{AA}-4C_{BB}-8C_{AB} \times [(q^2+3)^{3/2}-q(q^2+\tfrac{9}{2})]/27 \qquad (5\text{–}24)$$

Ici les deux premiers termes du second membre représentent les énergies (au facteur -2 près) des modes a.f. de $\{A\}$ et de $\{B\}$ séparément. Utilisant l'identité $a-b = (a^2-b^2)/(a+b)$ le terme d'interaction s'écrit

$$-8C_{AB}(1+q^2/4)/[(q^2+3)^{3/2}+q(q^2+\tfrac{9}{2})] \qquad (5\text{–}25)$$

Il est donc toujours positif. Factorisant des expressions trigonométriques on trouve que

$$(\lambda_A+2\lambda_B)_{\mathrm{I}}-(\lambda_A+2\lambda_B)_{\text{Néel}} = -4C_{AB}(1+u)^2(1+\tfrac{1}{2}\sqrt{(3)}-u)(1-\tfrac{1}{2}\sqrt{(3)}-u)/u \qquad (5\text{–}26)$$

d'où une condition de stabilité

$$u < 1-\sqrt{(3)}/2 \text{ ou } 164^\circ\,36' < X < 180^\circ \qquad (5\text{–}27)$$

et aussi [par (5–21)]

$$q > 2(\sqrt{(3)}-1) = 1{,}46 \qquad (5\text{–}28)$$

(Sans le terme d'interaction on aurait eu $q > 1{,}5$; voir aussi remarque finale sous 5.4.)

5.4. *Dégénérescence accidentelle et couplage de Yafet–Kittel pour* $\boldsymbol{k} = 0$

La positivité de λ_B fixe une limite supérieure au paramètre

$$y = C_{BB}/C_{AB} = S_B J_{BB}/(S_A J_{AB}) \qquad (5\text{–}29)$$

Selon (5–13) on doit avoir $y < 1$. Diagonalisant la matrice $M = ((\lambda)-\zeta(0))$, où (λ) est la matrice diagonale formée avec λ_A et λ_B, grâce aux vecteurs propres trouvés plus haut, on rencontre dans la diagonale principale trois fois la valeur λ_B+2C_{BB}. Il faut donc que l'on ait

$$\lambda_B > -2C_{BB} \text{ ou } y < \tfrac{3}{4} \qquad (5\text{–}30)$$

Pour $y = \frac{3}{4}$, il y a une forme très particulière de dégénérescence accidentelle. *Les valeurs de* λ_B *coincident alors pour les modes antiferromagnétiques et ferrimagnétiques.* Pourvu que leurs vecteurs propres $T_{\text{a.f.}}$ et $T_{AB\,\mathrm{III}}$ soient orthogonaux, toute combinaison linéaire sera solution.

Les équations (2–2) deviennent dans les spinelles

$$\begin{cases} \lambda_A\,\boldsymbol{\sigma}_A = C_{AA}\sum_1^4 \boldsymbol{\sigma}_A + 3C_{AB}\sum_1^4 \boldsymbol{\sigma}_{b_j} \\ \lambda_B\,\boldsymbol{\sigma}_{b_j} = 2C_{BB}\sum_{j\neq k}^{3} \boldsymbol{\sigma}_{b_k} + C_{AB}\sum_1^6 \boldsymbol{\sigma}_A \end{cases} \qquad (5\text{–}31)$$

$$= 2C_{BB}(-\boldsymbol{\sigma}_{b_j}+\sum_j^4 \boldsymbol{\sigma}_{b_j})+C_{AB}\sum_1^6 \boldsymbol{\sigma}_A$$

(a) *On ne semble pas avoir reconnu que l'énergie du mode composé ne dépend pas du mode a.f. particulier envisagé* ($\lambda = -2C_{BB}$).

Pour le prouver, notons

$$\sum_1^4 \boldsymbol{\sigma}_{b_{j\parallel}} = -K\boldsymbol{\sigma}_A\ ;\qquad \sum_1^4 \boldsymbol{\sigma}_{b_{j\perp}} = 0 \qquad (5\text{–}32)$$

Les équations (5–31) s'écrivent

$$\begin{cases} \lambda_A = 4C_{AA}-3C_{AB}K \\ \lambda_b K = 6C_{BB}K+24C_{AB} \\ \lambda_b\boldsymbol{\sigma}_{b_{j\perp}} = -2C_{BB}\boldsymbol{\sigma}_{b_{j\perp}} \end{cases} \qquad (5\text{–}33)$$

La dernière équation indique que *l'on a toujours* $\lambda_b = -2C_{BB}$ pour $\sigma_{b_{j\perp}} \neq 0$ (c'est-à-dire pour $y > \frac{3}{4}$). De la 2e équation (5–33), on déduit

$$K = 3C_{AB}/C_{BB} \qquad (5\text{–}34)$$

d'où

$$\lambda_A = 4C_{AA} - 9C_{AB}^2/C_{BB} \qquad (5\text{–}35)$$

L'énergie continue à être donnée par (5–14). On a (cf. Réf. 28)

$$H_{Y\text{–}K} = -2(4C_{AA} - 9C_{AB}^2/C_{BB} - 4C_{BB}) \qquad (5\text{–}36)$$

(b) *Les modèles particuliers ne diffèrent que par le choix du mode a.f.*

(i) Modèle de YAFET–KITTEL[7] : Ces auteurs choisissent un des modes $B_j(0)$ ($j = 2,3,4$). Les spins $\boldsymbol{\sigma}_{bj}$ forment des angles ϕ vec l'axe ferrimagnétique $0z$. On a, grâce à (5–32)

$$K = 4\cos\phi\,; \quad \cos\phi = 3/4y \qquad (5\text{–}37)$$

La dégénérescence de ce modèle est très élevée. On peut combiner le mode ferrimagnétique avec n'importe lequel des 3 modes $B_j(0)$ ($j = 2,3,4$). On peut même combiner $T_{AB\text{III}}$ avec la spirale $[h00]$ (5–7) où h est arbitraire.

(ii) Modèle binaire : Le mode a.f. est $(0,0,-1,1)$ c'est-à-dire $\boldsymbol{\sigma}_{b1}$ et $\boldsymbol{\sigma}_{b2}$ ne changent pas. Si ϕ est l'angle de $\boldsymbol{\sigma}_{b3,4}$ avec $0z$, on a

$$K = (1+\cos\phi)/2\,; \quad \cos\phi = -1+3/2y \qquad (5\text{–}38)$$

(iii) Modèle ternaire : Le mode a.f. est $(0,1,r_1,r_2)$ [cf. 5.2(a) et (c)]; $\boldsymbol{\sigma}_{b1}$ reste toujours antiparallèle à $\boldsymbol{\sigma}_A$; $\boldsymbol{\sigma}_{bj}$ ($j = 2,3,4$) forment un même angle ϕ avec $\boldsymbol{\sigma}_{b1}$ tandis que leurs composantes perpendiculaires forment un mode a.f. "en triangle". On a :

$$K = 1+3\cos\phi\,; \quad \cos\phi = 1/y - \tfrac{1}{3} \qquad (5\text{–}39)$$

Quand $y \to \infty$, cos $\phi \to -\frac{1}{3}$. Le modèle limite place $\boldsymbol{\sigma}_A$ selon $[\bar{1}\bar{1}\bar{1}]$ et les $\boldsymbol{\sigma}_{bj}$ ($j = 1,2,3,4$) dans les directions respectives [111], $[\bar{1}\bar{1}1]$, $[\bar{1}1\bar{1}]$, $[1\bar{1}\bar{1}]$ du modèle a.f. tétraédrique (cf. 5.2a).

KAPLAN[2] a montré que le modèle de Y–K est instable et que dans la direction $[hh0]$ le modèle de Néel devient instable déjà pour $y > \frac{2}{3}$. Nous ne pouvons que confirmer ce résultat que l'on retrouve facilement en explorant la matrice $((\lambda) - \zeta(hh0))$. Nous ne discutons pas les essais de KAPLAN de trouver l'état fondamental en superposant des modes $\boldsymbol{k} = 0$ et $\boldsymbol{k} = [hh0]$, ceci sortant du cadre du sujet. Il est certain cependant que l'invariance des λ_A et des λ_B doit se conserver pour que la superposition soit valable.

Remarque : Le modèle de Yafet–Kittel est moins stable que l'ensemble des modes a.f. de $\{A\}$ et de $\{B\}$ lorsque (LOTGERING[28])

$$xy > 9/8 \qquad (5\text{–}40)$$

dans nos notations (5–29) et avec $x = C_{AA}/C_{AB}$.

La présence du terme de couplage dans (5–24) reculera la valeur de 9/8 du produit xy à une valeur plus faible. En résumé, la spirale a.f. $[h00]$ est le mode stable quand les interactions C_{AA} et C_{BB} sont simultanément grandes et comparables à C_{AB}.

5.5. *Application de la méthode "naïve"*

Minimisons directement H (1–1) avec la condition (1–3)* (cf. Réf. 10). On a

$$H = -32[C_{AA}\cos X\cos Y\cos Z + 2C_{AB}(\cos X/2\cos Y/2\cos 3Z/2 + \text{ }) + C_{BB}(\cos X\cos Y + \text{ })] \qquad (5\text{–}41)$$

Nous laissons au lecteur de soin de vérifier que H est minimum pour $\boldsymbol{k} = [400]$ et $[444]$ et que les équations (2–2) sont satisfaites. On retrouve aussi correctement la spirale $[h00]$ de la Section 5.3(b).

On peut minimiser H (5–41) dans une direction $[hh0]$. Mais on trouve alors que les équations (2–2) et (5–31) ne sont plus satisfaites, car les λ_{b_j} prennent *deux* valeurs différentes (ce qui est incompatible avec les propriétés d'invariance des λ_j).

6. LES GRENATS

Depuis leur découverte au laboratoire du Professeur NÉEL[29, 30, 19, 31], les grenats ferrimagnétiques font l'objet d'un nombre toujours grandissant de travaux. Notre analyse se limite au cas où les interactions sont isotropes, les spins ordonnés, la maille chimique conservée ($\boldsymbol{k} = 0$). La formule des grenats est $A_2C_3D_3O_{12}$. Le groupe d'espace est $I\,a3d - (0_h^{10})$, donc cubique centré. Nous étudions successivement les modes des systèmes de spins $\{A\}$, $\{D\}$ et $\{C\}$ occupant respectivement les sites 16a) octaédriques, 24c) dodékaédriques (cubiques déformés) et 24d) tétraédriques.[32] Nous construisons ensuite les modes c uplés *complets*.

* Cela revient à admettre $\phi_{ij} = 0$ ou encore que $T(1,1,1,1,1,1)$ est solution. C'est effectivement le cas pour $\boldsymbol{k} = [444]$ et $[h00]$.

Vol. 21 1961

6.1. *Les modes*

6.1.1. *Modes de* $\{A\}$. Les 8 sous-réseaux de Bravais sont, dans l'ordre adopté ici 000 ; $0\frac{1}{2}\frac{1}{2}$; $\frac{1}{2}0\frac{1}{2}$; $\frac{1}{2}\frac{1}{2}0$; $\frac{3}{4}\frac{3}{4}\frac{1}{4}$; $\frac{1}{4}\frac{3}{4}\frac{3}{4}$; $\frac{3}{4}\frac{1}{4}\frac{3}{4}$; $\frac{1}{4}\frac{1}{4}\frac{1}{4}$. La matrice ζ_A, d'ordre 8, a la forme

$$\zeta_A = \begin{pmatrix} 0 & (a) \\ (a) & 0 \end{pmatrix} \tag{6-1}$$

où (a) est une matrice d'ordre 4

$$(a) = a \begin{pmatrix} 1 & 1 & 1 & 1 \\ 1 & 1 & 1 & 1 \\ 1 & 1 & 1 & 1 \\ 1 & 1 & 1 & 1 \end{pmatrix} \tag{6-2}$$

$$a = 2C_{AA} \tag{6-3}$$

(6–1) montre que les réseaux 1 à 4 n'interagisent qu'avec les réseaux 5 à 8. Une première réduction de (6–1) se fait par la matrice $\begin{pmatrix} 1 & 1 \\ 1 & -1 \end{pmatrix}$ qui transforme $\zeta_A(0) - (\lambda)$ en une matrice diagonale dont les termes sont $-(\lambda) \pm (a)$

Chacun de ces termes (eux-mêmes matrices) est réduit par la matrice Φ (4–9). Finalement la "matrice des phases" dont les colonnes A_j sont les vecteurs propres des modes $\{A\}$ est

$$(A) = \begin{pmatrix} \Phi & \Phi \\ \Phi & -\Phi \end{pmatrix}$$

$$= \left(\begin{array}{cccc|cccc} 1 & 1 & 1 & 1 & 1 & 1 & 1 & 1 \\ 1 & 1 & -1 & -1 & 1 & 1 & -1 & -1 \\ 1 & -1 & 1 & -1 & 1 & -1 & 1 & -1 \\ 1 & -1 & -1 & 1 & 1 & -1 & -1 & 1 \\ \hline 1 & 1 & 1 & 1 & -1 & -1 & -1 & -1 \\ 1 & 1 & -1 & -1 & -1 & -1 & 1 & 1 \\ 1 & -1 & 1 & -1 & -1 & 1 & -1 & 1 \\ 1 & -1 & -1 & 1 & -1 & 1 & 1 & -1 \end{array}\right) \tag{6-4}$$

Les modes A_j $(j = 1, ..., 8)$ ont les valeurs propres

$$\lambda_1 = \lambda_5 = 4a \; ; \; \lambda_2 = \lambda_3 = \lambda_4 = \lambda_6 = \lambda_7 = \lambda_8 = 0 \tag{6-5}$$

6.1.2. *Modes de* $\{D\}$. Les 12 réseaux de Bravais sont dans l'ordre adopté ici

$\frac{3}{8}0\frac{1}{4}$; $\frac{1}{4}\frac{3}{8}0$; $0\frac{1}{4}\frac{3}{8}$; $\frac{5}{8}0\frac{3}{4}$; $\frac{3}{4}\frac{5}{8}0$; $0\frac{3}{4}\frac{5}{8}$;
$\frac{1}{8}0\frac{3}{4}$; $\frac{3}{4}\frac{1}{8}0$; $0\frac{3}{4}\frac{1}{8}$; $\frac{7}{8}0\frac{1}{4}$; $\frac{1}{4}\frac{7}{8}0$; $0\frac{1}{4}\frac{7}{8}$;

La matrice $\zeta_D(0)$ d'ordre 12 a la forme

$$\zeta_D(0) = \begin{pmatrix} . & (d) & . & (d) \\ (d) & . & (d) & . \\ . & (d) & . & (d) \\ (d) & . & (d) & . \end{pmatrix} \tag{6-6}$$

où (d) est la matrice

$$(d) = d \begin{pmatrix} . & 1 & 1 \\ 1 & . & 1 \\ 1 & 1 & . \end{pmatrix} \tag{6-7}$$

$$d = C_{DD} \tag{6-8}$$

Une première réduction de (6–6) se fait par la matrice Φ (4–9) où l'on remplace l'élément 1 par la matrice diagonale (1) d'ordre 3 ce que nous noterons par $\Phi(1)$. Les termes de la diagonale de $\frac{1}{4}\,\tilde{\Phi}(1)\;\zeta_D(0)\;\Phi(1)$ sont $-(\lambda)+2(d)$; $-(\lambda)$; $-(\lambda)-2(d)$; $-(\lambda)$; ce qui montre déjà qu'il y a 6 racines dégénérées nulles. (d) est diagonalisé par

$$(v) = \begin{pmatrix} 1 & 1 & 1 \\ 1 & r_1 & r_2 \\ 1 & r_2 & r_1 \end{pmatrix} \tag{6-9}$$

où

$$r_1 = \exp 2\pi i/3 = r_2^* \tag{6-10}$$

La matrice de phases dont les colonnes D_j décrivent les modes possibles de $\{D\}$ est

$$(D) = \Phi(v) = \begin{array}{cccccccccccc} 1 & 1 & 1 & & 1 & 1 & 1 & & 1 & 1 & 1 & & 1 & 1 & 1 \\ 1 & r_1 & r_2 & & 1 & r_1 & r_2 & & 1 & r_1 & r_2 & & 1 & r_1 & r_2 \\ 1 & r_2 & r_1 & & 1 & r_2 & r_1 & & 1 & r_2 & r_1 & & 1 & r_2 & r_1 \end{array}$$

$$
\begin{array}{cccccccccccc}
1 & 1 & 1 & 1 & 1 & 1 & -1 & -1 & -1 & -1 & -1 & -1 \\
1 & r_1 & r_2 & 1 & r_1 & r_2 & -1 & -r_1 & -r_2 & -1 & -r_1 & -r_2 \\
1 & r_2 & r_1 & 1 & r_2 & r_1 & -1 & -r_2 & -r_1 & -1 & -r_2 & -r_1 \\
1 & 1 & 1 & -1 & -1 & -1 & 1 & 1 & 1 & -1 & -1 & -1 \\
1 & r_1 & r_2 & -1 & -r_1 & -r_2 & 1 & r_1 & r_2 & -1 & -r_1 & -r_2 \\
1 & r_2 & r_1 & -1 & -r_2 & -r_1 & 1 & r_2 & r_1 & -1 & -r_2 & -r_1 \\
1 & 1 & 1 & -1 & -1 & -1 & -1 & -1 & -1 & 1 & 1 & 1 \\
1 & r_1 & r_2 & -1 & -r_1 & -r_2 & -1 & -r_1 & -r_2 & 1 & r_1 & r_2 \\
1 & r_2 & r_1 & -1 & -r_2 & -r_1 & -1 & -r_2 & -r_1 & 1 & r_2 & r_1
\end{array} \qquad (6\text{–}11)
$$

La notation $\Phi(v)$ (6–11) signifie que l'on remplace dans Φ (4–9) 1 par (v) (6–9). Les seules racines λ_j nonnulles correspondant aux vecteurs D_j sont

$$\lambda_1 = -\lambda_7 = 4d \; ; \quad \lambda_2 = \lambda_3 = -\lambda_8 = -\lambda_9 = -2d \qquad (6\text{–}12)$$

Les modes 1,4,7,10 sont colinéaires. Les autres modes sont des "spirales rationnelles" d'angle $\phi = 120°$. Par exemple dans le mode D_2 les spins sont

$$\boldsymbol{\sigma_1} = \boldsymbol{x} = \boldsymbol{\sigma_4} = \boldsymbol{\sigma_7} = \boldsymbol{\sigma_{10}}$$

$$\boldsymbol{\sigma_2} = -\tfrac{1}{2}\boldsymbol{x} - \tfrac{1}{2}\sqrt{(3)}\boldsymbol{y} = \boldsymbol{\sigma_5} = \boldsymbol{\sigma_8} = \boldsymbol{\sigma_{11}}$$

$$\boldsymbol{\sigma_3} = -\tfrac{1}{2}\boldsymbol{x} + \tfrac{1}{2}\sqrt{(3)}\boldsymbol{y} = \boldsymbol{\sigma_6} = \boldsymbol{\sigma_9} = \boldsymbol{\sigma_{12}} \qquad (6\text{–}13)$$

où $\boldsymbol{x}$ et $\boldsymbol{y}$ sont des vecteurs orthogonaux unitaires.

6.1.3. *Modes de* $\{C\}$. Les 12 réseaux de Bravais sont dans l'ordre en

$$\tfrac{1}{8}0\tfrac{1}{4} \; ; \; \tfrac{1}{4}\tfrac{1}{8}0 \; ; \; 0\tfrac{1}{4}\tfrac{1}{8} \; . \; \tfrac{7}{8}0\tfrac{3}{4} \; ; \; \text{)} \; . \; \tfrac{3}{8}0\tfrac{3}{4} \; ; \; \text{)} \; . \; \tfrac{5}{8}0\tfrac{1}{4} \; ; \; \text{)} \; .$$

La matrice $\zeta_C(0)$ est

$$\zeta_C(0) = \begin{pmatrix} (c) & . & (c) & . \\ . & (c) & . & (c) \\ (c) & . & (c) & . \\ . & (c) & . & (c) \end{pmatrix} \qquad (6\text{–}14)$$

où

$$(c) = c \begin{pmatrix} . & 1 & 1 \\ 1 & . & 1 \\ 1 & 1 & . \end{pmatrix} \qquad (6\text{–}15)$$

$$c = C_{CC} = S_C^2 J_{CC} \qquad (6\text{–}16)$$

$\zeta_C(0)$ est en quelque sorte complémentaire de $\zeta_D(0)$ (zéros remplacés par (c) ; (d) remplacé par zéro). On vérifie aisement que $\zeta_C(0)$ a les mêmes vecteurs propres que $\zeta_D(0)$ ce que nous écrivons

$$(C) = (D) \qquad (6\text{–}17)$$

Parmi les racines toutes dégénérées, sont nonnulles

$$\lambda_1 = \lambda_7 = 4c \; ; \quad \lambda_2 = \lambda_3 = \lambda_8 = \lambda_9 = -2c \qquad (6\text{–}18)$$

La raison de la dégénérescence paire réside en ce que l'on peut scinder $\{C\}$ en deux sousensembles $\{C_1\}$ et $\{C_2\}$. $\{C_1\}$ comprend les réseaux 1,2,3; 7,8,9 et n'interagit qu'avec $\{C_1\}$. $\{C_2\}$ n'interagit qu'avec $\{C_2\}$. Il n'y a pas de mode a.f. colinéaire d'énergie nonnulle. Les seules modes a.f. d'énergie nonnulle sont les spirales rationnelles $C_{2,3,8,9}$.

6.2. *Couplage de modes*

Dans le cas général la matrice* $\zeta(\boldsymbol{k})$ a la forme

$$\zeta(\boldsymbol{k}) = \begin{pmatrix} \zeta_A & \zeta_{AD} & \zeta_{AB} \\ \zeta_{DA} & \zeta_D & \zeta_{DC} \\ \zeta_{CA} & \zeta_{CD} & \zeta_C \end{pmatrix} \qquad (6\text{–}19)$$

où ζ_A, ζ_D, ζ_C dans la diagonale principale sont des matrices dont nous connaissons déjà les vecteurs propres pour $\boldsymbol{k} = 0$ [cf. (6–4, 11, 17)]. Nous discuterons en détail le couplage A–D, plus

* Des matrices analogues aux nôtres ont été utilisées par DREYFUS[38] dans une étude du spectre d'ondes de spin.

Vol. 21
1961

brièvement les systèmes $\{AC\}$ et $\{CD\}$ et enfin le cas général $\{ACD\}$.

6.2.1. *Couplage A–D.* Chaque site de $\{A\}$ a 6 voisins de $\{D\}$. La matrice ζ_{AD} a la forme

$A \searrow D \rightarrow$	1	2	3	4	5	6	7	8	9	10	11	12
1	.	.	.	.	.	.	1	1	1	1	1	1
2	1	.	1	1	.	1	.	1	.	.	1	.
3	1	1	.	1	1	.	.	.	1	.	.	1
4	.	1	1	.	1	1	1	.	.	1	.	.
5	.	1	.	.	1	.	1	.	1	1	.	1
6	.	.	1	.	.	1	1	1	.	1	1	.
7	1	.	.	1	.	.	.	1	1	.	1	1
8	1	1	1	1	1	1	.	.	.	.	.	.

$$= \zeta_{AD}/e \qquad (6\text{–}20)$$

On a uniquement explicité les colonnes 1,4 à 6 et les lignes 1 à 4,6 et 8, contenant des éléments nonnuls. Avec les vecteurs $A_{2,4,6,8}$ d'une part, $D_{4,5,6}$ d'autre part on forme les combinaisons linéaires

$$A'_2 = \tfrac{1}{2}(A_2+A_4-A_6+A_8) = (1\bar{1}\bar{1}1\ ;\ 11\bar{1}\bar{1})$$
$$A'_4 = \tfrac{1}{2}(A_2-A_4+A_6+A_8) = 11,\bar{1}\bar{1}\ ;\ \bar{1}11\bar{1})$$
$$A'_6 = \tfrac{1}{2}(A_2+A_4+A_6-A_8) = (11\bar{1}\bar{1}\ ;\ 1\bar{1}\bar{1}1)$$
$$A'_8 = \tfrac{1}{2}(-A_2+A_4+A_6+A_8) = (1\bar{1}\bar{1}1\ ;\ \bar{1}\bar{1}11) \qquad (6\text{–}24)$$

où

$$e = C_{AD} = S_A J_{AD} S_D \qquad (6\text{–}21)$$

Les numéros des colonnes correspondent aux sousréseaux de $\{D\}$, ceux des lignes aux sousréseaux de $\{A\}$ dans l'ordre spécifié plus haut. Comme dans le cas de spinelles nous considérons la matrice (ad) (6–22) formée par les vecteurs propres des modes isolés de $\{A\}$ et de $\{D\}$

$$(ad) = \left(\begin{array}{c|c} (A) & 0 \\ \hline 0 & (D) \end{array}\right) \qquad (6\text{–}22)$$

(ad) ne diagonalise pas encore la matrice de perturbation (p) (2–15) On a

$(A)\,\zeta_{AD}\,(D)/e =$

	1	4	5	6
1	48	.	.	.
2	.	-16	$-8(1+r_1)$	$-8(1+r_2)$
3	.	-16	$-16r_2$	$-16r_1$
4	.	.	$-8(1-r_1)$	$-8(1-r_2)$
6	.	.	$8(1-r_1)$	$8(1-r_2)$
8	.	-16	$-8(1+r_1)$	$-8(1+r_2)$

(6–23)

$$D'_4 = D_4+D_5+D_6 = (100100\ ;\ \bar{1}00\bar{1}00)$$
$$D'_5 = D_4+r_1D_5+r_2D_6 = (010010\ ;\ 0\bar{1}00\bar{1}0)$$
$$D'_6 = D_4+r_2D_5+r_1D_6 = (001001\ ;\ 00\bar{1}00\bar{1}) \qquad (6\text{–}25)$$

Les 10 modes couplés suivants achèvent la diagonalisation de la matrice de perturbation

$$T(AD)_{\mathrm{I,II}} = A_1 \pm D_1\ ;\ T(AD)_{\mathrm{III,IV}} = A'_2 \pm D'_4$$
$$T(AD)_{\mathrm{V,VI}} = A'_4 \pm D'_5\ ;\ T(AD)_{\mathrm{VII,VIII}} = A_3 \pm D'_6$$
$$T(AD)_{\mathrm{IX}} = A'_6\ ;\ T(AD)_{\mathrm{X}} = A'_8 \qquad (6\text{–}26)$$

Les 10 vecteurs restants $A_{5,7}$ et $D_{2,3,7,8,9,10,11,12}$ sont indifférents au couplage. Dans (6–26) le signe supérieur correspond au premier chiffre

Vol. 21
1961

romain en indice, le signe inférieur au second chiffre. Avec la même convention on a

$$\lambda_{a\,\mathrm{I,II}} = 4a \pm 6e\ ;\ \lambda_{d\,\mathrm{I,II}} = 4d \pm 4e$$
$$\lambda_{a\,\mathrm{III,IV}} = \lambda_{a\,\mathrm{V,VI}} = \lambda_{a\,\mathrm{VII,VIII}} = \mp 2e$$
$$\lambda_{d\,\mathrm{III,IV}} = \lambda_{d\,\mathrm{V,VI}} = \lambda_{d\,\mathrm{VII,VIII}} = \mp 4e$$
$$\lambda_{a\,\mathrm{IX,X}} = 0 \qquad (6\text{–}27)$$

Les énergies : On vérifie que le mode II est celui de Néel, c'est à dire de $Y_3Fe_5O_{12}$ et que l'énergie d'interaction se partage également entre sites (*a*) et (*d*). On a

$$H_{\mathrm{I,II}} = -2(8\lambda_a + 12\lambda_d) \qquad (6\text{–}28)$$

Quant aux modes III, V, VII d'une part, IV, VI, VIII d'autre part, ils sont triplement dégénérés et *incomplets* (cf. D_j'). On peut précisément profiter de cette triple dégénérescence pour construire un mode *complet* en superposant les modes dégénérés selon 3 axes $\boldsymbol{x}, \boldsymbol{y}, \boldsymbol{z}$ orthogonaux, soit

$$T'(AD)_{\mathrm{III}} = (A_2'\boldsymbol{x} + A_4'\boldsymbol{y} + A_3\boldsymbol{z})/\sqrt{(3)} + (D_4'\boldsymbol{x} + D_5'\boldsymbol{y} + D_6'\boldsymbol{z}) \qquad (6\text{–}29)$$

Les équations (2–2) sont selon $0x$

$$\lambda_a'\,\sigma_{ax} = 2e\sigma_{dx}\ ;\quad \lambda_d'\sigma_{dx} = 4e\sigma_{ax} \qquad (6\text{–}30)$$

avec

$$\sigma_{ax} = 1/\sqrt{3}\ ;\quad \sigma_{dx} = -1 \qquad (6\text{–}30')$$

de sorte que

$$\lambda_a' = -2e\sqrt{3}\ ;\quad \lambda_d' = -4e/\sqrt{3} \qquad (6\text{–}31)$$

L'expression de l'énergie (6–28) s'applique de nouveau. On a

$$H_{\mathrm{III}}' = -2(32\sqrt{3})e \qquad (6\text{–}32)$$

Des vecteurs $T'(AD)_{\mathrm{V,\,VII}}$ analogues à (6–29) sont engendrés par l'opération d'un axe ternaire qui réalise les transformations $A_2' \to A_4' \to A_3$; $D_4' \to D_5' \to D_6' \to$ (cf. 2.4). Les mêmes considérations s'appliquent aux vecteurs $T(AD)_{\mathrm{IV,VI,VIII}}$. Il est assez remarquable que les modes $T(AD)$III à VIII ne doivent leur énergie qu'au couplage *a–d*.

Couplages Yafet–Kittel* : (i) L'existence du mode a.f. D_7 (non dégénéré) nous apprend que λ_d ne peut descendre audessous d :

$$\lambda_d = -4d \qquad (6\text{–}33)$$

Le mode $T(AD)_{\mathrm{II}}$ de Néel (selon $0z$) peut donc être couplé avec Dj (selon $0x$). On déduit des relations (2–2) selon $0z$

$$\lambda_a = 4a - 6e\cos\phi_a = 4a - 3e^2/d$$
$$\cos\phi_a = e/2d \qquad (6\text{–}33')$$

(ii) De même λ_a ne peut descendre audessous de la valeur propre du mode a.f. A_5

$$\lambda_a = -4a \qquad (6\text{–}34)$$

On déduit de (2–2)

$$\lambda_d = 4d - 4e\cos\phi_d = 4d - 3e^2/a$$
$$\cos\phi_d = 3e/(4a) \qquad (6\text{–}34')$$

ϕ_a et ϕ_d sont les angles avec $0z$ des spins $\boldsymbol{\sigma}_a$ et $\boldsymbol{\sigma}_d$ L'énergie est donnée par (6–28). Les modèles (α) et (β) de Y–K sont plus stables que le mode de Néel quand $\cos\phi$ existe et moins stable que le mode a.f. $A_5 + D_7$ quand

$$8\,ad > 3e^2 \qquad (6\text{–}35)$$

On peut montrer qu'entre le mode a.f. $A_5 + D_7$ et les modèles Y–K, il existe un domaine de stabilité pour $T'(AD)_{\mathrm{III,V,VII}}$(6–29).

6.2.2. *Couplage A–C.* Tout site *a*) a 6 voisins *c*). A cause de la complémentarité déjà notée de $\{C\}$ et de $\{D\}$, on obtient ζ_{AC} en remplaçant dans ζ_{AD} (6–20) zéro par 1,1 par zéro et e par f où

$$f = C_{AC} = S_A J_{AC} S_C \qquad (6\text{–}36)$$

Pour économiser l'espace nous n'explicitons ni ζ_{AC} ni la matrice $(A)\zeta_{AC}(C)$. En effet, celle-ci se déduit de (6–23) en y remplaçant e par f et $-8, -16, +8$ par $+8, +16, -8$ respectivement (le terme 48 restant inchangé).

On peut répéter presque mot à mot la discussion de la section précédente. On aura des modes I (ferro-m.) et II (ferri-m.)

$$T(AC)_{\mathrm{I,II}} = A_1 \pm C_1\ ;\quad \lambda_a = 4a \pm 6f\ ;$$
$$\lambda_c = 4c \pm 4f \qquad (6\text{–}37)$$

$$H = -2(8\lambda_a + 12\lambda_c) \qquad (6\text{–}38)$$

Comme précédemment on construit des vecteurs

* Ce couplage dans les grenats a déjà été discuté par DE GENNES[33].

$C'_{4,5,6}$ de même forme que les vecteurs $D'_{4,5,6}$ (6–25). A cause du changement du signe dans $(A)\zeta_{AC}(C)$ les modes $T(AC)_{III,V,VII}$ correspondent à des interactions positives et $T(AC)_{IV,VI,VIII}$ à des interactions négatives de sorte que les relations homologues de (6–27) sont

$$\lambda_{a\,III,VI} = \pm 2f\,; \quad \lambda_{c\,III,IV} = \pm 4f \qquad (6\text{–}39)$$

Un mode complet peut être construit avec

$$T'(AC)_{IV,VI,VIII} = (A'_2\boldsymbol{x}+A'_4\boldsymbol{y}+A_3\boldsymbol{z})/\sqrt{(3)} - (C'_4\boldsymbol{x}+C'_5\boldsymbol{y}+C'_6\boldsymbol{z}) \qquad (6\text{–}40)$$

$$\lambda'_a = -2f\sqrt{3}\,; \quad \lambda'_d = -4f\sqrt{3}\,; \quad H' = -2(32\sqrt{3})f \qquad (6\text{–}40')$$

Des considérations analogues s'appliquent à $T'(AC)_{III,V,VII}$.

Couplages Y–K : Dans $\{C\}$ il n'y a pas de mode a.f. colinéaire d'énergie nonnulle, mais un couplage Y–K est encore possible entre les modes de Néel $T(AC)_{II}$ selon $0z$ et l'un des 4 modes "en triangle" (spirales rationnelles) $C_{2,3,8,9}$ (angles sur $\{C\}$) ou le mode A_5 (angles sur $\{A\}$). Leurs énergies respectives sont

$$H_{Y\text{–}K}(C) = -2(32a-24c-32f^2/c)$$
$$H_{Y\text{–}K}(A) = -2(-32a+48c-36f^2/a) \qquad (6\text{–}41)$$

Dans le grenat $Fe_2^{3+}Mn_3^{2+}Ge_3^{4+}O_{12}$ (A = Fe ; C = Mn)[34] un *comportement a.f.*[35] *est observé.* Cela signifie ou bien que l'interaction A–C, notée f, est faible et que sur $\{A\}$ et $\{C\}$ il y a des modes a.f. $A_5+C_{2,3,8,9}$ en quel cas

$$f^2 < 2ac \qquad (6\text{–}42)$$

ou encore que, f n'étant pas négligeable, la maille chimique n'est pas conservée.

6.2.3. *Couplage C–D.* La matrice de couplage est

$$\zeta_{DC} = \zeta_{CD} = \begin{pmatrix} (g) & . & . & (g) \\ . & (g) & (g) & . \\ . & (g) & (g) & . \\ (g) & . & . & (g) \end{pmatrix} \qquad (6\text{–}43)$$

où

$$(g) = g(1)\,; \quad g = C_{CD} \qquad (6\text{–}44)$$

(1) est la matrice unité d'ordre 3. Les seules termes nonnuls de la matrice $(\tilde{D})\zeta_{DC}(C)$ sont les 3 premiers (1,2,3) et 3 derniers (10,11,12) de la diagonale principale, d'ailleurs tous égaux à $24g$. Les conbinaisons correctes de vecteurs propres sont par conséquent les 12 vecteurs $D_j \pm C_j$ (j = 1,2,3,10,11,12). Tout autre vecteur de $\{C\}$ et $\{D\}$ est indifférent au couplage C–D.
On a

$$T(CD)_{I,II} = D_1 \pm C_1\,; \quad \lambda_{c\,I,II} = 4c \pm 2g\,; \quad \lambda_{d\,I,II} = 4d \pm 2g\,. \qquad (6\text{–}45a)$$

$$\left.\begin{aligned} T(CD)_{III,IV} &= D_2 \pm C_2 \\ T(CD)_{V,VI} &= D_3 \pm C_3 \end{aligned}\right\} \quad \lambda_c = -2c \pm 2g\,; \quad \lambda_d = -2d \pm 2g \qquad (6\text{–}45b)$$

$$T(CD)_{VII,VIII,IX,X,XI,XII} = D_j \pm C_j (j = 10,11,12)\,; \quad \lambda_c = \lambda_d = \pm 2g. \qquad (6\text{–}45c)$$

L'énergie est

$$H = -2(12)(\lambda_c+\lambda_d) \qquad (6\text{–}46)$$

En supposant les interactions c et g négatives, il est remarquable que *le mode ferrimagnétique* $T(CD)_{II}$ *est moins stable que les modes non colinéaires* $T(CD)_{IV,VI}$.

$$H(CD)_{II} = -2(48)(c+d-g)\,;$$
$$H(CD)_{IV,VI} = -2(-24)(c+d+2g) \qquad (6\text{–}47)$$

La synthèse de grenats ayant des ions magnétiques uniquement en $\{C\}$ et $\{D\}$ n'a pas encore été réalisée.

6.2.4. *Couplage A C D.* C'est le cas général des grenats de terres rares. Que l'on couple $\{AC\}$ avec $\{D\}$ ou $\{AD\}$ avec $\{C\}$ ou $\{CD\}$ avec $\{A\}$, le résultat est le même. Parmi les $8+12+12 = 32$ modes possibles, 22 sont des modes couplés, notés Q_j (j = 1, ..., 22) dans le Tableau 4. Les 10 vecteurs restants ne participent à aucun couplage (sauf éventuellement celui de Y–K). Ce sont les modes isolés $A_{5,7}$, $A'_{6,8}$, $C_{7,8,9}$ et $D_{7,8,9}$ du texte.

Les modes $Q_{1,2,3}$ sont simples, Q_4 à Q_{12} triplement, Q_{13} à Q_{22} doublement dégénérés. Parmi les modes isolés A_5,C_7 et D_7 sont simples, $C_{8,9}$ et $D_{8,9}$ doublement, A_7,A'_6 et A'_8 triplement dégénérés (d'énergie nulle et reliés par un axe **3** cf. 2.4). Le mode ferrim. $A_1+D_1-C_1$ n'a pas été "oublié". En effet il est identique à $Q_1-Q_2+Q_3$.

Vol. 2
196

Tablea 4. *Couplage ACD dans les grenats. Cas général*

N°	Modes couplés	couplage	N°	Modes couplés	couplage
Q_1	$A_1+D_1+C_1$	a, c, d, e, f, g	Q_{13}	D_2+C_2	$c, d, g.$
Q_2	$A_1-D_1+C_1$	,,	Q_{14}	D_2-C_2	,,
Q_3	$A_1-D_1-C_1$	,,	Q_{15}	D_3+C_3	,,
Q_4	$A_2'+D_4'+C_4'$	e, f	Q_{16}	D_3-C_3	,,
Q_5	$A_2'-D_4'+C_4'$	,,			
Q_6	$A_2'-D_4'-C_4'$	,,	Q_{17}	$D_{10}+C_{10}$	g
			Q_{18}	$D_{10}-C_{10}$	,,
Q_7	$A_4'+D_5'-C_5'$	,,			
Q_8	$A_4'-D_5'+C_5'$	,,	Q_{19}	$D_{11}+C_{11}$	,,
Q_9	$A_4'-D_5'-C_5'$	,,	Q_{20}	$D_{11}-C_{11}$	,,
Q_{10}	$A_3+D_6'+C_6'$	,,	Q_{21}	$D_{12}+C_{12}$	,,
Q_{11}	$A_3-D_6'+C_6'$	,,	Q_{22}	$D_{12}-C_{12}$	,,
Q_{12}	$A_3-D_6'-C_6'$	,,			

Coefficients de couplage

$C_{ij} = S_i J_{ij} S_j$ (J_{ij} = intégrale d'échange)

$a = C_{AA}$; $c = C_{CC}$; $d = C_{DD}$

$e = C_{AD}$; $f = C_{AC}$; $g = C_{CD}$

Il y a 11 modes colinéaires : Q_1(f), $Q_{2,3}$ (ferrim.), $Q_{17,18}$ et $A_{5,7}$, $A_{6,8}'$, C_7, D_7 (a.f.).

Energies : Les 15 modes Q_4 à Q_{12} ; Q_{17} à Q_{22} ne doivent leur énergie qu'au couplage entre réseaux différents. Les modes Q_4 à Q_{12} sont incomplets. Mais de modes complets peuvent être construits selon le modèle de (6–29) tels que

$$\boldsymbol{Q}' = (A_2'\boldsymbol{x}+A_4'\boldsymbol{y}+A_3'\boldsymbol{z})/\sqrt{3}+(\boldsymbol{D}_4'-C_4')\boldsymbol{x} + (D_5'-C_5')\boldsymbol{y}+(D_6'-C_6')\boldsymbol{z} \quad (6\text{–}48)$$

$$H' = -2(32\sqrt{3})\,(e+f)$$

Le mode généralement observé dans les grenats de terres rares aux températures non trop basses est

$$Q_2 = A_1-D_1+C_1$$

où

$$\lambda_a = 4a-6e+6f\,; \quad \lambda_d = 4d-4e-2g\,; \quad \lambda_c = 4c+4f-2g \quad (6\text{–}49)$$

La forme de λ_c est intéressante. Si $2f$–$g > 0$, Q_2 est stable, si non Q_3 (non observé) serait stable. De toute façon, si toutes les interactions c,f et g sont négatives, λ_c (6–49) peut être très petit[31] et des influences autrement secondaires telles que le couplage de $\{C\}$ avec le champ cristallin peuvent être compétitives avec les forces d'échange.[36] Des couplages Y–K des modes ferrim. $Q_{2,3}$ avec les modes isolés A_5 D_7, $C_{8,9}$ peuvent être envisagés, mais n'expliquent certes pas la situation dans $Fe_5Ho_3O_{12}$ aux très basses températures.[36]

Les énergies des modes Q_{13} à Q_{22} et des modes isolés ont déjà été données dans le texte.

CONCLUSIONS

On a décrit une méthode matricielle (Section 2) et on l'a appliquée au cube centré, aux structures du type corindon, aux spinelles et aux grenats (Sections 3 à 6). *La méthode résoud en principe la détermination des modes fondamentaux de réseaux de spins ordonnés dans le cas d'interactions isotropes.* L'auteur est parfaitement conscient des limitations qui découlent de cette dernière restriction. L'expérience montre d'une part que *des interactions anisotropes* telles que le couplage antisymétrique de DZYALOSHINSKY[4]–MORIYA[37] *associent des modes fondamentaux* entre eux (ferromagnétisme faible superposé à l'antiferromagnétisme ; couplage de modes a.f. différents). Elle montre d'autre part que les différences d'énergie entre modes colinéaires et hélicoidaux sont en

général faibles et comparables aux énergies d'anisotropie pseudo-dipolaire, de couplage antisymétrique D–M,[4, 37] de couplage avec le champ cristallin.[36] Si ces derniers facteurs ont une influence secondaire en ce qui concerne les modes fondamentaux, leur rôle dans les transitions ne peut être négligé.

Remerciements—L'auteur tient à adresser ses remerciements à Monsieur le Professeur L. Néel pour ses encouragements et à MM. les Docteurs L. M. Corliss et E. A. Turov pour de nombreuses discussions.

REFERENCES

1. Villain J., *J. Phys. Chem. Solids* **11,** 303 (1959).
2. Kaplan T. A., *Phys. Rev.* **119,** 1460 (1960).
3. Yoshimori A., *J. Phys. Soc. Japan* **14,** 807 (1959).
4. Dzyaloshinsky I., *J. Phys. Chem. Solids* **4,** 241 (1958).
5. Turov E. A. et Najs B. E., *J. Met. et Metall. U.R.S.S.* **9,** 10 (1960).
6. Bertaut F., *C.R. Acad. Sci., Paris* **252,** 2078 (1961).
7. Yafet Y. et Kittel C., *Phys. Rev.* **87,** 290 (1952).
8. Luttinger J. M. et Tisza L., *Phys. Rev.* **70,** 954 (1946).
9. Lyons D. H. et Kaplan T. A., *Phys. Rev.* **120,** 1580 (1960).
10. Bertaut F., *C.R. Acad. Sci., Paris* **250,** 85 (1960).
11. Cooper B. R., *Phys. Rev.* **118,** 135 (1960).
12. Smart J. S., *Phys. Rev.* **86,** 968 (1952).
13. Gersch H. A. et Koehler W. C., *J. Phys. Chem. Solids* **5,** 180 (1958).
14. Corliss L. M., Hastings J. et Weiss R., *Phys. Rev. Letters* **3,** 211 (1959).
15. Kaplan T. A., *Phys. Rev.* **116,** 888 (1957).
16. Shull C. G., Strausser W. A. et Wollan E. O., *Phys. Rev.* **83,** 333 (1951).
17. Brockhouse B. N., *J. Phys. Chem.* **21,** 961 (1953).
18. Pauling L. et Hendricks S. B., *J. Amer. Chem. Soc.* **47,** 781 (1925).
19. Pauthenet R., Thèse, Grenoble n° 81 (1957).
20. Néel L., *Ann. Phys. Paris* **3,** 137 (1948).
21. Li Y., *Phys. Rev.* **102,** 1015 (1956).
22. Iida A., *J. Phys. Soc. Japan* **11,** 1300 (1956).
23. Shirane G., Pickart S. J. et Ischikawa Y., *J. Phys. Soc. Japan* **14,** 1352 (1959).
24. Anderson P. W., *Phys. Rev.* **102,** 1008 (1956).
25. Kaplan T. A., Report M.I.T. n° 53 G–0036, Lincoln Laboratory, Lexington, Mass. U.S.A. (1960).
26. Kouvel J. S., Techn. Report n° 210, Cruft Laboratory, Harvard (1955).
27. de Gennes P. G. et Villain J., *J. Phys. Chem. Solids* **13,** 10 (1960).
28. Lotgering F. K., *Philips Res. Rep.* **11,** 190 (1956).
29. Néel L., *C.R. Acad. Sci. Paris* **239,** 8 (1954).
30. Bertaut F. et Forrat F., *C.R. Acad. Sci. Paris* **242,** 382 (1956).
31. Aleonard R., *J. Phys. Chem. Solids* **15,** 167 (1960).
32. Menzer G., *Z. Kristallogr.* **69,** 300 (1928).
33. de Gennes P. G., *Phys. Rev. Letters* **3,** 209 (1959).
34. Tauber A., Banks E. et Kedesdy H., *Acta. Cryst. Camb.* **11,** 893 (1958).
35. Gilleo M. A. et Geller S., *J. Phys. Chem. Solids* **10,** 187 (1959).
36. Herpin A., Koehler W. C. et Meriel P., *C.R. Acad. Sci. Paris.* **251,** 1359 (1960).
37. Moriya T., *Phys. Rev.* **120,** 91 (1960).
38. Dreyfus B., *J. Phys. Chem. Solids*, à paraître.

APPENDICE A.1

Posons

$$\boldsymbol{\sigma}_{\boldsymbol{R}} = 1/\alpha \sum_{l'_j} \boldsymbol{\tau}\,(\boldsymbol{k}) \exp -2\pi i \boldsymbol{k}\cdot\boldsymbol{R} \qquad \text{(A–1)}$$

Ici α est une constante.

$$\boldsymbol{R} = \sum_j l_j\,\boldsymbol{a}_j\,; \quad \boldsymbol{k} = \sum_j (l'_j/L_j)\,\boldsymbol{b}_j \qquad \text{(A–2)}$$

On envisage un cristal dont les dimensions sont $L_j\boldsymbol{a}_j$ ($j = 1,2,3$) ; les vecteurs $\boldsymbol{a}_j$ et $\boldsymbol{b}_j$ sont les vecteurs translation des réseaux directs et réciproques respectivement. ($\boldsymbol{a}_j\cdot\boldsymbol{b}_k = \partial_{jk}$)·$l_j$ et l'_j sont entiers. $\boldsymbol{k}$ est un vecteur réduit à la première zone de Brillouin

$$-\tfrac{1}{2}\,L_j < l'_j < \tfrac{1}{2}\,L_j \qquad \text{(A–3)}$$

$\boldsymbol{\sigma}_{\boldsymbol{R}}$ est assujetti aux conditions

$$\begin{aligned} &1^\circ \quad \boldsymbol{\sigma}_{\boldsymbol{R}} \text{ est réel} \\ &2^\circ \quad |\boldsymbol{\sigma}_{\boldsymbol{R}}|^2 = 1 \\ &3^\circ \quad \sum |\boldsymbol{\sigma}_{\boldsymbol{R}}|^2 = L_1L_2L_3 \end{aligned} \qquad \text{(A–4)}$$

La première condition entraine

$$\boldsymbol{\tau}(\boldsymbol{k}) = \boldsymbol{\tau}^*(-\boldsymbol{k})$$

La 3e implique

$$\sum_k |\boldsymbol{\tau}(\boldsymbol{k})|^2 = \alpha^2 = L_1L_2L_3 \qquad \text{(A–5)}$$

Enfin la comparaison de la 2° condition (A–4) et de (A–5) entraîne la relation (2.8a) du texte où l'on a posé

$$\boldsymbol{T}(\boldsymbol{k}) = \boldsymbol{\tau}(\boldsymbol{k})/\alpha \qquad \text{(A–6)}$$

Dans le texte on a noté

$$\boldsymbol{k} = h\boldsymbol{b}_1 + k\boldsymbol{b}_2 + l\boldsymbol{b}_3 = [hkl]$$

APPENDICE A.2

Contrairement à ce que (2–6) suggère, on peut donner à (2–4) une forme qui ne dépend pas explicitement des coordonnées atomiques. Notons $\boldsymbol{R}_i$ ($i = 1, \ldots, n$) les

positions des origines des n réseaux de Bravais. Faisons la transformation

$$\boldsymbol{Q}_i(\boldsymbol{k}) = \boldsymbol{T}_i(\boldsymbol{k}) \exp(-2\pi i \boldsymbol{R}_i \cdot \boldsymbol{k}) \qquad \text{(A–7)}$$

Pour plus de clarté écrivons

$$\zeta_{ij} = \sum_{R^i_{js}} C_{ij} \exp[2\pi i \boldsymbol{k} \cdot (\boldsymbol{R}_i - \overset{i}{\boldsymbol{R}}_{js})] \qquad \text{(A–8)}$$

où $\boldsymbol{R}^i_{js}$ signifie un point, voisin de $\boldsymbol{R}_i$, *situé sur le réseau* j ; s est un indice de sommation sur les atomes équivalents de j (appartenant à une même valeur de C_{ij}). De même notons

$$\eta_{ij} = \sum_{R^i_{js}} C_{ij} \exp[2\pi i \boldsymbol{k} \cdot (\boldsymbol{R}_j - \boldsymbol{R}^i_{js})] \qquad \text{(A–9)}$$

Les équations (2–4) peuvent alors s'écrire

$$\lambda_i \boldsymbol{Q}_i(\boldsymbol{k}) = \sum_j \eta_{ij} \boldsymbol{Q}_j(\boldsymbol{k}) \qquad \text{(A–10)}$$

La matrice (η) possède les propriétés remarquables

1° Elle *est hermitique*

2° Elle *ne dépend pas des coordonnées atomiques*. En effet $\boldsymbol{R}_j - \boldsymbol{R}^i_{js}$ ne faisant intervenir que les différences de vecteurs de position d'un *même* réseau j de Bravais, est *un vecteur du groupe de translation* auquel appartient le cristal.

On a

$$\boldsymbol{\sigma}_i(\boldsymbol{R}) = \sum_{\boldsymbol{k}} \boldsymbol{Q}_i(\boldsymbol{k})$$

$$\sum |\boldsymbol{Q}_i(\boldsymbol{k})|^2 = 1$$

$$\sum_{k \neq k'} \sum \boldsymbol{Q}^*_i(\boldsymbol{k}) \boldsymbol{Q}_i(\boldsymbol{k}') = 0 \qquad \text{(A–11)}$$

APPENDICE A.3

Grâce au Tableau 1 et à la relation (2–6) la première équation du système matriciel (2–4) correspondant aux voisins de $00z$ (réseau 1) est

$$\lambda \boldsymbol{T}_1 = A\boldsymbol{T}_1 + B\boldsymbol{T}_2 + C\boldsymbol{T}_3 + D\boldsymbol{T}_4 \qquad \text{(A–12)}$$

avec les abréviations

$$A = 2J_0[\cos X + \cos Y + \cos(X+Y)]$$

$$B = J_4 (E \exp -iZ + E^* \exp iZ)$$

$$C = (J_1 + J_3 E \exp -2iZ) \exp 2\pi i 2lz$$

$$D = EJ_2 \exp -iZ \exp 2\pi i 2lz$$

$$E = \exp[-i(X+2Y)/3] + \exp[i(Y-X)/3] + \exp[i(2X+Y)/3] \qquad \text{(A–13)}$$

$$X = 2\pi h \; ; \quad Y = 2\pi k \; ; \quad Z = \pi l/3 \qquad \text{(A–14)}$$

ol. 21
1961

J. Phys. Chem. Solids Pergamon Press 1961. Vol. 21, Nos. 3/4, pp. 280–286. Printed in Great Britain.

GRAVIMETRIC STUDIES OF THE DEFECT STRUCTURE OF α-Nb_2O_5

PER KOFSTAD and PER BJØRN ANDERSON

Central Institute for Industrial Research, Blindern, Oslo, Norway

(*Received* 15 *June* 1961)

Abstract—The defect structure of non-stoichiometric α-Nb_2O_5 in the temperature range 900–1400°C has been studied by a gravimetric method. The relative, isothermal weight change of α-Nb_2O_5 equilibrated in mixtures of CO and CO_2 has been found to be proportional to $p_{O_2}^{-1/6}$. This clearly establishes that the defect structure of oxygen-deficient α-Nb_2O_5 involves oxygen vacancies. Thermodynamic properties of the defect equilibrium and the partial molar thermodynami cproperties of dissociation of oxygen in non-stoichiometric α-Nb_2O_5 have been calculated.

1. INTRODUCTION

NIOBIUM has in recent years received considerable attention as a possible high-temperature material. A major shortcoming of this metal, however, is its great reactivity with oxygen and other gases at elevated temperatures. Unfortunately little is known about the properties of the oxides formed during oxidation, resulting in a correspondingly incomplete understanding of the mechanism of oxidation.

The present studies were undertaken to obtain a better understanding of the defect structure of α-Nb_2O_5 which is the major oxidation product above 800°C.[1] Studies of this kind also give thermodynamic data of non-stoichiometric oxides. Such data have been lacking in the literature.

2. LITERATURE

Nb_2O_5 exhibits polomorphism and five crystalline modifications termed δ, γ (T), β (M), α (H), and α' have been reported.[2–9] The δ-form has been suggested to be a poorly crystallized state of the γ-phase,[7] while the β- and α-phases probably are identical with the β-modification existing as a two-dimensional array.[7] The transformation $\gamma \rightarrow \alpha$ has been found to take place at about 830°C.[7] However, it is probable that no specific transformation temperature can be assigned, as the transformation temperature has also been shown to be dependent upon the heating rate.[9] The transformation has been found to be irreversible suggesting that the γ-modification is metastable.[9] Both the γ- and α-modifications have been indexed on the basis of a monoclinic unit cell.[6, 7, 10]

Nb_2O_5 is non-stoichiometric. According to BRAUER[2] it may have an oxygen deficiency within the limits $NbO_{2.50}$–$NbO_{2.40}$ at temperatures of 1350 to 1400°C. The melting point of Nb_2O_5 is approximately 1450°C.

KLING[11] gives a qualitative description of some electrical conductivity measurements on Nb_2O_5 at a range of elevated temperatures. The conductivity was found to decrease with increasing oxygen pressure suggesting an *n*-type semiconductor.

The electrical conductivity of near-stoichiometric Nb_2O_5 single crystal and sintered specimens was studied by GREENER, *et al.*[12] Under constant ambient oxygen pressure in the temperature range 300–900°C the conductivity exhibited an exponential temperature dependence with an activation energy of 1·65 eV. The isothermal conductivity in the oxygen pressure range 0·002–1 atm was found to be proportional to $p_{O_2}^{-0.24\pm0.01}$. This result was interpreted in terms of a defect structure involving oxygen ion vacancies with one trapped electron.

Qualitative observations in connection with studies of oxidation of niobium suggests that the reaction takes place at the metal/oxide interface

and that oxygen is the most mobile ionic species in Nb_2O_5.[1, 13]

3. THEORY

The formation of non-stoichiometric Nb_2O_5 may be written as

$$Nb_2O_5 \leftrightharpoons Nb_2O_{5-x} + x/2\ O_2^{(g)} \quad (1)$$

In terms of a defect structure involving oxygen vacancies the reaction may be described by the equation

$$O_1^{=} \leftrightharpoons Ov + \tfrac{1}{2}\ O_2^{(g)} \quad (2)$$

where $O_1^{=}$ is an oxygen ion in a normal lattice position and Ov is an oxygen vacancy with two trapped electrons. The trapped electrons may be excited according to

$$Ov \leftrightharpoons Ov\cdot + e^- \quad (2a)$$

$$Ov\cdot \leftrightharpoons Ov\cdot\cdot + e^- \quad (2b)$$

e^- is an electron not associated with an oxygen vacancy, Ov· an oxygen vacancy with one trapped electron, and Ov·· is a vacancy from which both electrons have been excited.

Neglecting the contribution due to intrinsic conductivity and applying the law of mass action to equations (2), (2a) and (2b), the equilibria may be written as

$$[Ov]\, p_{O_2}^{1/2} = K_1 \quad (4)$$

$$[Ov\cdot]\,[e^-] = K_2[Ov] \quad (4a)$$

$$[Ov\cdot\cdot]\,[e^-] = K_3[Ov\cdot] \quad (4b)$$

Assuming essentially complete ionization of the two trapped electrons and applying the conditions of electro-neutrality, the concentration of oxygen vacancies as a function of oxygen pressure becomes

$$[Ov]_{total} = [Ov\cdot\cdot] = (\tfrac{1}{4} K_1K_2K_3)^{1/3} \times p_{O_2}^{-1/6} \quad (5)$$

If the first electron is completely ionized while the second is negligibly ionized

$$[Ov]_{total} = [Ov\cdot] = (K_1K_2)^{1/2} \times p_{O_2}^{-1/4} \quad (6)$$

This is the defect structure suggested by GREENER *et al.*[12] on the basis of electrical conductivity studies.

The above consideration of course only applies to a pure oxide. If impurities are present the relationships are somewhat changed.

An apparent oxygen deficit may of course also be the result of excess metal in interstitial positions. Such a defect structure may summarily be written

$$\tfrac{1}{2}\ Nb_2O_5 \leftrightharpoons Nb_i^{+n} + ne^- + \tfrac{5}{4}\ O_2^{(g)} \quad (7)$$

Considering the hypothetical and limiting case of a complete ionization of the interstitial niobium ion, one obtains:

$$\text{relative weight change} \propto p_{O_2}^{-5/24} \quad (8)$$

However, such a defect structure appears rather unlikely due to the large ionization energies involved. Whatever the defect structure, however, studies of the relative weight change of a Nb_2O_5 sample as a function of oxygen pressure may make it possible to decide as to the correct defect structure of the oxide.

4. EXPERIMENTAL METHODS

As the present work was carried out in conjunction with studies of high-temperature oxidation of niobium,[1] the niobium pentoxide was prepared by oxidation in air of high-purity niobium metal powder. Estimates of impurities present in the oxide were as follows: Ta: 0·30 per cent, Si and Ti: each 0·05 per cent, Fe: 0·03 per cent and Sn: 0·02 per cent. The specimens were prepared by sintering of cold-pressed oxide powder at 1300°C.

The gravimetric studies were carried out in a quartz helix type apparatus, which is shown schematically in Fig. 1. The measuring unit was enclosed in a vacuum system. The apparatus was made of Pyrex glass with the exception of the furnace tube, which consisted of Mullite. Constant temperature water was continuously circulated through a water jacket surrounding the quartz helix.

The furnace was wound with Pt–13 per cent Rh wire, and the sample was suspended in the furnace by a thin Pt–13 per cent Rh wire. The temperature was measured with a Pt–Pt 10 per cent Rh thermocouple situated next to the sample, and the thermocouple leads were taken out of the vacuum system through Araldite seals. The temperature in the furnace was controlled to within 3°C, and the constant temperature zone in the middle of the furnace had a length of approximately 5 cm.

Vol. 21
1961

The weight of the specimens was approximately 3 gm and the weight change could be read to $\pm 3\times10^{-5}$ gm. In order to obtain easily measurable weight changes, it was necessary to equilibrate the sample at low partial pressures of oxygen, and

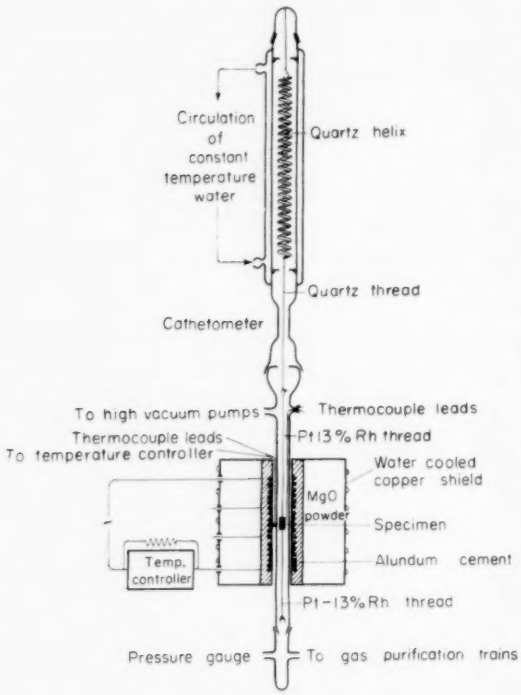

FIG. 1. Schematic representation of the quartz helix apparatus used in the gravimetric studies.

mixtures of CO and CO_2 were used for this purpose. The gases were led through purification trains consisting of heated Pd-asbestos, heated copper, silica gel, and cold traps. The relative amounts of the gases were determined by calibrated flow meters. Ratios of CO/CO_2 ranging from 1/20 to 20/1 were employed, and the partial pressure of oxygen were calculated from the well known equilibrium constant for the reaction $CO_2 = CO+\frac{1}{2}O_2$.[14] From 15–30 min were needed for filling the apparatus, and readings were taken 10 min after filling of the apparatus. Readings were taken at both decreasing and increasing temperature and partial pressures of oxygen. All measurements were carried out at a total gas pressure of 1 atm.

In measuring small relative weight changes of a sample at different temperatures and gas compositions, one of course has to correct for the buoyancy of the sample and quartz helix. In addition to the buoyancy due to the displacement of the gas, another unexpected buoyancy effect, termed the thermo-molecular[15] or "radiometer"[16] effect, became apparent during the course of the preliminary studies. Due to the large temperature gradient in the furnace, the gas molecules which collide with the suspending wire exert a "thermomolecular" force on the wire in the direction of the colder part of the furnace. The effect is a function of the temperature gradient in the furnace, the total gas pressure in the system, and the thickness of the suspending wire. The error due to this effect proved quite serious in the weight measurements and by far exceeded the actual weight change of the samples. Thus a Nb_2O_5 sample suspended by 0·5 mm thick wire at 1000°C exhibited an apparent weight change of approximately 4 mg when reducing the total gas pressure from 1 atm to 1 Torr. By employing wires of smaller diameter the error was reduced, but wires of 0·1 thickness were still found unsatisfactory.

In the studies the error was eliminated by attaching to the specimen an additional platinum wire which extended through the other end of the vertical furnace. Thus two wires of equal diameter extending through the furnace in opposite directions were attached to the specimens. In this way equal, but opposite "thermomolecular" forces were exerted on the two wires, and the effect on the measuring system thus essentially cancelled out.

5. RESULTS AND DISCUSSION

The change in weight of the sample as a function of temperature and oxygen pressure gives a measure of the corresponding change in the nonstoichiometry of the oxide. Assuming a defect structure in terms of oxygen ion vacancies, the weight change corresponds to the change in the number of vacant oxygen sites in the lattice.

The relative weight of the α-Nb_2O_5 sample as a function of temperature and oxygen pressure is shown in Fig. 2. The studies were carried out in two series (I and II in Fig. 2), as the suspending

Pt–13 per cent Rh wire broke during the course of the experiments. When reintroducing the specimen the absolute readings of the cathetometer were changed, and in Fig. 2 the relative weight changes of series I and II should thus be considered separately. The weight has been plotted as a function of $p_{O_2}^{-1/6}$, and as seen a straight-line relationship is obtained between w and $p_{O_2}^{-1/6}$. This is in accord with equation (5), and the conclusion is consequently drawn that the defect structure of non-stoichiometric α-Nb_2O_5 predominantly involves doubly charged oxygen ion vacancies according to the dissociation scheme (4), (4a) and (4b).

If one assumes that α-Nb_2O_5 is exactly stoichiometric at infinite oxygen pressure, the sample should of course at all temperatures have the same weight, w_0, at $p_{O_2}^{-1/6} = 0$. As seen in Fig. 2 the results of series II extrapolate to approximately the same weight at infinite oxygen pressure. For series I, however, one observes a slight shift in the apparent value of w_0.

In a plot of w as a function of $p_{O_2}^{-1/6}$ the straight portions of the curves should, however, not extrapolate to exactly the same weight. As one approaches stoichiometry, the relative importance

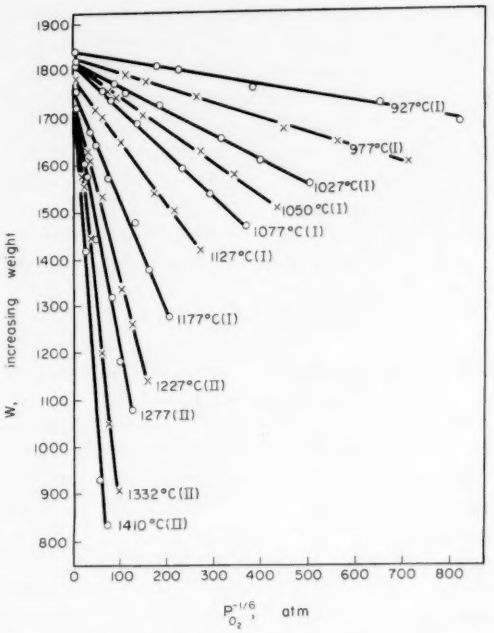

FIG. 2. The relative weight change of the α-Nb_2O_5 sample as a function of $p_{O_2}^{-1/6}$ in the temperature range 900–1400°C.

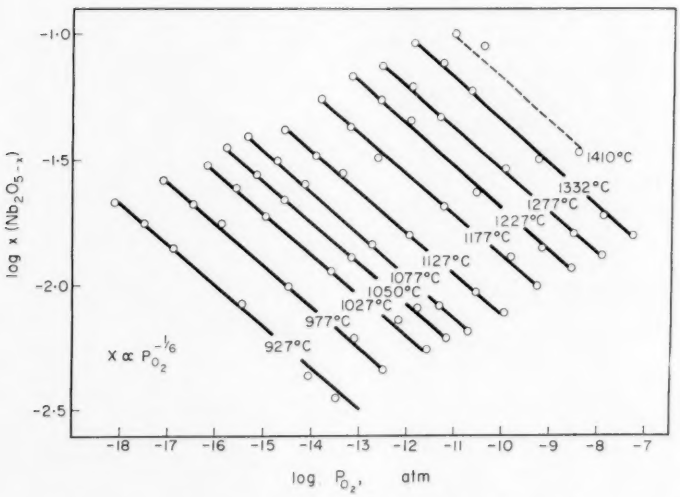

FIG. 3. The logarithm of x (in Nb_2O_{5-x}) as a function of log p_{O_2} in the temperature range 900–1400°C.

of the intrinsically excited electrons will increase and the oxygen pressure dependence will change. At or close to stoichiometry the concentration of electrons may be considered approximately constant resulting in $[Ov]_{total} \propto p_{O_2}^{-1/2}$. At small deviations from stoichiometry the effects of impurities and disorder in the niobium lattice may also affect the oxygen pressure dependence. Finally, the assumption of a stoichiometric oxide at infinite oxygen pressure may not be exactly correct. Under these conditions there is of course a possibility of interstitial oxygen atoms resulting in Nb_2O_5 with excess oxygen. All these factors may cause slight shifts in the extrapolated values of the weight at infinite oxygen pressure in Fig. 2.

In view of the lack of knowledge as to the oxygen pressure dependence of the weight change when approaching infinite oxygen pressure, the curves in Fig. 2 have been extrapolated to infinite oxygen pressure and the value of w_0 has been estimated at each temperature. From the weight changes, values of x in Nb_2O_{5-x} have been evaluated, and in Fig. 3 is shown a plot of log x as a function of log p_{O_2}. This plot accordingly yields straight lines with slopes of $-\frac{1}{6}$.

In view of the above considerations the present results thus only appear to establish that the defect structure involves doubly charged oxygen vacancies at concentration of x larger than approximately 4×10^{-3} (Fig. 3). The present results are thus not necessarily in disagreement with the studies of GREENER *et al.*, who on the basis of electrical conductivity studies concluded that the defect structure at partial pressures of oxygen from 1 to 0·002 atm predominantly involves singly charged oxygen vacancies. However, on the basis of the present results, one should expect the conductivity to be proportional to $p_{O_2}^{-1/6}$ at concentrations of $x > 4\times10^{-3}$ at temperatures above 900°C. Such studies are presently being carried out in this laboratory.

From the results in Fig. 3 the equilibrium constant $K = K_1K_2K_3$ has been evaluated according to the relationship:

$$K = K_1K_2K_3 = 4[O_V\cdot\cdot]^3 \times p_{O_2}^{1/2} = 4(x/5)^3 \times p_{O_2}^{1/2} \tag{9}$$

Values of K and $\Delta G^\circ = -RT \ln K$ at different temperatures are given in Table 1. As shown in

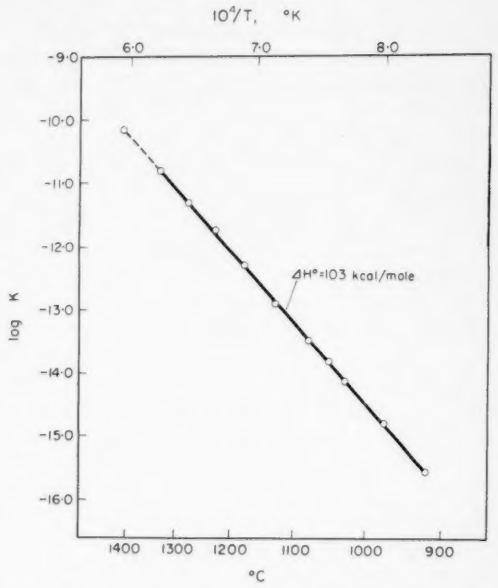

FIG. 4. The logarithm of the equilibrium constant for the defect equilibrium as a function of reciprocal absolute temperature.

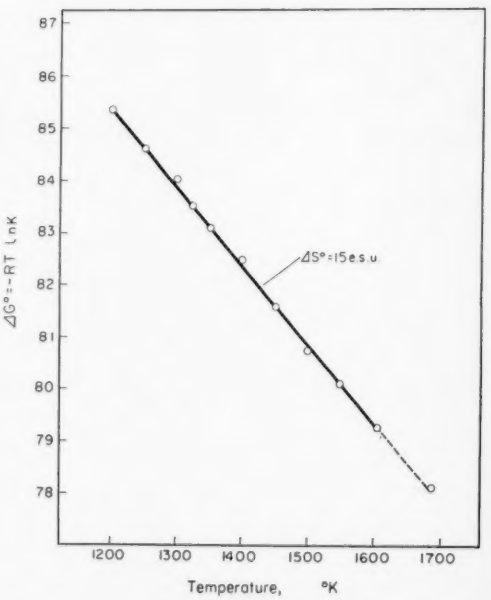

FIG. 5. The free energy change, ΔG°. of the defect reaction as a function of the absolute temperature.

Vol. 2
1961

Table 1. *Experimental values of* $K = K_1K_2K_3$ *and* ΔG°

Temperature (°C)	K	ΔG° (kcal/mole)
927	$2{\cdot}83\times10^{-16}$	85·34
977	$1{\cdot}60\times10^{-15}$	84·61
1027	$7{\cdot}85\times10^{-15}$	83·98
1050	$1{\cdot}60\times10^{-14}$	83·50
1077	$3{\cdot}59\times10^{-14}$	83·04
1127	$1{\cdot}27\times10^{-13}$	82·59
1177	$5{\cdot}07\times10^{-13}$	81·56
1227	$1{\cdot}80\times10^{-12}$	80·60
1277	$5{\cdot}07\times10^{-12}$	80·10
1332	$1{\cdot}60\times10^{-11}$	79·27
1410	$7{\cdot}16\times10^{-11}$	78·11

Fig. 4 a plot of log K as a function of reciprocal absolute temperature gives a value of ΔH° = 103 kcal/mole for the heat of formation of 1 mole of doubly charged oxygen vacancies. A plot of ΔG° as a function of absolute temperature gives a value of ΔS° = 15 e.u. This is shown in Fig. 5.

GRUBE and FLAD[17] measured equilibria in the system Nb_2O_5–H_2–NbO_2–H_2O at 920–1040 °C by means of a dynamic method. KUBASCHEWSKI[17] converted the results into enthalpies and free energies of dissociation of the oxides (Table 2). It was found that in the range Nb_2–$Nb_{2.42}$ the dissociation pressure remained constant at 980°C but then increased rapidly with oxygen concentration.

Table 2

N_0	x in Nb_2O_{5-x}	$\Delta\bar{G}_{1/2\,O_2}$ at 1253°K (kcal/mole)	$\Delta\bar{H}_{1/2\,O_2}$ at 1253°K (kcal/mole)
0	0·046	(−50·750)	(−82·500)
0·709	0·037	(−49·450)	(−63·500)
0·712	0·016	(−20·225)	
0·714	0		

The present studies gives a value of the partial enthalpy of dissociation of ½ mole of oxygen of $\Delta\bar{H}_{1/2\,O_2}$ = 103 kcal/mole for values of $x > 4\times10^{-3}$. Furthermore, within the experimental error, $\Delta\bar{H}_{1/2\,O_2}$ has been found to be independent of the concentration of oxygen vacancies.

Values of $\Delta\bar{G}_{1/2\,O_2}$ as a function of x are given in Fig. 6. As shown, the values of GRUBE and FLAD at compositions corresponding to x = 0·037 and 0·046 are in reasonable agreement with the present results. According to KUBASCHEWSKI[17] an extrapolation of the results of GRUBE and FLAD suggest

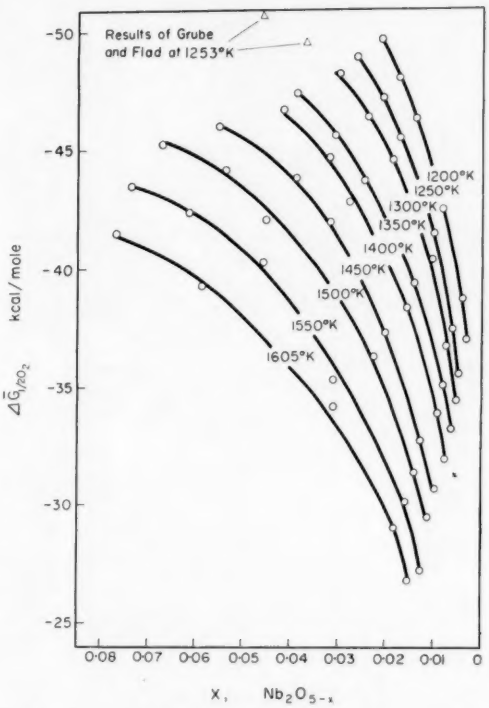

FIG. 6. The partial molar free energy of dissociation of oxygen in non-stoichiometric α-Nb_2O_5, $\Delta\bar{G}_{1/2\,O_2}$, as a function of x (in Nb_2O_{5-x}).

an oxygen pressure of 1 atm for stoichiometric Nb_2O_5 at 1253°K. It is obvious that no comparison can be made in this case as the present data have been evaluated on the assumption that Nb_2O_5 is exactly stoichiometric at infinite oxygen pressure, e.g. on the assumption that stoichiometric Nb_2O_5 is unattainable at any finite oxygen pressure. Furthermore, from the above consideration and due to the lack of detailed knowledge as to the defect structure at or close to stoichiometry, it does not appear possible at present to estimate $\Delta\bar{G}_{1/2\,O_2}$ at exact stoichiometry.

In the present study no attempts were made to determine the rate of diffusion of oxygen. The results suggest, however, a relatively rapid diffusion of oxygen as only short equilibration periods were needed.

Acknowledgement—The work has been sponsored by the Wright Air Development Division of the Air Research and Development Command, United States Air Force, through its European office.

REFERENCES

1. KOFSTAD P. and KJÖLLESDAL H., *Trans. A.I.M.E.* **221,** 285 (1961).
2. BRAUER G., *Z. anorg. Chem.* **248,** 1 (1941); *Naturwissenschaften* **28,** 30 (1940).
3. HAHN R. B., *J. Amer. Chem. Soc.* **73,** 5091 (1951).
4. SCHÄFER H. and BREIL C., *Z. anorg. Chem.* **267,** 265 (1952).
5. SCHÄFER H., DURKOP A. and JORI M., *Z. anorg. Chem.* **275,** 19 (1954).
6. FREVEL L. K. and RINN H. N., *Anal. Chem.* **27,** 1329 (1955).
7. HOLZBERG F., REISMAN A., BERRY M. and BERKENBLIT M., *J. Amer. Chem. Soc.* **79,** 2039 (1957).
8. SCHAFER M. W. and ROY R., *Z. Kristallogr.* **110,** 241 (1958).
9. GOLDSCHMIDT H. J., *J. Inst. Met.* **87,** 235 (1959).
10. MAGNELI A. and LAGERGREN S., A.S.T.M. Index Card 5–0379.
11. KLING H. P., *Technology of Columbium*, p. 87. John Wiley, New York (1958).
12. GREENER E. H., WHITMORE D. H. and FINE M. E., *J. Chem. Phys.* **34,** 1017 (1961).
13. KLOPP W. D., SIMS C. T. and JAFFEE R. I., *High-Temperature Oxidation and Contamination of Nb*, BMI–1170, Battelle Memorial Inst., February 19 (1957).
14. ROSSINI F. D., *Selected Values of Physical Thermodynamic Properties of Hydrocarbons and Related Compounds.* Carnegie Press, Pittsburgh, 1953.
15. FÖRLAND K. S., private communications.
16. SANDSTEDE G. and ROBENS E., *Chem.-Ing.-Tech.* **32,** 413 (1960).
17. KUBASCHEWSKI O. and CATTERALL J. A., *Thermochemical Data of Alloys*, p. 166. Pergamon Press, London (1956).

J. Phys. Chem. Solids Pergamon Press 1961. Vol. 21, Nos. 3/4, pp. 287–294. Printed in Great Britain.

SUR LA STRUCTURE ELECTRONIQUE DES METAUX DE TRANSITION LIQUIDES ET DE CERTAINES PHASES COMPLEXES

Y. A. ROCHER et J. FRIEDEL

Laboratoire de Physique des Solides, Groupe II, Faculté des Sciences d'Orsay, (S. et O), France.

(*Received* 8 *June* 1961)

Résumé—On détermine la fonction d'onde d'un électron dans l'approximation des liaisons fortes, à partir d'un modèle isotrope, pour la répartition des premiers voisins d'un atome. Ce modèle doit s'appliquer de façon approchée aux métaux liquides et est étendu à certaines phases complexes de métaux de transition : Mn α, Wβ, phases σ, phases de basse et moyenne températures des actinides. Malgré ses imperfections, le modèle permet de prévoir une très forte densité électronique au niveau de Fermi pour une bande *d* plus qu'au tiers remplie. Ces prévisions sont en accord avec l'expérience et suggèrent que les fortes supraconductibilités observées dans certaines de ces structures sont dues à cette forte densité électronique.

Abstract—In the tight-binding approximation, the wave function of an electron is calculated for an isotropic metal structure. This model should apply approximately to liquid metals and to some complex crystalline structures of transition metals: αMn, βW, σ phases and low and intermediate temperature phases of the actinides. Although somewhat rough, the model definitely predicts a very high electronic density at the Fermi level for a *d* band filled up to more than one-third. These predictions are in fair agreement with experiment. They suggest that the high temperature superconductivity observed in some of those structures is due to a very high electronic density.

INTRODUCTION

L'APPROXIMATION des liaisons fortes rend compte de façon satisfaisante de la structure électronique de bandes étroites, comme la bande *d* des métaux de transition.[1, 2]

Nous nous proposons de l'appliquer à un modèle simple, où l'on peut considérer chaque atome comme entouré d'un même nombre de premiers voisins statistiquement répartis à une certaine distance. Un tel modèle doit s'appliquer assez bien aux métaux de transition liquides. Nous pouvons aussi remarquer avec FRANK[3] et KRIPYAKEVITCH[4] qu'un certain nombre de structures, telles que Mnα, le chrome électrolytique, *W*β, les phases σ des métaux de transition, Uβ et sans doute Uα, Npα, Puα, Puβ, peuvent être considérées comme un empilement de sphères compactes, à forte co-ordinence et assez désordonné ; nous pouvons donc penser que notre modèle décrit également ces structures.

Chaque atome est entouré de p voisins ($p = 12$, 13, 14 ou davantage) à la distance interatomique moyenne b. Dans cette description, purement locale et isotrope, la notion de zone de Brillouin disparaît. Mais nous verrons que l'on peut introduire un nombre d'onde k associé à l'énergie E d'un électron. La variation de k définit une bande d'énergie à l'intérieur de laquelle on peut déterminer la densité électronique. Nous pouvons prévoir que la structure électronique ne sera correctement décrite que pour des longueurs d'onde de l'électron grandes vis-à-vis de la distance interatomique, c'est-à-dire pour les faibles valeurs de k.

Nous allons donc déterminer la fonction d'onde d'un électron itinérant. Puis nous calculerons la densité électronique associée à l'énergie E.

1. DETERMINATION DE LA FONCTION D'ONDE

1.1. *Formule générale*

La fonction d'onde d'un électron *d* s'écrit sous

la forme d'une combinaison linéaire de fonctions atomiques centrées aux sites j du métal :

$$\psi(\boldsymbol{r}) = \sum_{j,m} A_{jm}\phi_{jm}(\boldsymbol{r}-\boldsymbol{R}_j). \tag{1}$$

La sommation sur m correspond aux différentes fonctions, d, d'énergie E_0, cinq fois dégénérées dans l'état atomique.

Nous nous plaçons dans les hypothèses usuelles de l'approximation des liaisons fortes :[5, 6]

(a) chaque potentiel atomique U_j n'a de valeurs notables que dans la maille correspondante. Il en résulte

$$\int \phi_{jm}U_l\phi^*_{kn}\,d\tau \simeq 0 \text{ si } l \neq j \neq k \tag{2}$$

$$\int \phi_{jm}U_k\phi^*_{kn}\,d\tau \simeq 0 \text{ si } j \text{ et } k \text{ ne sont pas premiers voisins.} \tag{3}$$

(b) les fonctions d'onde atomiques centrées sur des sites différents sont quasi orthogonales :

$$\int \phi_{jm}\phi_{kn} \simeq \delta_{jk}\delta_{mn}. \tag{4}$$

On obtient dans ces conditions pour les coefficients A_{jm} de l'équation (1) une équation aux différences en général compliquée.[7] Cette équation se simplifie beaucoup si l'on fait *l'approximation supplémentaire*

$$A_{jm} = A_j \exp(i\lambda_m) \tag{5}$$

Ceci revient à supposer que dans la fonction d'onde ψ, les diverses fonctions $d(\phi_{jm})$ ont des amplitudes A_j égales et des phases λ_m indépendantes du site considéré : *les phases λ_m sont supposées constituer des variables aléatoires*, complètement indépendantes les unes des autres. Cette hypothèse est assez raisonnable pour les structures compactes et isotropes considérées où les diverses fonctions d d'atomes voisins ont peu tendance à se combiner pour former des liaisons covalentes.

Ces trois approximations conduisent par les méthodes usuelles à l'équation suivante pour les coefficients A_j

$$5A_j\,(E-E_0-\alpha) = \sum_{j' \text{ voisin } j} A_{j'} \times \int \sum_m \exp(i\lambda_m)\phi_{j'm}(V-U_{j'}) \sum \exp(-i\lambda_{m'})\phi^*_{jm'}d\tau \tag{6}$$

où

$$\alpha = \int \phi_{jm}(V-U_j)\phi^*_{jm}\,d\tau$$

indépendant de m.

E est l'énergie de l'électron, $V(\boldsymbol{r})$ est le potentiel du réseau ; $U_j\,(\boldsymbol{r}-\boldsymbol{R}_j)$ est le potentiel de l'atome au site j. La sphéricité du problème implique une probabilité de trouver un atome sur la sphère des premiers voisins indépendante de la position. $V(\boldsymbol{r})$ a donc une forme sphérique autour de j.

L'intégrale au deuxième membre de (6) se décomposent en deux termes :

(a) un terme

$$\sum_m \int \phi_{j'm}(V-U_{j'})\phi^*_{jm}\,d\tau$$

(b) un terme

$$\sum_{m,m'\neq m} \exp i(\lambda_m-\lambda_{m'}) \int \phi_{j'm}(V-U_{j'})\phi_{jm'}\,d\tau$$

Le premier terme est indépendant de la position de j' sur la sphère des premiers voisins de j. *Dans l'approximation de la phase aléatoire*, le terme $\exp\, i\,(\lambda_m-\lambda_{m'})$ est nul en moyenne et donc le deuxième terme est nul quel que soit j. Nous montrerons en appendice que la forme asymptotique des A_j reste la même, dans une approximation moins restrictive que la phase aléatoire.

Dans ces conditions, l'équation (6) peut s'écrire :

$$5A_j(E-E_0-\alpha) = \beta \sum_j A_{j'} \tag{7}$$

où

$$\beta = \sum_m \int \phi_{j'm}(V-U_{j'})\phi_{jm}\,d\tau.$$

1.2. *Forme asymptotique*

La forme asymptotique des coefficients A_j s'obtient en supposant les A_j continus dans l'espace ainsi que toutes leurs dérivées, ce qui est raisonable loin du site origine. Nous pouvons écrire :

$$A_{j'} = A_j + (\boldsymbol{b}_{jj'}\cdot\nabla)A_j + \ldots + \frac{1}{n!}(\boldsymbol{b}_{jj'}\cdot\nabla)^n A_j + \ldots \tag{8}$$

$\boldsymbol{b}_{jj'}$ est le vecteur joignant le site j au site j'. En sommant sur les p voisins j' de j, et en tenant compte

Vol. 2
196

de l'isotropie du modèle, il vient :

$$\sum_{j'} A_{j'} = p(A_j + \frac{b^2}{3!}\,\Delta A_j + \ldots + \frac{b^{2n}}{(2n+1)!} \times \Delta^n A_j + \ldots) \quad (9)$$

L'équation (7) peut être remplacée par l'équation différentielle

$$\Delta A_j + k^2 A_j = 0 \quad (10)$$

avec

$$E - E_0 - \alpha = \tfrac{1}{5}\, p\beta\, \frac{\sin kb}{kb}. \quad (11)$$

k apparaît comme un nombre d'onde et la solution asymptotique générale pour les A_j est

$$A_j = \sum_l a_l \times [\cos \delta_{lj} j_l(kR_j) - \sin \delta_l n_l(kR_j)]\, P_l(\cos\theta), \quad (12)$$

où les j_l et les n_l sont les fonctions sphériques de Bessel et Neumann. ψ est donc décomposée en harmoniques sphériques sur tous les sites. La densité électronique sur le site central ne dépend évidemment que de l'harmonique $l = 0$.

Or, pour obtenir (6), nous avons admis la quasi orthogonalité des ϕ_j. Dans la limite de cette approximation, *nous ne considérerons donc que l'harmonique $l = 0$ dans ce qui suit. Nous supposerons de plus que la formule asymptotique* (12) *est valable pour tous les sites autres que le site central.* A_0 est déterminé par la relation (7), et, finalement, la forme de la fonction d'onde est

(avec $\varphi_j = \sum_m \exp(i\lambda_m)\, \phi_{jm}$) :

$$\psi = a_0\, \frac{\sin(kb+\delta_0)}{\sin kb}\, \varphi_0(r) + \sum_{j\neq 0} a_0\, \frac{\sin(kR_j+\delta_0)}{kR_j}\, \varphi_j(r-R_j) \quad (13)$$

1.3. *Calcul du coefficient de normalisation* a_0

On écrit que la fonction d'onde ψ est nomalisée à dix électrons dans tout le volume considéré. Dans les approximations que nous avons faites, il vient

$$10 = \sum_j A_j^2 \quad (14)$$

En remplaçant la sommation sur tous les sites j par une intégrale dans tout le volume (sphère de rayon R), on obtient finalement :

$$a_0^2 = \frac{5\, v_0\, k^2}{\pi R} \quad (15)$$

où v_0 est le volume atomique.

1.4. *Calcul du déphasage* δ_0.

La relation (7) donne, pour le site central $j = 0$ et un site voisin $j = 1$:

$$A_0\, \frac{\sin kb}{kb} = a_0\, \frac{\sin(kb+\delta_0)}{kb} \quad (16)$$

$$p\, A_1\, \frac{\sin kb}{kb} = A + \sum_{j'_1} A_{j'_1} \quad (17)$$

Nous avons calculé la somme $\sum_{j'_1} A_{j'_1}$ en supposant les $p-1$ sites j'_1 voisins du site 1 répartis uniformément sur la sphère des premiers voisins du site 1, amputée d'une calotte d'aire $4\pi b^2/p$ centrée sur l'atome origine. En éliminant A_0, on obtient la relation donnant δ_0 :

$$\operatorname{tg}\delta_0 = \frac{p[\cos(2kb/\sqrt{p}) - \cos 2kb] + 2(k^2b^2 - p\sin^2 kb)}{p[\sin(2kb/\sqrt{p}) - \sin 2kb] - 2\operatorname{cotg} kb\,(k^2b^2 - p\sin^2 kb)} \quad (18)$$

Les variations de δ_0 en fonction de $k\,b$ sont représentés Fig. 1 pour $p = 12$. Nous avons calculé δ_0 dans les cas $p = 10$, 12 ou 14 et obtenu pour $\operatorname{tg}\delta_0$ des valeurs à peu près indépendantes de p. Comme la séparation mi-discrète, mi-continue des voisins du site 1 peut paraîte arbitraire, nous avons aussi calculé δ_0 quand les douze voisins du site 1 sont placés dans les positions du réseau cubique à faces centrées. Les résultats obtenus sont pratiquement identiques dans les deux cas. Ces considérations justifient dans une certaine mesure les approximations de notre modèle, en ce sens qu'elles montrent que les *résultats obtenus sont peu sensibles aux détalis du modèle employé.*

2. CALCUL DE LA DENSITE ELECTRONIQUE

Pour calculer la densité d'états, on peut supposer par exemple que les fonctions d'onde s'annulent sur la sphère de rayon R. La forme asymptotique

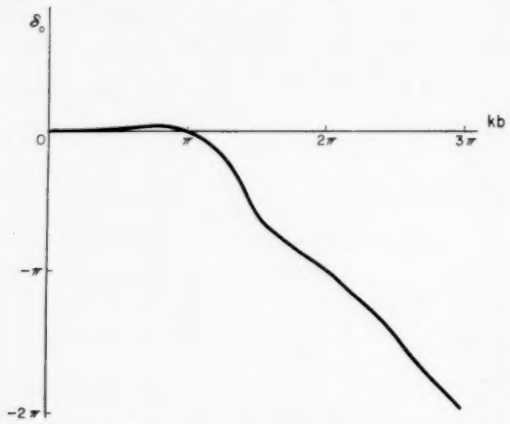

FIG. 1. Déphasage δ_0 en fonction du paramètre kb.

(12) montre que le nombre d'états $l = 0$ entre k et $k+dk$ est alors égal à

$$n(k)dk = \frac{1}{\pi}(R+d\delta_0/dk)\,dk \qquad (19)$$

Le nombre d'états $l = 0$ entre E et $E+dE$ est donc

$$n(E)dE = \frac{1}{\pi}\left(R+\frac{d\delta_0}{dk}\right)\frac{5\,k^2b}{|\beta(kb\cos kb-\sin kb)|}\,dE \qquad (20)$$

Dans la maille origine, le nombre d'électrons d'énergie comprise entre E et $E+dE$ est

$$d\rho = \int \psi_b\psi_b^* n(E)dE\,d\tau_0, \qquad (21)$$

puisque seuls contribuent à la densité électronique les états $l = 0$.

Nous pouvons définir *une densité électronique par atome et par unité d'énergie* $d\rho/dE$. En tenant compte de la dégénérescence totale de la bande d, et à l'aide des relations (13), (15) et (21), nous obtenons:

$$\frac{d\rho}{dE} = \frac{25v_0}{\pi^2 p|\beta|b^3}\,\frac{(kb)^4\sin^2(kb+\delta_0)}{\sin^2 kb|kb\cos kb-\sin kb|} \qquad (22)$$

Cette densité ne dépend que du paramètre $p\beta$ directement relié à la largeur ΔE de la bande d'énergie

$$\Delta E = \tfrac{1}{5}\,p|\beta|\left[1-\frac{\sin(k_0b)}{k_0b}\right] \qquad (23)$$

avec les conditions

$$k_0b = \operatorname{tg} k_0b$$
$$0 < k_0b < 3\pi/2.$$

On obtient alors

$$\Delta E = 0{,}243\,p|\beta|.$$

En sommant pour une certaine valeur de l'énergie toutes les contributions à la densité électronique provenant des différentes valeurs de k correspondant à cette énergie, nous obtenons les variations de la densité électronique en fonction de l'énergie. Des pics infinis de densité électronique apparaissent, correspondant aux valeurs de k, telles que

$$\operatorname{tg} kb = kb.$$

Les niveaux électroniques sont occupés jusqu'à une certaine énergie E_F, telle que

$$\int_{E_m}^{E_F}\frac{d\rho}{dE}\,dE$$

soit égale au nombre d'électrons par atome dans la bande ; on définit ainsi un niveau de Fermi. La bande calculée en faisant varier k de O à ∞ contient un nombre d'électrons par atome très peu inférieur au nombre théorique de 10. La différence provient certainement des approximations grossières du modèle.

Hors des pics, les contributions à la densité électronique provenant des grandes valeurs de k sont très faibles, comme on peut le voir Fig. 2. Pratiquement, on peut négliger toutes les contributions correspondant à $kb > 3\pi$. D'ailleurs, le modèle perd toute réalité physique pour les grandes valeurs de k. Nous avons obtenu la courbe de densité électronique représentée Fig. 3 en nous limitant aux valeurs de k, telles que $0 \leqslant kb \leqslant 3\pi$.

En prenant pour le chrome une fonction d'onde de Slater correspondant à la formule électronique

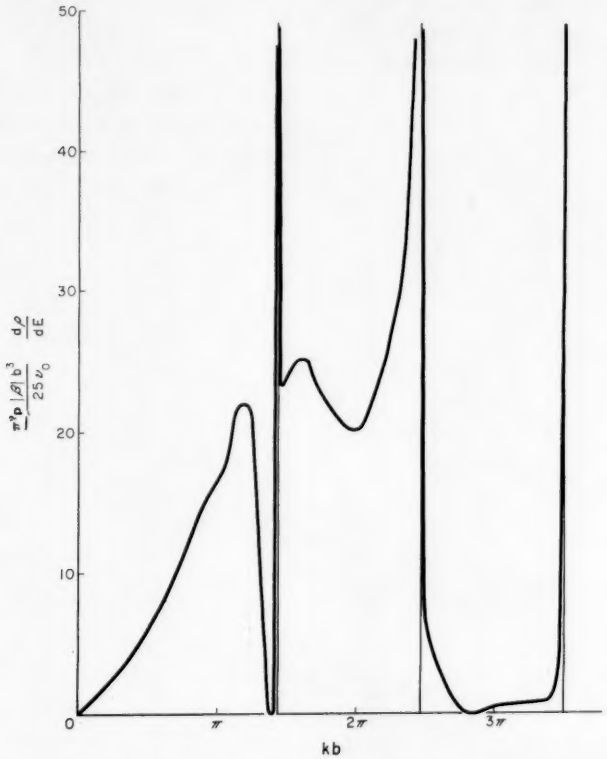

FIG. 2. Variations de la densité électronique $d\rho/dE$ en fonction du paramètre kb.

$3d^5\,4s^1$ (soit une charge efficace de 4,6), nous avons calculé une largeur de bande ΔE de l'ordre de 2,4 eV. Une estimation de la largeur de bande à partir de la densité au niveau de Fermi obtenue pour Mn α conduit à 2,3 eV. ASDENTE et FRIEDEL[2] ont calculé, à partir de la même fonction d'onde pour le chrome, une largeur de bande de 3,8 eV pour la structure cubique centrée. Notre modèle conduit donc à des bandes sensiblement plus étroites.

3. DISCUSSION

Il est possible de comparer l'énergie électronique d'un métal de transition dans la structure cubique centrée par exemple et dans une structure décrite par notre modèle. Si le métal considéré contient n électrons dans la bande d, nous aurons à comparer, par exemple, des termes tels que

$$\int_{E_m}^{E_F} \frac{d\rho(E)}{dE}\,(E-E_0-\alpha)\,dE.$$

E_m est l'énergie de bas de bande ; et l'énergie de Fermi E_F est telle que

$$n = \int_{E_m}^{E_F} \frac{d\rho(E)}{dE}\,dE.$$

On trouve alors, qu'à 0°K, la structure complexe doit être plus stable que la structure cubique centrée quand la bande d contient plus de 5 électrons par atome (Fig. 4). Ces structures sont alors

caractérisées par de très fortes densités électroniques au niveau de Fermi. Nous allons montrer que des propriétés physiques caractéristiques de fortes densités électroniques au niveau de Fermi

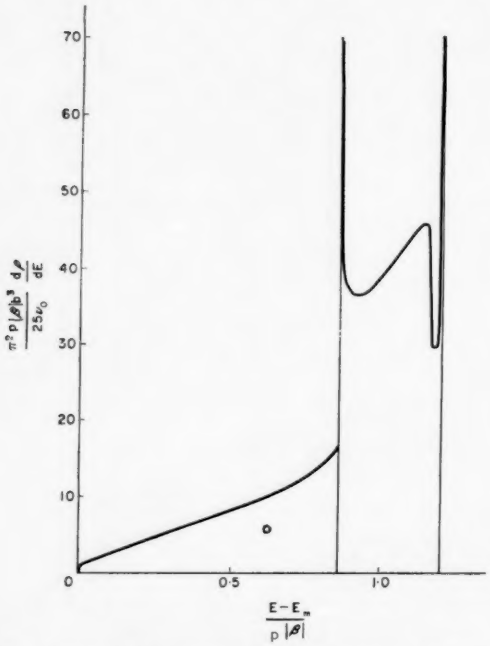

FIG. 3. Variations de la densité électronique $d\rho/dE$ en fonction de l'énergie.

s'observent effectivement dans les métaux de transition contenant de 5 à 7 électrons *d* par atome et susceptibles d'être décrits par ce modèle "liquide".

4. PROPRIETES DES METAUX : Mnα, PHASES σ, METAUX DE LA DERNIERE SERIE

Tous ces métaux cristallisent à basse température dans des phases complexes qui peuvent être assez bien décrites par le modèle liquide. La concentration électronique varie de 5 à 7 électrons *d* par atome et leurs propriétés physiques sont effectivement liées à une très forte densité électronique au niveau de Fermi :

Mnα[8] : la chaleur spécifique électronique

$$(\gamma = 4{,}2\times10^{-3}\text{cal/mole/deg}^2),$$

la susceptibilité magnétique

$$(\chi \simeq 10\times10^{-6}\text{ e.m.u./g à }20°\text{C}),$$

sont très élevées et s'accordent avec une forte densité électronique au niveau de Fermi. La phase liquide a une susceptibilité particulièrement élevée :

$$\chi = 12{,}5\times10^{-6}\text{ e.m.u./g à }1{,}250°\text{C}.$$

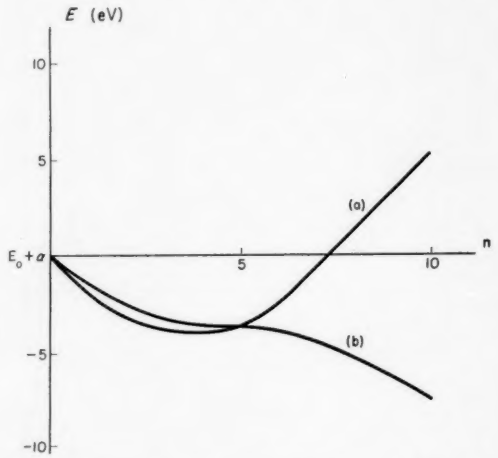

FIG. 4. Variation de l'énergie électronique *E* en fonction du numbre *n* d'électrons *d* par atome :
(a) structure cubique centrée
(b) structure liquide.

Phases σ des métaux de transition : la chaleur spécifique électronique est très forte ($\gamma = 6{,}4\times10^{-3}$ cal/mole/deg^2 pour une phase σ Fe Cr à 44,1 at. pour cent de Cr). Ces phases possèdent des propriétés de supraconductivité et la température de transition présente un maximum particulièrement élevé[10, 11] pour environ 6,5 électrons de valence par atome. On a des raisons de penser que ces fortes températures sont dues à de fortes densités d'états du niveau de Fermi.

Wβ : Des composés de structure Wβ sont supraconducteurs. Les températures de transition sont élévées,[11] parfois même exceptionnellement élevées, comme c'est le cas de Nb_3Sn.[12]

Métaux de la dernière série : U, Np, Pu : Ces métaux ont respectivement 6, 7 et 8 électrons périphériques qui, à basse température, occupent surtout des orbitales 6*d*.[13] Les phases de basse température sont très complexes mais peuvent

Vol. 2
1961

être déduites de phases σ (Uβ) et sont bien décrites par le modèle liquide. Les chaleurs spécifiques électroniques sont élevées : pour Uα, $\gamma = 2 \pm 1 \times 10^{-3}$ cal/mole/deg^2 [14] ; pour Puα, les résultats expérimentaux varient de $\gamma = 11{,}7 \times 10^{-3}$ cal/mole/deg^2 à $20{,}5 \times 10^{-3}$ cal/mole/deg^2.[15] Le terme de Pauli de la susceptibilité magnétique est élevé : $\chi = 4{,}5 \times 10^{-6}$ e.m.u./g pour Uα et $\chi = 5{,}6 \times 10^{-6}$ e.m.u./g pour Puα.

CONCLUSION

Nous voyons donc que notre modèle liquide semble décrire dans ses grandes lignes la structure électronique de ces métaux à structure cristalline complexe et à très grande maille. Il prévoit, en effet, la très forte densité électronique au niveau de Fermi qui les caractérise, alors que les calculs effectués dans l'approximation des liaisons fortes pour des structures c.c.[2] ou c.f.c.[1] prévoient, pour une concentration électronique de 5 à 7 électrons par atome, une densité électronique nettement plus faible. On peut également penser que les fortes températures critiques de supraconductibilité observées dans ces alliages sont liées à ces fortes densités d'états.

La stabilité de ces phases semble limité à une concentration de 5 à 7 électrons par atome dans la bande *d*. Un calcul du terme d'énergie électronique pour les structures c.f.c. ou h.c. permettrait peut-être d'expliquer la stabilité de ces structures pour les grands nombres d'électrons par atome. La stabilité du fer c.c. est sans doute liée à un terme d'énergie magnétique.

BIBLIOGRAPHIE

1. Fletcher G. C. et Wohlfarth E. P., *Phil. Mag.* **42,** 106 (1951).
2. Asdente M. et Friedel J., *Phys. Rev.*, à paraître.
3. Frank F. C. et Kasper J. S., *Acta Cryst., Camb.* **11,** 184 (1958); **12,** 483 (1959).
4. Kripyakevitch P. I., *Kristallographiya* **5,** 1, 79 (1960).
5. Mott N. F. et Jones H., *The Theory of the Properties of Metals and Alloys*, Oxford University Press (1936).
6. Leman G., *J. Phys. Chem. Solids*, à paraître.
7. Koster G. F. et Slater J. C., *Phys. Rev.* **95,** 1167 (1954).
8. Sully A. H., *Manganese*. Butterworths Scientific Publications, London (1955).
9. Hoare F. E. et Matthews J. C., *Proc. Phys. Soc. Lond.* **71,** 2, 220 (1958).
10. Blaugher R. D. et Hulm J. K., *J. Phys. Chem. Solids* **19,** 134 (1961).
11. Matthias B. T., Compton V. B. et Corenzwit E., *J. Phys. Chem. Solids* **19,** 130 (1961).
12. Matthias B. T., Geballe T. H., Geller S. et Corenzwit E., *Phys. Rev.* **95,** 1435 (1954).
13. Friedel J., *J. Phys. Chem. Solids* **1,** 175 (1956).
14. Goodman B. B. et Shoenberg D., *Nature, Lond.*, **165,** 441 (1950).
15. Sandenaw T. A., Olsen C. E. et Gibney R. B., *Conf. Int. Pu, mémoire* 42. Grenoble (1960).

APPENDICE

Solution asymptotique générale de l'équation (6)

Nous allons chercher la forme asymptotique des coefficients A_{jm} dans le cas où nous avons :

$$A_{jm} = \sum_m g_m A_j. \tag{A.1}$$

Cette forme est plus générale que la forme (5), puisque nous supposons seulement que l'amplitude et la phase des diverses fonctions ϕ_{jm} sont indépendantes du site considéré. Dans ces conditions, nous obtenons une relation plus générale que l'équation (6)

$$A_j(E - E_0 - \alpha) = \sum_{j'} A_{j'} \beta_{j'} \tag{A.2}$$

$$\beta_{j'} = \tfrac{1}{5} \int \sum_m g_m \phi_{j'm}(V - U_{j'}) \sum_m g_m^* \phi_{jm}^* \, d\tau$$

$$\alpha = \tfrac{1}{5} \sum_m g_m g_m^* \int \phi_{jm}(V - U_j) \phi_{jm}^* \, d\tau$$

Nous pouvons développer $\beta_{j'}$ en harmoniques sphériques

$$\beta_{j'} = \sum_{lm} \beta_l^m Y_l^m(j') \tag{A.3}$$

La forme asymptotique des coefficients A_j s'obtient comme précédemment. En développant $A_{j'}$ au voisinage de A_j en fonction des dérivées successives de A_j le deuxième membre de (A.2) devient :

$$\sum_{j'} A_{j'} \beta_{j'} = \sum_{j'} \sum_{n=0}^{\infty} \sum_{l=0}^{\infty} \sum_{m=-l}^{+l}$$

$$\frac{1}{n!} (\boldsymbol{b}_{j'} \cdot \nabla)^n A_j \beta_l^m P_l^m (\cos \theta_{j'})$$

$$\times \exp(im\varphi_{j'}) \sqrt{\left[\frac{2l+1}{4\pi} \frac{(l-|m|)!}{(l+|m|)!}\right]} \tag{A.4}$$

En définissant l'opérateur $\boldsymbol{k}$ tel que

$$-i\nabla = \boldsymbol{k}, \tag{A.5}$$

on obtient, en faisant la moyenne sur toutes les positions j' de la sphère des premiers voisins de j :

$$\sum_{j'} A_{j'}\beta_{j'} = \frac{p}{2} A_j \sum_{l=0}^{\infty} \sqrt{\left(\frac{4l+1}{4\pi}\right)} \beta_{2l}^{\circ}$$

$$\times \int_{-1}^{+1} \cos kbtP_{2l}(t)\, dt \tag{A.6}$$

Nous retrouvons donc que A_j est solution de l'équation (10)

$$\Delta A_j + k^2 A_j = 0$$

L'énergie E est reliée en nombre d'onde k par la relation:

$$E - E_0 - \alpha = \tfrac{1}{2} p \sum_{l=0}^{\infty} \sqrt{\left(\frac{4l+1}{4\pi}\right)} \beta_{2l}^{\circ} \int_{-1}^{+1} \cos kbtP_{2l}(t)\, dt \tag{A.7}$$

avec

$$\beta_{2l}^{\circ} = \sqrt{\left(\frac{4l+1}{4\pi}\right)} \int_{\Omega_{j'}} \beta_{j'} P_{2l}(\cos\theta_{j'})\, d\Omega_{j'} \tag{A.8}$$

L'intégrale au deuxième membre de (A.7) représente une moyenne sur toutes les positions j' sur la sphère des premiers voisins de j.

Nous pouvons développer (A.6) de la manière suivante:

$$E - E_0 - \alpha = \tfrac{1}{2} p\beta \frac{\sin kb}{kb}$$

$$+ \tfrac{1}{2} p \sum_{l=1}^{\infty} \sqrt{\left(\frac{4l+1}{4\pi}\right)} \beta_{2l}^{\circ} \int_{-1}^{+1} \cos kbtP_{2l}(t)\, dt, \tag{A.9}$$

où β a la valeur indiquée au paragraphe 1.1. Nous n'avons conservé que le premier terme du deuxième membre, pour la solution générale de l'équation (6) donnée au paragraphe 1.2.

On voit sans peine que β_{2l}° s'écrit.

$$\beta_{2l}^{\circ} = \sqrt{\left(\frac{4l+1}{4\pi}\right)} \sum_{m} g_m g_m^*$$

$$\times \int_{\Omega_{j'}} \left\{ P_{2l}(\cos\theta_{j'})\, d\Omega_{j'} \int \phi_{j'm}(V - U_{j'}) \phi_{jm}^*\, d\tau \right\} \tag{A.10}$$

Si les coefficients g_m sont tous égaux en module, le terme

$$\sum_{m} \int \phi_{j'm}(V - U_{j'}) \phi_{jm}^*\, d\tau$$

étant indépendant de la position de j' sur la sphère des premiers voisins, nous obtenons immédiatement la relation

$$\beta_{2l}^{\circ} = C\, \delta_{0l} \tag{A.11}$$

Dans ce cas donc, nous retrouvons la solution asymptotique obtenue au paragraphe 1.2 en utilisant l'approximation de la phase aléatoire.

Vol. 2
1961

J. Phys. Chem. Solids Pergamon Press 1961. Vol. 21, Nos. 3/4, pp. 295–305. Printed in Great Britain.

CONFIGURATIONS MAGNÉTIQUES. LA MÉTHODE DIRECTE*

E. F. BERTAUT

Laboratoire d'Electrostatique et de Physique du Métal et Centre d'Etudes Nucléaires, Grenoble, France

(*Received* 5 *July* 1960; *revised* 1 *May* 1961)

Résumé—Une méthode simple, basée sur l'hypothèse de voisinages équivalents permet l'énumération de plus de modes de spins que les méthodes de GERSCH et KOEHLER et de Fourier–Villain.

Abstract—A simple method, based on the equivalent neighborhood hypothesis allows enumeration of more spin modes than the GERSCH and KOEHLER and the Fourier–Villain methods.

1. INTRODUCTION

1.1. *Historique. Le problème de périodicité*

ON DISPOSE actuellement de deux méthodes permettant de prévoir la configuration de spins dans les structures magnétiques. L'une est empruntée à la théorie des groupes, l'autre, plus physique s'appuie directement sur la notion de l'intégrale d'échange en utilisant, soit l'énergie d'échange de Heisenberg soit le champ moléculaire de NÉEL[1].

Dans la première méthode, on assimile le spin à un vecteur axial de symétrie $\infty/m\ 2'/m'$, et, naturellement, tout groupe qui admet un sous-groupe ayant cette symétrie, est un groupe magnétique possible. Toutefois, il ne s'agit pas du cadre des 230 groupes d'espace habituels de Fedoroff et Schoenflies, mais des groupes de Shubnikov dits "bicolores"[2], au nombre de 1651, et que l'on peut dériver des 230 groupes cristallographiques par l'introduction d'éléments d'antisymétrie. C'est ainsi que le symbole $2'$ représente un antiaxe d'ordre deux qui fait tourner un vecteur de 180° et *change son sens*. Pour une revue de la question nous renvoyons aux références indiquées.[3, 4, 5] Au même titre que les 230 groupes cristallographiques fournissent le cadre des structures tripériodiques des cristaux, la méthode des groupes bicolores permet de dénombrer tous les groupes magnétiques à *vecteurs tripériodiques*, le spin étant toujours considéré comme un vecteur axial de symétrie $\infty/m\ 2'/m'$.

La deuxième méthode a été utilisée par VAN VLECK[6], ANDERSON[7], SMART[8], YAFET et KITTEL[9] et récemment par GERSCH et KOEHLER[10] Ces auteurs énumèrent, dans des réseaux de Bravais les configurations de spins compatibles avec les hypothèses suivantes :

(a) chaque spin "voit" le même voisinage ou un voisinage énergétiquement équivalent,

(b) les spins sont colinéaires.

Ces hypothèses entraînent comme conséquence que les spins forment des réseaux à vecteurs tripériodiques.

Un point de vue nouveau voit le jour lorsque, abandonnant l'hypothèse de la colinéarité, YOSHIMORI[11] montre sur l'exemple de MnO_2 la possibilité d'arrangements spiralés dont la période n'est plus commensurable avec celle de la structure cristalline support. VILLAIN[12], partant de la notion du champ moléculaire, démontre que la "transformée de Fourier" de l'intégrale d'échange doit être maximum dans les réseaux de Bravais. Signalons aussi le travail contemporain de KAPLAN[13] sur les spirales dans Cr et sur la stabilité de la configuration ferrimagnétique dans les spinelles[14].

Remarquons ici que les configurations spiralées ne rentrent pas dans le cadre des groupes bicolores. Cependant, les structures spiralées sont encore

* In à la Neutron Diffraction Convention, Gatlinburg, Tennessee, U.S.A., April, 1960.

"périodiques", à condition de choisir une définition de périodicité plus large. C'est ce que nous ferons dans ce mémoire.

1.2. *Definition. Hypothèse P*

L'énergie d'échange d'un cristal est

$$W = -2\sum_{i,j} J_{ij}\boldsymbol{S}_i\cdot\boldsymbol{S}_j = -2\sum_{ij} J_{ij}S_iS_j\cos\Theta_{ij} \tag{1-1}$$

Ici, $\boldsymbol{S}_i$ est le spin au point $\boldsymbol{R}_i$, Θ_{ij} l'angle entre les spins en $\boldsymbol{R}_i$ et $\boldsymbol{R}_j$ que nous noterons plus explicitement par $\Theta(\boldsymbol{R}_i, \boldsymbol{R}_j)$. J_{ij} est l'intégrale d'échange habituelle. La sommation est étendue à tous les couples d'atomes du cristal.

Par définition, les spins forment un réseau périodique lorsque pour tout couple de spins $\boldsymbol{S}_i$ et $\boldsymbol{S}_j$ on peut trouver un couple de spins $\boldsymbol{S}_i'$, $\boldsymbol{S}_j'$ aux points $\boldsymbol{R}_i' = \boldsymbol{R}_i+\boldsymbol{L}$ et $\boldsymbol{R}_j' = \boldsymbol{R}_j+\boldsymbol{L}$ tel que

$$\Theta(\boldsymbol{R}_i, \boldsymbol{R}_j) = \Theta(\boldsymbol{R}_i, \boldsymbol{R}_j') \tag{1-2}$$

$$S_i = S_i';\ S_j = S_j' \tag{1-3}$$

$\boldsymbol{L}$ étant le vecteur

$$\boldsymbol{L} = l_1\boldsymbol{A}_1+l_2\boldsymbol{A}_2+l_3\boldsymbol{A}_3 \tag{1-4}$$

Ici $\boldsymbol{A}_j$ ($j = 1, 2, 3$) est un vecteur translation du réseau cristallographique et l_j ($j = 1, 2, 3$) un nombre entier.

Lorsqu'on ne peut trouver qu'un vecteur $\boldsymbol{L}_1$, la périodicité sera à une dimension. Lorsqu'on peut trouver trois vecteurs $\boldsymbol{L}_1$, $\boldsymbol{L}_2$, $\boldsymbol{L}_3$, tels que (1-4), la périodicité sera tridimensionnelle. Comme en cristallographie, on a intérêt à choisir les translations $\boldsymbol{L}_1$, $\boldsymbol{L}_2$, $\boldsymbol{L}_3$ les plus petites possibles pour définir la maille magnétique.

Notre définition de périodicité angulaire est plus générale que celle de périodicité vectorielle de la théorie des groupes bicolores. En particulier elle inclut le cas des modes spiralés [Figs. 1(a) et 1(b)].

Nous n'étudions pas* dans ce mémoire l'hypothèse P dans toute sa généralité, mais sous une forme plus restrictive en adoptant l'hypothèse (a) de GERSCH et KOEHLER[10] (équivalence des voisinages), mais en remplaçant leur hypothèse (b) de spins colinéaires par celle (b') de spins coplanaires. Nous montrons que nous trouvons en plus de leurs arrangements colinéaires ceux spiralés. Nous allons d'abord confronter les résultats des méthodes de G. et K., de Fourier–Villain et de la méthode directe sur l'exemple instructif de la chaîne linéaire.

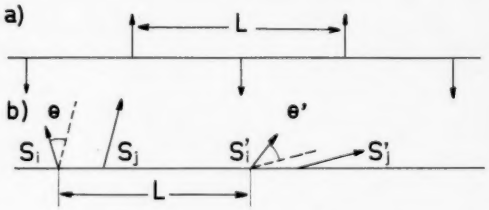

FIG. 1 (a) Périodicité vectorielle
(b) Périodicité angulaire.

2. LA CHAINE LINEAIRE

2.1. *Droite isotope*

2.1.1. *Methode directe.* Soit d l'équidistance d'atomes situés sur un réseau linéaire et porteurs de spins S égaux. Soient X_- et X_+ les angles que fait le spin $\boldsymbol{S}_n$ avec les spins $\boldsymbol{S}_{n-1}$ et $\boldsymbol{S}_{n+1}$ respectivement. Le fait de se donner X_- et X_+, combiné avec nos hypothèses (a) et (b') *fixe aussitôt les angles dans toute la chaîne.*

En effet, si $\boldsymbol{S}_{n+1}$ fait l'angle X_+ avec $\boldsymbol{S}_n$, $\boldsymbol{S}_{n+1}$ doit faire l'angle X_- avec $\boldsymbol{S}_{n+2}$ (en vertu de l'hypothèse P). Il s'ensuit plus généralement que $\boldsymbol{S}_{n+m}$ fait avec $\boldsymbol{S}_n$ l'angle

$$\varphi_m = \frac{m}{2}(X_++X_-)$$

si m est pair, et

$$\varphi_m = \frac{m-1}{2}(X_++X_-)+X_+$$

si m est impair [cf. Fig. 2(a)].

L'énergie d'échange W_e par spin $\boldsymbol{S}_n$, compte tenu des premiers et seconds voisins

$$(S_{n+1}, S_{n-1};\ S_{n+2}, S_{n-2})$$

est

$$W_e = -2S^2[J_1(\cos X_++\cos X_-)+2J_2\cos(X_++X_-)] \tag{2-1}$$

* L'exemple suivant est dû au referee. L'arrangement ↑ ↑ ↑ ↓ ↓ ↓ ↑ ↑ ↑ ... satisfait à l'hypothèse P, mais pas à celle de l'équivalence des voisinages. Nos hypothèses (a) et (b') satisfont naturellement à P.

Vol. 2
1961

Tableau 1

Catégorie	X_+	X_-	$W_E/4S^2$	Conditions de stabilité	Périodicité vectorielle	Périodicité angulaire
A 1	0	0	$-J_1 \quad -J_2$	$J_1 > 0$; $4J_2+J_1 > 0$	d	d
A 2	π	π	$J_1 \quad -J_2$	$J_1 < 0$; $4J_2-J_1 > 0$	$2d$	d
A 3a	0	π	J_2	instable	$2d$	$2d$
A 3b	π	0	J_2	instable	$2d$	$2d$
B 1	$X_+ =$	X_-	$J_2+\frac{1}{8}J_1^2/J_2$	$J_2 < -\frac{1}{4}\lvert J_1\rvert$	non rationnelle	d
	$\cos X = -J_1/4J_2$					

Les conditions d'énergie minimum impliquent immédiatement que

$$\sin X_+ = \sin X_- \qquad (2\text{–}2)$$

Le Tableau 1 résume les deux classes de solutions possibles (classe A : sin $X = 0$; classe B : sin $X \neq 0$) ainsi que leurs énergies, conditions de stabilité et enfin les périodicités *vectorielles* et *angulaires* qui ne sont pas toujours égales.

Les modes 3a et 3b ne sont pas distincts, de sorte que nous trouvons quatre modes distincts possibles. Les solutions A1 ($\uparrow\ \uparrow\ \uparrow\ \uparrow$), A2 ($\uparrow\ \downarrow\ \uparrow\ \downarrow$), A3a ($\uparrow\ \uparrow\ \downarrow\ \downarrow$) et A3b ($\uparrow\ \downarrow\ \downarrow\ \uparrow$) ont déjà été prévues par GERSCH et KOEHLER. On a toujours

$$W_e(B1) < W_e(A3) \qquad (2\text{–}3)$$

de sorte qu'en négligeant l'énergie magnétocristalline, le mode B1 *spiralé est plus stable que le mode* A3.

2.1.2. *Méthode de Fourier–Villain*[12]

$$W_e = 4S_0^2(J_1 \cos 2\pi kd + J_2 \cos 4\pi kd) \qquad (2\text{–}4)$$

La méthode de Fourier–Villain fournit par annulation des dérivées premières de (2–4) les solutions déjà signalées A1, 2, et B, mais *non pas* les solutions A3a et 3b. La raison physique en est que (2–4) ne distingue pas entre voisins gauches et droits

$$\cos[2\pi k(R_{n+1}-R_n)] = \cos[2\pi k(R_{n-1}-R_n)]$$

alors que dans les modes A3a et A3b, il y a une anisotropie manifeste des voisinages premiers (voisin gauche parallèle/voisin droit anti-parallèle). On ne doit pas en conclure que la méthode de Fourier échoue dans ce cas. Envisageons, en effet, une droite dans laquelle les distances entre voisins immédiats soient alternativement d et d', les intégrales d'échanges respectives étant J_1 et J_1' [Fig. 2(b)].

2.2. *Droite anisotrope*

2.2.1. L'énergie d'échange devient alors

$$W_e = -2S_0^2[J_1 \cos 2\pi kd + J_1' \cos 2\pi kd' + 2J_2 \cos 2\pi k(d+d')] \qquad (2\text{–}5)$$

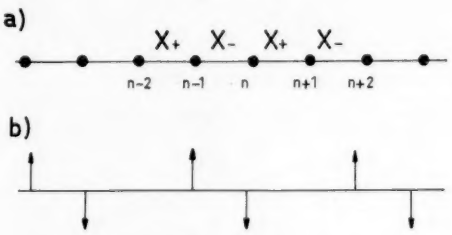

FIG. 2. Chaîne linéaire
(a) Droite isotrope
(b) Droite anisotrope.

Les modes A3a et A3b auront cette fois-ci des énergies différentes

$$W_e(A3a)/S_0^2 = J_2 - \tfrac{1}{2}(J_1 - J_1') \qquad W_e(A3b)/S_0^2 = J_2 + \tfrac{1}{2}(J_1 - J_1') \qquad (2\text{–}6)$$

A la limite, c'est-à-dire quand J_1' tend vers J_1, et d' vers d, on obtient l'énergie du mode A3 du Tableau 1.

En général, la méthode directe fournit un nombre de configurations plus élevé. Nous admettrons que la méthode de Fourier–Villain permette de les retrouver par un abaissement convenable de la symétrie du modèle.

Remarque. A la droite anisotrope correspond

encore un mode spiralé B, mais avec des angles X_+ et X_- *différents* et *alternants*. On trouve :

$$\left.\begin{aligned}\cos X_+ &= \cos 2\pi kd = -\tfrac{1}{4}r'-(1-t^2)/r' \\ \cos X_- &= \cos 2\pi kd' = -\tfrac{1}{4}r-(1-t^{-2})/r\end{aligned}\right\} \quad (2\text{–}7)$$

$$W_e(B) = 2J_2S_0^2\,(t+t^{-1})+\tfrac{1}{4}\,rr' \quad (2\text{–}8)$$

Ici, nous avons introduit les abréviations

$$r = J_1/J_2;\ r' = J_1'/J_2;\ t = J_1'/J_1 \quad (2\text{–}9)$$

On démontre encore que si cos X_- existe, on a toujours

$$W_e(B) < W_e(A3) \quad (2\text{–}10)$$

2.3. *Conditions de stabilité*

Le critère classique de stabilité est la positivité de la forme quadratique :

$$(\partial X_+)^2\,\frac{\partial^2 W}{\partial X_+^2}+2\partial X_+\partial X_-\,\frac{\partial^2 W}{\partial X_+\partial X_-} +(\partial X_-)^2\frac{\partial^2 W}{\partial X_-^2} > 0 \quad (2\text{–}11)$$

Cela exige que l'on ait simultanément :

$$\frac{\partial^2 W}{\partial X_+^2} > 0;\ \frac{\partial^2 W}{\partial X_-^2} > 0 \quad (2\text{–}12a)$$

$$D = \begin{vmatrix} \dfrac{\partial^2 W}{\partial X_+^2} & \dfrac{\partial^2 W}{\partial X_+\partial X_-} \\ \dfrac{\partial^2 W}{\partial X_+\partial X_-} & \dfrac{\partial^2 W}{\partial X_-^2} \end{vmatrix} > 0 \quad (2\text{–}12b)$$

Les conditions de stabilité sont résumées dans la sixième colonne du Tableau 1. Le mode spiralé B est toujours stable pourvu que $J_2 < 0$ et que cos X (cf. Tableau 1) existe. Le mode A3 où l'on a $D = -4S^2J_1^2$ est instable sauf pour $J_1 = 0$. Dans ce dernier cas, le mode A3 peut être considéré comme un ensemble de deux réseaux, l'un constitué par les spins pairs S_{2n}, l'autre par les spins impairs S_{2n+1}, chacun des réseau étant antiferromagnétique, mais sans couplage entre eux. L'existence du mode spiralé montre cependant que par continuité, l'angle entre les réseaux S_{2n} et S_{2n+1} est l'angle droit (cos $X = 0$) (en absence d'anisotropie cristalline). Les conditions (2–12) sont surabondantes. Il faut et il suffit que la matrice dans (2–12b) ait des racines positives. Cette dernière condition se généralise facilement au cas de plusieurs variables.

2.4. *Influence de l'énergie magnétocristalline*

Malgré la valeur généralement faible de l'énergie magnéto-cristalline par rapport à l'énergie d'échange, une direction de facile aimantation favorise les modes colinéaires au détriment des modes spiralés. Le modèle que l'auteur a en vue est celui utilisé par NÉEL[15] d'un réseau magnétique en couches, les forces d'échange dans la couche (J_0) étant fortement ferromagnétiques tandis que celles entre couches, premiers et deuxièmes voisins (J_1, J_2) sont faibles et d'un même ordre de grandeur que les forces magnéto-cristallines. Le modèle linéare est suffisant pour la discussion suivante.

Anisotropie uniaxe. On suppose qu'en première approximation, l'énergie magnétocristalline par spin est donnée par

$$W_a = -K\cos^2\Theta \quad (2\text{–}13)$$

où Θ est l'angle entre le spin et l'axe Oz.

Lorsque K est grand et négatif, Oz sera une direction de difficile aimantation et dans tous les modes, colinéaires et spiralés, les spins se trouvent dans le plan P, perpendiculaire à Oz ($\Theta = \pi/2$). Donc, en l'absence ou présence d'une direction de difficile aimantation, rien ne sera changé par rapport aux résultats précédents.

Par contre, lorsque K est positif, $\Theta = 0$ est la position d'équilibre des modes colinéaires dont l'énergie par spin est :

$$W = W_e-K \quad (2\text{–}14)$$

Dans le mode spiralé, on a par spin

$$W_a = -\frac{K}{2}-\frac{K}{2}\langle\cos 2\Theta_n\rangle \quad (2\text{–}15)$$

Si l'on néglige le terme en $\langle\cos 2\Theta_n\rangle$ qui, en première approximation, est un terme aléatoire, le mode A_3 devient plus stable que le mode B lorsque

$$K > -\tfrac{1}{2}\,S^2J_1^2/J_2 \quad (2\text{–}16)$$

Ce raisonnement est très schématique, car il néglige la variation en fonction de n de l'intervalle angulaire X_n sous l'influence de K (cf. Appendice

Tableau 2. Parité des coordonnées et angle de rotation

m	n	$\varphi(m,n)$	
pair	pair	$\frac{m}{2}(X_+ + X_-) +$	$\frac{n}{2}(Y_+ + Y_-)$
pair	impair	$\frac{m}{2}(X_+ + X_-) +$	$\frac{n-1}{2}(Y_+ + Y_-) + Y_+$
impair	pair	$\frac{m-1}{2}(X_+ + X_-) + X_+$	$\frac{n}{2}(Y_+ + Y_-)$
impair	impair	$\frac{m-1}{2}(X_+ + X_-) + X_+ +$	$\frac{n-1}{2}(Y_+ + Y_-) + Y_+$

I) mais illustre suffisamment la possibilité de transitions entre un mode spiralé et colinéaire. (par exemple, par suite de la variation thermique de K).

Anisotropie orthohombique. Envisageons le cas où

$$W_a = -K_1 \cos^2 \Theta - K_2 \sin^2 \Theta \cos 2\varphi \quad (2\text{–}17)$$

où K_1 est négatif, K_2 positif avec $K_1 > K_2$. $\Theta = \pi/2$ est encore une position d'équilibre. Les spins resteront dans le plan P dans lequel la direction $\varphi = 0$ est axe de facile aimantation. On a par spin

$$W_a(A) = -K_2; \; W_a(B) = 0 \quad (2\text{–}18)$$

En particulier, le mode A3 est plus stable que le mode B lorsque

$$K_2 > -\tfrac{1}{4} S^2 J_1^2 / J_2 \quad (2\text{–}19)$$

Couplages pseudodipolaires. NÉEL[15] a établi que les couplages dipolaires et pseudodipolaires favorisent les transitions antiferromagnétiques → ferromagnétiques sous l'action d'un champ extérieur. Nous remettons à plus tard l'étude de l'influence de tels couplages dans les modes spiralés.

3. CAS DE DEUX OU TROIS DIMENSIONS

On peut postuler que dans toute direction d'espace, les seuls modes capables de se propager sont les modes discutés dans le cas de la chaîne linéaire. On peut énumérer leurs combinaisons distinctes [cf. Ref. (10)].

On peut aussi généraliser l'alternance d'angles X_+ et X_- au cas de plusieurs axes. C'est cette méthode que nous utiliserons. Dans le cas plan, les modes seront notés (X_+, X_-; Y_+, Y_-), dans celui de l'espace (X_+, X_-; Y_+, Y_-; Z_+, Z_-).

La méthode décrite s'applique à toutes les structures magnétiques coplanaires. Le nombre de variables est généralement surabondant et l'on doit écrire les conditions dans lesquelles les voisinages considérés sont énergétiquement équivalents. Ces conditions ont une signification géométrique évidente.

3.1. *Reseaux à deux dimensions*

L'angle de rotation $\varphi(m, n)$ du spin $\boldsymbol{S}_{m,n}$ par rapport au spin à l'origine $\boldsymbol{S}_{0,0}$ est donné dans le Tableau 2 en fonction de la parité des coordonnées m, n. Il est alors aisé de former les différences $\Delta\varphi$ [telles que $\Delta\varphi = \varphi(m+1, n) - \varphi(m,n)$ par exemple, etc.] qui représentent les rotations relatives des spins des premiers et seconds voisinages d'un spin fixe $\boldsymbol{S}_{m,n}$. Illustrons la procédure suivie par l'exemple du réseau hexagonal plan.

3.1.1. *Réseau hexagonal plan.* Dans les premières et deuxièmes lignes du Tableau 3 on a porté les coordonnées respectives des premiers et seconds voisinages du point (m,n). Dans la troisième ligne figurent les angles de rotation relatifs du premier

voisinage de $S_{m,n}$ lorsque m et n sont pairs (par exemple $m = 0$, $n = 0$). Dans la quatrième ligne figurent les angles de $S_{m,n}$ avec son premier voisinage lorsque m est impair et n pair (par exemple $m = 1$, $n = 0$). L'inspection du tableau montre que les premiers voisinages de $S_{0,0}$ et $S_{1,0}$ deviennent énergétiquement équivalents si l'on impose l'une des conditions

$$X_+ = X_- = X \text{ ou } Y_+ = Y_- = Y \quad (3\text{–}1)$$

On peu vérifier que, l'une des deux conditions étant satisfaite, l'équivalence des premiers voisinages autour de $S_{m,n}$ est assurée quelle que soit la parité de m et de n. Il en est de même des seconds voisinages (cf. 5ème et 6ème lignes du Tableau 3). Adoptant la seconde des conditions (3–1) l'énergie d'échange devient

$$\begin{aligned} W = -2S^2 \{ & J_1 [\cos X_+ + \cos X_- + 2\cos Y \\ & + \cos(X_+ + Y) + \cos(X_- + Y)] + J_2 [\cos(X_+ + 2Y) \\ & + \cos(X_- + 2Y) + \cos(X_+ - Y) + \cos(X_- Y) \\ & + 2\cos(X_+ + X_- + Y)]\} \end{aligned} \quad (3\text{–}2)$$

L'étude des dérivées premières montre l'existence de deux classes de solutions, A et B.

$$\begin{aligned} &\text{A} : \sin X_+ = \sin X_- = \sin Y = 0 \\ &\text{B} : \sin X \neq 0 \end{aligned} \quad (3\text{–}3)$$

Dans le Tableau 4 et la Fig. 3(a), nous avons représenté les quatre modes colinéaires A_1 à A_4 déjà obtenus par G. et K. Les modes A_3 et A_4 sont en général instables (en effet, le déterminant (2–12) et $\partial^2 W/\partial X^2$ sont de signe contraire) et ne peuvent être retrouvés par la méthode de Fourier–Villain sans introduire d'interactions anisotropes.

Modes spiralés. Aussi bien par la méthode directe que par celle de Fourier–Villain[12] on retrouve les modes A_1 et A_2 ainsi que deux modes spiralés stables B_1 et B_2 (cf. Fig. 3 et Tableau 4). Les deux conditions (3–1) sont satisfaites dans tous ces cas. Posons alors pour faire la liaison entre les deux méthodes

$$X = 2\pi h; \quad Y = 2\pi k \quad (3\text{–}4)$$

Les modes pourront être notés $[h,k]$, h et k étant les composantes du vecteur de propagation. Les modes A_1 et A_2 s'écriront par exemple [0,0] et $[\frac{1}{2},0]$ respectivement.

Tableau 3. Réseau hexagonal plan—angles de rotation

Voisins premiers de (m, n)	$m, n+1$	$m, n-1$	$m+1, n$	$m-1, n$	$m+1, n+1$	$m-1, n-1$
Voisins seconds de (m, n)	$m+1, n-1$	$m-1, n+1$	$m+1, n+2$	$m+2, n+1$	$m-1, n-2$	$m-2, n-1$
Angles relatifs des premiers voisins de $S_{0,0}$	Y_+	$-Y_-$	X_+	$-X_-$	$X_+ + Y_+$	$-(X_- + Y_-)$
A.r. des premiers voisins de $S_{1,0}$	Y_+	$-Y_-$	X_-	$-X_+$	$X_- + Y_+$	$-(X_+ + Y_-)$
A.r. des seconds voisins de $S_{0,0}$	$X_+ - Y_-$	$-X_- + Y_+$	$X_+ + Y_+ + Y_-$	$X_+ + X_- + Y_+$	$-(X_- + Y_+ + Y_-)$	$-(X_+ + X_- + Y_-)$
A.r. des seconds voisins de $S_{1,0}$	$X_- - Y_-$	$-X_+ + Y_+$	$X_- + Y_+ + Y_-$	$X_+ + X_- + Y_+$	$-(X_+ + Y_+ + Y_-)$	$-(X_- + X_+ + Y_-)$

Vol. 21
1961

Tableau 4. *Modes hexagonaux plans*

Modes	Rotations X_+ X_- Y	Vecteur de propagation*	Energie $W_e/4S^2$	Stabilité
A_1	0 0 0	[0 0 0]	$-3(J_1+J_2)$	$J_1>0$; $J_1+3J_2>0$
A_2	π π π	[½ 0 ½]	(J_1+J_2)	$J_2<0$; $J_1-J_2<0$; $-J_1+8J_2<0$
ou	π π 0			
ou	0 0 π			
A_3	0 π π		(J_1-J_2)	instable
A_4	0 π 0		$-(J_1-J_2)$	instable
B_1	$\cos X=-\frac{1}{2}(1+J_1/J_2)$ $Y=0$	$[h \quad 0 \quad \bar{h}]$	$(J_1^2+3J_2^2)/(2J_2)$	$J_2<0$; $J_1-J_2>0$; $J_1+3J_2<0$
B_{2a}	$\cos X=-\frac{1}{2}$ $X=Y$	$[h \quad h \quad 2\bar{h}]$	$3(\frac{1}{2}J_1-J_2)$	$J_1<0$; $-J_1+8J_2>0$

* Le vecteur de propagation est ici donné avec trois indices (permutables) $[h\ k\ i]$ où $i=-(h+k)$. Cela fait mieux ressortir l'équivalence des modes $[\frac{1}{2}\ 0]$, $[0\ \frac{1}{2}]$, $[\frac{1}{2}\ \frac{1}{2}]$.

Mode B_1 $[h,0]$. Les modes $[h,\bar{h}]$, $[0,h]$ $[\bar{h},0]$ sont équivalents. On trouve

$$\cos X = -(J_1+J_2)/(2J_2) \qquad (3\text{–}5)$$

Les conditions de stabilité se réduisent à

$$J_2 < 0 \qquad (3\text{–}6)$$

L'existence de cos X exige que l'on ait

$$(J_1+3J_2)(J_1-J_2) < 0 \qquad (3\text{–}7)$$

L'énergie d'échange devient

$$W = 2S^2(J_1^2+3J_2^2)/(J_2) \qquad (3\text{–}8)$$

On vérifie que lorsque (3–6) et (3–7) sont satisfaites W (3–8) est toujours inférieure à l'énergie des deux modes colinéaires $[0,0]$ et $[\frac{1}{2}\,\frac{1}{2}]$.

Le Tableau 3 (3ème et 5ème lignes) en y faisant $X_+ = X_- = X$; $Y = 0$ montre les angles de rotation du premier et second voisinage autour de $S_{0,0}$. Les vecteurs spins du mode $[h,0]$ sont

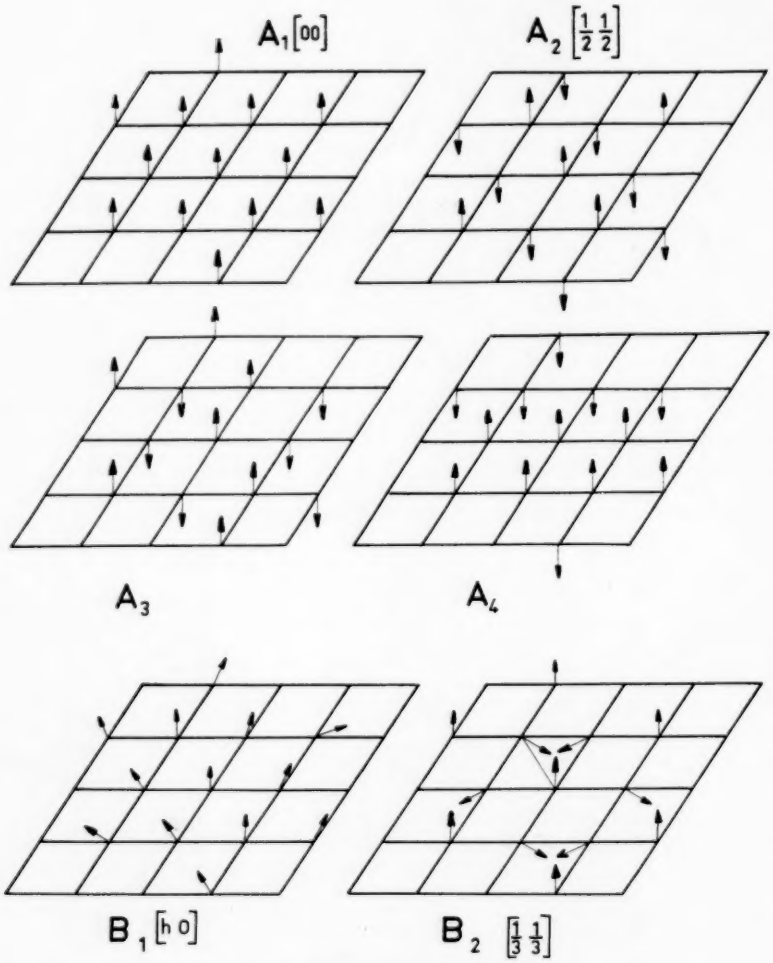

FIG. 3 (a) Modes hexagonaux colinéaires
(b) Modes hexagonaux spiralés.

parallèles selon l'axe [1 1 0] (Les modes équivalents sont parallèles aux axes équivalents Ox ou Oy).

Mode B_2 $[h,h]$. Dans ce mode, on obtient

$$\frac{\partial We}{\partial X}/4S^2 = J_1(\sin X + \sin 2X) + 3J_2 \sin 3X$$

$$= \sin X(1+2\cos X)\,[J_1 + 3J_2(2\cos X - 1)] \quad (3\text{–}9)$$

Une autre solution de (3–9) est

(2) $$\cos X = +\tfrac{1}{2} - J_1/(6J_2) \quad (3\text{–}13)$$

solution instable, car on trouve après quelques calculs

$$D = -2J_2^2(1-\cos X)^2(1+2\cos X)^2 \sin^2 X \quad (3\text{–}14)$$

quantité toujours négative.

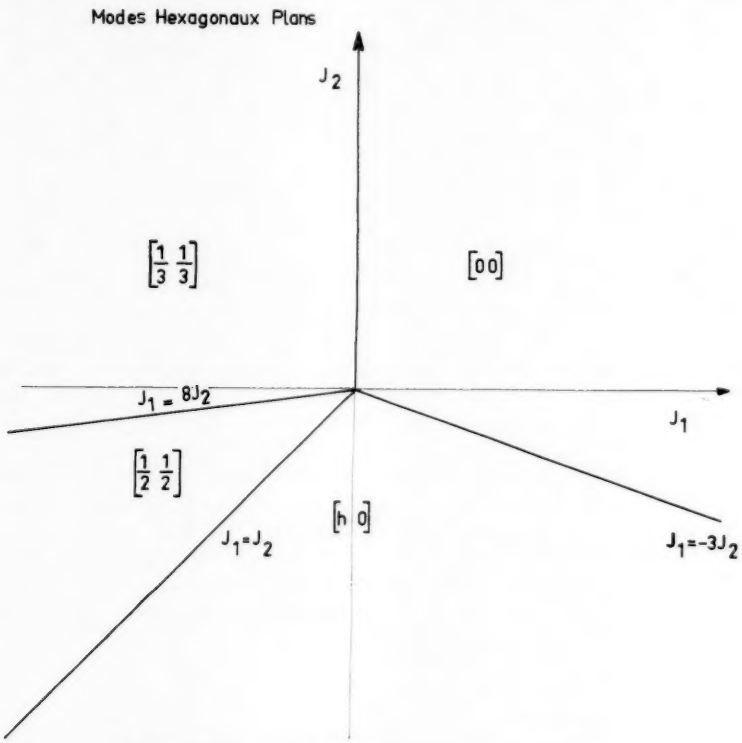

FIG. 4. Domaine de stabilité des modes hexagonaux.

Ecartant la solution triviale $\sin X = 0$, on trouve une solution particulièrement intéressante

(1) $$\cos X = -\tfrac{1}{2} \text{ ou } X = 2\pi/3 = 120° \quad (3\text{–}10)$$

Les conditions de stabilité (2–12) se réduisent à

$$-J_1 + 6J_2 > 0 \quad (3\text{–}11)$$

L'énergie d'échange devient

$$W = 6S^2(J_1 - 2J_2) \quad (3\text{–}12)$$

En résumé, la seule solution possible du mode $[h,h]$ est $X = 2\pi/3$. Ce mode peut encore se noter $[\frac{1}{3},\frac{1}{3}]$ et semble avoir été observé la première fois dans CrSe par CORLISS et HASTINGS[16]. Nous n'avons pas étudié de modes d'ordre plus élevé. Il est douteux qu'ils soient stables.

Domaines d'existence. Des conditions de stabilité, d'existence de $\cos X$ dans les modes spiralés et de la comparaison des énergies entre elles

Vol. 21
1961

Tableau 5. *Cube simple*

Modes		Angles de rotation X Y Z_+ Z_-	Energie $W/4S^2$	N° G. et K.
I	A_1	0 0 0 0	$-3J_1 - 6J_2$	1
	A_2	π π π π	$3J_1 - 6J_2$	10
	A_3	0 0 π π	$-J_1 + 2J_2$	3
	A_4	π π 0 00	$J_1 + 2J_2$	7
	B_1	X X X X	$J_1^2/2J_2$	—
		$\cos X = -J_1/4J_2$		
II	A_5	0 0 0 π	$-2J_1 - 2J_2$	2
	A_6	π π 0 π	$2J_1 - 2J_2$	9
	A_7	0 π 0 π	$2J_2$	6
	B_2	X X 0 π	$J_1^2/2J_2$	—
		$\cos X = -J_1/2J_2$		
III		$X_+ = Y_+$ $X_- = Y_-$ $Z_+ = Z_-$		
	A_8	0 0π 0	$-J_1$	4
	A_9	0 π π	$+J_1$	8
IV	A_{10}	$X_+ = Y_+ = Z_+ = 0$		
		$X_- = Y_- = Z_- = \pi$		5

résultent des conditions parmi lesquelles on prend toujours les plus restrictives. Elles limitent les domaines d'existence des modes, en absence d'énergies magnétocristallines négatives (cf. Tableau 4 et Fig. 4).

3.2. *Réseau a trois dimensions*

Nous ne traitons que le cas du cube simple. Les voisins proches du point (l, m, n) sont les six points $(l \pm 1, m, n)$, $(l, m \pm 1, n)$ $(l, m, n \pm 1)$. Les douze voisins seconds sont $(l \pm 1, m \pm 1, n)$, $(l, m \pm 1, n \pm 1)$ $(l \pm 1, m, n \pm 1)$. Comme précédemment, on pourra évaluer les angles de rotation des spins du premier et second voisinages d'un spin donné et écrire ensuite les conditions pour les voisinages de même espèce soient équivalents. On trouve que les premiers voisinages sont toujours équivalents. Quant aux seconds voisinages, l'équivalence est certainement obtenue lorsque

$$X_+ = X_- = X;\ Y_+ = Y_- = Y;\ Z_+ = Z_- = Z \tag{3-15}$$

Dans ces conditions, la méthode directe et de Fourier–Villain fournissent la même expression pour l'énergie d'échange.

$$W_e = -4S^2[J_1(\cos X + \cos Y + \cos Z) + 2J_2(\cos X \cos Y + \cos Y \cos Z + \cos Z \cos X)] \tag{3-16}$$

On trouve quatre modes stables que l'on note par $(0, 0, 0)$; (π, π, π) ; $(0, 0, \pi)$ et $(\pi, \pi, 0)$ et un mode spiralé $B(X, X, X)$ instable (le critère de stabilité est $J_2 < 0$; mais de plus, la comparaison des énergies montre que $W(XXX) < W(A_3)$ implique $\cos X < -\frac{1}{3}$ et $J_1 < 0$; alors que $W(XXX) < W(A_4)$ implique $\cos X < \frac{1}{3}$ et $J_1 > 0$; ces conditions sont contradictoires). Les modes stables A_1, A_2 A_3, A_4 sont numérotés 1, 10, 3 et 7 chez G. et K.[10]

II—*La conditions* (3–15) *est suffisante, mais pas nécessaire*. L'équivalence des seconds voisins est aussi obtenue en posant

$$X_+ = X_- = X;\ Y_+ = Y_- = Y;\ Z_+ \neq Z_- \tag{3-17}$$

On trouve alors les modes colinéaires $(0 ; 0 ; 0, \pi)$, $(\pi ; \pi ; 0, \pi)$ $(0 ; \pi ; 0, \pi)$ caractérisés par quatre indices correspondant aux quatre variables X, Y, Z_+ et Z_- et un mode spiralé $(X ; X ; 0, \pi)$ avec $\cos X = J_1/2J_2$.

Les modes 5, 6, 7 sont numérotés 2, 9 et 6 chez G. et K.

III–La condition

$$X_+ = Y_+ = X;\ Y_+ = Y_- = Y;\ Z_+ = Z_- = Z \tag{3-18}$$

ne rend les seconds voisinages équivalents que

pour les valeurs particulières $X = 0$; $Y = \pi$ et $Z = 0$ ou π. Les deux modes correspondants A_8 et A_9 sont numérotés 3 et 4 chez G. et K.

IV–Enfin, la condition

$$X_+ = Y_+ = Z_+ = X_1; X_- = Y_- = Z_- = X_2 \tag{3-19}$$

ne fournit de seconds voisinages équivalents que pour $X_1 = 0$; $X_2 = \pi$. Le mode correspondant A_{10} est noté 5 chez G. et K.

Tous les modes sous II, III et IV sont instables. La méthode de Fourier–Villain[12] ne fournit que les modes sous I.

CONCLUSION

L'intérêt de la méthode directe réside non seulement dans son extrême simplicité, mais aussi dans le fait qu'elle est à la fois plus riche que les méthodes de G. et K.[10] et de F–V[12]. En effet, en plus des modes colinéaires de G. et K. elle contient les modes spiralés. En plus des modes trouvés par la méthode de F–V elle contient des modes, il est vrai, instables, mais stabilisables soit par une énergie magnétocristalline, soit par un abaissement de symétrie.

BIBLIOGRAPHIE

1. Néel L., *Ann. Phys. Paris* **3,** 137 (1948).
2. Belov N. V., Neronova N. N. et Smirnova T. S., *Trud. Inst. Krist. Akad. Nauk SSSR.* **11,** 33 (1955); *Kristallografia* **2,** 315 (1957).
3. Donnay G., Corliss L. M., Donnay J. D. H., Elliott N. et Hastings J. M., *Phys. Rev.* **112,** 1917 (1958).
4. le Corre Y., *Bull. Soc. Fr. Min. Crist.* **81,** 120 (1958).
5. Donnay J. D. H. et Donnay G., *C.R. Acad. Sci. Paris* **248,** 3317 (1959).
6. van Vleck J. H., *J. Phys. Radium* **12,** 262 (1951).
7. Anderson P. W., *Phys. Rev.* **79,** 705 (1950).
8. Smart J. S., *Phys. Rev.* **86,** 968 (1952).
9. Yafet Y. et Kittel C., *Phys. Rev.* **87,** 290 (1952).
10. Gersch H. A. et Koehler W. C., *J. Phys. Chem. Solids* **5,** 180 (1958).
11. Yoshimori A., *J. Phys. Soc. Japan* **14,** 807 (1959).
12. Villain J., note C.E.A., juillet 1959; *J. Phys. Chem. Solids* **11,** 303 (1959).
13. Kaplan T. A., *Phys. Rev.* **116,** 888 (1957).
14. Kaplan T. A., *Phys. Rev.*, **119,** 1460 (1960).
15. Neel L., *Rapport* 10^e *Congrès Solvay*, 1954. Cf. *Nuovo Cim.* **6,** 942 (1957).
16. Corliss L. M. et Hastings J., non publié.

APPENDICE

Influence de l'Anisotropie Cristalline, Chaîne linéaire

On considère l'anisotropie comme une petite perturbation. L'équation (2–1), combinée avec (2–15), peut s'écrire comme une équation aux différences

$$W_n = -K\cos 2\varphi_n - 2S^2 \times \{J_1[\cos(\varphi_{n+1}-\varphi_n)-\cos(\varphi_n-\varphi_{n-1})] + J_2[\cos(\varphi_{n+2}-\varphi_n)-\cos(\varphi_n-\varphi_{n-2})]\} \tag{A-1}$$

$$W = \sum_n W_n \tag{A-2}$$

Posons

$$\varphi_n = n\varphi_0 + \epsilon_n \tag{A-3}$$

où φ_0 est solution de l'équation sans perturbation

$$\cos\varphi_0 = -J_1/4J_2 \tag{A-4}$$

Ecrivons

$$\frac{\partial W}{\partial \epsilon_n} = 0 \tag{A-5}$$

Négligeons tous les produits de la forme $K\epsilon_n$ et utilisons l'approximation $\sin\epsilon_n = \epsilon_n$, $\cos\epsilon_n = 1$. (A–5) devient

$$2K\sin 2n\varphi_0 + 2S^2[J_1(2\epsilon_n - \epsilon_{n+1} - \epsilon_{n+1})\cos\varphi_0 + J_2(2\epsilon_n - \epsilon_{n+2} - \epsilon_{n-2})\cos 2\varphi_0] = 0 \tag{A-6}$$

Posons

$$\epsilon_n = A\sin 2n\varphi_0 \tag{A-7}$$

On a par identification et compte tenu de (A–4)

$$\epsilon_n = K\sin 2n\varphi_0/(8S^2J_2\sin^2\varphi_0\sin^2 2\varphi_0) \tag{A-8}$$

relation valable pour A petit.

LETTERS TO THE EDITOR

The energy and the configuration of the atoms in a simple model of an edge dislocation

(*Received* 3 *July* 1961)

THE ENERGIES and the positions of the atoms around a dislocation can be calculated from elastic theory except at the dislocation core, where elastic theory is not applicable; applied formally, it would give an infinite value for the energy there.

A correct description of the dislocation core can only be obtained from an atomistic model; such a model was used for the first time by HUNTINGTON *et al.*[1] in 1955, for a crystal of NaCl. A first approximation for the positions of the atoms is obtained from elastic theory and the positions are then adjusted to minimize the energy; in regions where elastic theory is applicable the positions given by it are already those of minimum energy.

We have carried out such a calculation for a model of a crystal of argon, where the interatomic forces can be regarded as two-body forces decreasing rapidly with increasing distance. To evaluate the total energy one need only consider nearest-neighbour interactions, which greatly facilitates the work and enables one to compute the total energy of any arbitrary configuration of a large number of atoms. Argon is thus a model substance for the study of lattice imperfections and has been used as such for the study of the atoms around a vacancy[2] and near the surface.[3]

Once one has obtained the configuration of the atoms around a dislocation one can attack the problem of the distribution of impurity atoms around it; the properties of solutions of argon and of similar substances have often been studied.[4]

We report here the results of the calculation of the positions and energies of the atoms at a two-dimensional edge dislocation in a plane close-packed lattice; such a dislocation has been realized and photographed by BRAGG and NYE[5] in their famous bubble-raft experiments.

We have taken the energy of interaction e_{ij} of two atoms i and j a distance r_{ij} apart to be given by the Lennard–Jones potential

$$e_{ij} = e_A[(r_A/r_{ij})^{12} - 2(r_A/r_{ij})^6] \qquad (1)$$

where e_A and r_A are parameters characterizing the depth and the position of the potential well. The total reduced energy of a configuration is

$$U = 1/2 \sum e_{ij}/e_A. \qquad (2)$$

It is easily verified that interactions between other than nearest neighbours on the plane close-packed lattice contribute only 12 per cent to the total energy and we have felt justified therefore to consider in our calculations nearest-neighbour interactions only. The interatomic distance a_0 in the perfect lattice at 0°K is then equal to r_A; the reduced energy of interaction u_0 of an atom with its six neighbours equals -6 and the total energy U_0 of N atoms is $-3N$.

The calculations have been carried out in the following manner. Initial positions of the atoms were calculated from elastic theory; expressions for the displacements in the x and y directions have been given by HUNTINGTON *et al.*[1] and represent the deformations in an infinite lattice. These expressions contain two parameters, the Burgers vector and Poisson's constant. The former equals a for a simple edge dislocation, the latter is 1/4 in the model used. We have placed the neutral line, where $\sigma_{xx} = \sigma_{yy} = 0$, half-way between two rows of atoms.

The positions of the atoms are then adjusted so as to minimize the total energy, at first in a region containing one layer of atoms around the dislocation core. The calculations were carried out numerically, by means of a program written for the IBM 650 computer. The coordinates of the atoms are changed one by one so as to minimize their energy; the program is iterative in the sense that it returns to the first atoms after the last, until none of the changes in the coordinates exceeds a predetermined value ($10^{-4}a$ or $10^{-5}a$). The energies of the initial configuration, U_i, and of the final configuration, U, are also computed.

The region is then increased layer by layer and the whole computation repeated for each region; the final configuration in each step is taken as the initial configuration of the next, the positions given by elastic theory are taken as the initial positions of the atoms in the layer added. The difference $U_i - U$ decreases steadily as the region considered is increased. The largest region

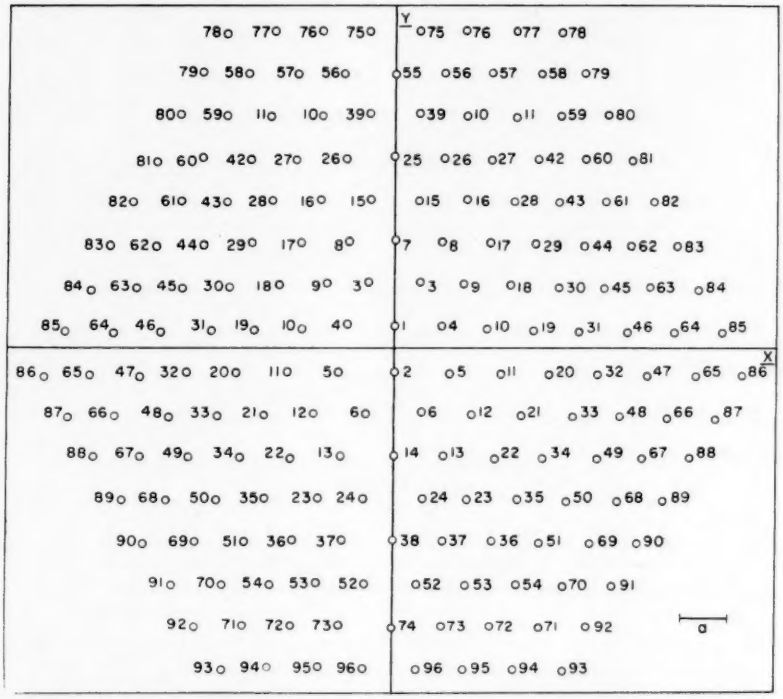

FIG. 1. Position of atoms on an edge dislocation in a close-packed plane, as determined from the condition of minimum energy for an array of 184 atoms.

considered in our computations contained 184 atoms; since we had taken the symmetry of the problem into account, we have used a maximum of 96 atoms.

Figure 1 shows the final configurations of the atoms for this region; the atoms are numbered to permit identification. Table 1 gives the values of

Table 1. *Initial and final energies of regions of increasing size, tolerance* $10^{-4}a$

Number of last layer added	Number of atoms in region	$U_i - U_0$	$U - U_0$	$U_i - U$
1	10	8·036	4·372	3·664
2	24	6·102	5·615	0·487
3	44	6·741	6·482	0·259
4	70	7·298	7·174	0·124
5	102	7·819	7·740	0·079
6	140	8·275	8·227	0·048
7	184	8·687	8·650	0·037

Table 2. *Energies of atoms* 1 *to* 14; *region of* 184 *atoms, tolerances* $10^{-5}a$

Number of atom	Number of layer	$u - u_0$	$\frac{u-u_0}{-u_0}$
1	0	1·435	0·24
2	0	1·084	0·18
3	1	0·152	0·02
4	1	1·067	0·18
5	1	0·819	0·14
6	1	0·371	0·06
7	2	0·083	0·01
8	2	0·080	0·01
9	2	0·127	0·02
10	2	0·629	0·10
11	2	0·308	0·05
12	2	0·171	0·03
13	2	0·131	0·02
14	2	0·180	0·03

Vol. 21
1961

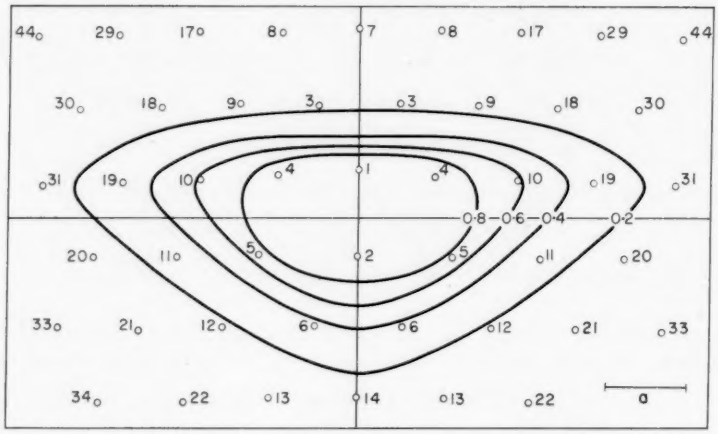

FIG. 2. Lines of equal energy, expressed as $u-u_0$, in a close-packed plane with an edge dislocation.

U_i-U_0, $U-U_0$, and U_i-U for the regions considered consecutively; the convergence of U_i-U is seen to be rather slow.

The final energies u of the atoms in the dislocation core and in the first two layers (atoms 1 to 14) are given in Table 2.

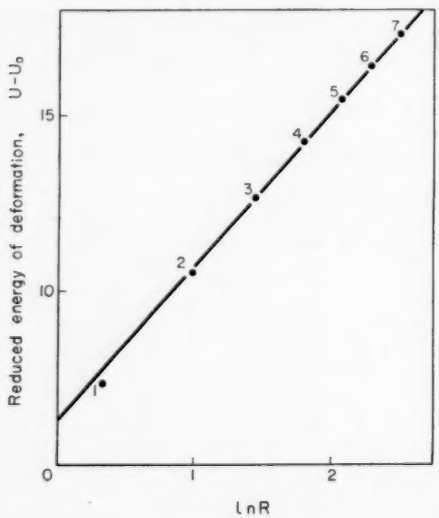

FIG. 3. The dependence of the reduced energy of deformation $U-U_0$ on ln R. The numbers indicated are the number of layers in the region considered.

The relative error in $u-u_0$ is not likely to exceed 0·1 and results primarily from the lack of precision with which first-order elasticity theory gives the positions of the atoms on the boundary of the regions considered.

It is instructive to compare the values of $u-u_0$ with the energy of fusion, which for argon is about 15 per cent of the energy of sublimation; the energies of atoms 1, 2, 4 and 5 exceed this energy or are of this order, but all other atoms have energies much below this value.

Figure 2 shows some equipotential lines for the region of 184 atoms. The width of the dislocation, using Peierls' definition, is one and a half atomic distances.

Figure 3 shows the total energy of each region as a function of ln R where R is the "equivalent radius" of the region; within the accuracy of the diagram, the energy is a linear function of ln R, as required by elastic theory, after about three layers.

These calculations are now being extended to a three-dimensional lattice; the results, with relevant details, will be reported in a later publication.

Acknowledgements—We are indebted to Mr. J. MOMMENS of the Centre Numérique de Calcul of IBM Belgium, under whose supervision the numerical computations were carried out.

This work is part of a project supported by the Union

Carbide Corporation, New York, and we acknowledge gratefully this support.

European Research Associates, s.a. A. ENGLERT
95, *rue Gatti de Gamond* H. TOMPA
Brussels 18, *Belgium*

References

1. HUNTINGTON H. B., DICKEY J. E. and THOMSON R., *Phys. Rev.* **100,** 1117 (1955).
2. HALL G. L., *J. Phys. Chem. Solids* **3,** 210 (1957).
3. ALDER B. J., VAISNIJS J. R. and JURA G., *J. Phys. Chem. Solids* **11,** 182 (1959).
4. PRIGOGINE I., *Molecular Theory of Solutions.* North Holland Publishing Company, Amsterdam (1957)
5. BRAGG W. L. and NYE J. F., *Proc. Roy. Soc.* A**190,** 474 (1947).

Paramagnetic resonance absorption in molecular crystals: some comments on the paper by WIGEN and COWEN

(*Received* 29 *May* 1961)

RECENTLY, WIGEN and COWEN[1] reported paramagnetic resonance absorption in some inorganic molecular crystals after electron irradiation at 77°K. In lithium sulfate monohydrate they observed two sets of anisotropic doublets, corresponding to the two distinguishable sites in the monoclinic crystal. These doublets were identified as arising from the interaction of a "hole" with a single proton, the principal values of the interaction tensor being -21, -16, and -4 G. In interpreting this tensor, WIGEN and COWEN have assumed that the interaction must be axially symmetric, and they have attributed the observed deviation from axial symmetry to a further interaction with a lithium nucleus of spin 3/2. This part of their interpretation is incorrect.

In the following argument, the paramagnetic species will be regarded as an electron occupying a half-filled molecular orbital. The interaction between the unpaired electron and a single proton will be axially symmetric only if the wave function of the electron has axial symmetry about a radius vector originating at the proton. Thus, if the unpaired electron is located mainly in an atomic orbital of a particular atom and its wave function has π-orbital character, the interaction will not have axial symmetry. This has been observed in free radicals produced by radiation damage in organic single crystals[2–4] and has been considered theoretically.[3, 5]

The deviation from axial symmetry cannot arise from an interaction with a further nucleus. The spin states of such a nucleus would be independent of the spin state of the proton and, to a very good approximation, the additional interaction would merely split or broaden each line of the original doublet. The centers of gravity of the split or broadened doublet would coincide with the positions of the lines in the absence of the additional interaction. The observed coupling tensor must therefore arise entirely from the electron–proton interaction.

In the *ac* crystal plane, the projection of A_{zz} lies close to the projection of the hydrogen bond direction [Ref. (1), Fig. 4]. In the *bc* plane, the projection of A_{zz} is not in such good agreement with the hydrogen bond direction [Ref. (1), Fig. 5]. However, the anisotropy in this direction appears to be small [Ref. (1), Fig. 6] which would make an accurate estimation of the projected direction of A_{zz} difficult. It is therefore reasonable to assume that A_{zz} lies close to the hydrogen bond direction.

With the present choice of sign, the isotropic component is $-13{\cdot}7$ G while the anisotropic components are $+9{\cdot}6$ G along A_{zz}, with $-2{\cdot}3$ G and $-7{\cdot}3$ G perpendicular to A_{zz}. These can be compared with the estimation by MCCONNELL and STRATHDEE of the dipole–dipole coupling between a $2p$ electron on a carbon atom, and a proton bonded to it by a sp^2 hybrid.[5] Their calculated values are: $+15{\cdot}4$ G along the C–H bond, $-1{\cdot}6$ G along the density axis of the p orbital, and $-13{\cdot}8$ G along the perpendicular direction. Spin polarization of the C–H bond gives rise to an isotropic component of about -23 G.[2–6] Thus the tensor observed here is similar, except for a reduction in magnitude, to that of the C–H case. This indicates that the electron is located mainly in a p orbital of an oxygen atom. The smallest component, $-2{\cdot}3$ G along A_{yy}, should lie along the density axis of the p orbital. Unfortunately, this direction is not given in Ref. (1).

The paramagnetic center was regarded as a hole localized on that sulfate group oxygen atom which

takes part in the hydrogen bond.[1] It is interesting to consider as an alternative, the removal of the hydrogen atom not involved in the hydrogen bond with the sulfate oxygen, to give an unpaired electron localized on the oxygen atom of the water molecule. The resulting species could be regarded as a hydroxyl radical hydrogen bonded to the sulfate group. To a first approximation, the p_z oxygen orbital of this radical will take part in the σ bond to the remaining hydrogen, a second p orbital will contain two non-bonding electrons and the third will contain the unpaired electron. To account for the non-axial symmetry of the coupling tensor, these two last orbitals must have a fixed spacial orientation. Their degeneracy is probably lifted by a hydrogen bond to the neighboring water molecule.[7]

The g tensor was axially symmetric, with $g_{\parallel} = 2{\cdot}04 \pm 0{\cdot}001$ and close to the original hydrogen bond direction, and $g_{\perp} = 2{\cdot}002 \pm 0{\cdot}001$. The above model is qualitatively consistent with these values. When the field is along the O–H direction, promotion of an electron from the non-bonding (or hydrogen bonding) p orbital into the half-full p orbital, under spin–orbit coupling, will cause a positive g shift.[8] With the field along the density axis of the half-full p orbital, symmetry considerations indicate that g will be close to the free-spin value of 2·0023. In the direction perpendicular to these, the perpendicular p orbital takes part in the σ bond, the energy required for electron promotion will be large, and g will again be close to the free-spin value.

WYARD and SMITH[9] have studied electron paramagnetic resonance in irradiated frozen solutions of hydrogen peroxide and deuterium peroxide. Their spectra indicated the presence of polyoriented free radicals with an axially symmetric g-factor. Analysis of a spectrum from u.v. irradiated D_2O_2 in D_2O gave $g_{\parallel} = 2{\cdot}0419 \pm 0{\cdot}0040$ and $g_{\perp} = 2{\cdot}0002 \pm 0{\cdot}0007$. These g-values are similar to those found for the doublet in irradiated $Li_2SO_4 \cdot H_2O$. Warmed up samples of u.v. irradiated H_2O_2 in H_2O showed a doublet hyperfine splitting of $13{\cdot}5 \pm 3$ G. This value lies within the range of the tensor elements found for irradiated $Li_2SO_4 \cdot H_2O$ and is equal to the isotropic component of $-13{\cdot}7$ G. WYARD and SMITH concluded that the radicals present in irradiated hydrogen peroxide might be OH, or HO_2, but that there was insufficient evidence to favor one or the other.

Physics Division D. W. OVENALL
Battelle Memorial Institute
Geneva, Switzerland

References

1. WIGEN P. E. and COWEN J. A., *J. Phys. Chem. Solids* **17,** 26 (1960).
2. MCCONNELL H. M., HELLER C., COLE T. and FESSENDEN R. W., *J. Amer. Chem. Soc.* **82,** 766 (1960).
3. GHOSH D. K. and WHIFFEN D. H., *Mol. Phys.* **2,** 285 (1959).
4. MIYAGAWA I., KURITA Y. and GORDY W., *J. Chem. Phys.* **33,** 1599 (1960).
5. MCCONNELL H. M. and STRATHDEE J., *Mol. Phys,* **2,** 129 (1959).
6. MCCONNELL H. M. and CHESNUT D. B., *J. Chem. Phys.* **28,** 107 (1958).
7. LARSON A. C. and HELMHOLTZ L., *J. Chem. Phys.* **22,** 2149 (1954).
8. MCCONNELL H. M. and ROBERTSON R. E., *J. Phys. Chem.* **61,** 1018 (1957).
9. WYARD S. J. and SMITH R. C., *Bull. Groupement Ampère, Compte Rendu 9th Colloque, Pisa,* p. 224 (1960).

The specific heats of single Cu–Mn crystals between 1·4 and 5°K

(*Received* 15 *May* 1961; *revised* 23 *June* 1961)

THE LOW temperature specific heats of polycrystalline dilute alloys of manganese in copper have recently been reported.[1] These measurements indicate the existence of an anomaly that is linear in temperature and independent of concentration, and which terminates at a temperature that is a linear function of concentration. OVERHAUSER[2] has proposed that the magnetic properties which cause this anomaly can be explained in terms of a spin-density wave ordering of the manganese ions below the Néel temperature. On the other hand, MARSHALL[3] has suggested that these properties are fully accounted for by the Yosida interaction, and do not require the use of the spin-density wave concept. In the Overhauser interpretation, macroscopic imperfections such as grain boundaries could conceivably affect some of these properties. Since no experimental data of the

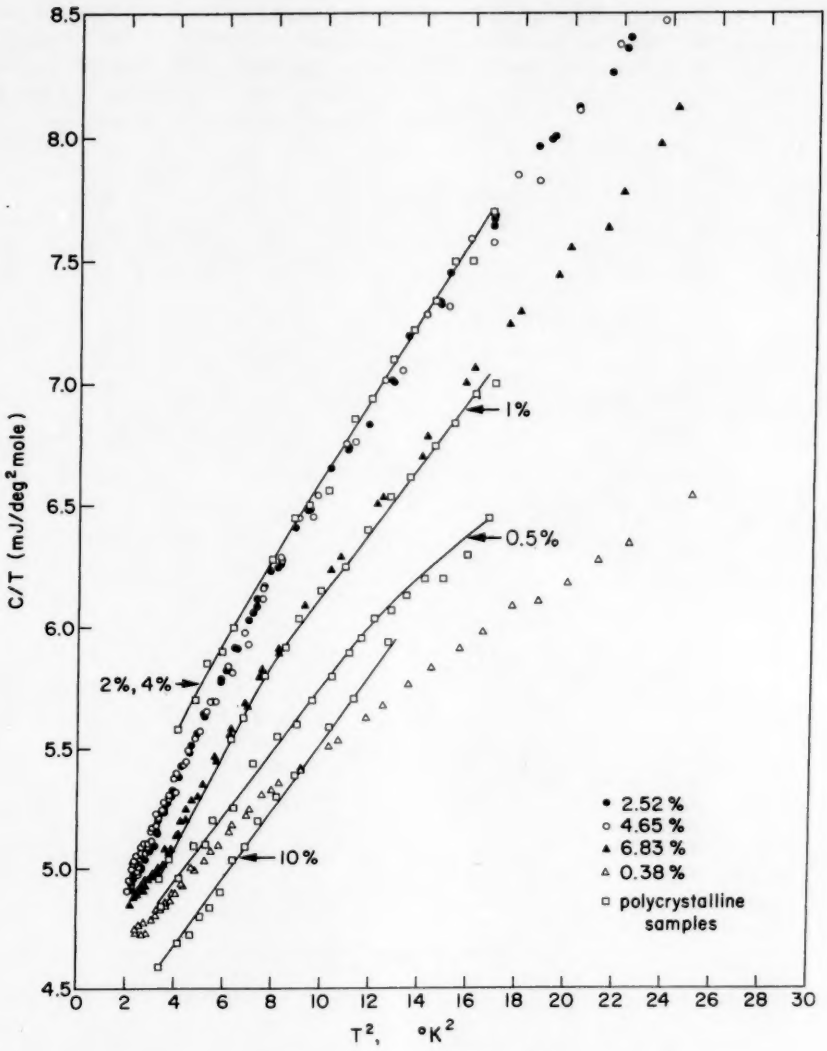

FIG. 1. C/T vs. T^2 plot of the single crystal data with the polycrystalline data superimposed.

thermal properties of single crystals were available in the literature, it was thought desirable that such measurements be made on a single crystal of a copper–manganese alloy.

The reported specific heat measurements in copper–manganese were taken using polycrystalline samples whose grain size varied from needles about 0·1 mm in diameter and 5 mm long to single crystals of almost 0·5 cm³ volume and roughly cubic in shape. A needle structure comprised about 25 per cent of the volume in each sample, with 10 or 20 per cent of the remaining volume being comprised of 1 mm³ sized crystals. Because large and carefully annealed single crystals of Cu–Mn

were available in this laboratory following the ultrasonic measurements of the elastic constants of these alloys by WALDORF[4], it was decided to measure the specific heats of these to provide a comparison to the polycrystalline data.

specimens having between 2 and 5 weight per cent manganese ion concentration. Both sets of data also show that the specific heats of samples of differing manganese concentration do not maintain constant differences in magnitude over the

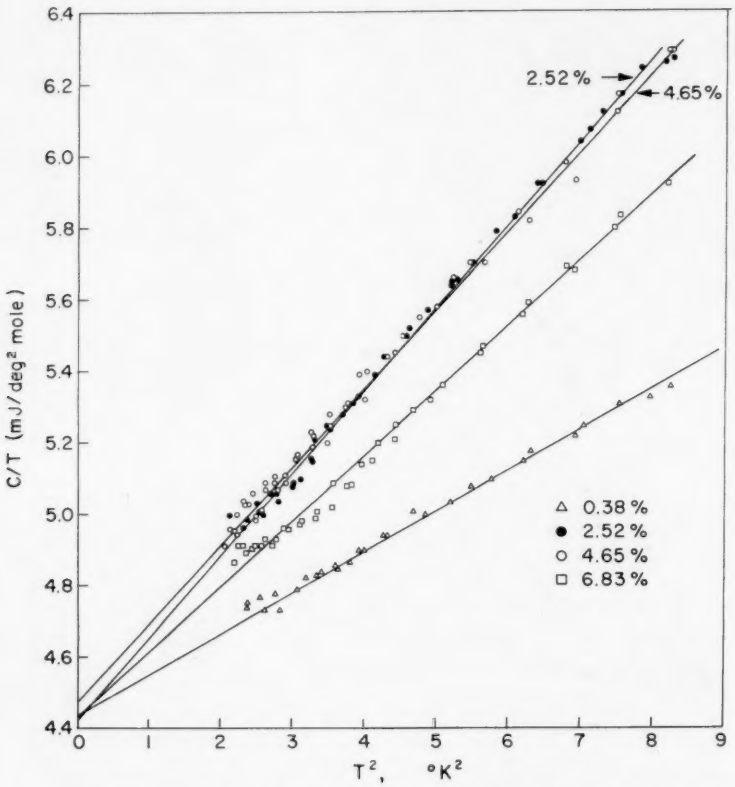

FIG. 2. Expanded plot of C/T vs. T^2 for single crystal data below 3°K. Solid lines indicate least square values.

Measurements were taken using a mechanical thermal switch calorimeter and are shown in Fig. 1, in which the polycrystalline data are indicated by the solid lines. It is obvious that there is no important difference between these two sets of data. Although the specific heat in excess of that of pure copper is said to be independent of concentration, both sets of measurements show that it really varies over a range of about 20 per cent of its magnitude, with a maximum value for temperature range below the Néel temperature, but diverge slightly with increasing temperature for concentrations below 10 weight per cent, beyond which concentration some new processes seem to be occurring in the magnetic ordering.

Above 3°K the single crystal data are in very close accord with all details of the polycrystalline data insofar as comparison is possible, while below that temperature the single crystal data show two systematic tendencies which are possibly indicated

Vol. 2
1961

in the polycrystalline data for the 1 weight per cent sample, but are not established in general. In the first place the single crystal data all extrapolate to the same value of C_p/T at absolute zero. Secondly the data are linear on a C_p/T vs. T^2 plot below 3°K. The single crystal data below 3°K are shown on an expanded plot in Fig. 2. A least squares calculation shows that the common intercept at 0°K is at $C_p/T = 4{\cdot}44 \pm 0{\cdot}03$ mJ/deg^2 mole and that the linearity of C_p/T vs. T^2 has an r.m.s. deviation of less than 0·6 per cent for all four samples. Thus, below 3°K the specific heats have the form $AT+B(c)T^3$, where $A = 4{\cdot}44$ mJ/deg^2 mole and B is concentration dependent as indicated. Above 3°K the specific heats break away from the linear region rather suddenly, especially in the case of the 0·38 per cent sample, and assume the slopes and magnitudes characteristic of the polycrystalline samples.

The meaning of the $AT+B(c)T^3$ form of the specific heat is not clear at present, but the range of concentration of these samples is so broad that a process of general importance is indicated.

Scientific Laboratory L. T. CRANE
Ford Motor Company J. E. ZIMMERMAN
Dearborn
Michigan

References

1. ZIMMERMAN J. E., *J. Phys. Chem. Solids* **17,** 52 (1960).
2. OVERHAUSER A. W., *Phys. Rev. Letters* **3,** 414 (1959); *J. Phys. Chem. Solids* **13,** 71 (1959).
3. MARSHALL W., *Phys. Rev.* **118,** 1519 (1960).
4. WALDORF D. L., *J. Phys. Chem. Solids* **16,** 90 (1960).

Photocapacitance effects in additively colored alkali halide crystals

(*Received* 27 *March* 1961)

KAHN and GLASS[1] have recently published a paper under the above title in which it appears that theoretical work of the present author is misapplied, leading to conclusions outside the scope of the theory and at variance with conclusions of similar experimental work of the author.[2] (This paper will be referred to as I hereafter.) The main experiment consists of measurements of the capacitance and conductance of a photoconducting crystal containing F-centers as a function of light intensity, frequency, d.c. bias, and a.c. signal amplitude. The work in I differed from that of KAHN and GLASS in that U-centered crystals were generally used, largely avoiding bleaching effects[3, 4] arising from the applied light which occur with additively colored crystals. The F-centers were produced by gamma irradiation of U-centered crystals. In addition, the earlier measurements were made by a bridge method instead of the less accurate differencing method of KAHN and GLASS. Finally, evaporated as well as silver paint contacts were used, and the effect of thin mica blocking layers was investigated as well.

The main point at issue is that KAHN and GLASS interpret their low frequency limiting capacitance as arising from electrode space charge associated with conduction-band electrons released from F-centers by light absorption, while this conclusion was found to be untenable for the results obtained in I. Space charge theory[5, 6] shows that in the case of blocking electrodes (zero conduction current), the zero-frequency or static space-charge capacitance in the limit of zero a.c. and d.c. applied potentials (practically, for potentials less than kT/e) depends on the free electron concentration in the bulk of the material, and the high-frequency limiting conductance depends on electron mobility as well. When the application of these results to experimental measurements is appropriate, both electron concentration and mobility can thus be calculated.

For practical experimental light intensities, the concentration of conduction-band electrons is very much smaller than the concentration of filled F-centers and the recombination factor[6, 7] R is very large. Under these conditions, empty F-centers (positively charged negative-ion vacancies) are mobilized by recombination, and over an appreciable applied potential range accumulation of charge can occur simultaneously at or near anode and cathode when these electrodes are blocking. Such accumulation leads to an over-all space-charge capacitance which increases essentially exponentially with applied static potential.[6,7] No such increase was observed by KAHN and GLASS, who applied low-frequency potentials of

up to 5 V r.m.s., or by the author, who found, in fact, a slight decrease instead.[2] For a fixed light intensity, theory[6] indicates that beyond a certain applied potential, of the order of one volt in the present case, the space-charge capacitance should stop increasing and should decrease proportionally to the (applied potential)$^{-m}$, where m is one-half or less. Such decrease occurs when an exhaustion layer (here a region where all F-centers are ionized) starts to form at one electrode.

The dependence of static space-charge capacitance on light intensity with bimolecular recombination can be very complicated[6] since it is affected by the applied potential and electrode separation. However, the static space-charge capacitance in the limit of low applied potentials should be proportional to the square or fourth root of light intensity, with the choice depending on the recombination mechanism[2] and electrode separation.[6] No light dependence at all was found in I. On the other hand, KAHN and GLASS mention that they found a fourth-root dependence, indicating bimolecular recombination, for a KBr crystal. No details or results of measurements were presented. Because of the clear dependence of photoconductance and time constant on light intensity, some parallel capacitance light dependence can be observed at any frequency above that where the final low-frequency limiting capacitance appears. This apparent change occurs even when the actual low-frequency limiting capacitance change is zero, and it is felt that KAHN and GLASS observed this effect rather than a true change. Detailed measurements presented in I failed to indicate any true static capacitance change.

The above result found by KAHN and GLASS was evidently obtained with an applied potential whose magnitude far exceeded the maximum value for which the linearized theory[5] they used applies. In addition, if true fourth-root capacitance light dependence were found, it should have associated with it square-root dependence of the high-frequency limiting conductance.[2, 8] Instead a linear dependence of conductance on light intensity was found in I, consistent with the monomolecular trapping which may be expected in a situation where there will be far more shallow traps than ionized F-centers.[2] KAHN and GLASS's failure to demonstrate bimolecular recombination makes suspect their derivation of recombination constants and electron lifetimes from measured capacitance vs. frequency curves.

Electrodes made using silver paint were termed rectifying in I, implying that conduction-band electrons could be removed relatively easily from the crystal in the forward direction of current flow but could only be brought in from the electrodes in the reverse direction with difficulty. The current–voltage relation to be expected with two such electrodes in series would be antisymmetrical in applied voltage, in good agreement with results found by KAHN and GLASS. The measurements of I indicated that the parallel capacitance (excluding the geometric contribution) of a crystal with rectifying contacts decreased at high frequencies less rapidly than the usual inverse-square power of the frequency, indicating the presence of a series capacitance dependent on frequency. The less accurate results of KAHN and GLASS show somewhat similar behavior although fitting to Debye curves is attempted. Only when the contact was made blocking in the earlier work by insertion of a thin mica sheet between the metal and the crystal was the usual frequency-independent series capacitance observed. However, the resulting over-all series capacitance was not appreciably affected by the capacitance of the mica itself, although it was quite different from that found with rectifying contacts.

The above results indicate that the character of the electrode has an important effect on the measured capacitance and that again a theory appropriate for blocking electrodes does not give a good description of the experimental results found with rectifying ones. KAHN and GLASS obtain a V^2 dependence of current on applied d.c. voltage V and interpret this result as a space-charge-limited current situation.[9, 10] Results of VON HIPPEL *et al.*[11] show, however, that internal field emission is possible for applied voltages in the range applied by KAHN and GLASS. It is likely that such emission has an important effect when a.c. potentials of 5 V r.m.s. are applied, and it may account for the difference between the series capacitance associated with the region near an electrode found with rectifying and with blocking electrodes.

In an effort to explain the voltage independence of the photo-capacitance, KAHN and GLASS have presented an approximate theoretical treatment of

current flow in which the influence of positively charged ionized *F*-centers is omitted. This approximate treatment does indeed lead to a voltage-independent capacitance, but it turns out that when the usual space-charge-limited current result is used for the proportionality factor *a* introduced by KAHN and GLASS, their capacitance result simplifies to just the geometrical capacitance of the system in the absence of space charge. This capacitance is, of course, constant by definition. Further, it is inconsistent to justify the use of a capacitance result derived for blocking electrodes by means of a theory of non-zero conduction current which is applied over a range of potentials far greater than is appropriate for the original calculation.

The above considerations suggest that the conclusions of I are still valid. No true photocapacitance is measured. Instead, there is a thin region near each electrode in which there may be no *F*-centers (Mott barrier) or where many traps (initially probably neutral) capture electrons.[10,12] If electrons from the bulk of the crystal cannot enter this region freely and its charge, if any, therefore changes little with applied potential, it will produce an approximately potential-and-frequency independent differential capacitance in series with the bulk conductance of the rest of the crystal. The effect of such a potential-independent capacitance in series with space-charge capacitance has been considered elsewhere.[7] *F*-center light will increase crystal conductance and therefore cause the parallel capacitance of the system to depend on frequency except at frequencies far below the frequency corresponding to the time constant of the system. In the dark, little or no parallel capacitance will be measured at practical frequencies because the time constant will be so long. Apparently, any photo-controlled space-charge capacitance associated with the motion of free electrons in the crystal is much greater than the capacitance of the initial layers next to the electrodes and has little influence on the over-all capacitance. Measurements of the static or limiting low-frequency differential capacitance of the system as a function of temperature would be of great value in determining the cause of the potential-independent electrode capacitance.

Since the formula for low-voltage space-charge capacitance is not applicable to KAHN and GLASS's results, the approximate agreement of the electron mobilities they calculate with directly measured values must be a coincidence. They have failed to demonstrate the applicability of the linearized a.c. space-charge theory to their experiments, and their conclusion that their data is in striking agreement with this theory must be rejected.

J. ROSS MACDONALD

Texas Instruments Incorporated
Dallas 22, Texas

References

1. KAHN D. and GLASS A. J., *J. Phys. Chem. Solids* **17,** 210 (1961).
2. MACDONALD J. R., *J. Chem. Phys.* **23,** 275 (1955).
3. CASLER R., PRINGSHEIM P. and YUSTER P., *J. Chem. Phys.* **18,** 887 (1950).
4. HARDTKE F. C., SCOTT A. B. and WOODLEY R. E., *Phys. Rev.* **119,** 544 (1960).
5. MACDONALD J. R., *Phys. Rev.* **92,** 4 (1953).
6. MACDONALD J. R., *J. Chem. Phys.* **30,** 806 (1959).
7. MACDONALD J. R., *J. Chem. Phys.* **29,** 1346 (1958).
8. KLASENS H. A., *J. Phys. Chem. Solids* **7,** 175 (1958).
9. MOTT N. and GURNEY R., *Electronic Processes in Ionic Crystals* (2nd Ed.) p. 172. Oxford University Press (1948).
10. RHYS-ROBERTS C. and TREDGOLD R. H., *Proc. Phys. Soc. Lond.* **76,** 497 (1960).
11. VON HIPPEL A., GROSS E. P., JELATIS J. G. and GELLER M., *Phys. Rev.* **91,** 568 (1953).
12. MOTT N. and GURNEY R., *Electronic Processes in Ionic Crystals* (2nd Ed.) p. 173. Oxford University Press (1948).

Effects of gaseous impurities on the magnetic properties of copper

(*Received* 1 *May* 1961)

RECENT experiments on the influence of gaseous impurities on the resistance minimum and residual resistance of copper[1,2] have shown that oxidation of 99·999 per cent copper causes a reduction in residual resistance and the disappearance of the anomalous resistance minimum. Since small concentrations of iron are known to induce a resistance minimum in copper, it was felt worthwhile to investigate the magnetic behavior of nominally pure copper upon annealing in reducing and oxidizing atmospheres.

In the Faraday method of measuring the magnetic susceptibility, a change in force due to a

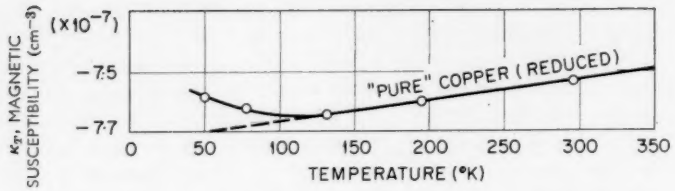

FIG. 1. Temperature dependence of the magnetic susceptibility of 99·999 per cent pure copper.

magnetic field gradient is measured with a sensitive balance. If the field strength and gradient are assumed constant along the length of the sample (i.e. if the sample is small), the susceptibility, κ_t, of a sample having a small amount of ferromagnetism is given by ${}^3\kappa_t = \kappa + c\sigma/H$, where κ is the field-independent, paramagnetic or diamagnetic susceptibility per cm^3, H is the magnetic field strength, and c and σ are the concentration and magnetic moment per gram of ferromagnetic material respectively. The intercept of a plot of κ_t vs. $1/H$ will therefore yield the net diamagnetic susceptibility (this includes paramagnetic contributions of dissolved impurities) of the material; the slope of the plot will yield the amount of ferromagnetic constituent. In the case of the equipment used in these measurements, the field variation along the full length of the specimen is appreciable causing the plot of κ_t vs. $1/H$ to deviate from a straight line. This, however, has no effect upon the

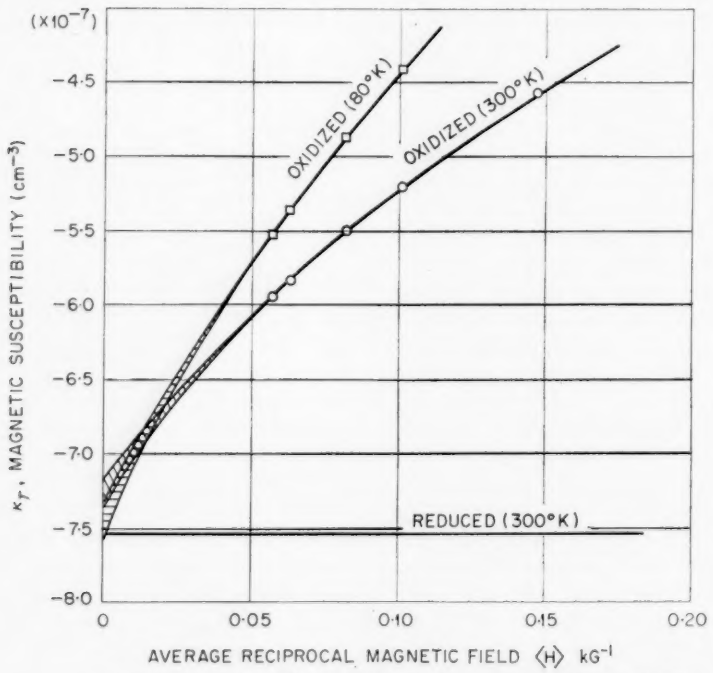

FIG. 2. Magnetic field dependence of the susceptibility of 99·999 per cent pure copper after reducing and oxidizing treatments. The shading at low $1/\langle H \rangle$ indicates uncertainty in extrapolation.

Vol. 2
196

accuracy of determining the susceptibility of purely diamagnetic or paramagnetic samples and only decreases the accuracy of determining κ and c in samples that contain a ferromagnetic constituent.

Figure 1 shows the behavior of a "reduced" (annealed for 2 hr at 900°C under 15 μ of CO) sample of 99·999 per cent copper as a function of temperature. The increase of paramagnetism below $\sim$ 100°K indicates the presence of a paramagnetic impurity. The data can be accounted for by assuming approximately 5×10^{17} magnetic centers per cm^3, each having a magnetic moment of the order of two Bohr magnetons.

Figure 2 shows the field dependence of the susceptibility of the same sample in "reduced" and "oxidized" (annealed for 4 hr at 900°C under 20 μ of air) states, the latter measured at 300 and 80°K. It is clear that there is no field dependence discernible when the sample is "reduced". The curves for the "oxidized" case, however, show a fairly steep slope. If approximately 2×10^{17} iron atoms were precipitated either as metallic iron or as a ferrite, slopes of the magnitude observed would result.

The number, 2×10^{17}, that is consistent with the slopes of the κ_t vs. $1/H$ plots is slightly less but is of the same order of magnitude as the number of dissolved impurity atoms deduced from Fig. 1. It should be borne in mind that the reduction and oxidation treatments used to remove or create the ferromagnetism is the same as that found to produce or remove a resistance minimum[1] and a high residual resistance.[2]

CONSTANT and his co-workers had found by use of remanence measurements that most "commercial" metals contained a small amount of ferromagnetic impurity.[4] They found that in copper this ferromagnetism could be removed by a hydrogen anneal[5] and could be recreated by annealing in air. He attributed the effect to oxidation of iron impurity. These effects have also been studied by others, most recently by DOMENICALI and CHRISTENSON[6]. In order to compare our results with those of other investigators, a sample of copper containing 0·1 per cent iron was prepared. The temperature dependence of κ_t of this sample in the reduced state indicated that almost all (99·9 per cent) of the iron was in a paramagnetic state. However, when the sample was oxidized, it was too strongly magnetic to permit measurement in the susceptibility balance. The sample, when hung on a string, was quite easily attracted by a small bar magnet.

It seems fairly certain that trace amounts of iron can contribute strongly to the magnetic as well as electrical properties of copper of purity as high as 99·999 per cent. Moreover, preferential oxidation causes precipitation of iron, even when only 10^{17}–10^{18} atoms/cm^3 are present in the copper. This would imply that great care is necessary in interpreting results of resistance minimum measurements in copper alloys (which almost surely contain trace amounts of iron) and in using residual resistance as a gauge of purity. Moreover, magnetic susceptibility measurements as described here might be useful in estimating iron content in high purity copper.

One further point of interest might be noted. In Fig. 2 the slope for the oxidized sample is greater at 80°K than it is at room temperature. This might indicate that some of the precipitate particles are small enough to be ferromagnetic at 80°K but paramagnetic (superparamagnetic[7]) at 300°K. Such particles would be, roughly, 100–300 Å in diameter.

Acknowledgement—The authors are indebted to T. H. BLEWITT for suggestion of the problem and for many helpful discussions.

Solid State Division
*Oak Ridge National Laboratory**
Oak Ridge
Tennessee

E. SONDER
S. T. SEKULA

References

1. SEKULA S. T., *Phys. Rev. Letters* **3,** 416 (1959).
2. REDMAN J. K., *et al.*, Solid State Division Annual Progress Report, ORNL-2829, p. 74 (1959); *Bull. Amer. Phys. Soc.* (II) **4,** 150 (1959).
3. BATES L. F., *Modern Magnetism* p. 115. Cambridge University Press, London (1948).
4. CONSTANT F. W. and FORMWALT J. M., *Phys. Rev.* **56,** 373 (1939).
5. CONSTANT F. W., FAIRES R. E. and LENANDER H. E., *Phys. Rev.* **63,** 441 (1943).

* Oak Ridge National Laboratory is operated by Union Carbide Corporation for the U.S. Atomic Energy Commission.

6. DOMENICALI C. A. and CHRISTENSON E. L., *J. Appl. Phys.* **31,** 1730 (1960); also Ref. (1) through (7) in that paper.
7. PAINE T. O., *Magnetic Properties of Metals and Alloys*, p. 158. American Society for Metals, Cleveland (1959).

The effect of arsenic pressure on impurity diffusion in gallium arsenide*

(*Received* 13 *July* 1961; *revised* 25 *August* 1961)

BECAUSE effects directly attributable to non-stoichiometry in GaAs have not been reported, the role of an important variable in many high-temperature physico-chemical processes in this material, the arsenic pressure, has with few exceptions been ignored (cf. Refs. 1, 2). Diffusion of impurities from the vapor into the solid is one such process, and since diffusion coefficients are intimately related to defect concentrations, small variations in surface composition during diffusion might be expected to have a measurable effect even if the deviations from stoichiometry attainable in intrinsic material are considerably below normal detection limits.

In order to test this hypothesis, diffusion of various impurities into gallium arsenide was studied as a function of the ambient arsenic pressure. The p–n junction method was used to obtain penetration data because of its simplicity, although in some cases (particularly sulfur) quantitative results cannot be obtained in this manner. Polished wafers of GaAs, together with a small amount of diffusant and a weighed chip of deoxidized arsenic, were sealed under high vacuum into a quartz ampoule of known volume. The diffusants (except sulfur) were present in the form of either a 3–5 mg chip of metal or an evaporated layer on the back side of the wafer. In the case of sulfur diffusion, a vapor source density of 3 $\mu g/cm^3$ was used to prevent the formation of a separate sulfide phase at the surface.

Temperatures during diffusion were controlled to $\pm 10°C$. The ampoules were allowed to cool in air to about 600°C and were then water quenched at one end to prevent condensation of the vapor on the wafer. Junction depths were measured by angle lapping and staining, and whenever possible the sheet resistance was determined by the four-point probe method. Several crystals of different carrier concentration and orientation were used as substrates; blanks were used to check for conversion and other spurious effects.

The results of several typical experiments are shown in Fig. 1. The diffusants can be divided into three groups: acceptors (zinc and manganese),

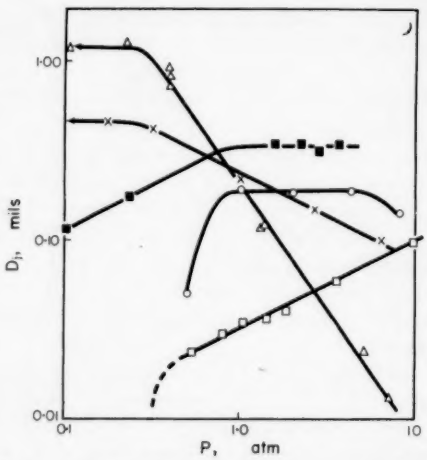

FIG. 1. Junction depth vs. arsenic pressure for various diffusants.

○	Sulfur,	1000°C, t = 45 min.
△	Manganese,	900°C, t = 30 min.
×	Zinc,	800°C, t = 45 min.
□	Tin,	1000°C, t = 60 min.
■	Silicon,	1150°C, t = 90 min.

which are assumed to occupy gallium sites preferentially by virtue of their s^2 configurations; donors (sulfur), which occupy arsenic sites; and amphoteric (Group IV) elements, which may occupy both sites.

Zinc and manganese show pressure-independent behavior at pressures below P_K, which represents the points at which the knee in the curves appears for the various diffusants. Above this pressure, the data can be represented by simple power law plots, which in the case of manganese extend over two orders of magnitude decrease in the junction depth. The decrease in penetration of zinc in the presence of excess

* The work described was performed under the sponsorship of the Electronic Technology Laboratory, Aeronautical Systems Division, Air Force Systems Command, United States Air Force.

arsenic is in qualitative agreement with the radiotracer data of CUNNELL and GOOCH[1]. Above P_K, curves of the junction depth as a function of the square root of time at constant pressure are not linear, implying time-dependent diffusion coefficients. The slopes of the junction-depth–pressure curves decrease with increasing temperature (for all diffusants studied), and are therefore functions of the diffusant, temperature, time, and, very likely, the surface concentration.

The diffusion of sulfur is generally independent of pressure above P_K, and decreases sharply below the knee. A slight decrease in penetration is also observed at high pressures. Sheet resistances could not be measured after sulfur diffusion; this behavior is characteristic of low ($<10^{18}$) concentration n-type material. Junction penetration follows the square root of time law in the pressure independent region. It is therefore reasonable to assume complementary error function penetration, and to calculate an activation energy for diffusion from the variation of junction depth with temperature at constant pressure. Results obtained over the range 900–1075°C at two atmospheres of arsenic pressure give a value of $E_a = 1{\cdot}8 \pm 0{\cdot}8$ eV, which is substantially lower than the value obtained at low pressure by radiotracer techniques.[3]

Of the Group IV elements, the most extensively studied is tin. At 1000°C the junction depth is proportional to the square root of the pressure above P_K, with a sharp cutoff at P_K when bulk tin is used as the diffusion source. A large increase in sheet resistance precedes the cutoff, the apparent surface concentration falling from $3\times10^{19}/\text{cm}^3$ to $3\times10^{18}/\text{cm}^3$ within a few tenths of an atmosphere around P_K. Thermal probe measurements reveal an n-type layer on wafers diffused below P_K. The use of a thin evaporated layer as the diffusion source results in the smoothing of the knee, with a constant surface concentration over the range 0·1–10 atm. At 1150°C, diffusion above one atmosphere appears to be independent of pressure. Similar behavior is observed for silicon, as shown in the figure.

In the case of metallic diffusants, the appearance of the knee results from the reaction between the diffusant and arsenic, which makes the P values used in Fig. 1 too high in the intermediate range, but does not affect the terminal points.

A hypothesis which has been employed with some success in explaining diffusion in compound semiconductors is that of movement along a sublattice.[3,4] Group II elements (Zn and Cd) and Group IV elements (S, Se) are considered to be confined to the gallium and arsenic sublattices respectively. The basic diffusion process is a jump to a second nearest neighbor vacancy. Experimentally, it is observed that the activation energies for Group II elements are lower than those for Group VI, just as the activation energy for gallium is lower than that for arsenic.[3]

The expected effect of arsenic pressure would be straightforward. Any means by which excess vacancies are introduced into the sublattice of the diffusant should increase the diffusion rate, D being directly proportional to the number of such vacancies. Even at equilibrium, however, the effect is small, since it is readily shown that the vacancy concentrations for Schottky disorder (neglecting electronic terms) are given by:

$$[V_{Ga}] = k_1 P_{As4}^{1/4}$$

and

$$[V_{As}] = k_2 P_{As4}^{-1/4}$$

As4 being the predominant vapor species.

The observed effects for zinc and sulfur (and probably manganese) are not compatible with the sublattice mechanism, being both too large and in the wrong direction, and strongly suggest the participation of nearest neighbor vacancies in the diffusion process. Additional evidence comes from the low activation energy for sulfur found here. The previously reported value of 4·04 eV was obtained at reduced pressures.[5] This discrepancy can be attributed to the fact that there is more than one diffusion path available to sulfur, the low energy path predominating at high arsenic pressures.

Acknowledgements—The author wishes to thank N. ALMELEH for providing some of the data published here and for his helpful discussions of the work.

Radio Corporation of America L. J. VIELAND
Semiconductor and Materials Division
Somerville
New Jersey

Vol. 21
1961

References

1. CUNNELL F. A. and GOOCH C. H., *J. Phys. Chem. Solids* **15**, 127 (1960).
2. MCCALDIN J. O. and HARADA R., *J. Appl. Phys.* **31**, 2065 (1960).
3. GOLDSTEIN B., *Phys. Rev.* **121**, 1305 (1961).
4. EISEN F. and BIRCHENALL C., *Acta Met.* **5**, 265 (1957).
5. GOLDSTEIN B., private communication.

Indium antimonide tunnel diodes in high magnetic fields

(*Received* 27 *March* 1961; *revised* 5 *June* 1961)

CALAWA and co-workers[1], and ESAKI and PRICE[2], have observed that the tunnel current is reduced when a magnetic field is applied to an indium antimonide tunnel diode. They interpret this reduction by introducing Landau sub-bands into the theory of tunnelling through a linear potential barrier as developed by KELDYSH[3] and KANE[4]. We have carried the measurements of CALAWA and co-workers to higher magnetic fields and have interpreted the results on a theory of tunnelling through a parabolic potential barrier which contains no disposable parameters. The variation of peak current with magnetic field was measured at 77°K for three diodes with different donor concentrations; the variation of the tunnel current at reverse bias with magnetic field was measured for one diode. We used pulsed magnetic field and oscillographic techniques to make the measurements. The theory has also been used to analyse data on peak current densities at zero magnetic field for a large number of diodes with various doping concentrations.

The diodes were made by alloying discs of pure cadmium (0·010 in. diameter, 0·04 in. thick) on to the (110) faces of dice cut from single crystals of *n*-type indium antimonide. The temperature cycle used involved a peak temperature of approximately 410°C and the dice was above 300°C for about 4 min. The *n*-type crystals were grown from tellurium-doped melts by J. B. MULLIN and O. JONES of this laboratory. A ⟨110⟩ growth-axis was used to avoid the facet effect[5] and to obtain crystals of good cross-sectional uniformity. The carrier concentrations were calculated from the Hall constants measured at 77°K. The principal parameters of the diodes at 77°K in zero magnetic field are given in Table 1.

Table 1. *Diode parameters at* 77°K

Diode	*n*-type carrier concentration (cm^{-3})	Peak current (mA)	Valley current (mA)
A	$1{\cdot}8\times10^{17}$	5·8	2·8
B	$3{\cdot}2\times10^{17}$	154	28
C	$4{\cdot}3\times10^{17}$	207	20

A pulsed magnetic field was obtained by discharging a 4000 μF condenser through an air-cored solenoid with 0·375 in. bore. The *p*–*n* junction was oriented perpendicular to the magnetic field. The current–voltage characteristic of the diode was displayed on an oscilloscope (A); the trace was brightened at the peak of the magnetic field by a 0·5 msec pulse. The magnetic field was measured by observing the search coil output on another oscilloscope (B); the time of observation of the diode sweep was recorded by marking the trace with the same brightening pulse as that applied to oscilloscope A. The peak value of the magnetic field could be varied from 10 kG to 180 kG by varying the initial charge on the condenser.

In calculating the tunnelling probability we use a Cartesian coordinate system *Oxyz* with the *z*-axis normal to the plane of the junction. The *p*-type regrowth layer in our diodes is more heavily doped than the *n*-type starting material. Hence the potential barrier is largely confined to the *n*-type material and is closely approximated by the parabolic form $V(z) = az^2$, where $a = 2\pi N_d e^2/\epsilon_r$; N_d is the density of donor atoms and ϵ_r is the relative dielectric constant. In subsequent calculations we identify N_d with the *n*-type carrier concentration given in Table 1. The tunnelling probability of an electron with total energy E and transverse energy E_t is[6]

$$T(E,E_t) = \exp\left[-2\int_{z_1}^{z_2}|k_z|\,dz\right] \qquad (1)$$

where k_z is the local longitudinal component of the wave vector and z_1 and z_2 are the classical

turning points at which k_z vanishes. For indium antimonide the relation between k_z and the local energy $\epsilon = E - V(z)$ can be approximated by[7]

$$E_t + \frac{\hbar^2}{2m^*}k_z^2 = \epsilon(\epsilon - E_g)/E_g \qquad (2)$$

where m^* is the effective mass at the bottom of the conduction band and E_g is the energy gap. Hence the tunnelling probability for the parabolic barrier is

$$T(E,E_t) = \exp[-\gamma(M + M'E_t/E_g)] \qquad (3)$$

where

$$\gamma = 2E_g(2m^*)^{1/2}/3\hbar a^{1/2},$$

and

$$M = w^{1/2}[(2w-1)E(w^{-1/2}) - 2wK(w^{-1/2})]$$

and

$$M' = 3K(w^{-1/2})/2w^{1/2};$$

we have written $w = E/E_g$. The functions $K(w^{-1/2})$ and $E(w^{-1/2})$ are complete elliptic integrals of the first and second kinds respectively.

In zero magnetic field the transverse energy is unquantized, $E_t = \hbar^2(k_x^2 + k_y^2)/2m^*$, and the net tunnel current per unit area is[6]

$$J(0) = \frac{4\pi em^*}{h^3}\int_{E_g}^{B} dE[f_n(E) - f_p(E)]\int_0^{E_m} dE_t T(E,E_t) \qquad (4)$$

where B is the barrier height, E_m is the smaller of the two quantities $E(E-E_g)/E_g$ and $(E-B)\times(E-B-E_g)/E_g$, and $f_n(E)$ and $f_p(E)$ are the Fermi distribution functions on the two sides of the junction. When a longitudinal magnetic field H is applied the transverse energy is quantized into Landau levels: $E_t = (n+\frac{1}{2})\hbar\omega_c \pm \frac{1}{2}g\beta H$ where $\omega_c = eH/m^*c$ is the cyclotron frequency, g is the effective g-factor, β is the Bohr magneton.[8] The net tunnel current is then obtained by replacing

$$\int_0^{E_m} dE_t T(E,E_t)$$

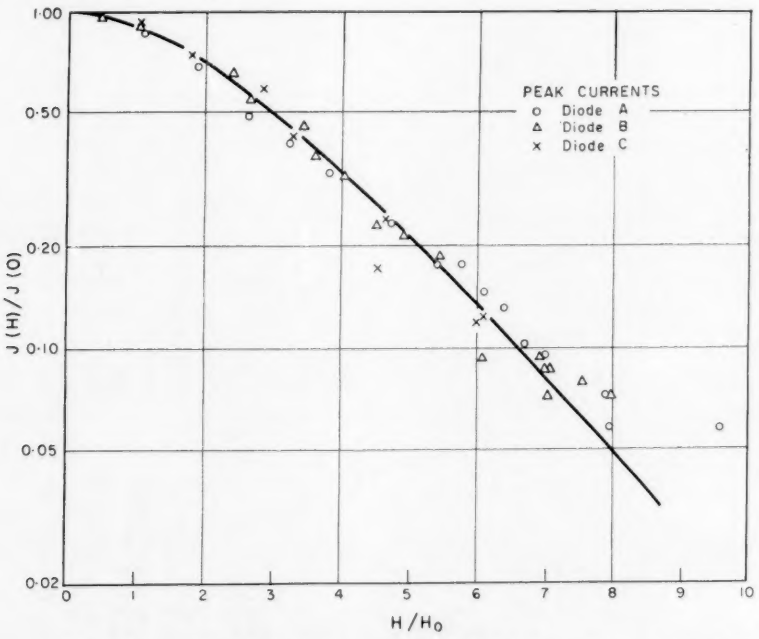

FIG. 1. The ratio of the peak currents with and without applied magnetic field plotted against the reduced magnetic field for three differently doped diodes. The continuous curve shows the variation predicted by equation (5).

Vol. 21
1961

in equation (4) by

$$\frac{\hbar\omega_c}{2}\sum_{E_t=0}^{E_m} T(E,E_t).$$

A simple approximation to the ratio $J(H)/J(0)$ is adequate for the interpretation of the experimental results. Since $T(E,E_t)$ falls off rapidly with increasing E_t, we replace E_m by infinity. Moreover, since M' is a slowly-varying function of E and $\exp(-\gamma M)$ increases with E, we may replace M' in the integrals by its value at the higher of the two Fermi levels. Thus we obtain the simple result

$$\frac{J(H)}{J(0)} = \frac{H}{H_0}\frac{\cosh\left(\frac{1}{2}g\frac{m^*}{m}\cdot\frac{H}{H_0}\right)}{\sinh\left(\frac{H}{H_0}\right)} \qquad (5)$$

where $H_0 = m^*E_g/\gamma\beta mM'$. CALAWA and co-workers[1] and HAERING and ADAMS[13] have derived a similar expression for $J(H)/J(0)$. However, they assume a linear potential barrier and obtain a different expression for H_0. We measured the ratio of the peak currents of diodes A, B and C with and without a longitudinal magnetic field† and the ratio $J(H)/J(0)$ at 33, 66 and 100 mV reverse bias for diode A. The experimental results are presented in Fig. 1 for peak currents and in Fig. 2 for reverse bias. The full lines are theoretical curves obtained from equation (5) by using the values $g = 56$ and $m^*/m = 0{\cdot}013$. The experimental points have been fitted to these curves by calculating in each case the value of H_0 to give a

† Equation (5) gives the ratio of the currents at a fixed voltage. The voltage at which the peak current occurs appeared to change slightly with applied field. The error introduced by ignoring the voltage change and taking the ratio of peak currents was negligible.

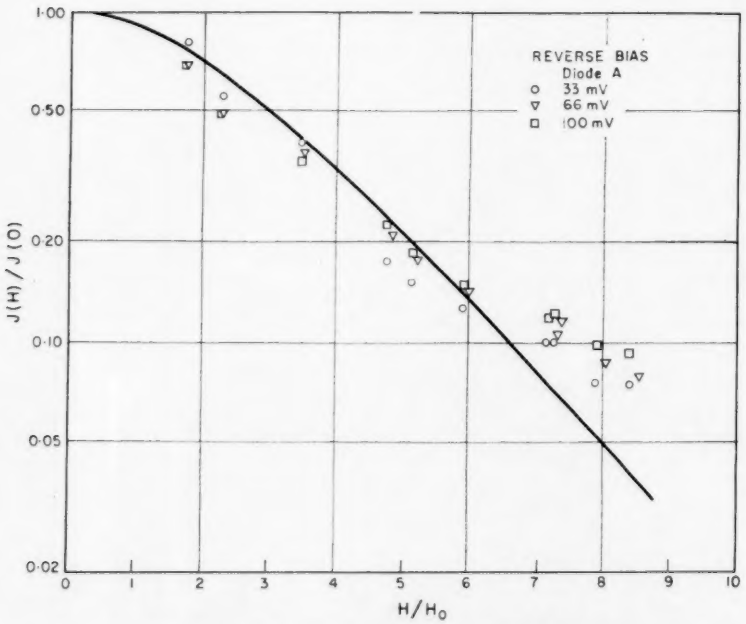

FIG. 2. The ratio of the currents, at a given reverse bias voltage, with and without the applied magnetic field plotted against the reduced magnetic field for the most lightly doped diode. Results are plotted for three values of the reverse bias voltage. The continuous curve shows the variation predicted by equation (5).

Vol. 2
1961

good fit. The values of H_0 thus obtained are given in Table 2. Also given are the theoretical values of H_0 obtained using the values $E_g = 225$ meV, $\epsilon_r = 15{\cdot}9$ and the n-type carrier concentrations set out in Table 1. The corresponding n-type Fermi levels were derived from the empirical relation found by SMITH *et al.*[9]

Table 2. Magnetic field scaling factor

Diode	Experimental H_0 (kOe)	Theoretical H_0 (kOe)
A (peak current)	16	20
B (peak current)	19	29
C (peak current)	23	35
A (33 mV reverse bias)	16	22
A (66 mV reverse bias)	16	24
A (100 mV reverse bias)	16	26

The dependence of the peak current on donor concentration allowed an additional comparison between theory and experiment. The peak current in zero magnetic field is found experimentally to be very sensitive to the donor concentration in the n-type material, while the voltage V_p at the peak is always about 20–30 mV. These observations imply that the p-type regrowth layer is always more heavily doped than the n-type starting material. A simple approximation will suffice to interpret the data. We replace

$$\int_0^{E_m} T(E,E_t)\,dE_t$$

in equation (4) by the value it has at the n-type Fermi level and pull it behind the integration sign. The remaining integral is approximately equal to eV_p. Hence we obtain the relation:

$$J_p(0)M'/N_d^{1/2} = \mu \exp(-\lambda M/N_d^{1/2}) \qquad (6)$$

where $\lambda = 2E_g(\epsilon_r m^*)^{1/2}/3\hbar e\pi^{1/2}$ and $\mu = 4\pi e^2 m^* E_g V_p/h^3\lambda$. By using the numerical values $E_g = 225$ meV, $m^*/m = 0{\cdot}013$, $\epsilon_r = 15{\cdot}9$ and $V_p = 30$ mV we obtain the theoretical estimates of λ and μ: $\lambda = 3{\cdot}67 \times 10^9$ cm$^{-3/2}$, $\mu = 3{\cdot}87 \times 10^{-4}$ A cm$^{-1/2}$.

In Fig. 3 we have plotted the experimental values of $J_p(0)M'/N_d^{1/2}$ against $M/N_d^{1/2}$. Each point represents the average of a number of diodes made on n-type material with a particular donor concentration. The junction areas, required in the calculation of the peak current densities, were measured by microscopic examination. The experimental values of λ and μ obtained by fitting a straight line to the measured points are $\lambda = 4{\cdot}3 \times 10^9$ cm$^{-3/2}$ and $\mu = 0{\cdot}60 \times 10^{-4}$ A cm$^{-1/2}$.

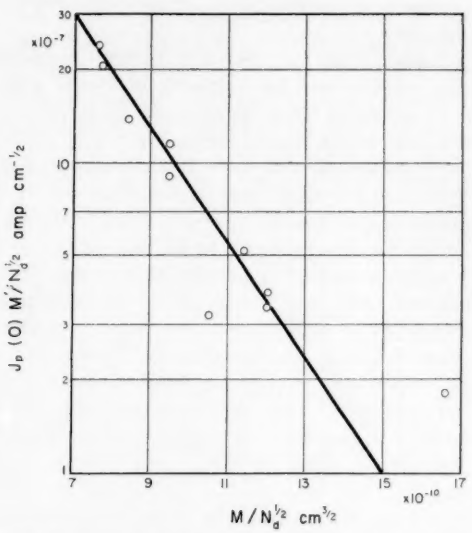

FIG. 3. Experimental data on the variation of the peak current density in zero magnetic field with the donor concentration in the n-type material. Each point represents the average result for a number of diodes in which the n-type material had a particular donor concentration. The straight line has been drawn to fit the experimental results, bearing in mind the approximate statistical weights of the points.

The theory used employs a realistic form of potential barrier, and takes account of the non-parabolic band-shape of indium antimonide. Thus the variation of effective mass with magnetic field[10] is automatically allowed for. It is clear that the theory provides an adequate explanation of the general features of the experimental results for forward bias. At high magnetic fields there is slight tendency for the experimental values of $J(H)/J(0)$ to lie above the theoretical curve.

Moreover, the theoretical values of H_0 are somewhat higher than those needed to fit the experimental results, and the discrepancy becomes more pronounced as the donor concentration increases. For reverse bias the situation is similar; the tendency for the experimental points to lie above the theoretical curve at high magnetic fields is more pronounced in this case, for all three reverse bias voltages. The theory is also in reasonably good agreement with the magnitudes of the peak current densities obtained from various donor concentrations in zero magnetic field; this is a very sensitive test.

An improved agremeent between theory and experiment could be obtained for the magnetic field results if it were assumed that drift and diffusion of the impurities during the fabrication of the diode had spread out the barrier, and if the carrier space charge, both in the bands and in the forbidden energy gap were treated rigorously. The improvement would be at the expense of the zero magnetic field agreement. The diode spreading resistance may account for some of the discrepancies at reverse bias, and we do not attach great weight to the discrepancy between theory and experiment at high magnetic fields in Fig. 2.

In view of the fact that the theory contains no adjustable parameters we conclude that the major assumptions involved concerning barrier shape and the predominance of tunnelling to the light-hole band are substantially correct. The assumption of light-hole band tunnelling alone has been criticized by CHYNOWETH and co-workers[11], but the criticism is not necessarily valid as has been pointed out by HAERING and MILLER[12].

Acknowledgements—We are indebted to J. B. MULLIN and O. JONES for the uniformly doped crystals, to MARGARET A. STARKEY who fabricated and mounted the diodes, to P. H. DAVIES who assisted in setting-up the measuring equipment, and to D. W. BROWN who carried out most of the measurements. We also wish to thank T. P. MCLEAN for helpful discussions. This communication is published by permission of the Controller, H.B.M. Stationery Office.

Royal Radar Establishment P. N. BUTCHER
Ministry of Aviation J. A. HULBERT
Great Malvern, Worcestershire K. F. HULME
England

References

1. CALAWA A. R., REDIKER R. H., LAX B. and MCWHORTER A. L., *Phys. Rev. Letters* **5,** 55 (1960).
2. ESAKI L. and PRICE P. J., private communication.
3. KELDYSH L. V., *Soviet Phys. JETP* **6,** 763 (1958).
4. KANE E. O., *J. Phys. Chem. Solids* **12,** 181 (1959).
5. HULME K. F. and MULLIN J. B., *Phil. Mag.* **4,** 1286 (1959); MULLIN J. B. and HULME K. F., *J. Phys. Chem. Solids* **17,** 1 (1960).
6. KANE E. O., *J. Appl. Phys.* **32,** 83 (1961).
7. KANE E. O., *J. Phys. Chem. Solids* **1,** 249 (1957).
8. BOWERS R. and YAFET Y., *Phys. Rev.* **115,** 1165 (1959).
9. SMITH S. D., MOSS T. S. and TAYLOR K. W., *J. Phys. Chem. Solids* **11,** 131 (1959).
10. LAX B. and MAVROIDES J. G., *Solid State Physics* Vol. XI, p. 261. Academic Press, New York (1960).
11. CHYNOWETH A. G., LOGAN R. A. and WOLFF P. A., *Phys. Rev. Letters* **5,** 548 (1960).
12. HAERING R. R. and MILLER P. B., *Phys. Rev. Letters* **6,** 269 (1961).
13. HAERING R. R. and ADAMS E. N., *J. Phys. Chem. Solids* **19,** 8 (1961).

The absorption edge of zinc telluride

(*Received* 17 *March* 1961)

AMONG the II–VI compounds, crystals with the hexagonal structure, e.g. CdS,[1] ZnO[2] and ZnS[3] have been extensively studied by optical techniques. However, no detailed measurements have been reported for cubic ZnTe. Initial measurements[4] on bulk crystals indicated that the band gap is ZnTe of $\sim 2{\cdot}1$ eV at room temperature. Recently, optical measurements on ZnTe thin films have been reported.[5] In this note, we present some detailed optical measurements of bulk ZnTe crystals near the absorption edge.

ZnTe single crystals of about a centimeter on an edge were grown from the melt by a vertical Bridgman technique. A stoichiometric mixture of the elements was enclosed in an evacuated quartz capsule and slowly lowered through a vertical platinum furnace maintained at $\sim 1250°C$. For transmission measurements, crystals having thicknesses ranging from seven microns to one millimeter were employed. These were polished with a Linde *B* powder using either H_2O or diluted HNO_3 as the lubricating fluid. The cleaved surface of a

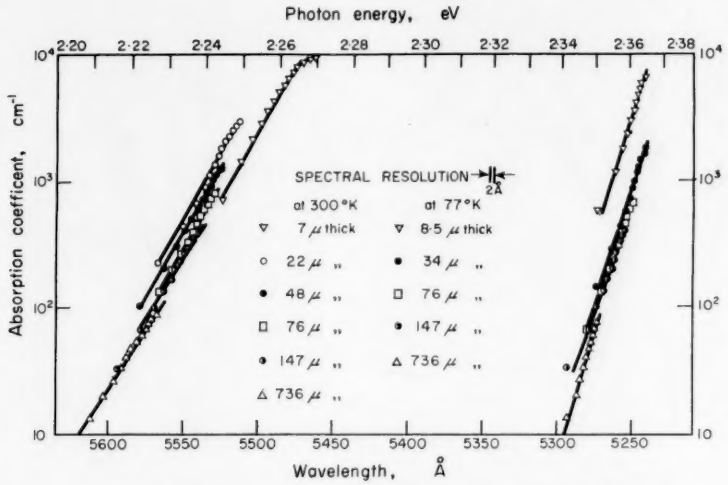

FIG. 1. Absorption spectra of ZnTe crystals at 300°K and 77°K.

crystal several millimeters thick was used for reflectance measurements. Optical measurements were made on a Perkin Elmer Model 112 spectrometer equipped with a Bausch and Lomb grating (7500 Å blaze, 1200 lines/mm). A spectral resolution of about 2 Å (~ 0·001 eV) was employed.

The reflection coefficient was evaluated from measurements of transmission in the transparency region. Values of relative reflectivity in the strong absorption region were directly measured and normalized with respect to the reflection coefficient in the transparency region.

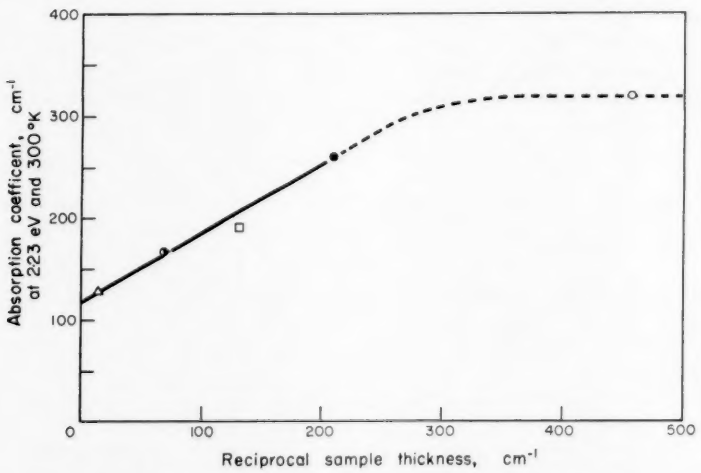

FIG. 2. Absorption coefficient, at 2·23 eV and room temperature, of mechanically polished ZnTe crystals vs. reciprocal of sample thickness.

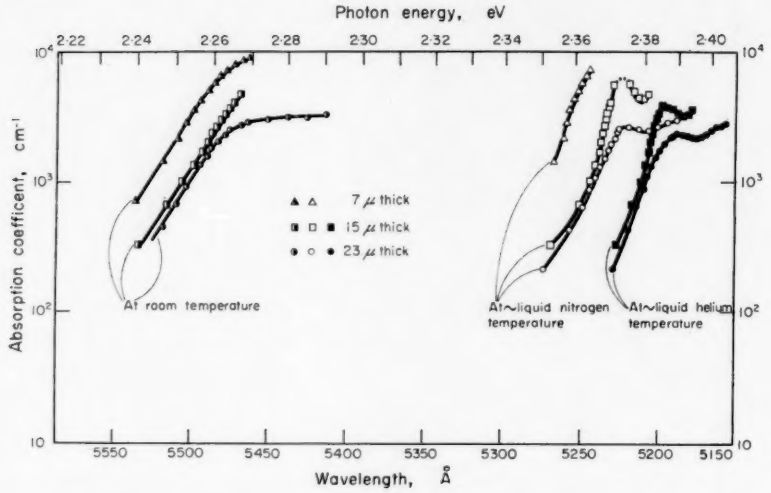
Photon energy, eV
2·22 2·24 2·26 2·28 2·30 2·32 2·34 2·36 2·38 2·40
Absorption coefficent, cm⁻¹
7 μ thick
15 μ thick
23 μ thick
At room temperature
At ~liquid nitrogen temperature
At ~liquid helium temperature
5550 5500 5450 5400 5350 5300 5250 5200 5150
Wavelength, Å

FIG. 3. Absorption spectra of ZnTe crystals showing exciton peak at low temperatures.

Figure 1 shows the measured absorption spectra of ZnTe crystals at 300°K and 77°K. The general pattern of the absorption spectra is similar to that of CdS.[1] At 300°K, the slope of the absorption coefficient is one decade/0·02 eV while at 77°K it is one decade/0·01 eV. The absorption edge shifts about 0·1 eV toward higher photon energy as the sample is cooled from 300°K to 77°K.

Using mechanically polished samples of different thicknesses, a systematic trend in the data was noted. Namely, measured absorption coefficients at a particular energy increase as the thickness of the polished crystal decreases. By assuming a constant depth of damage, s, for similarly polished samples of all thicknesses, d ($d > s$), one can write

$$\alpha d = \alpha_s s + \alpha_b (d - s) \qquad (1)$$

where α_s and α_b are respectively absorption coefficients of the surface damaged region and the bulk undamaged core of the sample and b is the thickness of the undamaged bulk.

Equation (1) can be rewritten as:

$$\alpha = (\alpha_s - \alpha_b)\, s/d + \alpha_b. \qquad (2)$$

A plot of α vs. $1/d$ for mechanically polished samples at room temperature at a fixed photon energy, say at 2·23 eV is shown in Fig. 2. This figure shows that for samples of thicknesses greater than about 50μ, equation (2) holds and the corresponding points fall on a straight line. As the samples are made thinner by polishing, d approaches s and hence α approaches α_s as suggested by the dotted line in Fig. 2. Similar results have been observed in other materials such as ZnO.[2]

The presence of an exciton peak at the absorption edge at low temperatures is shown in Fig. 3.

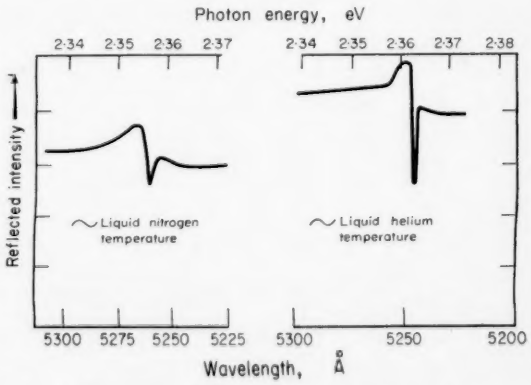

FIG. 4. Reflection spectra of cleaved ZnTe crystal at low temperature.

Vol. 21
1961

The data for this figure were obtained from samples polished using 20–50 volumetric per cent HNO_3 to reduce the mechanical damage. The prominence of the exciton peak is a function of sample treatment. The peak was exhibited most clearly in the thicker acid polished samples. Mechanically polished samples of similar thickness showed no structure at all. Reflection spectra are reproduced in Fig. 4. The locations of the single maximum–minimum structure are about the same as those of the exciton peak observed in absorption at the corresponding temperatures. Unfortunately, the observation of a single exciton peak is insufficient to yield any further quantitative information. However, the present observations indicate that, in common with other II–VI compounds, the steep absorption edge in ZnTe is associated with the onset of an exciton absorption process.

Acknowledgement—We would like to thank E. CRAMER for the polishing of the thin samples.

Semiconductor Materials Department
Hughes Research Laboratories
Newport Beach
California, U.S.A.

E. LOH
R. NEWMAN*

References

1. DUTTON D., *Phys. Rev.* **112,** 785 (1958).
2. THOMAS D. G., *J. Phys. Chem. Solids* **15,** 86 (1960).
3. PIPER W. W., JOHNSON P. D. and MARPLE D. T. F., *J. Phys. Chem. Solids* **8,** 457 (1959).
4. LIND E. L. and BUBE R. H., *Bull. Amer. Phys. Soc.* **1,** 110 (1956).
5. ZHOLKEVICH G. A., *Soviet Physics—Solid State* **2,** 1009 (1960).
6. KLICK C. C., *Phys. Rev.* **89,** 274 (1953).

* Present address: Sperry Rand Research Center, Sudbury, Mass.

NOTICES

Chemical Abstracts

Abstractors are needed by *Chemical Abstracts*. Busy chemists make time for abstracting. They believe that *CA*, their co-operative enterprise, is indispensible. Chemists and chemical engineers find abstracting interesting. It promotes effective reading of new research papers and patents, and gives experience in clear, concise writing. Abstractors who can handle German patents and chemical papers published in Russian are needed especially. However, abstractors for all fields of chemistry and all languages (including English) are sought to take care of the chemical literature that doubled in the last 8·3 years. Assignments of papers for abstracting are adjusted to languages, fields of chemistry, and time of abstractors. To find out more about becoming an abstractor write to:

CHARLES L. BERNIER, *Chemical Abstracts*, The Ohio State University, Columbus 10, Ohio, U.S.A.

International Conference on the Physics of Semiconductors

The Institute and Society on behalf of the International Union of Pure and Applied Physics, and the British National Committee for Physics is arranging an International Conference on the Physics of Semiconductors, which will be held at the University of Exeter from the 16–20 July, 1962. The Conference is planned to follow the previous sequence of Conferences on the Physics of Semiconductors, which were held in Reading in 1950, Amsterdam in 1954, Garmisch in 1956, Rochester in 1958 and Prague in 1960.

Accommodation will be provided in Halls of Residence at the University. Further information regarding the Conference may be obtained from the Administration Assistant, The Institute of Physics and The Physical Society, 47 Belgrave Square, London S.W.1.

First International Conference on Paramagnetic Resonance

The First International Conference on Paramagnetic Resonance will be held at the Hebrew University of Jerusalem, Israel, during July 16th to 20th, 1962. The Conference is sponsored by the International Union of Pure and Applied Physics. Topics to be covered are represented by the preliminary program.

The Organizing Committee is:

A. ABRAGAM, Commissariat à l'Energie Atomique, France
B. BLEANEY, The Clarendon Laboratory, England
G. FEHER, University of California, U.S.A.
C. J. GORTER, Kamerlingh Onnes Laboratorium, Holland
C. KITTEL, University of California, U.S.A.
W. LOW, The Hebrew University of Jerusalem, Israel
M. H. L. PRYCE, University of Bristol, England
J. H. VAN VLECK, Harvard University, U.S.A.

In order to achieve a program of interest and balance, the Organizing Committee will make a careful selection of the papers. An Abstract of about 200 words should reach W. Low, Conference Secretary, The Hebrew University of Jerusalem, Israel, by February 1, 1962.

For further information please contact the Conference Secretary: W. LOW, The Hebrew University of Jerusalem, Israel.

Vol. 21
1961

Preliminary Program

1. Paramagnetic Resonance of Transition Elements
   the iron group — the uranium group
   the rare earth group — the palladium and platinum group
2. Double Resonance ENDOR Experiments
3. Theoretical Advances in Energy Level Calculations
4. Resonance Spectra of Point Defects and Radiation Centers in Single Crystals
5. Spectra of Ion Pairs
6. Relaxation Phenomena and Line Shape
   correlation with paramagnetic relaxation experiments
7. Correlation of Paramagnetic Resonance Spectra with Optical Spectra
8. Advances in Experimental Techniques